



# Challenging fission cross section simulation with long standing macro-microscopic model of nucleus potential energy surface

Pierre Tamagno

## ► To cite this version:

Pierre Tamagno. Challenging fission cross section simulation with long standing macro-microscopic model of nucleus potential energy surface. Atomic Physics [physics.atom-ph]. Université de Bordeaux, 2015. English. NNT : 2015BORD0123 . tel-01316791

**HAL Id: tel-01316791**

**<https://theses.hal.science/tel-01316791>**

Submitted on 17 May 2016

**HAL** is a multi-disciplinary open access archive for the deposit and dissemination of scientific research documents, whether they are published or not. The documents may come from teaching and research institutions in France or abroad, or from public or private research centers.

L'archive ouverte pluridisciplinaire **HAL**, est destinée au dépôt et à la diffusion de documents scientifiques de niveau recherche, publiés ou non, émanant des établissements d'enseignement et de recherche français ou étrangers, des laboratoires publics ou privés.

THÈSE PRÉSENTÉE  
POUR OBTENIR LE GRADE DE  
**DOCTEUR DE**  
**L'UNIVERSITÉ DE BORDEAUX**

ÉCOLE DOCTORALE DES SCIENCES PHYSIQUES ET DE L'INGÉNIEUR  
SPÉCIALITÉ ASTROPHYSIQUE, PLASMAS, NUCLÉAIRE

Par Pierre TAMAGNO

**CHALLENGING FISSION CROSS SECTION SIMULATION  
WITH LONG STANDING MACRO-MICROSCOPIC MODEL  
OF NUCLEUS POTENTIAL ENERGY SURFACE**

Soutenue le 19 Octobre 2015

Membres du jury :

M. TSEKHANOVICH, Igor Dr, Professeur, Université de Bordeaux (CENBG)	Président
Mme GOUTTE, Héroïse Dr, HDR, Chef de Service au CEA-DSM (Saclay)	Rapporteuse
M. KONING, Arjan Dr, Professeur, Physicien à NRG (Petten, Pays-Bas)	Rapporteur
M. MÖLLER, Peter Dr, Physicien au Los Alamos National Laboratory (USA)	Examineur
M. QUENTIN, Philippe Dr, Professeur émérite (CENBG)	Examineur
M. AÏCHE, Mourad Dr, MC, Université de Bordeaux (CENBG)	Directeur de thèse
M. BOULAND, Olivier Dr, HDR, Physicien au CEA-DEN (Cadarache)	Encadrant
M. SEROT, Olivier Dr, HDR, Physicien au CEA-DEN (Cadarache)	Encadrant

---

**Titre :** De la phénoménologie à la microscopie, une nouvelle approche pour l'évaluation des sections efficaces de fission

**Résumé :** Les travaux présentés visent à améliorer les modèles de physique nucléaire utilisés dans l'évaluation des sections efficaces neutroniques de fission. Le résultat de ces travaux donne les clefs pour une percée significative dans ce domaine et a permis d'étendre fortement les capacités du code d'évaluation CONRAD. Les sections partielles étant naturellement corrélées entre-elles pour respecter la valeur de la section totale, ces améliorations bénéficient à l'ensemble des sections partielles. Un cadre solide pour la modélisation des processus concurrent à la fission a dû être établi sur le modèle du code de référence TALYS. Après s'être assuré de la fiabilité et de la cohérence du cadre, les investigations spécifiques concernant la fission ont pu être réalisées. Les perspectives d'applications offertes par les modèles macro-microscopiques FRDM et FRLDM ont été analysées. Ces modèles ont été implémentés et validés sur des données expérimentales et des benchmarks. Afin d'obtenir des temps de calcul compatibles avec les besoins de l'évaluation, des méthodes numériques sophistiquées ont été sélectionnées et une partie des calculs a été portée sur GPU. Ces modèles macro-microscopiques peuvent être utilisés pour construire des surfaces d'énergie potentielle qui sont à leur tour traitées afin d'obtenir des barrières de fission à une dimension, puis des coefficients de transmission fission. Ces derniers sont alors utilisés dans le cadre de modélisation des sections efficaces moyennes du domaine statistique sur la base d'un modèle Hauser-Feshbach. Les résultats de cette approche seront présentés sur le cas du  $^{239}\text{Pu}(n,f)$ .

**Mots clés :** Physique nucléaire, évaluation, modèle macro-microscopique, FRLDM, FRDM, sections efficaces, Hauser-Feshbach, barrière de fission, GPU

---

**Title:** Challenging fission cross section simulation with long standing macro-microscopic model of nucleus potential energy surface

**Abstract:** The work presented here aims to improve models used in the fission cross-section evaluation. The results give insights for a significant breakthrough in this field and yielded large extensions of the evaluation code CONRAD. Partial cross sections are inherently strongly correlated together as of the competition of the related reactions must yield the total cross section. Therefore improving fission cross section benefits to all partial cross sections. A sound framework for the simulation of competitive reactions had to be settled in order to further investigate on the fission reaction; this was implemented using the TALYS reference code as guideline. After ensuring consistency and consistency of the framework, focus was made on fission. Perspective resulting from the use of macroscopic-microscopic models such as the FRDM and FRLDM were analyzed; these models have been implemented and validated on experimental data and benchmarks. To comply with evaluation requirements in terms of computation time, several specific numerical methods have been used and parts of the program were written to run on GPU. These macroscopic-microscopic models yield potential energy surfaces that can be used to extract a one-dimensional fission barrier. This latter can then be used to obtain fission transmission coefficients that can be used in a Hauser-Feshbach model. This method has been finally tested for the calculation of the average fission cross section for  $^{239}\text{Pu}(n,f)$ .

**Keywords:** Nuclear physics, evaluation, macroscopic-microscopic model, FRLDM, FRDM, cross section, Hauser-Feshbach, fission barrier, GPU

---

**Unité de recherche**

Laboratoire d'Études de Physique, CEA/DEN/DER/SPRC/LEPh CEA de Cadarache  
13108 St Paul Lez Durance, France

---

# Remerciements

Je tiens tout d’abord à remercier la personne à l’origine de cette thèse, Oliver Bouland, merci beaucoup pour ton soutien et ta bienveillance durant ces trois années. Merci également à Olivier Serot pour tes conseils pertinents et ta vision globale des thématiques autour de la fission. Merci à Gilles Noguère et Olivier Litaize pour nos discussions enrichissantes sur certains points de physique nucléaire. Pour continuer la litanie des saints, merci à Cyrille De Saint Jean pour m’avoir accueilli dans le labo, pour tes conseils en matière de physique nucléaire, de programmation, et sur les autres aspects de la vie du physicien. Enfin, un immense merci à Pascal Archier, « l’encadrant de l’ombre », pour le temps et l’énergie que tu as passés à m’aider à décortiquer les entrailles de CONRAD et de TALYS.

Merci aux membres du jury et spécialement aux rapporteurs Héloïse Goutte et Arjan Köning. Merci tout particulièrement à Peter Möller pour nos nombreux échanges concernant les modèles macro-microscopiques et pour les commentaires sur le manuscrit.

Merci également à Stéphane Hilaire du CEA/DAM-DIF pour tes judicieux conseils lors de mon séjour à Bruyères le Châtel.

Un grand merci à l’équipe complète du LEPH pour m’avoir accueilli pendant ces trois dernières années, je suis très heureux de continuer l’aventure avec vous !

Je tiens également à rendre hommage aux Oompa Loompas de la science : les doctorants et les stagiaires. Je ne peux pas tous vous remercier individuellement sans ajouter une nouvelle annexe à ce manuscrit déjà bien long, je me limiterai donc à : David Regnier (pour nos travaux sur « l’armure d’iron man »), Simon Ravaux (pour nos discussions à la machine à café), Guillaume Truchet (pour notre long parcours commun et pour tes relectures), Amine Nasri (pour la passion avec laquelle tu as réalisé ton travail de stage). Merci à ceux que je n’ai pas nommé directement pour les bons moments passés ensemble.

Enfin Léonie Berge, un immense merci pour tes relectures approfondies et pour ton soutien.

Merci à toute ma famille pour m’avoir porté et pour avoir fait de moi qui je suis aujourd’hui.



---

---

# Résumé Étendu

## Introduction à l'Évaluation des Sections Efficaces

Les données nucléaires telles que les sections efficaces sont des « ingrédients » d'entrée des calculs de physique des réacteurs. La physique des réacteurs est régie par l'équation du transport qui décrit la population neutronique dans un réacteur. C'est une équation difficile à résoudre du fait de la géométrie des réacteurs (géométrie récursivement imbriquée) et de la grande gamme énergétique à traiter (de 20 MeV à  $10^{-5}$  meV). Jusqu'aux années 90, l'incertitude associée à la résolution de l'équation du transport était supérieure à celle associée aux données nucléaires d'entrée. Depuis, la montée en puissance des ordinateurs a rendu possible un emploi plus routinier de méthodes de résolution plus rigoureuses utilisant la simulation Monte-Carlo. L'incertitude liée aux données nucléaires est aujourd'hui le premier facteur d'incertitude dans les calculs de physique des réacteurs. De plus, le renforcement des normes de sûreté des réacteurs pousse à améliorer les modélisations afin de quantifier plus précisément le processus en jeu et de restaurer si possible les marges d'exploitation.

Le but de ce travail de thèse est de démontrer la faisabilité de l'utilisation de modèles de structure nucléaire avancés dans l'évaluation des sections efficaces de fission. L'évaluation des sections efficaces repose d'une part sur des modèles, d'autre part sur des données expérimentales à partir desquelles les paramètres de modèle sont ajustés. à basse énergie, la précision expérimentale est en général suffisante pour pouvoir obtenir une représentation exacte de la section. Pour les actinides, cette section présente des structures résonnantes comme montré dans la figure 1. à plus hautes énergies, la précision expérimentale ne permet plus de décrire ces structures, une approche statistique moyenne doit être utilisée pour modéliser la section. Le domaine à basse énergie est appelé le domaine des résonances résolues. Au delà de ce domaine, les résonances existent toujours, mais il n'est pas possible d'obtenir des paramètres de résonance pouvant les décrire, c'est le domaine des résonances non résolues. à plus hautes énergies encore, la densité des résonances et leur largeur augmentent, ce qui les amène à se recouvrir mutuellement. Dans ce domaine énergétique, même avec une précision expérimentale infinie, les résonances ne sont plus visibles. Ce domaine est appelé le continuum. Le domaine des résonances non résolues et le continuum sont regroupés sous le nom de domaine statistique.

Plusieurs pistes d'amélioration sont ouvertes afin d'obtenir des évaluations de sections efficaces plus satisfaisantes et sont présentées dans le manuscrit. On retiendra uniquement ici que le processus de fission est le moins bien modélisé et que du fait de la compétition entre les voies de réactions différentes, une amélioration spécifique à la section de fission bénéficierait aux autres sections partielles. En particulier, un des problèmes soulignés dans le manuscrit est que les mesures de sections efficaces de fission montrent des structures qui ne se retrouvent pas dans la section totale, ce qui est révélateur d'un phénomène propre au processus de fission. De plus, on montrera dans le manuscrit que les modèles utilisés à l'heure actuelle dans la modélisation du processus de fission ne peuvent pas permettre

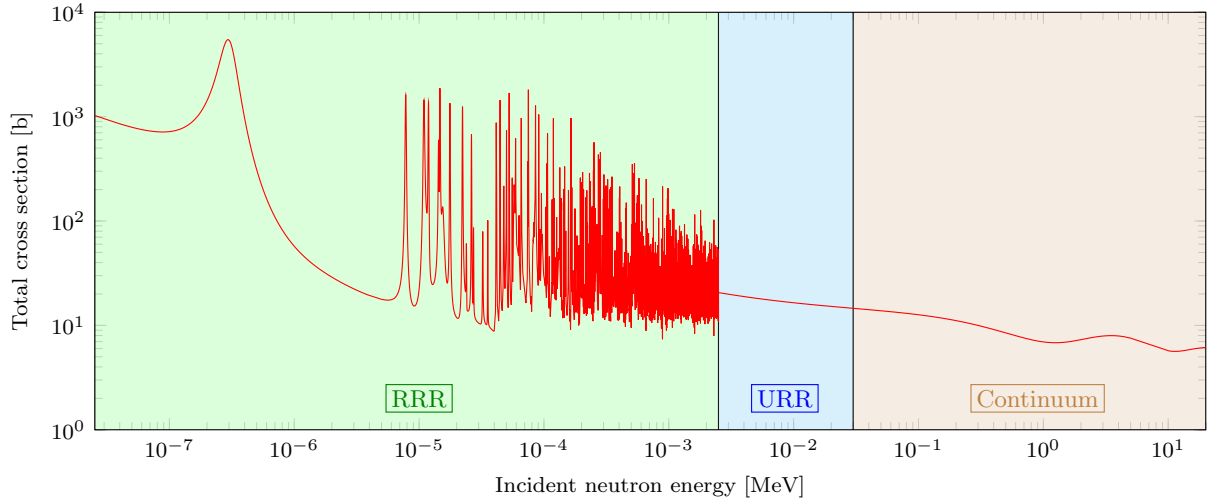


FIGURE 1 – Exemple d'évaluation de la section efficace totale du  $^{239}\text{Pu}$ . Les différents domaines en énergie impliqués dans la modélisation de la section sont illustrés.

de modéliser les structures observées dans les données expérimentales.

## Théorie des Collisions et Sections Efficaces

Avant de rentrer dans le cœur du sujet, il est important de préciser dans quel cadre les sections efficaces sont modélisées. Du fait de la taille des « particules » impliquées en physique des réacteurs (neutrons et noyaux), leurs interactions doivent être modélisées dans le cadre de la mécanique quantique. C'est à dire que là où le neutronicien considère une particule incidente avec une direction donnée frappant un noyau et repartant dans une autre direction (avec une certaine probabilité associée), le physicien nucléaire ou l'évaluateur considère quant à lui une onde plane caractérisant le neutron incident se réfléchissant au contact du noyau cible. L'onde plane incidente peut se décomposer en une superposition d'ondes sphériques. Les ondes réfléchies sont également des ondes sphériques. C'est donc en terme de probabilité de réflexion d'une onde sphérique donnée en une autre que le physicien nucléaire est amené à finalement quantifier ce phénomène via une grandeur appelée la section efficace  $\sigma_{cc'}$  qui connecte l'onde incidente  $c$  en une onde réfléchie  $c'$ . On dit que cette section relie la voie  $c$  à la voie  $c'$ . De façon plus générale, une voie peut également correspondre à une autre paire de particules (neutron+noyau cible ou proton+noyau résiduel dans le cas de la réaction (n,p)). La voie décrit également les moments angulaires des deux particules de la voie, leur état d'excitation intrinsèque, etc. On notera ici que le moment angulaire total  $J$  et la parité totale  $\pi$  sont de « bons nombres quantiques », ce qui signifie qu'ils sont conservés dans le processus. Un phénomène de collision entre deux particules fait intervenir une infinité de processus « parallèles » ayant des  $J^\pi$  associés différents.

Pour finir, plusieurs code de modélisation de réactions nucléaires sont présentés. Ils correspondent à des codes utilisés dans cette étude, principalement le code ECIS [1] permettant d'obtenir une section efficace totale dans le domaine statistique, le code TALYS [2] permettant de décomposer la section efficace totale en sections partielles. Ces deux codes représentent des approches de référence dans le travail de mise à niveau du code CONRAD [3] qui a été le réceptacle des développements réalisés durant le travail de thèse.

---

## Section Efficace de Fission dans le Domaine Résolu

La modélisation des sections efficaces dans le domaine des résonances résolues repose sur la théorie de la matrice- $\mathfrak{R}$  [4, 5]. Cette théorie (et ses nombreuses approximations qui sont utilisées en pratique) permet d'obtenir une paramétrisation de la section efficace dans laquelle la dépendance énergétique est explicite. En d'autres termes, la théorie donne une formule mathématique dépendante de l'énergie et avec des paramètres ( $\gamma_{\lambda c}$ ) ne dépendant pas de l'énergie. La théorie de la matrice- $\mathfrak{R}$  est un formalisme *exact*. En effet, elle ne suppose pas d'hypothèses supplémentaires que celles de la théorie des collisions, ce qui en a fait sa grande force et explique que le formalisme soit toujours utilisé aujourd'hui. Le contrecoup de cette exactitude se paie dans le fait que la théorie ne décrit pas la valeur des paramètres qui interviennent dans l'expression de la section. Ces paramètres doivent donc être obtenus à partir de données expérimentales, ce qui réduit considérablement le caractère prédictif du modèle.

Les modèles basés sur une approche type matrice- $\mathfrak{R}$  ne peuvent donc pas prétendre à la prédictivité pour décrire une section efficace donnée pour un isotope non mesuré. De plus, la qualité des mesures nécessaires est relativement importante afin de pouvoir en extraire des paramètres utilisables. Dans la pratique, cela n'est possible qu'à faible énergie du neutron incident. à plus haute énergie, il est difficile d'obtenir une statistique et une précision satisfaisantes avec les installations expérimentales actuelles. Cependant, si les mesures à basses énergies sont suffisamment précises, les paramètres de résonance qui en sont extraits peuvent servir à obtenir des données statistiques qui peuvent être utilisées dans une modélisation de la valeur moyenne de la section, dans une approche dite « matrice- $\mathfrak{R}$  moyenne ».

Dans la pratique, une approche de type matrice- $\mathfrak{R}$  rigoureuse n'est pas possible pour la réaction de fission. Cela est dû au fait que pour cette réaction de trop nombreuses voies sont ouvertes, correspondantes aux différentes fragmentations, répartitions d'énergies cinétique et de moment angulaire entre les fragments, etc.. Il en est de même pour la réaction de capture radiative pour les actinides à cause du grand nombre de niveaux d'arrivée dans le noyau composé après émission du photon. Dans la pratique, l'approximation Reich-Moore [6] de la matrice- $\mathfrak{R}$  permet, pour les actinides, de considérer une voie moyenne dont les paramètres associés ont une faible dispersion. Le traitement habituel des voies de fission fait que les paramètres non dépendants de l'énergie ( $\gamma_{\lambda f}$ ) absorbent une partie de la dépendance. Ceci est dû au manque de description physique des voies de fission. Il est également observé que l'utilisation de deux « voies » de fission suffit à reproduire les mesures. Cela s'explique par le fait que le passage du noyau composé par *peu* d'états corrèle fortement les  $\gamma_{\lambda f}$ , ce qui réduit le degré de liberté associé.

J. E. Lynn [7] a élaboré une extension du formalisme matrice- $\mathfrak{R}$  à ces « voies de fission ». Dans cette approche, le potentiel d'interaction utilisé dans la théorie de la matrice- $\mathfrak{R}$  est assimilé à la barrière de fission correspondant à un état intrinsèque donné. La description de cette barrière ainsi qu'une mise en équation propre aux voies de fission permet de décrire la dépendance en énergie manquante, qui biaise l'ajustement des  $\gamma_{\lambda f}$  sur les mesures de section efficace de fission. Cette théorie est présentée dans le manuscrit, ainsi qu'une approche pragmatique permettant de retranscrire cette dépendance. Cette méthode est ensuite mise en application sur un cas pratique, le  $^{240}\text{Pu}(n, f)$ . Pour cet isotope, dit « non fissile », les mesures (n,f) présentent des groupes de résonances appelés clusters. Ces clusters sont la manifestation de l'effet de la barrière de fission dans la distribution de la valeur des  $\gamma_{\lambda f}$ . L'analyse de ces clusters de résonances permet d'obtenir des valeurs de  $\gamma_{\lambda f}$  avec un biais de modélisation réduit. Ces valeurs peuvent ainsi être utilisées dans

---

les extrapolations à plus hautes énergies de façon plus fiable.

## Etat de l'Art dans le Domaine Statistique

L'impact de la barrière de fission ne se retrouve pas seulement dans le domaine des résonances résolues. à plus hautes énergies, dans le domaine statistique, des fluctuations dans les sections efficaces moyennes peuvent être attribuées à la barrière de fission. Du fait que les sections partielles sont en réalité définies comme une fraction de la section totale, celles-ci sont donc naturellement corrélées ; leur somme doit redonner la valeur de la section totale qui provient d'une modélisation séparée.

Deux modèles sont utilisés pour la modélisation de la section efficace totale, le modèle dit « matrice- $\mathfrak{R}$  moyenne » et le modèle optique. C'est l'utilisation de ces deux modèles qui amène à séparer le domaine statistique en deux sous-domaines, le modèle des résonances non résolues (URR) et le domaine du continuum.

Ces deux modèles permettent de décrire la probabilité qu'un neutron de pénétrer à l'intérieur du noyau cible et de former un noyau composé. L'hypothèse du noyau composé permet de dire que cette probabilité de former le noyau composé à partir d'un neutron est reliée à la probabilité d'émettre un neutron à partir de ce noyau composé. Pour quantifier ces phénomènes, les coefficients de transmission  $T_c$  sont introduits. Ils permettent également dans le formalisme Hauser-Feshbach [8] de décrire les probabilités de décroissance suivant les différentes voies à partir d'un noyau composé. Dans une forme simplifiée, le formalisme Hauser-Feshbach donne la probabilité  $P_{\text{CN} \rightarrow c}$  de décroître, à partir du noyau composé, dans la voie  $c$  comme

$$P_{\text{CN} \rightarrow c} = \frac{T_c}{\sum_{c'} T_{c'}}.$$

Dans cette image, la probabilité de former le noyau composé est décorrélée de la probabilité de décroître dans la voie  $c$ . Dans la pratique, un facteur de correction est appliqué pour tenir compte de la corrélation entre la voie d'entrée et la voie de sortie. Ce terme appelé facteur de correction de fluctuation des largeurs n'est pas davantage développé dans le manuscrit mais reste inclus dans les calculs. Pour pouvoir calculer une section efficace partielle, il faut donc un modèle donnant la section totale, un modèle Hauser-Feshbach et un modèle donnant les coefficients de transmission pour toutes les autres voies que celles d'entrées (les coefficients de transmission liés aux voies d'entrées sont donnés par le modèle donnant la section totale). Il est donc nécessaire, même pour modéliser une section efficace de fission seule, de disposer de modèles décrivant les autres processus de décroissance comme par exemple la décroissance radiative.

Avant le début de cette thèse, la modélisation haute énergie du code CONRAD, issue d'un travail préparatoire, était assez rudimentaire. En effet un moteur Hauser-Feshbach préexistait ainsi que certains modèles rudimentaires permettant le calcul de sections partielles limitées. Dans ce cadre, seul le modèle matrice- $\mathfrak{R}$  moyenne pouvait être utilisé. Une refonte complète de cette partie du code a donc été effectuée afin d'être plus générique dans les modèles utilisables pour les différentes voies.

Concernant le traitement de la voie d'entrée, le modèle matrice- $\mathfrak{R}$  moyenne a été préservé (afin d'assurer l'isocapacité du code), mais a été modifié afin de permettre de s'articuler de façon générique au reste du code. Un couplage avec le code ECIS (modèle optique utilisant le formalisme des voies couplées décrit en annexe du manuscrit) a été réalisé afin de pouvoir traiter un domaine en énergie plus grand. En effet, il a été dit plus haut que le modèle matrice- $\mathfrak{R}$  moyenne utilise des données issues de l'analyse de

domaine résolu, or dans ce domaine, seules quelques voies jouent un rôle significatif. à plus hautes énergies, le poids « s'équilibre » entre les différentes voies et leur nombre augmente très rapidement. Il est donc impossible d'utiliser le modèle matrice- $\mathfrak{R}$  moyenne à hautes énergies car trop de paramètres doivent être ajustés sur des mesures. à hautes énergies des modèles optiques sont utilisés de façon à limiter le nombre de paramètres phénoménologiques à ajuster *in fine* sur des mesures. Ce type de modèle réussit très bien à reproduire les sections efficaces totales. Afin de maîtriser complètement la chaîne de modélisation des sections efficaces partielles, un modèle optique par voies couplées a également été implémenté de façon à pouvoir se passer à terme du code ECIS utilisé depuis plus de 50 ans et dont la maintenance est difficile à assurer. La nouvelle implémentation pourra également faciliter l'arrivée de nouveaux modèles optiques, par exemple de type rotor moue. L'implémentation du nouveau modèle optique et le couplage au code ECIS ont été testés et ont donné des résultats satisfaisants permettant de passer à la modélisation des autres réactions. Pour effectuer cette vérification, deux isotopes ont été testés : le  $^{56}\text{Fe}$  et le  $^{157}\text{Gd}$ . Le  $^{56}\text{Fe}$  permet de tester un potentiel sphérique alors que le  $^{157}\text{Gd}$ , déformé dans son état fondamental, requiert l'utilisation d'un potentiel de type rotor rigide.

Le plus naturel est de commencer par traiter le processus de capture radiative. Ce processus n'est pas un processus à seuil, il peut se produire à n'importe quelle énergie d'excitation du noyau composé. Il rentre donc en jeu même à basse énergie. Le photon émis par décroissance fait « retomber » le noyau composé dans un état de moindre énergie et de spin-parité différent. De nombreux états d'arrivée sont disponibles, tout spécialement pour les noyaux lourds. Ainsi, de nombreux coefficients de transmission doivent être calculés pour chacun de ces états. En pratique, seule une partie des états de basse énergie est connue. Pour traiter les autres états, une densité de niveau phénoménologique est utilisée. Le code CONRAD partage avec un autre code (le code FIFRELIN) une bibliothèque de modèles de physique nucléaire dans laquelle des modèles de densité de niveau  $\rho$  sont disponibles. Ces modèles ont donc été raccordés au code CONRAD afin de pouvoir traiter ce « continuum » de niveaux. Le modèle utilisé dans ce travail est le modèle phénoménologique de Gilbert-Cameron [9]. La description des niveaux n'est pas suffisante pour décrire le processus de décroissance radiative. Pour décrire la probabilité de décroissance entre deux niveaux séparés d'une énergie  $\epsilon_\gamma$ , un modèle phénoménologique dit de fonction force gamma est utilisé. La bibliothèque de modèles de physique nucléaire contient également des modèles de fonction force gamma qui ont été couplés au code CONRAD. Ces modèles sont cohérents avec ceux de la base RIPL-3 [10]. Au final, le coefficient de transmission gamma est donné par la formule

$$T_\gamma^{J^\pi} = \sum_{X \in \{E, M\}} \sum_{\ell} \left[ \sum_{i=1}^N T_{X\ell}(\epsilon_\gamma(i)) f(J_i, \pi_i, J, \pi, X, \ell) + \sum_{J' \pi'} \int_{E_{\text{cont}}}^{E^*} d\epsilon_\gamma \rho(E^* - \epsilon_\gamma, J', \pi') T_{X\ell}(\epsilon_\gamma) f(J', \pi', J, \pi, X, \ell) \right].$$

Dans cette formule, la fonction  $f$  sert à sélectionner les transitions permettant de conserver le moment angulaire et la parité. Les coefficients de transmission liée à l'émission de neutron sont déjà connus soit via le modèle de matrice- $\mathfrak{R}$  moyenne soit via le modèle optique. Il est donc possible de calculer la section efficace de capture radiative en utilisant la formule d'Hauser-Feshbach

$$\sigma_{n,\gamma} \propto \frac{T_n T_\gamma}{T_n + T_\gamma}$$

L'implémentation de ce modèle a été vérifiée avec le code TALYS. Pour effectuer cette vérification les deux isotopes  $^{56}\text{Fe}$  et  $^{157}\text{Gd}$  ont été réutilisés. Le code CONRAD et le code TALYS présentent des écarts inférieurs 0.05%.

Le même type de mise à niveau du code a été réalisé pour la réaction inélastique, toujours en utilisant le code TALYS comme référence. à la différence de la réaction de capture, une partie dite directe doit être ajoutée. Cette partie directe peut provenir soit du calcul par voies coupées pour les niveaux inélastiques, considérés dans le calcul du modèle optique, soit d'un calcul séparé de type DWBA. Les résultats avec le code TALYS ont été encore une fois satisfaisants. Cependant, à plus hautes énergies, l'émission d'un gamma suivi de l'émission d'un neutron devient de plus en plus probable. Ce type de réaction n'est pas prévu dans le code CONRAD, et son traitement a dû être désactivé dans le code TALYS afin de faire des comparaisons pertinentes. Malgré tout, cela ne doit pas poser de problème pour le reste de cette étude car, dans le domaine énergétique traité, cette contribution reste marginale. Le cadre présenté jusqu'à présent permet maintenant de traiter spécifiquement la réaction de fission. Afin de réaliser des comparaisons pertinentes et de porter le code CONRAD au niveau de l'état de l'art de la modélisation des sections efficaces fission, le traitement standard de la fission utilisant un modèle de type Hill-Wheeler [11] avec deux barrières non corrélées a été implémenté. Le modèle Hill-Wheeler repose sur la description des barrières de fission comme étant de simples paraboles inversées. De plus, dans la modélisation usuelle, les deux barrières non corrélées ne sont pas reliées par un puits intermédiaire. Or ce puits intermédiaire est responsable des structures observées sur les sections efficaces de fission. L'obtention et l'utilisation d'un potentiel continu seront le sujet des deux prochains chapitres.

## Les Modèles Macro Microscopiques

En physique nucléaire, les barrières de fission sont obtenues en étudiant l'évolution de l'énergie du noyau à mesure que celui-ci se déforme. La description de cette énergie en fonction des paramètres de déformation collectifs est appelée surface d'énergie potentielle. Plusieurs approches existent pour obtenir de telles surfaces, les méthodes purement microscopiques, bien qu'intellectuellement plus satisfaisantes, amènent à des durées de calcul rédhibitoires pour l'évaluation. La méthode concurrente, appelée macro microscopique, combine l'approche historique de type goutte liquide à une modélisation simplifiée des fonctions d'onde individuelles de chacun des nucléons. Le modèle retenu pour cette étude est le modèle Finite-Range Liquid-Drop-Model de Peter Möller [12]. Dans cette approche, la forme de noyau est imposée à l'aide d'une fonction géométrique dépendant des paramètres de déformation collectifs. Un historique est présenté retraçant les différentes améliorations successives apportées au modèle macroscopique de type goutte liquide, dont la formulation originale de type Bethe-Weizsäcker [13, 14] donnée par

$$B(Z, N) = a_V A - a_S A^{2/3} - a_C \frac{Z^2}{A^{1/3}} - a_A \frac{(N - Z)^2}{A} - \delta(Z, N).$$

Cette modélisation a notamment été améliorée par l'apport successif de termes correctifs décrivant la diffusivité de la surface du noyau, la taille finie des protons, etc. Cette vision macroscopique du noyau présente certains défauts. Notamment dans cette description, tous les noyaux ont une forme sphérique dans leur état fondamental. De plus, la forme de la barrière de fission obtenue ne présente qu'un seul pic. Pour finir, il faut noter que cette formulation ne permet pas de coller aux masses expérimentales pour certains noyaux. En effet, pour des noyaux ayant un nombre de protons ou de neutrons proche



des nombres magiques 2, 8, 20, 28, 50, 82 et 126, des écarts significatifs avec le modèle macroscopique sont observés. Ces écarts sont dus au fait que les nucléons du noyau ne sont pas répartis de façon homogène et ont un comportement régi par la mécanique quantique.

Le modèle macro microscopique devint populaire à partir des travaux de Strutinsky [15] qui fournit une méthode pour calculer une correction de couche à partir des énergies simples particuliers nucléons. Ces énergies sont obtenues par la résolution de l'équation de Schrödinger pour des particules indépendantes

$$\hat{H}\psi_\nu = (\hat{T} + \hat{V})\psi_\nu = \epsilon_\nu\psi_\nu.$$

Dans le travail présenté, seules des formes à symétrie axiale seront étudiées. La résolution de cette équation repose sur la donnée du potentiel moyen ressenti par les nucléons. Dans l'approche utilisée dans le modèle macro microscopique, ce potentiel est donné par un modèle de Yukawa calqué sur la forme du noyau. à ce potentiel nucléaire moyen est ajouté un second potentiel scalaire tenir compte, pour les protons, de l'interaction coulombienne. De plus, afin d'obtenir un potentiel réaliste, un potentiel de couplage spin orbite est aussi introduit. La résolution de l'équation est donc réalisée séparément pour les protons et neutrons, et ce pour chaque forme du noyau. Un modèle microscopique à particules indépendantes a donc dû être implémenté dans le code CONRAD. Dans le cas d'un noyau sphérique, les nombres magiques sont retrouvés. D'autres vérifications sont également effectuées, portant notamment sur la valeur des énergies simple particule obtenues lorsque le potentiel utilisé est analytique.

La méthode utilisée pour obtenir la correction de couche à partir des énergies simple particule est présentée. En réalité, deux types de correction sont calculés. Une première correction caractérise l'effet de la quantification des énergies des nucléons dans le noyau. Une deuxième correction caractérise l'effet des énergies discrètes par rapport à l'énergie continue sur l'énergie d'appariement des nucléons. Le calcul de ces deux types de correction a été vérifié sur un benchmark. Une dernière correction doit être appliquée à la surface d'énergie potentielle afin de pouvoir la comparer à une donnée expérimentale. Cette correction s'appelle l'énergie vibrationnelle de point zéro. Elle correspond au fait, que lorsque le noyau se trouve dans un puits de potentiel de la surface, il ne peut se trouver « au fond du puits », mais à une énergie légèrement au dessus. Ce phénomène est courant en mécanique quantique : une particule liée dans un puits harmonique se trouve dans le premier état vibrationnel accessible. Il en est de même pour le noyau dans le puits de la surface de potentiel. Afin de pouvoir comparer l'énergie potentiel du noyau avec l'énergie de liaison expérimentale, cette énergie de vibration doit être ajoutée. L'implémentation modèle a donc pu être vérifiée sur des données publiées [12] et sur les masses expérimentales. Pour obtenir une analyse plus fine des différences entre l'implémentation originale du modèle et celle réalisée pour le travail de thèse, un deuxième modèle du même type (le Finite-Range Droplet Model [12]) a été implémenté. Ce modèle diffère du premier seulement par sa composante macroscopique. Ceci a permis d'identifier partiellement l'origine des différences vis-à-vis de l'implémentation originale. En conclusion, les écarts observés avec les données publiées permettent d'utiliser avec confiance le programme pour l'étude des surfaces d'énergie potentielle afin d'en extraire une barrière de potentiel à une dimension.

## Obtention d'une Barrière de Fission à une Dimension

La surface d'énergie potentielle obtenue à l'aide d'un modèle macro microscopique ne peut pas être utilisée directement dans un calcul de section efficace type Hauser-Feshbach. Un



coefficient de transmission fission doit en être extrait. Il serait possible d'utiliser pleinement tous les degrés de liberté décrits par la surface en utilisant par exemple des formalismes sophistiqués tels que « time-dependent generator coordinate method ». Cependant, de telles méthodes nécessitent un temps de développement et de calcul qui n'est pas compatible avec la présente étude. La surface de potentiel est multidimensionnelle. Des méthodes plus simples à mettre en place permettent d'obtenir un coefficient de transmission à partir d'une « surface » à une dimension (une barrière de fission), et ce, quelle que soit la forme de cette surface. Il a donc été choisi de réduire la surface multidimensionnelle à un chemin 1D. Deux types de méthodes ont été étudiés, la méthode dite de « moindre énergie », et la méthode de moindre action.

La méthode de moindre énergie se comprend intuitivement en imaginant une surface 2D correspondant par exemple à un profil topologique d'une région géographique montagneuse. En étudiant l'écoulement de l'eau sur cette surface, on obtient une idée d'un chemin 1D « optimal ». La généralisation de ce problème à  $N$  dimensions est plus complexe, car si les minima locaux sont faciles à identifier, les points selles les connectant, ainsi que le chemin complet entre ces différents points particuliers ne sont pas aisés à déterminer pour des dimensions supérieures. L'algorithme élaboré afin de déterminer ce parcours est présenté dans le manuscrit. Il s'appuie notamment sur la méthode d'immersion [16] pour déterminer les points selles connectant chaque couple de minima locaux. Le point faible de cette méthode se trouve dans la définition de « l'abscisse de fission ». En effet cette méthode donne la suite de formes (et les énergies de déformation associées) que prend le noyau durant le processus de fission. Cependant la notion de distance entre deux formes n'est pas naturelle. Un ersatz de solution a été choisi en utilisant une distance « de Pythagore » entre deux formes en utilisant les valeurs des paramètres de forme. Le cas du  $^{240}\text{Pu}$  (fissionnant) a été étudié, et les hauteurs de barrière obtenues sont cohérentes avec celles trouvées dans la littérature.

La deuxième méthode étudiée est la méthode de moindre action. Cette méthode a l'avantage de naturellement donner une abscisse de fission. Cependant cette méthode requiert un paramètre supplémentaire par rapport à la méthode de moindre énergie : le tenseur d'inertie. Ce tenseur d'inertie  $B$  caractérise l'inertie qu'a le noyau à se déformer dans certaines « directions ». En réalité, ces directions sont les paramètres collectifs de forme du noyau. Le parcours de moindre action est ensuite défini comme étant le parcours  $L$  qui minimise l'intégrale d'action  $S$  définie par

$$S = \int_L ds \sqrt{\sum_{ij} B_{ij}(\vec{q}) \frac{dq_i}{ds} \frac{dq_j}{ds} [V(\vec{q}) - V(\vec{q}^{\text{GS}})]}.$$

Deux modèles ont été étudiés pour obtenir le tenseur d'inertie, le model Werner-Wheeler [17] et le modèle de cranking [18, 19].

Le modèle de Werner-Wheeler modélise le noyau comme un liquide incompressible et irrotationnel (de façon cohérente avec l'approche macroscopique de l'énergie de déformation du noyau). Cette méthode présente l'avantage de donner une solution rapide car elle ne nécessite que la connaissance du volume, de la masse et de la forme du noyau. Cependant, ce modèle n'a pas été utilisé plus loin dans l'étude du fait des résultats non satisfaisants donnés par une modélisation aussi simple du noyau. L'insuffisance du modèle est montrée lors du passage à un calcul de chemin explorant l'asymétrie de masse. En effet, l'ordre du tenseur (et le nombre de degrés de déformation collectifs) est donné par le nombre de paramètres utilisés dans la description de la forme du noyau. Dans l'étude, la paramétrisation de Brack [20] a été utilisée. Cette paramétrisation permet de jouer sur l'élongation du noyau, la « taille du col » et optionnellement l'asymétrie de masse. On

étudie donc des surfaces d'énergie potentielle à deux ou trois dimensions. Dans tous les cas les valeurs propres du tenseur d'inertie doivent toujours être positives. Or, dans le cas de la surface à trois dimensions, cela n'est plus le cas. C'est la raison pour laquelle ce modèle n'a pas été utilisé plus loin dans l'étude.

Un deuxième modèle a été étudié pour obtenir le tenseur d'inertie : le modèle de cranking. Dans ce modèle, les fonctions d'onde simple particule du modèle microscopique  $\psi_\nu$  sont réutilisées, de même que les énergies quasi-particule  $E_\nu$  obtenues à partir du modèle de correction d'appariement. Le tenseur d'inertie s'obtient alors par

$$B_{ij}^{\text{cr}}(\vec{q}) = 2\hbar^2 \sum_{\mu\nu} \frac{\left\langle \nu \left| \frac{\partial \hat{H}}{\partial q_i} \right| \mu \right\rangle \left\langle \mu \left| \frac{\partial \hat{H}}{\partial q_j} \right| \nu \right\rangle}{(E_\nu + E_\mu)^3} (u_\nu v_\mu + v_\nu u_\mu)^2 + P_{ij}.$$

Contrairement au modèle Werner-Wheeler, une solution analytique a été développée de façon à vérifier l'implémentation du modèle.

Une fois le tenseur d'inertie connu, l'intégrale d'action est minimisée à l'aide d'une méthode de Ritz. L'avantage de la méthode de moindre action par rapport à la méthode de moindre énergie est qu'en plus de donner une définition plus rigoureuse de l'abscisse de fission, elle donne également un paramètre d'inertie dépendant de l'abscisse de fission (appelée déformation après réduction à une dimension). Dans le cas du chemin de moindre énergie, ce paramètre est choisi constant et indépendant de la déformation. Ce paramètre a un effet significatif sur le calcul des coefficients de transmission. Malheureusement, l'utilisation du modèle de cranking dans le cas 3D mène à un parcours ayant des hauteurs de barrière peu réalistes. Une façon d'obtenir des hauteurs de barrière plus réalistes est de sélectionner parmi les chemins de moindre action étudiés, celui correspondant à la barrière la plus basse. Cette méthode arbitraire est appelée LA- $V_{\min}$ . Cela est bien sûr peu satisfaisant mais permettra dans le reste de l'étude de montrer l'impact de la dépendance de l'inertie en fonction la déformation.

Trois modèles sont donc testés pour l'obtention d'une barrière à une dimension : la méthode de moindre énergie avec paramètre d'inertie constant, la méthode LA- $V_{\min}$  avec un paramètre constant et avec un paramètre dépendant de la déformation. Une fois ces barrières connues, il a fallu mettre en place une méthode pour calculer un coefficient de transmission à partir d'une barrière de forme quelconque. Dans le cas d'un paramètre d'inertie constant, la méthode de Numerov [21] peut être appliquée. Dans le cas d'un paramètre d'inertie dépendant de la déformation, une méthode de Runge-Kutta a été utilisée. Cela a notamment permis de montrer l'effet spectaculaire de la dépendance du paramètre d'inertie sur le coefficient de transmission (et *in fine* sur la section efficace). Ce phénomène est d'autant plus marqué que le paramètre d'inertie est complètement négligé dans les approches « traditionnelles » type Hill-Wheeler ou Cramer-Nix [22]. Non seulement, dans ces approches le paramètre d'inertie est constant, mais sa valeur n'a pas d'effet sur le coefficient de transmission final.

Pour obtenir des coefficients de transmission fission utilisables dans un calcul de section efficace, il est nécessaire de traiter les états de transition. Ces états de transition sont reliés au fait qu'un noyau se déformant peut se trouver dans l'état qui minimise l'énergie intrinsèque, ou alors dans le premier état excité, ou le deuxième, etc. Ces états excités sont obtenus en réutilisant les énergies simple particules du calcul microscopique et en les combinant avec des états vibrationnels harmoniques afin d'obtenir des têtes de bandes rotationnelles. Cette opération est réalisée en utilisant une routine issue du code AVXSf [23, 24]. Les têtes de bandes rotationnelles obtenues sont alors déroulées en utilisant un moment d'inertie, calculé lui aussi à l'aide du modèle de cranking. Dans l'étude,

---

l'hypothèse adiabatique est faite et le premier état excité reste le premier état excité, peu importe l'évolution du niveau simple particule correspondant. Pour finir, la section efficace de fission  $^{239}\text{Pu}(n,f)$  est obtenue en réinjectant les coefficients de transmission dans un calcul de section efficace moyenne (de type Hauser-Feschbach). Les résultats sont présentés et commentés : un écart d'environ 30% par rapport aux données évaluées a pu être obtenu, et ce *sans ajustement*.

## Conclusions et Perspectives

Ce travail de thèse a eu pour but de démontrer la possibilité de fonder la modélisation de la section efficace de fission à partir d'un modèle moins phénoménologique que dans les pratiques actuelles. Ce travail ne s'est pas focalisé sur un seul des domaines en énergie impliqué dans l'évaluation des sections efficaces pour la neutronique mais sur tous (domaine des résonances résolues et domaines statistiques). Dans le domaine des résonances résolues, il a été montré qu'il était possible de donner davantage de sens physique aux paramètres de résonances associés à la réaction de fission. Dans le domaine statistique, un modèle de structure nucléaire a été implémenté de façon à fournir des données qui ne pouvaient jusqu'à présent qu'être intuitées, puis ajustées sur des mesures. Ce travail a de plus permis de montrer l'importance d'une grandeur complètement ignorée dans les méthodes actuelles : le paramètre d'inertie. Dans une approche pragmatique de moindre énergie, il a été possible de montrer que la méthode intégrée d'utilisation de la surface d'énergie potentielle macro microscopique et l'utilisation d'une barrière de fission *continue* permettent de retrouver l'ordre de grandeur de la section expérimentale. De plus, il est montré que moyennant un ajustement raisonnable des paramètres, l'accord avec les données expérimentales peut être accru.

# Contents

<b>1</b>	<b>Introduction</b>	<b>1</b>
1.1	Objectives of present PhD Work . . . . .	2
1.2	General Context of Nuclear Data Evaluation . . . . .	3
1.3	Evaluation Methods and Status of Evaluated Cross Sections . . . . .	7
1.3.1	Consistency of Evaluated Nuclear Data . . . . .	7
1.3.2	Consistency of Nuclear Data Modeling . . . . .	8
1.3.3	Variance-Covariance Data . . . . .	10
1.3.4	Predictability and Reproduction of Experimental Data . . . . .	11
<b>2</b>	<b>Collision Theory, a Background to Cross-Section Evaluation</b>	<b>15</b>
2.1	Theoretical Framework . . . . .	16
2.1.1	Channels and Channel Wave Functions . . . . .	16
2.1.2	Normalization of Wave Functions . . . . .	19
2.1.3	Wave Functions and Cross Sections . . . . .	20
2.2	Models and Codes Overview . . . . .	22
<b>3</b>	<b>RRR-Related Fission Model Improvements</b>	<b>25</b>
3.1	General Theory and Practical Aspects . . . . .	26
3.1.1	$\Re$ -Matrix Theory . . . . .	26
3.1.2	Single- and Multi-Level Breit-Wigner Formalism . . . . .	30
3.1.3	Reich-Moore . . . . .	32
3.2	Lynn Extension to Fission Channels . . . . .	33
3.2.1	Double-Humped Barrier Textbook Example . . . . .	34
3.2.2	Penetration Factor Modeling . . . . .	37
3.3	Sub-Threshold Analysis of $^{240}\text{Pu}(\text{n},\text{f})$ . . . . .	38
<b>4</b>	<b>Upgrading the CONRAD Code to the State of the Art of Evaluation Models in the Statistical Range</b>	<b>43</b>
4.1	Hauser-Feshbach Framework . . . . .	44
4.2	Unresolved Resonance Range – Average $\Re$ -Matrix . . . . .	46
4.3	Continuum Range – Optical Model . . . . .	48
4.4	Capture Reaction and Level Density Models . . . . .	50
4.4.1	Level Density Models . . . . .	52
4.4.2	Gamma Strength Functions . . . . .	54
4.4.3	Verification on Capture and Elastic Cross Sections . . . . .	54
4.5	Inelastic Scattering . . . . .	55
4.6	Fission Reaction . . . . .	58
4.6.1	Hill-Wheeler Approach . . . . .	58
4.6.2	Cramer-Nix Approach . . . . .	59
4.6.3	Current Pragmatical Approach for Fission . . . . .	62

4.6.3.1	Uncorrelated Hill-Wheeler Humps . . . . .	62
4.6.3.2	Transition States . . . . .	65
4.6.3.3	Ersatz Solution for Intermediate-Well Fluctuation . . . . .	65
4.6.3.4	“Classical” Fission Treatment in CONRAD . . . . .	66
4.7	Summary and Remaining Limitations of the Code . . . . .	67
4.7.1	“CONRAD 2.0” . . . . .	67
4.7.2	“CONRAD 2.0-beta” . . . . .	67
<b>5</b>	<b>Implementation and Verification of Macroscopic-Microscopic Models</b>	<b>69</b>
5.1	General Macroscopic-Microscopic Approach . . . . .	70
5.2	Macroscopic Models . . . . .	72
5.2.1	Historical Semi-Empirical Bethe-Weizsäcker Formula . . . . .	72
5.2.2	Liquid Drop Model . . . . .	75
5.2.3	Finite-Range Liquid-Drop Model . . . . .	75
5.2.3.1	Finite Range of Nuclear Forces . . . . .	75
5.2.3.2	The Yukawa Plus Exponential Formula . . . . .	77
5.2.3.3	Proton Form Factor . . . . .	78
5.2.3.4	Binding Energy of Electrons . . . . .	79
5.2.3.5	Neutron-Proton Asymmetry terms . . . . .	79
5.2.3.6	Pairing Effects . . . . .	80
5.2.4	Summary and Effect of Deformation . . . . .	80
5.2.5	Macroscopic Model Verification . . . . .	82
5.3	Microscopic Models . . . . .	82
5.3.1	Nilsson Harmonic Oscillator Model and Basis Wave Functions . . . . .	82
5.3.2	More Realistic Phenomenological Potentials . . . . .	84
5.3.2.1	Average Scalar Potential . . . . .	84
5.3.2.2	Spin-Orbit Coupling Potential . . . . .	85
5.3.3	Single-Particle States and Deformation . . . . .	87
5.3.4	Microscopic Model Verifications . . . . .	89
5.4	Macroscopic-Microscopic Model . . . . .	93
5.4.1	Shell and Pairing Corrections . . . . .	93
5.4.1.1	Shell Correction Term . . . . .	94
5.4.1.2	Pairing Correction Term (BCS model) . . . . .	96
5.4.1.3	Pairing Correction Term (Lipkin-Nogami Model) . . . . .	97
5.4.1.4	Pairing Models Comparison . . . . .	99
5.4.2	Macroscopic-Microscopic Model Verification and Results . . . . .	99
5.4.2.1	Zero-Point Vibrational Energy . . . . .	99
5.4.2.2	Results for Masses . . . . .	101
5.4.2.3	Results for Potential Energy Surface . . . . .	104
5.5	Evaluation-Compliant Implementation . . . . .	106
5.5.1	Base Expansion of Wave Functions . . . . .	106
5.5.2	Efficient Numerical Integration Methods . . . . .	107
5.5.3	Exploitation of Computational Resources . . . . .	110
<b>6</b>	<b>From Potential Energy Surface to Fission Cross Section</b>	<b>113</b>
6.1	Least-Energy Path . . . . .	114
6.1.1	Immersion Technique . . . . .	114
6.1.2	Full Least-Energy Path . . . . .	116
6.1.3	2D-Verification and 3D-Application . . . . .	118
6.2	Least-Action Path . . . . .	121

6.2.1	Deformation Inertia Tensor . . . . .	121
6.2.1.1	Werner-Wheeler Approximation . . . . .	121
6.2.1.2	Cranking Model for Deformation Inertia Tensor Calculation . . . . .	123
6.2.2	Action Minimization and Path . . . . .	128
6.3	Least-Energy V.S. Least-Actions . . . . .	129
6.4	Numerical Transmission Coefficients . . . . .	132
6.4.1	Deformation-Independent Effective Mass Parameter . . . . .	132
6.4.1.1	Numerov Method . . . . .	133
6.4.1.2	Verification and Comparison of the Methods . . . . .	134
6.4.2	Deformation-Dependent Effective Mass Parameter . . . . .	136
6.4.3	Effects of Path Searching Method and Deformation Inertia Tensor on Transmission Coefficient . . . . .	138
6.4.3.1	A Test Case . . . . .	138
6.4.3.2	Actual Barriers and Inertia Parameters . . . . .	139
6.5	Transition states . . . . .	141
6.5.1	Rotational Band . . . . .	142
6.5.2	Rotational Band-Heads . . . . .	142
6.5.3	Rotational Moments of Inertia . . . . .	143
6.5.3.1	Rigid Body (Sharp- and Diffuse-edge) . . . . .	144
6.5.3.2	Cranking Model . . . . .	144
6.5.3.3	Model Comparison and Validation . . . . .	145
6.6	Fission Cross Section . . . . .	146
<b>7</b>	<b>Conclusion &amp; Perspectives</b> . . . . .	<b>151</b>
7.1	Overview of the Work . . . . .	152
7.1.1	Impact of the Fission Barrier in the RRR . . . . .	152
7.1.2	Integration of a Nuclear Structure Model . . . . .	152
7.1.3	Fission Cross Section in the Statistical Energy Range . . . . .	153
7.1.4	Summary of the Developments . . . . .	154
7.2	To Be Continued... . . . .	154
7.2.1	Consistency and Accuracy of the Current Method . . . . .	154
7.2.1.1	PES Reduction to a One-Dimensional Fission Barrier . . . . .	155
7.2.1.2	Inertia Parameter . . . . .	155
7.2.1.3	Continuum of Transition States . . . . .	155
7.2.2	Further Refinements of the Presented Method . . . . .	155
7.2.2.1	Fission Barrier Described down to the Scission Point . . . . .	156
7.2.2.2	Axially-Asymmetric Shapes . . . . .	156
7.2.2.3	Vibrational Phonons, Inertia Momentum and Transition States . . . . .	156
7.2.2.4	Odd Compound Nuclei . . . . .	157
7.2.2.5	Nuclear Structure Models . . . . .	157
<b>A</b>	<b>Coupled Channel Equations</b> . . . . .	<b>159</b>
A.1	Overview . . . . .	160
A.2	Expansion of the Interaction Potential . . . . .	161
A.2.1	Nucleus Coupling Matrix Element $\langle I_f M_f   Y_\lambda^\mu(\hat{r}')^*   I_i M_i \rangle_{\hat{r}'}$ . . . . .	163
A.2.2	Particle Coupling Matrix Element $\langle j_f m_f   Y_\lambda^\mu(\hat{r})   j_i m_i \rangle_{\hat{r}}$ . . . . .	164
A.2.3	Full Matrix Element $\langle \Psi_f^{JM}   Y_\lambda^\mu(\hat{r}) Y_\lambda^\mu(\hat{r}')^*   \Psi_i^{JM} \rangle_{\hat{r}, \hat{r}'}$ . . . . .	165
A.3	Special Cases . . . . .	167
A.3.1	Spin- $\frac{1}{2}$ Projectile . . . . .	167

A.3.2 Spin-0 Projectile . . . . .	168
A.4 Spin-Orbit Term . . . . .	168
<b>B Macroscopic-Microscopic Models in the CONRAD code</b>	<b>173</b>
B.1 Generating Shapes . . . . .	174
B.1.1 Legendre Polynomials Expansion . . . . .	174
B.1.2 Hill-Wheeler Parameterization . . . . .	175
B.1.3 Perturbed Spheroid . . . . .	175
B.1.4 Generalized Spheroid . . . . .	176
B.1.5 Three Quadratic Surfaces (3QS) . . . . .	178
B.2 About Shell and Pairing Correction . . . . .	179
B.2.1 Shell Correction . . . . .	179
B.2.2 Discussion about the Shell Correction . . . . .	183
B.2.3 Pairing Correction . . . . .	185
B.3 Finite Range Droplet Model . . . . .	185
B.3.1 Droplet Model . . . . .	185
B.3.2 Finite Range Droplet Model . . . . .	189
B.4 Computational Forms . . . . .	194
B.4.1 Reduction of Integration Domain . . . . .	194
B.4.1.1 $r(\theta)$ Parameterization . . . . .	194
B.4.1.2 $\rho(z)$ Parameterization . . . . .	197
B.4.2 Coulomb Potential in $\rho(z)$ Parameterization . . . . .	198
B.4.3 Principal Curvatures of 2D-Surfaces . . . . .	203
B.4.3.1 $\rho(z)$ Parameterization . . . . .	203
B.4.3.2 $r(\theta)$ Parameterization . . . . .	205
<b>C Matrix Elements of the Single-Particle Hamiltonian</b>	<b>209</b>
C.1 Wave-Functions Basis $ n_r n_z \Lambda \Sigma\rangle$ . . . . .	210
C.2 Kinetic Matrix Element $\langle \Psi_f   \hat{T}   \Psi_i \rangle$ . . . . .	210
C.2.1 Kinetic Operators . . . . .	210
C.2.2 $\xi$ -Diagonal Matrix Element $\langle \Psi_{n'_z}   \hat{T}_\xi   \Psi_{n_z} \rangle$ . . . . .	211
C.2.3 $\eta$ -Diagonal Matrix Element $\langle \Psi_{n'_r}^\Lambda   \hat{T}_{\Lambda\eta}   \Psi_{n_r}^\Lambda \rangle$ . . . . .	213
C.2.4 General Kinetic Matrix Element . . . . .	215
C.3 Scalar Potential Matrix Element $\langle \Psi_f   \hat{V}_{C+N}   \Psi_i \rangle$ . . . . .	216
C.4 Spin-Orbit Coupling Matrix Element $\langle \Psi_f   \hat{V}_{s.o.}   \Psi_i \rangle$ . . . . .	216
C.4.1 Diagonal Spin-Orbit Matrix Element ( $\Sigma' = \Sigma$ ) . . . . .	217
C.4.2 Cross Spin-Orbit Matrix Element ( $\Sigma' = -\Sigma$ ) . . . . .	219
<b>D Numerical Transmission Coefficients</b>	<b>225</b>
D.1 Numerical Methods for Transmission Coefficient Calculation . . . . .	225
D.1.1 Piece-wise Methods . . . . .	226
D.1.2 JWKB Method . . . . .	228
D.1.3 Derivation of the Numerov Method . . . . .	228
D.2 Analytical Cases . . . . .	229
D.2.1 Step Potential . . . . .	230
D.2.2 Triangular Potential . . . . .	231
D.2.3 Cramer-Nix Original Potential . . . . .	234
D.2.4 Cramer-Nix “Modified” Potential . . . . .	236
<b>Bibliography</b>	<b>241</b>

# Chapter 1

## Introduction

*The general treatment of nuclear data in order to supply industry with usable data, called “evaluation”, is presented in this chapter. The evaluation process is introduced along with a general background of evaluated data libraries, application data libraries, engineering codes, etc. Focus will be made on neutron cross section evaluation and deficiencies of current evaluated cross sections will be presented.*

### Contents

---

<b>1.1</b>	<b>Objectives of present PhD Work</b>	<b>2</b>
<b>1.2</b>	<b>General Context of Nuclear Data Evaluation</b>	<b>3</b>
<b>1.3</b>	<b>Evaluation Methods and Status of Evaluated Cross Sections</b>	<b>7</b>
1.3.1	Consistency of Evaluated Nuclear Data	7
1.3.2	Consistency of Nuclear Data Modeling	8
1.3.3	Variance-Covariance Data	10
1.3.4	Predictability and Reproduction of Experimental Data	11

---



## 1.1 Objectives of present PhD Work

The purpose of present PhD work is to demonstrate the feasibility of using advanced theoretical models as underlying tools for *fission cross section evaluation*. Two main energy ranges are considered in cross section evaluation: the *Resolved Resonance Range* (RRR), relying on the  $\mathfrak{R}$ -matrix theory and the *statistical energy range* relying on the *Hauser-Feshbach theory*. Directions for improvements of fission cross section modeling will be given for both energy ranges. These improvements aim to give adjusted parameters a sound physical meaning. The physical meaning for parameters (and for related models) restrain arbitrariness of the evaluation choices that are made in current approaches.

In the RRR, the fission penetration factor is currently assumed to be unity ( $P_f = 1$ ), which deteriorates both the meaning and the statistical quality of the fission resonance parameters ( $\gamma_{\mathfrak{M}}$ ). In the statistical energy range, the usual *Hill-Wheeler formalism* fails to reproduce experimental structures. To compensate this model default, *ad hoc* solutions are selected but rely on phenomenological parameters that limit the predictive power of this approach. The present study will focus on the effects of considering detailed and reliable fission barrier (namely a barrier having a double-hump shape provided by a macroscopic-microscopic model) in fission cross section modeling. Results of present work will be presented as follows.

First, the general context of evaluated data and, more specifically, of evaluated cross sections will be introduced (this chapter). Focus will be made on the remaining data inconsistencies and on sources of improvement.

In Chapter 2, the general *collision theory* that drives cross section modeling will be detailed. All the programming developments required for this work have been implemented in the CONRAD evaluation code that will be presented.

The  $\mathfrak{R}$ -matrix theory is an exact frame that gives a *parameterization* of resonant cross sections in which the energy dependency is made explicit. It relies on the knowledge of the interaction potential operating in the different reaction channels. This potential, and the related wave functions, are used to define penetration factors that carry a part of the energy dependency of the cross section. Theory describing fission-specific penetration factors in the RRR will be introduced in Chapter 3. An analysis of the fission resonance parameters of the  $^{240}\text{Pu}(n, f)$  cross section will be performed using will highlights the effect of fission-dedicated treatment in the RRR cross section analysis.

The fission barrier shape is a decisive ingredient in the fission penetration factor modeling. It is also a key feature in average fission cross section modeling in the statistical energy range. In Chapter 5, a long-standing macroscopic-microscopic model, the *Finite Range Liquid Drop Model*, will be presented. This model can be used to describe the potential energy of nucleus as this latter deforms and provides what is called the *Potential Energy Surface* (PES).

The multidimensional PES cannot be directly used in a Hauser-Feshbach model to calculate average cross sections in the statistical energy range. The PES must be converted into a one-dimensional fission barrier. Out of this latter, a fission transmission coefficient usable in a Hauser-Feshbach model can be calculated. This reduction to a one-dimension fission barrier, and the computation of the related fission transmission coefficient will be treated in Chapter 6. An application example for the  $^{239}\text{Pu}(n, f)$  cross section will be finally presented.

Significant efforts have been provided in this PhD work in terms of code development. Several verifications on analytical cases, and validations on experimental data were made all along this work to ensure the reliability of the present approach.

## 1.2 General Context of Nuclear Data Evaluation

Nuclear data are necessary inputs for numerous applications such as reactor physics, nuclear medicine, nuclear marine propulsion<sup>1</sup>, and non-proliferation efforts. It is also used for less known applications such as archaeology (radiocarbon dating), food conservation, material science and astrophysics. In France, the aging of nuclear plants leads to question the medium-term future of power production and considering alternative sources of energy. In case where nuclear energy production is favored, two main options are open

- Extent current power plant lifetimes, the so-called Generation II reactors<sup>2</sup>, engaging heavy and costly renovations.
- Building a new generation of reactors (the Generation III), with highly upgraded safety and operability standards.

In both cases, advanced studies regarding safety and efficiency must be performed using accurate input data. Safety upgrades are imposed by the national nuclear regulatory commission (named *Autorité de Sûreté Nucléaire* in France). Unless operators prove that current procedures comply with the new safety standards, reactor operation margins can be drastically reduced. This necessitates detailed studies of how to reduce model uncertainties so that safety can be ensured with reasonably restored operation margins. In recent years, new computational resources made affordable the use of *reference* methods in reactor physics. These methods, based on Monte-Carlo simulations, are more appropriate because of they do not rely on the various approximations present in the analytical deterministic methods that are more commonly used. Yet Monte-Carlo simulation is often too time-consuming considering the number of studies required for instance to operate reactors. The reference methods are thus mainly used to quantify and correct biases carried by analytical deterministic calculations.

*Reactor physics* computations require a large amount of *nuclear physics* input data, namely the cross section values. Nowadays, reactor physics calculations exhibit input-related uncertainties that are larger than those related to computation method itself, thanks to Monte-Carlo reference methods.

In parallel to the two above options concerning future of nuclear power production in France, there is a medium-term project related to a fourth generation of reactors that is expected to coexist with, or replace Generation III reactors. The fourth reactor generation is designed to consume the most abundant isotope of uranium,  $^{238}\text{U}$  present in natural ore<sup>3</sup>. Generation II and III reactor reactors use only the scarce  $^{235}\text{U}$ , which isotopic fraction amounts to only 0.720% of the natural element. This change of consumed material is achieved by transmuting  $^{238}\text{U}$  into  $^{239}\text{Pu}$  by neutron capture. This process actually occurs in any reactor, as long as it contains  $^{238}\text{U}$ . In light water reactors (Generation II and III for instance), plutonium can be responsible for up to a third of fissions. In France, some current reactors<sup>4</sup> use plutonium as fuel. It is obtained from uranium-based spent fuel recycling, yet this type plutonium fuel recycling can only be performed once as the

<sup>1</sup>Nuclear marine propulsion refers to both naval nuclear propulsion of warships and to the very few civil nuclear ships.

<sup>2</sup>In France, the Generation I corresponds to the first industrially developed reactors built in the 50's. They used natural uranium as fuel and graphite as moderator; the technology then switched to enriched uranium as fuel and light water as moderator for in Generations II and III.

<sup>3</sup>There are scenarii and studies that involve thorium as the source of nuclear fuel, yet the related technology is likely to be ready in a more remote future than for uranium-base fuel cycle.

<sup>4</sup>Only some of the 900 MWe reactors use plutonium fuel. Yet, it amounts to only a third of the nuclear fuel used, the remaining being the usual  $^{235}\text{U}$  fuel.

plutonium isotopic quality is degraded after being used once more in a Generation II or III reactor. Generation IV reactors are designed to allow multi-recycling of spent fuel, and are also expected to burn minor actinides that are responsible for long-term radiotoxicity of current nuclear wastes. All these reasons (new reactor design, renovation of existing plants and highlight of nuclear data-related uncertainties) advocate for quality enhancement of nuclear data and of related uncertainties.

A large amount of nuclear data is required in order to design, operate and even de-commission a nuclear reactor plant. These nuclear data can be of very various types, for example:

- *Partial and total cross-sections*; When two particles collide, for instance a neutron and a uranium nucleus, the probability for a given reaction to occur (*e.g.* capture, elastic scattering, fission, etc.) can be quantified in terms of *cross-sections*. The partial cross section is related to a given reaction type and the total cross section stands for the total interaction probability, regardless of the type of reaction.
- *Multiplicity* of produced particles; for some reactions, various types of particle (neutron, proton, alpha particle, fission fragments, *etc.*) can be emitted. In particular, for the fission reaction, these quantities are separately named *fission yields* when referring to the fission fragments; *fission multiplicity* when referring to the number of neutrons emitted by fission; and *fission gamma multiplicity* when referring to prompt gamma emissions.
- *Angular and energetic distributions* of produced particles.
- *Radioactive decay* data.
- Reaction energy; *e.g.* the amount of energy released per fission or the energy transferred by inelastic scattering.
- Data related to nuclear structure (discrete levels); for example energy, angular momentum and parity of excited states of nuclei.
- Nuclear data can also be extended to some *electronic* properties data, for instance for the electronic stopping power along with the nuclear stopping power.

Nuclear data can be either obtained from by experiments or, whenever no experimental information is available, predicted by theoretical models. On the contrary, when several experimental measurements and/or several models are available, a necessary balance must be found in order to weight all “versions” and to reach the best data estimate. This cumbersome process is called *evaluation*. Figure 1.1 shows the upstream position of the nuclear data evaluation in the whole process that eventually leads to industrial applications.

For a specific type of nuclear data, all relevant **microscopic experimental information** can be merged and averaged to form a **standard**. The cross section standards are not often used in applications because of two main reasons:

- First, data for which many related measurements are available are scarce. For neutron cross section, standards only involve few reactions [25]  $^1\text{H}(n, n)$ ,  $^3\text{He}(n, p)$ ,  $^6\text{Li}(n, t)$ ,  $^{10}\text{B}(n, \alpha)$ ,  $^{10}\text{B}(n, \alpha_1\gamma)$ ,  $\text{C}(n, n)$ <sup>5</sup>,  $^{197}\text{Au}(n, \gamma)$ ,  $^{235}\text{U}(n, f)$  and  $^{238}\text{U}(n, f)$ . Related data are also often restricted to a limited energy range.

---

<sup>5</sup>For the  $\text{C}(n, n)$  cross section, the standard is related to carbon of natural isotopic abundance.

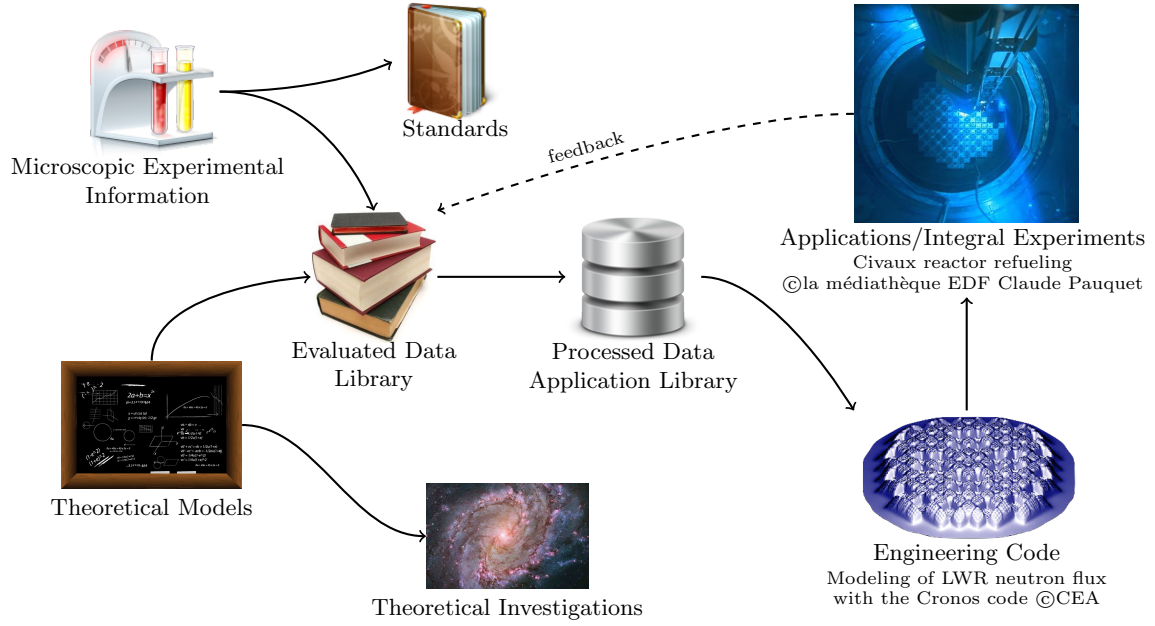


Figure 1.1 – Schematic of the nuclear data path from experimental and/or theoretical sources to industrial applications.

- The second reason that limits the use of standards is that careful *evaluation* analyses, combining **theoretical models** and selected experimental data, usually increases the consistency of *evaluated nuclear data* with **integral experiments**. These latter integral experiments involve several partial cross sections of many isotopes for a wide energy range. Standards are based on **microscopic experiments** designed to be as sensitive as possible to *one* reaction involving *one* isotope and for a specific energy range only.

Even though *standards* are not directly used for applications, they remain a source of verification of the evaluation process. *Evaluated nuclear data* are gathered into **evaluated data libraries**. On the opposite to the **standards** way, there are the pure **theoretical investigations**. This approach is envisaged whenever lack of microscopic and integral experimental data is encountered. Nuclear data are very specific to the related isotope, yet systematics (or trends) can be found for some types of data across the periodic table.

The present work focuses on one specific type of nuclear data: the neutron-induced fission cross section, for which experimental data are usually available and for which large reactor application feedback exists (*i.e.* integral experiments). This feedback is used more and more to produce new evaluated data that are expected to correct possible biases in microscopic measurements. Finally, it must be also noticed that evaluated data libraries are usually not directly used in **engineering codes**. A **processed data application library** must be created specifically for each engineering code. The processing is not only a change of format but can consists of several treatments, for instance the zero-Kelvin cross sections can be broadened to actual reactor temperatures. Further dedicated treatments [26,27] can also be performed such as the production of self-shielded multigroup cross sections [28,29].

Due to the very nature of nuclear physics, nuclear data can be highly fluctuating and finely structured. For instance, cross sections can “oscillate” several times (varying of several orders of magnitude) within a range of 1 eV of the incident particle energy, and the reactor data must cover the range from 0 to several millions of eV! Figure 1.2 shows an

example of evaluation of such fluctuating data, pictured here by the total neutron cross section of  $^{239}\text{Pu}$ .

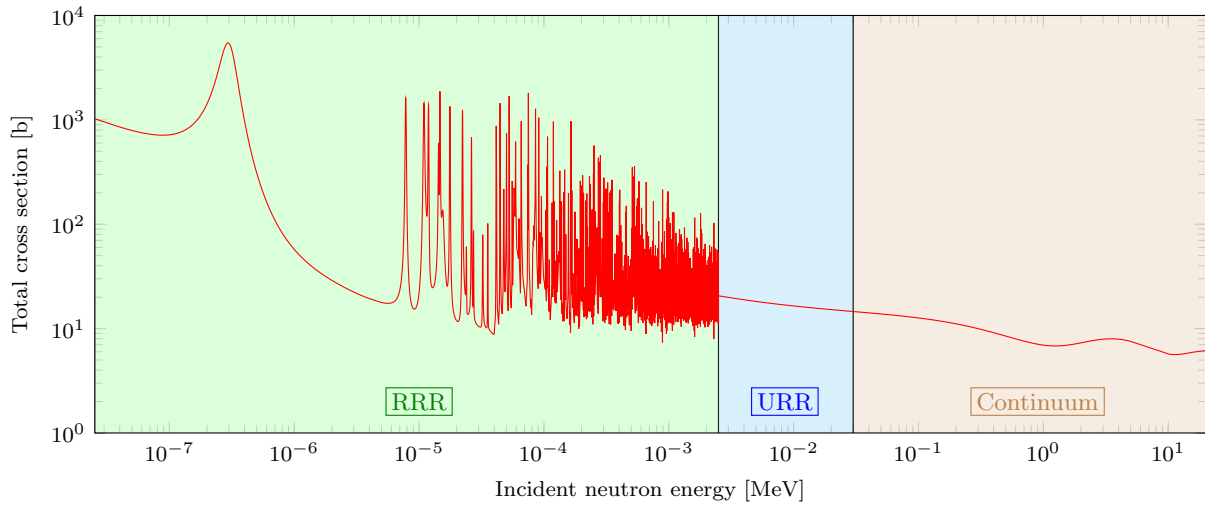


Figure 1.2 – JEFF-3.2 evaluation of the  $^{239}\text{Pu}$  total cross section. The different energy ranges involved for the description of the cross section are also highlighted.

At low incident neutron energies, well energy-resolved resonances can be observed (green background), they correspond to the *Resolved Resonance Range* (RRR). At higher energies the lack of experimental information and the difficulty to separate resonances lead to consider an average value of the cross section, this energy range is referenced as the *Unresolved Resonance Range* (URR) (blue background).

In this energy range, resonances still exist and cannot be neglected for reactor physics applications. In the reactor core, neutrons collide with isotopes present in the reactor core. The resonance width that is “seen” by the moving neutron depends on the relative velocity between the neutron and the collided isotope. This relative kinetic energy is modified by the medium temperature as thermal motion modifies the velocity of the collided isotope. By Doppler effect, the resonance widths are broadened when the medium temperature increases, for instance as a result of an increase in power production in the reactor. This phenomenon is a key point for reactor safety, as this effect has to result in a negative feedback which stabilizes the reactor reactivity. In the URR, the effect of the medium temperature must be “somehow” treated. Since no pointwise data can be recommended for resonance description in this range, they are treated using *probability tables* that contain the statistical properties of the resonances. This description is more suitable to handle self-shielding and Doppler effect.

At even higher energies, the resonance density becomes so high that resonances overlap and no fine resonance structures can be identified anymore. The resonance widths also become larger with increasing incident neutron energy, which enhances the overlapping phenomenon. This energy range, where no resonance can physically be observed, is called the neutron *Continuum* range (red background in Fig. 1.2).

The amount of numerical values to be stored in order to reproduce the complexity of the cross section is tremendous. In order to make evaluated data available to any application, these latter are formatted into specific *evaluated nuclear data files*. The definition of an international format has been a long term effort from the pioneer definitions [30,31] to the current ENDF-6 standard [32] as more and more types of nuclear data became needed to be processed and stored. Although the ENDF-6 format seems nowadays like



an old-fashioned and highly FORTRAN-oriented *Man Machine Interface*, it is still the international reference format used world wide. The reason being that the processing of evaluation files is a heavy task that needs to be done specifically for every reactor physics computer code. A change in the format would imply tremendous modifications in all subsequent processing codes. Still, a working group of the OECD/NEA WPEC (subgroup 38 [33]) is currently in charge of studying the relevance of different modern formats that could be more appropriate to a new generation of nuclear data storage.

## 1.3 Evaluation Methods and Status of Evaluated Cross Sections

The recent renewed interest from nuclear industry in improved nuclear data, pushes for new experiments and more sophisticated theoretical models, also pushes for changes in evaluation methods. The improvements in evaluation methods are related to already identified deficiencies in current evaluations:

- Consistency of evaluated nuclear file. For instance, the same type of information can be found several times in a single evaluated file, thus consistency is not always ensured.
- Consistency of modeling of nuclear data. For instance the data evaluated in different energy ranges can have common features (*e.g.* parameters) that are not consistent between the ranges.
- Lack of accurate variance-covariance data. These types of information stand for both uncertainties and correlations between nuclear data.
- Predictability of not-measured nuclear data by improving the theoretical ground; a continuous effort is carried on in that field as experiments cannot be always performed (cost, feasibility, international treaties<sup>6</sup>).
- Capability to reproduce experimental data.

All these points will be discussed and exemplified in the following sections.

### 1.3.1 Consistency of Evaluated Nuclear Data

Improving consistency of evaluated nuclear data may seem like the most trivial way to enhance data quality. Figure 1.3 shows an example of inconsistency; the JEFF-3.2 evaluation of the  $^{240}\text{Pu}$  total cross section exhibits a nonphysical discontinuity at 40 keV.

This issue results from the fact that the cross section has been evaluated separately according to the range of incident neutron energy (URR or Continuum). For reactor physics applications, neutron cross sections are evaluated for incident neutron energies from about  $10^{-5}$  eV up to 20 MeV, that is to say on an energy range about twelve orders of magnitude wide. In practice there is no unique model able to treat cross sections over such a wide energy range, hence different models are used depending on the range of the incident neutron energy. As each range may be treated by different people, at different

---

<sup>6</sup>For instance, fission cross section of  $^{241}\text{Am}$ ,  $^{242\text{m}}\text{Am}$  and  $^{234}\text{U}$  where measured [34,35] in the 60's by the means of nuclear explosions as neutron source. This technique is now prohibited by the *Comprehensive Nuclear-Test-Ban Treaty*.

locations<sup>7</sup> and at different times, complete consistency is difficult to achieve. Consistency is not only related to man-power issues but may also be related to intrinsic differences in model behavior depending on the energy range. Some ongoing studies attempt to analyze the effects of constraining consistency between models in terms of cross section values and propagated variance-covariance matrices [36].

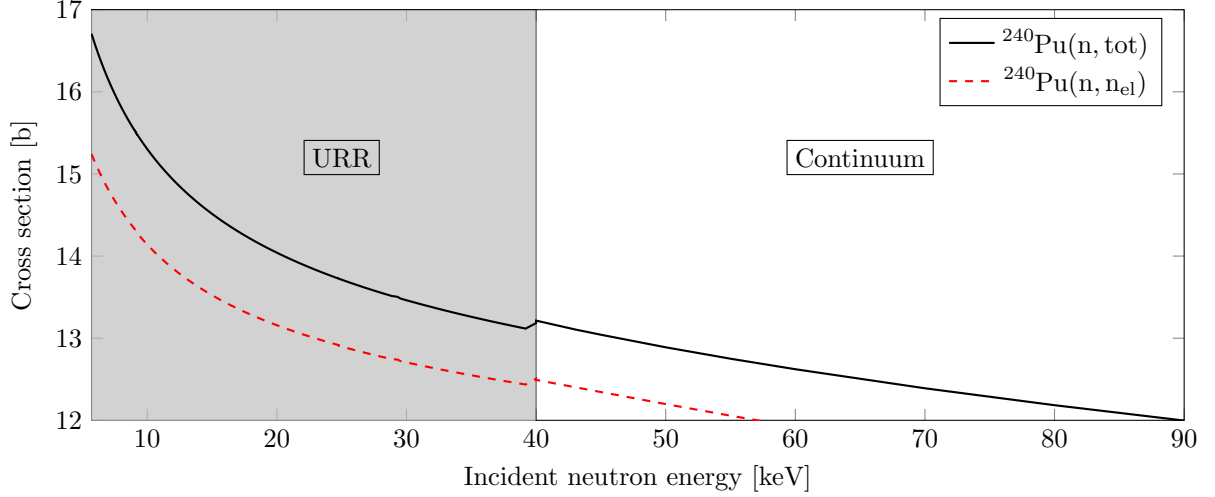
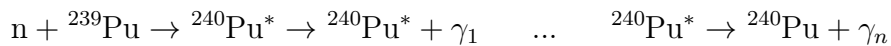


Figure 1.3 – JEFF-3.2 evaluation of the  $^{240}\text{Pu}$  total and elastic scattering cross sections. A mismatch can be observed at 40 keV between the Unresolved Resonance Range (gray background) and the Continuum Range.

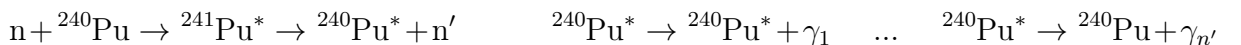
Similar issues can also occur for partial cross sections. Indeed total and partial cross sections are provided in evaluated files, but the summation of partial cross sections does not necessarily equal the total cross section. This is also related to the fact that total and partial cross sections can be evaluated separately or may result from addition of “extra” cross sections in the evaluation file. These extra cross sections are used to provide data wherever the ENDF-6 format has no dedicated container, the use of such tricks remains hazardous but should vanish with upcoming new formats.

### 1.3.2 Consistency of Nuclear Data Modeling

Another source of inconsistency in current evaluations is related to the underlying models (and parameters) used to produce evaluated data. In Chapter 4, it will be clearly shown that models operating in different energy ranges have common features. Connections between the model parameters, and consequently between different evaluated data sets, emerge because models provides not only the required observable but also tend to describe the complete nuclear process and thus some common intermediate properties are also involved and should be consistent. Figure 1.4 shows an example of such a situation. Here the radiative capture reaction  $^{239}\text{Pu}(n, \gamma)$  is considered:



Underlying parameters describe the  $^{240}\text{Pu}$  excited states involved in photon emission. Another reaction called the inelastic scattering  $^{240}\text{Pu}(n, n')$  or  $^{240}\text{Pu}(n, n_{\text{inel}})$  is:



<sup>7</sup>For instance, several contributors and institutes are involved in the JEFF project of evaluated cross section library, namely CEA-Bruyères-le-Châtel and CEA-Cadarache (France), NRG (Netherlands), Karlsruhe Institute of Technology (Germany), UKAEA (United-Kingdom) and many others.

Here again, parameters are required to describe the  $^{240}\text{Pu}$  excited states involved in the decays of  $^{241}\text{Pu}^*$  and  $^{240}\text{Pu}^*$ . Both reactions  $^{239}\text{Pu}(n, \gamma)$  and  $^{240}\text{Pu}(n, n')$  involve the same  $^{240}\text{Pu}$  nucleus but in different roles. In the inelastic reaction,  $^{240}\text{Pu}$  is the target and residual nucleus, whereas for the capture reaction it is the compound nucleus. This implies that model parameters are correlated (and expected to be consistent); therefore the same nuclear structure database must be used for evaluation of both reactions.

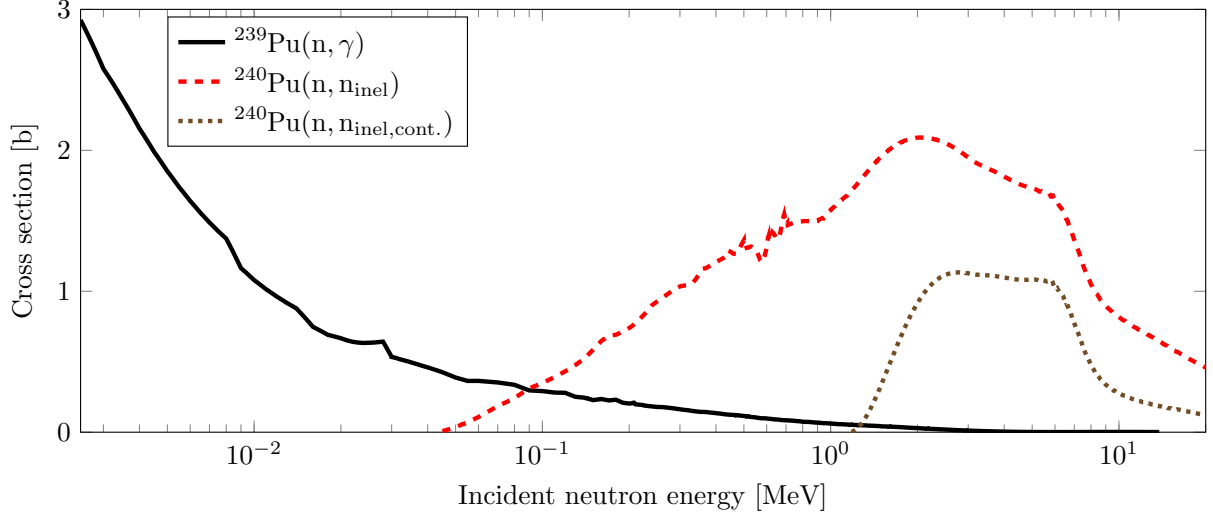
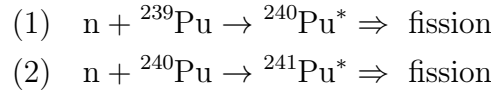


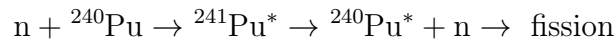
Figure 1.4 – JEFF-3.2 evaluations of the  $^{239}\text{Pu}(n, \gamma)$  and  $^{240}\text{Pu}(n, n_{\text{inel}})$  cross sections. The “continuum” contribution to the  $^{240}\text{Pu}(n, n_{\text{inel}})$  cross section,  $^{240}\text{Pu}(n, n_{\text{inel, cont.}})$  is also shown. The word “continuum” used here is not related to the continuum energy range of incident neutron energy introduced previously. Instead it is related to an average treatment of residual nucleus levels.

A second example, related to fission cross sections, is shown in Fig. 1.5. Here the reaction models involve a neutron colliding with an actinide isotope, forming a compound nucleus that undergoes fission. This reaction process is called *first chance fission*. However for high enough incident neutron energies, the compound nucleus can emit a neutron and still have a significant probability of fissioning. This latter process is called *second chance fission*.

The two first chance fission reactions involved in Fig. 1.5 are



Let say that, in the  $^{241}\text{Pu}^*$  decay (reaction (2)), a neutron is emitted prior to fission and ignites a second-chance fission



The  $^{240}\text{Pu}^*$  isotope is formed by two different processes, by the first chance fission in  $^{239}\text{Pu}(n, f)$  and by the second chance fission in  $^{240}\text{Pu}(n, nf)$ . However in this example, common features do not relate to  $^{240}\text{Pu}$  states as decay arrival states, like in the first example, but as initial states prior to fission decay. Here model parameters describing  $^{240}\text{Pu}^*$  tendency to decay toward fission must be the same. Physics consistency requires thus that common shared parameters must be used in the evaluation of  $^{239}\text{Pu}(n, f)$  and  $^{240}\text{Pu}(n, f)$ , yet this is not always the case. It must be stated here that the large number of related parameters can be difficult to estimate with the desired degree of confidence.



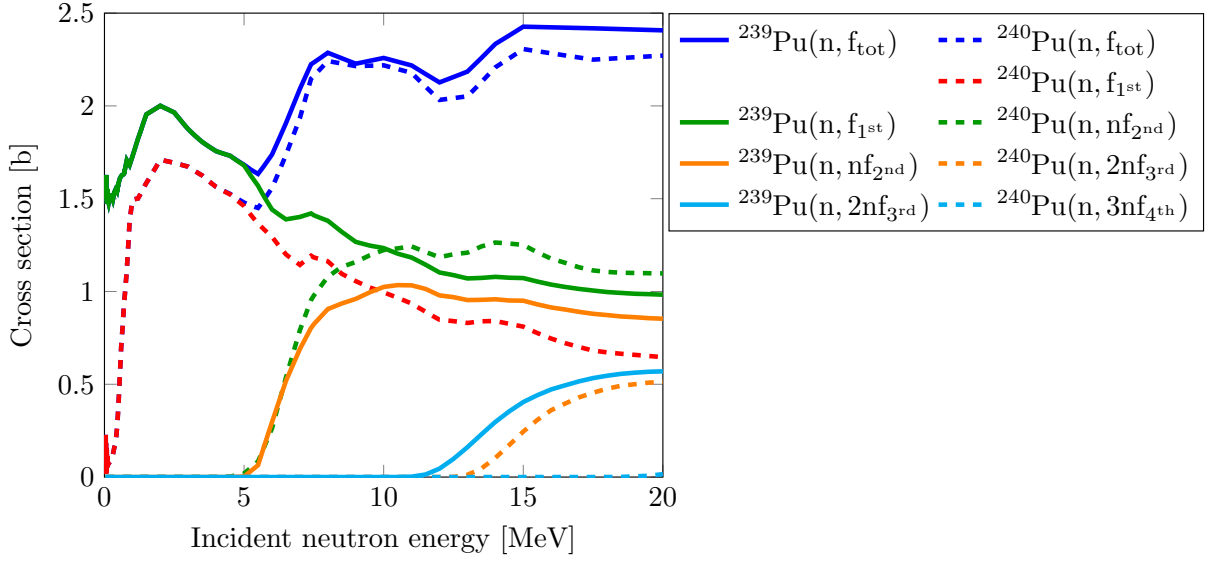


Figure 1.5 – JENDL-4.0 evaluations [37] of the  $^{239}\text{Pu}$  and  $^{240}\text{Pu}$  neutron-induced fission cross sections. The solid and dashed lines correspond to the partial cross sections related to  $^{239}\text{Pu}$  and to  $^{240}\text{Pu}$  respectively. Dark blue curves correspond to total fission cross sections, *i.e.* the sum of all chance fission cross sections. Except for dark blue curves, dashed and solid curves of the same color are related to the fission decay of the same compound nucleus, namely  $^{241}\text{Pu}^*$ ,  $^{240}\text{Pu}^*$ ,  $^{239}\text{Pu}^*$  and  $^{238}\text{Pu}^*$ . Partial fission cross sections of identical “chance order” correspond to the same decay process but for different isotopes. However curves with same colors relate to decay of the same isotope, and thus rely on common parameters.

### 1.3.3 Variance-Covariance Data

As operation margins tend to be reduced in nuclear industry due to enhanced safety standards, efforts are made to quantify more accurately uncertainties related to nuclear data. Uncertainties on nuclear data are provided by evaluators in terms of variance-covariance matrices. These matrices contain uncertainties on data themselves but also the interdependence, or *correlation*, between two given data, *e.g.* the cross section values at two different energies or between two different partial cross sections. Significant efforts were put in this direction in recent years, and should be maintained because:

- Variance-covariance matrices do not exist for all nuclear data types and isotopes.
- When full experimental matrices are used, the eventual  $\chi^2$  of the fit can be improved while deteriorating the agreement with experimental data (see Peelle’s Pertinent Puzzle [38]).
- For experiments with a tremendous number of data points, the eventual computed uncertainty is sometimes too low to be relevant. Yet, the marginalization technique [38], recently applied in evaluation for the propagation of systematic uncertainty, reduces this effect.
- Correlations between isotopes are quite rare although measurements are often made with respect to reference data (*e.g.* the  $^{235}\text{U}$  neutron fission cross section) or are made with natural-abundance samples containing several different isotopes.
- Models correlate data as they give “trends” regardless of their parameter values.

- Evaluated data related to processes involving decay of identical isotopes must use common parameters that describe the decays, thus correlating the data.

### 1.3.4 Predictability and Reproduction of Experimental Data

Development of Fast Reactor technology and concerns about long-life minor actinides waste increase interest in nuclear data related to heavy nuclei. Unfortunately experimental investigation on nuclear data is often expensive, and sometimes hardly practical due to radio-toxicity or to short lifetime of the involved isotopes. Therefore alternative methods are investigated. In the experimental field, surrogate reactions are used to produce identical compound nuclei by substitute reactions. For instance, the  $^{238}\text{U}(^3\text{He}, \text{tf})^{238}\text{Np}$  reaction leads to fission decays of  $^{238}\text{Np}$  and can be considered an indirect measurement of the  $^{237}\text{Np}(\text{n}, \text{f})$  reaction.

In the theoretical field, investigations can be made using extrapolated model parameters. Systematics (trends) in parameter values for known isotopes may exhibit approximate dependencies on the mass number  $A$  and/or on the atomic charge number  $Z$ . Hence specific data can be extrapolated from known isotopes to exotic ones. This technique is often used to supply data for astrophysics applications that deal with very short-life isotopes. Unfortunately these extrapolations can be done only in cases where few parameters are involved. When highly structured data are involved, such as resonant cross sections, this systematics approach cannot be considered. A related example is shown in Fig. 1.6 representing the JEFF-3.2 neutron-induced fission cross section of  $^{240}\text{Pu}$ . Fluctuations in the evaluated cross section in the continuum range results from the addition of *ad hoc* parameters (*i.e.* not provided by underlying nuclear structure model) used here to reproduce experimental data. Details about the method used to produce the right-hand side of this evaluation will be given in Section 4.6.

In the URR range (*cf.* Fig. 1.6), one can also notice that evaluated data [43] (red lines) do not reproduce all features observed in the experimental data since the model used in this range provides only energy-averaged values of the fission cross section. To emphasize that such an average treatment is a limiting point for reactor physics applications, the ECCO-1968 [42] multigroup energy structure is also shown on the upper parts of the frames in Fig. 1.6. This energy group structure is used by some reactor physics codes to defined multigroup cross sections, which can be regarded here as energy-averaged cross sections over the group energy width. One can see that the reactor physics energy discretization is quite more refined than the one chosen for the evaluated data<sup>8</sup>. This highlights that some experimental structures are discarded in the evaluation treatment and that engineering codes are readily able to deal with more finely structured input cross sections.

On the lower part of Fig. 1.6, the experimental fission cross section structures that are not reproduced in the evaluation are about 100 eV wide, and have a mean spacing of about 200 eV. These structures should not be mixed up with the low-energy resonances that are considered in the RRR (*cf.* Fig. 1.2). These latter resonances are much narrower (100 meV wide). This can be verified in Fig. 1.7 where  $^{240}\text{Pu}$  total and fission cross sections are shown for energies corresponding to the upper part of the RRR (in this example the RRR is [0, 5.7 keV] and Fig. 1.6 shows the lower part of the URR). Low energy resolved resonances can be observed on the total cross section measured by Kolar *et al.* [46] and on the JEFF-3.2 evaluation.

---

<sup>8</sup>The nearly piece-wise constant structures in the low energy part of Fig. 1.6 results from the inclusion of an integral experiments feedback [44] based on the ERALIB adjusted library [45].

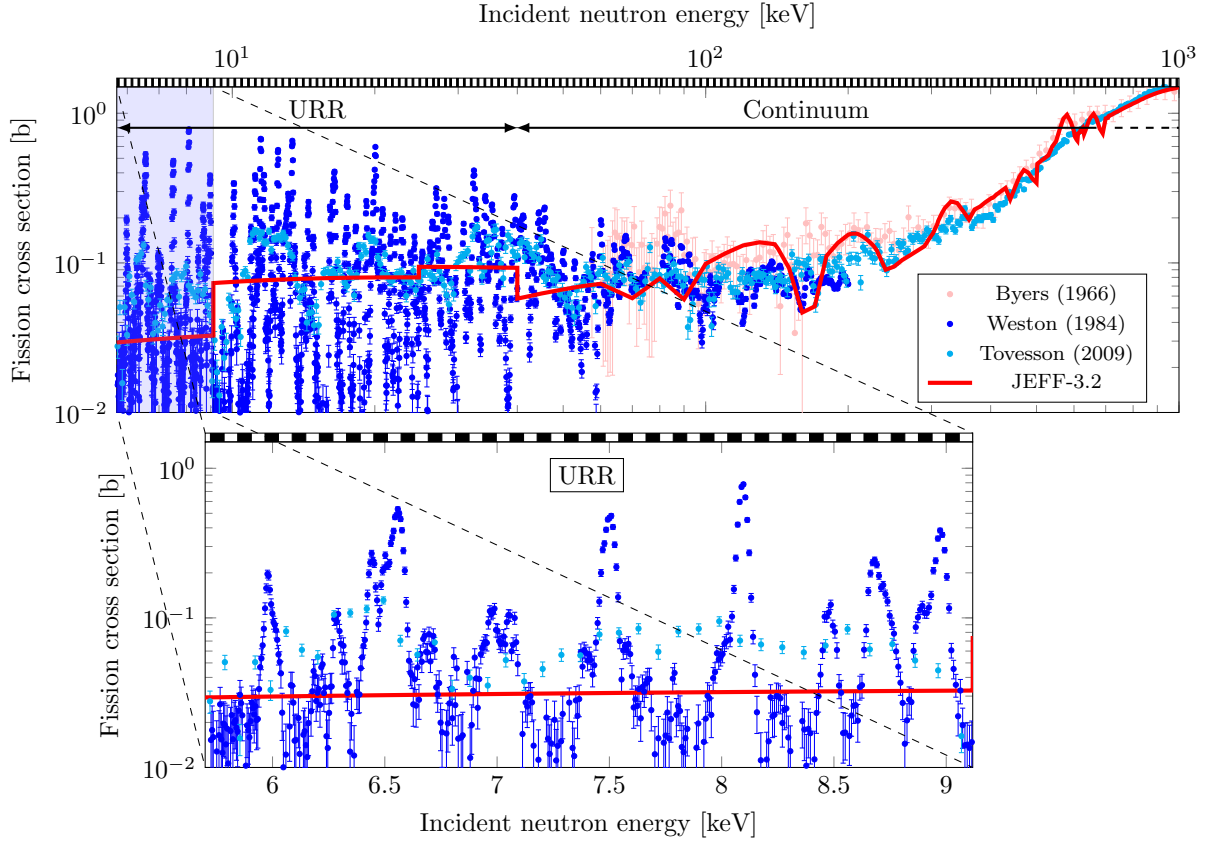


Figure 1.6 – Comparison between the JEFF-3.2  $^{240}\text{Pu}(n,f)$  cross section evaluation and related experimental data [39–41]. The blue background corresponds to the enlarged frame shown in the lower figure. The black and white bar codes, on the top of each figure, show the 1968-groups energetic mesh used by the ECCO reactor cell code [42].

These *resolved* resonances have an average width smaller than 100 meV, and a mean spacing of about 13 eV. The broad structures (100 eV wide) in the fission cross section shown in Fig. 1.6 are much wider than the narrow resolved resonances of the total cross section. Differences in experimental resolution cannot explain alone these broad structures. If so, average fluctuations should be similar between fission and total cross sections but this is not what is observed in Fig. 1.7. Average JEFF-3.2 total and fission cross sections are shown to highlight differences in behavior between total and fission cross sections. The average values are obtained using a 15 eV bin. Broad structures are visible on the average fission cross section whereas the average total cross section remains roughly constant. This proves that the fluctuations shown in Fig. 1.6 are not partially-resolved narrow resonances but are instead originating from a fission-specific phenomenon.

This phenomenon also shows up for fissile isotopes. In Fig. 1.8 one can compare the JEFF-3.2 total and fission cross sections for  $^{235}\text{U}$  and  $^{239}\text{Pu}$ . The broad fluctuation behavior of the fission cross sections is reduced compared with  $^{240}\text{Pu}$ , especially for  $^{235}\text{U}$ , and the visible fluctuations seem correlated to the total cross section. This can be understood referring to by the Hauser-Feshbach (HF) formalism that will be detailed in Chapter 4. For the present explanation, it will be understood that HF parameters like  $T_n$  describes the tendency of the compound nucleus to emit a neutron and  $T_f$  is the related parameter for undergoing fission. Neglecting capture reaction<sup>9</sup>, the HF formalism yields the

<sup>9</sup>In practice this assumption is invalid for low incident neutron energies. But it is reasonably assumed that, for heavy nuclei, the capture reaction does not produce structures in neutron cross section for the

following results:

$$T_f \ll T_n \Rightarrow \bar{\sigma}_{n,f} \propto T_f \quad T_f \gg T_n \Rightarrow \bar{\sigma}_{n,f} \propto T_n \quad (1.1)$$

and

$$\bar{\sigma}_{n,tot} \propto T_n. \quad (1.2)$$

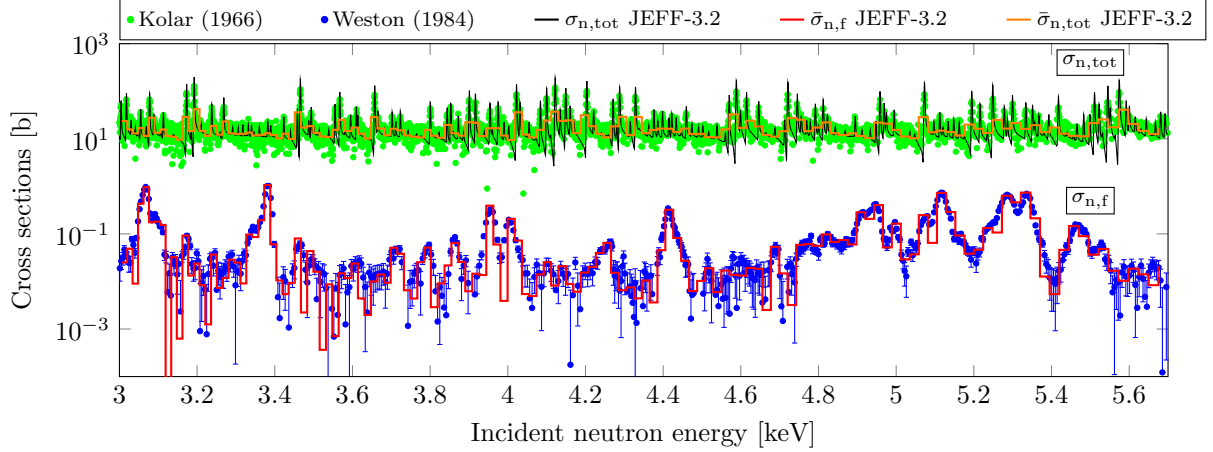


Figure 1.7 – Comparison of structures in  $^{240}\text{Pu}$  total and fission evaluated and experimental [39, 46] cross sections.

One can yet see uncorrelated broad structures between total and fission cross sections of  $^{239}\text{Pu}$  near 2.2 keV. About this energy, the fission reaction is less favored (the gap between total and fission cross sections is the largest of the energy range of Fig. 1.8). This can be interpreted using Eqs. 1.1 and 1.2. In this range, fission is somehow hindered, so that  $\bar{\sigma}_{n,f} \propto T_f$ , and as  $\bar{\sigma}_{n,tot} \propto T_n$ , uncorrelated structures can appear. When fission is more favored (in the rest of the considered energy range),  $\bar{\sigma}_{n,f} \propto T_n$  and thus correlations appear.

Uncorrelated structures are not visible for  $^{235}\text{U}$  because the fission probability is higher for this isotope than for  $^{239}\text{Pu}$ , as it can be seen in the lower part of Fig. 1.8. This higher probability to fission can be explained using empirical data [10] for fission barrier heights and neutron binding energies. For  $^{235}\text{U}$ , thermal neutrons lead to a compound nucleus excited to about 0.86 MeV above its related fission barrier, whereas for  $^{239}\text{Pu}$  this quantity is reduced to about 0.52 MeV. Hence fission is less favored for  $^{239}\text{Pu}$  and thus fission-related structures are more visible on the  $^{239}\text{Pu}$  fission cross section (as explained by the Hauser-Feshbach frame) than in  $^{235}\text{U}$  fission cross section.

The present study will focus on the fission cross section modeling, in both the RRR and the statistical energy range. Yet before showing how the fission process description can be improved in the RRR, the general collision theory, that is a common framework for resonant and average cross section modeling, will be introduced.

---

considered energy range.

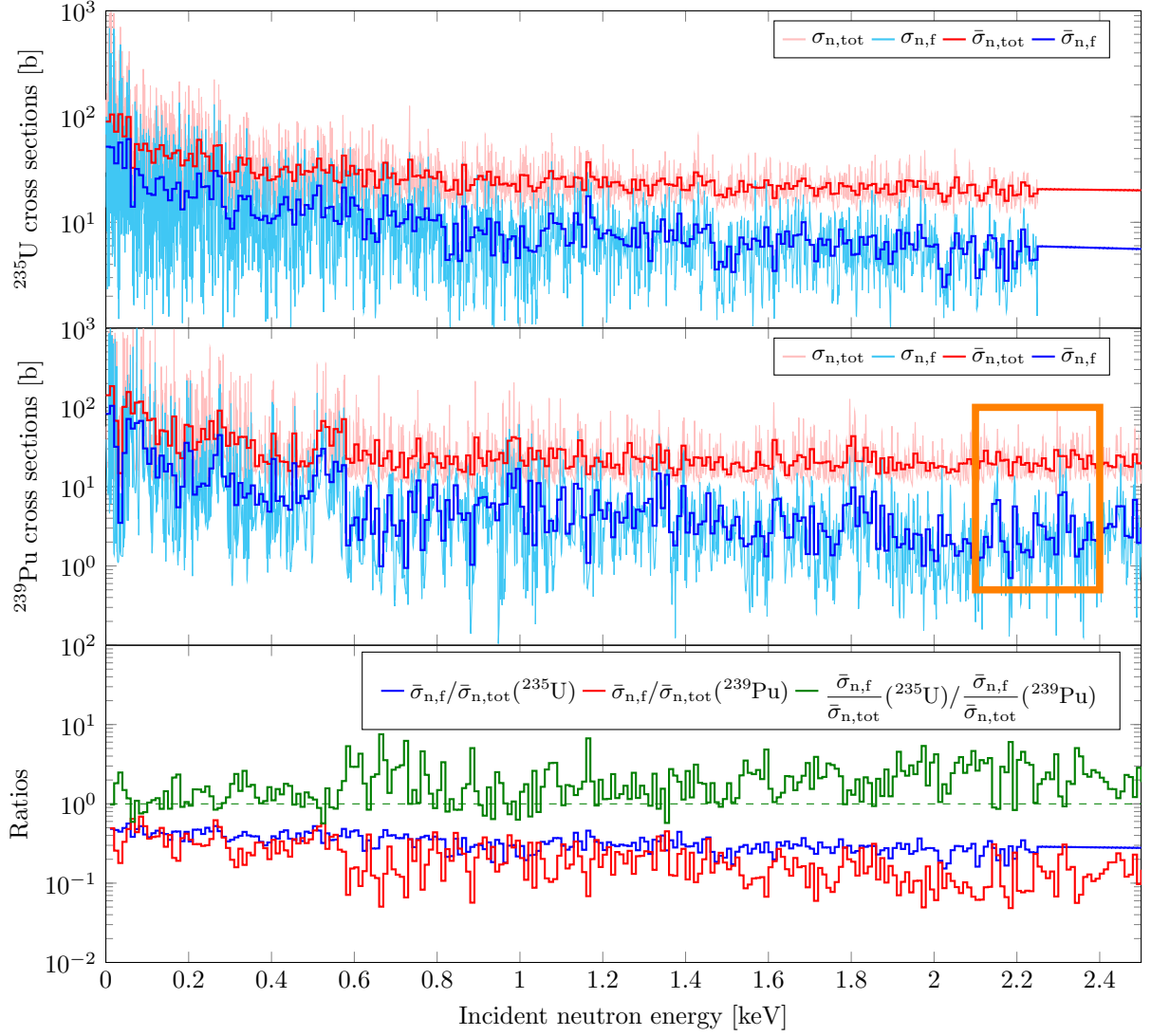


Figure 1.8 – Comparison of the JEFF-3.2 total and fission cross sections of  $^{235}\text{U}$  and  $^{239}\text{Pu}$ . To make comparison easier, cross section are averaged using a 10 eV bin.

## Chapter 2

# Collision Theory, a Background to Cross-Section Evaluation

*In this chapter the general theoretical framework used to described cross sections will be presented. It quantifies the transition probability from one state, a channel mode of two colliding particles with some properties, to another state. Wave functions related to all of the possible channels must be properly defined and combined together to obtain the total system wave function that is in turn used to define the collision matrix. The total and partial cross sections can finally be expressed in terms of the collision matrix that carries all physical information related the collision process. A general scheme of models and theories related to cross section modeling will be presented, along with some computer codes that are related to the present study.*

### Contents

---

<b>2.1</b>	<b>Theoretical Framework</b>	<b>16</b>
2.1.1	Channels and Channel Wave Functions	16
2.1.2	Normalization of Wave Functions	19
2.1.3	Wave Functions and Cross Sections	20
<b>2.2</b>	<b>Models and Codes Overview</b>	<b>22</b>

---

## 2.1 Theoretical Framework

Cross section evaluation models mostly rely on collision theory regardless of the energy range the models are used for. A reader familiar with collision theory can readily jump to Section 2.2.

### 2.1.1 Channels and Channel Wave Functions

Due to the small size of particles involved in nuclear reactions, their behavior must be described within the framework of quantum mechanics. Collision theory is used to provide an efficient way of deriving cross section expressions as a function of the particles relative velocity. This section will deal with scattering of an incident particle or *projectile* (*e.g.* a neutron) colliding a *target* (*e.g.* an actinide nucleus). The collision may change the nature and properties of the initial particles, leading to an ejectile (usually this term is used for the lighter of the final particles) and a residual nucleus. This is schematically shown in Fig. 2.1 where both classical and quantum mechanics representations are displayed.

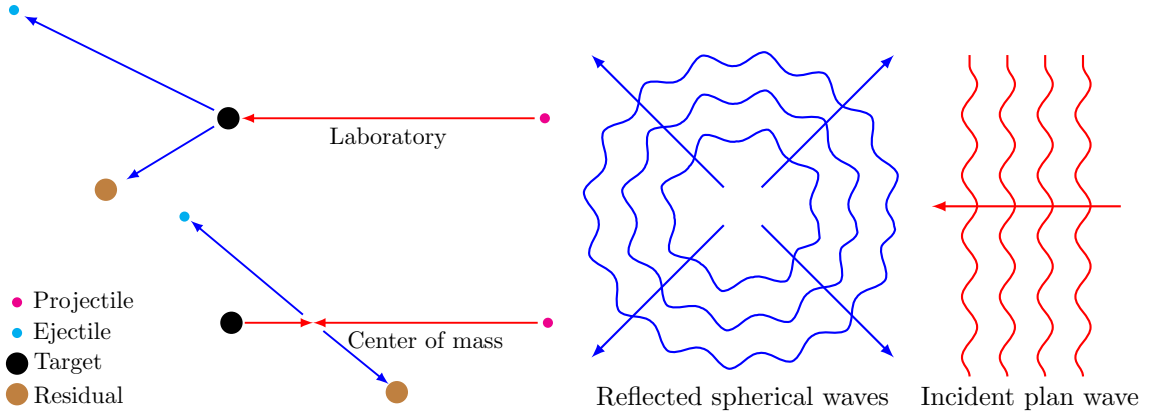


Figure 2.1 – (left) Classical representation of particle scattering in both laboratory and center-of-mass systems. (right) Equivalent representation with quantum mechanics wave functions in the center-of-mass system. Red lines correspond to the initial configuration, blue lines to the final one.

In the following,  $\alpha = (\alpha_1, \alpha_2)$  stands for a pair of particles. Parameter  $\alpha_1$  and  $\alpha_2$  describe the nature of either of the colliding particles, (*e.g.*, neutron, proton, alpha, nucleus, etc.) but also the particle internal configurations. For instance, the ground state and an excited state of the same given nucleus will be labeled by two different values of  $\alpha_1$ . When two particles collide, the total angular momentum  $J$  and the parity  $\pi$  of the system are “good quantum numbers”<sup>1</sup>. This means they are conserved along the whole collision process. A *channel*  $c$  is specified by a pair of particles in their given internal states  $\alpha$ , a set of good quantum numbers  $J^\pi$  and an additional set of the remaining quantum numbers required to precisely define the channel. These quantum numbers are sometimes referred as asymptotically good quantum numbers. For example a channel in which two particles have intrinsic spins  $I_1$  and  $I_2$  and relative orbital angular momentum  $\ell$  is labeled by

$$c = \{\alpha, J, \pi, \ell, I_1, I_2, \dots\},$$

with any additional parameters characterizing the coupling between angular momenta.

<sup>1</sup>Actually the  $\vec{J}$  projection  $M_J$  along an arbitrary axis is also a good quantum number. However unless non-spherically-symmetric external field is introduced, most of the equations are independent of  $M_J$ .



Some channel-related parameters will be used in the following such as:

- The channel reduced mass  $M_c$ :

$$M_c = \frac{M_{\alpha_1} M_{\alpha_2}}{M_{\alpha_1} + M_{\alpha_2}}, \quad (2.1)$$

where  $M_{\alpha_1}$  (reps.  $M_{\alpha_2}$ ) is the mass of particle  $\alpha_1$  (reps. particle  $\alpha_2$ ).

- The channel wave number  $k_c$ :

$$k_c = \sqrt{2M_c(E - \epsilon_c)/\hbar^2}, \quad (2.2)$$

where  $E$  is the total energy of the system and  $\epsilon_c$  is the intrinsic excitation energies of particles in channel  $c$ , *i.e.* the energy carried by the internal configuration of each particle.

- The channel Coulomb field parameter  $\eta_c$ :

$$\eta_c = \frac{Z_{\alpha_1} Z_{\alpha_2} e^2}{4\pi\epsilon_0} \frac{M_c}{\hbar^2 k_c}, \quad (2.3)$$

where  $Z_{\alpha_1}$  (reps.  $Z_{\alpha_2}$ ) is the atomic charge number of particle  $\alpha_1$  (reps. particle  $\alpha_2$ ) and  $e$  is the electric charge of an electron. In Eq. 2.3,  $\pi$  stands for the mathematical constant, not the system parity. This ambiguous notation can be found elsewhere in this document, yet it is often obvious which definition must be understood.

Target and projectile can be made of nucleons, their related spatial degrees of freedom define the nucleons *configuration space*. In collision theory, the nucleons configuration space is divided into one internal region and several external regions, the *channels*. The internal region is defined by the condition that nucleons are spatially close enough so that nuclear interactions cannot be neglected to describe the system. Compound nucleus states are included in this internal region that is shown in Fig. 2.2a.

In a given external region (or channel), nucleons are spatially gathered to form two subgroups distant enough from each other so that no “complex” (unknown) nuclear interactions between the subgroups is effective. Nuclear interactions exist within a subgroup; the nucleon configuration within a subgroup can be different from the ground state configuration of this subgroup and different from channel to channel. This leads to “labeling” channels according to their internal configurations or *excitation states* as explained before. In a given channel, the interaction potential between the two subgroups is assumed to be known, thus the wave function  $\Psi$  associated to the two subgroups can be analytically solved in the channel region and is called the *channel wave function*  $\Psi_c$ .

These external regions are shown in Fig. 2.2b. Each “tube” corresponds to a channel that expands from internal region border along a certain degree of freedom  $r_c$  that is the distance between the subgroups’ centers of mass. The  $r_c$  parameter is not defined everywhere in the configuration space as the subgroups of nucleons must be separated enough so that their centers-of-mass can be properly identified. All channels are connected to the internal region but not directly together. This means that a system of two colliding particles can only evolve from an *entrance* channel to an *exit* channel by traveling through the configuration space along an entrance “tube” to the internal region and finally along the exit “tube”. The external system total wave function (*i.e.*, the combining of all channel wave functions) is zero in the configuration space zone that is not a channel.



As  $J^\pi$  is conserved along the collision process, processes with different  $J^\pi$  do not interact, regions such as illustrated in Fig. 2.2 are specific to a given  $J^\pi$ . The bordering region between a channel  $c$  and the internal region is named the *channel surface*  $\mathcal{S}_c$ . The internal region completely enclosed within the total surface  $\mathcal{S}$  defined as

$$\mathcal{S} = \sum_c \mathcal{S}_c. \quad (2.4)$$

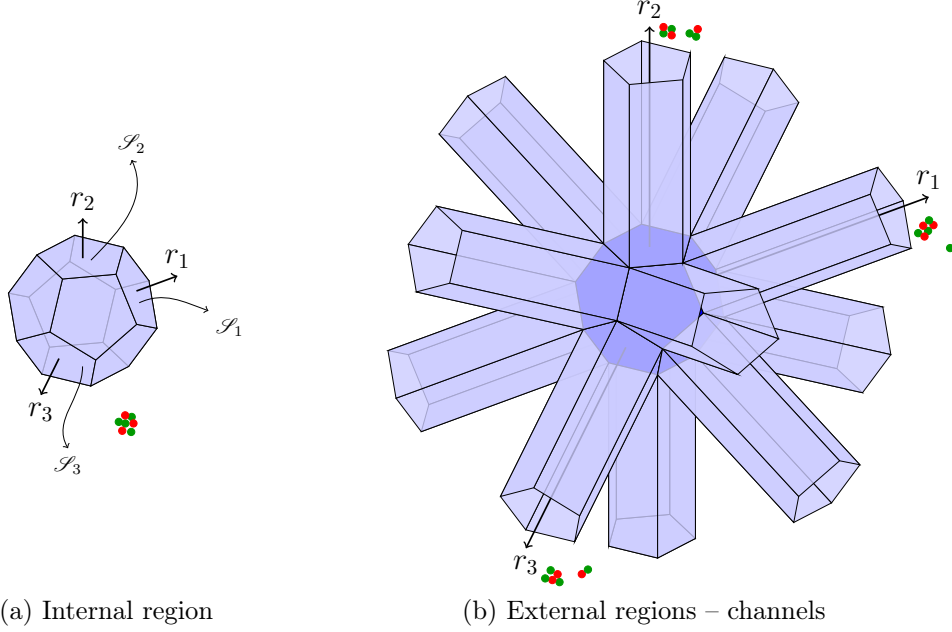


Figure 2.2 – Representation of the configuration space regions [47]. The internal region corresponds to the compound nucleus configurations. In the channel regions two “sub-groups” of nucleons are already well separated. Some channel surfaces  $\mathcal{S}_c$  and the related channel degrees of freedom  $r_c$  are shown. Illustration of nucleon configurations is shown for the compound nucleus region and for some channels.

To obtain the global (internal and external) system wave function, channel waves have to be smoothly matched at the border between the channels and the internal region. As channel  $c$  evolves along the  $r_c$  degree of freedom (see Fig. 2.2b), the border is defined by the *matching radius* or *channel radius*  $a_c$  so that  $r_c = a_c$ . The smooth matching conditions are given by

$$\forall c, \left\{ \begin{array}{l} \Psi^{\text{int}}|_{r_c=a_c} = \Psi_c|_{r_c=a_c} \\ \text{grad}_n \Psi^{\text{int}}|_{r_c=a_c} = \text{grad}_n \Psi_c|_{r_c=a_c} \end{array} \right., \quad (2.5)$$

where  $\text{grad}_n$  is the gradient normal to the internal surface. Equations 2.5 are verified on the channel surface  $\mathcal{S}_c$ . As long as  $r_c$  is a relevant degree of freedom in the configuration space, this  $\mathcal{S}_c$  region can be defined by  $r_c = a_c$ . This region splitting approach (distinct wave functions defined in different external regions and matched at a certain radius with the internal region wave) is common in both resonance and statistical energy ranges. Two methods for matching these waves at boundaries will be detailed in Chapters 3 and 4. They lead to the formalisms used respectively for the modeling of resonant and average cross sections. In the following, focus will be made on how cross sections can be obtained providing that these wave functions are smoothly matched.

In a given channel  $c$ , the potential is asymptotically symmetric and the wave function  $\Psi_c$  can be expanded using spherical harmonics  $Y_{m_\ell}^\ell(\hat{\Omega}_c)$ , where  $\hat{\Omega}_c$  is the normalized

direction vector pointing from particle  $\alpha_1$  to particle  $\alpha_2$ , it reads

$$\Psi_c \propto i^\ell Y_{m_\ell}^\ell(\hat{\Omega}_c) \frac{u_c(r_c)}{r_c}, \quad (2.6)$$

where the radial wave function  $u_c$  is solution of the radial Schrödinger equation

$$\left[ \frac{d^2}{dr_c^2} - \frac{\ell(\ell+1)}{r_c^2} - 2\frac{\eta_c k_c}{r_c} + k_c^2 \right] u_c(r_c) = 0, \quad (2.7)$$

which is the wave equation when no potentials but the centrifugal and Coulomb fields are effective. Defining the variable  $\rho_c = k_c r_c$ , Eq. 2.7 becomes

$$\left[ \frac{d^2}{d\rho_c^2} - \frac{\ell(\ell+1)}{\rho_c^2} - 2\frac{\eta_c}{\rho_c} + 1 \right] u_c(\rho_c) = 0. \quad (2.8)$$

There are two real and linearly independent solutions of the radial equation 2.8. They are known as the *regular*  $F_c$  and *irregular*  $G_c$  Coulomb wave functions [48]. Their names regular and irregular refer to the fact that  $\lim_{\rho_c \rightarrow 0} F_c(\rho_c) = 0$  whereas  $\lim_{\rho_c \rightarrow 0} G_c(\rho_c) \neq 0$ . Another couple of linearly independent solutions are defined by

$$\begin{cases} I_c(r_c) &= [G_c(\rho_c) - iF_c(\rho_c)]e^{i\omega_c} \\ O_c(r_c) &= [G_c(\rho_c) + iF_c(\rho_c)]e^{-i\omega_c} \end{cases}. \quad (2.9)$$

The  $\omega_c$  parameter is related to the Coulomb phase shift  $\sigma_c = \arg \Gamma(1 + \ell + i\eta_c)$  ( $\Gamma$  being the gamma function [48]) by

$$\omega_c = \sigma_c - \sigma_{c|\ell=0} = \sum_{n=1}^{\ell} \arctan\left(\frac{\eta_c}{n}\right). \quad (2.10)$$

Those functions have interesting asymptotic properties that are needed to obtained cross section expressions and that are presented in the following blue insert. From the radial wave functions (Eq. 2.9), two linearly independent forms of the channel wave function  $\Psi_c$  can be defined:

$$\begin{cases} \mathcal{J}_c(r_c) &= i^\ell Y_{m_\ell}^\ell(\hat{\Omega}_c) \frac{I_c(r_c)}{v_c^{1/2} r_c} \\ \mathcal{O}_c(r_c) &= i^\ell Y_{m_\ell}^\ell(\hat{\Omega}_c) \frac{O_c(r_c)}{v_c^{1/2} r_c} \end{cases}, \quad (2.11)$$

where  $v_c = \hbar k_c / M_c$  is the asymptotic relative velocity of the two particles in channel  $c$ . This velocity is introduced here so that wave functions are normalized to a one unit flux of probability current.

### 2.1.2 Normalization of Wave Functions

For  $\mathcal{J}_c$ , (resp.  $\mathcal{O}_c$ ) the current flows to (resp. from) the internal region. This can be shown if one considers the probability current defined by

$$\vec{j}[\Psi] = \frac{\hbar}{2iM_c} \left[ \Psi^* \vec{\nabla} \Psi - \Psi \vec{\nabla} \Psi^* \right], \quad (2.12)$$

where  $\Psi$  can be either of the wave functions  $\mathcal{J}_c$  and  $\mathcal{O}_c$ . The del operator  $\vec{\nabla}$  can be written using the spherical coordinate system as

$$\vec{\nabla} = \frac{\partial}{\partial r_c} \hat{r}_c + \frac{1}{r_c} \vec{\nabla}_{\hat{\Omega}_c}, \quad (2.13)$$

where  $\hat{r}_c = \frac{\vec{r}_c}{r_c}$  and  $\vec{\nabla}_{\hat{\Omega}_c}$  operates on  $\hat{\Omega}_c$  only. Considering for instance  $\Psi = \mathcal{J}_c$ , the probability current can be written

$$\vec{j}[\mathcal{J}_c] = \frac{\hbar}{2iM_c} \left[ \frac{Y_{m_\ell}^{\ell*} Y_{m_\ell}^\ell}{v_c r_c} \left( I_c^* \frac{d}{dr_c} \frac{I_c}{r_c} - I_c \frac{d}{dr_c} \frac{I_c^*}{r_c} \right) \hat{r}_c + \frac{|I_c|^2}{v_c r_c^3} \left( Y_{m_\ell}^{\ell*} \vec{\nabla}_{\hat{\Omega}_c} Y_{m_\ell}^\ell - Y_{m_\ell}^\ell \vec{\nabla}_{\hat{\Omega}_c} Y_{m_\ell}^{\ell*} \right) \right]. \quad (2.14)$$

The second term tends to zero faster than the first one due to the  $r_c$  dependence<sup>2</sup>. It is also the only term that will lead to a component in the  $\hat{r}_c$  direction. One can thus only consider the first term

$$\vec{j}[\mathcal{J}_c] \cdot \hat{r}_c = \frac{\hbar}{2iM_c} \frac{Y_{m_\ell}^{\ell*} Y_{m_\ell}^\ell}{v_c r_c} \left( \frac{I_c^* I_c'}{r_c} - \frac{|I_c|^2}{r_c^2} - \frac{I_c I_c'^*}{r_c} + \frac{|I_c|^2}{r_c^2} \right) = \frac{Y_{m_\ell}^{\ell*} Y_{m_\ell}^\ell}{2ik_c r_c^2} (I_c^* I_c' - I_c I_c'^*), \quad (2.15)$$

where  $v_c$  was replaced by its expression. From Eq. 2.9 it can be seen that  $I_c^* = O_c$ . The probability flux passing through a sphere of radius  $r_c$  is obtained by integration of Eq. 2.15 over the related sphere:

$$\Phi[\mathcal{J}_c] = \int_{4\pi} d^2\hat{\Omega}_c r_c^2 \vec{j}[\mathcal{J}_c] \cdot \hat{r}_c = \frac{1}{2ik_c} \mathcal{W}(O_c, I_c) = \mathcal{W}(F_c, G_c), \quad (2.16)$$

where  $\mathcal{W}$  is the Wronskian operator. The derivative of the Coulomb functions is made with respect of  $\rho_c$ , with the consequence of removing the  $k_c$  coefficient. Finally, considering the probability currents related to both  $\mathcal{J}_c$  and  $\mathcal{O}_c$  functions, and using the Wronskian property of the Coulomb functions [48], the probability fluxes are

$$\begin{cases} \Phi[\mathcal{J}_c] &= -1 \\ \Phi[\mathcal{O}_c] &= 1 \end{cases}, \quad (2.17)$$

which correspond to an inward (respectively outward) propagating, one-unit-flux wave function for  $\mathcal{J}_c$  (respectively  $\mathcal{O}_c$ ).

### 2.1.3 Wave Functions and Cross Sections

The unit-flux-normalized incoming plane wave, propagating downward the  $z$ -axis, can be expressed in terms of Coulomb wave functions  $F_c$  as<sup>3</sup> [5]

$$\Psi_\alpha^{\text{inc}} = \frac{1}{k_\alpha v_\alpha^{1/2}} \sum_{\ell=0}^{\infty} i^\ell \sqrt{4\pi(2\ell+1)} e^{i\omega_\alpha \ell} \frac{F_{\alpha\ell}}{r_\alpha} Y_\ell^0(\hat{\Omega}_\alpha). \quad (2.18)$$

Here the  $\alpha$  and  $\ell$  indices have been used instead of  $c$  to exhibit specific dependencies, and especially no specific dependency on  $J^\pi$ .  $\Psi_\alpha^{\text{inc}}$  can be written in terms of  $\mathcal{J}_c$  and  $\mathcal{O}_c$  using Eq. 2.11 as

$$\Psi_\alpha^{\text{inc}} = \sum_{\ell=0}^{\infty} \underbrace{\frac{i\sqrt{\pi(2\ell+1)}}{k_\alpha}}_{y_c} (\mathcal{J}_c - e^{2i\omega_c} \mathcal{O}_c). \quad (2.19)$$

<sup>2</sup>It can be shown that this term can be rigorously omitted if one considers afterward probability current, for a given  $\ell$ , summed over all possible  $m_\ell$  values.

<sup>3</sup>In case of no Coulomb field, *i.e.*  $\eta_c = 0$ , this expression has a more common form:  $\Psi_\alpha^{\text{inc}} = v_\alpha^{-1/2} e^{ik_\alpha r_\alpha}$ .

It can be noticed that for all partial incoming waves included in the sum of Eq. 2.18, the  $z$ -projection of their relative orbital momentum  $m_\ell$  is zero. As the total angular momentum  $J$  (and also the parity  $\pi$ ) is a result of the coupling between all angular momenta ( $\vec{J} = \vec{I}_1 + \vec{I}_2 + \vec{\ell}$ ), an infinity of processes with different  $J^\pi$  are induced by the incident plane wave  $\Psi_\alpha^{\text{inc}}$  defined in Eq. 2.18.

The channel wave function can be written in a general way as

$$\Psi_c = x_c \mathcal{O}_c + y_c \mathcal{I}_c, \quad (2.20)$$

where  $x_c$  and  $y_c$  are expansion coefficients. The *collision matrix*  $\mathbf{U}$  (and its coefficients  $U_{cc'}$ ) is defined by the general relation

$$x_c = - \sum_{c'} U_{cc'} y_{c'}. \quad (2.21)$$

This expression transposes the fact that the probability flux flowing out of channel  $c$  is a result of the sum of the probability fluxes flowing from channels  $c'$  (through the internal volume). Using the collision matrix, the channel wave function can still be written in a general way as

$$\Psi_c = \sum_{c'} (\mathcal{I}_c \delta_{cc'} - U_{cc'} \mathcal{O}_c) y_{c'}. \quad (2.22)$$

The total wave function in the external region is

$$\Psi = \sum_c \Psi_c = \sum_{cc'} (\mathcal{I}_c \delta_{cc'} - U_{cc'} \mathcal{O}_c) y_{c'}. \quad (2.23)$$

The incident plane wave  $\Psi_\alpha^{\text{inc}}$  of Eq. 2.19 is added and removed from the total wave function  $\Psi$  (Eq. 2.23) so that

$$\Psi = \Psi_\alpha^{\text{inc}} + \sum_{cc'} (\mathcal{I}_c \delta_{cc'} - U_{cc'} \mathcal{O}_c) y_{c'} - \sum_{cc'} (\mathcal{I}_c \delta_{cc'} - e^{2i\omega_c} \mathcal{O}_c \delta_{cc'}) y_{c'}, \quad (2.24)$$

$$= \Psi_\alpha^{\text{inc}} + \sum_{cc'} (e^{2i\omega_c} \delta_{cc'} - U_{cc'}) \mathcal{O}_c y_{c'}. \quad (2.25)$$

The incident wave function has thus been isolated out of the total wave. The second term of Eq. 2.25 is related to the probability of flowing out of channel  $c$  ( $\mathcal{O}_c$ ), from flowing in from channel  $c'$  ( $y_{c'}$ ).

As mentioned earlier, many processes with different  $J^\pi$  occur independently, hence the collision matrix  $\mathbf{U}$  is a block diagonal matrix, with blocks corresponding to different  $J^\pi$  values. It is more usual to work with such  $J^\pi$  blocks written  $\mathbf{U}^{J^\pi}$ . The partial cross section can be obtained from the current probability related to  $(e^{2i\omega_c} \delta_{cc'} - U_{cc'}) \mathcal{O}_c y_{c'}$  and is given by [5]

$$\sigma_{cc'}^{J^\pi} = \frac{\pi}{k_c^2} g_J |e^{2i\omega_c} \delta_{cc'} - U_{cc'}^{J^\pi}|^2, \quad (2.26)$$

where

$$g_J = \frac{2J+1}{(2I_1+1)(2I_2+1)} \quad (2.27)$$

is called the *spin factor*<sup>4</sup>. As the collision matrix is unitary [5], the total cross section depends only on the collision matrix diagonal terms and can thus be obtained easily from

$$\sigma_{c,\text{tot}}^{J^\pi} = \sum_{c'} \sigma_{cc'}^{J^\pi} = \frac{2\pi}{k_c^2} g_J (1 - \text{Re}[U_{cc}^{J^\pi}]). \quad (2.28)$$

---

<sup>4</sup> The derivation of this term involves summation over  $z$  projections of all angular momenta [5]. This summation is responsible of the disappearance of the  $(2\ell+1)$  term in  $y_c$ .

## 2.2 Models and Codes Overview

Collision theory is a keystone in cross section modeling. Other related specialized theories and frameworks ( $\mathfrak{R}$ -matrix theory for resonant cross sections and Hauser-Feshbach for average cross sections) are built on this former general theory. The different energy ranges involved in cross section evaluation (RRR, URR, Continuum) directly reflect this change in the underlying models (respectively an  $\mathfrak{R}$ -matrix approximation, the average  $\mathfrak{R}$ -matrix model and the optical model). The relation between these energy ranges, on one side, and related models and theories, on the other side, is illustrated in Fig. 2.3.

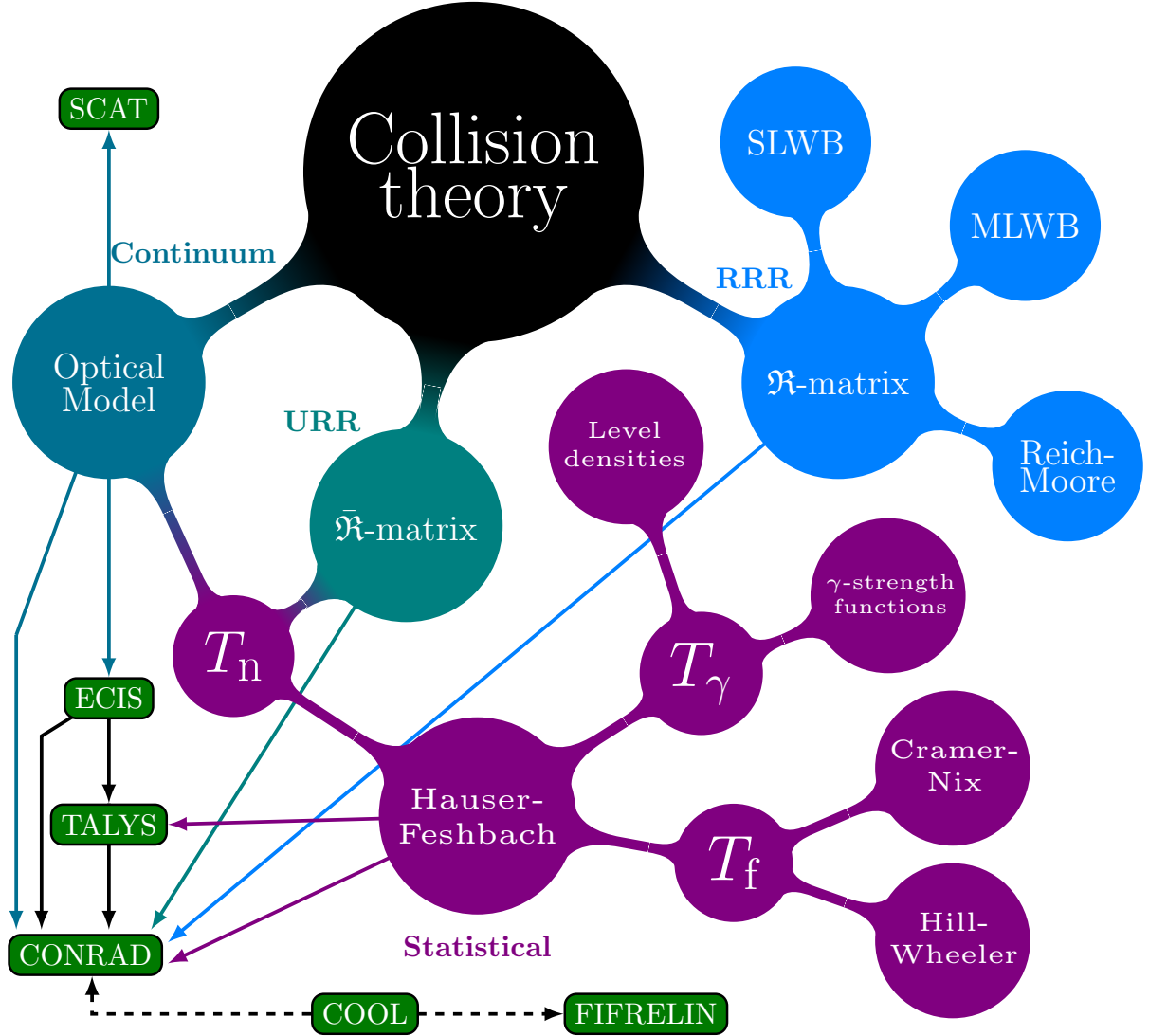


Figure 2.3 – Overview of models and codes used in cross section modeling. Bubble colors correspond to the different energy ranges. Computer codes related to the present study are shown in green boxes.

$\mathfrak{R}$ -matrix approximations (SLBW, MLBW and Reich-Moore) used in practice in the RRR will be presented along with the general  $\mathfrak{R}$ -matrix in Chapter 3. The Hauser-Feshbach framework and its related sub-models (including the average  $\mathfrak{R}$ -matrix and optical models) will be detailed in Chapter 4. All code developments related to this PhD work were performed in the CONRAD code [3]. Yet CONRAD is not the only code dealing with cross section modeling. Other computer codes related to the present work are also indicated in Fig. 2.3. They can be briefly introduced as follows:

- The SCAT spherical optical model code [49], developed at CEA-Bruyères-le-Châtel (France) by Olivier Bersillon. This program is not directly used in the present work, but a similar implementation has been introduced in the CONRAD code in 2011 by Pascal Archier [50].
- The ECIS coupled channel optical model code [1] has been widely used for half a century and developed since the 60' by Jacques Raynal at CEA-Saclay (France).
- The TALYS nuclear reaction code [51] is a widely used reference code developed from the end of the 90' by Arjan Koning and Marieke Duijvestijn at NRG/Petten (The Netherlands) and Stéphane Hilaire at CEA-Bruyères-le-Châtel. It contains many nuclear reaction models that makes it suitable for calculations in the energy range [1 keV, 200 MeV] and can deal with many observables: cross sections, spectra, angular distributions, *etc.* This energy range corresponds to high-energy reactions<sup>5</sup> making associated models particularly suited, for instance, for astrophysics applications.
- The FIFRELIN code [52] that simulates various fission observables, has been developed at CEA-Cadarache (France) by Oliver Litaize, Olivier Serot and David Regnier. This code is not used in the present study, but is mentioned here since it shares with the CONRAD code the jointly-developed COOL libraries containing nuclear physics models.
- The AVXSF code [23, 24], not represented in Fig. 2.3, is an average fission cross section modeling code developed by J. Eric Lynn from LANL (USA) and Olivier Bouland from CEA-Cadarache (France). This code is, in particular, able to treat the intermediate structures in the second well and the coupling of class-I and class-II states by Monte Carlo sampling and combinatorial level densities. This code is mentioned here because its combinatorial routine has been coupled to the CONRAD code for the present studies.

CONRAD [3] is an evaluation-dedicated computer code developed at CEA-Cadarache to produce evaluated data along with related variance-covariance matrices. The initial purpose of the code was the treatment of the resolved resonances. It has recently been extended to the treatment of various data types: prompt neutron fission spectrum [53], fission yields [54], *etc.* The code has the capability of analyzing both microscopic and integral experiments. The code contains an internal library of nuclear models (the COOL library) but is also coupled with external nuclear-reaction programs like the TALYS and ECIS codes using them as black boxes.

The purpose of the present work is to improve very significantly the models used for the description of fission cross sections. Few capabilities were present in CONRAD for the treatment of average cross sections in the statistical range. It was then necessary to develop a proper frame making possible investigations on fission cross section in the statistical range. TALYS has been used as a reference guideline for the implementation of this framework for the calculation of average cross sections in the statistical range. Other partial cross sections must be properly treated so that improvements brought along the present work are relevant. Although applications presented in this document are mostly related to the statistical range (URR and Continuum), some investigations in the RRR will also be presented in Chapter 3.

---

<sup>5</sup>The meaning of the term “high energy” depends on the considered field. For particle physics it will be related to colliding particles with energies above 1 GeV, for astrophysics it may be used for energies up to 200 MeV whereas for nuclear reactor physics, energies near 1 MeV can be regarded as high.





# Chapter 3

## RRR-Related Fission Model Improvements

*In this chapter, the general method for modeling cross sections in the Resolved Resonance Range (RRR) will be presented. It will be followed by an introduction to the standard approximations used in practice. The extension of the formalism to fission channels will be presented, and exemplified by an analysis of the fission resonance parameters involved in the modeling of the  $^{240}\text{Pu}(n,f)$  cross section.*

### Contents

---

<b>3.1</b>	<b>General Theory and Practical Aspects</b>	<b>26</b>
3.1.1	$\mathfrak{R}$ -Matrix Theory	26
3.1.2	Single- and Multi-Level Breit-Wigner Formalism	30
3.1.3	Reich-Moore	32
<b>3.2</b>	<b>Lynn Extension to Fission Channels</b>	<b>33</b>
3.2.1	Double-Humped Barrier Textbook Example	34
3.2.2	Penetration Factor Modeling	37
<b>3.3</b>	<b>Sub-Threshold Analysis of <math>^{240}\text{Pu}(n,f)</math></b>	<b>38</b>

---

## 3.1 General Theory and Practical Aspects

All cross section evaluation techniques in the RRR rely on the  $\Re$ -matrix theory or on related approximations. The general theory of resonance cross section modeling will be presented as well as some practical approximations commonly used in evaluation work.

### 3.1.1 $\Re$ -Matrix Theory

The  $\Re$ -matrix theory was elaborated [4, 55] in the 40's to give a proper framework in the interpretation of the resonance phenomena observed in two-body collisions. Several authors [5, 47] have developed the theory and gave full mathematical details of its derivation. Therefore only explanations necessary to the understanding of the rest of this document will be provided here. The complete derivation can be found in the encyclopedic paper of Lane and Thomas [5]. This derivation is made for channels involving particles, it could seem tedious and not directly related to the fission reaction applications, yet it makes the extension to fission reaction, that is presented later in this chapter, more straightforward. Most of the notations of Ref. [5] are adopted here.

The purpose of the  $\Re$ -matrix theory, that will be discussed now, is to obtain a parameterization of the collision matrix that exhibits an explicit energy dependence, and that thus relies on energy-independent parameters only. The principal assumption of the theory is that the wave function in the internal region<sup>1</sup>  $\Psi$  can be expanded on a set of eigenfunctions  $X_\lambda$  of the system Hamiltonian  $\hat{H}$ :

$$\Psi = \sum_{\lambda} A_{\lambda} X_{\lambda}. \quad (3.1)$$

These eigenfunctions  $X_\lambda$  are defined by an eigenvalue boundary condition, more details can be found about their definition in Ref. [5]. The  $A_\lambda$  coefficients are obtained by integration of  $\Psi$  over the internal region  $V_{\text{int}}$

$$A_{\lambda} = \int_{V_{\text{int}}} d\tau X_{\lambda}^* \Psi, \quad (3.2)$$

where  $d\tau$  is an infinitesimal integration volume of the configuration space. The channel “surface” wave functions are defined by either

$$\begin{aligned} \varphi_{c=\alpha i \ell s}^{J^\pi M_J} &= \sum \langle i m_i I M_I | s m_s \rangle \langle \ell m_\ell s m_s | J M_J \rangle a_c^{-1} i^\ell Y_{m_\ell}^\ell \\ &\text{or} \\ \varphi_{c=\alpha i \ell j}^{J^\pi M_J} &= \sum \langle i m_i \ell m_\ell | j m_j \rangle \langle I M_I j m_j | J M_J \rangle a_c^{-1} i^\ell Y_{m_\ell}^\ell \end{aligned} \quad (3.3)$$

where  $I$ ,  $i$  and  $s$  are respectively the target, projectile and channel spins. The bracket signs correspond to the usual Clebsch-Gordan coefficients [56]. The channel radii  $a_c$  are defined in Chapter 1, and  $Y_{m_\ell}^\ell$  are the usual spherical harmonics. The channel spin  $s$  is obtained by coupling  $I$  and  $i$ ,  $\vec{s} = \vec{i} + \vec{I}$ . The total angular momentum of the system  $J$  is thus obtained by coupling  $s$  with the relative orbital momentum  $\ell$ ,  $\vec{J} = \vec{s} + \vec{\ell}$ . The alternative representation would consist in first coupling  $\ell$  and  $i$  to obtain the projectile total angular momentum  $\vec{j} = \vec{i} + \vec{\ell}$ , that is then coupled to  $I$  to obtain  $\vec{J} = \vec{j} + \vec{I}$ . These two definitions are correct, in the RRR and URR it is usually the coupling scheme involving  $s$  that is used, whereas for the continuum energy range (treated with an optical

---

<sup>1</sup>cf. Chapter 1

model), it is coupling scheme involving  $j$  that is used. For instance in resonance models the channel spin  $s$  is preferred, whereas in optical models (statistical range) the projectile total angular momentum  $j$  is favored. The term “surface” must be understood in the sense of internal region boundary surface (*cf.* Chapter 1, Fig. 2.2). The surface wave function  $\varphi_c$  has finite values on  $\mathcal{S}_c$  only and is zero elsewhere. The channel surface wave functions are orthogonal and normalized on the internal surface  $\mathcal{S} = \sum_c \mathcal{S}_c$ , so that

$$\int_{\mathcal{S}} d\mathcal{S} \varphi_c^* \varphi_{c'} = \delta_{cc'}. \quad (3.4)$$

The  $X_\lambda$  eigenfunction is related to the eigenvalue  $E_\lambda$  and depends on a set of boundary conditions  $\{B_c\}_c$  defined at the surface  $\mathcal{S}$  by

$$\frac{\delta_{\lambda c}}{\gamma_{\lambda c}} = B_c, \quad (3.5)$$

where the *value quantity*  $\gamma_{\lambda c}$  and the *derivative quantity*  $\delta_{\lambda c}$  are defined as

$$\begin{aligned} \gamma_{\lambda c} &= \sqrt{\frac{\hbar^2}{2M_c a_c}} \int_{\mathcal{S}} d\mathcal{S} \varphi_c^* X_\lambda, \\ \delta_{\lambda c} &= \sqrt{\frac{\hbar^2}{2M_c a_c}} \int_{\mathcal{S}} d\mathcal{S} \varphi_c^* \text{grad}_n(r_c X_\lambda), \end{aligned} \quad (3.6)$$

where  $M_c$  is defined in Chapter 1. The proper definition of  $X_\lambda$  and the choice of the arbitrary conditions are beyond the scope of the present work. One should refer to Refs. [5, 47] for discussion about this point. It should yet be noted that the boundary conditions  $\{B_c\}_c$  are independent of both  $\lambda$  and  $E$ , however the  $A_\lambda$  coefficients do depend on  $E$ .

The derivation of the  $\mathfrak{R}$ -matrix theory using the Green’s functions can be obtained as done in Ref. [5]. Considering the waves  $\Psi$  and  $X_\lambda$ , eigenfunctions of the system Hamiltonian  $\hat{H}$ , that are related to the eigenvalues  $E$  and  $E_\lambda$  respectively so that

$$\hat{H}X_\lambda = E_\lambda X_\lambda, \quad \hat{H}\Psi = E\Psi. \quad (3.7)$$

The complex conjugate of the first of these expressions is multiplied by  $\Psi$ , and the second expression is multiplied by  $X_\lambda^*$ , so that

$$\Psi[\hat{H}X_\lambda]^* = \Psi E_\lambda X_\lambda^*, \quad X_\lambda^* \hat{H}\Psi = X_\lambda^* E\Psi. \quad (3.8)$$

The second expression is subtracted from the first one, and the result is integrated over the internal region  $V_{\text{int}}$

$$(E_\lambda - E) \int_{V_{\text{int}}} d\tau \Psi X_\lambda^* = \int_{V_{\text{int}}} d\tau \left( \Psi[\hat{H}X_\lambda]^* - X_\lambda^* \hat{H}\Psi \right). \quad (3.9)$$

The potential part  $\hat{V}$  in  $\hat{H}$  is assumed to be self-adjoint, so that

$$\int_{V_{\text{int}}} d\tau \left( \Psi[\hat{V}X_\lambda]^* - X_\lambda^* \hat{V}\Psi \right) = 0. \quad (3.10)$$

Only the kinetic operator  $\hat{T}$  remains in the right-hand-side of Eq. 3.9. Then using Eq. 3.2 and the Green's theorem, Eq. 3.9 reduces to

$$(E_\lambda - E)A_\lambda = \int_{\mathcal{S}} d\mathcal{S} \frac{-\hbar^2}{2M_c} (\Psi \text{grad}_n X_\lambda^* - X_\lambda^* \text{grad}_n \Psi). \quad (3.11)$$

Similarly to  $\gamma_{\lambda c}$  and  $\delta_{\lambda c}$ , the *value quantity*  $V_c$  and the *derivative quantity*  $D_c$  can be defined for  $\Psi$  as

$$\begin{aligned} V_c &= \sqrt{\frac{\hbar^2}{2M_c a_c}} \int_{\mathcal{S}} d\mathcal{S} \varphi_c^* \Psi, \\ D_c &= \sqrt{\frac{\hbar^2}{2M_c a_c}} \int_{\mathcal{S}} d\mathcal{S} \varphi_c^* \text{grad}_n (r_c \Psi). \end{aligned} \quad (3.12)$$

Expansion of  $\Psi$  and  $\text{grad}_n(r_c \Psi)$  on  $\mathcal{S}$  using the channel surface functions is assumed to be complete, so that

$$\begin{aligned} \Psi &= \sum_c \sqrt{\frac{2M_c a_c}{\hbar^2}} V_c \varphi_c, \\ \text{grad}_n r_c \Psi &= \sum_c \sqrt{\frac{2M_c a_c}{\hbar^2}} D_c \varphi_c = a_c \text{grad}_n \Psi + \Psi. \end{aligned} \quad (3.13)$$

Similarly for  $X_\lambda$ , one has

$$\begin{aligned} X_\lambda &= \sum_c \sqrt{\frac{2M_c a_c}{\hbar^2}} \gamma_{\lambda c} \varphi_c, \\ \text{grad}_n r_c X_\lambda &= \sum_c \sqrt{\frac{2M_c a_c}{\hbar^2}} \delta_{\lambda c} \varphi_c = a_c \text{grad}_n X_\lambda + X_\lambda. \end{aligned} \quad (3.14)$$

Using these four relations into Eq. 3.11, the  $A_\lambda$  coefficients are expressed as

$$A_\lambda = \frac{1}{E_\lambda - E} \sum_c \gamma_{\lambda c} (D_c - B_c V_c). \quad (3.15)$$

Using this expression in the  $\Psi$  expansion (Eq. 3.1), after a projection on  $\varphi_{c'}^*$ , a relation between different value quantities  $V_c$  is obtained

$$V_{c'} = \sum_{c\lambda} \frac{\gamma_{\lambda c} \gamma_{\lambda c'}}{E_\lambda - E} (D_c - B_c V_c). \quad (3.16)$$

In matrix form it becomes

$$\vec{V} = \mathfrak{R}(\vec{D} - \mathbf{B}\vec{V}), \quad (3.17)$$

where  $\mathbf{B}$  being a diagonal matrix (so that  $\mathbf{B}_{cc'} = B_c \delta_{cc'}$ ). This introduces the  $\mathfrak{R}$ -matrix, whose coefficients  $R_{cc'}$  are given by

$$R_{cc'} = \sum_\lambda \frac{\gamma_{\lambda c} \gamma_{\lambda c'}}{E_\lambda - E}. \quad (3.18)$$

The channel wave function expression  $\Psi_c = x_c \mathcal{O}_c + y_c \mathcal{I}_c$  (*cf.* Chapter 2, Eq. 2.20) is now used to obtain the value and derivative quantities. Using this  $\Psi_c$  in Eq. 3.12,  $V_c$  and  $D_c$  can be calculated as

$$\begin{aligned} V_c &= \sqrt{\frac{\hbar^2}{2M_c a_c v_c}} (x_c \mathcal{O}_c + y_c \mathcal{I}_c) = \sqrt{\frac{\hbar}{2}} \rho_c^{-\frac{1}{2}} (x_c \mathcal{O}_c + y_c \mathcal{I}_c), \\ D_c &= \sqrt{\frac{\hbar^2 a_c}{2M_c v_c}} k_c (x_c \mathcal{O}'_c + y_c \mathcal{I}'_c) = \sqrt{\frac{\hbar}{2}} \rho_c^{\frac{1}{2}} (x_c \mathcal{O}'_c + y_c \mathcal{I}'_c). \end{aligned} \quad (3.19)$$

These must verify Eq. 3.17, which is written in matrix notation

$$(1 - \Re(\rho \mathbf{O}' \mathbf{O}^{-1} - \mathbf{B})) \mathbf{O} \rho^{-\frac{1}{2}} \vec{x} = -(1 - \Re(\rho \mathbf{I}' \mathbf{I}^{-1} - \mathbf{B})) \mathbf{I} \rho^{-\frac{1}{2}} \vec{y}, \quad (3.20)$$

where  $\rho, \mathbf{I}, \mathbf{O}$  are diagonal matrices and  $\vec{x}, \vec{y}$  are column vectors. The collision matrix  $\mathbf{U}$  is obtained by identification of its definition  $\vec{x} = -\mathbf{U} \vec{y}$  (cf. Chapter 1, Eq. 2.21) with Eq. 3.20, so that  $\mathbf{U}$  is expressed as

$$\mathbf{U} = \rho^{\frac{1}{2}} \mathbf{O}^{-1} (1 - \Re(\rho \mathbf{O}' \mathbf{O}^{-1} - \mathbf{B}))^{-1} (1 - \Re(\rho \mathbf{I}' \mathbf{I}^{-1} - \mathbf{B})) \mathbf{I} \rho^{-\frac{1}{2}}. \quad (3.21)$$

Defining the following diagonal matrices:

$$\begin{aligned} \mathbf{L} &= \rho \mathbf{O}' \mathbf{O}^{-1}, & \mathcal{L} &= \rho \mathbf{I}' \mathbf{I}^{-1}, \\ \mathbf{L}^0 &= \mathbf{L} - \mathbf{B}, & \mathcal{L}^0 &= \mathcal{L} - \mathbf{B}, \\ \mathbf{\Omega} &= \mathbf{I}^{\frac{1}{2}} \mathbf{O}^{-\frac{1}{2}}, & \mathfrak{P} &= \rho \mathbf{I}^{-1} \mathbf{O}^{-1}. \end{aligned} \quad (3.22)$$

The final relation between  $\Re$  and  $\mathbf{U}$  becomes

$$\mathbf{U} = \mathbf{\Omega} \mathfrak{P}^{\frac{1}{2}} (1 - \Re \mathbf{L}^0)^{-1} (1 - \Re \mathcal{L}^0) \mathfrak{P}^{-\frac{1}{2}} \mathbf{\Omega}. \quad (3.23)$$

Dependencies of the parameters involved in this equation are now discussed. The diagonal matrices  $\rho, \mathbf{I}$  and  $\mathbf{O}$  only depend on the channel definition and on the choice of channel radii  $\{a_c\}_c$  at which they are evaluated. They depend on the system energy  $E$  only through their dependency on  $k_c$ . Hence in this last formulation, matrices  $\mathbf{\Omega}, \mathbf{L}, \mathfrak{P}$  and  $\mathcal{L}$  depend on  $k_c$  and on the choice of  $a_c$ . The remaining parameters are  $\gamma_{\lambda c}$  and  $E_\lambda$  are present in the  $\Re$ -matrix definition (cf. Eq. 3.18) and that are related to the properties of the internal region. These internal parameters must be obtained from adjustments on experimental cross sections. This formulation explicitly exhibits energy dependence of the collision matrix  $\mathbf{U}$ , and consequently, of the cross sections. It provides an *exact* way to reproduce cross sections by: first choosing arbitrary channel parameters  $\{a_c\}_c$  and  $\{B_c\}_c$ , then adjusting the internal region parameters  $\{\gamma_{\lambda c}\}_{c\lambda}, \{E_\lambda\}_\lambda$  on measured data. It must be reminded that the values of the internal region parameters  $\gamma_{\lambda c}, E_\lambda$  depend on the prior arbitrary choice of the channel parameters  $a_c$  and boundary condition  $B_c$ . Discussions about the choice of  $a_c$  and  $B_c$  can be found in Refs. [47, 57–59].

The method presented here is particularly well adapted for “particle” channels, *i.e.* when one of the colliding particle is a nucleon or a light nucleus. For capture reaction on heavy nuclei, *i.e.* for gamma emission, many channels are available but it is most of the time impossible to distinguish gamma channels experimentally. In such cases, a special treatment (cf. the Reich-Moore model that will be detailed later) is made so that these numerous channels are considered as a whole. Additionally in the case of fission reaction, there is a tremendous number of available channels because namely of the different possible fragmentations, so that such a general approach is not possible. A similar treatment (Reich-Moore) cannot be done for fission cross section. The reason is that, when the nucleus deforms towards fission, it can only pass by few “transition states” (cf. Chapter 4). These transition states will correlate the fission amplitude widths and their effects cannot statistically cancel as in the case of gamma channels. This effect for gamma channels will be detailed in Section 3.1.3.

Restraining the rest of this section to “proper” particle channels, and because of the analytical relation between  $I_c$  and  $O_c$  and the Coulomb wave functions  $F_c$  and  $G_c$ , it can be shown that  $\mathcal{L} = \mathbf{L}^*$ . Matrix  $\mathbf{L}$  can be written as  $\mathbf{L} = \mathbf{S} + i\mathbf{P}$ , where matrices  $\mathbf{S}$  and  $\mathbf{P}$  are real and respectively called *shift* and *penetration* factors. One can also show that

$\mathfrak{P} = \mathbf{P}$  and  $\Omega_c = e^{i(\omega_c - \phi_c)}$ , where  $\phi_c$  is called the *hard-sphere phase shift* and is defined by  $\phi_c = \arctan[F_c/G_c]$ . It describes the direct interaction between target and projectile. Hence  $\mathbf{S}$ ,  $\mathbf{P}$  and  $\mathbf{\Omega}$  can be computed using  $F_c$  and  $G_c$ . If one of the two particles involved carries no charge (*i.e.*, when a neutron is involved), the Coulomb wave functions reduce to spherical Bessel functions, from which analytical expressions can be obtained for  $\mathbf{S}$ ,  $\mathbf{P}$  and  $\Omega_c = e^{-i\phi_c}$ . Their expression can be found in Tab. 3.1.

Table 3.1 – Analytical expressions corresponding to shift and penetration factors and to the hard-sphere phase shift for channels involving a neutron.

$\ell$	$S_c$	$P_c$	$\phi_c$
0	0	$\rho_c$	$\rho_c$
1	$-\frac{1}{1 + \rho_c^2}$	$\frac{\rho_c^3}{1 + \rho_c^2}$	$\rho_c - \arctan \rho_c$
$\ell$	$\frac{\rho_c^2(1 - S_{c \ell-1})}{(1 - S_{c \ell-1})^2 + P_{c \ell-1}^2} - \ell$	$\frac{\rho_c^2 P_{c \ell-1}}{(1 - S_{c \ell-1})^2 + P_{c \ell-1}^2}$	$\rho_{c \ell-1} - \arctan \left[ \frac{P_{c \ell-1}}{\ell - S_{c \ell-1}} \right]$

The channel phase shift has a special role. Indeed if no eigenstate is assumed in the internal region ( $\mathfrak{R} \equiv 0$ ), then Eq. 3.23 reduces to

$$\mathbf{U} = \mathbf{\Omega}^2, \quad U_{cc'} = \delta_{cc'} e^{-2i\phi_c}. \quad (3.24)$$

In practice it is almost impossible to perform full  $\mathfrak{R}$ -matrix analysis. As mentioned above, measurements are necessary to obtain the  $\gamma_{\lambda c}$  and  $E_\lambda$  parameters and the tremendous number of possible channels undermines the rigorous modeling of resonances. For example, if one considers neutron spectroscopy of a medium-size nucleus, for a given resonance  $\lambda$ , each gamma decay process will correspond to a different photon-channel  $c$  to which a  $\gamma_{\lambda c}$  parameter must be associated. For heavier nuclei, fission channels worsen the entanglement. Approximate treatments of the general  $\mathfrak{R}$ -matrix framework must thus be settled. Even for total cross section, where only diagonal terms of the collision matrix are involved (*cf.* Chapter 1, Eq. 2.28), measurement overlays all entrance channels. It can be noted here that polarized scattering experiments may reduce this effect, unfortunately such experimental data are scarce.

### 3.1.2 Single- and Multi-Level Breit-Wigner Formalism

In case of well-spaced levels<sup>2</sup>, a convenient approximation can be made so that the  $\mathfrak{R}$ -matrix can be decomposed as  $\mathfrak{R} = \mathbf{R}^0 + \mathbf{R}^{\text{SL}}$ , where  $\mathbf{R}^0$  varies slowly with energy, and  $\mathbf{R}^{\text{SL}}$  is an  $\mathfrak{R}$ -matrix-like single-level matrix, so that its components  $R_{cc'}^{\text{SL}}$  verify

$$R_{cc'}^{\text{SL}} = \frac{\gamma_{\lambda c} \gamma_{\lambda c'}}{E_\lambda - E} \quad (3.25)$$

This leads to splitting the expression of the collision matrix  $\mathbf{U} = \mathbf{U}^0 + 2i \frac{\vec{\tau}_\lambda \times \vec{\tau}_\lambda}{\epsilon_\lambda}$ , where  $\mathbf{U}^0$  is also slowly varying with energy, both  $\vec{\tau}_\lambda$  and  $\epsilon_\lambda$  are defined in Ref. [5]. Finally, assuming negligible effect of remote levels, the collision matrix can be written

$$U_{cc'} = (U_{cc}^0 U_{c'c'}^0)^{1/2} \left[ \delta_{cc'} + \frac{i\Gamma_{\lambda c}^{1/2} \Gamma_{\lambda c'}^{1/2}}{E_\lambda + \Delta_\lambda - E - \frac{i}{2}\Gamma_\lambda} \right], \quad (3.26)$$

<sup>2</sup>A proper definition of the “well-spaced” condition will be given in the following.

where

$$\Gamma_{\lambda c} = 2P_c \gamma_{\lambda c}^2, \quad (3.27)$$

and  $\Delta_{\lambda c} = -(S_c - B_c) \gamma_{\lambda c}^2$  are the channel width and channel shift, associated to level  $\lambda$ . The  $\Gamma_{\lambda}$  parameter can be, to first order, considered the “natural width” of the resonance, *i.e.* the half-height width of the resonance observed in cross sections measurements. The well-spaced level condition can thus be more rigorously defined as  $\langle E_{\lambda} - E_{\lambda+1} \rangle_{\lambda} \gg \langle \Gamma_{\lambda} \rangle_{\lambda}$ . The bracket sign  $\langle \rangle_{\lambda}$  stands for an average over levels. The total level width and shift are given respectively by  $\Gamma_{\lambda} = \sum_c \Gamma_{\lambda c}$  and  $\Delta_{\lambda} = \sum_c \Delta_{\lambda c}$ . Expression 3.26 can be inserted in Eq. 2.26 of Chapter 2 that is recalled below

$$\sigma_{cc'}^{J\pi} = \frac{\pi}{k_c^2} g_J \left| e^{2i\omega_c} \delta_{cc'} - U_{c'c}^{J\pi} \right|^2, \quad (3.28)$$

to obtain channel-to-channel cross sections

$$\sigma_{cc'}^{J\pi}(E) = \frac{\pi}{k_c^2} g_J \frac{\Gamma_{\lambda c} \Gamma_{\lambda c'}}{(E_{\lambda} + \Delta_{\lambda} - E)^2 + \frac{1}{4} \Gamma_{\lambda}^2}, \quad c \neq c', \quad (3.29)$$

$$\sigma_{cc}^{J\pi}(E) = \frac{\pi}{k_c^2} g_J \left[ 4 \sin^2 \phi_c - \Gamma_{\lambda c} \frac{2(E_{\lambda} + \Delta_{\lambda} - E) \sin 2\phi_c + \Gamma_{\lambda} (1 - \cos 2\phi_c)}{(E_{\lambda} + \Delta_{\lambda} - E)^2 + \frac{1}{4} \Gamma_{\lambda}^2} + \frac{\Gamma_{\lambda c}^2}{(E_{\lambda} + \Delta_{\lambda} - E)^2 + \frac{1}{4} \Gamma_{\lambda}^2} \right]. \quad (3.30)$$

The last term of Eq. 3.30 is called the *resonance* term and corresponds to interactions of the projectile within the internal region of the target with all nucleons. In this region complex many-body nuclear interactions are effective and lead to the many resonances visible on cross sections. The first term, on the contrary, can be seen as corresponding to the projectile interacting with the an average potential surrounding the target nucleus and is called the *potential* term. It has a slight energy dependency that can often be neglected in the vicinity of a given resonance. Finally the term in the middle corresponds to interference between the potential and resonance terms.

Nowadays, this type of modeling is obsolete in evaluation work as it neglects coupling terms between levels and between channels and because current computers can cope with more refined models. It is presented here because it can be used to make a simple connection between the RRR and the statistical energy range frameworks, as will be shown in Chapter 4. It can be seen in Eq. 3.29 that the only difference between  $\sigma_{cc'}^{J\pi}$  and  $\sigma_{cc''}^{J\pi}$  lies in the width  $\Gamma_{\lambda c'/c''}$  of the exit channel; no coupling between the *entrance* and *exit* channels, nor between exit *channels*. Additionally, the fluctuations of the cross sections in the RRR are due to the presence of many levels, and can be approximated as a sum of expressions of type 3.29. Again in this case, no interference or coupling is considered between *levels*. An extension, called Multi-Level Breit-Wigner, in which the coupling terms between *levels only* exists and is still commonly used and gives satisfactory results for isotopes where the fission reaction is negligible.

The fission channels, in the rigorous sense of the  $\Re$ -matrix formalism, are numerous because each fragmentation (and each internal configuration of each fragment) leads to new channels. In practice, due to the fact that only few *transition states* are effective in the resonance region, satisfactory results are obtained using one or two fission channels. However as no proper wave functions are defined in the outer region, the penetration factor related to fission is arbitrarily set to 1 for simplicity.



### 3.1.3 Reich-Moore

As mentioned before, the general  $\mathfrak{R}$ -matrix theory is hardly practical for actual computation, especially for heavy nuclei, because of the too many radiative decay channels that are open. An alternative treatment has been proposed by Reich and Moore [6], that consists in writing the general  $\mathfrak{R}$ -matrix as follows

$$\mathfrak{R} = \begin{pmatrix} \mathfrak{R}_{11} = \begin{pmatrix} R_{1,1} & \cdots & R_{1,m} \\ \vdots & \ddots & \vdots \\ R_{m,1} & \cdots & R_{m,m} \end{pmatrix} & \begin{pmatrix} R_{1,m+1} & \cdots & R_{1,n} \\ \vdots & \ddots & \vdots \\ R_{m,m+1} & \cdots & R_{m,n} \end{pmatrix} \\ \begin{pmatrix} R_{m+1,1} & \cdots & R_{m+1,m} \\ \vdots & \ddots & \vdots \\ R_{n,1} & \cdots & R_{n,m} \end{pmatrix} & \begin{pmatrix} R_{m+1,m+1} & \cdots & R_{m+1,n} \\ \vdots & \ddots & \vdots \\ R_{n,m+1} & \cdots & R_{n,n} \end{pmatrix} \end{pmatrix} \quad (3.31)$$

where indices  $i \in \llbracket 1, m \rrbracket$  relate to non-gamma channels, and accordingly  $i \in \llbracket m+1, n \rrbracket$  relates to gamma channels. They also split the collision matrix  $\mathbf{U}$  using the same pattern. In their derivation, they used the original Wigner and Eisenbud formula [4] that relates the  $\mathfrak{R}$ -matrix to the collision matrix  $\mathbf{U}$ :

$$\mathbf{U} = \mathbf{\Omega}[\mathbf{1} - i(\mathfrak{B}\mathfrak{R}\mathfrak{B} + \mathfrak{C})]^{-1}[\mathbf{1} + i(\mathfrak{B}\mathfrak{R}\mathfrak{B} + \mathfrak{C})]\mathbf{\Omega}, \quad (3.32)$$

instead the collision matrix expression of Eq. 3.23. The  $\mathfrak{B}$  and  $\mathfrak{C}$  terms used in Eq. 3.32 are defined in Ref. [4]. The full derivation of their calculation [6] is not reported here. It is only emphasized here that they derived a relation between  $\mathfrak{R}_{11}$  and its counterpart  $\mathbf{U}_{11}$ , and that this relation can be put in a form similar to Eq. 3.32

$$\mathbf{U}_{11} = \mathbf{\Omega}_{11}[\mathbf{1}_{11} - i(\mathfrak{B}_{11}\mathbf{R}\mathfrak{B}_{11} + \mathfrak{C}_{11})]^{-1}[\mathbf{1}_{11} + i(\mathfrak{B}_{11}\mathbf{R}\mathfrak{B}_{11} + \mathfrak{C}_{11})]\mathbf{\Omega}_{11}, \quad (3.33)$$

but where the genuine  $\mathfrak{R}$ -matrix components are replaced by a slightly modified expression

$$[\mathfrak{R}]_{cc'} = \sum_{\lambda} \frac{\gamma_{\lambda c} \gamma_{\lambda c'}}{E_{\lambda} - E} \Rightarrow [\mathbf{R}]_{cc'} = \sum_{\lambda} \frac{\gamma_{\lambda c} \gamma_{\lambda c'}}{E_{\lambda} - E - \frac{1}{2}i\Gamma_{\gamma}} \quad (3.34)$$

In Eq. 3.34,  $\Gamma_{\gamma}$  is the total width related to gamma channels only. It can be stated at this point that Eq. 3.33 is obtained by assuming random sign of the amplitude width  $\gamma_{\lambda c}$  (where  $c$  is related to gamma channels only), so that while summing expression such as

$$\sum_{\lambda\mu} \gamma_{\lambda c} \gamma_{\mu c}, \quad (3.35)$$

for  $c \in \gamma$ , only “diagonal” terms remain

$$\sum_{\lambda\mu} \gamma_{\lambda c} \gamma_{\mu c} \approx \sum_{\lambda} \gamma_{\lambda c}^2. \quad (3.36)$$

Partial cross sections not related to gamma channels can be obtained by using the regular  $\mathfrak{R}$ -matrix framework but using the Reich-Moore form of that matrix (right side of Eq. 3.34). The capture cross section is obtained by subtraction of all other partial cross sections from the total cross section (that is obtained from the diagonal components of  $\mathbf{U}$ )

$$\sigma_{c\gamma}^{J\pi} = \sigma_{c,\text{tot}}^{J\pi} - \sum_{c' \neq \gamma} \sigma_{cc'}^{J\pi}. \quad (3.37)$$

Concerning fission channels this formalism still carries some deficiencies. Just like in the Multi-Level Breit-Wigner formalism, the penetration factor related to fission channel is arbitrarily set to 1. As width amplitudes  $\gamma_{\lambda c}$  are adjusted on experimental data, adjustment that balance modeling deficiency. However this leads to statistical bias when considering statistical properties of the width amplitudes related to fission channels.

## 3.2 Lynn Extension to Fission Channels

Lynn [7,60] extended the  $\mathfrak{R}$ -matrix formalism presented in Section 3.1.1 to fission channels. Yet this extension has never been used in practice for actual evaluations. Like the  $r_c$  degree of freedom of the “true” particle channels, an adequate fission channel degree of freedom  $\eta$  must be defined. A related kinetic operator  $\hat{T}_\eta$  for the fission channel and an “interaction” potential  $\hat{V}(\eta)$  also have to be defined. The general formula of the kinetic operator<sup>3</sup> is

$$\hat{T}_\eta = -\frac{\hbar^2}{2B_\eta(\eta)f^2(\eta)}\frac{\partial}{\partial\eta}\left(f^2(\eta)\frac{\partial}{\partial\eta}\right), \quad (3.38)$$

where the  $f$  function definition depends on the type of fission channel degree of freedom  $\eta$  that is considered. For instance  $\eta$  can be chosen to be the quadruple moment  $Q$  of the system of  $A$  nucleons, defined by

$$\eta \equiv Q = \sum_{i=1}^A (3\bar{z}_i^2 - \bar{r}_i^2), \quad (3.39)$$

where  $\bar{z}_i$  and  $\bar{r}_i$  are the  $i^{\text{th}}$  nucleon cylindrical coordinates in the center-of-mass. In this case,  $f$  is simply the identity function  $f \equiv 1$ . The  $B_\eta$  coefficient is the inertia parameter corresponding to the deformation variable  $\eta$ . Its definition also depends on the choice of the deformation  $\eta$ . In the case of  $\eta \equiv Q$ , it is given by

$$B_Q = \frac{m}{4Q + 8A\bar{r}^2}, \quad (3.40)$$

where  $m$  is the mass of a nucleon and  $\bar{r}^2$  is the average value of  $\bar{r}_i^2$  given by

$$\bar{r}^2 = \frac{1}{A} \sum_{i=1}^A \bar{r}_i^2. \quad (3.41)$$

In the following,  $B_Q$  is assumed not to depend on the deformation  $\eta$ . As fission coordinate is considered, the eigenstates  $X_\lambda$  of the internal region are expanded on functions  $\Psi_{\mu\nu}$ , associated to coefficient  $C_{\lambda(\nu\mu)}$ . The  $\Psi_{\mu\nu}$  functions are defined as a product of quasi-vibrational functions  $\Psi_\nu^{(\mu)}(\eta)$  and an intrinsic function  $\chi_\mu$  (defined at the channel deformation  $\eta_c$ )

$$X_\lambda = \sum_{\nu\mu} C_{\lambda(\nu\mu)} \Psi_{\mu\nu} = \sum_{\nu\mu} C_{\lambda(\nu\mu)} \Psi_\nu^{(\mu)} \chi_\mu. \quad (3.42)$$

The superscript  $(\mu)$  implies that a different set of quasi-vibrational functions  $\Psi_\nu^{(\mu)}(\eta)$  can be defined for each intrinsic state  $\chi_\mu$ . The quasi-vibrational functions  $\Psi_\nu^{(\mu)}(\eta)$  satisfy the energy-independent boundary condition

$$\frac{1}{f(\eta_c)\Psi_\nu^{(\mu)}(\eta_c)} \left( \frac{\partial f \Psi_\nu^{(\mu)}}{\partial \eta} \right)_{\eta_c} = B_\mu. \quad (3.43)$$

These considerations lead to the definition of new *value* and *derivative* quantities (as in Eq. 3.12) related here to the fission channel

$$\begin{aligned} V_\mu &= \left( \frac{\hbar^2}{2B_\eta f(\eta_c)} \right)^{1/2} \int_{\mathcal{S}|\eta=\eta_c} d\mathcal{S} \chi_\mu^* f^{-1} \Psi, \\ D_\mu &= \left( \frac{\hbar^2}{2B_\eta f(\eta_c)} \right)^{1/2} \int_{\mathcal{S}|\eta=\eta_c} d\mathcal{S} \chi_\mu^* f^{-1} \frac{\partial f \Psi}{\partial \eta}. \end{aligned} \quad (3.44)$$

<sup>3</sup>This form actually depends on the choice of the deformation coordinate  $\eta$ . It is yet a general expression for deformation coordinates considered in Ref. [7].

Following the same approach than in Section 3.1.1, the corresponding shift and penetration factors are defined as

$$\left[ \frac{1}{f\Psi^{(\mu)}} \frac{\partial(f\Psi^{(\mu)})}{\partial\eta} \right]_{\eta=\eta_c} = S_\mu + iP_\mu, \quad (3.45)$$

where  $\Psi^{(\mu)}$  is the outgoing wave function, solution of

$$[\hat{T}_\eta + \hat{V}(\eta)]\Psi^{(\mu)} = [E - \epsilon_\mu(\eta)]\Psi^{(\mu)}, \quad (3.46)$$

where  $\epsilon_\mu$  is the intrinsic excitation energy corresponding to state  $\chi_\mu$  and  $E$  is the total excitation energy.

### 3.2.1 Double-Humped Barrier Textbook Example

To illustrate what are the expected effects of this approach on resonance analysis, let us detail an example inspired by Ref [7]. The fission barrier shape  $V(\eta)$  of Fig. 3.1 is considered. A constant inertia parameter will be assumed with value  $B_\eta = 0.054A^{5/3}\hbar^2 \text{ MeV}^{-1}$ , the fissioning isotope is  $^{241}\text{Pu}$ , thus  $A = 241$ . Considering only the fundamental barrier (*i.e.*  $\epsilon_\mu = 0$ ) the wave function  $\Psi^{(\mu)}$  can be computed for any value of  $E$ .

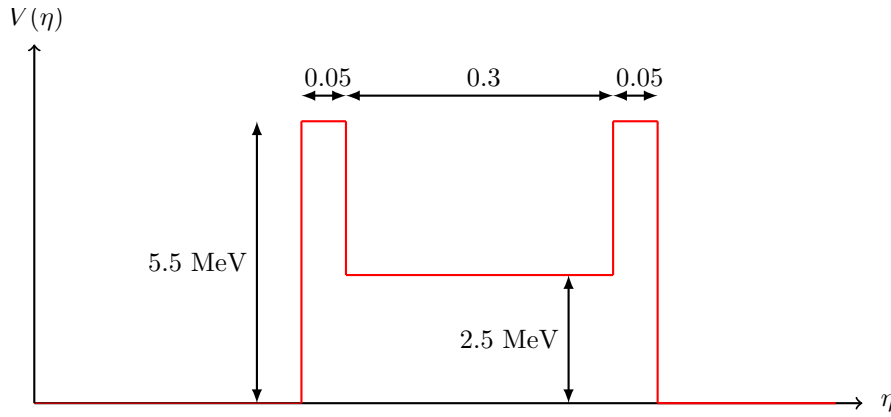


Figure 3.1 – Schematic representation of a double-humped fission barrier. Deformations ( $\eta$  axis) are in arbitrary units.

Defining an equivalent fission channel radius  $\eta_c$  as the deformation corresponding to the top of the first barrier hump,  $P_\mu$  and  $S_\mu$  can be computed from Eq. 3.45. A relevant numerical method [61] used for the wave function  $\Psi^{(\mu)}$  computation also provides the barrier transmission coefficient. In this numerical method, the wave function  $\Psi^{(\mu)}$  is expressed differently on each piecewise constant parts  $V_n$  of the potential

$$\Psi_n^{(\mu)}(\eta) = b_n e^{ik_n \eta} + c_n e^{-ik_n \eta}, \quad (3.47)$$

where  $b_n$  and  $c_n$  are expansion coefficients for the  $n^{\text{th}}$  potential constant segment and

$$k_n = \left[ \frac{2B_\eta}{\hbar^2} (E - V_n) \right]^{1/2} \in \mathbb{C}^*. \quad (3.48)$$

The rightmost potential segment is labeled  $\infty$ . The outgoing wave function requirement leads to setting  $c_\infty = 0$ . The rightmost condition  $c_\infty = 0$  is then “propagated” to the leftmost segment (labeled 0). The barrier transmission coefficient is finally given by

$$T_f = \frac{k_\infty}{k_0} \left| \frac{b_\infty}{b_0} \right|^2. \quad (3.49)$$

Some numerical methods that can be used for this type of problem will be detailed in Chapter 6 and Appendix D.

In Fig. 3.2 the results for the transmission coefficient (Eq. 3.49), the penetration and the shift factor (Eq. 3.45) are shown. On the right part of the figure, the potential is shown again (red lines) with the densities probabilities  $|\Psi^{(\mu)}|^2$  computed for some special energies. These energies are those for which the transmission coefficient shown on the right part of the figure (black dotted curve) is maximal. These energies are shown on both part of the figure, on the right part by colored dots on the top of the frame and on the left part by straight solid lines accordingly colored.

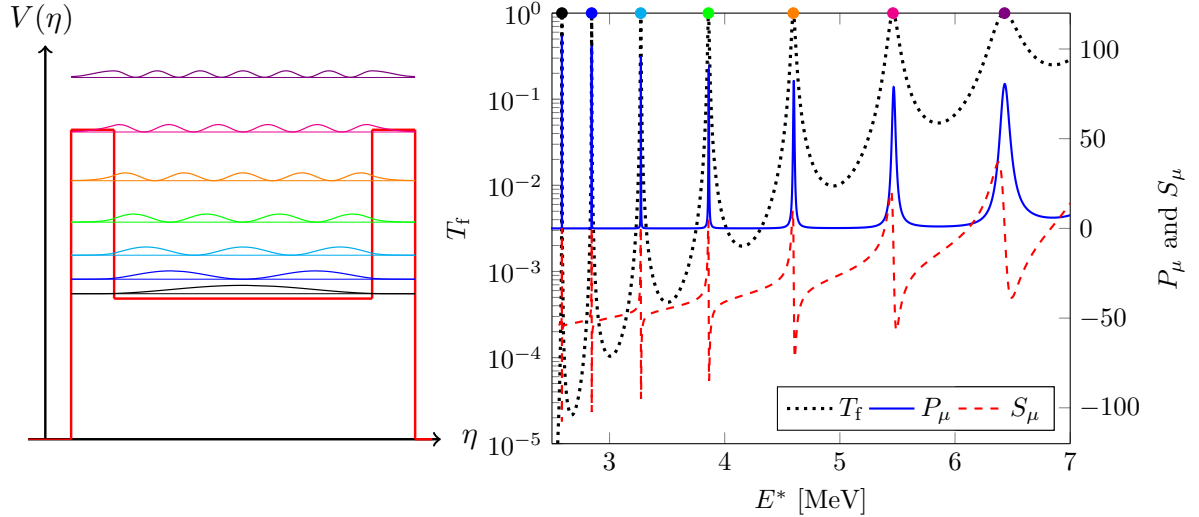


Figure 3.2 – (Left) Potential used for the computation of the wave function  $\Psi^{(\mu)}$  and probability densities  $|\Psi^{(\mu)}|^2$  associated with the resonance energies of the transmission coefficient  $T_f$  shown on the right. (Right) Transmission coefficient ( $T_f$ ), shift ( $S_\mu$ ) and penetration ( $P_\mu$ ) factors for the barrier shape of Fig. 3.1. Pseudo eigenstates are shown on the left plot, the related energies are shown with corresponding-colored dots on the right plot.

From Fig. 3.2 it can be seen that the three functions  $T_f$ ,  $P_\mu$  and  $S_\mu$  exhibit distinct resonant structures at similar energies. The structures do not exist if the considered barrier does not have an intermediate well. The transmission coefficient has much broader resonant structures compared to those of the penetration factor. For energies at which resonant structures exist, the probability density  $|\Psi^{(\mu)}(\eta)|^2$  shows that the wave is mostly located in the intermediate well. Energies at which resonances occur are directly related to the barrier shape. They are pseudo-eigenenergies of the intermediate well; the term “pseudo” is used because the intermediate well is not infinite. The resonant structures of the transmission coefficient are evidences of states spatially located in the intermediate well, the so-called class-II states. States mostly located in the first well (not represented in the figure) are respectively named class-I states. Resonance energies showing up in the transmission coefficient thus correspond to energies of the class-II states.

One can notice from Fig. 3.2 that the maximum value of the penetration factor is not identical for all resonant structures of blue curve. This is a feature related to the fission barrier description. Instead of the potential described by Fig. 3.1, one can consider the barrier used in Ref. [7], reported in Fig. 3.3. In this case the potential is also described (from the second saddle point) down to the “scission point”.

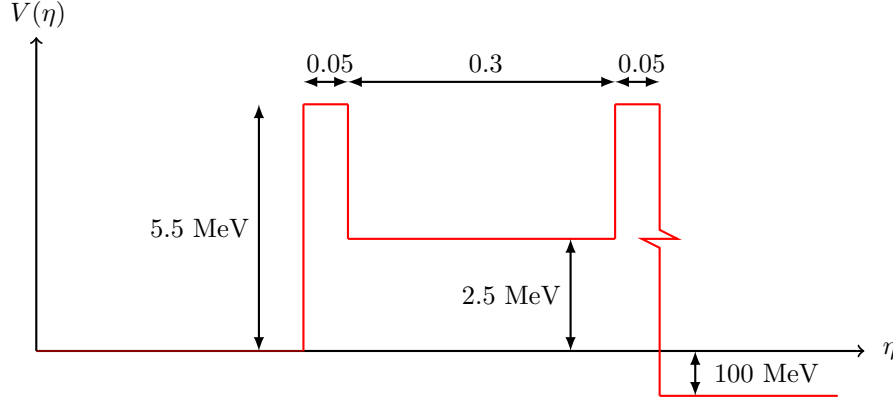


Figure 3.3 – Schematic representation of a double-humped fission barrier with a description down to the scission point. Deformations ( $\eta$  axis) are in arbitrary units.

This description is of course very schematic, yet if this actual potential is used to obtain  $T_f$ ,  $P_\mu$  and  $S_\mu$ , the results can be slightly different. The corresponding results are shown on Fig. 3.4.

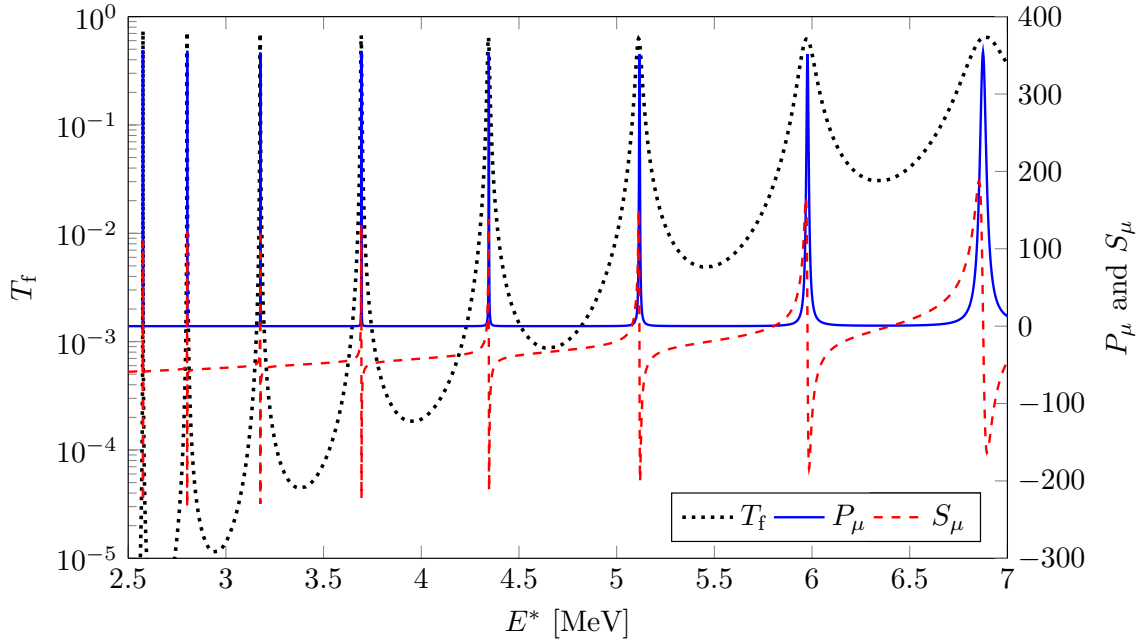


Figure 3.4 – Transmission coefficient ( $T_f$ ), shift ( $S_\mu$ ) and penetration ( $P_\mu$ ) factors related to the barrier shape of Fig. 3.3.

In Fig. 3.4, several features should be noticed. First, the shift factor is not strongly modified apart from the increase of the maximum values at resonances. The second feature is related to the maximal values of the transmission coefficient that are not equal to unity anymore. This is due to the first ratio in Eq. 3.49, in which the two wave numbers are no longer identical. This is physically related to the fact that the probability current used in the definition of the transmission coefficient<sup>4</sup>, involve the asymptotic velocity waves that are thus different on the right and left sides of the potential. This feature should not be

<sup>4</sup>In Eq. 2.12 of Chapter 2, the probability current is defined as  $\vec{j}[\Psi] = \frac{\hbar}{2iB_\eta}[\Psi^* \vec{\nabla} \Psi - \Psi \vec{\nabla} \Psi^*]$  and the transmission coefficient is defined by  $T_f = |j_{\text{right}}/j_{\text{left}}|^2$ , where  $j_{\text{left}}$  and  $j_{\text{right}}$  are respectively the probability current on the left (resp. the right) part of the barrier.

a concern in this chapter as only the penetration factor will be used. The last feature is related to the penetration factor. The maximal values for each resonance of  $P_\mu$  are now roughly equal. This would be an important condition in the sub-threshold analysis of the  $^{240}\text{Pu}$  fission cross section.

### 3.2.2 Penetration Factor Modeling

Prior to attempting to use these concepts to perform an actual analysis, a practical method to include the fluctuations of the penetration factor must be defined. Zooming on a particular resonance structure, as shown in Fig. 3.5, one sees a shift in energy between the transmission coefficient and the penetration factor maxima.

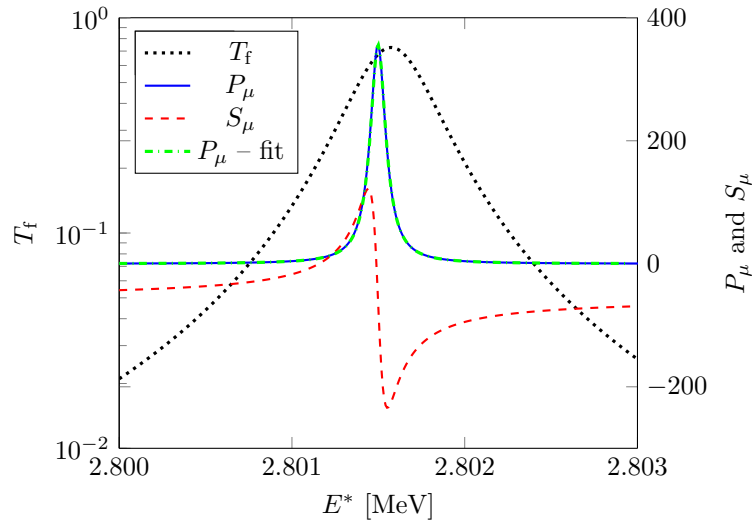


Figure 3.5 – Barrier transmission coefficient ( $T_f$ ), shift ( $S_\mu$ ) and penetration ( $P_\mu$ ) factors, related to the schematic barrier of Fig. 3.3, for the second class-II resonance of Fig. 3.4 near 2.8 MeV. An approximation of the penetration factor by a Lorentzian ( $P_\mu - \text{fit}$ ) is also shown.

The energy shift in Fig. 3.5 indicates that the maximal amplification of the penetration factor occurs at energies slightly different from the class-II states energies. This will have a visible effect when analyzing clusters of resonances for fertile isotopes as will be detailed in the following. For practical reasons the whole modeling of the fission channel, by defining both kinetic operator  $\hat{T}_\eta$  and deformation potential  $V(\eta)$ , will not be carried out in resonance analysis. Instead of using a full description of the barrier shape, one can approximate the amplification effect of the penetration factor by the following Lorentzian expression

$$P_\mu(E) = \frac{\sigma_C \Gamma_C^2 / 4}{(E - E_C)^2 + \Gamma_C^2 / 4}. \quad (3.50)$$

Parameters  $E_C$  and  $\Gamma_C$  are respectively the cluster resonance energy (roughly the class-II state energy) and the cluster width. Parameter  $\sigma_C$  characterizes the magnitude of the penetration factor. Figure 3.5 also demonstrates the quite satisfactory representation of the actual penetration factor  $P_\mu$ , obtained with the potential of Fig. 3.3, by such a phenomenological Lorentzian ( $P_\mu - \text{fit}$ ).

### 3.3 Sub-Threshold Analysis of $^{240}\text{Pu}(n,f)$

The dramatic local amplification of the penetration factor can account for the presence of clusters of resonances in fission cross-section of fertile isotopes such as  $^{240}\text{Pu}(n,f)$ . This sub-threshold resonance phenomenon is exemplified in Fig. 3.6. Between 600 eV and 2100 eV, three structures located around 800, 1400 and 1900 eV are visible. They are called clusters of resonances. A fourth one, quite smaller, can be seen near 1000 eV if one considers the cumulative fission width “Cumul.  $\Gamma_f$ ” defined as

$$\text{Cumul. } \Gamma_f(E) = \sum_{\lambda|E_\lambda \leq E} \Gamma_{\lambda f}. \quad (3.51)$$

This cumulative fission width is also shown in Fig. 3.6. It reveals that within each cluster a few (actually only one) resonances contribute significantly to the cumulative fission width.

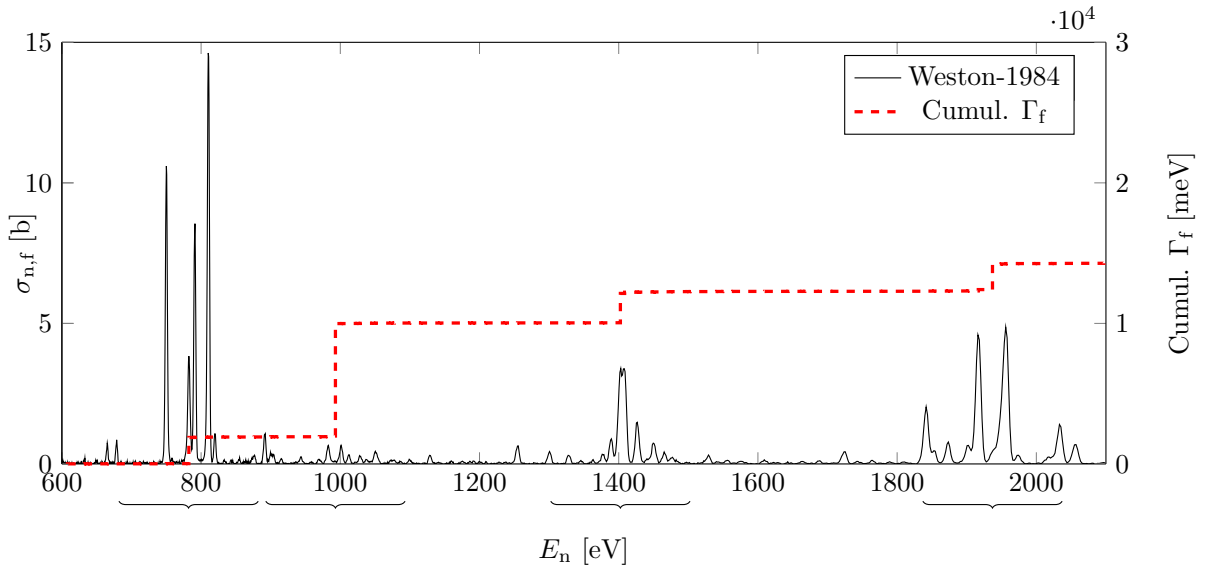


Figure 3.6 – Measurement of the lowest-energy clusters of resonances for  $^{240}\text{Pu}(n,f)$  (Weston-1984 [39]). The cumulative fission width (Cumul.  $\Gamma_f$ ) is also shown.

The phenomenological method (penetration factor approximation by a Lorentzian) will now be used to analyze the resonances of the  $^{240}\text{Pu}$  fission cross section. The JEFF-3.2 evaluation is used as the basis for the analysis. This does not mean that the JEFF-3.2 parameters are necessarily used in the present analysis, instead the fission cross section is reconstructed using the relevant RRR formalism<sup>5</sup> and used as if it were experimental data. Some fission widths in the evaluation are not related to measurements but are introduced to represent the average resonance spacing, and must be discarded from the statistical analysis. As these resonances are very small, they do not significantly affect the reproduced cross section. For the present analysis these resonance widths are not retained. Within each cluster of resonances, a particular resonance with an extremely large fission width (a thousand times larger than the surrounding ones) and a quite small neutron width can be identified. These resonances are considered as evidence of wave function located in the intermediate well and identified as the class-II states. Those class-II resonances should be considered separately in the analysis because their physical origin

<sup>5</sup>In this case, the  $^{240}\text{Pu}(n,f)$ -JEFF-3.2 fission cross section must be reconstructed using the Reich-Moore formalism, cf. Section 3.1.3.



differs from the surrounding class-I resonances. Their distinctive property is striking when considering the zero-Kelvin cross section as shown in Fig. 3.7. A resonance with an extremely large width is observed near 1400 eV. It should be noted that in the vicinity of this large resonance, other narrow resonances have their maximum values amplified. The maximum of this amplification phenomenon (*cf.* red dashed curve in Fig. 3.7) seems not to be centered on the large width resonance (blue arrow) but rather on the right of the most amplified narrow resonance, near 1410 eV (red arrow). This can be seen as an illustration of the energy shift in the resonance structures of Fig. 3.5. The maximum of the transmission coefficient (meaning the energy of the broad 0 K resonance) is shifted compared to the maximum of the penetration factor (energy of the most amplified narrow resonance).

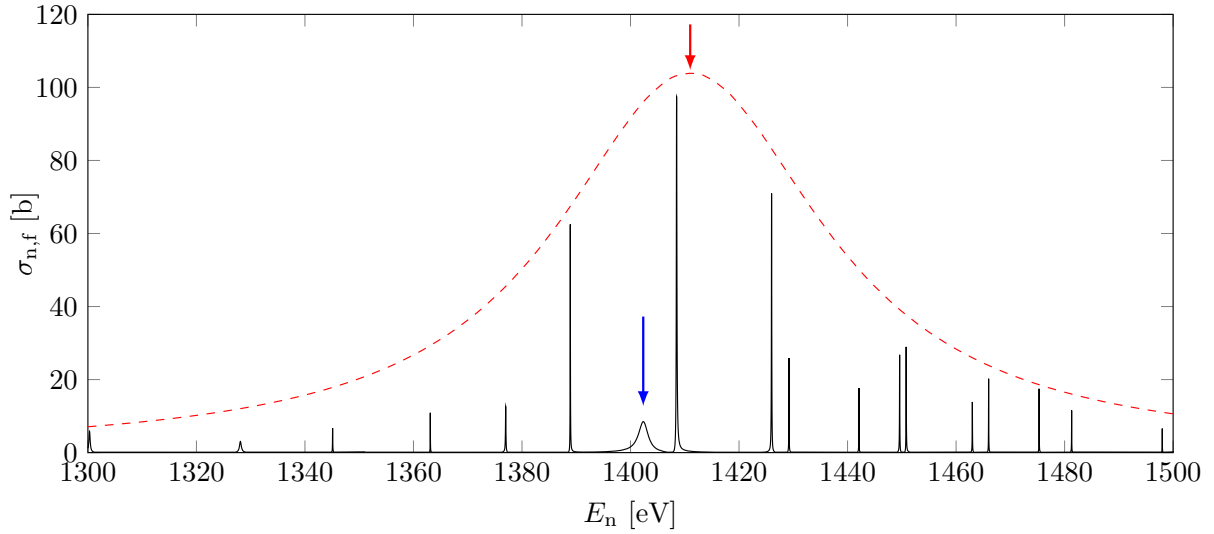


Figure 3.7 – Neutron-induced fission cross section of  $^{240}\text{Pu}$  reconstructed at zero Kelvin from the JEFF-3.2 evaluation resonance parameters (solid black curve). The class-II state is indicated with the blue arrow. The class-I amplification envelope is shown in dashed red line. The envelope is centered about an energy indicated with a red arrow.

In the vicinity of the class-II resonance of each cluster, the class-I resonances have amplified fission widths (although a hundred times smaller than the class-II one). To highlight this phenomenon the averaged reduced widths  $\gamma_{\lambda f}^2 / \langle \gamma_{\lambda f}^2 \rangle$  are shown in Fig. 3.8 (black marks). Only the class-I assumed resonances are considered in the calculation of  $\langle \gamma_{\lambda f}^2 \rangle$  (the broad class-II states are discarded). It can be seen that, when the usual treatment of the penetration factor, *i.e.*  $P_\mu \equiv P_f \equiv 1$  (black marks), some class-I resonances have quite large width amplitudes  $\gamma_{\lambda f}$ . This is due to the omission of the amplifying penetration factor that is balanced by the  $\gamma_{\lambda f}$  fit in the JEFF-3.2 analysis to reproduce experimental data.

For the present study, an analysis has been done using a penetration factor defined as the sum of four Lorentzians centered on the most amplified class-I state of each cluster. All Lorentzians have a width of 60 eV except for the one in the second cluster near 1000 eV. In that cluster the class-II state has a fission width twice larger than for other class-II states. Because of that, a twice-larger Lorentzian width (120 eV) was taken for this cluster. In a proper evaluation, those parameters should be adjustable, or even better, directly deduced from an underlying penetration barrier calculation as done in the previous section. Here they were not adjusted.

As was shown on the previous section, the maximum value of the penetration factor  $\sigma_C$

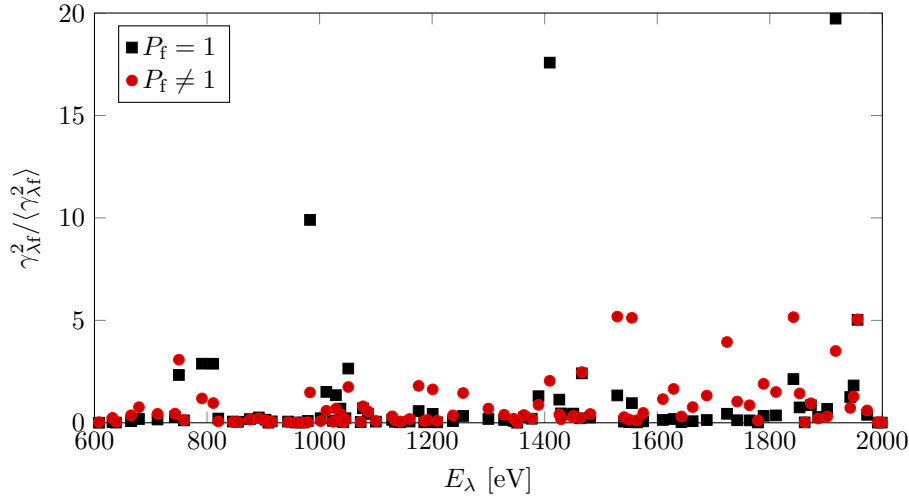


Figure 3.8 – Averaged fission reduced width amplitudes of  $^{240}\text{Pu}(n,f)$  analyzed using either a unit penetration factor ( $P_f = 1$ ) *i.e.* the JEFF-3.2 data, or using four Lorentzian enhancers defined by Eq. 3.50 ( $P_f \neq 1$ ).

is identical for all Lorentzians. The  $\sigma_C$  parameter has no effect on practical resonance parameter analysis. Considering a Single-Level Breit-Wigner description of the resonances, the resonance width  $\Gamma_{\lambda f}$  is related to the resonance amplitude  $\gamma_{\lambda f}$  by

$$\Gamma_{\lambda f} \approx 2P_\mu(E_\lambda)\gamma_{\lambda f}^2 \quad (3.52)$$

The reduced width amplitudes  $\gamma_{\lambda f}$  are obtained by “fitting the resonance width  $\Gamma_{\lambda f}$ ”, by fitting the cross section. Thus the  $\sigma_C$  parameter will have the effect of a normalization factor that will vanish in the resonance parameter analysis as the quantity of interest is the relative distribution  $\gamma_{\lambda f}^2 / \langle \gamma_{\lambda f}^2 \rangle$ . Using the four Lorentzians, class-I  $\gamma_{\lambda f}$  parameters are fitted to the JEFF-3.2 reconstructed cross section. In Fig. 3.8 the result of this analysis is shown ( $P_f \neq 1$ , red marks). It can be seen that the local amplification of the class-I states in the vicinity of the class-II is somehow removed since the cluster envelopes produce the amplification. Here again the class-II reduced width amplitudes are not used for the statistical analysis.

Figure 3.9 shows another visible effect of this treatment. The JEFF-3.2 evaluation is compared to an artificially reconstructed cross section, ( $P_f \neq 1$ ), for which an identical average reduced width amplitude  $\langle \gamma_{\lambda f} \rangle$  was taken for all class-I resonances<sup>6</sup>. In one case a constant penetration factor is used and yields no structures ( $P_f = 1$ , middle figure). In the second case, the penetration factor used contains the four Lorentzian described earlier ( $P_f \neq 1$ , lower figure). It can be seen that this rough approach tends to reproduce properly gross structures.

A “cleaner” statistics feedback for the distribution  $f$  of the class-I fission reduced width amplitudes  $\gamma_{\lambda f}$  may be expected from the present approach. The distribution  $f$  is defined so that  $f(x)dx$  is the probability for an average reduced width amplitude  $\gamma_{\lambda f}^2 / \langle \gamma_{\lambda f}^2 \rangle$  to have a value between  $x$  and  $x + dx$ . In Fig. 3.10 such a distribution is shown. It can be seen that despite the rather low statistics between 600 eV and 2100 eV (less than a hundred resonances), the replacement of the one-unit penetration factor by the

<sup>6</sup>The reduced width amplitudes  $\gamma_{\lambda f}$  are signed quantities (positive or negative). In the present case, the sign of the evaluated parameter is conserved but the magnitude is fixed to the average magnitude value.

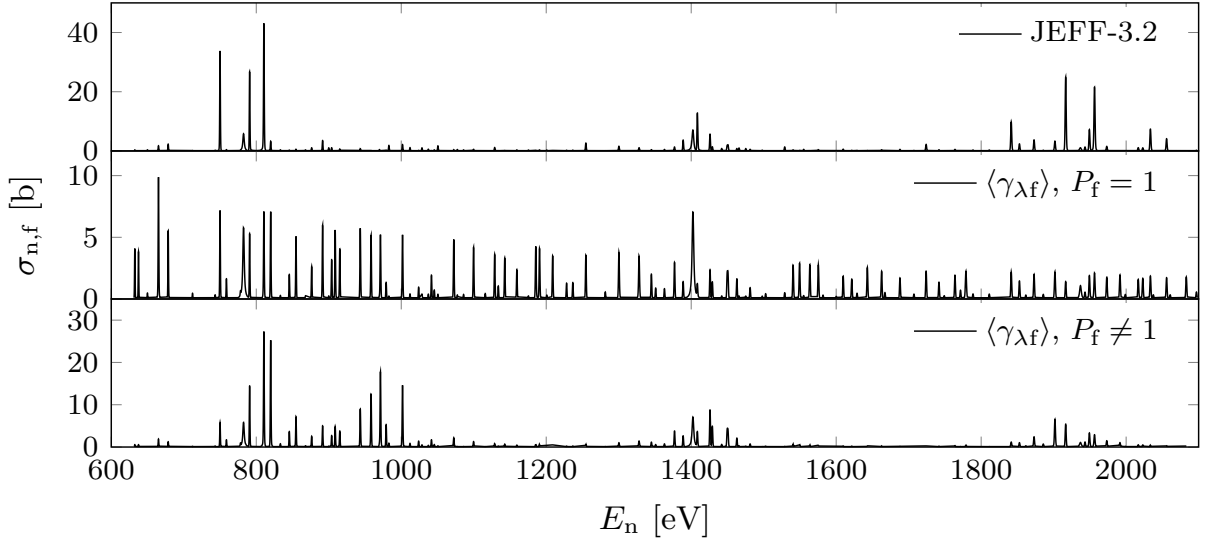


Figure 3.9 – Clusters of resonances in the  $^{240}\text{Pu}(n,f)$  cross section. The upper figure shows the JEFF-3.2 evaluation reproducing the observed fission cross section but (a standard Reich-Moore formalism). The middle plot shows a theoretical calculation using an average fission reduced width amplitude  $\langle\gamma_{\lambda f}\rangle$  for all resonances and a unit fission penetration factor. The lower plot shows a theoretical calculation also using an averaged fission reduced width amplitude  $\langle\gamma_{\lambda f}\rangle$  for all resonances but with the Lorentzians as fission penetration factor. In the middle and lower plots, the JEFF-3.2 parameters are used for all reactions but fission.

four Lorentzians brings the “experimental” distribution closer to the expected Porter-Thomas distribution [62]. It thus brings consistency with the class-I neutron reduced width amplitude analyses.

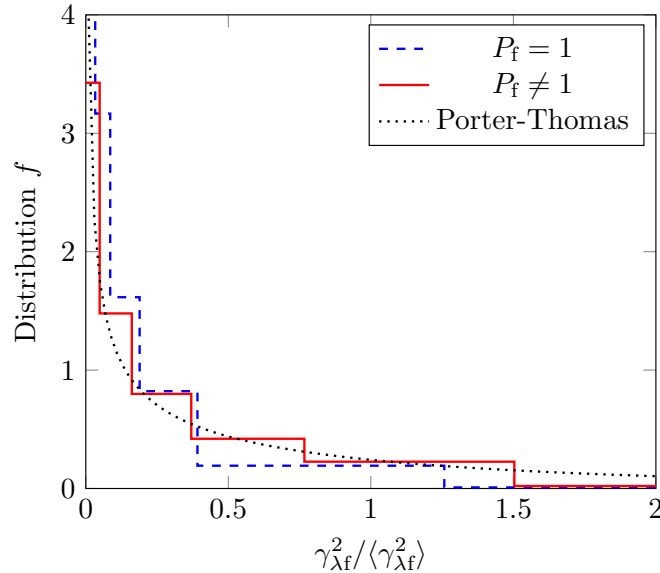


Figure 3.10 – Distribution of the  $^{240}\text{Pu}(n,f)$  fission reduced width amplitudes using a unit penetration factor ( $P_f = 1$ , blue dashed curve), reproduced from the JEFF-3.2 evaluation. The similar quantity obtained while performing the analysis with the four cluster Lorentzian enhancers is also shown ( $P_f \neq 1$ , red solid curve). A Porter-Thomas theoretical distribution is also shown for comparison.

The present analysis highlights that the consideration of the fission barrier shape in the RRR analysis leads to different evaluated parameters. These parameters are believed to have a better physical meaning. In the presented analysis, the fission penetration factor was not directly obtained by treatment of the fission barrier but instead by a phenomenological way by introducing Lorentzians. The more rigorous method would require a proper physical description of the barrier shape to be used as a starting point of the fission resonance analysis. In the next chapter a model providing such a fission barrier description will be presented.

## Chapter 4

# Upgrading the CONRAD Code to the State of the Art of Evaluation Models in the Statistical Range

*In this chapter, some of the models currently used for cross section evaluation in the statistical energy range will be presented. The aim of this chapter is not to introduce all models that can be used for evaluation. It will be restricted to the necessary developments that have been brought to the CONRAD code in order to improve and extend the code capability in the statistical range.*

### Contents

---

<b>4.1</b>	<b>Hauser-Feshbach Framework . . . . .</b>	<b>44</b>
<b>4.2</b>	<b>Unresolved Resonance Range – Average <math>\mathfrak{R}</math>-Matrix . . . . .</b>	<b>46</b>
<b>4.3</b>	<b>Continuum Range – Optical Model . . . . .</b>	<b>48</b>
<b>4.4</b>	<b>Capture Reaction and Level Density Models . . . . .</b>	<b>50</b>
4.4.1	Level Density Models . . . . .	52
4.4.2	Gamma Strength Functions . . . . .	54
4.4.3	Verification on Capture and Elastic Cross Sections . . . . .	54
<b>4.5</b>	<b>Inelastic Scattering . . . . .</b>	<b>55</b>
<b>4.6</b>	<b>Fission Reaction . . . . .</b>	<b>58</b>
4.6.1	Hill-Wheeler Approach . . . . .	58
4.6.2	Cramer-Nix Approach . . . . .	59
4.6.3	Current Pragmatical Approach for Fission . . . . .	62
<b>4.7</b>	<b>Summary and Remaining Limitations of the Code . . . . .</b>	<b>67</b>
4.7.1	“CONRAD 2.0” . . . . .	67
4.7.2	“CONRAD 2.0-beta” . . . . .	67

---

This chapter will focus on the cross section modeling in the statistical energy range (*cf.* Fig. 2.3 of Chapter 2). It must be emphasized that the CONRAD code [3] had only few statistical range capabilities prior the start of the present PhD work. Indeed, the code has been linked to the ECIS code [1] to adjust average total cross sections and to the TALYS code [51] for the various partial cross sections (*cf.* Chapter 2, Section 2.2). However, CONRAD uses this latter code as a “black-box” and implementation of new fission models required to assimilate parts of the TALYS code into the CONRAD code. An average  $\mathfrak{R}$ -matrix model was already implemented along with a spherical optical model similar to the SCAT-2 [49] program. Despite these previous developments, a lack of generic programming was limiting the use of “neutron transmission coefficients” (*e.g.* obtained from ECIS, the internal spherical optical model or the average  $\mathfrak{R}$ -matrix) to obtain partial cross sections. This latter comment will become clearer in the following as the Hauser-Feshbach frame for the calculation of statistical range cross section will be introduced.

## 4.1 Hauser-Feshbach Framework

The energy-averaged total cross section derived in Chapter 2 (*cf.* Eq. 2.28), leads to the definition of two “partial cross sections”,

$$\bar{\sigma}_{c,\text{tot}} = \frac{2\pi}{k_c^2} g_J (1 - \text{Re}[\bar{U}_{cc}^{J\pi}]) = \underbrace{\frac{\pi}{k_c^2} g_J |1 - \bar{U}_{cc}^{J\pi}|^2}_{\sigma_c^{\text{shape}}} + \underbrace{\frac{\pi}{k_c^2} g_J (1 - |\bar{U}_{cc}^{J\pi}|^2)}_{\sigma_c^{\text{reaction}}} \quad (4.1)$$

The first term,  $\sigma_c^{\text{shape}}$ , is called the *shape* elastic cross section and is related to the probability that the incoming particle is reflected on the target without penetrating into the nuclear matter. The second term,  $\sigma_c^{\text{reaction}}$ , on the contrary, is the complementary *reaction* cross section. The reaction cross section is not exactly the cross section for the formation of the compound nucleus (or absorption cross section), other direct cross sections, such as the direct inelastic cross sections should be subtracted from the reaction cross section to obtain the compound nucleus formation cross section.

A model providing  $\bar{U}_{cc}^{J\pi} - c$  being the entrance channels, in the present case, the neutron channels – would be enough to provide the average total cross section. However the shape elastic cross section does not correspond to the final elastic cross section as neutrons can be emitted “elastically” after having been absorbed by the target. It can be compared to the potential term of the Single Level Breit-Wigner (SLBW) expression (*cf.* 3.29 of Chapter 3). Thus, a model is necessary to decompose the absorption cross section into partial *compound* cross sections. The statistical Hauser-Feshbach [8] framework is used for that purpose. It can be derived from the SLBW formula. Considering the partial compound cross section related to a given level  $\lambda$  in the SLBW formalism

$$\sigma_{cc'\lambda}^{\text{comp}J\pi}(E) = \frac{\pi}{k_c^2} g_J \frac{\Gamma_{\lambda c} \Gamma_{\lambda c'}}{(E_{\lambda} + \Delta_{\lambda} - E)^2 + \frac{1}{4} \Gamma_{\lambda}^2}, \quad (4.2)$$

the actual partial cross section is obtained by summation over all levels

$$\sigma_{cc'}^{\text{comp}J\pi}(E) = \sum_{\lambda} \sigma_{cc'\lambda}^{\text{comp}J\pi}(E). \quad (4.3)$$

Here it is convenient to assume that  $\Delta_{\lambda} = 0$ . Equation 4.2 corresponds to process involving formation of a compound nucleus. Considering the resonance integral  $I_{\lambda}$  of a SLBW cross

section of Eq. 4.2,

$$I_\lambda = \int_0^\infty dE \sigma_{cc'\lambda}^{\text{comp}J^\pi}(E) = \int_0^\infty dE \frac{\pi}{k_c^2} g_J \frac{\Gamma_{\lambda c} \Gamma_{\lambda c'}}{(E - E_\lambda)^2 + \frac{1}{4} \Gamma_\lambda^2} \approx \frac{\pi}{k_c^2} g_J \int_\Delta dE \frac{\Gamma_{\lambda c} \cdot \Gamma_{\lambda c'}}{(E - E_\lambda)^2 + \frac{1}{4} \Gamma_\lambda^2} \quad (4.4)$$

The right-hand-side of Eq. 4.4 is obtained by assuming that the resonance is narrow enough so that its amplitude is almost entirely contained in the integration range  $\Delta$ . The range  $\Delta$  is supposed to be small enough so that the energy dependency of  $k_c$  can be neglected in the  $\Delta$  range. Assuming again that the resonance is narrow compared with  $\Delta$  (*i.e.*  $\Gamma_\lambda \ll \Delta$ ), the integration range can be reset to  $[0, +\infty[$  so that analytical integration can be performed. One obtains

$$I_\lambda \approx \frac{\pi}{k_c^2} g_J \int_0^\infty dE \frac{\Gamma_{\lambda c} \Gamma_{\lambda c'}}{(E - E_\lambda)^2 + \frac{1}{4} \Gamma_\lambda^2} = \frac{\pi}{k_c^2} 2\pi g_J \frac{\Gamma_{\lambda c} \Gamma_{\lambda c'}}{\Gamma_\lambda}. \quad (4.5)$$

Finally, the average value of the SLBW cross section  $\bar{\sigma}_{cc'}^{\text{comp}J^\pi}$  can be obtained by considering  $N$  resonances in an energy range  $D \times N$ ,  $D$  being the average resonance spacing

$$\bar{\sigma}_{cc'}^{\text{comp}J^\pi} = \frac{N \times \langle I_\lambda \rangle_\lambda}{N \times D} = \frac{\pi}{k_c^2} g_J \frac{2\pi}{D \times N} \left( N \times \left\langle \frac{\Gamma_{\lambda c} \Gamma_{\lambda c'}}{\Gamma_\lambda} \right\rangle_\lambda \right) = \frac{\pi}{k_c^2} g_J \frac{2\pi}{D} \left\langle \frac{\Gamma_{\lambda c} \Gamma_{\lambda c'}}{\Gamma_\lambda} \right\rangle_\lambda. \quad (4.6)$$

The bracket signs correspond to the average over the  $N$  resonances contained in the  $D \times N$  energy bin. This average is not an *energy* average but a *level* average. In practice, a width fluctuation correction term  $W_{cc'}$  is further introduced to take into account of the fact that

$$\left\langle \frac{\Gamma_{\lambda c} \Gamma_{\lambda c'}}{\Gamma_\lambda} \right\rangle_\lambda \neq \frac{\langle \Gamma_{\lambda c} \rangle_\lambda \langle \Gamma_{\lambda c'} \rangle_\lambda}{\langle \Gamma_\lambda \rangle_\lambda}. \quad (4.7)$$

The  $W_{cc'}$  coefficient has a significant effect on partial cross sections but as this is not the point of the present study, it is often omitted here but is present in the computations. The average total cross section can also be simply expressed as

$$\bar{\sigma}_{c,\text{tot}}^{\text{comp}J^\pi} = \sum_{c'} \bar{\sigma}_{cc'}^{\text{comp}J^\pi} = \frac{\pi}{k_c^2} g_J \frac{2\pi}{D} \langle \Gamma_{\lambda c} \rangle_\lambda, \quad (4.8)$$

where relation  $\Gamma_\lambda = \sum_c \Gamma_{\lambda c}$  has been used. As Eq. 4.2 is related to compound processes only, Eq. 4.8 is actually the total *compound* cross section or the compound nucleus formation cross section. This relation can be compared to Eq. 4.1 and leads to the definition of a new quantity named the *transmission coefficient*  $T_c$  defined by

$$T_c = 1 - |\bar{U}_{cc}^{J^\pi}|^2 = \frac{2\pi}{D} \langle \Gamma_{\lambda c} \rangle_\lambda. \quad (4.9)$$

Finally, the Hauser-Feshbach formula, provides the compound partial cross sections, according to

$$\bar{\sigma}_{cc'}^{\text{comp}J^\pi} = \frac{\pi}{k_c^2} g_J \frac{T_c T_{c'}}{\sum_{c''} T_{c''}} W_{cc'}. \quad (4.10)$$

The width fluctuation correction factor  $W_{cc'}$  vanishes when considering the total compound cross section, as an effect of the “flux conservation”

$$\bar{\sigma}_{c,\text{tot}}^{\text{comp}J^\pi} = \sum_{c'} \frac{\pi}{k_c^2} g_J \frac{T_c T_{c'}}{\sum_{c''} T_{c''}} W_{cc'} = \frac{\pi}{k_c^2} g_J T_c \frac{\sum_{c'} T_{c'} W_{cc'}}{\sum_{c''} T_{c''}} = \frac{\pi}{k_c^2} g_J T_c. \quad (4.11)$$



These two last expressions (Eqs. 4.10 and 4.11) are keystones of a global framework in which many sub-models provide transmission coefficients for a specific reaction type using their own physical description and parameters. They provide the compound nucleus part of all partial cross sections. One can however notice that, except for the total cross section that only depends on the entrance transmission coefficient  $T_c$  (*i.e.* neutron absorption or emission<sup>1</sup>), all other partial cross sections will depend on the transmission coefficients related to all reactions. This intrinsic competition between partial reactions increases dramatically the complexity of partial cross section analyses. This is caused by the fact that any change in one of the transmission coefficients will affect all partial cross sections. To make the CONRAD code able to calculate fission cross sections it was thus necessary to have reliable transmission coefficients for all other reactions. Some of the transmission coefficient sub-models available in CONRAD will be presented in the following. Most of them have been implemented specifically for the present PhD work.

## 4.2 Unresolved Resonance Range – Average $\Re$ -Matrix

As recalled above (*cf.* Eq. 4.1), a model providing  $\bar{U}_{cc}^{J\pi}$  can readily be used to provide entrance-channel-related transmission coefficients. In neutron cross section evaluation, two models are used to produce such average matrix coefficients. The first model considered here is a direct extension of the  $\Re$ -Matrix formalism explained above. At intermediate energies, resonances are not fully detailed due to energy resolution limitation of microscopic differential measurements and to the partial overlapping of resonances. Evaluation of *resolved* resonance parameters becomes equivocal. This energy domain, called Unresolved Resonance Range (URR), needs a proper treatment [63]. The URR is analyzed on the basis of prior average parameter values extracted from the RRR. An average treatment of the diagonal terms of the collision matrix leads to [5]

$$\bar{U}_c^{J\pi} \equiv \bar{U}_{cc}^{J\pi} \simeq e^{2i\phi_c} \frac{1 + iP_c(E) \left( \bar{R}_c^\infty + i\pi \frac{s_c \sqrt{E}}{2P_{\ell=0}(E)} \right)}{1 - iP_c(E) \left( \bar{R}_c^\infty + i\pi \frac{s_c \sqrt{E}}{2P_{\ell=0}(E)} \right)}, \quad (4.12)$$

where the *pole strength function*<sup>2</sup> parameters  $s_c$  can be estimated from the RRR analysis as

$$s_c = 2\pi \frac{\langle \gamma_{\lambda c}^2 \rangle_\lambda}{D_{J\pi}}. \quad (4.13)$$

The average level spacing  $D_{J\pi}$  involved in Eq. 4.13 is related to levels having quantum numbers  $J\pi$  similar to those in channel  $c$ <sup>3</sup>. The distant level parameters  $\bar{R}_c^\infty$  characterizes the effect of distant resonances, and need to be adjusted on experimental data. In the

<sup>1</sup>In this framework the entrance or exit transmission coefficients are identical quantities.

<sup>2</sup>The *pole* pole strength function is defined by Eq. 4.13, whereas the *strength function*  $S_c$  is given by  $S_c = 2\pi \frac{\langle \Gamma_{\lambda c} \rangle_\lambda}{D_{J\pi}}$ , which still contains a remaining energy-dependency because of the penetration factor  $P_c$ , *cf.* Eq. 3.27.

<sup>3</sup>In practice, it can be difficult to identify definitively the  $J\pi$  values of a resonance as measurements are cumulating events from different  $J\pi$  processes. Yet interference patterns on cross sections can give some clues about the difference in  $J\pi$  from a resonance to another. Sometimes this identification is not possible but the value of the incident neutron orbital momentum  $\ell$  can be identified. In such cases, the  $D_{J\pi}$  value is estimated as an average value for these  $\ell$ -tagged resonances.

case of neutron cross section evaluation, using Eqs. 4.9 and 4.12, a neutron transmission coefficient can be defined.

The parameters used in this model are obtained from the RRR analysis or from adjustments on experimental data at higher energies. It was explained in Chapter 2 that the reactor physics cross sections (related to plane wave scattering) involve many processes having specific  $J^\pi$  values. At low energy only few of these processes are contributing to the cross sections, hence data extracted from the RRR analysis [64] can be used to describe only few of these processes. It is thus difficult to use this formalism for high energies as more and more  $J^\pi$  processes are involved. An alternative approach, relying on optical models (described in the following) do not suffer from this limitation.

To explain why this model is still used in evaluation, it is necessary to details some phenomena that play effective roles in reactor physics. Even if the resonances in the URR are not experimentally resolved they exist. The cross sections depend on the relative velocity between the projectile and the target nucleus. As resonances can be quite narrow, the thermal motion of the target may be significant enough so that it has some effect on the relative velocity. This effect is known as the Doppler-broadening and cannot be taken into account if only an average value of the resonance is known. In practice this effect can be rendered if average resonance parameters (as those used by the average  $\Re$ -matrix) are known. A fictive (but representative) cross section can be reconstructed from these average parameters, broadened then averaged so that the effect of the thermal motion can be propagated to the cross section values. In practice this has no strong effects in reactor physics applications if multigroup formalism is used. Indeed, if resonances are narrow enough so that they are mostly contained in a single energy group, as the resonance integral is conserved by the broadening, the resulting average cross section remains unchanged. Yet this may have effect if a continuous energy description is used or if *probability tables* are used along with multigroup cross sections. These tables contain the distribution of the cross section values within an energy group. Even if the average value does not change in the group, if the medium temperature is modified, the distribution of the cross section values *do* change. This is illustrated in Fig. 4.1, where the total cross section and related cross section probability density are shown (in the energy range [300 eV,320 eV]) for two temperatures 0 K (red curves) and 300 K (blue curves). The average cross sections are also shown with dashed lines on the left part of Fig. 4.1. This average is made over the energy range [300 eV,320 eV], thus the Doppler broadening has little effect on the cross section average value (about 0.05%). If only a part of a resonance was contained in the energy range, the average value would have change more. On the other side, the cross section probability density (right part of Fig. 4.1) is strongly affected by the change in temperature. As probability tables are computed from the cross section probability density, they are significantly modified by Doppler-broadening.

At high enough energies, this treatment is no longer necessary because resonances overlap each other and Doppler broadening is no longer effective. The energy boundaries of the URR are determined, for the low energies, by the available experimental data, and for the higher energies by the effective range of the Doppler broadening. The emerging standard procedure (SPRT [65]) for the treatment of the URR relies on the alternative optical models to obtain transmission coefficients and phase shifts, then to extract from them the required averaged parameters used in the URR treatment. Before this PhD work, the average  $\Re$ -matrix formalism was already implemented in the CONRAD code, however its use in a generic and validated Hauser-Feshbach framework was still to be done.

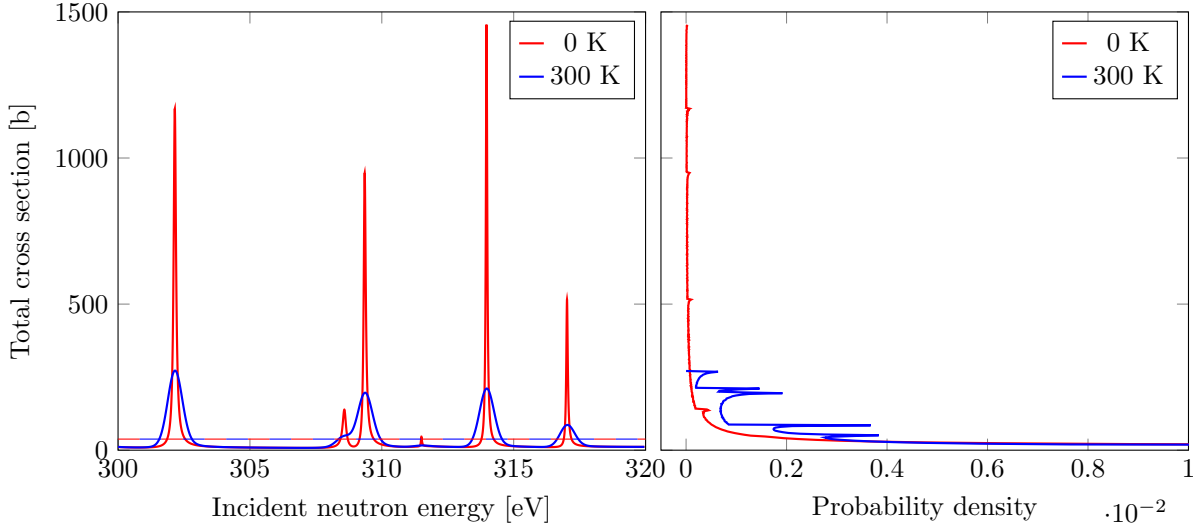


Figure 4.1 – Effect of Doppler broadening on the  $^{239}\text{Pu}(n, \text{tot})$  cross section (left) and on the cross section probability density (right). The average values of the cross sections is shown in dashed lines on the left plot.

### 4.3 Continuum Range – Optical Model

The main liability of the average  $\Re$ -matrix approach is that the number of parameters to be fitted becomes tremendous as incident neutron energy increases. As the energy increases, the number of significantly contributing channels increases, as well as the number of average parameters to be evaluated. An alternative model for supplying neutron transmission coefficients is the optical model. For comprehensive information about optical models see Refs. [1, 66–70]. In the following, the global scheme of the optical models will be sketched, more details about the coupled channel equations that are solved can be found in Appendix A.

Optical models share many common features with the  $\Re$ -matrix theory. Phenomenology is introduced in optical models through the description of the interaction potential  $\hat{V}_{cc'}(r_c, \hat{\Omega}_{c'})$  that is effective between the two particles of channel  $c$ . As in Eq. 2.6, the channel wave function is

$$\Psi_c = i^\ell Y_{m_\ell}^\ell(\hat{\Omega}_c) \frac{u_c(r_c)}{r_c}. \quad (4.14)$$

The Schrödinger equation (*cf.* Eq. 2.8) becomes

$$\left[ -\frac{\hbar^2}{2M_c} \left( \frac{d^2}{dr_c^2} - \frac{\ell(\ell+1)}{r_c^2} - 2\frac{\eta_c k_c}{r_c} \right) + \epsilon_c - E \right] u_c(r_c) = - \sum_{c'} \left[ \int_{4\pi} d^2\hat{\Omega}_c Y_\ell^{m*}(\hat{\Omega}_c) \hat{V}_{cc'}(\vec{r}_{c'}) Y_{\ell'}^{m'}(\hat{\Omega}_{c'}) \right] u_{c'}(r_{c'}). \quad (4.15)$$

In Eq. 4.15, the interaction potential is present in the right-hand-side. In case of spherically symmetric interaction potential,  $\hat{V}_{cc'}(r_c, \hat{\Omega}_{c'})$  does not depend on  $\hat{\Omega}_{c'}$  and most of terms in the summation vanish. Therefore for such potentials, only channels having the same  $\ell$  and  $m$  can be coupled. The channel-to-channel coupling potential is defined by

$$W_{cc'}(r) = \frac{2M_c}{\hbar^2} \int_{4\pi} d^2\hat{\Omega}_c Y_\ell^{m*}(\hat{\Omega}_c) \hat{V}_{cc'}(\vec{r}_{c'}) Y_{\ell'}^{m'}(\hat{\Omega}_{c'}). \quad (4.16)$$

Finally the coupled channel equation is

$$\left[ \frac{d^2}{dr_c^2} - \frac{\ell(\ell+1)}{r_c^2} - 2\frac{\eta_c k_c}{r_c} + k_c^2 \right] u_c(r_c) = - \sum_{c'} W_{cc'}(r_{c'}) u_{c'}(r_{c'}). \quad (4.17)$$

Just like in the  $\mathfrak{R}$ -matrix theory, only channels coupled to the same  $J^\pi$  value are considered. Hence several coupled equations are to be solved separately according to the  $J^\pi$  value of the process. In practice, as  $\hat{V}_{cc'}(r_{c'}, \hat{\Omega}_{c'})$  is an operator, the coupled channel equation can become quite complex because of terms such as spin-orbit coupling (involving wave function first order derivatives) are involved. Further details are beyond the scope of this work. It can be stated that, from the numerical resolution of the coupled channel equation, the radial waves  $u_c$  are obtained and matched to the analytical asymptotic wave functions of Eq. 2.9, for which the coupling potential  $W_{cc'}(r_{c'})$  is zero. This finally leads to the definition of the average collision matrix  $\bar{U}$  (called the scattering matrix  $\mathcal{S}$  in optical models). As in Eq. 2.26, calculated collision matrix elements are used to obtain the channel-to-channel cross sections

$$\bar{\sigma}_{cc'}^{J^\pi} = \frac{\pi}{k_c^2} g_J \left| \delta_{cc'} - \bar{U}_{cc'}^{J^\pi} \right|^2. \quad (4.18)$$

A common interface was developed in CONRAD for all models that can provide the value of the average collision matrix  $\bar{U}_{cc'}^{J^\pi}$  (optical models and average  $\mathfrak{R}$ -matrix). They can now be easily tested and interchanged in the Hauser-Feshbach framework.

Since the total cross section depends only on the neutron transmission coefficients (*cf.* Eq. 4.1) and can be compared with representative evaluated data, they are chosen as a first checking comparison. This was also a test to validate a newly implemented C++ coupled channels program based on the same algorithm than the ECIS code<sup>4</sup> that has been implemented for during this PhD. The simplest reaction to be considered is  $^{56}\text{Fe}(n, \text{tot})$  that involves an even-even medium-mass target and for which a spherical optical model potential can be assumed to be relevant. The even-even nature of  $^{56}\text{Fe}$  leads to a zero intrinsic spin for the target ground state. This in turns reduces the complexity of the angular momentum coupling involved in the coupled channel optical models. In this particular case, for  $^{56}\text{Fe}(n, \text{tot})$ , equations solved by from the spherical optical model (channels not coupled) and by the more refined coupled channel optical models are identical. Left part of Fig 4.2 shows results obtained for the calculation using the ECIS code, the CONRAD internal spherical optical model implemented by P. Archier [50] and the new coupled channel algorithm. Comparison with the TALYS code is not necessary in this case as TALYS actually drives ECIS internal calculations to obtain the total cross section (*i.e.* both shape elastic cross sections and transmission coefficients). A second test shown on the right part of Fig 4.2 corresponds to a similar calculation but for  $^{157}\text{Gd}(n, \text{tot})$ . In this case the target nucleus has no longer a zero-spin ground state and is deformed. Because of these two additional features, the equation coupling in the coupled channel model becomes more complex. It was thus a relevant second test case. More details are provided in Appendix A about the coupled channel equations. Four rotational levels are included in this calculation. The new implementation was found to be roughly as fast as the ECIS calculation and can further benefit from the native parallelism of the CONRAD code.

One can notice that all optical models are very consistent. However the comparison with evaluated data and calculated results is rather discrepant as shown for  $^{56}\text{Fe}(n, \text{tot})$

---

<sup>4</sup>First version of the ECIS code were written about 50 years ago in an old-fashioned FORTRAN-IV language, which makes the code difficult to maintain.

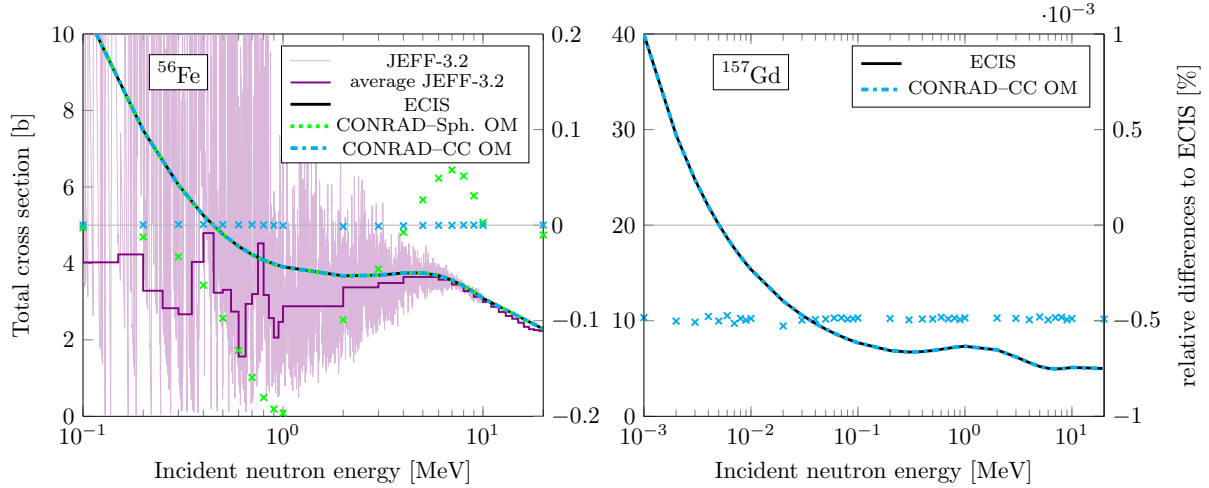


Figure 4.2 – (left) Comparison of the average total cross section of  $(n + {}^{56}\text{Fe})$  calculated using the various options available in the CONRAD code. Solid lines correspond to cross sections obtained with optical models. To make comparison between optical model results easier, relative differences to ECIS results are shown with x-marks. (right) Same but for the  $(n + {}^{157}\text{Gd})$  reaction.

for energies below 3 MeV. This of course may be due to the limited relevance of using average cross section models (optical models) for such low energies with this type of medium-mass isotope, but this can also be explained by the choice of the optical model *potential*. The selected optical model potential was taken from the RIPL database [10], (an international database containing reference input data for numerous nuclear data applications). The potential parameter set (RIPL-1416), is designed to cover a large energy range (0-200 MeV), wider than the present one. One can notice that small differences exist between the coupled channel results (ECIS and CONRAD-CC OM) and the spherical optical model (CONRAD-Sph. OM), in the case of  ${}^{56}\text{Fe}(n, \text{tot})$ . This may be caused by some extra angular discretization that is considered in the coupled channel programs. For the total cross section, the differences between ECIS and CONRAD-CC OM are below 0.001%, which is close to the digit precision of the ECIS output files. In the case of  ${}^{157}\text{Gd}(n, \text{tot})$ , differences are even smaller (about 0.0005%). Obtaining satisfactory comparison with evaluated data is not the objective of the work presented here, which is to obtain satisfactory modeling for partial reactions so that fission models can be tested. Model parameter evaluation is not performed here, therefore verification will be limited to comparisons between codes (TALYS and CONRAD mainly). Codes are of course supplied with identical input parameters<sup>5</sup>.

## 4.4 Capture Reaction and Level Density Models

The next step in the quest of better fission cross section modeling is to obtain compound partial cross sections and to do so, reaction-dedicated transmission coefficients are necessary. As explained before, both average  $\mathfrak{R}$ -matrix and optical models can provide neutron transmission coefficients<sup>6</sup> that can be in turn used to provide the total compound cross section. To extend the modeling capability of the code, beyond total cross section, to

<sup>5</sup>Consistency with code internal databases (*e.g.* low-lying levels and deformations) had also to be ensured for these comparisons.

<sup>6</sup>They also provide the shape elastic cross section.

partial cross section calculations, the Hauser-Feshbach model has been implemented. It must be “fed” with transmission coefficients in order to calculate compound partial cross sections. As photon radiative emission is always possible, the simplest step further is to introduce a gamma transmission coefficient  $T_\gamma^{J^\pi}$  that will allow calculation of both capture and elastic cross sections. In reactor physics, the capture cross section corresponds to radiative emission of photons and no re-emission of the incident particle. The elastic cross section corresponds to the re-emission of the incident particle – or of another particle of the same nature – where the residual nucleus is identical to the target nucleus. For instance if the target is in its ground state, which is often the case, the residual nucleus is also in its ground state. The elastic cross section is the addition of the shape elastic and the compound elastic cross sections, whereas only compound radiative capture occurs.

The gamma transmission coefficient is actually a sum of many photon-channel transmission coefficients. Each channel is related to a given type  $X$  of transition having a multipolarity  $\ell$ . The  $X$  term labels either the electric E or magnetic M nature of the photon-decay, as for instance E1, M2, *etc.* Each channel is also characterized by a “reaction transition energy”  $\epsilon_\gamma$  that is the amount of energy taken away by the photon. The multipolarity  $\ell$  is the amount of angular momentum carried away by the photon. After the decay, the nucleus lies in a state  $i$  of its related level scheme. This state is described by its related energy  $E_i$ , angular momentum  $J_i$  and parity  $\pi_i$ . The energy of the photon  $\epsilon_\gamma$  is thus the difference between the compound nucleus excitation energy  $E^*$  and the energy of ending state  $E_i$ . It is given by

$$\epsilon_\gamma(i) = E^* - E_i. \quad (4.19)$$

As angular momentum and total parity of the whole system must be conserved. Some photon-decay channels are forbidden (suppressed) because they would break these conservation rules. One can finally write

$$T_\gamma^{J^\pi} = \sum_{X \in \{E, M\}} \sum_{\ell} \sum_i T_{X\ell}(\epsilon_\gamma(i)) f(J_i, \pi_i, J, \pi, X, \ell), \quad (4.20)$$

where the  $f$  function ensures the conservation rules:

$$f(J_i, \pi_i, J, \pi, E, \ell) = \begin{cases} 1, & |J - \ell| \leq J_i \leq J + \ell \text{ and } \pi = (-1)^\ell \pi_i \\ 0, & \text{otherwise} \end{cases}, \quad (4.21)$$

$$f(J_i, \pi_i, J, \pi, M, \ell) = \begin{cases} 1, & |J - \ell| \leq J_i \leq J + \ell \text{ and } \pi = (-1)^{\ell+1} \pi_i \\ 0, & \text{otherwise} \end{cases}. \quad (4.22)$$

In practice, the nucleus level scheme is not known up to energies corresponding to the neutron binding energy (4 to 10 MeV). Hence the summation of Eq. 4.20 can be done only for the known levels (usually only the lowest energy levels). The remaining levels are treated using a phenomenological average level density  $\rho(E, J, \pi)$ . If the  $N$  first levels are known up to a certain energy  $E_{\text{cont}}$ , Eq. 4.20 becomes:

$$T_\gamma^{J^\pi} = \sum_{X \in \{E, M\}} \sum_{\ell} \left[ \sum_{i=1}^N T_{X\ell}(\epsilon_\gamma(i)) f(J_i, \pi_i, J, \pi, X, \ell) + \sum_{J' \pi'} \int_{E_{\text{cont}}}^{E^*} d\epsilon_\gamma \rho(E^* - \epsilon_\gamma, J', \pi') T_{X\ell}(\epsilon_\gamma) f(J', \pi', J, \pi, X, \ell) \right]. \quad (4.23)$$



This computation of gamma transmission coefficients has been implemented in the CONRAD code using the TALYS reference code as guideline. The CONRAD implementation has been verified to be consistent with the TALYS results, yet the selected integration method used in the calculation of the last term of Eq. 4.23 has been found to be a possible source of significant differences, about 2% for  $^{56}\text{Fe}(n, \gamma)$  and 0.6% for  $^{157}\text{Gd}(n, \gamma)$ .

#### 4.4.1 Level Density Models

In order to obtain gamma transmission coefficients, level density models are required. Phenomenological level density models usually decompose the level density  $\rho(E^*, J, \pi)$ , into a product of a state density  $\rho(E^*)$ , an angular momentum probability of the level  $P(J)$  and its parity probability  $P(\pi)$ , so that

$$\rho(E^*, J, \pi) = \rho(E^*)P(J)P(\pi). \quad (4.24)$$

Therefore  $\rho(E^*, J, \pi)dE^*$  is the number of levels having a total angular momentum  $J$  and parity  $\pi$  in the energy interval  $dE^*$  around the excitation energy  $E^*$ . Therefore each term can be specifically treated by dedicated models. The implementation of a gamma transmission coefficient model has been eased by the use of the C++ nuclear physics model library that is shared by the CONRAD and the FIFRELIN [52] codes. This library contains “tools” that can benefit to both codes. This library already contained level density models before this present PhD work started thanks to D. Regnier PhD work [71]. Concerning the level densities, a Composite Gilbert-Cameron Model [9] (CGCM) is used. This model is widely used for three reasons:

- It relies on a small amount of parameters.
- Its implementation is quite easy.
- It can be used to reproduced quite satisfactorily the few observables related to level densities, namely low-lying average values and the mean level spacing at neutron spectroscopy energies (called  $D_0$ ).

This composite model consists in a Constant Temperature Model (CTM) for low excitation energies and a Fermi Gas Model (FGM) at higher energies. These two models are smoothly joint at a matching excitation energy  $E_M$

$$\rho^{\text{CGCM}}(E^*) = \begin{cases} \rho^{\text{CTM}}(E^*) = \frac{1}{T} \exp \left[ \frac{E^* - E_0}{T} \right], & E^* \leq E_M \\ \rho^{\text{FGM}}(E^*) = \frac{\sqrt{\pi}}{12} \frac{\exp \left[ 2\sqrt{a(E^* - \Delta)} \right]}{a^{1/4}(E^* - \Delta)^{5/4}}, & E^* \geq E_M \end{cases}. \quad (4.25)$$

Here  $T$  and  $E_0$  are parameters adjusted on low-lying levels and  $\Delta$  is an average pairing energy. The level density parameter  $a$  is set using the Ignatyuk’s prescription [72] with thus a dependence on the excitation energy  $E^*$

$$a(E^*) = \tilde{a} \left[ 1 + \delta W(A, Z) \frac{1 - \exp[-\gamma(E^* - \Delta)]}{E^* - \Delta} \right], \quad (4.26)$$

where  $\delta W(A, Z)$  is a shell correction for the considered nucleus. The asymptotic level density parameter  $\tilde{a}$  and the  $\gamma$  parameter are obtained using systematics:

$$\tilde{a} = \alpha A + \beta A^{2/3} \quad \text{and} \quad \gamma = \frac{\gamma_0}{A}. \quad (4.27)$$



The  $\alpha$ ,  $\beta$  and  $\gamma_0$  parameters are obtained from the RIPL [10] database.

Both CTM and FGM rely on the assumption of equiprobability of the parity distribution  $P(\pi = \pm 1) = \frac{1}{2}$ , and on a Rayleigh-type distribution law for the angular momentum probability

$$P(J) = \frac{J + \frac{1}{2}}{\sigma^2} \exp \left[ -\frac{(J + \frac{1}{2})^2}{2\sigma^2} \right], \quad (4.28)$$

where  $\sigma$  is a parameter called the *spin cutoff* and  $J$  is expressed in units of  $\hbar$ . This distribution (Eq. 4.28) is not normalized for discrete values. To compensate this problem, two normalization options are present in the code, the piece-wise normalization<sup>7</sup>:

$$P^{\text{pw}}(J) = \frac{P(J)}{\sum_{J'} P(J')}, \quad (4.29)$$

and the integral normalization:

$$P^{\text{int}}(J) = \int_{J-\frac{1}{2}}^{J+\frac{1}{2}} \frac{j}{\sigma^2} \exp \left[ -\frac{j^2}{2\sigma^2} \right] dj, \quad (4.30)$$

where the integration boundaries must be shifted if one considers integer angular momenta instead of half-integer ones. This normalization can have effects up to 0.3% (respectively 2.3%) on the level densities for the  $P^{\text{int}}$  (respectively  $P^{\text{pw}}$ ) normalization. This effect is calculated by comparison with the case with no-normalization (Eq. 4.28).

A model of the spin-cutoff  $\sigma$  is also required, the Back-Shifted, following the TALYS standard route [73] is defined as follow<sup>8</sup>

$$\sigma^2(E^*) = \begin{cases} \sigma_d^2, & 0 \leq E^* \leq E_d \\ \sigma_d^2 + \frac{E^* - E_d}{B_n - E_d} (\sigma_F(B_n) - \sigma_d^2), & E_d \leq E^* \leq B_n \\ \sigma_F^2(E^*), & E^* \geq B_n \end{cases}, \quad (4.31)$$

where again  $E_d$  and  $\sigma_d$  are extracted from low-lying levels as described in Ref. [73], and  $\sigma_F$  is the Fermi-gas spin-cutoff given by

$$\sigma_F^2(E^*) = \frac{I_0/\hbar^2}{\tilde{a}} \sqrt{a(E^* - \Delta)}, \quad (4.32)$$

where  $I_0$  is the rotational moment of inertia of the nucleus, assumed here to be a rigid spherical body and is thus given by

$$I_0 = \frac{2}{5} m_0 R^2 A \approx 0.01389 A^{5/3} \hbar^2 \text{ MeV}^{-1}, \quad (4.33)$$

where  $m_0$  is the neutron mass and  $R$  is the nucleus radius that is here  $R = 1.2A^{1/3}$  fm.

As said above, all parameters involved in the level density parameterization are not completely free, the low-lying levels and the mean level spacing measurements obtained by neutron spectroscopy are used to constrain the model parameters<sup>9</sup>.

<sup>7</sup>In practice, the sum span over the first 50 possible  $J$  values.

<sup>8</sup>To obtain better agreement between CONRAD and TALYS, the binding energy  $B_n$  in Eq. 4.31 is replaced by the matching energy  $E_M$  used in Eq. 4.25.

<sup>9</sup>The mean level spacing obtained with slow neutrons is directly related to the level density at  $E^* = B_n$ .

### 4.4.2 Gamma Strength Functions

To obtain the gamma transmission coefficient of Eq. 4.23, the multipolar transmission coefficients  $T_{X\ell}(\epsilon_\gamma)$  must be provided. This can be done by use of gamma strength functions  $f_{X\ell}$  so that

$$T_{X\ell}(\epsilon_\gamma) = 2\pi f_{X\ell}(\epsilon_\gamma) \epsilon_\gamma^{2\ell+1}. \quad (4.34)$$

Gamma strength functions are often a part of photo-absorption cross section models. Usual gamma strength models are independent of the excitation energy of the nucleus. However some models incorporate a slight dependency on this energy.

Several gamma strength function models were already present in the shared library mentioned above thanks again to D. Regnier PhD work [71]. The already implemented models are the *Enhanced Generalized Lorentzian* (EGLO) model defined in RIPL-3 [10], and the Brink-Axel [74] model, also called Standard Lorentzian (SLO) in RIPL-3. The CONRAD code could use the SLO model with minor implementation work. The TALYS standard route uses a slightly different version of the EGLO model<sup>10</sup>. To maintain differences between the CONRAD and TALYS codes as small as possible (for the present objective to have a “safe” framework to work further on fission cross sections) an identical model had to be implemented.

Following the TALYS standard route, the Kopecky-Uhl [75] model is used for the  $X\ell \equiv E1$  transitions and the Brink-Axel [74] model (SLO) for other transitions. In the Kopecky-Uhl model, the strength function is given by

$$f_{E1}(\epsilon_\gamma, E^*) = \frac{\sigma_{X\ell} \Gamma_{E1}}{(2\ell+1)\pi^2 \hbar^2 c^2} \left[ \frac{\epsilon_\gamma \tilde{\Gamma}_{E1}(\epsilon_\gamma, T_f)}{(\epsilon_\gamma^2 - E_{E1}^2)^2 + \epsilon_\gamma^2 \tilde{\Gamma}_{E1}^2(\epsilon_\gamma, T_f)} + 0.7 \frac{\tilde{\Gamma}_{E1}(0, T_{f,i})}{\epsilon_\gamma^3} \right], \quad (4.35)$$

where

$$T_{s \in \{f,i\}}(E^*) = \sqrt{\frac{E^* - \Delta - \epsilon_\gamma \delta_{sf}}{a(S_n)}} \quad \text{and} \quad \tilde{\Gamma}_{E1}(\epsilon_\gamma, T) = \Gamma_{E1} \frac{\epsilon_\gamma^2 + 4\pi^2 T^2}{E_{E1}^2}. \quad (4.36)$$

The difference between this model and the EGLO lies in the temperature of the second term of Eq. 4.35. The RIPL-3 states  $T_i$  for the EGLO whereas TALYS implementation is  $T_f$  for the Kopecky-Uhl model.

For multiplicities different than  $E1$ <sup>11</sup>, the strength function model is the SLO defined by

$$f_{X\ell}(\epsilon_\gamma) = \frac{1}{(2\ell+1)\pi^2 \hbar^2 c^2} \frac{\sigma_{X\ell} \epsilon_\gamma \Gamma_{X\ell}^2}{(\epsilon_\gamma^2 - E_{X\ell}^2)^2 + \epsilon_\gamma^2 \Gamma_{X\ell}^2}. \quad (4.37)$$

In both models  $E_{X\ell}$ ,  $\Gamma_{X\ell}$  and  $\sigma_{X\ell}$  are parameters that can be adjusted.

### 4.4.3 Verification on Capture and Elastic Cross Sections

In the TALYS code, it is possible to obtain intermediate results such as the level density  $\rho(E, J)$  and the gamma strength functions  $f_{X\ell}(E)$  that are used in the calculations. Comparisons were made with the corresponding CONRAD intermediate results to check consistency. However, this step is not reported here, but the agreement was satisfactory,

<sup>10</sup>The TALYS code uses a strength function model based on the Kopecky-Uhl original model [75] whereas the EGLO model is based on a modified version defined in Ref. [76]

<sup>11</sup>The only transitions considered in the present work are  $E1$ ,  $E2$ ,  $M1$  and  $M2$ , following the TALYS standard route, no other multiplicities are considered.

below 0.1% of difference for strength functions and about 0.0001% for level densities. Comparison on capture and elastic cross sections are presented instead. These compound cross sections are calculated using the Hauser-Feshbach formula (Eq. 4.10) and are added, for the elastic cross section, to the shape elastic cross section obtained by the optical model. Results can be seen in Fig. 4.3 for the elastic scattering and radiative capture cross sections of the ( $^{56}\text{Fe} + n$ ) and ( $^{157}\text{Gd} + n$ ) colliding systems. The TALYS and CONRAD results (respectively, the blue solid and green dashed curves) are so close that the relative difference must be shown in the right axis. For all considered cases, the differences are quite satisfactory, the maximum of difference is for the  $^{56}\text{Fe}(n, n)$  reaction, below 0.05%. This test thus verifies the implementation of the Hauser-Feshbach engine and the calculation of the gamma transmission coefficient from the gamma strength functions and level density.

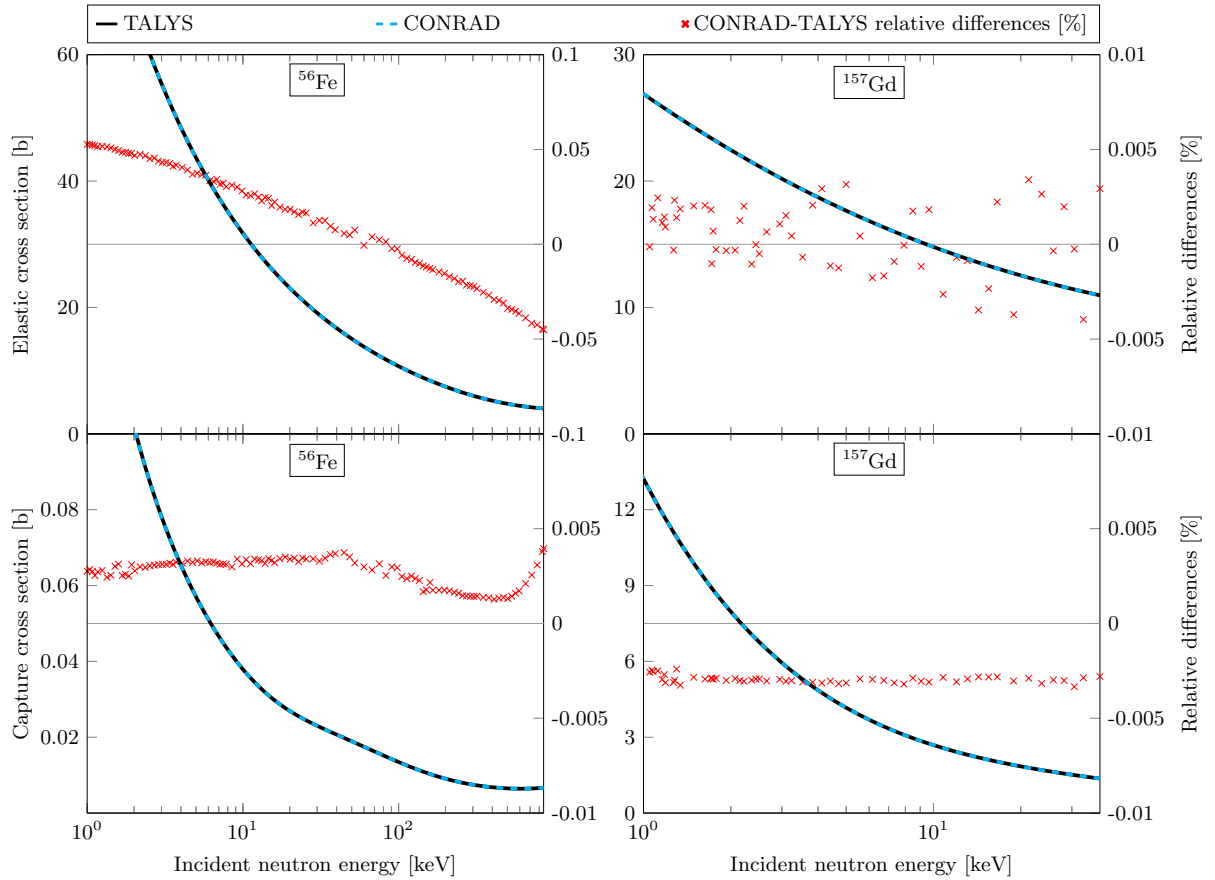


Figure 4.3 – Verification of the CONRAD Hauser-Feshbach model with the TALYS code for  $^{56}\text{Fe} + n$  (left plots) and  $^{157}\text{Gd} + n$  (right plots).

## 4.5 Inelastic Scattering

Prior to focusing on fission cross section modeling, a last reaction must be considered, the neutron inelastic scattering. This reaction cannot be neglected because the Hauser-Feshbach formula enforces that the sum of all partial cross sections remains equal to the total cross section (*cf.* Eq. 4.11). This is due to the constraint on  $W_{cc'}$  for the conserving flux

$$\sum_{c'} \frac{T_c T_{c'}}{\sum_{c''} T_{c''}} W_{cc'} = T_c. \quad (4.38)$$

Omitting inelastic cross section would lead to either restraining the energy range of calculation of fission cross section below the first inelastic threshold energy, or to highly overestimate all partial cross sections. This is especially true for fertile isotopes for which the inelastic cross section can be as large as the fission cross section. The eventual compensation on fission and capture cross section would undermine all efforts made so far to obtain a suitable framework for fission cross section modeling. The inclusion of inelastic reaction in the model is yet somehow different from the capture reaction because a direct component must be taken into account. These direct terms are rather similar in nature to the shape elastic cross section. They correspond to incident neutron interacting with collective states of the target (the ground state and some collective excited states). These *direct inelastic* terms can be seen as a kind of “shape inelastic” terms. The incident neutron is thus scattered but some of its energy has been transferred to a collective state of the target nucleus. In case of coupled channel calculations, some direct terms are directly provided by the couple channel calculation. In this study, these terms involve levels and related inelastic channels that are included in the coupled channel calculation as part of the ground state rotational band. For other levels or for spherical nuclei, following the TALYS code as guideline, a vibrational model is assumed and treated in the Distorted Wave Born Approximation (DWBA) [1, 70]. The ECIS code can be used to provide such direct terms. Since the DWBA and coupled channel formalisms have many similarities, a DWBA model was also implemented in the CONRAD code for the present study.

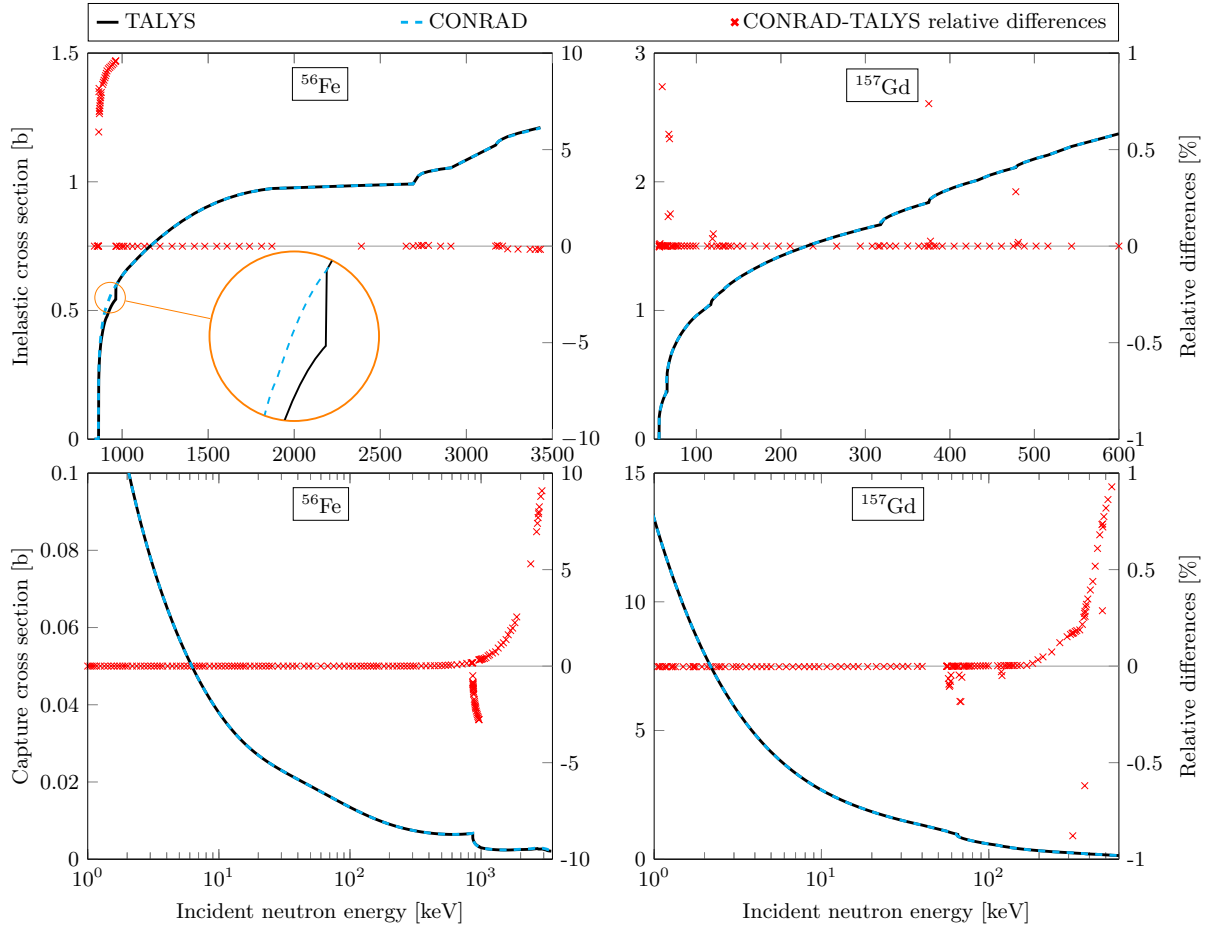


Figure 4.4 – Same as Fig. 4.3 but with the elastic cross section substituted by the inelastic cross section (direct and compound).

It can be seen in Fig. 4.4 that larger differences are present between code results compared with those of Fig. 4.3. One first notices large differences in the vicinity of certain energies. This is obvious on the low energy side of the  $^{56}\text{Fe}$  inelastic cross section. Although both codes seem to have similar threshold energies related to the first inelastic level (near 800 keV), they provide different values up to a certain energy near 1000 keV whereas above that point consistency is restored. These differences come from different threshold energies used for the treatment of the direct and compound inelastic cross sections in the TALYS code. This explains most of the differences observed in Fig. 4.4. Another striking difference is visible over the high energy part of the capture cross sections for both  $^{56}\text{Fe}$  and  $^{157}\text{Gd}$ . These deviations are due to the  $(n, \gamma n)$  reaction that was neglected in the CONRAD code but not in TALYS. At low energies, this reaction is negligible, which can be explained by the two following arguments:

- First, the gamma strength function shape implies that photons are more likely to be emitted at energies around 1 MeV, with small dependency on nucleus excitation energy. To be able to emit a neutron after a gamma emission, the gamma must be of energy smaller than  $E^* - B_n$ , thus the  $(n, \gamma n)$  becomes more favored as  $E^* - B_n$  tends to 1 MeV.
- Second, as excitation energy increases, the level density near the final energy (*cf.* Eq. 4.23) increases exponentially.

This explains the exponential shape of the differences now attributed to the  $(n, \gamma n)$  reaction. Such “second chance” (or two-steps) reactions (*cf.* Chapter 1) are not considered in the CONRAD code. For the remaining section of this chapter that is related to fission cross section modeling, these features have been deactivated in the TALYS code so that comparison with the CONRAD are not biased.

To illustrate the effect of this “second chance” removal, a calculation similar to the lower-left part of Fig. 4.4 is performed and a new comparison is made between CONRAD and TALYS (“second chance” deactivated). The results are shown in Fig. 4.5. It can be seen that differences between codes have been cut by about one order of magnitude (from 10% to about 0.6%) compared to results shown in Fig. 4.4.

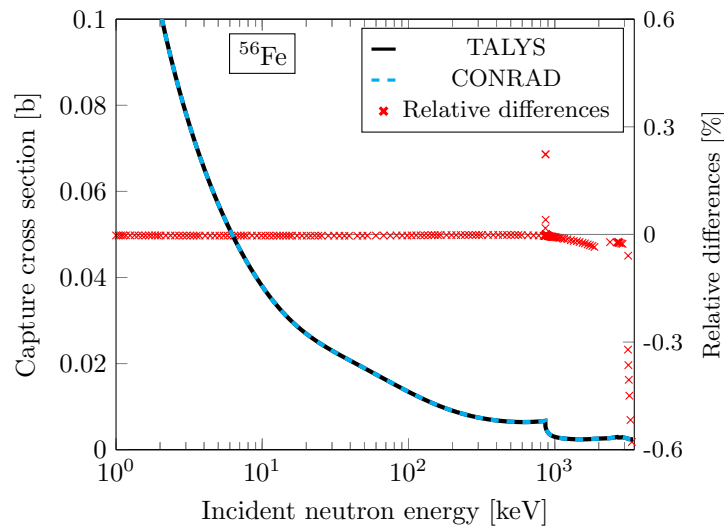


Figure 4.5 – Verification of the CONRAD Hauser-Feshbach model with the TALYS code for  $^{56}\text{Fe}(n, \gamma)$  with two steps reactions deactivated in the TALYS code.

Remaining differences can be seen around 800 keV corresponding to the first inelastic level. This could be explained this time by small change in the *compound* inelastic cross section. At higher energies (above 1 MeV), the difference between codes raises again, but this is much smaller than in Fig. 4.4. For the time being these differences remain unexplained, but are acceptable for the purpose of the present work which will be now focused on fission models.

Besides checking model implementations, one must keep in mind that possible differences between numerical implementations and also between nuclear databases can have significant eventual effects. Both CONRAD and TALYS codes use their own nuclear data input library, describing for instance the experimental low-lying levels of the various isotopes. Some nuclear levels present some differences in level energies and more often in assigned angular momenta and parities.

## 4.6 Fission Reaction

Some of the necessary developments realized for the present work to provide a proper framework for evaluation were summarized in the previous sections. These are related to all partial cross sections but fission. In this last section, current models for obtaining fission transmission coefficients will be discussed. Focus will be made on the well-known and extensively used Hill-Wheeler model [11]. Final comparisons with the TALYS reference code will be presented on actual actinide fission cross section calculations.

### 4.6.1 Hill-Wheeler Approach

To understand the underlying phenomenon in the Hill-Wheeler [11] famous formula, one can consider a nucleus deforming from a spheroidal shape to an elongated dumbbell shape, and eventually to two nascent fragments. The nucleus deformation is hindered by attractive nuclear forces. At a certain deformation, the Coulomb repulsive force prevails and increases deformation. The potential felt by the nucleus can be approximated, at least locally, by its second order Taylor expansion in the vicinity of the potential maximum<sup>12</sup>. The system behavior is thus modeled by a fictive particle interacting with an inverted parabola potential as represented in Fig. 4.6. The wave function  $\Psi$  of the equivalent fictive particle is solution of

$$-\frac{\hbar^2}{2\mu} \frac{d^2\Psi}{d\eta^2} + (V - \frac{1}{2}\mu\omega^2\eta^2)\Psi = E\Psi, \quad (4.39)$$

where  $\eta$  is a general deformation parameter (often written  $\beta$ ) related to a degree of freedom relevant to the fission process (elongation). The  $\mu$  parameter is the inertia of the fictive particle “with respect of  $\eta$ ”,  $V$  and  $\hbar\omega$  are respectively the barrier height and curvature. Using the variable change  $x = \eta\sqrt{\mu\omega/\hbar}$  and writing  $b = (V - E)/\hbar\omega$ , one obtains

$$\frac{d^2\Psi}{dx^2} + (x^2 - 2b)\Psi = 0. \quad (4.40)$$

The solutions of this wave equation are expressed in terms of parabolic cylinder functions [48]. The corresponding asymptotic behavior [11] for  $x > 0$  is

$$\Psi \sim T \equiv 2^{-\frac{1}{4}}x^{-\frac{1}{2}} \exp \left[ i\frac{x^2}{2} - i\frac{b}{2} \ln 2x^2 + i\frac{\pi}{8} - \pi\frac{b}{4} \right], \quad (4.41)$$

---

<sup>12</sup>As the expansion is made in the vicinity of the potential maximum, the first order derivative term in this expansion vanishes.

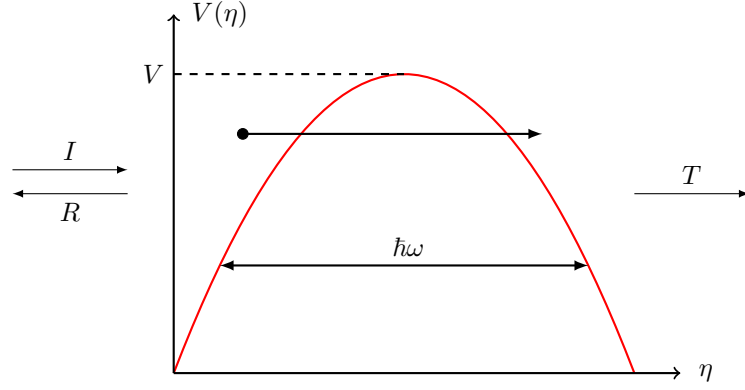


Figure 4.6 – Schematic representation of the fission process in the Hill-Wheeler usual approach: a fictive particle of inertia  $\mu$  (black mark) tunnels through an inverted parabolic potential. The asymptotic forms of the wave function  $I$ ,  $R$  and  $T$  are also shown on both sides of the barrier.

and for  $x < 0$  the asymptotic behavior is a combination of an incident wave  $I$  and a reflected wave  $R$

$$\begin{aligned} I &\equiv \frac{\sqrt{2\pi} 2^{-\frac{1}{4}} |x|^{-\frac{1}{2}}}{\Gamma(\frac{1}{2} + ib)} \exp \left[ -i \frac{x^2}{2} + i \frac{b}{2} \ln 2x^2 + i \frac{\pi}{8} + \pi \frac{b}{4} \right], \\ R &\equiv 2^{-\frac{1}{4}} |x|^{-\frac{1}{2}} \exp \left[ i \frac{x^2}{2} - i \frac{b}{2} \ln 2x^2 - 3i \frac{\pi}{8} + 3\pi \frac{b}{4} \right]. \end{aligned} \quad (4.42)$$

Conservation of the probability current defined as  $j = \frac{\hbar}{2\mu i} (\Psi^* \frac{\partial \Psi}{\partial x} - \Psi \frac{\partial \Psi^*}{\partial x})$  implies that

$$|I|^2 = |R|^2 + |T|^2. \quad (4.43)$$

The barrier transmission coefficient  $T_f$  is defined by

$$T_f = \left| \frac{T}{I} \right|^2 = \frac{|T|^2}{|T|^2 + |R|^2} = \frac{1}{1 + \left| \frac{R}{T} \right|^2}. \quad (4.44)$$

Substituting Eqs. 4.41 and 4.42 in Eq. 4.44, it reads

$$\frac{R}{T} = \exp(-2i\pi + \pi b) = \exp(\pi b), \quad (4.45)$$

eventually yielding the famous formula, commonly used in cross section evaluation works

$$T_f = \left[ 1 + \exp \left( 2\pi \frac{V - E}{\hbar\omega} \right) \right]^{-1}. \quad (4.46)$$

A representation of the energy dependence of the Hill-Wheeler transmission coefficient will be shown in the following.

### 4.6.2 Cramer-Nix Approach

Prior to detailing how the Hill-Wheeler formula is used in practice, an alternative modeling of the barrier tunneling will be presented. When evidence began to show that fission barrier may consist of several humps, Cramer and Nix [22] extended the Hill-Wheeler



model to more complex barrier shapes. They considered a barrier made of three smoothly joint parabolae as shown in Fig. 4.7.

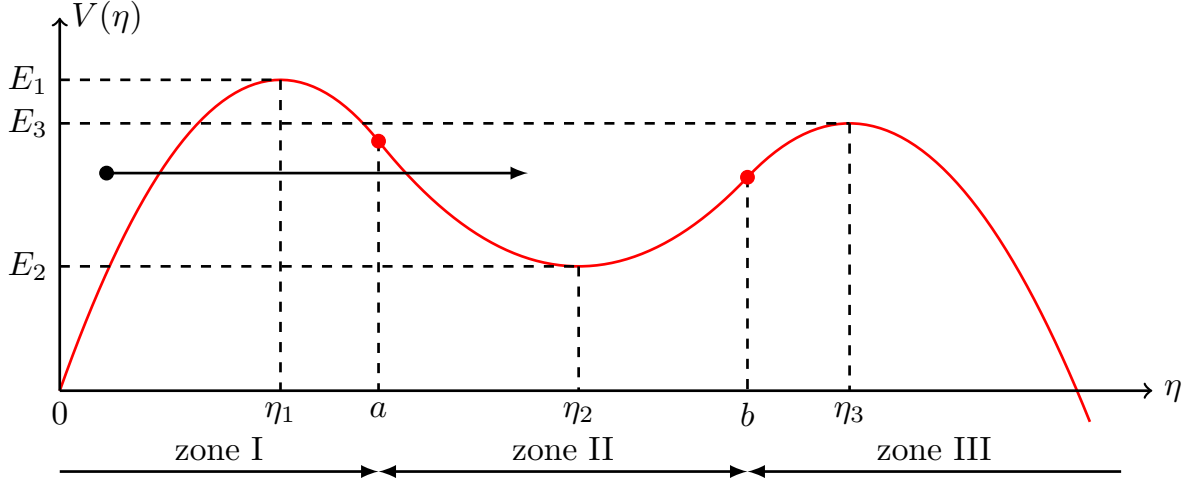


Figure 4.7 – Schematic representation of the fission tunneling process in the Cramer-Nix approach: a fictive particle of inertia  $\mu$  (black dot) tunnels through a potential made of three smoothly joint parabola.

In this approach, the deformation potential is defined by

$$V(\eta) = \begin{cases} E_1 - \frac{1}{2}\mu\omega_1^2(\eta - \eta_1)^2, & \eta \leq a \\ E_2 + \frac{1}{2}\mu\omega_2^2(\eta - \eta_2)^2, & a \leq \eta \leq b \\ E_3 - \frac{1}{2}\mu\omega_3^2(\eta - \eta_3)^2, & \eta \geq b \end{cases} \quad (4.47)$$

This potential is defined by 12 parameters out of which 4 can be regarded as interdependent because of the smooth matching conditions at  $\eta = a$  and  $\eta = b$ . Two additional degrees of freedom vanish as the eventual transmission coefficient is insensitive to the inertia parameter  $\mu$  and to any  $\eta$ -shift of the barrier. The 6 parameters usually retained are the energies  $E_1$ ,  $E_2$  and  $E_3$  and the curvatures  $\omega_1$ ,  $\omega_2$  and  $\omega_3$  as defined by Eq. 4.47 and shown in Fig. 4.7. The deformation space related to  $\eta$  can be divided into three zones, over each of which an analytical wave function  $\Psi$  can be computed using parabolic cylinder functions [48]. Two types of solutions exist; one can be regarded as a wave  $\psi$  propagating towards  $\eta > 0$ , the other one  $\varphi$  as a wave propagating towards  $\eta < 0$ . The wave function equation is separately solved in each of the different potential zone and then wave functions and their first derivatives are matched at the zone boundaries. The zone-waves are

$$\begin{aligned} \Psi_{\text{I}} &= A\psi_{\text{I}} + B\varphi_{\text{I}}, & \eta \leq a, \\ \Psi_{\text{II}} &= C\psi_{\text{II}} + D\varphi_{\text{II}}, & a \leq \eta \leq b, \\ \Psi_{\text{III}} &= F\psi_{\text{III}} + G\varphi_{\text{III}}, & \eta \geq b. \end{aligned} \quad (4.48)$$

To select solutions corresponding to an outgoing wave function (from which the transmission coefficient can be obtained), one needs to consider global waves propagating towards  $\eta > 0$  in the rightmost part of the potential (*i.e.*  $G = 0$ ). Defining the intermediate

quantities

$$\begin{aligned} u(\eta) &= \sqrt{\frac{2\mu\omega_1}{\hbar}}(\eta - \eta_1), & \alpha_1 &= \frac{E_1 - E}{\hbar\omega_1}, \\ v(\eta) &= \sqrt{\frac{2\mu\omega_2}{\hbar}}(\eta - \eta_2), & \alpha_2 &= \frac{E_2 - E}{\hbar\omega_2}, \\ w(\eta) &= \sqrt{\frac{2\mu\omega_3}{\hbar}}(\eta - \eta_3), & \alpha_3 &= \frac{E_3 - E}{\hbar\omega_3}. \end{aligned} \quad (4.49)$$

The barrier transmission coefficient is defined by

$$T = \sqrt{\frac{\omega_3}{\omega_1}} \left| \frac{F}{A} \right|^2, \quad (4.50)$$

where

$$\frac{F}{A} = \frac{v'u'2i\sqrt{2/\pi}}{\det M}, \quad (4.51)$$

and where  $M$  is a matrix whose components are defined using the parabolic cylinder functions [48]  $\mathcal{V}$ ,  $\mathcal{U}$  and  $\mathcal{E}$ .

$$M = \begin{bmatrix} \mathcal{E}_a(\alpha_1, -u) & -\mathcal{V}_a(\alpha_2, v) & -\mathcal{U}_a(\alpha_2, v) & 0 \\ -u'\mathcal{E}_a^{(-u)}(\alpha_1, -u) & -v'\mathcal{V}_a^{(v)}(\alpha_2, v) & -v'\mathcal{U}_a^{(v)}(\alpha_2, v) & 0 \\ 0 & \mathcal{V}_b(\alpha_2, v) & \mathcal{U}_b(\alpha_2, v) & -\mathcal{E}_b(\alpha_3, w) \\ 0 & v'\mathcal{V}_b^{(v)}(\alpha_2, v) & v'\mathcal{U}_b^{(v)}(\alpha_2, v) & -w'\mathcal{E}_b^{(w)}(\alpha_3, w) \end{bmatrix}. \quad (4.52)$$

Here above the function superscript stands for the argument with respect of which the derivative of the function is calculated. The function subscript stands for the deformation point  $\eta$  at which the function is evaluated.

In Fig. 4.8, transmission coefficients obtained with both the Cramer-Nix and the Hill-Wheeler models are shown. It can be seen that the Cramer-Nix model leads to transmission coefficient with resonant structures where the Hill-Wheeler model only produces a smooth variation of the transmission coefficient.

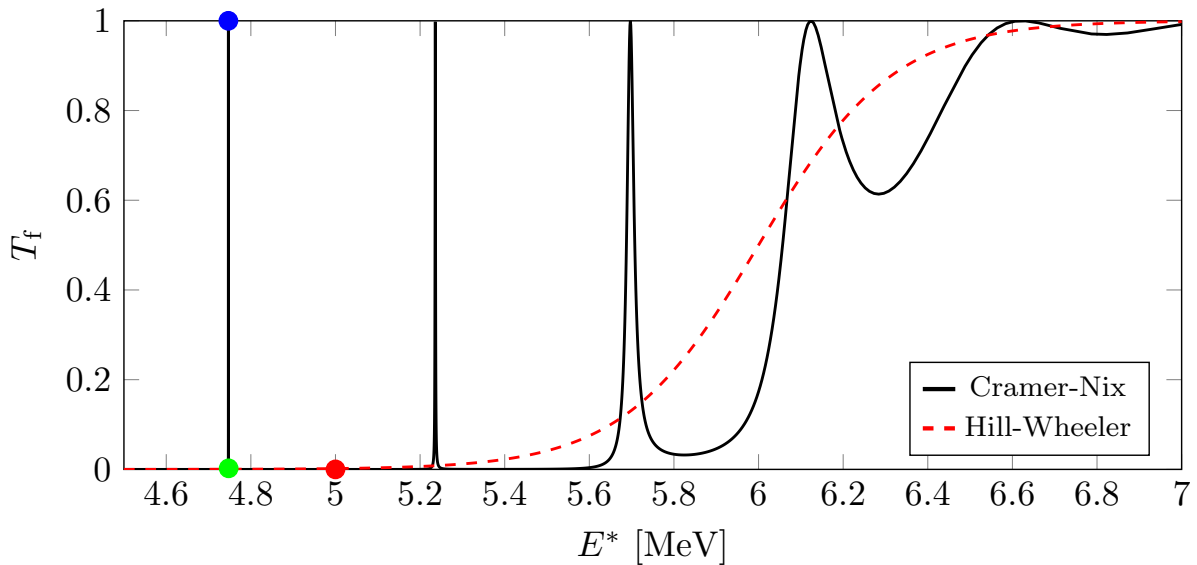


Figure 4.8 – Example of fission transmission coefficients obtained using the Cramer-Nix model and a single-humped Hill-Wheeler model. The three colored dots correspond to special energies that are analyzed in Fig. 4.9.

Three special energies are chosen for a more in dept analysis. They are highlighted by colored dots in Fig. 4.8. The first energy (blue dot) corresponds to the first resonance energy of the Cramer-Nix transmission coefficient in the figure. The second energy (green dot) is chosen few hundreds of eV above to the first one (but already “out” of the resonance). The last energy (red dot) is chosen to be approximately between the two first resonance energies. The corresponding wave functions are illustrated in Fig. 4.9. It becomes obvious while comparing the “red” and “green” states, that the spatial localization of the wave function is responsible for the dramatic change in the transmission coefficient value. For the “red” state (out of the resonance) the wave is mostly located in the first well, whereas for the “blue” state it is mostly located in the intermediate well (zone-II). Both blue and green curves of Fig. 4.9 are related to close energies in the vicinity of the first resonance, as shown in Fig. 4.8. The small change shown in the wave functions (blue and green curves in the orange enlargement circle Fig. 4.9) leads to a drop of the value of the transmission coefficient from nearly unity (blue dot in Fig. 4.8) to about  $2.5 \times 10^{-3}$  (green dot in Fig. 4.8). For comparison, the transmission coefficient related to the red curve in Fig. 4.9 is about  $10^{-6}$  (red dot in Fig. 4.8).

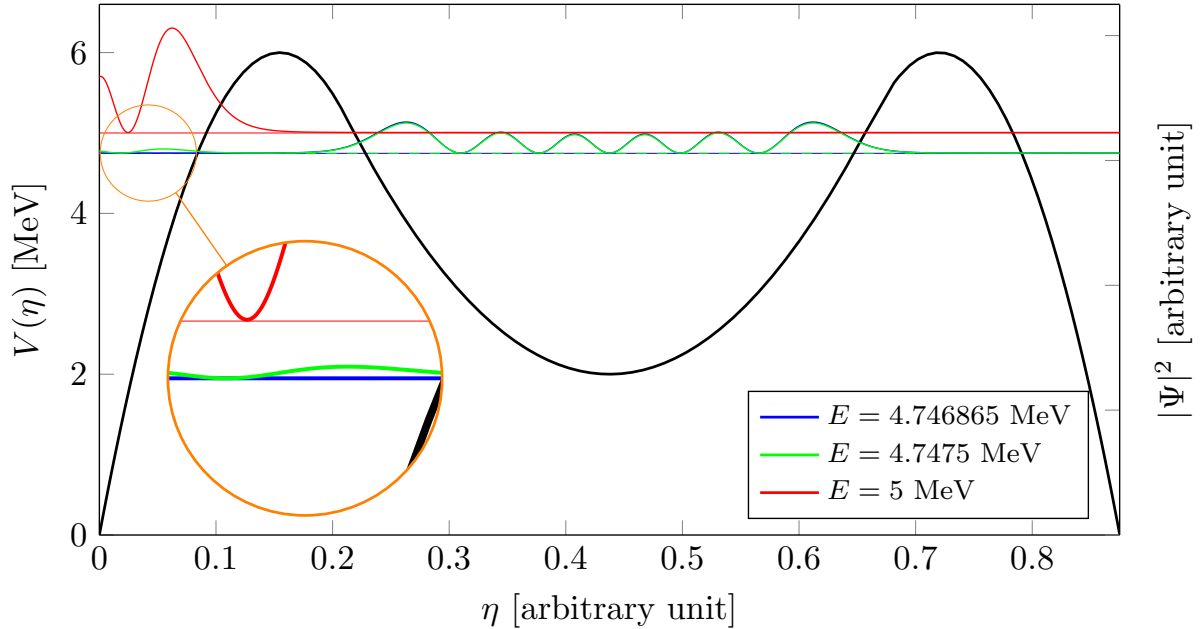


Figure 4.9 – Cramer-Nix potential (black curve) used to obtain the transmission coefficient show in Fig. 4.8. The probability amplitudes  $|\Psi(\eta)|^2$  for three peculiar energies is represented.

This type of barrier potential and analytical transmission coefficient has also be extended to a triple-humped fission barriers [77] and numerical methods have been developed to solve this type of problem with arbitrary barrier shapes [78]. Some of these latter methods will be detailed in Chapter 6 and Appendix D.

### 4.6.3 Current Pragmatical Approach for Fission

#### 4.6.3.1 Uncorrelated Hill-Wheeler Humps

In practice, the Cramer-Nix model is not used in evaluation. The uncorrelated Hill-Wheeler barriers model, that will be presented below, is often favored because it relies on fewer adjustable parameters. To account for the double-humped nature of the fission

barrier, the two humps are dissociated and a statistical equilibrium (Hauser-Feshbach formalism) is assumed in the intermediate well [79]. This is illustrated in Fig. 4.10. In the following,  $T_A$  is related to the Hill-Wheeler transmission coefficient related to the first hump, and  $T_B$  to the second one. The derivation of the commonly used formula  $T_f^{\text{eq}} = T_A T_B / (T_A + T_B)$  is now presented.

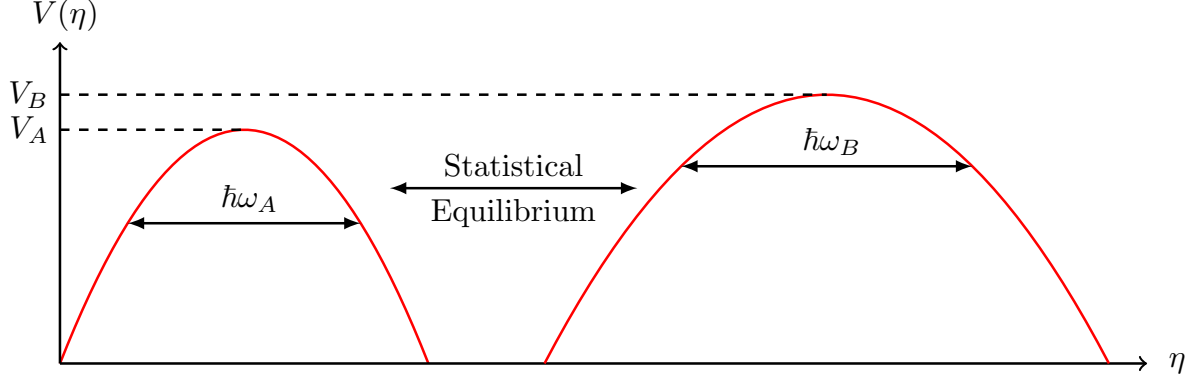


Figure 4.10 – Schematic picture of the double-hump fission barrier in the uncorrelated Hill-Wheeler approach. The potential shown here is not continuous (not defined between the two humps) and is not used to calculate wave propagation and probability current as in the single-hump Hill-Wheeler model.

Let us define the following probabilities:

1. to pass from the first well to the second well:

$$P_{\text{I} \rightarrow \text{II}} = \frac{T_A}{T_A + T_{\text{I}}} \quad (4.53)$$

2. to pass from the second well to fission:

$$P_{\text{II} \rightarrow \text{f}} = \frac{T_B}{T_A + T_B + T_{\text{II}}} \quad (4.54)$$

3. to pass from the second well to the first well :

$$P_{\text{II} \rightarrow \text{I}} = \frac{T_A}{T_A + T_B + T_{\text{II}}} \quad (4.55)$$

$T_{\text{I}}$  (resp.  $T_{\text{II}}$ ) stands for sum of the transmission coefficients related to any decay from the first well (resp. the second well) without passing through any barrier. Hence the fission probability is obtained by

$$P_{\text{I} \rightarrow \text{f}} = P_{\text{I} \rightarrow \text{II}} P_{\text{II} \rightarrow \text{f}} + P_{\text{I} \rightarrow \text{II}} (P_{\text{II} \rightarrow \text{I}} P_{\text{I} \rightarrow \text{II}}) P_{\text{II} \rightarrow \text{f}} + \dots \quad (4.56)$$

$$= P_{\text{I} \rightarrow \text{II}} P_{\text{II} \rightarrow \text{f}} \sum_{n=0}^{\infty} (P_{\text{II} \rightarrow \text{I}} P_{\text{I} \rightarrow \text{II}})^n = \frac{P_{\text{I} \rightarrow \text{II}} P_{\text{II} \rightarrow \text{f}}}{1 - P_{\text{II} \rightarrow \text{I}} P_{\text{I} \rightarrow \text{II}}} \quad (4.57)$$

Finally, the probability that the nucleus undergoes fission from an initial state located in the first well is [79]

$$P_{\text{I} \rightarrow \text{f}} = \frac{T_A T_B}{(T_A + T_{\text{I}})(T_A + T_B + T_{\text{II}}) - T_A^2} \quad (4.58)$$

From this, an *effective* or *equivalent* fission transmission coefficient  $T_f^{\text{eq}}$  can be defined so that it can be used in a “first well” Hauser-Feshbach formula. It is defined such as

$$P_{I \rightarrow f} = \frac{T_f^{\text{eq}}}{T_f^{\text{eq}} + T_I}, \quad (4.59)$$

which leads to

$$T_f^{\text{eq}} = \frac{T_I T_A T_B}{T_A T_{\text{II}} + T_I (T_A + T_B + T_{\text{II}})}. \quad (4.60)$$

If no absorption or particle emission is considered in the second well (*i.e.*  $T_{\text{II}} = 0$ ), the equivalent fission transmission coefficient becomes

$$T_f^{\text{eq}} = \frac{T_A T_B}{T_A + T_B}. \quad (4.61)$$

This expression is usually used for “first well” Hauser-Feshbach calculation, *i.e.* a calculation leading to a fission cross section that can be expressed as

$$\sigma_{\text{nf}} \propto \frac{T_f^{\text{eq}}}{T_f^{\text{eq}} + T_I}. \quad (4.62)$$

The derivation of the  $T_f^{\text{eq}}$  expression shows why it is not normalized to unity. This property leads to different asymptotic plateau values in both fission cross section and fission decay probability calculations [80] depending on the chosen number of barrier humps. This is illustrated in Fig. 4.11 where it can be seen that the plateau value of the transmission coefficient plateau is approximately halved<sup>13</sup>.

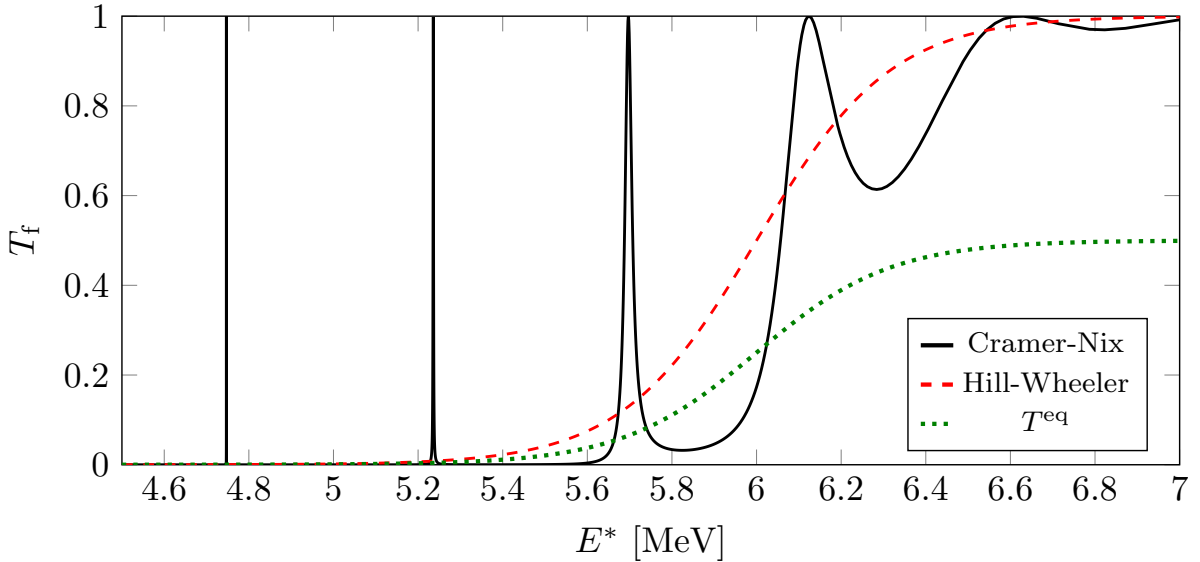


Figure 4.11 – Effect of the uncorrelated Hill-Wheeler hump model ( $T_f^{\text{eq}}$ ) on the transmission coefficient plateau value. The Cramer-Nix and single-humped Hill-Wheeler models are also shown for comparison.

<sup>13</sup>The precise effect of the reduction depends on the choice of the barrier parameters (heights and curvatures).

### 4.6.3.2 Transition States

The plateau value can be restored by addition of transition states [80,81]. These transition states were introduced by Bohr and Wheeler [81,82] to account for the states of internal excitation of the nucleus as it passes the barrier. They were later characterized [83] in terms of coupling between collective and individual degrees of freedom in the picture of the “cold fissioning nucleus”. In the vicinity of the hump maximum, the total energy  $E^*$  that is available for deformation can be reduced because some energy  $E_{\text{int}}$  is drained out by discrete intrinsic excitation. The deformation energy  $E_{\text{def}}$  is constrained by the energy conservation

$$E^* = E_{\text{int}} + E_{\text{def}} \quad (4.63)$$

This property can be understood as if there were many way of crossing the barrier. The total transmission coefficient for the barrier  $X$  is

$$T_X^{J\pi}(E^*) = \sum_{c|J\pi} T_{Xc}^{J\pi}(E^*), \quad X \in \{A, B\}, \quad (4.64)$$

where the sum runs over the possible transition states  $c$ , these being significantly different from the  $\mathfrak{R}$ -matrix channels. The transmission coefficient related to a transition state  $c$  is given by Eq. 4.46 with an energy shift

$$T_{Xc}^{J\pi}(E^*) = \left[ 1 + \exp \left( 2\pi \frac{V_X - (E^* - \epsilon_{Xc}^{J\pi})}{\hbar\omega_{Xc}} \right) \right]^{-1}, \quad (4.65)$$

where  $V_X$  is the height of barrier  $X$ ,  $\hbar\omega_{Xc}$  is the barrier curvature energy and  $\epsilon_{Xc}$  is the intrinsic excitation energy. In practice  $\hbar\omega_{Xc}$ ,  $V_X$  and  $\epsilon_{Xc}$  are adjustable parameters. Transition states are not channels in the sense of the  $\mathfrak{R}$ -matrix theory but they are used to reduce the tremendous number of  $\mathfrak{R}$ -matrix channels related to fission. In practice the transition state energy  $\epsilon_{Xc}$  is calculated as part of a rotational band. The rotational band is characterized by a band-head energy, and by two quantum numbers: the band-head parity  $\pi$  and the quantum number  $K$ . This latter is the magnitude of the projection of the total angular momentum  $J$  on the nucleus deformation axis<sup>14</sup>. For a barrier hump  $X$ , a band-head energy can thus be written  $E_X^{K\pi}$ , a transition state related to the  $J\pi$  quantum numbers and related to the band-head  $E_X^{K\pi}$  would be given by

$$\epsilon_{Xc}^{J\pi} = E_X^{K\pi} + \frac{J(J+1) - K(K+1)}{2I_X} \quad (4.66)$$

where  $I_X$  is the moment of inertia of the nucleus for a deformation corresponding to the hump maximum.

### 4.6.3.3 Ersatz Solution for Intermediate-Well Fluctuation

The presence of an intermediate well should create fluctuations in the overall tunneling phenomenon. The uncorrelated Hill-Wheeler barrier model does not reproduce such fluctuations (regardless of the addition of transition states). As energy gets close to a pseudo-eigenstate of the intermediate well, the transmission is amplified and, even if energy is below the barriers heights, one can observe (assuming ideal experimental energy

<sup>14</sup>The quantum number  $K$  is a good quantum number only for axially symmetric shapes.

resolution) an amplified overall transmission coefficient. This model deficiency is, in practice, compensated by adding local enhancement factors [84]

$$F_{AB}(E) = 1 + \sum_{\text{class II}} \left[ \frac{4}{T_A + T_B} + \left( \frac{E - E_{\text{II}}}{\Gamma_{\text{II}}/2} \right)^2 \left( 1 - \frac{4}{T_A + T_B} \right) - 1 \right] f_{\text{II}}(E) \quad (4.67)$$

where  $f_{\text{II}}$  is 1 if  $E \in [E_{\text{II}} \pm \Gamma_{\text{II}}/2]$  and 0 otherwise. However, this method, which uses phenomenological parameters, leads to issues mentioned in the introduction, in particular it lacks of predictability for the  $E_{\text{II}}$  and  $\Gamma_{\text{II}}$  class-II parameter values. To be able to predict new data, attempts are made to connect model parameters to quantities obtained from less phenomenological approaches. For instance, the barrier heights and width can be obtained from underlying HFB calculations [85]. Yet, in the approach of Ref. [85] the fission transmission coefficient is still obtained using uncorrelated Hill-Wheeler humps.

#### 4.6.3.4 “Classical” Fission Treatment in CONRAD

As a final step of the upgrade of the CONRAD code that has been achieved during this PhD work, the “usual” treatment of the fission transmission coefficients was also implemented (*i.e.* Hill-Wheeler transmission coefficients supplemented by transition states). A comparison was made with the TALYS code for both  $^{238}\text{U}(n, f)$  and  $^{239}\text{Pu}(n, f)$  cross sections, the results are shown in Fig. 4.12.

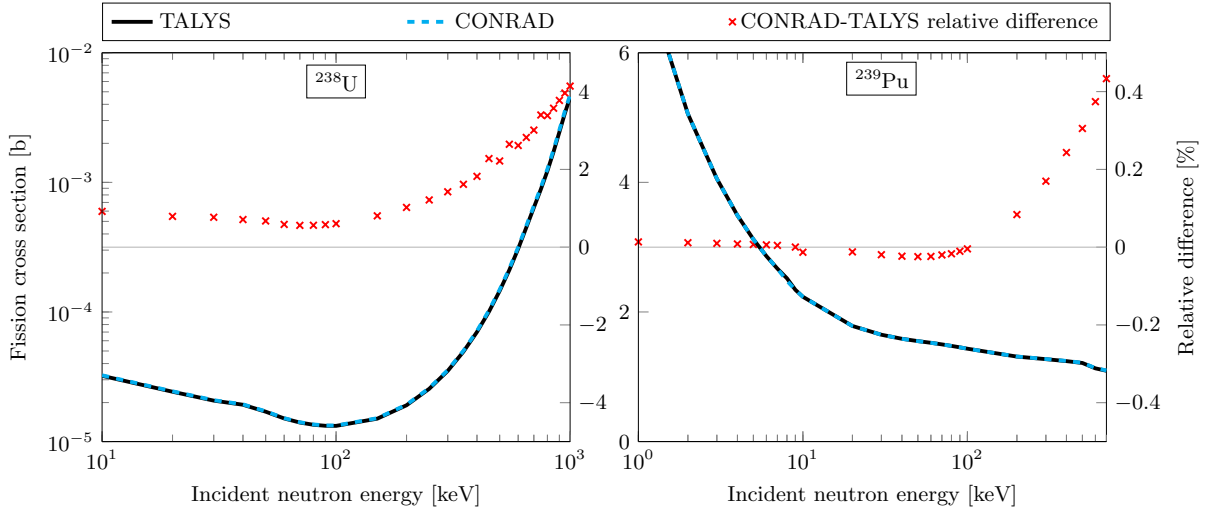


Figure 4.12 – Test of the fission cross section model implemented in CONRAD by comparison with TALYS on the ( $^{238}\text{U} + n$ ) and ( $^{239}\text{Pu} + n$ ) systems.

The differences between code results for the fission cross sections are larger than for the other partial cross sections detailed in the previous sections. The reason was found to lie in the numerical integration related to the transition states. Just like the gamma transmission coefficient (given by Eq. 4.23) that is a sum over discrete states plus an integral over a “continuum” energy range, the fission transmission coefficient expression can be split on the same ground, namely

$$T_X^{J\pi}(E^*) = \sum_{\text{discrete states } c} T_{Xc}^{J\pi}(E^*) + \int_{E_X^{\text{cont.}}}^{E^*} d\epsilon T_X^{J\pi}(\epsilon) \rho_X(J, \pi, \epsilon), \quad (4.68)$$



where  $T^{J^\pi}(\epsilon)$  is the continuum extension of Eq. 4.65,  $\rho_X$  is the transition state density related to the barrier hump  $X$  and  $E_X^{\text{cont.}}$  is the continuum lower boundary energy. It was found, just like for the gamma transmission coefficient Eq. 4.23, that most of the remaining differences between the CONRAD and the TALYS calculations are related to the numerical computation of the continuum integrals.

## 4.7 Summary and Remaining Limitations of the Code

### 4.7.1 “CONRAD 2.0”

Deep modifications have been brought to the CONRAD code in terms of “high energy” cross section modeling. These modifications and implementations mainly consist in:

- A generic Hauser-Feshbach engine able to be rapidly extended to new models and new reactions.
- A brand new coupled channel optical model that could be more easily upgraded than the ECIS legacy code.
- Generic transmission coefficients for neutron-related reactions (*i.e.* elastic and inelastic compound scattering).
- A customizable gamma transmission coefficient relying on the COOL library nuclear physics models (*e.g.* level densities and gamma strength functions).
- A shape inelastic DWBA model, inspired also by the ECIS code and the TALYS standard route (first order vibrational model for uncoupled levels).
- Standard fission transmission coefficients using the Hill-Wheeler and Cramer-Nix approaches.

These developments were made by generic programming<sup>15</sup> allowing the code to keep evolving with further new models and new reactions. All these upgrades have been introduced in the CONRAD code, which make them readily usable as tool for complete evaluations (*i.e.* adjustment on experimental data with production of accurate variance-covariance data).

### 4.7.2 “CONRAD 2.0-beta”

However several shortcomings remain and prevent from the covering of the whole evaluation range  $[0, 20 \text{ MeV}]$ . These limiting points are yet quite acceptable for the present study concerning fission-dedicated models. The further limitations are:

- No continuum inelastic scattering is considered. The “continuum” term refers here to the excitation energy domain of the residual nucleus (*i.e.* after re-emission of the incident particle) that cannot be described by experimentally known low-lying levels. This is not a serious gap to fill because the treatment is similar to the one involved for gamma transmission coefficients and fission transition states<sup>16</sup>. However in the

<sup>15</sup>This “spirit” was already present in the TALYS code that has been a precious help for the work presented in this chapter.

<sup>16</sup>A slight difference with respect to gamma of fission reactions lies in the direct inelastic cross section treatment in the continuum.

presented applications it is the first limitation to be encountered as calculations are made with increasing incident particle energies. It is this limiting point that defines the high energy border in Fig. 4.12.

- No *deformed* spin-orbit coupling is yet possible in the new coupled channel optical model.
- No charged particle emission is yet possible. This is no serious gap either because the optical models implemented in or driven by CONRAD can treat Coulomb interaction, but the related channels must be properly managed.
- The most sever change that should be brought to the code, so that cross sections can be evaluated to higher energies, is the treatment of multiple chance reactions (two-steps or more). These would mostly consist in as second chance fission (n, nf) and (n,  $\gamma$ n) reactions, then to reactions involving charged particles and multiple neutrons emission.
- Finally for quite high energies, a new phenomenon starts to play a significant role. The compound nucleus hypothesis becomes less and less valid as incident particle energy increases. A pre-equilibrium model would be necessary as the probability of particle emission prior to reach the compound nucleus state increases at higher incident particle energies are reached.

To conclude this chapter, it should be stated that the vast modifications brought to the CONRAD evaluation code make it usable in the low energy part of the statistical energy range. Despite the remaining limitations of the code, preventing from performing evaluations over the whole energy range [0, 20 MeV] of reactor physics, the code can be used to test new approaches of fission cross section evaluations for neutron incident energies up to 1 MeV for actinides. These new approaches will be detailed in the two following chapters.

# Chapter 5

## Implementation and Verification of Macroscopic-Microscopic Models

Chapters 3 and 4 showed that the fission barrier shape is a key requirement for the fission cross section models. Such barriers can be obtained by studying Potential Energy Surfaces (PES). These PES represent the nuclear deformation energy with respect to multidimensional coordinates  $\vec{q}$  that describe the shape of the nucleus. A long-standing macroscopic-microscopic model has been implemented to calculate these PES: the Finite-Range Liquid-Drop Model (FRLDM) that is presented in this chapter. The FRLDM is composed of two parts (macroscopic and microscopic) that will be detailed. The necessary verification and validation of the newly implemented program will also be presented. Finally, insights are given about the computational methods that have been set up during this work to make this model computationally fast enough to meet evaluation requirements.

### Contents

---

<b>5.1</b>	<b>General Macroscopic-Microscopic Approach</b>	<b>70</b>
<b>5.2</b>	<b>Macroscopic Models</b>	<b>72</b>
5.2.1	Historical Semi-Empirical Bethe-Weizsäcker Formula	72
5.2.2	Liquid Drop Model	75
5.2.3	Finite-Range Liquid-Drop Model	75
5.2.4	Summary and Effect of Deformation	80
5.2.5	Macroscopic Model Verification	82
<b>5.3</b>	<b>Microscopic Models</b>	<b>82</b>
5.3.1	Nilsson Harmonic Oscillator Model and Basis Wave Functions	82
5.3.2	More Realistic Phenomenological Potentials	84
5.3.3	Single-Particle States and Deformation	87
5.3.4	Microscopic Model Verifications	89
<b>5.4</b>	<b>Macroscopic-Microscopic Model</b>	<b>93</b>
5.4.1	Shell and Pairing Corrections	93
5.4.2	Macroscopic-Microscopic Model Verification and Results	99
<b>5.5</b>	<b>Evaluation-Compliant Implementation</b>	<b>106</b>
5.5.1	Base Expansion of Wave Functions	106
5.5.2	Efficient Numerical Integration Methods	107
5.5.3	Exploitation of Computational Resources	110

---

## 5.1 General Macroscopic-Microscopic Approach

The quest for relevant Potential Energy Surfaces (PES) has been a long-term effort in nuclear physics. These surfaces can be in turn used for deriving fission transmission coefficients that can be used in a Hauser-Feshbach for the calculation of average fission cross sections. In the present study, the Finite-Range Liquid-Drop Model [12] (FRLDM) has been selected to provide these PES. This macroscopic-microscopic model is composed of two sub-models: the macroscopic and the microscopic parts. In the macroscopic model, the nucleus is regarded as a homogeneous liquid, whereas in the microscopic model, nucleons in the nucleus are considered as individual particles.

Even if macroscopic models can be used to describe the overall behavior of nuclear masses throughout the periodic table, some discrepancies remain. These are due to quantum mechanics-related phenomena that cannot be taken into account in the macroscopic approach. For specific numbers of neutrons or protons, the nucleus is more tightly bound than other nuclei having similar numbers of nucleons. This effect occurs for numbers known as the *magic numbers*: 2, 8, 20, 28, 50, 82 and 126. This specificity comes from the fact that bound nucleons have discrete energies, which cannot be rendered by the homogeneous liquid picture.

Solutions were proposed to account for the microscopic (quantum mechanics) effects, see for example Ref. [86], but these were based on an *analytical expression* relying on adjustable parameters. The macroscopic-microscopic method became widely used after Strutinsky introduced a quantitative method [15, 87] to *calculate* the microscopic corrections using single-particle levels as a starting point. It is this macroscopic-microscopic model that has been selected for the present study to obtain the required PES. The macroscopic deformation energy  $E_{\text{macro}}$  describes the overall energy of the nucleus as it deforms. The microscopic model is used to provide single-particle orbits  $(\psi_i, \epsilon_i)$ . From these orbits, corrections can be extracted in order to account for the discrete nature of the nucleons inside the nucleus. The microscopic corrections are calculated independently for neutrons,  $E_{\text{micro,n}}$  and protons  $E_{\text{micro,p}}$ . The macroscopic-microscopic “deformation energy”  $E^{\text{def}}$  is finally obtained as the sum of these three components

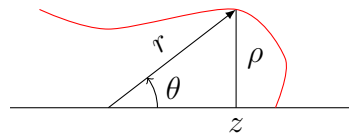
$$E^{\text{def}} = E_{\text{macro}} + E_{\text{micro,n}} + E_{\text{micro,p}}. \quad (5.1)$$

Microscopic corrections are composed of a shell correction  $\delta E_{\text{shell}}$  and pairing correction  $\delta E_{\text{pair}}$ . For instance, the neutron microscopic correction is given by

$$E_{\text{micro,n}} = \delta E_{\text{shell(n)}} + \delta E_{\text{pair(n)}}. \quad (5.2)$$

The general scheme of the macroscopic-microscopic approach, shown in Fig. 5.1, can be summarized as:

1. Selecting a parameterization for the nucleus shape. For instance the shape can be defined as a “geometrical” function  $\rho(z)$  or  $r(\theta)$  (defined here in the cylindrical coordinate system) relying on a set of parameters  $\vec{q}$ .



The  $\vec{q}$  parameters are only involved in the  $\rho(z)$  or  $r(\theta)$  expressions.

2. Calculating the macroscopic energy according to the model described in Section 5.2 using the selected shape.
3. Generating an average potential for both neutrons and protons using the selected shape, then computing the related wave functions with the microscopic model described in Section 5.3.
4. The corrections due to the discrete energy levels of nucleons are computed and added to the macroscopic energy. This point will be developed in Section 5.4.1.

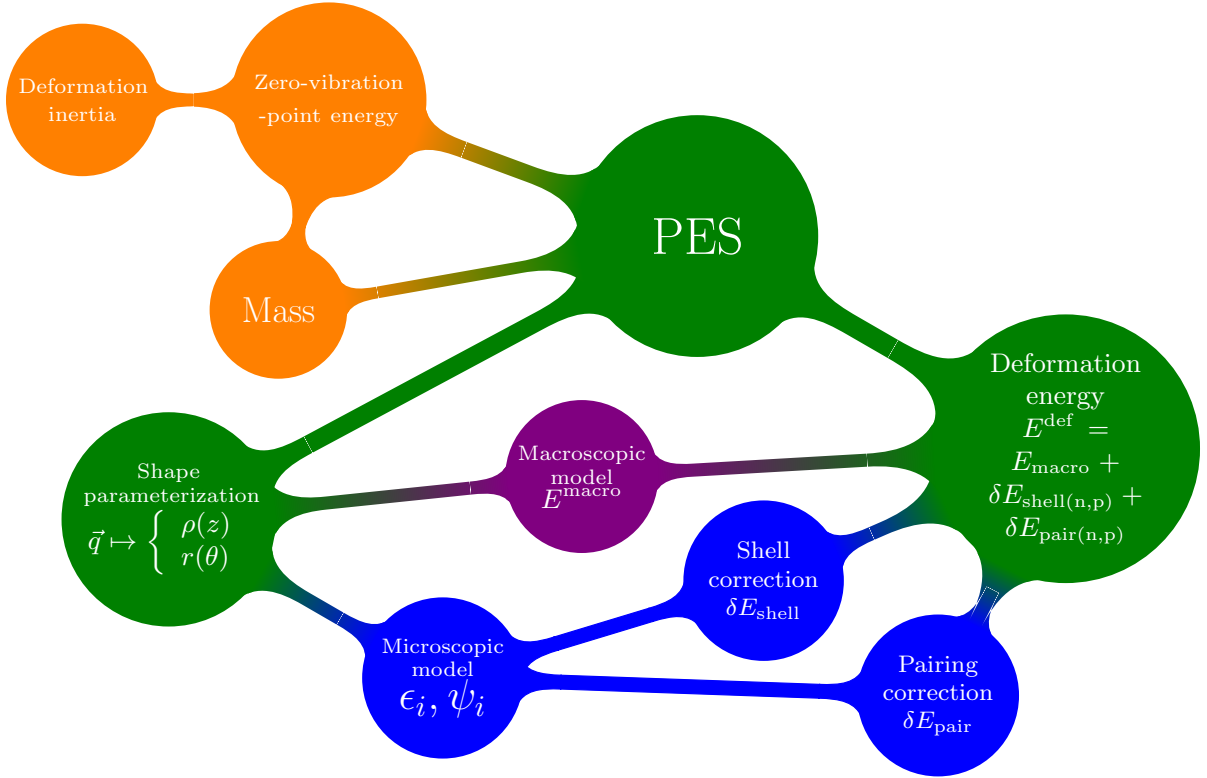


Figure 5.1 – Macroscopic-microscopic general scheme.

The first step of the macroscopic-microscopic approach is the definition of the nucleus shape. In this approach, the shape of the nucleus is not an output of the model but an input. To study the evolution of the shape of a fissioning nucleus, one would need to compute the nucleus energy for many deformations (or shapes), then to track back which shapes are relevant for the study. The notion of shape is rather abstract. To “quantify” a shape, a parameterization is used. This parameterization would connect a given set of *shape parameters* to a geometrical function, for instance  $\rho(z)$  or  $r(\theta)$ . In the present study, only axially symmetric shapes are studied.

In case of diffuse-edge shapes, the geometrical functions  $\rho(z)$  and  $r(\theta)$  are the *generating shapes*. For diffuse-edge shapes, nuclear matter density must be handled instead of sharp-edge volume. However the geometrical functions can be used as folding function to obtain the desired structure of the nuclear matter density. This leads to nuclear matter density having spacial features similar to the geometrical folding functions. Hence parameterized geometrical shapes can still be used for diffuse-edge calculations.

Several parameterizations have been used for macroscopic-microscopic studies. In Tab. 5.1, some properties of the parameterizations used in the present study are summarized. More details related to shape parameterization are given in Appendix B.1.

Table 5.1 – Characteristics of the shape parameterizations used in the present work.

Parameterization name	Type	Number of degrees of freedom	Parameter names
Legendre Polynomials <sup>a</sup>	$r(\theta)$	1.. $\infty$	$\beta_2, \beta_3, \dots$
Hill-Wheeler	$r(\theta)$	1	fissility $y$
Perturbed Spheroid <sup>a</sup>	$r(\theta)$	1..5	$\epsilon_2, \epsilon_3, \epsilon_4, \epsilon_5, \epsilon_6$
Generalized Spheroid <sup>a</sup>	$\rho(z)$	2..3	$c, h, \alpha$
Three Quadratic Surfaces	$\rho(z)$	5	$Q_2, \alpha_g, \varepsilon_{f1}, \varepsilon_{f2}, d$

<sup>a</sup>A generalization to axially-asymmetric shapes exists.

## 5.2 Macroscopic Models

In this section, the macroscopic model will be detailed. The basic idea is to consider the atomic nucleus as a liquid whose properties are solely due to collective average behavior of nucleons. This model was first proposed by George Gamow [88] then fully theorized into its more final and mature form by Carl Friedrich von Weizsäcker in 1935. Several refinements have been introduced since – that will be presented in the following – and yielded to the current macroscopic model composing the FRLDM. Not all these refinements would have eventual effects on the PES that will be used later in the calculation of average fission cross section. Indeed some of these refinements have no dependence on the nucleus shape and thus only leads to uniform shift in the PES energy. The PES used in this study are “shifted” so that the zero-deformation energy corresponds to the ground-state shape. These shape-independent features must yet be implemented in the code so that the program can be verified against published tables and validated with experimental data.

### 5.2.1 Historical Semi-Empirical Bethe-Weizsäcker Formula

An easily measurable manifestation of nuclear properties is the nuclear binding energy. Systematic differences were measured between masses of nuclei and the sum the separated nucleon masses. For a given atom with  $Z$  protons and  $N$  neutrons and of mass  $M(Z, N)$ , the binding energy  $B(Z, N)$  is given by

$$B(Z, N) = ZM_H + NM_n - M(Z, N), \quad (5.3)$$

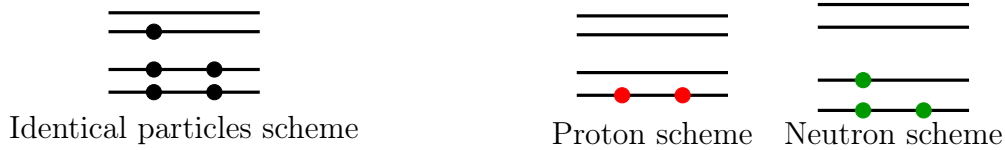
where  $M_H$  is the mass of a hydrogen atom<sup>1</sup>, and  $M_n$  is the mass of a neutron. The binding energy or *mass defect* is the result of the existence of a strong attractive force acting between nucleons and counteracting the repulsive Coulomb interaction between protons. The positive sign of the binding energy (as defined above) means that the corresponding system of nucleons is more stable if nucleons are gathered into a small region (the nucleus) than separated. One of the pioneering attempts to understand nuclear energy was modeling the nuclear binding energy. It yielded the famous Semi-Empirical Bethe-Weizsäcker formula [13, 14]

$$B(Z, N) = a_V A - a_S A^{2/3} - a_C \frac{Z^2}{A^{1/3}} - a_A \frac{(N - Z)^2}{A} - \delta(Z, N), \quad (5.4)$$

where  $A = Z + N$  is the total number of nucleons. Even though more sophisticated models exist today, the physical meaning of the formula terms are still quite relevant.

<sup>1</sup>As  $M(Z, N)$  is the atomic mass, the mass of electrons and the related electronic binding energies must be removed. This is done by using the hydrogen *atomic* mass instead of the proton mass.

- The first term, known as the *volume* term, stands for the existence of an attractive force between nucleons and thus has a dependence on the total number of nucleons  $A$ .
- The second term, called the *surface* term, stands for the fact that nucleons in the surface region of the nucleus have less neighbors to interact with and thus reduces the first term proportionally to the nuclear surface area (which is proportional to  $A^{2/3}$ , assuming a spherical shape of the nucleus).
- The third term is also negative and results from the Coulomb interaction between protons. It is given by the Coulomb energy of a uniformly charged sphere of radius proportional to  $A^{1/3}$ .
- The fourth term, known as the *asymmetry* term, is related to the quantum nature of the nucleus. Nucleons can only occupy discrete energy levels. The system energy is the sum of the energies for all occupied states. Because of the Pauli exclusion principle, only two nucleons can occupy a given level. If protons and neutrons were identical particles (as in the level scheme below), the system energy is obtained by summing a large number of level energies. On the contrary, if they could occupy states in different level schemes, only the low-lying levels are occupied and the system energy is reduced. It is observed that for heavy nuclei this phenomenon is less effective (due to the reduction of energy gap between levels and/or higher level degeneracy).



- The last term stands for the *pairing* interaction that tends to strongly bind nucleons pairwise (protons with protons, neutrons with neutrons) as pairs of nucleons in time-reversed orbits<sup>2</sup>. This term introduces changes between neighbor nuclei but has a limited effect on mass formula except for very light nuclei. Its main  $Z$  and  $N$  dependence is given by:

$$\delta(Z, N) = \begin{cases} +\delta_0, & Z \text{ and } N \text{ even} \\ 0, & A \text{ odd} \\ -\delta_0, & Z \text{ and } N \text{ odd} \end{cases} \quad (5.5)$$

Figure 5.2 shows the effect of successive addition these five terms for the binding energy per nucleon. Experimental data are taken from Ref. [90]. For each mass number  $A$ , only the most stable nuclide of the isobar family is considered. The addition of the Coulomb term leads to saw-tooth shape structure that are only due to the fact that for the volume and surface term there is no dependence on  $Z$ . It may seem that all terms are required to get a proper match with experimental data, however one has to keep in mind that the present parameters are fitted so that the whole formula gives proper results. One would

<sup>2</sup>Unless magnetic field is effective, neutrons and protons levels are – at least – doubly degenerate. They can be more degenerate, for instance in case of spherically symmetric field with no spin-orbit coupling. The two nucleons of a doubly-degenerate level have identical quantum numbers except for the quantum number related to the projection of their total angular momentum. These are identical in magnitude but of opposite sign. Two nucleons in the same doubly-degenerate level are said to be in time-reversed orbits because of the symmetry of their related wave functions under time reversal [89].



have obtained different parameters while fitting data with a mass formula containing less terms. One can see that despite the agreement on the global trend of the curve, some structures are not reproduced. Discrepancies occur for isotopes having a number of neutrons or protons close to the so-called “magic number”: 2, 8, 20, 28, 50, 82 and 126. For very light isotopes large differences are visible, however one can consider that the global approach of the “liquid drop” concept for the nucleus becomes increasingly less accurate with decreasing number of nucleons. However, for medium and heavier nuclei shell effects tend to organize nucleons in such a way that less energy is required to gather nucleons. Some residual peaks are present on the curve around  $^{138}_{56}\text{Ba}_{82}$  and  $^{140}_{58}\text{Ce}_{82}$  and around the doubly magic nucleus  $^{208}_{82}\text{Pb}_{126}$ . These structures cannot be reproduced by “smooth” curves such as those used in terms of Eq. 5.4. For lighter isotopes near  $^{36}_{16}\text{S}_{20}$  or  $^{88}_{38}\text{Sr}_{50}$ , structures are also visible although because the gap between magic numbers 8 and 20 is smaller than between 126 and 82, shells are more difficult to distinguish.

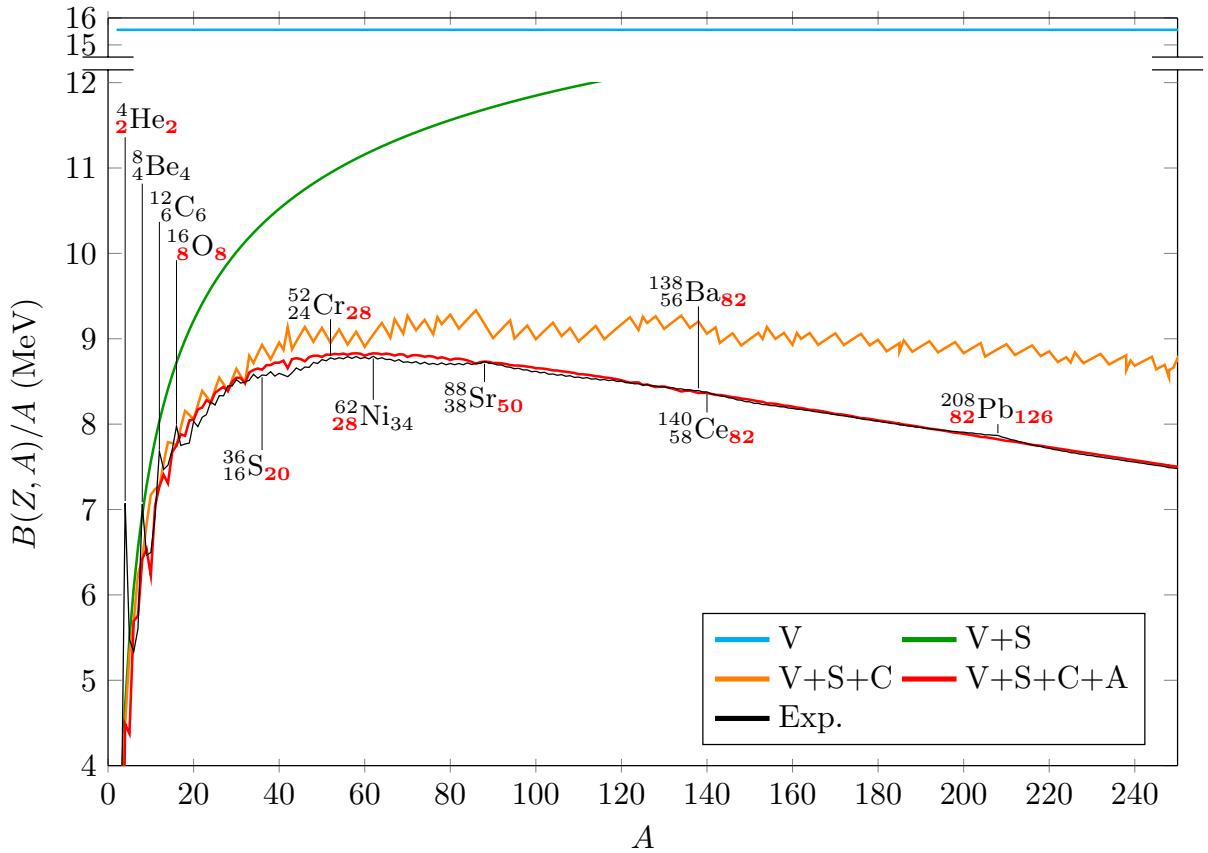


Figure 5.2 – Binding energy per nucleon also known as the Aston’s curve. The different contributions of the Bethe-Weizsäcker formula are shown as successive addition of its terms: Volume (V), Surface (S), Coulomb (C) and Asymmetry (A). Experimental data [90] (Exp.) are also shown (for each isobar family only the most tightly bound nuclide is considered). For readability the pairing term is not shown. Some of the nuclides with “magic numbers”, for which shell structures occur, are shown in format  $^A_Z X_N$  with magic numbers written in bold red.

An early correction of the formula was introduced to include Pauli exclusion principle in the calculation of the Coulomb energy term. It yields [14]

$$a_C \frac{Z^2}{A^{1/3}} \rightarrow a_C \left[ \frac{Z^2}{A^{1/3}} - 5 \left( \frac{9}{2^8 \pi^2} \right)^{1/3} \frac{Z^{4/3}}{A^{1/3}} \right]. \quad (5.6)$$

## 5.2.2 Liquid Drop Model

To obtain the Bethe-Weizsäcker Formula (Eq. 5.4), the nucleus is seen as a homogeneous sphere of radius proportional to  $A^{1/3}$ . However there is no *a priori* reason for the nucleus to be spherical. Additionally, when nuclear reaction such as fission are studied, it is interesting to let the nucleus shape evolve. A straightforward extension of the Bethe-Weizsäcker formula is the Liquid Drop Model (LDM). In this model the nuclear matter, following what scattering experiments of that time indicated, is assumed to be a homogeneous (uniformly charged), incompressible liquid. Additionally, nuclear matter is assumed to be contained within a sharp-edge surface characterized by an *arbitrary* shape  $\vec{q}$ . Eq. 5.4 becomes

$$B(Z, N) = a_V A - a_S B_S(\vec{q}) A^{2/3} - a_C B_C(\vec{q}) \frac{Z^2}{A^{1/3}} - a_A \frac{(N - Z)^2}{A} - \delta(Z, N). \quad (5.7)$$

The surface term  $B_S$  is the surface area of the nucleus, the Coulomb term  $B_C$  is the Coulomb energy of the related liquid. Both terms are normalized to the related value for a spherical nucleus having the same volume. The radius  $R$  of such a spherical nucleus is proportional to  $A^{1/3}$  and can be written as

$$R = r_0 A^{1/3}, \quad (5.8)$$

where  $r_0$  is a model parameter that can be estimated from electron-nucleus scattering experiments. For the surface term one obtains

$$B_S(\vec{q}) = \frac{1}{4\pi R^2} \int_S d^2 S, \quad (5.9)$$

where  $d^2 S$  is the surface element. For the Coulomb term one has:

$$a_C = \frac{3}{5} \frac{e^2}{4\pi\epsilon_0 r_0} \quad \text{and} \quad B_C(\vec{q}) = \frac{15}{32\pi^2 R^5} \int_V \int_V \frac{d^3 \vec{r}_1 d^3 \vec{r}_2}{\|\vec{r}_1 - \vec{r}_2\|}, \quad (5.10)$$

where  $\epsilon_0$  is the vacuum permittivity.

This classical Liquid Drop Model was later modified to take into account several refinements, such as the surface diffuseness. These refinements led to the Finite-Range Liquid-Drop Model (FRLDM) that is presented in the following section.

## 5.2.3 Finite-Range Liquid-Drop Model

### 5.2.3.1 Finite Range of Nuclear Forces

The actual nucleus surface is not sharp but has a certain diffuseness, hence the charge density has also a diffuse-edge aspect. For instance, the sharp-edge charge density  $\rho_C^{\text{sharp}}$  is defined as

$$\rho_C^{\text{sharp}}(\vec{r}) = \begin{cases} \frac{Ze}{\frac{4}{3}\pi R^3} & , \vec{r} \in V \\ 0 & , \vec{r} \notin V \end{cases}, \quad (5.11)$$

that is used in the Coulomb term calculation must be replaced by a diffuse-edge charge density  $\rho_C^{\text{diff}}$ .

Swiatecki and Myers refined the mass formula by inclusion of the surface diffuseness in the calculation of the Coulomb energy [91, 92]. This diffuseness was modeled using a Wood-Saxon form for the nuclear matter density. For the charge density it becomes

$$\rho_C^{\text{diff}}(\vec{r}) = \frac{Ze}{\frac{4}{3}\pi R^3} \frac{1}{1 + e^{n/d}}, \quad (5.12)$$

where  $d$  is a “skin parameter” and  $n$  is the distance between the point at  $\vec{r}$  and the surface of the nucleus. The skin parameter characterizes the diffuseness range of nuclear matter density at the nucleus edge. The correction term to the Coulomb energy for the surface diffuseness is defined as the effect of the density change  $\rho_C^{\text{diff}} - \rho_C^{\text{sharp}}$  on the Coulomb energy. This correction term is then added to the usual sharp-edge term. Swiatecki and Myers defined the surface diffuseness Coulomb correction term  $\delta E_C$  as

$$\delta E_C = \int_{-\infty}^{\infty} d^3\vec{r} [\rho_C^{\text{diff}}(\vec{r}) - \rho_C^{\text{sharp}}(\vec{r})] V(\vec{r}), \quad (5.13)$$

where  $V(\vec{r})$  is the Coulomb potential created by the sharp distribution. Using a first-order Taylor expansion of the Coulomb potential and applying the Gauss theorem they found

$$\delta E_C = -4\pi Ze \int_{-\infty}^{\infty} dn \cdot n [\rho_C^{\text{diff}}(\vec{r}) - \rho_C^{\text{sharp}}(\vec{r})], \quad (5.14)$$

where  $n$  is the normal distance between  $\vec{r}$  and the sharp surface. To first order in  $\frac{d}{R}$  it yields:

$$\delta E_C = -\frac{\pi^2 e^2 Z^2 d}{2 r_0 A R}. \quad (5.15)$$

Later, Davies and Nix derived an exact formulation of the Coulomb term for a diffuse-edge shape [93]. Instead of the Wood-Saxon density they used a Yukawa-folded density defined as

$$\rho_C^{\text{diff}}(\vec{r}_1) = \frac{Ze}{\frac{4}{3}\pi R^3} \int_V d^3\vec{r}_2 \frac{1}{4\pi a^3} \frac{e^{-\|\vec{r}_1 - \vec{r}_2\|/a}}{\|\vec{r}_1 - \vec{r}_2\|/a}, \quad (5.16)$$

where  $a$  is the range of the Yukawa density. Its meaning is closely related to the skin parameter  $d$ . In this expression, integration is performed over a volume  $V$  circumscribed by a surface, defined by a *generating shape*. This generating shape can be defined as a sharp-edge shape with a parameterized geometrical function  $\rho(z)$  or  $r(\theta)$ . But the generating shape must not be understood as the actual sharp-edge surface of the nucleus, since in the present case the nucleus has a diffuse surface. Yet this generating surface is used to *fold* a nuclear matter density model (such as the Yukawa-folded density) that will reproduced the features of the generating shape on the density. The exact Coulomb energy term can be calculated as

$$E_C = \frac{1}{2} \int_{-\infty}^{\infty} \int_{-\infty}^{\infty} \frac{d^3\vec{r}_1 d^3\vec{r}_2}{\|\vec{r}_1 - \vec{r}_2\|} \rho_C^{\text{diff}}(\vec{r}_1) \rho_C^{\text{diff}}(\vec{r}_2). \quad (5.17)$$

In the case of the Yukawa-folded charge density, it yields [94, 95]

$$E_C = \frac{1}{2} \left( \frac{Ze}{\frac{4}{3}\pi R^3} \right)^2 \int_V \int_V \frac{d^3\vec{r}_1 d^3\vec{r}_2}{\|\vec{r}_1 - \vec{r}_2\|} \left( 1 - \left( 1 + \frac{1}{2} \frac{\|\vec{r}_1 - \vec{r}_2\|}{a} \right) e^{-\|\vec{r}_1 - \vec{r}_2\|/a} \right). \quad (5.18)$$

In parallel Krappe, Nix and Sierk [96,97] included diffuse-edge shape in the calculation of the nuclear energy term. They also used a Yukawa-folded model and replaced the  $B_S(\vec{q})A^{2/3}$  term by

$$E_S(\vec{q}) = -\frac{1}{8\pi^2 r_0^2 a^4} \int_V \int_V d^3\vec{r}_1 d^3\vec{r}_2 \frac{e^{-\|\vec{r}_1 - \vec{r}_2\|/a}}{\|\vec{r}_1 - \vec{r}_2\|/a} + \frac{2}{3} \frac{r_0}{a} A. \quad (5.19)$$

This expression presents several advantages: it makes the nuclear energy term less sensitive to high multipole wriggles on the nuclear surface. It also leads to an attractive contribution when used to model heavy ions collisions. It removes excessively high surface-energy contributions from the neck region of nuclei at scission when the size of the neck is of the order of the nuclear interaction range. Finally it is readily appropriate to any types of shape. The last term in the expression is present so that for spherical nuclei and for  $a/r_0 \ll 1$ , one obtains the usual Liquid Drop Model term:

$$E_S(\vec{q} = \vec{0}) = A^{2/3} - \frac{a^2}{r_0^2} + \left( A^{1/3} + \frac{a}{r_0} \right)^2 \exp\left(-2\frac{r_0}{a} A^{1/3}\right) \xrightarrow{a/r_0 \rightarrow 0} A^{2/3}. \quad (5.20)$$

### 5.2.3.2 The Yukawa Plus Exponential Formula

Later again Krappe et al. [98] showed that this formulation in terms of Yukawa-folded potential has two deficiencies. The first issue was that the Yukawa range  $a$ , required to obtain suitable heavy-ion interaction barrier-heights, was incompatible with the one obtained from heavy-ion elastic scattering analyses. The second issue arises when one considers the (Yukawa-folded) interaction energy between two semi-infinite nuclear matter slabs. Krappe showed that the interaction potential between slabs  $E_{\text{int}}$  is

$$E_{\text{int}} = -\frac{a_S}{2\pi r_0^2} e^{-s/a}, \quad (5.21)$$

where  $s$  is the distance between the slabs and  $a_S$  characterizes the strength of the interaction. It happens that this interaction energy is not minimal when slabs are touching ( $s = 0$ ). One can get rid of this feature by considering a potential given as the difference between two Yukawa-folded functions:

$$E_{\text{int}} = E_{\text{int},1} - E_{\text{int},2}. \quad (5.22)$$

However one has now to deal with four parameters (two ranges  $a$  and two strengths  $a_S$ ). The minimum of slab interaction energy is obtained by the condition

$$\left. \frac{\partial E_{\text{int},1} - E_{\text{int},2}}{\partial s} \right|_{s=0} = 0, \quad (5.23)$$

where indices 1, 2 stand for the two Yukawa folding functions. This condition, also known as the *saturation condition*, yields

$$\frac{a_{S,1}}{a_1} = \frac{a_{S,2}}{a_2}. \quad (5.24)$$

If one writes the effective strength  $a_S$  as

$$a_S = a_{S,1} - a_{S,2}, \quad (5.25)$$

one gets the relations

$$a_{S,1} = \frac{a_S a_1}{a_1 - a_2} \quad \text{and} \quad a_{S,2} = \frac{a_S a_2}{a_1 - a_2} . \quad (5.26)$$

Hence the interaction energy can be written

$$E_{\text{int}} = -\frac{a_S}{2\pi r_0^2} \frac{a_1 e^{-s/a_1} - a_2 e^{-s/a_2}}{a_1 - a_2} . \quad (5.27)$$

Heavy-ion scattering experiments suggested that both Yukawa-folded functions have similar ranges ( $a_1 \sim a_2$ ). In the limit case  $a_1 \rightarrow a_2$ , one has

$$E_{\text{int}} = -\frac{a_S}{2\pi r_0^2} \frac{\partial}{\partial a} a e^{-s/a} . \quad (5.28)$$

The generalization to arbitrary shape comes by the differentiation of the first term of Eq. 5.19 with respect to  $a$ :

$$E_S(\vec{q}) = -\frac{1}{8\pi^2 r_0^2 a^4} \int_V \int_V d^3\vec{r}_1 d^3\vec{r}_2 \left( \frac{\|\vec{r}_1 - \vec{r}_2\|}{a} - 2 \right) \frac{e^{-\|\vec{r}_1 - \vec{r}_2\|/a}}{\|\vec{r}_1 - \vec{r}_2\|/a} . \quad (5.29)$$

It can be noted that, in the case of spherical nuclei, this term becomes

$$E_S(\vec{q} = \vec{0}) = \left\{ 1 - 3 \left( \frac{a}{R} \right)^2 + \left( \frac{R}{a} + 1 \right) \left[ 2 + 3 \frac{a}{R} + 3 \left( \frac{a}{R} \right)^2 \right] e^{-R/a} \right\} A^{2/3} . \quad (5.30)$$

In the limit of zero range of nuclear forces and no diffuse-edge of the nuclear surface ( $a = 0$ ), one gets again the usual Liquid Drop Model term  $A^{2/3}$ . However it can be noted that, in the opposite case  $a/r_0 \sim 1$ , the second term of the equation leads to a term that is not associated with any power of  $A$  (also known as  $A^0$  terms). This leads to include an  $A^0$  term in the mass formula that appears to have a significant effect for mass tabulation [94].

### 5.2.3.3 Proton Form Factor

In the calculation of the Coulomb energy, one assumes that the nuclear charge is homogeneous within the nucleus. The Coulomb energy between two elementary volumes  $d^3\vec{r}_1$  and  $d^3\vec{r}_2$ , in the sharp-edge case, is given by

$$d^6 E_C = \left( \frac{Ze}{V} \right)^2 \frac{d^3\vec{r}_1 d^3\vec{r}_2}{\|\vec{r}_1 - \vec{r}_2\|} . \quad (5.31)$$

In this expression, the potential at a point  $\vec{r}_1$  created by a charge density  $Ze/V$  at point  $\vec{r}_2$ , can be easily recognized. However scattering experiments showed that protons have a finite-range radius and that the related proton charge distribution is exponential [99]. The effective potential between two protons is [100]

$$V(\vec{r}_1, \vec{r}_2) = \frac{e^2}{\|\vec{r}_1 - \vec{r}_2\|} \left[ 1 - e^{-x} \left( 1 + \frac{11}{16}x + \frac{3}{16}x^2 + \frac{1}{48}x^3 \right) \right] , \quad (5.32)$$

where  $x = \sqrt{12}\|\vec{r}_1 - \vec{r}_2\|/r_p$  and  $r_p \approx 0.8$  fm is the proton r.m.s. radius. From that potential, a correction to the Coulomb energy that takes into account the “shape” of

protons can be calculated. This *proton form factor correction energy*  $\Delta E_{\text{p.f.f.}}$  is given by [94]

$$\Delta E_{\text{p.f.f.}} = -\frac{1}{8} \frac{r_{\text{p}}^2 e^2}{r_0^2} \left[ \frac{145}{48} - \frac{327}{2880} (k_{\text{F}} r_{\text{p}})^2 + \frac{1527}{1209600} (k_{\text{F}} r_{\text{p}})^4 + \dots \right] \frac{Z^2}{A}, \quad (5.33)$$

where  $k_{\text{F}}$  is the Fermi wave number given by

$$k_{\text{F}} = \frac{1}{r_0} \left( \frac{9\pi Z}{4A} \right)^{1/3}. \quad (5.34)$$

The proton form factor correction is assumed to be independent of the deformation.

### 5.2.3.4 Binding Energy of Electrons

The mass model parameters are often adjusted on experimental atomic masses. Hence the mass of electrons is removed to obtain the nucleus mass. Additionally the binding energy of electrons  $B_{\text{el}}(Z)$  must also be removed. Foldy suggested [101] that the binding energy of electrons can be written as a function of powers of  $Z$ :

$$B_{\text{el}}(Z) = 15.73 Z^{7/3} \text{ eV} \quad (5.35)$$

Seeger seems to have been the first to include this correction [102, 103] in atomic mass models. He used:

$$B_{\text{el}}(Z) = 14.33 Z^{2.39} \text{ eV} \quad (5.36)$$

More recent estimations [104] suggest:

$$B_{\text{el}}(Z) = 14.4381 Z^{2.39} + 1.55468 \times 10^{-6} Z^{5.35} \text{ eV} \quad (5.37)$$

It should be noted that if one uses this formula for the electron binding energy, the atomic mass of hydrogen  $M_{\text{H}}$  should not be used anymore but must be replaced by the masses of the proton and electron. Indeed in Eq. 5.3,  $M_{\text{H}} = M_{\text{p}} + M_{\text{e}} - B_{\text{el}}(1)$ , where  $B_{\text{el}}(1) = 13.6 \text{ eV}$ . This electron binding energy correction is very small compared to the nuclear binding energy. The related parameters are not adjusted with other mass parameters but obtained from dedicated adjustments on ionization energies. This correction is introduced so that adjustable parameters are not falsified by the fitting process.

### 5.2.3.5 Neutron-Proton Asymmetry terms

Studies of neutron and proton densities in nucleus [105] led to consider that the difference in the neutron and proton “effective radii” should be taken into account in the mass formula as an asymmetry component in the surface term [92, 94, 106]. The asymmetry term  $a_{\text{A}}(N - Z)^2/A = a_{\text{A}}I^2A$  of the Bethe-Weizsäcker formula 5.4 can be regarded as a similar effect but for the volume term. Hence  $a_{\text{S}}$  should be replaced by  $c_{\text{S}} = a_{\text{S}}(1 - \kappa_{\text{S}}I^2)$ , where  $I$  is the relative neutron excess:  $I = (N - Z)/A$ . Similarly  $a_{\text{V}}$  can be replaced by  $c_{\text{V}} = a_{\text{V}}(1 - \kappa_{\text{V}}I^2)$  and the asymmetry term  $a_{\text{A}}(N - Z)^2/A$  can be dropped. The new parameters  $a_{\text{S}}$ ,  $a_{\text{V}}$ ,  $\kappa_{\text{S}}$  and  $\kappa_{\text{V}}$  must be adjusted on experimental data.

It was first considered that this treatment of asymmetry was good enough to include all asymmetry effects. However Negele [100] argued that the unexplained failure of the mass formula to reproduce mass difference between mirror nuclei  $^{41}\text{Sc}$  and  $^{41}\text{Ca}$  was due

to a small asymmetry in the nuclear force [94]. To first order, this effect was included by a charge-asymmetry energy  $\Delta E_A$  given by

$$\Delta E_A = c_A \frac{Z^2 - N^2}{A} = c_A(Z - N), \quad (5.38)$$

where  $c_A$  is a new adjustable parameter.

An other failure of the mass formula is visible for light nuclei having  $Z = N$  [92]. This effect cannot be explained by usual shell or pairing effects [107] and led to the inclusion of an additional term called the “Wigner term”, defined by

$$E_{\text{Wigner}} = (|I| + d)W, \quad (5.39)$$

where

$$d = \begin{cases} 1/A, & Z \text{ and } N \text{ odd, and } Z = N \\ 0, & \text{otherwise} \end{cases}. \quad (5.40)$$

The  $d$  term is justified experimentally [108].

### 5.2.3.6 Pairing Effects

In the early Bethe-Weizsäcker formula, the pairing term makes no distinction between pairs of neutrons or pairs of protons. An extension of this approach may consider different pairing forces between neutrons and protons [109]. This approach includes nevertheless a “residual interaction” between an unpaired neutron and an unpaired proton that leads to bring more stability than if one considers protons and neutrons as non-interacting systems. This last refinement leads to a pairing term  $\delta(Z, N)$  defined as

$$\delta(Z, N) = \begin{cases} \bar{\Delta}_p + \bar{\Delta}_n - \delta_{np}, & Z \text{ and } N \text{ odd}, \\ \bar{\Delta}_p, & Z \text{ odd and } N \text{ even}, \\ \bar{\Delta}_n, & Z \text{ even and } N \text{ odd}, \\ 0, & Z \text{ and } N \text{ even}. \end{cases} \quad (5.41)$$

Here the average pairing gap parameters  $\bar{\Delta}_p$  and  $\bar{\Delta}_n$  and average residual interaction  $\delta_{np}$  are given by

$$\begin{aligned} \bar{\Delta}_p &= \frac{r B_S}{Z^{1/3}} e^{+sI - tI^2}, \\ \bar{\Delta}_n &= \frac{r B_S}{N^{1/3}} e^{-sI - tI^2}, \\ \delta_{np} &= \frac{h}{B_S A^{2/3}}, \end{aligned} \quad (5.42)$$

where  $B_S$  is defined by Eq. 5.9. Parameters  $r$ ,  $s$ ,  $t$  and  $h$  are to be adjusted on experimental data. An extensive study of pairing models, comparing macroscopic, BCS and Lipkin-Nogami models, was performed by Möller and Nix [110] and concluded that no real benefit is obtained by varying  $t$  and  $s$  parameters. Hence the final parameters retained for the average pairing terms are  $h$  and  $r$ , both parameters  $s$  and  $t$  are taken to be zero.

### 5.2.4 Summary and Effect of Deformation

The global expression of the macroscopic energy of the finite-range liquid-drop model,  $E_{\text{macro}}^{\text{FRLDM}}(Z, A, \vec{q})$ , is obtained by gather all features presented here-above. The expression of the atomic mass in the macroscopic model is given by [12]



$$\begin{aligned}
E_{\text{macro}}^{\text{FRLDM}}(Z, A, \vec{q}) = & M_{\text{H}}Z + M_{\text{n}}N \\
& - a_{\text{V}}(1 - \kappa_{\text{V}}I^2)A + a_{\text{S}}(1 - \kappa_{\text{S}}I^2)B_1(\vec{q})A^{2/3} + f(k_{\text{F}}r_{\text{p}})\frac{Z^2}{A} \\
& + a_0A^0 + c_1\frac{Z^2}{A^{1/3}}B_3(\vec{q}) - c_4\frac{Z^{4/3}}{A^{1/3}} - c_{\text{a}}(N - Z) \\
& + W\left(|I| + \frac{1}{A}\delta_{ZN}\delta_{Z\text{odd}}\right) + \begin{cases} \bar{\Delta}_{\text{p}} + \bar{\Delta}_{\text{n}} - \delta_{\text{np}}, & Z \text{ and } N \text{ odd} \\ \bar{\Delta}_{\text{p}}, & Z \text{ odd and } N \text{ even} \\ \bar{\Delta}_{\text{n}}, & Z \text{ even and } N \text{ odd} \\ 0, & Z \text{ and } N \text{ even} \end{cases} - a_{\text{el}}Z^{2.39}. \quad (5.43)
\end{aligned}$$

where

$$c_1 = \frac{3}{5} \frac{e^2}{4\pi\epsilon_0 r_0} \quad \text{and} \quad c_4 = \frac{5}{4} c_1 \left(\frac{3}{2\pi}\right)^{2/3}. \quad (5.44)$$

The expression of the shape-dependent terms in Eq. 5.43,  $B_1$  and  $B_3$ , are, as stated previously given by

$$B_1(\vec{q}) = \frac{A^{-2/3}}{8\pi^2 r_0^2 a^4} \int_V d^3\vec{r}_1 \int_V d^3\vec{r}_2 \left(2 - \frac{\|\vec{r}_1 - \vec{r}_2\|}{a}\right) \frac{e^{-\|\vec{r}_1 - \vec{r}_2\|/a}}{\|\vec{r}_1 - \vec{r}_2\|/a}, \quad (5.45)$$

$$B_3(\vec{q}) = \frac{15A^{-5/3}}{32\pi^2 r_0^5} \int_V d^3\vec{r}_1 \int_V \frac{d^3\vec{r}_2}{\|\vec{r}_1 - \vec{r}_2\|} \left[1 - \left(1 + \frac{1}{2} \frac{\|\vec{r}_1 - \vec{r}_2\|}{a_{\text{den}}}\right) e^{-\|\vec{r}_1 - \vec{r}_2\|/a_{\text{den}}}\right]. \quad (5.46)$$

In the present study, the model parameters are not adjusted, their values can be found in Ref. [12].

In Fig. 5.3, the deformation energy of  $^{240}\text{Pu}$  obtained using the macroscopic FRLDM energy is shown, as a function of the deformation, using the Hill-Wheeler shape parameterization (*cf.* Eq. B.4 of Appendix B.1). It can be seen that the calculated ground state is spherical ( $y = 0$ ) and that the fission barrier has a single hump. The barrier height seems quite low (less than 4 MeV), yet it should be kept in mind that the macroscopic parameters used here are those of the macroscopic-microscopic model. These parameters have been adjusted to reproduce experimental data (masses) but using the macroscopic-microscopic model, not the macroscopic model alone. A similar calculation with the macroscopic-microscopic model would lead to more realistic barrier heights (about 6 MeV) and also to a non-spherical ground state. It is also this latter unsatisfactory feature of the macroscopic model that historically led to introduce the macroscopic-microscopic model.

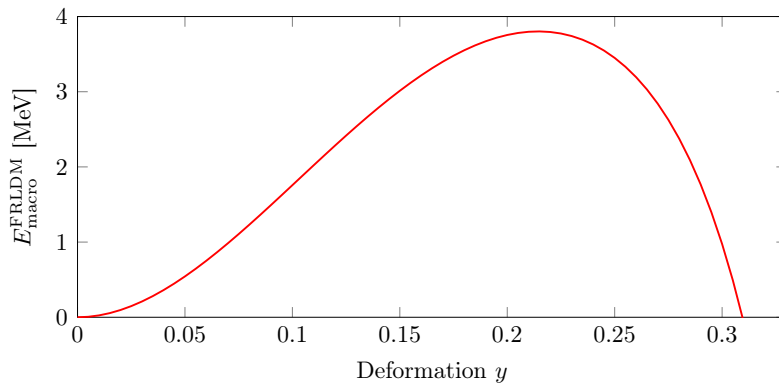


Figure 5.3 – Macroscopic deformation energy of the FRLDM using the Hill-Wheeler shape parameterization for  $^{240}\text{Pu}$ .

### 5.2.5 Macroscopic Model Verification

In the FRLDM macroscopic expression (*cf.* Eq 5.43), few terms need specific numerical verification, it only relates to the  $B_1$  and  $B_3$  terms that depend not only on the considered isotope but also on its shape. A macroscopic shape-dependent term,  $B_S$  is used in the microscopic shell correction that will be detailed later in this chapter. The numerical computation of this term must also be verified. The computation of the  $B_1$ ,  $B_3$  and  $B_S$  terms can be verified against sphere shapes (of radius  $R = r_0 A^{1/3}$ ) for which analytical expression exists, Eqs. 5.45, 5.46 and 5.9 become respectively:

$$B_S(\vec{q}_{\text{sphere}}) = 1, \quad (5.47)$$

$$B_1(\vec{q}_{\text{sphere}}) = 1 - \frac{3}{x_0^2} + (1 + x_0) \left( 2 + \frac{3}{x_0} + \frac{3}{x_0^2} \right) e^{-2x_0}, \quad (5.48)$$

$$B_3(\vec{q}_{\text{sphere}}) = 1 - \frac{5}{y_0^2} \left[ 1 - \frac{15}{8y_0} + \frac{21}{8y_0^3} - \frac{3}{4} \left( 1 + \frac{9}{2y_0} + \frac{7}{y_0^2} + \frac{7}{2y_0^3} \right) e^{-2y_0} \right], \quad (5.49)$$

where

$$x_0 = \frac{r_0 A^{1/3}}{a} \quad \text{and} \quad y_0 = \frac{r_0 A^{1/3}}{a_{\text{den}}}. \quad (5.50)$$

Additionally it can be noted that, depending on the shape parameterization, the shape can be represented by two kinds of functions  $\rho(z)$  or  $r(\theta)$ , thus two types of integration methods must be implemented for  $B_1$ ,  $B_3$  and  $B_S$  (Eqs. 5.9, 5.45 and 5.46). For shapes for which both representations are possible, the two integration methods lead to consistent results.

## 5.3 Microscopic Models

An alternative way of considering the atomic nucleus is the microscopic approach, in which nucleons are individually modeled in a quantum mechanics framework. This approach is widely investigated with Hartree-Fock-Bogoliubov self-consistent methods. However the following study will be limited to phenomenological mean-fields that will be later used in the macroscopic-microscopic model. Additionally, only axially-symmetric shapes will be considered.

In this approach nucleon properties are described by an independent-particle Hamiltonian  $\hat{H}$  given by

$$\hat{H} = \hat{T} + \hat{V}, \quad (5.51)$$

where the kinetic operator  $\hat{T}$  can be written, using the cylindrical coordinate system defined in Fig. 5.4, as

$$\hat{T} = -\frac{\hbar^2}{2m} \left( \frac{1}{\rho} \frac{\partial}{\partial \rho} \left( \rho \frac{\partial}{\partial \rho} \right) + \frac{1}{\rho^2} \frac{\partial^2}{\partial \varphi^2} + \frac{\partial^2}{\partial z^2} \right), \quad (5.52)$$

where  $m$  is the mass of a nucleon. In the following, a few different models for the potential operator  $\hat{V}$  will be discussed.

### 5.3.1 Nilsson Harmonic Oscillator Model and Basis Wave Functions

A single-particle Hamiltonian that often appears in microscopic models is the Nilsson Harmonic Oscillator model [111]. In this model, a spinless nucleon of mass  $m$  feels an

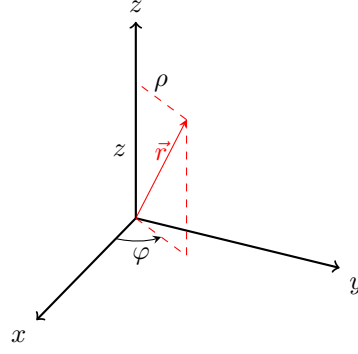


Figure 5.4 – Definition of the cylindrical coordinate system.

average three-dimensional harmonic oscillator potential  $\hat{V}^{\text{HO}}$  defined as

$$\hat{V}^{\text{HO}} = \frac{1}{2}m\omega_x^2\hat{x}^2 + \frac{1}{2}m\omega_y^2\hat{y}^2 + \frac{1}{2}m\omega_z^2\hat{z}^2, \quad (5.53)$$

where  $\omega_x$ ,  $\omega_y$  and  $\omega_z$  are the harmonic oscillator frequencies associated with the  $x$ ,  $y$  and  $z$  axes respectively. In the case of axially symmetric potentials, one defines  $\omega_{\perp} = \omega_x = \omega_y$ , so that the potential  $\hat{V}$  simplifies to

$$\hat{V}^{\text{HO}} = \frac{1}{2}m\omega_{\perp}^2\hat{\rho}^2 + \frac{1}{2}m\omega_z^2\hat{z}^2. \quad (5.54)$$

It is often convenient to introduce the following variable changes

$$\eta = \frac{m\omega_{\perp}}{\hbar}\rho^2 \quad \text{and} \quad \xi = \sqrt{\frac{m\omega_z}{\hbar}}z. \quad (5.55)$$

The kinetic operator  $\hat{T}$  can thus be written as

$$\hat{T} = -\frac{1}{2}\hbar\omega_{\perp} \left( 4\frac{\partial}{\partial\eta} \left( \eta\frac{\partial}{\partial\eta} \right) + \frac{1}{\eta}\frac{\partial^2}{\partial\varphi^2} \right) - \frac{1}{2}\hbar\omega_z\frac{\partial^2}{\partial\xi^2}. \quad (5.56)$$

Using variables  $\eta$  and  $\xi$ , the potential operator  $\hat{V}^{\text{HO}}$  can be written

$$\hat{V}^{\text{HO}} = \frac{1}{2}\hbar\omega_{\perp}\eta + \frac{1}{2}\hbar\omega_z\xi^2. \quad (5.57)$$

In practice,  $\omega_{\perp}$  and  $\omega_z$  are not chosen independently, the usual approach is to enforce  $\omega_{\perp}^2\omega_z = \omega_0^3$  to be independent of the harmonic oscillator “elongation”. The eigenfunctions of the corresponding Hamiltonian  $\hat{H}$  are defined by

$$\Psi_{n_r, n_z, \Lambda}(\rho, z) = \Psi_{n_r}^{\Lambda}(\eta)\Psi_{n_z}(\xi)\Psi_{\Lambda}(\varphi), \quad (5.58)$$

where

$$\begin{aligned} \Psi_{\Lambda}(\varphi) &= N_{\Lambda}e^{i\Lambda\varphi}, & N_{\Lambda} &= \frac{1}{\sqrt{2\pi}}, \\ \Psi_{n_z}(\xi) &= N_{n_z} \left[ \frac{m\omega_z}{\hbar} \right]^{\frac{1}{4}} e^{-\frac{\xi^2}{2}} H_{n_z}(\xi), & N_{n_z} &= \frac{1}{\sqrt{\sqrt{\pi}2^{n_z}n_z!}}, \\ \Psi_{n_r}^{\Lambda}(\eta) &= N_{n_r}^{\Lambda} \left[ \frac{2m\omega_{\perp}}{\hbar} \right]^{\frac{1}{2}} \eta^{\frac{|\Lambda|}{2}} e^{-\frac{\eta}{2}} L_{n_r}^{|\Lambda|}(\eta), & N_{n_r}^{\Lambda} &= \sqrt{\frac{n_r!}{(n_r + |\Lambda|)!}}, \end{aligned} \quad (5.59)$$

and  $(n_r, n_z) \in \mathbb{N}^2$ ,  $\Lambda \in \mathbb{Z}$ . Here  $H_{n_z}$  and  $L_{n_r}^{|\Lambda|}$  are respectively the Hermite and associated Laguerre polynomials [48].  $\Psi_{n_r, n_z, \Lambda}$  is also an eigenfunction of the  $\hat{l}_z$  operator, which is the orbital angular momentum projection on the deformation axis  $z$ , with eigenvalue  $\Lambda$ . The eigenvalue  $\epsilon_{n_z, n_r, \Lambda}$  associated with  $\Psi_{n_r, n_z, \Lambda}$  for the Hamiltonian operator  $\hat{H}$  is given by

$$\epsilon_{n_z, n_r, \Lambda} = \frac{1}{2} \hbar \omega_{\perp} (2n_r + |\Lambda| + 1) + \frac{1}{2} \hbar \omega_z (n_z + \frac{1}{2}). \quad (5.60)$$

One can easily see (from the modulus sign  $|\cdot|$ ) that the energy level associated with  $\epsilon_{n_z, n_r, \Lambda}$  is always degenerate if  $\Lambda \neq 0$ . In this latter case two eigenfunctions with opposite value of  $\Lambda$  are associated with the  $\epsilon_{n_z, n_r, \Lambda}$  energy. Hence one can consider only doubly-degenerate levels with eigenfunctions for which  $\Lambda \in \mathbb{N}^*$ , with special care of non-degenerate eigenfunctions having  $\Lambda = 0$ . The eigenfunction  $\Psi_{n_r, n_z, \Lambda}$  can be written in Dirac notation:

$$\Psi_{n_r, n_z, \Lambda} = |n_r n_z \Lambda\rangle \quad (5.61)$$

This type of potential may seem simplistic, however it is still widely used as a computing base in more sophisticated approaches. This point will be detailed in Section 5.5.1.

### 5.3.2 More Realistic Phenomenological Potentials

More realistic potentials have been introduced since. In the following, only phenomenological potentials will be presented, *i.e.* potentials defined by *ad-hoc* parameters, not obtained from an effective nucleon-nucleon interaction. These parameterized approaches can yet be used to produce shape-dependent potentials.

#### 5.3.2.1 Average Scalar Potential

The most commonly used phenomenological potential is known as the Wood-Saxon potential [112]. It has been introduced as an optical model interaction potential as described in Section 4.3 of Chapter 4. The potential well felt by a nucleon is given by

$$\hat{V}_N = -\frac{V_0}{1 + e^{n(\vec{r})/a}}, \quad (5.62)$$

where  $n(\vec{r})$  is the normal distance from  $\vec{r}$  to the surface of the nucleus. Although this type of parameterization could be used for deformed nuclei ( $n(\vec{r})$  depends not only on  $r$  but also on  $\frac{\vec{r}}{r}$ ), another parameterization, known as the Yukawa-folded model, is more suitable for arbitrary shapes. It is defined by

$$\hat{V}_N = -\frac{V_0}{4\pi a^3} \int_V \frac{e^{-\|\vec{r}-\vec{r}'\|/a}}{\|\vec{r}-\vec{r}'\|/a} d^3\vec{r}'. \quad (5.63)$$

For protons, an additional scalar potential  $\hat{V}_C$  resulting from the Coulomb interaction must be added. It reads

$$\hat{V}_C = \frac{Ze^2}{\frac{4}{3}\pi R^3} \int_V \frac{d^3\vec{r}'}{\|\vec{r}-\vec{r}'\|}. \quad (5.64)$$

Figure 5.5 shows an example of such potentials for neutrons and protons using the Yukawa-folded model. The generating shape is defined using the three-quadratic surface parameterization (3QS) that is detailed in Appendix B.1. One can observe structures on the well bottom for protons that do not exist for neutrons. They are due to long-range of the Coulomb interaction.

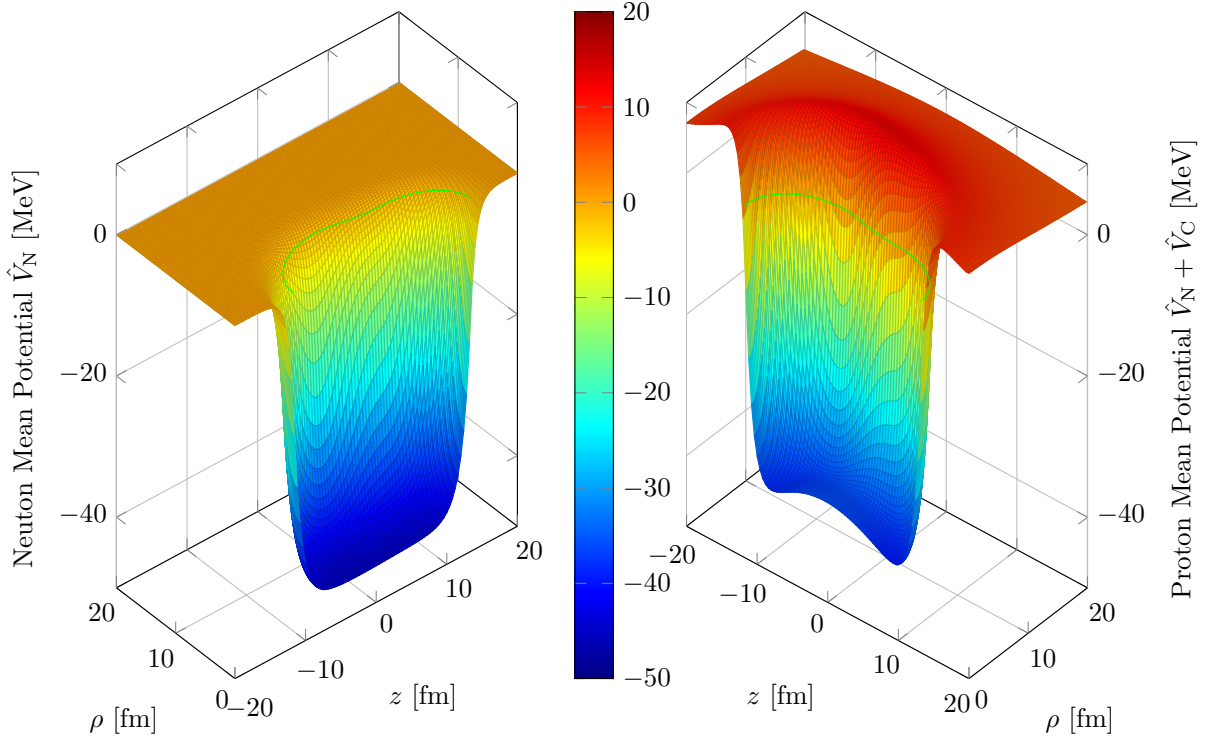


Figure 5.5 – Example of scalar mean potentials calculated by a folded-Yukawa model for  $^{236}\text{U}$ . Here  $a = 0.8$  fm,  $V_0 \approx 45$  MeV for neutrons and  $V_0 \approx 60$  MeV for protons. The 3QS generating shape used here (*cf.* Appendix B.1), is symbolized by a solid green line on plane  $V = 0$ .

The parameters used in the model are listed in Ref. [12]. The spherical-equivalent radius definition is obtained from Ref. [113], the proton and neutron well depths are taken from Ref. [87]. Finally the spin-orbit coupling strength is defined in Ref. [94] from interpolation of experimental data fitting [114] in regions  $A \approx 160$  and  $A \approx 240$ .

### 5.3.2.2 Spin-Orbit Coupling Potential

In addition to the mean scalar potential, a spin-orbit coupling potential  $\hat{V}_{\text{s.o.}}$  must be added in the Hamiltonian. In spherically symmetric potentials, this term is proportional to  $\hat{\vec{S}} \cdot \hat{\vec{L}}$ , where  $\hat{\vec{S}}$  is the nucleons intrinsic spin operator and  $\hat{\vec{L}}$  is its relative angular momentum operator. However, for arbitrary shapes, a more general form of the coupling potential must be considered, known as *full-Thomas term* [115]. It is given by

$$\hat{V}_{\text{s.o.}} = -\lambda \left( \frac{\hbar}{2mc} \right)^2 \bar{\vec{\sigma}} \cdot \vec{\nabla} V_N \times \frac{\vec{p}}{\hbar}, \quad (5.65)$$

where  $\bar{\vec{\sigma}}$  is the Pauli spin vector

$$\bar{\vec{\sigma}} = \begin{pmatrix} \sigma_x \\ \sigma_y \\ \sigma_z \end{pmatrix}_{(x,y,z)} = \begin{pmatrix} \sigma_\rho \\ \sigma_\varphi \\ \sigma_z \end{pmatrix}_{(\rho,\varphi,z)} = \begin{pmatrix} \sigma_r \\ \sigma_\theta \\ \sigma_\varphi \end{pmatrix}_{(r,\theta,\varphi)}. \quad (5.66)$$

In cylindrical coordinate system, one has the Pauli matrices

$$\sigma_\rho = \begin{bmatrix} 0 & e^{-i\varphi} \\ e^{i\varphi} & 0 \end{bmatrix}, \quad \sigma_\varphi = \begin{bmatrix} 0 & -ie^{-i\varphi} \\ ie^{i\varphi} & 0 \end{bmatrix}, \quad \sigma_z = \begin{bmatrix} 1 & 0 \\ 0 & -1 \end{bmatrix}. \quad (5.67)$$

This coupling potential, because of the presence of the Pauli spin vector  $\vec{\sigma}$ , will introduce mixing between states with different  $\Lambda$  and  $\Sigma$  values,  $\Sigma$  being the quantum number related to the projection of  $\hat{S}$  on the  $z$  axis. However the total angular momentum projection on the  $z$  axis,  $\Omega = \Lambda + \Sigma$ , remains a good quantum number. The spin-orbit potential  $\hat{V}_{\text{s.o.}}$  operates on wave functions that can be written as

$$\Phi(\rho, z) = \begin{pmatrix} \psi^{\uparrow\uparrow}(z, \rho) \\ \psi^{\uparrow\downarrow}(z, \rho) \end{pmatrix}, \quad (5.68)$$

where  $\psi^{\uparrow\uparrow}$  and  $\psi^{\uparrow\downarrow}$  are wave functions for which  $\Omega = \Lambda + \frac{1}{2}$  and  $\Omega = \Lambda - \frac{1}{2}$  respectively. Hence the spin-orbit potential operator can be written in a matrix form [116] as

$$\hat{V}_{\text{s.o.}} = \lambda \left( \frac{\hbar}{2mc} \right)^2 \begin{bmatrix} -\frac{(\Omega - \frac{1}{2})}{\rho} \frac{\partial V_N}{\partial \rho} & \left[ \frac{(\Omega + \frac{1}{2})}{\rho} \frac{\partial V_N}{\partial z} + \frac{\partial V_N}{\partial z} \frac{\partial}{\partial \rho} - \frac{\partial V_N}{\partial \rho} \frac{\partial}{\partial z} \right] \\ \left[ \frac{(\Omega - \frac{1}{2})}{\rho} \frac{\partial V_N}{\partial z} - \frac{\partial V_N}{\partial z} \frac{\partial}{\partial \rho} + \frac{\partial V_N}{\partial \rho} \frac{\partial}{\partial z} \right] & \frac{(\Omega + \frac{1}{2})}{\rho} \frac{\partial V_N}{\partial \rho} \end{bmatrix}. \quad (5.69)$$

In case of nucleons ( $\Sigma = \pm \frac{1}{2}$ ) no states with  $\Omega = 0$  exists, hence there are only doubly-degenerate eigenstates<sup>3</sup> ( $i, \bar{i}$ ) having opposite signs of  $\Omega$ . Considering eigenstate  $i$  with  $\Omega > 0$ , the state wave can be written

$$\Phi_i(\rho, z) = \begin{pmatrix} \psi_{i+}^{\uparrow\uparrow}(z, \rho) \\ \psi_{i+}^{\uparrow\downarrow}(z, \rho) \end{pmatrix}, \quad (5.70)$$

the corresponding eigenstate  $\bar{i}$  with  $\Omega < 0$  is obtained [117] from  $\Phi_i$  as

$$\Phi_{\bar{i}}(\rho, z) = \begin{pmatrix} -\psi_{i+}^{\uparrow\downarrow}(z, \rho) \\ \psi_{i+}^{\uparrow\uparrow}(z, \rho) \end{pmatrix}. \quad (5.71)$$

Considering  $\Omega > 0$ , one can write

$$|\Sigma\rangle = \begin{cases} \begin{pmatrix} 1 \\ 0 \end{pmatrix}, & \text{for } \Sigma = +\frac{1}{2} \\ \begin{pmatrix} 0 \\ 1 \end{pmatrix}, & \text{for } \Sigma = -\frac{1}{2} \end{cases}. \quad (5.72)$$

The wave function  $\Phi_i$  can thus be written

$$\Phi_i(\rho, z) = \psi_{i+}^{\uparrow\uparrow}(z, \rho) |\Sigma = +\frac{1}{2}\rangle + \psi_{i+}^{\uparrow\downarrow}(z, \rho) |\Sigma = -\frac{1}{2}\rangle. \quad (5.73)$$

In case of non-zero spin particles, the harmonic oscillator wave functions  $|n_z n_r \Lambda\rangle$  can be used to define a new base of functions

$$|n_z n_r \Lambda \Sigma\rangle = |n_z n_r \Lambda\rangle |\Sigma\rangle. \quad (5.74)$$

These new functions will be used as an expansion base for the numerical computation of the actual wave functions as described in Section 5.5.1, this method will namely rely on the calculation of coupling terms between different functions of the base.

---

<sup>3</sup>If  $i$  is one of the doubly-degenerate state (for instance with  $\Omega > 0$ ), its time-reversed counterpart is written  $\bar{i}$ .

### 5.3.3 Single-Particle States and Deformation

Given a parameterized shape, a folded nuclear potential  $\hat{V}_N$ , a Coulomb potential  $\hat{V}_C$  and a spin-orbit coupling potential  $\hat{V}_{s.o.}$  can be defined. The Schrödinger equation of independent particles [87], written

$$\hat{H}\psi = \left[ \hat{T} + \hat{V}_N + \hat{V}_C + \hat{V}_{s.o.} \right] \psi = \epsilon\psi, \quad (5.75)$$

is solved and leads to single-particle wave functions  $\psi_i$  and related single-particle energies  $\epsilon_i$ .

An illustration of such wave functions is shown in Fig. 5.6. One can notice that nucleons are not necessarily localized in a specific spatial region; in this example it is particularly true for the proton state. The wave reflection-asymmetry in the figure is due to the mass-asymmetry of the generating shape (green line). The wave functions are not directly required for the calculation of the microscopic corrections that must be brought to the macroscopic energy, however they will be required for the calculation of inertia quantities. This will be detailed in Chapter 6.

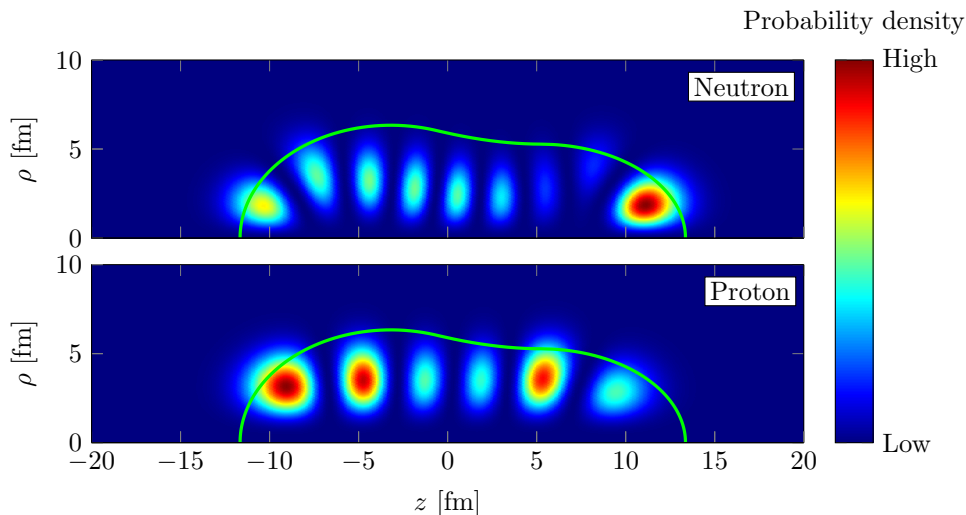


Figure 5.6 – Example of nucleon probability density  $|\psi_i|^2$  for the last occupied level of  $^{240}\text{Pu}$ . The generating shape, here a 3QS one (*cf.* Appendix B.1), is drawn as a solid green line.

Figure 5.7 (respectively 5.8) shows single-particle energies  $\epsilon_i$  for neutrons (respectively protons) calculated for different shapes. Here described by the Hill-Wheeler shape parameter  $y$  (*cf.* Appendix B.1). This figure shows results obtained with the newly implemented single-particle program, for comparison with results from Ref. [87]. For the spherical shape, the magic numbers appear. They can be found by filling levels with two nucleons per level, from the first (most negative) level. Magic numbers occur when a significant gap between level energies exists. Considering two neighboring nuclei having the same level scheme, one has all levels filled with nucleons up to a gap, the other one has just one more nucleon that is at an energy quite above than the former one. The binding energy *per nucleon*, would be quite reduced in the latter case compared to the former one.

In Figs. 5.7 and 5.8, only the less tightly bound levels are shown, so only largest magic number can be seen. There are the experimentally observed numbers 82 and 126 and the predicted number 184 for neutrons and the experimentally observed 50 and 82



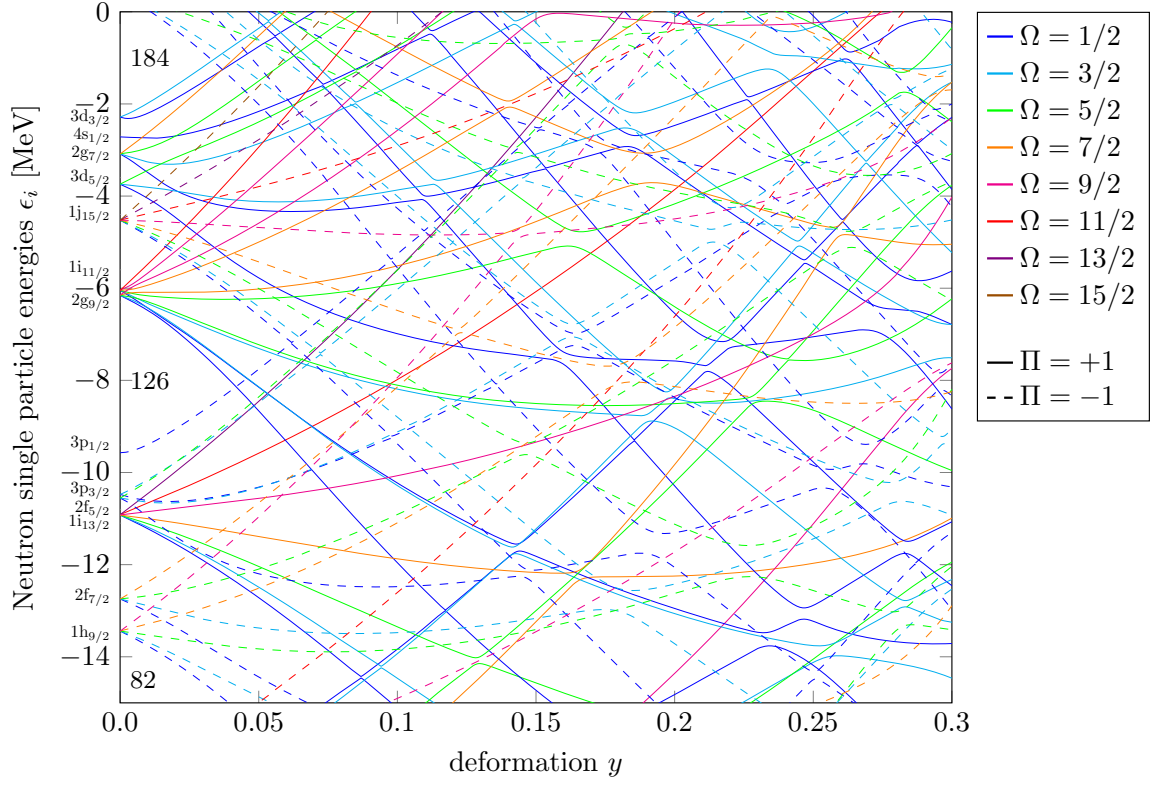


Figure 5.7 – Example of Nilsson diagram showing the single-particle energies  $\epsilon_i$  as a function of the Hill-Wheeler “deformation” parameter  $y$  (*cf.* Appendix B.1 on shape parameterization). Each line corresponds to a doubly-degenerate level ( $M_J = \pm\Omega$ ).

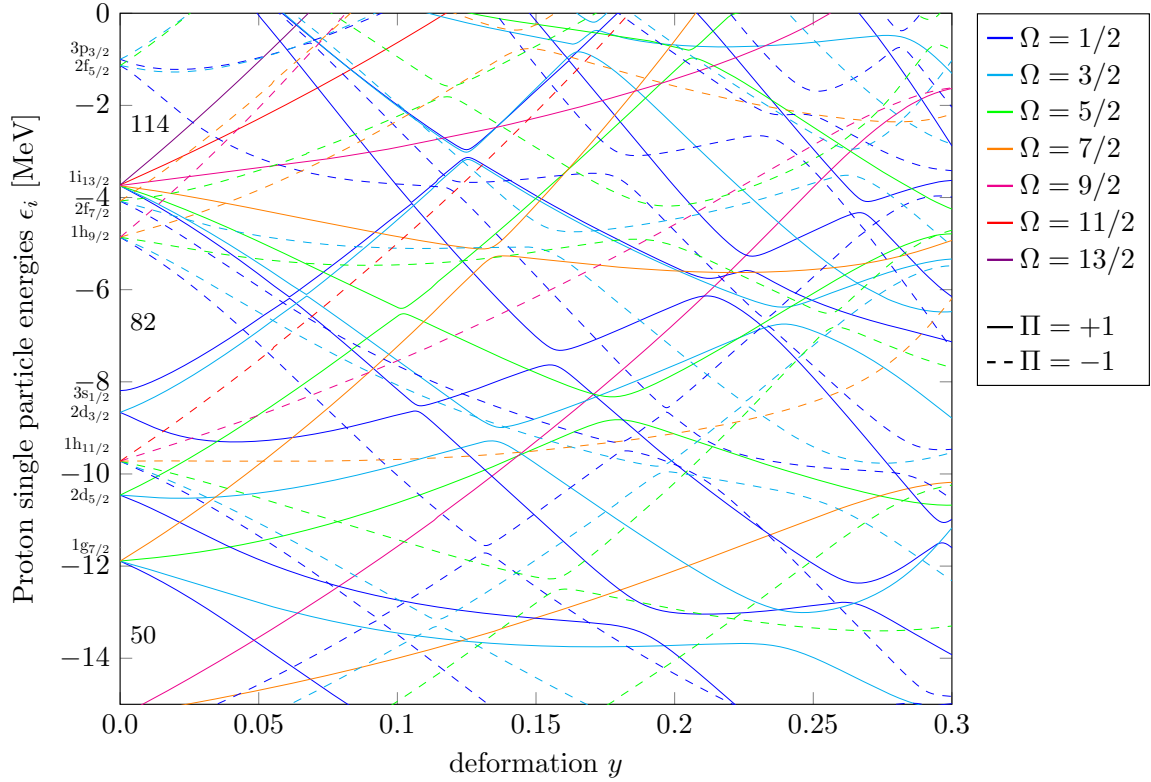


Figure 5.8 – Same as Fig. 5.7 but for protons.

numbers and the predicted 114 number for protons. In the case of spherically symmetric potential, the “spectroscopy” levels correspond to *good quantum numbers*  $N\ell_j$ , shown in the figures. The degeneracy is broken for non-spherical shapes. The von Neumann-Wigner non-crossing rule [118] is also verified; levels with similar  $\Omega$  and parity  $\Pi$  quantum numbers do not cross when deformation increases. Finally one can notice that as the shape evolves from sphere to dumbbell-like shape (with two nascent fragments), the high- $\Omega$  levels increase in energy and the low- $\Omega$  levels decrease in energy.

Figures 5.7 and 5.8 show the level energies for the  $^{240}\text{Pu}$  nucleus as a function of the deformation. The nucleus “starts” from a spherical shape and evolves to a dumbbell shape corresponding to two nascent fragments. The  $^{240}\text{Pu}$  nucleus contains many nucleons and, in its ground state, it has low-lying levels with high-angular momenta. On the contrary, fragments are smaller and have not these high-angular-momentum levels in their low-lying level schemes. As the levels energies are continuous functions of deformation, the high-angular-momentum levels must “disappear” otherwise they would be present in the fragment level schemes. Thus these level energies must raise as deformation increases. To compensate this reduction of available levels, extra low-angular-momentum levels must “appear”, *i.e.* as the nucleus deforms, levels from the positive energy region (for spherical shapes) fall down to the low-lying negative energy region (for elongated shapes), as can be seen in the figures. For instance in Fig. 5.8, orange lines ( $\Omega = \frac{7}{2}$ ) seem to rise with deformation whereas blue lines ( $\Omega = \frac{1}{2}$ ) tend to go down.

### 5.3.4 Microscopic Model Verifications

Several verifications of the microscopic model have been done.

- A first natural verification consists in considering a deformed harmonic oscillator potential  $\hat{V}^{\text{HO}}$  for the nuclear average potential  $\hat{V}_{\text{N}}$  ( $\omega_{\perp} \neq \omega_z$ ), no Coulomb potential  $\hat{V}_{\text{C}} = 0$  and no spin-orbit coupling potential  $\hat{V}_{\text{s.o.}} = 0$ . In this case, the eventual Hamiltonian matrix  $\mathbf{H}_{\Omega}$  used in the expansion method described in Section 5.5.1 is diagonal. The diagonal matrix element, corresponding to the base function  $|n_r n_z \Lambda \Sigma\rangle$  has an analytical expression (*cf.* Eq. 5.60)

$$\epsilon_{n_z, n_r, \Lambda} = \frac{1}{2} \hbar \omega_{\perp} (2n_r + |\Lambda| + 1) + \frac{1}{2} \hbar \omega_z (n_z + \frac{1}{2}), \quad (5.76)$$

which is the eigenvalue associated with  $|n_r n_z \Lambda\rangle$ . With this simplified potential, there is no dependence on  $\Sigma$ , and thus the diagonalization of the Hamiltonian matrix<sup>4</sup>  $\mathbf{H}_{\Omega}$  must yields twice to each eigenvalues. For this test, the implemented computer code recovers exactly the analytical values of  $\epsilon_{n_z, n_r, \Lambda}$  within errors smaller than  $10^{-3}\%$ .

- The second verification deals with the above potential specifications, but where the  $\hat{V}_{\text{N}}$  potential is taken to be spherical ( $\omega_{\perp} = \omega_z$ ). This case is just a particular configuration of the above general verification. However it is well known that for spherically symmetric potentials,  $\ell$ ,  $s$  and  $j$  are good quantum numbers and that corresponding energy levels are  $2(2\ell + 1)$ -degenerate (this degeneracy corresponds to the  $s_z$  and  $\ell_z$  quantum numbers). For this test the code gives consistent results as well. Even if numerical values are not exactly identical for all degenerate states (differences less than  $10^{-3}\%$  between them), these differences are much smaller than the energy differences between degenerate levels.

<sup>4</sup>This is correct if both  $|n_r n_z \Lambda, +\frac{1}{2}\rangle$  and  $|n_r n_z (\Lambda + 1), -\frac{1}{2}\rangle$  are contained in the base of  $\mathbf{H}_{\Omega}$  ( $\Omega = \Lambda + \Sigma$ ). If the base is truncated using all base functions having a  $\Lambda$  value below a given  $\Lambda_{\text{max}}$ , then eigenvalues  $\epsilon_{n_z, n_r, \Lambda_{\text{max}}}$  are found only once among the matrix  $\mathbf{H}_{\Omega}$  eigenvalues.

- A third verification of the code can be made using again a spherical harmonic oscillator  $\hat{V}^{\text{HO}}$  and no Coulomb potential but this time using a spin-orbit coupling potential with a special form. Indeed, in such spherically symmetric case, the full Thomas term (*cf.* Eq. 5.65) becomes

$$\hat{V}_{\text{s.o.}} = -\frac{\kappa}{\hbar} \vec{\sigma} \cdot \vec{\nabla} V_N \times \frac{\vec{p}}{\hbar} = -\frac{\kappa}{\hbar} \vec{\sigma} \cdot \frac{dV_N}{dr} \frac{\vec{r}}{r} \times \frac{\vec{p}}{\hbar} \quad (5.77)$$

$$= -2 \frac{\kappa}{\hbar} \frac{1}{r} \frac{dV_N}{dr} \frac{1}{\hbar^2} \vec{S} \cdot \underbrace{\vec{r} \times \vec{p}}_{\vec{L}} = -2 \frac{\kappa}{\hbar} \frac{1}{r} \frac{dV_N}{dr} \frac{\vec{S} \cdot \vec{L}}{\hbar^2}, \quad (5.78)$$

where  $\frac{\kappa}{\hbar} = \lambda \left( \frac{\hbar}{2mc} \right)^2$ . The  $\vec{S} \cdot \vec{L}$  operator can be written  $\hat{J}^2 - \hat{L}^2 - \hat{S}^2$  so that  $2 \frac{\vec{S} \cdot \vec{L}}{\hbar^2}$  has for eigenvalue  $j(j+1) - \ell(\ell+1) - s(s+1)$ . As the wave functions associated with the spherical harmonic oscillator (without spin-orbit coupling) are also eigenfunctions of  $\vec{S} \cdot \vec{L}$ , thus  $\hat{H}$  and  $\hat{V}_{\text{s.o.}}$  commute, providing that

$$\frac{1}{r} \frac{dV_N}{dr} = \text{const.}/r. \quad (5.79)$$

A proper substitution of  $V_N$  leads to an analytical shift of the energy levels (this replacement of  $V_N$  is made in the  $\hat{V}_{\text{s.o.}}$  expression only, not for the scalar mean field that remains a spherical harmonic oscillator  $\hat{V}^{\text{HO}}$ ). If the replacement form for  $V_N$  is chosen to be

$$\frac{C\hbar r^2}{\kappa} \frac{r^2}{2}, \quad C \in \mathbb{R}, \quad (5.80)$$

it leads to an energy shift  $\Delta E_{\text{s.o.}}$  (with respect to level energy without spin-orbit coupling) of

$$\Delta E_{\text{s.o.}} = -C [j(j+1) - \ell(\ell+1) - s(s+1)]. \quad (5.81)$$

This term lifts the spherical level degeneracy related to  $\ell$  and  $s$ . Only the degeneracy related to  $j$  remains. The  $C$  parameter will quantify the magnitude of the energy shift. As nucleons are spin- $\frac{1}{2}$  particles, only two  $(\ell, s)$  coupling are possible:

$$\Delta E_{\text{s.o.}} = \begin{cases} C\ell(\ell+1), & j = \ell - \frac{1}{2}, \\ -C\ell, & j = \ell + \frac{1}{2}. \end{cases} \quad (5.82)$$

Therefore “large”  $j$  levels will have lower energies than “small”  $j$  levels. This special configuration (spherical harmonic oscillator potential with “special” spin-orbit coupling potential) was tested with the code and gave very satisfactory results.

When a realistic phenomenological spin-orbit coupling is included, the proper level degeneracy lift can be observed. An example is shown in Fig. 5.9 for  $^{208}\text{Pb}$ . The spin-orbit coupling is introduced progressively (*i.e.* a “strength” of the coupling is used to vary the magnitude of the spin-orbit potential used for the figure, 0% means no spin-orbit coupling potential, 100% means full realistic potential). As the strength is varied from 0 to 100% it is observed that, for all levels but the  $s$  ones, the spin-orbit coupling potential “splits” the 0% levels into two levels. These two levels correspond to two different possible values of  $j = \ell \pm \frac{1}{2}$ , as  $\ell$  is no longer a good quantum number. Given a 0%-strength level (labeled  $N\ell$ ), two  $j$ -levels appears with increasing the strength, with the larger  $j$  that is the lower energy level, in agreement with Eq. 5.82.

It must be noted here that the program computes states as doubly-degenerate levels having  $\Omega = |j_z| \geq \frac{1}{2}$ . When no deformation is considered, *i.e.* for spherical potentials,  $j$

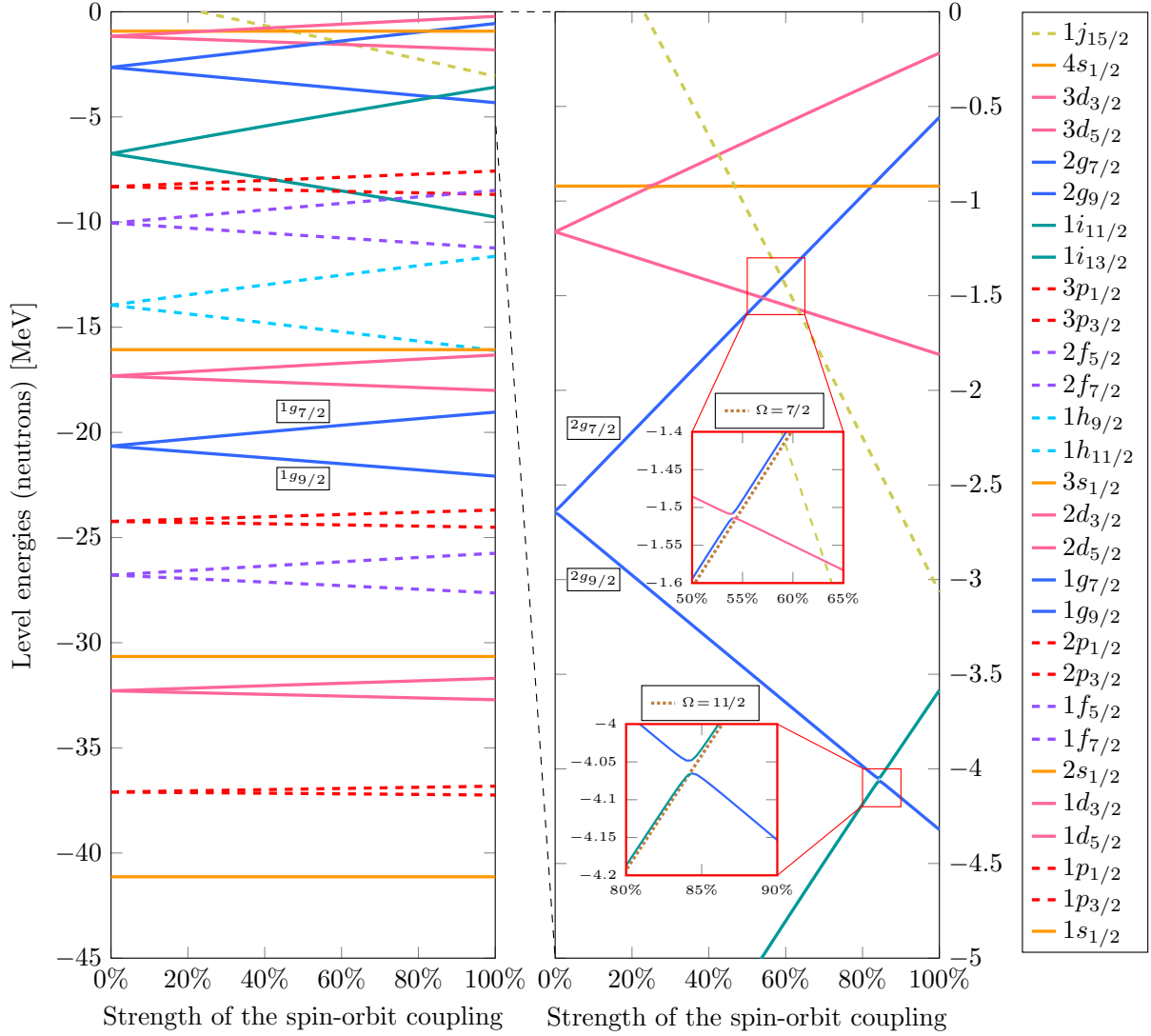


Figure 5.9 – Variation of the single-particle level energies of  $^{208}\text{Pb}$  with the strength of the spin-orbit coupling. Unless other specification, energies are given for states with  $\Omega = \frac{1}{2}$ . Solid and dashed lines refer respectively to positive and negative parities. Spectroscopic labels  $N\ell_j$  are used, where  $N$  is the principal quantum number,  $\ell$  and  $j$  are quantum numbers related respectively to the orbital and total angular momentum. Colors are related to the  $\ell$  quantum numbers. To avoid overloaded figure, the same colors are used for all principal quantum numbers  $N$ . Levels in the legend box are ordered according to the level order for the 0% coupling strength situation. Finally, for a given  $N\ell$  level if two corresponding  $j$  levels exist, the level with the larger  $j$  value is always the lower of the two. An example is given with  $1g$  and  $2g$  levels.

is a good quantum number, and the degenerate states of a given  $j$ -level have  $j_z$  quantum numbers spanning from  $-j$  to  $+j$ , meaning a  $2j + 1$  degeneracy that is also found when analyzing code results. The levels shown in Fig. 5.9 correspond to the doubly-degenerate levels with  $\Omega^\pi = \frac{1}{2}^\pm$  as these states are present in all degenerate  $j$ -levels and are thus representative of these  $j$ -levels. Just like in Section 5.3.3, levels with the same  $\Omega^\pi$  quantum numbers do not cross. Enlargements are shown for confirmation on the right side of Fig. 5.9, where levels corresponding to states  $\Omega^\pi \neq \frac{1}{2}^\pm$  are also shown. From enlargements it can be seen that levels with identical  $\Omega^\pi$  do not cross. To make levels shown in Fig. 5.9 having constant degeneracy when the spin-orbit coupling strength varies, the colors change



## 5.4 Macroscopic-Microscopic Model

The macroscopic and microscopic models have now been introduced. To obtain the macroscopic-microscopic energy, the microscopic shell and pairing corrections  $\delta E_{\text{shell}}$  and  $\delta E_{\text{pair}}$  must be calculated using the single-particle-state  $(\psi_i, \epsilon_i)$ . It is recalled here that these corrections are calculated independently for neutrons and protons.

### 5.4.1 Shell and Pairing Corrections

The discrete character of the nucleon energy levels is responsible for properties that cannot be reproduced by a macroscopic model alone. Examples of such properties are for instance a non-zero quadrupole deformation at the ground state or the double-humped shape of fission barrier. Corrections corresponding to this discrete nature are to be brought to the macroscopic energy that is obtained considering a uniform and homogeneous model of the nucleus [15]. These corrections are calculated independently for neutrons and protons. Figure 5.11 shows the effect of a discrete distribution of levels on the cumulative number of levels  $N_{\text{disc}}^{\text{cumul}}$ , counted up to a certain energy compared with the case of the continuous distribution  $N_{\text{cont}}^{\text{cumul}}$ . It can be seen that the continuous distribution sometimes underestimates, sometimes overestimates the total number of levels. The shell correction, originally introduced by Strutinsky [15], is calculated with the same idea but considering the energy of the level instead of the number of levels. Details on the shell correction will be given in the following.

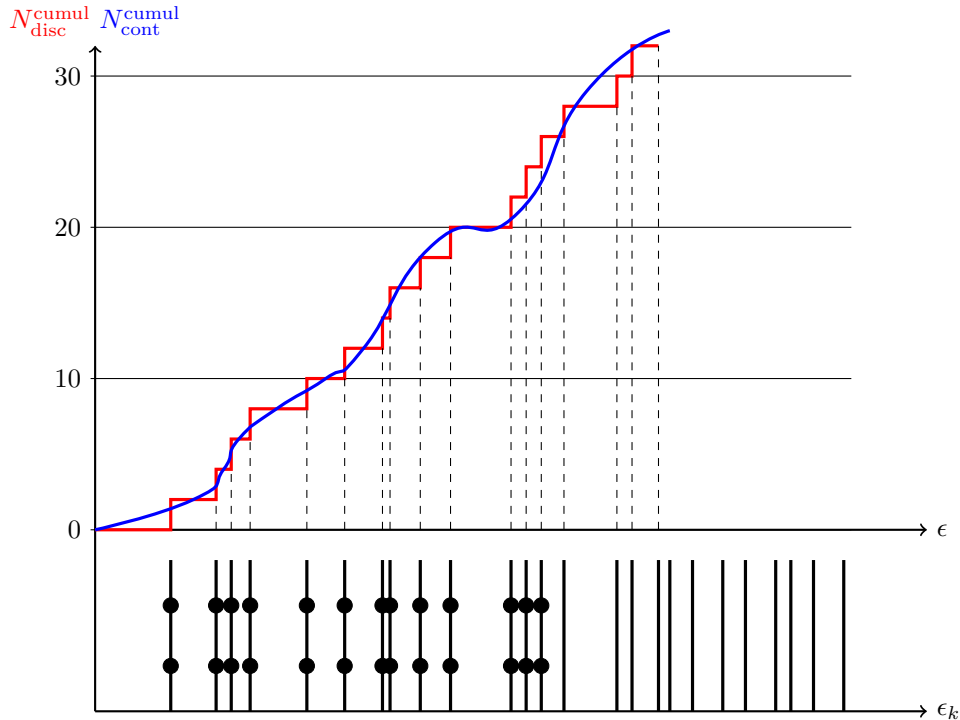


Figure 5.11 – Schematic illustration of the discrete nature of nucleon levels. The cumulative number of levels is shown as a function of the level energy for a discrete distribution  $N_{\text{disc}}^{\text{cumul}}$  (red curve) and for a continuous distribution  $N_{\text{cont}}^{\text{cumul}}$  (blue curve). The corresponding level scheme is shown in the lower part of the figure.

Corrections that are included in macroscopic-microscopic models are related to the shell structure of the energy levels [87, 120] but also to its impact on the pairing en-



ergy [110]. In microscopic models, the effect of nucleons pairing on the total energy depends on the single-particle states. It differs from its macroscopic definition, for which it only depends on odd-even property of  $N$  and  $Z$ . The inclusion of a pairing interaction “destroys” the sharp nature of the Fermi surface<sup>5</sup>. On a Nilsson diagram, the occupation number  $v_k^{\text{disc}}$  of a state  $k$  is no longer 1, or 0 according if the level is below or above the Fermi surface. As only even system will be considered here, the last occupied level has a pair-occupancy of 1. In the interest of simplicity and clarity, introduction of the pairing correction will be restrained in the following to even number of nucleons. Extensions to odd numbers of nucleons exist and can be found, for instance, in Ref. [110]. Instead of having integer values, the occupation number  $v_k$  becomes a real number that can take any values between 0 and 1 (it is actually an occupation number of the pair at the considered level and thus the maximum value is 1 and not 2). This is schematically shown in Fig. 5.12. The effect of this pairing correction depends on the “spread” of levels and is thus different depending if one considers a set of discrete levels or a continuous distribution. This is why a pairing correction must be included as energy-related “shell effect”. Two models for the pairing correction will be presented: the Bardeen, Cooper, and Schrieffer (BCS) and Lipkin-Nogami models. In practice, it is the Lipkin-Nogami model that is used for the calculation presented in this study, yet the BCS is more suitable for a first introduction to pairing correction.

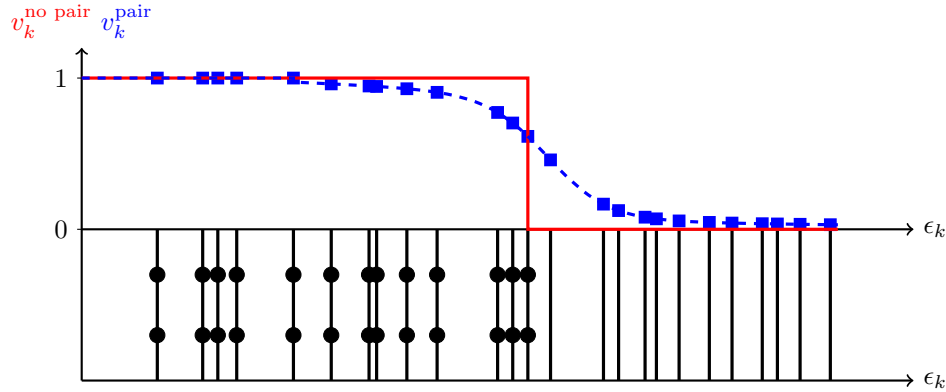


Figure 5.12 – Schematic effect of pairing interaction on level occupation numbers. The occupation numbers are shown with ( $v_k^{\text{pair}}$ ) and without ( $v_k^{\text{no pair}}$ ) pairing considered. The corresponding level scheme is shown below the figure.

#### 5.4.1.1 Shell Correction Term

The usual calculation of the shell correction considers a set of discrete energy levels  $\{\epsilon_k\}_k$ , from which a smooth level density must be extracted. The eventual shell correction is calculated as the difference between the cumulative energy of the discrete distribution and the one obtained with the smooth distribution. The method described in Refs. [87, 120] has been implemented in the CONRAD code for the present study in order to obtain the smooth distribution is reported here. More details are provided in Appendix B.2.1. The cumulative number of levels of the discrete distribution  $n$  at a given energy  $\epsilon$  is given by

$$n(\epsilon) = \int_{-\infty}^{\epsilon} \frac{dn}{d\epsilon'} d\epsilon' = \int_{-\infty}^{\epsilon} g(\epsilon') d\epsilon', \quad (5.83)$$

<sup>5</sup>The Fermi surface is the name of the energy region below the energy of the least tightly bound nucleon.



where the discrete level density  $g$  is expressed from the single-particle energies  $\epsilon_n$  as

$$g(\epsilon) = \sum_{n=1}^{\infty} \delta(\epsilon - \epsilon_n). \quad (5.84)$$

The shell correction calculation method requires to have an equivalent smooth level density  $\bar{g}$ . To obtain  $\bar{g}$ , the discrete density  $g$  is written with Gaussian weighting, where the Dirac functions  $\delta$  are expanded in terms of Hermite polynomials [87],  $g$  becomes

$$g(\epsilon) = \frac{1}{\gamma} \sum_{n=1}^{\infty} \delta\left(\frac{\epsilon - \epsilon_n}{\gamma}\right) = \frac{1}{\gamma\sqrt{\pi}} \sum_{n=1}^{\infty} e^{-u_n^2} \sum_{m=0}^{\infty} c_m H_m(u_n), \quad (5.85)$$

where

$$u_n = \frac{\epsilon - \epsilon_n}{\gamma}, \quad (5.86)$$

and

$$c_m = \begin{cases} \frac{(-1)^{m/2}}{2^m(m/2)!}, & m \text{ even}, \\ 0, & m \text{ odd}. \end{cases} \quad (5.87)$$

The smoothing parameter  $\gamma$  has a smoothing effect on  $\bar{g}$ . The smooth density  $\bar{g}$  can be obtained from  $g$  by cutting off the  $\delta$ -function expansion up to a certain order  $p$ , so that

$$\bar{g}(\epsilon) = \frac{1}{\gamma\sqrt{\pi}} \sum_{n=1}^{\infty} e^{-u_n^2} \sum_{m=0}^p c_m H_m(u_n). \quad (5.88)$$

From this smooth level distribution, it is possible to calculate the smooth cumulative number of levels up to energy  $\epsilon$ ,  $\bar{n}(\epsilon)$ , which can be written

$$\bar{n}(\epsilon) = \int_{-\infty}^{\epsilon} \bar{g}(\epsilon') d\epsilon' = \sum_{n=1}^{\infty} \left\{ \frac{1}{2} [1 + \text{erf}(u_n)] - \frac{1}{\sqrt{\pi}} e^{-u_n^2} \sum_{m=1}^p c_m H_{m-1}(u_n) \right\}. \quad (5.89)$$

The cumulative number of levels  $\bar{n}$  is not directly used to calculate the correction energy but is used to obtain the smooth-distribution Fermi energy  $\bar{\lambda}$  that satisfies

$$\bar{n}(\bar{\lambda}) = N, \quad (5.90)$$

where  $N$  is the total number of nucleon considered (neutrons and protons are treated separately). The eventual shell correction is defined as

$$\delta E_{\text{shell}} = \sum_{n=1}^N \epsilon_n - \int_0^N \bar{\epsilon}(n) dn, \quad (5.91)$$

where  $\bar{\epsilon}$  is the smooth equivalent to  $\epsilon_n$ . The second term of Eq. 5.91 can be transformed using  $\bar{g}$  as

$$\int_0^N \bar{\epsilon}(n) dn = \int_{-\infty}^{\bar{\lambda}} \epsilon \bar{g}(\epsilon) d\epsilon. \quad (5.92)$$

So that the second term of Eq. 5.91 can be written as a function of the discrete level energies:

$$\int_0^N \bar{\epsilon}(n) dn = \sum_{n=1}^{\infty} \left\{ \frac{1}{2} \epsilon_n [1 + \operatorname{erf}(\bar{u}_n)] - \frac{1}{2\sqrt{\pi}} \gamma e^{-\bar{u}_n^2} - \frac{1}{\sqrt{\pi}} e^{-\bar{u}_n^2} \sum_{m=1}^p c_m \left[ \frac{1}{2} \gamma H_m(\bar{u}_n) + \epsilon_n H_{m-1}(\bar{u}_n) + m \gamma H_{m-2}(\bar{u}_n) \right] \right\}, \quad (5.93)$$

where

$$\bar{u}_n = \frac{\bar{\lambda} - \epsilon_n}{\gamma}. \quad (5.94)$$

Equation 5.93 can be used in Eq. 5.91 to provide finally the shell correction energy  $\delta E_{\text{shell}}$ . A discussion about the shell correction treatment, namely the effect of level in the continuum, can be found in Appendix B.2.2.

In practice, the smoothing parameter  $\gamma$  used in the shell calculation (Eq. 5.93) carries an empirical dependence on the  $B_S$  term defined in Eq. 5.9,  $\gamma$  is expressed as

$$\gamma = \hbar \omega_0 B_S(\text{shape}). \quad (5.95)$$

#### 5.4.1.2 Pairing Correction Term (BCS model)

The pairing correction is calculated in a similar way than for the shell correction. The term pairing correction should be used carefully as a pairing correction can also be brought to single-particle calculation in a microscopic approach. In the present case, the pairing correction actually refers to a shell correction for the pairing effect. A pairing correction is calculated with both types of energy distribution  $g$  and  $\bar{g}$ , yielding respectively  $E_{\text{pc}}$  and  $\bar{E}_{\text{pc}}$ , then the difference between the two gives the correction  $\delta E_{\text{pair}}$  to the macroscopic energy

$$\boxed{\delta E_{\text{pair}} = E_{\text{pc}} - \bar{E}_{\text{pc}}}. \quad (5.96)$$

The first inclusions [15, 87, 121] of a microscopic correction related to pairing in the nuclear deformation energy were based on the BCS [122]. This model has been developed by Bardeen, Cooper, and Schrieffer to explain the superconductivity property of electrons in metals. Given a pairing strength  $G$  and a pairing gap  $\Delta$ , the pairing interaction leads to a new expectation value of the total binding energy [19]  $E^{\text{BCS}}$  that is given by

$$E^{\text{BCS}} = 2 \sum_{k=1}^{N_p} \epsilon_k v_k^2 - G \sum_{k=1}^{N_p} v_k^4 - \frac{\Delta^2}{G}, \quad (5.97)$$

where the summation is taken over all doubly-degenerate levels considered in the pairing calculation. The pairing correction for a discrete energy level distribution  $E_{\text{correction}}^{\text{BCS}}$  is given by

$$E_{\text{correction}}^{\text{BCS}} = E^{\text{BCS}} - 2 \sum_{k=1}^{\frac{1}{2} N_p} \epsilon_k. \quad (5.98)$$

The pairing *correlation*  $E_{\text{pc}}^{\text{BCS}}$  may be considered instead of the above expression [87, 123]. However it only results in a shift in energy of  $+\frac{1}{2} G N_p$  compared with the above expression. As this energy shift occurs for both terms  $E_{\text{pc}}^{\text{BCS}}$  and  $\bar{E}_{\text{pc}}^{\text{BCS}}$  this has no effects on the eventual correction  $\delta E_{\text{pair}}$  brought to the macroscopic energy. The pairing correlation of the discrete energy level scheme  $E_{\text{pc}}^{\text{BCS}}$  is given by

$$E_{\text{pc}}^{\text{BCS}} = 2 \left( \sum_{k=1}^{N_p} \epsilon_k v_k^2 - \sum_{k=1}^{\frac{1}{2} N_p} \epsilon_k \right) - \frac{\Delta^2}{G} - G \left( \sum_{k=1}^{N_p} v_k^4 - \sum_{k=1}^{\frac{1}{2} N_p} 1 \right), \quad (5.99)$$

where the level occupancy numbers  $v_k$ , the Fermi energy  $\lambda$  and the pairing gap  $\Delta$  satisfy the BCS equations:

$$2N_p = 2 \sum_{k=1}^{N_p} v_k^2, \quad (5.100)$$

$$\frac{2}{G} = \sum_{k=1}^{N_p} \frac{1}{[(\epsilon_k - \lambda)^2 + \Delta^2]^{1/2}}, \quad (5.101)$$

$$\forall k \in \llbracket 1, N_p \rrbracket, v_k^2 = \frac{1}{2} \left\{ 1 - \frac{\epsilon_k - \lambda}{[(\epsilon_k - \lambda)^2 + \Delta^2]^{1/2}} \right\}. \quad (5.102)$$

The equivalent expression  $\bar{E}_{pc}^{BCS}$  for a continuous energy distribution is obtained using a linearized expression of  $\bar{\epsilon}(n)$  near the Fermi level. The pairing strength  $G$  can be calculated [87] as

$$\frac{1}{G} = \bar{\rho} \ln \left\{ \left[ \left( \frac{N_p}{2\bar{\rho}\Delta} \right)^2 + 1 \right]^{1/2} + \frac{N_p}{2\bar{\rho}\Delta} \right\}, \quad (5.103)$$

where  $\bar{\rho}$  is the average density of doubly-degenerate levels and is given by

$$\bar{\rho} = \frac{1}{2} \bar{g}(\bar{\lambda}). \quad (5.104)$$

The pairing correlation for the continuous energy distribution is finally given by

$$\bar{E}_{pc}^{BCS} = -\frac{1}{4} \frac{N_p^2}{\bar{\rho}} \left\{ \left[ 1 + \left( \frac{2\bar{\rho}\Delta}{N_p} \right)^2 \right]^{1/2} - 1 \right\} + \frac{1}{2} \bar{\rho} \Delta G \arctan \frac{N_p}{2\bar{\rho}\Delta}. \quad (5.105)$$

#### 5.4.1.3 Pairing Correction Term (Lipkin-Nogami Model)

The BCS model fails to describe the pairing effect when the level gap at the Fermi energy is too large. To solve this liability, a refined model was developed by Lipkin and Nogami [124–128]. It has been then adapted to the nuclear pairing correction that is required for the macroscopic-microscopic approach [110]. In this model, the average pairing gap, written  $\Delta_G$ , is a model parameter. The following notation will be used: the pairing interaction involved  $N_{tot}$  nucleons dispatched between the levels  $N_1$  and  $N_2$ ,  $N_p$  levels are thus involved. Here again, in the interest of simplicity, only cases with  $N_{tot}$  even are treated. The pairing strength  $G$  is obtained by [110]

$$\frac{2}{G} = \bar{\rho} \left[ \ln \left( \sqrt{y_2^2 + \Delta_G^2} + y_2 \right) - \ln \left( \sqrt{y_1^2 + \Delta_G^2} + y_1 \right) \right], \quad (5.106)$$

where  $\bar{\rho}$  is again the average density of doubly-degenerate levels and is given by

$$\bar{\rho} = \frac{1}{2} \bar{g}(\bar{\lambda}), \quad (5.107)$$

and

$$y_1 = \frac{N_1 + 1 - \frac{1}{2}N_{tot}}{\bar{\rho}} \quad \text{and} \quad y_2 = \frac{N_2 - \frac{1}{2}N_{tot}}{\bar{\rho}}. \quad (5.108)$$

The smooth pairing term  $\bar{E}_{pc}^{LN}$  is given by

$$\begin{aligned} \bar{E}_{\text{pc}}^{\text{LN}} = \frac{1}{2}\bar{\rho} & \left[ (y_2 - G) \left( y_2 - \sqrt{y_2^2 + \Delta_G^2} \right) + (y_1 - G) \left( y_1 + \sqrt{y_1^2 + \Delta_G^2} \right) \right] \\ & + \frac{1}{4}(G - 4\bar{\lambda}_2)\bar{\rho}\Delta_G \left[ \arctan\left(\frac{y_2}{\Delta_G}\right) - \arctan\left(\frac{y_1}{\Delta_G}\right) \right], \end{aligned} \quad (5.109)$$

where  $\bar{\lambda}_2$  is given by

$$\bar{\lambda}_2 = \frac{G}{4} \left( \frac{A - C}{B - C} \right), \quad (5.110)$$

where

$$A = \left( \frac{\bar{\rho}\Delta_G}{4} \right)^2 \left\{ \left( \frac{2}{G\bar{\rho}} \right)^2 - \left[ \ln \left( \frac{\sqrt{y_2^2 + \Delta_G^2}}{\sqrt{y_1^2 + \Delta_G^2}} \right) \right]^2 \right\}, \quad (5.111)$$

$$B = \frac{\Delta_G^2 \bar{\rho}^2}{16} \left[ \arctan\left(\frac{y_2}{\Delta_G}\right) - \arctan\left(\frac{y_1}{\Delta_G}\right) \right]^2, \quad (5.112)$$

$$C = \frac{\bar{\rho}\Delta_G}{32} \left[ \Delta_G \left( \frac{y_2}{y_2^2 + \Delta_G^2} - \frac{y_1}{y_1^2 + \Delta_G^2} \right) + \arctan\left(\frac{y_2}{\Delta_G}\right) - \arctan\left(\frac{y_1}{\Delta_G}\right) \right]. \quad (5.113)$$

The discrete pairing term  $E_{\text{pc}}^{\text{LN}}$  is obtained by solving the  $2N_p + 3$  coupled equations:

$$N_p = \sum_{k=1}^{N_p} v_k^2, \quad (5.114)$$

$$\forall k \in \llbracket 1, N_p \rrbracket, v_k^2 = \frac{1}{2} \left\{ 1 - \frac{e_k - \lambda}{[(e_k - \lambda)^2 + \Delta^2]^{1/2}} \right\}, \quad u_k^2 = 1 - v_k^2, \quad (5.115)$$

$$\forall k \in \llbracket 1, N_p \rrbracket, e_k = \epsilon_k + (4\lambda_2 - G)v_k^2, \quad (5.116)$$

$$\frac{2}{G} = \sum_{k=1}^{N_p} \frac{1}{[(e_k - \lambda)^2 + \Delta^2]^{1/2}}, \quad (5.117)$$

$$\lambda_2 = \frac{G}{4} \left[ \frac{\left( \sum_{k=1}^{N_p} u_k^3 v_k \right) \left( \sum_{k=1}^{N_p} u_k v_k^3 \right) - \sum_{k=1}^{N_p} u_k^4 v_k^4}{\left( \sum_{k=1}^{N_p} u_k^2 v_k^2 \right)^2 - \sum_{k=1}^{N_p} u_k^4 v_k^4} \right]. \quad (5.118)$$

From these equations the pairing energy  $\Delta$ , the Fermi energy  $\lambda$ , the number fluctuation constant  $\lambda_2$  and the occupation numbers  $v_k$  are determined. The discrete pairing term  $E_{\text{pc}}^{\text{LN}}$  is finally obtained by

$$E_{\text{pc}}^{\text{LN}} = \sum_{k=1}^{N_p} (2v_k^2 - n_k) \epsilon_k - \frac{\Delta^2}{G} - \frac{G}{2} \sum_{k=1}^{N_p} (2v_k^4 - n_k) - 4\lambda_2 \sum_{k=1}^{N_p} u_k^2 v_k^2, \quad (5.119)$$

where  $n_k$  takes the values 2 or 0 according to the discrete distribution.

Both pairing models (BCS and Lipkin-Nogami) have been implemented. The BCS implementation was easier in a first approach but the Lipkin-Nogami was necessary for the complete verification of the macroscopic-microscopic model.

#### 5.4.1.4 Pairing Models Comparison

Figure 5.13 shows the pairing correction  $\delta E_{\text{pair}}$  obtained by both the BCS and Lipkin-Nogami models. This figure is obtained using a shape described using the perturbed spheroid parameterization (*cf.* Appendix B.1), where the two shape parameters  $\epsilon_2$  and  $\epsilon_4$  are varied. It can be seen that the two models lead to quite similar results, yet in two areas, highlighted with green circles, small differences can be observed. As the Lipkin-Nogami is a more robust model than the traditional BCS, and because the FRLDM parameters are given [12] for this model, it was also selected as for the present work.

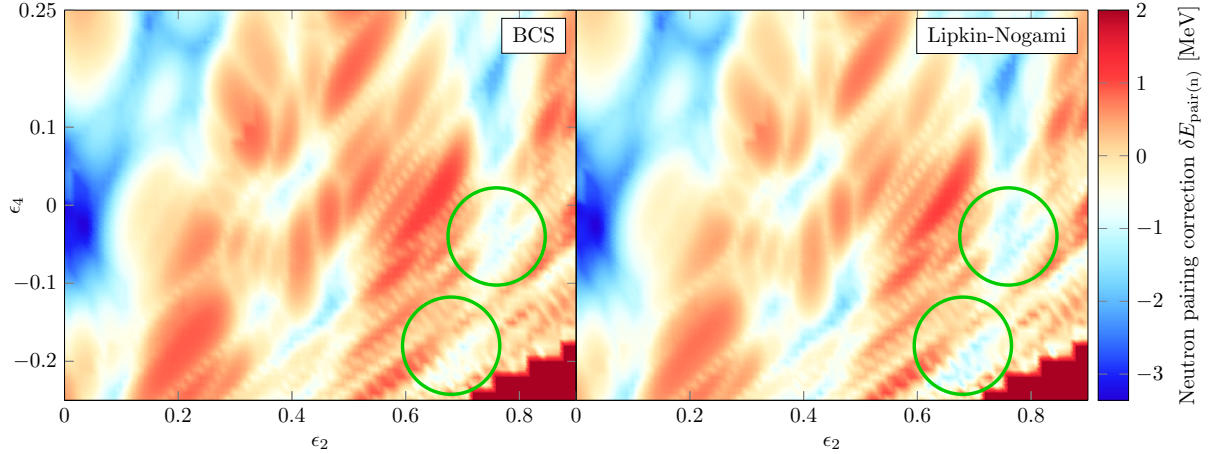


Figure 5.13 – Comparison of the BCS and Lipkin-Nogami corrections obtained using a perturbed spheroid parameterization (*cf.* Appendix B.1).

### 5.4.2 Macroscopic-Microscopic Model Verification and Results

#### 5.4.2.1 Zero-Point Vibrational Energy

In order to verify the present implementation of the macroscopic-microscopic model, it was necessary to be able to calculate nuclear masses. The nuclear masses are obtained from the minimum value of the PES<sup>6</sup> to which a *zero-point vibrational energy* is added. Therefore in addition to all previous contributing terms, a last one must be added. This term stands for the fact that the PES model provides the deformation potential “felt” by the nucleus. The experimental mass is related to the actual energy level of the nucleus at rest inside its deformation potential well. As the nucleus cannot have zero kinetic energy (forbidden by quantum mechanics), a certain offset must be added to the deformation potential minimum. In Fig. 5.14, an example is shown for a harmonic oscillator potential. The first energy level is shifted from the ground state deformation potential  $V_{\text{g.s.}} = V(\eta_{\text{g.s.}})$ . The ground state deformation still remains defined as the minimum of the deformation energy but the actual nucleus wave function spreads over certain deformation range.

There is some arbitrariness in the choice of collective coordinates for the zero vibration(s) point (one or several degrees of freedom can be considered). For the calculation of this last term, the procedure described in Refs. [12, 94] is applied. Only one degree of freedom is retained, here is this degree of freedom is  $\epsilon_2$  and corresponds to the perturbed spheroid parameterization of the nuclear shape that is defined in Appendix B.1.3.

<sup>6</sup>A restricted area in the PES must be considered to avoid scission shapes to be considered as the ground states as these shapes may have related deformation energies lower than the ground state one.

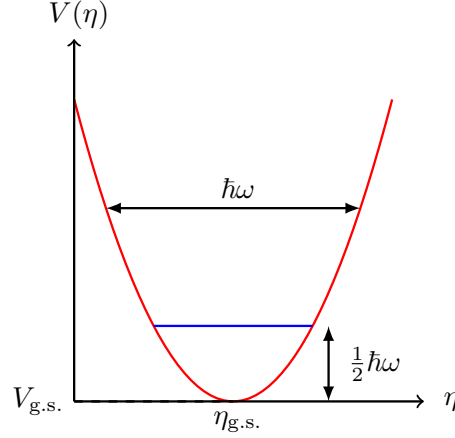


Figure 5.14 – Illustration of the first level construction from the addition of the zero point energy to the minimum energy of a harmonic oscillator potential. The harmonic oscillator potential operates on an arbitray deformation parameter  $\eta$ .

The actual potential is locally approximated by a harmonic oscillator. First, the actual potential energy surface stiffness  $C_{\epsilon_2}$  is calculated for the ground state deformation

$$C_{\epsilon_2} = \left. \frac{\partial^2 V_{\text{actual}}}{\partial \epsilon_2^2} \right|_{\text{g.s.}}. \quad (5.120)$$

Then the inertia parameter  $B_{\epsilon_2}$  is obtained considering the nuclear matter as an irrotational liquid [94]:

$$B_{\epsilon_2}^{\text{irr}}(\epsilon_2) = \frac{2}{15} \frac{1 + \frac{2}{9}\epsilon_2^2}{(1 - \frac{1}{3}\epsilon_2^2)^2} \left( 1 - \frac{1}{3}\epsilon_2^2 - \frac{2}{27}\epsilon_2^3 \right)^{-4/3} M_0 R^2, \quad (5.121)$$

where  $M_0 = A \times m$  ( $m$  is the mass of a nucleon,  $A$  is the mass number), and  $R = r_0 A^{1/3}$ . The local curvature  $\omega_{\epsilon_2}^{\text{irr}}$  is defined by

$$\omega_{\epsilon_2}^{\text{irr}} = \left( \frac{C_{\epsilon_2}}{B_{\epsilon_2}^{\text{irr}}} \right)^{1/2}. \quad (5.122)$$

Following Ref. [12] the final zero-point vibrational energy is given by

$$E_{\text{zp}} = \frac{1}{2} \hbar \omega_{\epsilon_2}, \quad (5.123)$$

where

$$\omega_{\epsilon_2} = \Re \omega_{\epsilon_2}^{\text{irr}}. \quad (5.124)$$

The  $\Re$  parameter is adjusted so that for spherical shape the inertia  $B_{\epsilon_2}$  equals the inertia determined from an adjustment to spontaneous-fission half-lives of actinides.

Finally, all these refinements can be gathered to form the finite-range liquid-drop model. Although the number of refinements seems rather large, only few terms are shape-dependent. Therefore they will mostly only produce an energy shift of the PES but will have a significant effect on the predicted ground-state masses. This confrontation of the implemented model with experimental masses is a validation that cannot be overlooked.

### 5.4.2.2 Results for Masses

At this point, both macroscopic and microscopic models have been presented, and the related implementation in the CONRAD code has been verified. The calculation of the shell and pairing corrections from the single-particle orbitals have been verified on a benchmark kindly provided by P. Möller [129]. As the FRLDM parameters are adjusted to reproduce experimental masses it is interesting to test the mass prediction power of the newly implemented model as a final validation point. In the beginning of this chapter the Aston curve was presented along with its modeling with the Bethe-Weizsäcker formula (*c.f.* Fig. 5.2). A similar plot can be made with values obtained from the FRLDM, this is shown in Fig. 5.15.

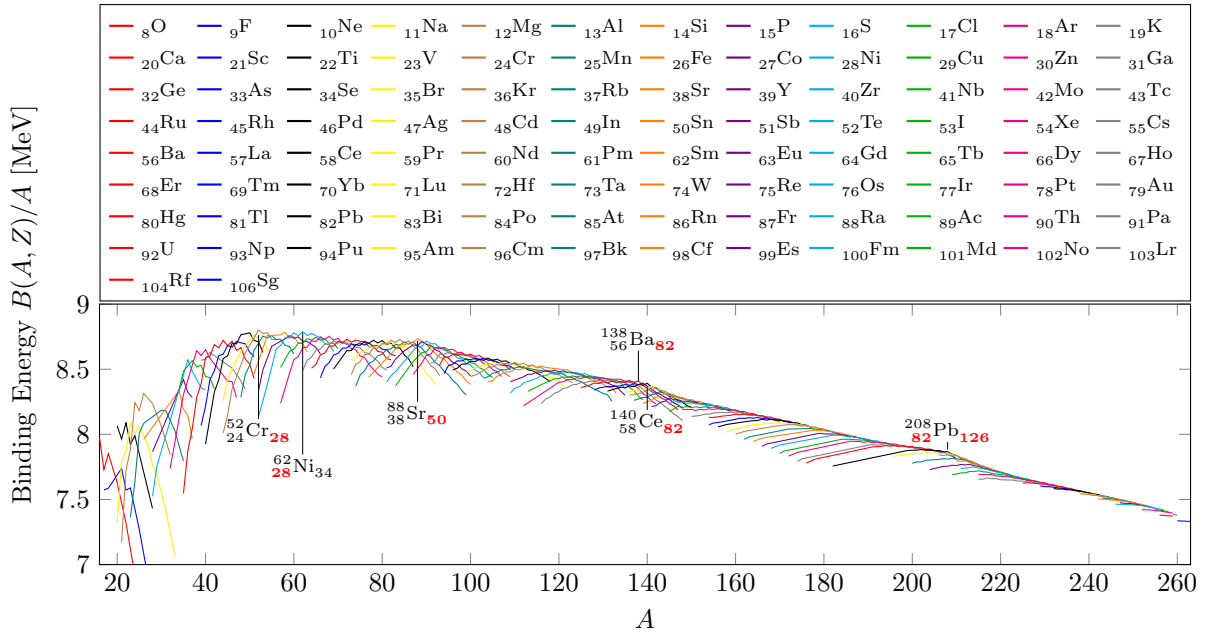


Figure 5.15 – Results of newly implemented FRLDM for binding energies per nucleon. Red numbers are magic numbers for which small structures are visible. This figure must be compared with the Aston curve in Fig. 5.2.

One obtains the expected structure around the particular mass number (related to the magic numbers) as in the experimental Aston curve of Fig 5.2. Some related “magical” isotopes are placed on the curve to highlight shell structures. To investigate remaining differences between experimental and theoretical data, examining the binding energy per nucleon is not appropriate. Instead, error on mass excess, will be used, *i.e.* the difference between the experimental and predicted mass excesses. Comparison with results from the original model [12] are shown in Fig. 5.16. The lower part of Fig 5.16 is related to a second model, the finite-range droplet model, which is detailed in Appendix B.3. This model differs from the FRLDM only for its macroscopic component. Both models have been implemented, yet only the FRLDM model is used to calculate the eventual PES. The implementation of the FRDM is nevertheless important for the present study as it helps to identify the source of the remaining differences between the present implementation and the original one [12].

In Fig 5.16, gross structures are reproduced, however many small differences remain. For instance, structures near  $A = 240$  seem similar between the present and the original implementations. However structures near  $A = 140$  present more similarities between the two implementations from the same *author* rather than between two implementations of



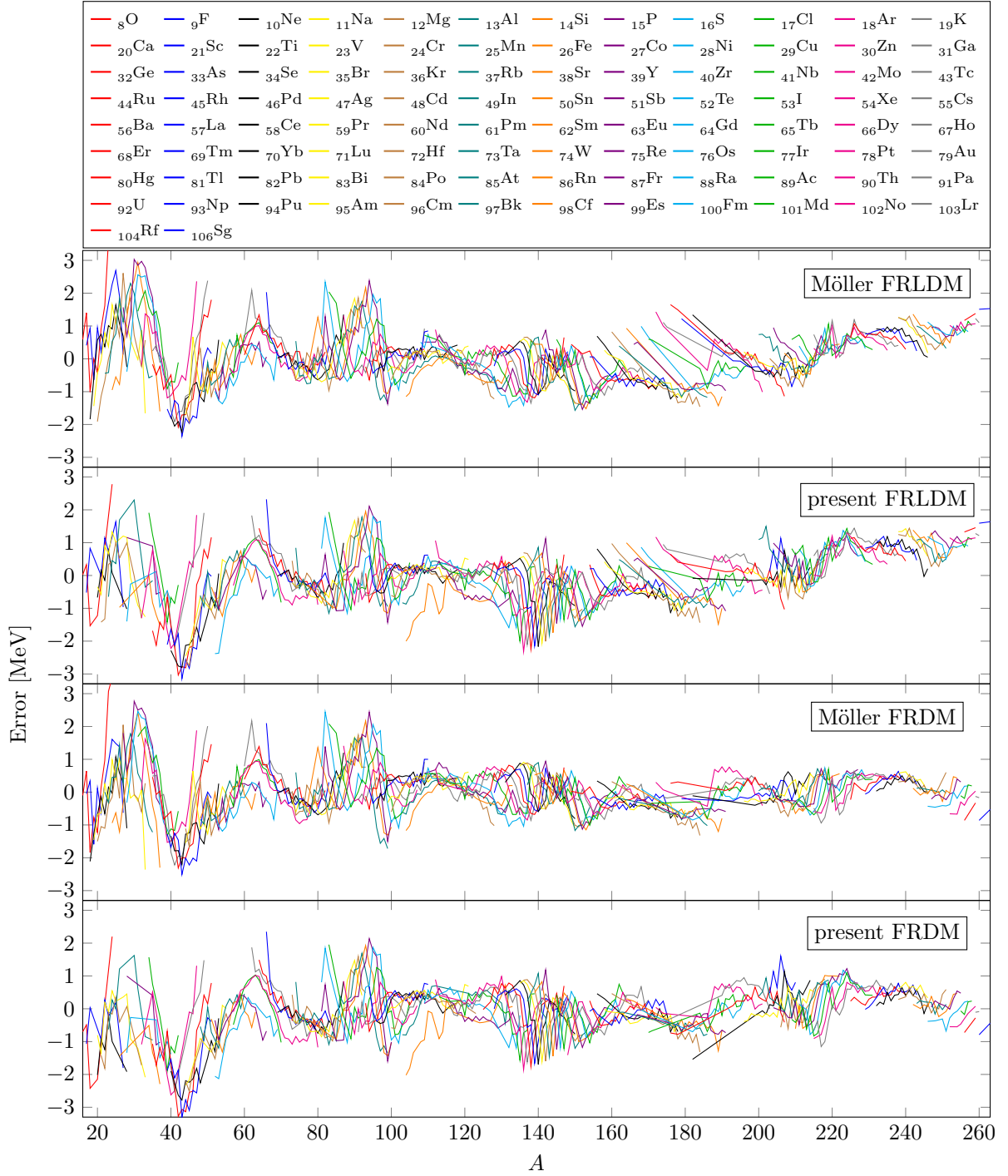


Figure 5.16 – Comparison of the errors on masses obtained by Peter Möller with his original implementation [12] and with the present implementation. The two upper plots are related to the FRLDM, and the two lower ones, to the FRDM.

the same *model*. The origin of the remaining differences is quite difficult to identify due to the complexity of the model. The FRDM and FRLDM only differ by their macroscopic components, *i.e.* shell and pairing corrections are the same for both models. Therefore, the difference of the FRDM and FRLDM values should be rather insensitive to the microscopic components (with the exception of the zero-point vibrational energy that still depends on the surface curvature of the complete<sup>7</sup> deformation energy). Figure 5.17 shows

<sup>7</sup>The comparison is made on  $E_{\text{def}} = E_{\text{macro}} + \delta E_{\text{pair}(n)} + \delta E_{\text{pair}(p)} + \delta E_{\text{shell}(n)} + \delta E_{\text{shell}(p)} + E_{\text{zp}}$ .

the difference  $\Delta E_{\text{macro}}$  between macroscopic energies of the two models.

$$\Delta E_{\text{macro}} = E_{\text{macro}}^{\text{FRDM}} - E_{\text{macro}}^{\text{FRLDM}} \quad (5.125)$$

The agreement is much better than in the comparison of full models (*cf.* Fig. 5.16). This indicates that remaining differences come from the microscopic terms. As shell and pairing corrections were properly verified from P. Möller benchmark [129], the remaining differences must be due to the single-particle energies. A preliminary study indicated that the choice the base of wave functions used in the expansion method (*cf.* Section 5.5.1) may explain the remaining differences on single-particle energies.

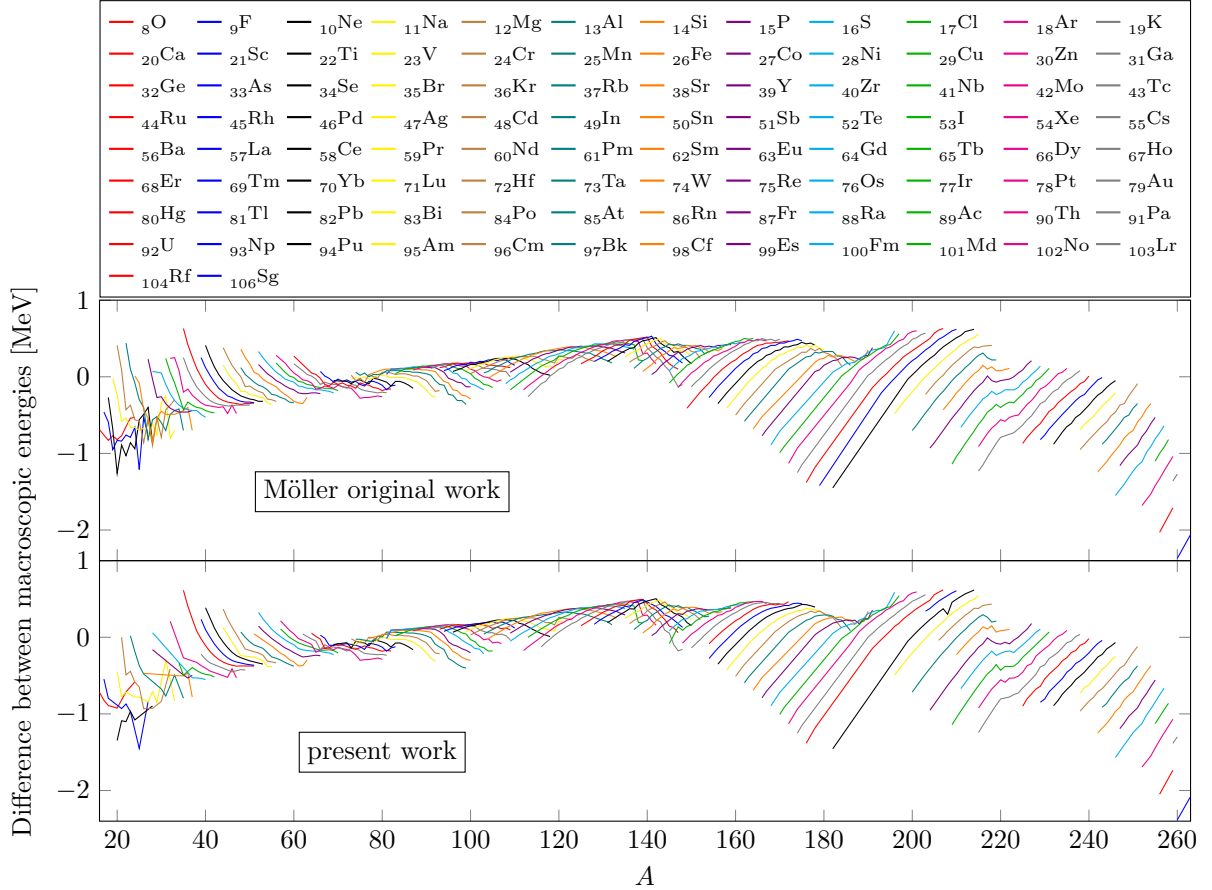


Figure 5.17 – Comparison of the difference between the macroscopic energies  $\Delta E_{\text{macro}}$  obtained with Möller original implementation [12] (above) and with present implementation (below).

To quantify the error on mass excess predictions for the two implementations, the method given in Ref. [12] was used to estimate the deviation from experimental masses for both FRDM and FRLDM models and results were compared with those from Ref. [12]. Out of the 1654 data points (*i.e.* isotope masses) used in Ref. [12], the present program leads to 174 non-calculable points. For almost all of the non-calculable points the program failure was due to non-positive potential stiffness  $C_{\epsilon_2}$  for the calculation of the zero-point vibrational energy. This is easily explained by the fact that small changes in the model implementation can change the actual ground state shape and thus, for isotopes with shallow ground-state minima on the potential energy surface, the potential stiffness  $C_{\epsilon_2}$  becomes negative for the tabulated ground-state shape. If the program is “allowed” to search for its own local minimum, most of the crash points are processed correctly. Finally

six remaining failure points were due to another reason. The failures happened for isotopes far from the stability valley. For these isotopes, too few levels were found available for the calculation of the shell and pairing corrections. Finally Tab. 5.2 summarizes the comparison of the present mass calculations with the original implementation results [12]. The results seems quite satisfactory, especially for the FRLDM that is the model used eventually for the calculation of the PES that are used in the next chapter.

Table 5.2 – Root-Mean-Square errors (in MeV) for the implementations of the two macroscopic-microscopic models.

Implementation	FRDM	FRLDM	Number of masses
Möller et al. [12]	0.669	0.779	1654
Present work	0.724	0.793	1590

### 5.4.2.3 Results for Potential Energy Surface

To conclude this chapter on PES calculation, Fig 5.18 shows the PES obtained using the FRLDM and the generalized spheroid shape parameterization (see Appendix B.1), for four different values of the mass-asymmetry parameter  $\alpha$ . The ground state shape can be identified by searching the minimum of the PES in a restrained area of small elongations. It is located in the present case at  $(c, h, \alpha) = (1.25, -0.18, 0)$ . This means that the calculated ground state has a mass-symmetric shape. A second minimum can be observed for slightly more elongated shapes (for larger  $c$  values), for instance at  $(c, h, \alpha) = (1.45, 0, 0)$ . This minimum is responsible for the double-humped shape of the fission barrier. The “dark sea” on the right upper part of the plots is the entrance valley of shapes leading eventually to scission configurations. Two barrier humps can thus be defined, one connecting the ground state shape to the intermediate minimum, the second connecting this latter to the “dark sea”. In Fig 5.18, the first hump can be identified to be related a mass-symmetric shape ( $\alpha = 0$ ), and to be located around  $(c, h, \alpha) = (1.3, 0.2, 0)$ . The second hump would be quite larger (about 10 MeV) if only mass-symmetric shapes are considered. Extending the searching area to mass-asymmetric shapes, one can find a lower second hump (with height of about 6 MeV) located near  $(c, h, \alpha) = (1.6, 0, 0.1)$ .

With very high mass-asymmetry ( $\alpha = 0.15$ ), the fission barrier increases again to exceed 12 MeV. This is consistent with evaluated independent fission yields<sup>8</sup>, as shown in Fig. 5.19 for the thermal neutron-induced fission on  $^{239}\text{Pu}$ . It can be noticed that the symmetrical fission (120/120) is hindered, just like the very asymmetric one (58/155). However, the “reasonably” mass-asymmetric fission (103/137) is favored.

The FRLDM model (and its related implementation) that has been presented in this chapter can readily be used to study the variation of the nuclear potential energy as its shape evolves. In the first versions of the newly implemented FRLDM, a complete calculation for a given nucleus shape took few seconds. As a typical PES can contains up to millions of shapes, a run would thus last more than 100 days! Therefore special care was brought in the present work about mathematical, numerical and computational solutions to make the computing time compatible with evaluation requirements.

<sup>8</sup>These fission yields are obtained from the JEFF-3.1.1 evaluation, the term *independent* means that they correspond to yields before prompt neutron emissions.

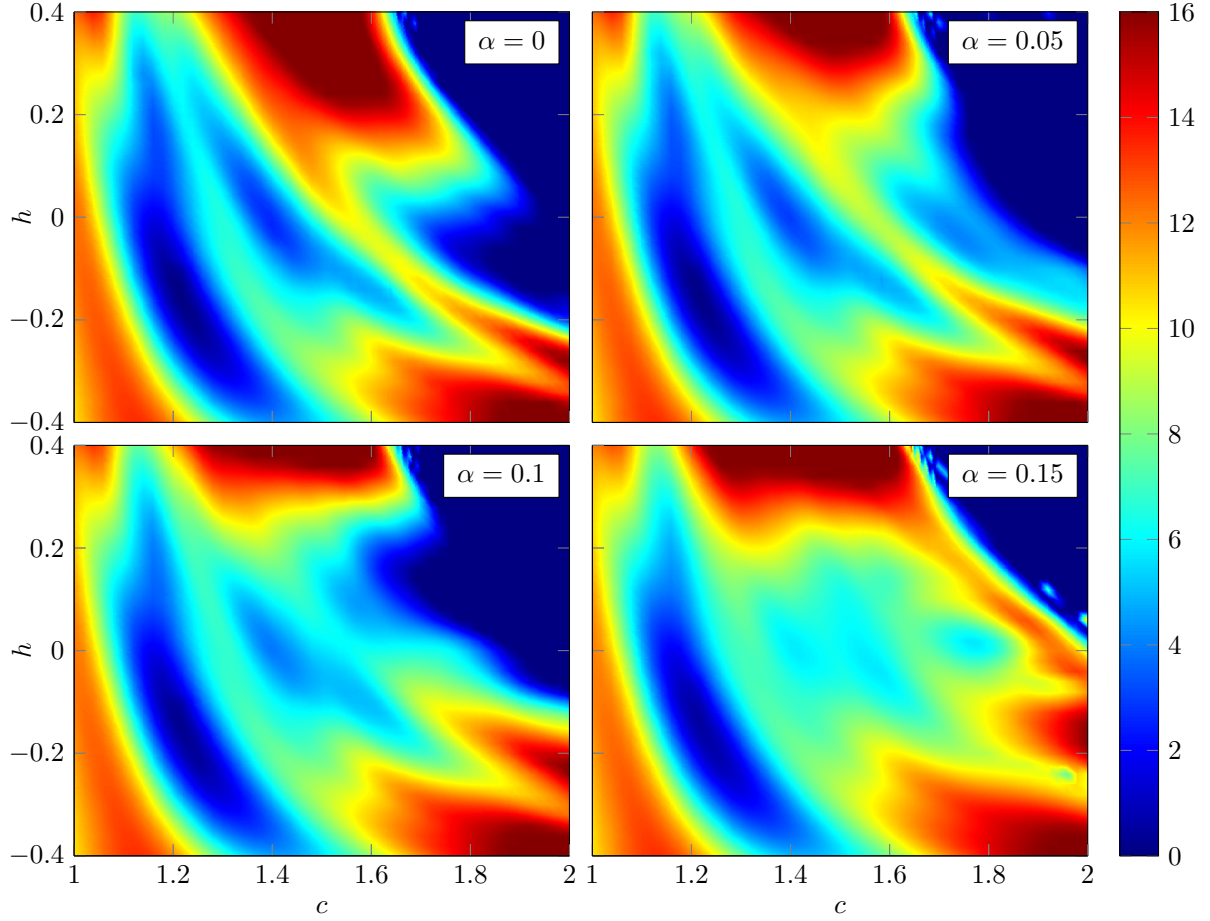


Figure 5.18 – Example of potential energy surfaces obtained using the generalized spheroid shape parameterization and the FRLDM for  $^{240}\text{Pu}$ .

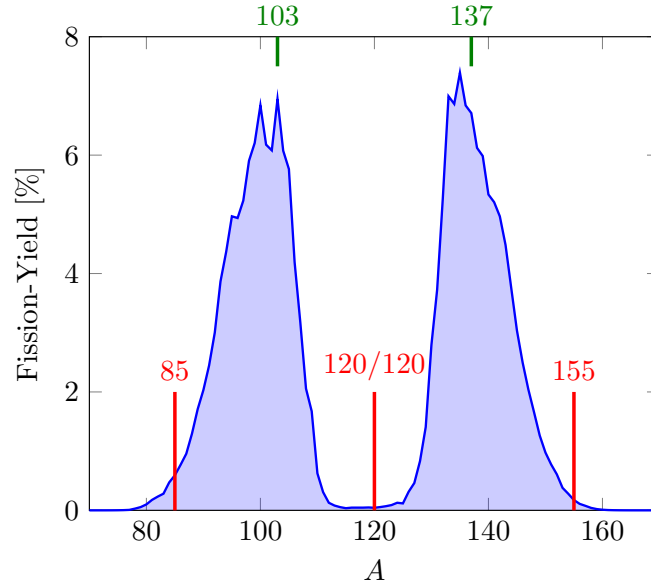


Figure 5.19 – JEFF-3.1.1 evaluation of the  $n + ^{239}\text{Pu}$  thermal-neutron-induced independent fission yields. A favored splitting is shown in green on the upper part of the figure, two less likely scission configurations are shown in red.

## 5.5 Evaluation-Compliant Implementation

Evaluations rely on experimental data but also on accurate theoretical models. The macroscopic-microscopic model presented here is a good candidate for the improvement of physics in evaluations. Other models, for instance based on the Hartree-Fock-Bogoliubov theory, may seem more accurate, or at least more intellectually satisfactory. Yet their use in evaluation is often difficult in practice because of three reasons. First, computational models may not be available and their implementation would require a lot of work. Second, they may be not flexible enough so that their parameters could not balance remaining model inaccuracy. Yet this point cannot be checked before the model is implemented. Finally the computation may take much too long time to be compatible with adjustment procedures. This latter statement must be taken with consideration as nothing is more time-dependent than computation power. As this last point was a major challenge for this PhD work, some of the features that led to an evaluation-compliant program will be detailed.

### 5.5.1 Base Expansion of Wave Functions

The first point that will be developed in this section is not a brand new method (neither a specific contribution of this PhD work) but remains a key point to obtain fast single-particle states computation. Once kinetic, scalar potential and spin-orbit potentials operators are defined, a numerical method must be chosen to obtain the related single-particle orbitals (*i.e.* energies and wave functions). The two most common methods for the computing single-particle orbitals are the finite-difference method [116] and the base functions expansion method<sup>9</sup> [117, 131]. However it was early reported [87] that the expansion method is accurate enough as long as accuracy on the asymptotic behaviors of the wave functions is not required, and is much faster than the finite-difference method. This method will be briefly detailed here, extensive details can be found in Appendix C.

In the expansion method, a set of arbitrary functions  $\{|\varphi_j\rangle\}_j$  will be assumed to be properly chosen, so that any eigenfunction  $|\psi_i\rangle$  of the single-particle Hamiltonian<sup>10</sup>  $\hat{H}$  can be expanded using  $\{|\varphi_j\rangle\}_j$ . In other “words”:

$$\forall i \begin{cases} \hat{H}|\psi_i\rangle = E_i|\psi_i\rangle, \\ \exists \{a_j^i\}_j : |\psi_i\rangle = \sum_j a_j^i |\varphi_j\rangle. \end{cases} \quad (5.126)$$

It is recalled here that the eigenfunctions of  $\hat{H}$  are orthonormal:

$$\forall (\ell, i), \quad \langle \psi_\ell | \hat{H} | \psi_i \rangle = E_i \langle \psi_\ell | \psi_i \rangle = E_i \delta_{i\ell} = \sum_{kj} a_k^\ell a_j^i \langle \varphi_k | \hat{H} | \varphi_j \rangle. \quad (5.127)$$

As  $\hat{H}$  is Hermitian, it can be shown that Eq. 5.127 is equivalent to the diagonalization of the symmetric matrix  $\mathbf{H}$  whose coefficients  $[\mathbf{H}]_{kj}$  are given by

$$[\mathbf{H}]_{kj} = \langle \varphi_k | \hat{H} | \varphi_j \rangle. \quad (5.128)$$

If  $\mathbf{E}$  is a diagonal matrix containing the  $[\mathbf{H}]$  eigenvalues  $E_i$ , the hermitian properties of  $\mathbf{H}$  implies that there is an orthogonal matrix  $\mathbf{P}$  satisfying

$$\mathbf{P}^\dagger \mathbf{H} \mathbf{P} = \mathbf{E}, \quad (5.129)$$

<sup>9</sup>Reference [130] corrects misprints of Ref. [131].

<sup>10</sup>See for instance Eq. 5.75 of this chapter.

which can be written

$$\forall(\ell, i), \quad \sum_{jk} P_{ji} H_{jk} P_{kl} = E_i \delta_{i\ell}, \quad (5.130)$$

and compared to Eq. 5.127.

The key point of this approach is thus the definition of the base functions and the calculation of the related Hamiltonian matrix elements. The base functions used in the present work is the deformed harmonic oscillator base described in Section 5.3.1. The eigenvalues and eigenvectors of  $\mathbf{H}$  are obtained using the vectorized library Eigen [132]. It can be stated here that due to the fact that only axially spherical shapes are considered, the  $\Omega$  quantum number is a good quantum number, therefore  $\mathbf{H}$  is a block diagonal matrix. Each block  $\mathbf{H}_\Omega$  can be treated separately, reducing both the number of matrix elements to compute and the time required for the matrices diagonalization<sup>11</sup>.

## 5.5.2 Efficient Numerical Integration Methods

As is mentioned in Section 5.3.2, the use of more realistic potential such as the Yukawa-folded potential requires performing numerical integrations over the nucleus surface. Prior to detailing how efficient numerical integrations can be performed, it should be stated that the Gauss-divergence theorem can usually be used to reduce the dimensional range of integration. For instance by transforming a volume integration into a surface integration<sup>12</sup>, or a double volume integration into a double surface integration<sup>13</sup> [93]. These integral transformations, detailed in Appendix B.4.1, provide forms that can be efficiently computed. Additionally, for Coulomb potential related to a sharp-edge volume, a special treatment using *complete elliptic integrals* [48] can reduce the the surface integral to a one dimensional integral. This is detailed in Appendix B.4.2. Finally, as detailed in Appendix C.4, the use of integration by parts may also remove scalar potential gradient terms that are time-consuming to evaluate in the spin-orbit matrix elements computation.

Numerical integration can be highly time-consuming. Therefore efficient numerical procedures have been implemented. In the following, the Gauss-Patterson [133, 134] *quadrature rule* and the related *sparse grid* extension will be detailed.

A *quadrature rule* can be seen as an implicit expansion, of the function  $f$  to integrate, on a given set of polynomials. The most “famous” type of quadrature rule is the Gauss-Legendre rule, relying on Legendre polynomials, that can be used to perform integrations over the range  $[-1, 1]$ . This range can be easily converted by linear variable change to any finite range  $[a, b]$ .

$$\int_b^a dx f(x) = \frac{b-a}{2} \int_{-1}^1 dy f\left(\frac{b-a}{2}y + \frac{b+a}{2}\right) \quad (5.131)$$

For integrals over semi-infinite  $[0, +\infty[$  and infinite  $]-\infty, +\infty[$  ranges, other polynomials must be used. In the present implementation, the Gauss-Laguerre and Gauss-Hermite

<sup>11</sup>For reflection-symmetric shapes, *i.e.* for mass-symmetric shapes, the parity  $\pi$  is also a good quantum number, in this case each matrix  $\mathbf{H}_\Omega$  can be divided into two additional sub-matrices. This is not done in practice to keep a unified procedure in the computation as the program is intended to extensively investigate mass-asymmetric shapes.

<sup>12</sup>This is the case for the computation of scalar microscopic potentials, *cf.* Eqs. 5.64 and 5.63.

<sup>13</sup>For instance, for the computation of the Coulomb and surface terms  $B_1$  and  $B_3$  of the FRLDM macroscopic part, *cf.* Eqs. 5.45 and 5.46.



quadrature rules [135] have been used respectively for semi-infinite and infinite ranges. Eventually the integral of a function  $f$  over the range  $R$  will be computed as

$$I_R[f] = \int_R dx f(x) \approx \sum_{i=1}^N w_i^{(N)} f(x_i^{(N)}). \quad (5.132)$$

The integral  $I_R$  is estimated by evaluating the function  $f$  for certain predetermined abscissa  $x_i^{(N)}$ , the function results  $f(x_i^{(N)})$  will be weighted by the predetermined coefficients  $w_i^{(N)}$  and summed to obtain the integral estimate. This integral is only an estimation of  $I_R[f]$  as the underlying polynomial expansion is truncated to a given order related to the quadrature order<sup>14</sup>  $N$ . These quadrature methods usually reduce the number of function evaluations<sup>15</sup> necessary to obtain a decent estimation.

A key point in the use of quadrature rules is the choice of the quadrature order. The quadrature rule will provide an estimate of the integral, but no *accuracy* estimation. A trivial way to obtain an estimate of the integration error is to compare with another estimate obtained with an order  $N-1$  or  $N+1$ . Yet this method may require a significant number of extra function calls. Several methods have been developed in order to obtain an estimate of the error from a subset of the previously evaluated function results; for instance the Gauss-Kronrod [136] and Gauss-Bond [137] quadrature rules. These methods still have the liability that if the estimated error is too large, a completely new set of function calls must be computed to obtain an integral estimate of order  $N+1$ .

This burden is removed if *nested* quadratures are used. For nested quadrature rules, the evaluation abscissa of order  $N$  are partially or fully contained in the abscissa of order  $N+1$ . Thus, to perform an integration with a higher order, some (or all) of the previous function evaluations can be reused to provide a new estimate. This is illustrated in Fig. 5.20, it can be seen that for the nested Gauss-Patterson quadrature rule, the lower order abscissa ( $x_i$ ) can be reused for higher order integral estimates. This is not possible for the unnested Gauss-Legendre quadrature rule.

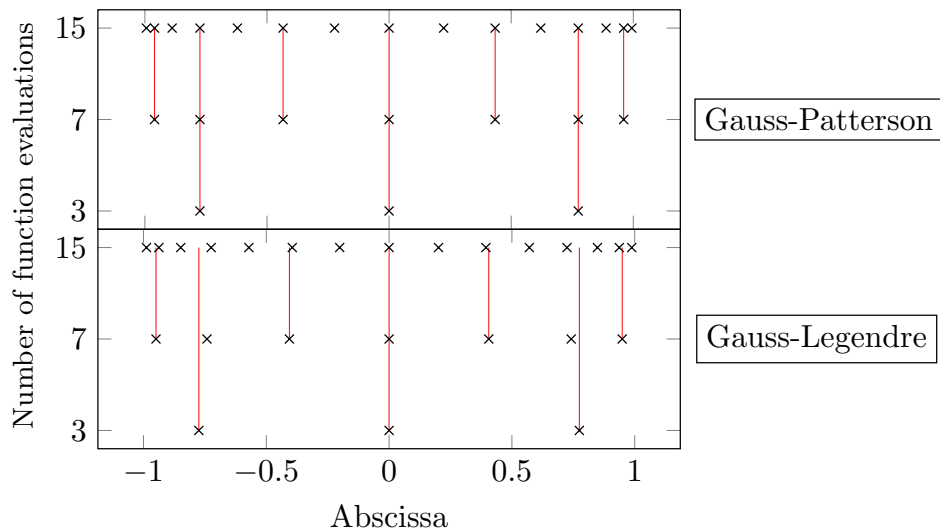


Figure 5.20 – Comparison of the abscissa for the Gauss-Legendre and Gauss-Patterson quadrature rules. The red lines highlight the fact that a quadrature rule is nested or not.

<sup>14</sup>The quadrature order  $N$  is not necessarily the highest order of polynomial used.

<sup>15</sup>Compared with discretization methods such as the Simpson method [135].



With nested quadrature rules, the error estimation can be obtained by comparing convergence of the integral estimate between orders  $N$  and  $N - 1$ . The precision<sup>16</sup> of such nested rules is slightly reduced compared with other types of quadrature (*e.g.* Gauss-Legendre) as can be seen in Tab 5.3. The high-precision of the Gauss-Legendre quadrature rule is traded off to get nestedness. Yet in practice the Gauss-Patterson rule leads to a significant speed-up of the integration as the convergence of the integral can be tested much faster than if a higher order Gauss-Legendre quadrature had to be estimated. It also reduces the number of function calls if the function to integrate varies “nicely”.

Table 5.3 – Comparison of precision for the Gauss-Legendre and Gauss-Patterson quadrature rules.

Number of function calls	Precision	
	Gauss-Patterson	Gauss-Legendre
1	1	1
5	5	5
13	11	13
29	23	29
61	47	61
125	95	125
253	191	253
509	383	509
1021	767	1021

In practice, two or three-dimensional integrals must be computed in the present work. This can be easily performed by use of the Fubini’s theorem and using recursive calls of one-dimensional quadrature rule, for instance

$$\int_{X \times Y} d(x, y) f(x, y) = \int_X dx \left( \int_Y dy f(x, y) \right). \quad (5.133)$$

This approach combined with the Gauss-Patterson method would enforce convergence on each “ $x$  evaluation point” whereas a convergence on the integral estimate would be enough.

The generalization of quadrature rules to higher dimensions is called *sparse grid* and is obtained by Smolyak construction [138]. Tensor product of one-dimensional quadrature rules is used to form product rules, then a weighted sum of product rules, provides sparse grid. One-dimensional types of quadrature rule can be combined to define a sparse grid. For instance, it allows to handle integration ranges  $[-1, 1]$  and  $[0, +\infty[$  for two different dimensions. Details about Smolyak construction [138] is beyond the scope of this document, an example is shown in Fig. 5.21. In the figure only evaluation points are shown. It can be seen that they spread similarly on each dimension, and this, accordingly to the one-dimension Gauss-Patterson quadrature rule. The weight related to each evaluation points is not shown, and their computation is quite tedious. To tabulate the Gauss-Patterson evaluation points and weights for one dimensional quadrature rule (and two and three dimensional sparse-grids) the SANDIA\_RULES program of John Burkardt [139, 140] has been used.

<sup>16</sup>Precision, order and number of function evaluations are different quantities. The quadrature order is simply an index labeling a given quadrature rule in its quadrature rule family. The precision stands for the highest order of polynomial that the quadrature is able to integrate *exactly*.

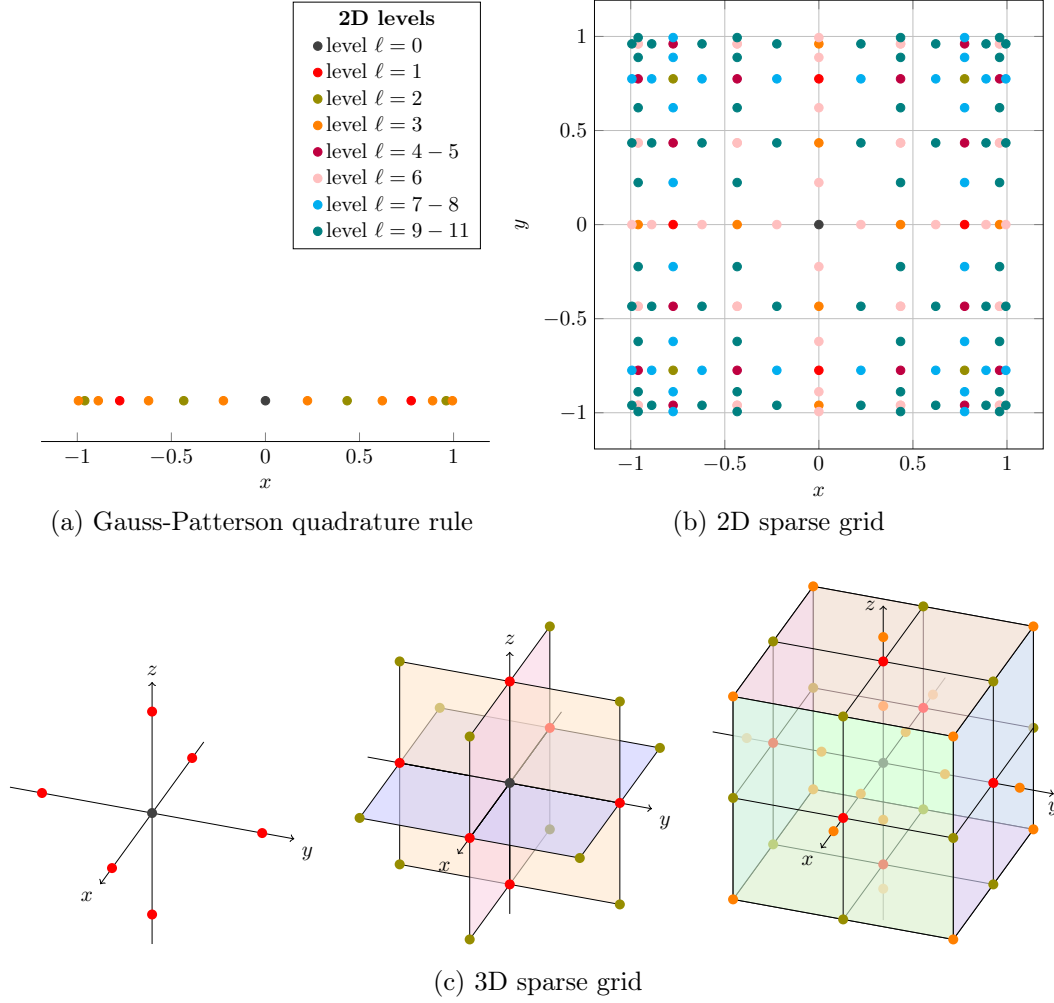


Figure 5.21 – Illustration of a 1D nested quadrature rule (5.21a) and of a 2D (5.21b) and a 3D sparse grids (5.21c) obtained with the Gauss-Patterson quadrature rule. Only evaluation points are shown, related weights are not represented. The *level* is a generalization of the one-dimensional *order*. For 1D and 3D cases the level colors are identical (for presented levels) to the 2D levels. Levels 4 and 5, levels 7 and 8 and levels 9 to 11 correspond to identical 2D sparse grids.

### 5.5.3 Exploitation of Computational Resources

Even with the here-above mentioned mathematical and numerical sophisticated methods, a modern program intended to be used for evaluation purposes should take advantage of all speed-up opportunities. The last point in this section about implementation efficiency will deal with hardware-related implementation. Figure 5.22 shows the evolution of the processor frequency in the last 40 years, along with the evolution of the number of cores per processor during the same period. It can be seen that the exponential increase of the processor frequency has been dramatically reduced from the beginning in the decade 2000-2010. Additionally, one can see that the number of cores per processor has taken over the computing power race.

In parallel of this effort to compensate the so-called “frequency wall” by adding more and more cores per processor, manufacturers also increased vectorized computation capabilities of cores. This type of computing capability relies on the Single Instruction Multiple Data (SIMD) treatment. An example of application of this technology could be

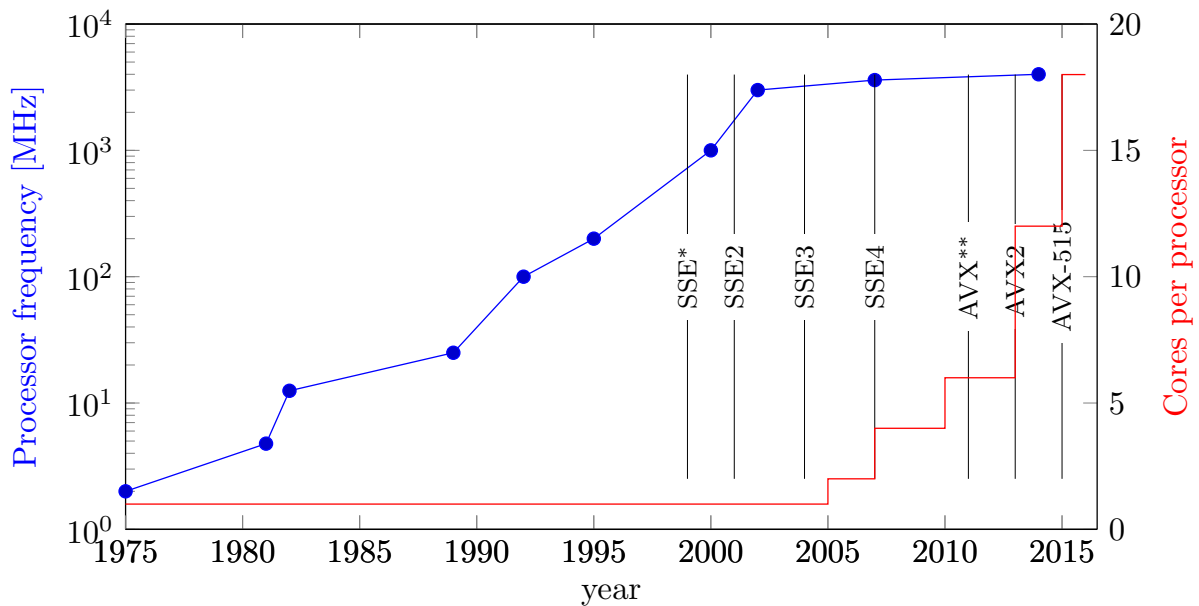


Figure 5.22 – Evolution of the processor frequency and the number of cores per processor since 1975. \*Streaming SIMD Extensions. \*\*Advanced Vector eXtensions.

understood when one needs to perform an element-wise addition of two arrays. Instead of looping on array elements and performing “one-by-one” additions, the core performs two additions at the same time. Speed-up becomes less easy than in the “good old days” when the chip frequency kept increasing, but if this type of operation is a bottle-neck in the program, significant enhancement can be expected. Figure 5.22 also shows some *instruction set architectures* (SSE and AVX). They correspond either to:

- An increase of the vectorized register size (128-bits, 256-bits, 512-bits, etc.)<sup>17</sup>.
- A new data-type capability, for instance operations on floating point numbers (not only integers).
- More complex or composed operations, multiplication (not only addition). Recently fused multiply-add (FMA) operations became available, *i.e.* performing multiplication and addition at the same time or more exactly, during the same clock cycle.

Graphical processing has been for a long time a specific field of computer sciences. Although it has been used for large scale computing for a long time, it has been investigated for scientific computation – namely genomic research – only for less than a decade. Among the main motivations was the fact that programming for Graphic Processing Unit (GPU) was a much more difficult task than for usual Central Processing Unit (CPU). In recent years, General-Purpose computing on GPU (GPGPU) developed thanks to Application Programming Interfaces (API) such as OpenCL [141] of the Khronos Group or CUDA [142] of NVIDIA. This later was used for the present implementation work. These API ease the programming on GPU even if some hardware-related features must be handled at the programming level, whereas it is often compiler-level for most CPU programs<sup>18</sup>. Interest from the High Performance Computing (HPC) community for GPU

<sup>17</sup> This corresponds to the capability of either processing more data at the same time (four-by-four), or treating “larger” type of data (64-bits integers, double-precision floating point numbers).

<sup>18</sup> This is actually different when performances are targeted. In this case, specific programming features must be inserted in order to take advantage of the many cores or of the vectorized operations.

is additionally driven by the energy efficiency of GPU by comparison with CPU for a similar computation power<sup>19</sup>.

Two versions of the FRLDM have been implemented, one using CPU-only, the second combining CPU and GPU (in this version only the Hamiltonian diagonalization is performed by the CPU<sup>20</sup>). Both versions will not be detailed any further; it will simply emphasized that both implementations use the same mathematics and numerical algorithms (*cf.* the two subsections above concerning mathematical and numerical methods). A typical calculation with the implemented models of the FRLDM would consist in defining a large list of nucleus shapes. For each of these, an independent calculation (a shape-task) as described in the previous section is performed. For computation of the many shape-tasks, the list of shape-tasks is dispatched, by a “master” workstation, to all available workstations installed in the group laboratory. On each workstation, the program splits its list of shape-tasks and distributes tasks to available CPU cores. As mentioned above the implementation using GPU is not GPU-only, a part of the computation is performed by the CPU. It should be stated here that standalone GPU programs are not (yet?) possible, GPUs are still driven by a CPU. The latter CPU only starts the GPU computation and waits for GPU calculation to be complete. GPU must still be considered a co-processor. The difference between the two implementations rely in the following: in the CPU implementation, a list of shape-tasks is attributed to each CPU, they perform the required computations using as much as possible vectorized loops. In the GPU implementation, in order to use GPU at their maximal capacities, all CPU submits a specific shape-task to the GPU and performed diagonalization when GPU computation is completed. When all shape-tasks assigned to the workstation are treated, the related results are sent back to the master workstation.

To complete this section about computational efficiency, qualitative results with two implementations of the FRLDM (CPU and GPU) will be given for the computation of PES. The calculation grid of the example<sup>21</sup> consists in a 3D grid containing  $42 \times 42 \times 26 \approx 5 \times 10^4$  shape-tasks. Only one workstation is used (no workstation dispatching) but the 12 cores of the workstation are used. In this case the computation time for the CPUs alone is about 20 minutes, whereas for GPUs enhanced computation this falls to 5 minutes, which means a speed-up factor of 4. Considering a single-CPU computation for an equivalent case, the speed-up factor would be about 50. The workstation dispatching has a nice scalability (*i.e.* it does not loose too much performance while dispatching tasks and gathering results), while using only few of the available workstation in the group laboratory, one easily gets a factor 100.

---

<sup>19</sup>The computation power is often measured in terms of highest achievable number of Floating Point Operations per Second (FLOPs), the energy efficiency of the computation is measured in FLOPS per Watt.

<sup>20</sup>This part remains performed by the CPU because the CUDA version available at that time did not provide eigen-problem library. This is now the case with the CUDA-7 version.

<sup>21</sup>In Ref. [16], for a 5D grid, more than  $5 \times 10^6$  shapes are considered.

## Chapter 6

# From Potential Energy Surface to Fission Cross Section

*In the previous chapter, Potential Energy Surfaces (PES) are obtained using the FRLDM macroscopic-microscopic model. The present chapter deals with several methods that have been settled in order to extract from the multidimensional PES, a one-dimensional fission barrier. To obtain a fission transmission coefficient from this barrier, numerical methods have been tested and compared. The influence of a deformation-dependent inertia parameter on fission transmission coefficient is studied. Global transition states are also introduced as the extension of those from Chapter 4 and the eventual macroscopic-microscopic-based fission cross section is computed.*

### Contents

---

<b>6.1</b>	<b>Least-Energy Path</b>	<b>114</b>
6.1.1	Immersion Technique	114
6.1.2	Full Least-Energy Path	116
6.1.3	2D-Verification and 3D-Application	118
<b>6.2</b>	<b>Least-Action Path</b>	<b>121</b>
6.2.1	Deformation Inertia Tensor	121
6.2.2	Action Minimization and Path	128
<b>6.3</b>	<b>Least-Energy V.S. Least-Actions</b>	<b>129</b>
<b>6.4</b>	<b>Numerical Transmission Coefficients</b>	<b>132</b>
6.4.1	Deformation-Independent Effective Mass Parameter	132
6.4.2	Deformation-Dependent Effective Mass Parameter	136
6.4.3	Effects of Path Searching Method and Deformation Inertia Tensor on Transmission Coefficient	138
<b>6.5</b>	<b>Transition states</b>	<b>141</b>
6.5.1	Rotational Band	142
6.5.2	Rotational Band-Heads	142
6.5.3	Rotational Moments of Inertia	143
<b>6.6</b>	<b>Fission Cross Section</b>	<b>146</b>

---

In the previous chapter it was shown how to obtain multidimensional Potential Energy Surfaces (PES). These PES are related to a shape parameterization, each parameter of the parameterization corresponds to one dimension of the PES. In this last chapter, the generalized spheroid parameterization (*cf.* Appendix B.1) will be used for all the calculations. This parameterization can be easily used with two or three shape parameters corresponding approximately to the elongation  $c$ , the neck size  $h$  and the mass-asymmetry  $\alpha$ . For a better description of the nucleus shape “between” the “fission point” (defined below) and the scission point, a more sophisticated shape parameterization such as the 3QS (*cf.* Appendix B.1) should be used. As this deformation range is not studied in the present work, the three dimensional generalized spheroid parameterization seems appropriate.

In practice, a multi-dimensional PES cannot be directly used to perform cross section modeling. Ongoing works are investigating in this direction, for instance using the time-dependent generator coordinate method [143], but it implies performing time-dependent wave propagation, which is for the time being far too time-consuming for direct use in evaluation. To use the multidimensional PES obtained from the macroscopic-microscopic model, one needs to determine a relevant one-dimensional path. This path consists in a list of shapes taken by the nucleus from its ground state shape to a “fission shape”<sup>1</sup>. Two approaches to obtain this one-dimensional barrier have been implemented in the CONRAD code, they are namely the least-energy and least-action methods. These methods extract a one-dimensional deformation potential (“fission barrier”) from the multidimensional PES. To calculate the transmission coefficient related to this one-dimensional potential, numerical methods must be chosen. Several options have been tested and compared. The least-action method also provides a deformation-dependent inertia parameter (defined later in this chapter) that has a significant effect on transmission coefficient. Finally, global transition states are introduced and an actual fission cross section calculation can be performed.

## 6.1 Least-Energy Path

An intuitive approach to obtain a one-dimensional path consists in considering that, along the fission path, the nucleus takes a shape that minimizes “somehow” the potential energy. The least-energy path method, described in the following, relies on that principle. As the PES spans over several dimensions (more than 2), visual verification is not always possible. If the following, one can consider the PES a multidimensional array, most of the discussion below can be more easily understood if one keeps in mind a 2D array. The algorithm may seem trivial, yet while considering arbitrary 2D surface or higher dimensions it becomes necessary to have a sound method.

### 6.1.1 Immersion Technique

The first step in the least-energy path method is the identification of all PES local minima. This is trivially done by checking, for each point of the PES, if all neighboring points are higher in energy. These minima can also be at an edge of the calculation grid, in this case the point checked has just fewer neighbors. In the present work it seems not necessary to check if two neighboring points have exactly identical energies as the program stores energies in double precision, the probability for this situation is highly improbable to the difference in Ref. [16] where only few digits were stored.

---

<sup>1</sup>This type of shape corresponds here to elongated shapes having the same deformation energy than the ground state.

Once all local minima have been identified, the next step is to obtain the saddle points between all pairs of minima. This is done using the immersion technique well described in Ref. [16], this method is only briefly described below. To easily understand the method, one should consider the deformation-energy a “landscape” with hills, valleys and ridges. The immersion technique allows to obtain the saddle points connecting two valley bottoms. Considering two selected valley bottoms (two local minima), one artificially considers that water is flowing out of one of the local minima (the spring). The second minimum will be called the sink point. The flowing water slowly fills the first valley containing the spring, the water level increases iteratively up to a level where the water reaches the saddle point and flows down to the second valley to sink point. The implementation of the immersion technique must then focus on how properly “wet” points of the PES as water level increases and also how to wet points as the water flows down a saddle point.

The saddle point is obtained with this method by identifying the point of the PES that is the lowest to become “wet” as the water level is raised and flows down to the sink valley. The water level is increased at each iteration with a given water-level step until the sink point becomes wet. If the water-level step used is small enough, there is only one wet point between the two last iterative water levels. A trivial one-dimensional case is shown in Fig. 6.1. One can consider that water is flowing out of one of the local minima (red dots), the water level is iteratively raised with a constant water-level step. When the water level exceeds the saddle point<sup>2</sup>, the number of points located between the two last water levels (here corresponding to steps 3 and 4) are counted. If this number is larger than one, the program resumes raising water level from step 3 with a smaller water-level step (here leading to step 5). This operation is repeated until only one point is identified.

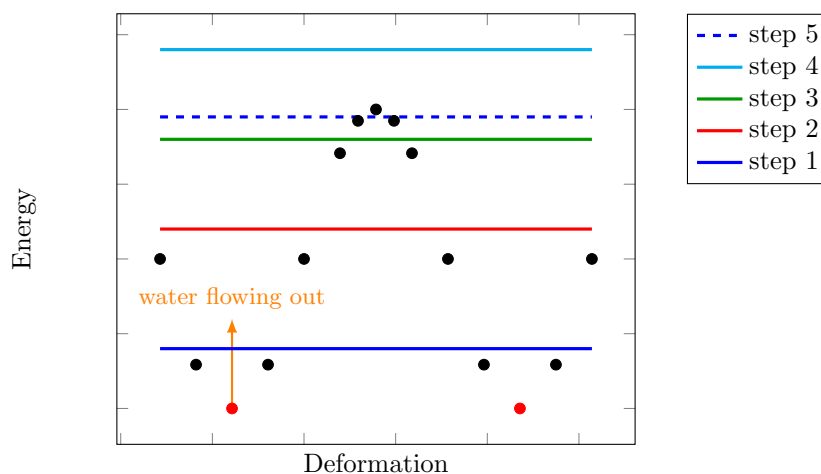


Figure 6.1 – Example of application of the immersion technique in a one-dimension case.

The generalization of this concept and its application to the PES saddle point search is well detailed in Ref. [16]. Since this method is well suited and robust for high-dimensional PES, it has been implemented in the CONRAD code during this PhD work, and verified for 2D cases. Whenever high-dimensional PES are considered (for instance 5D), several hundreds of local minima can be identified and the immersion technique must be applied for each pair of minima. As a saddle point between two minima can also be the saddle between two others, this reduces the number of times of the immersion technique must be applied. Yet, as this operation can still take a significant amount of time, this search of saddle points has been multithreaded (*i.e.* parallelized) in the CONRAD code.

<sup>2</sup>In the multidimensional case, this event is detected by a method described in Ref. [16].



### 6.1.2 Full Least-Energy Path

In order to obtain the full least-energy path, the following steps are followed

1. Get all minima,
2. Get saddle points between each pair of minima,
3. For each saddle point, get all minima that are reached solely by going down from the saddle,
4. Get the succession of minima and saddle points between a specific local minimum (the ground-state) and a “fission point”,
5. Select a relevant “fission point”,
6. Get the succession of saddle points and intermediate wells between the ground-state and the “fission point”,
7. Find paths between the ground-state and the selected “fission point” (down the saddles).

The two first points have been treated in the previous sub-section. The third point can be addressed by the definition of “only-going-down” paths. Considering a saddle point identified in the previous step, the saddle point is set as “wet” and added to a group of wet points (the just-wet-group), then all neighbors below that saddle point are labeled as wet and added to the just-wet-group. The saddle point is then removed from the just-wet-group (but is still wet). This operation is performed as long as there are points in the just-wet-group; a new point is picked out of the just-wet-group at each step and some of its neighbors can be added (if below the running point and not already wet). Once the just-wet-group is empty, all minima that could become wet by water going solely down from the saddle, with no intermediate saddles, have been found. A mapping can be obtained between each saddle point and all minima that can “get wet by water, flowing out of the saddle point, without accumulating somewhere”. This is exemplified in Fig 6.2, where two paths are shown, starting from the higher saddle point on the right. Path 2 goes directly to the lowest local minimum and, all along the path, the deformation energy only decreases. In case of Path 1, the path reaches first an intermediate local minimum, after what the deformation energy increases again until the path reaches the second saddle point.

At the fourth step, the ground-state point must be identified. This is done by searching the *global* minimum among *local* minima. As very elongated shapes can have energy below the ground-state shape, they must be discarded, thus a maximal “elongation” criterion must be set. Then *exit* points must be defined; these points are local minima with energy below the ground-state energy, they are the “fission shapes”. From step 2, the saddle points between all these minima and the ground state are known. Thus a first selection is made among the exit points to retain only those corresponding to the lowest global saddle point. At this stage, the ground-state and the global saddle points are known. Yet the eventual fission point is not uniquely determined as several exit points may correspond to the lowest saddle point connected to the ground state. Here a first arbitrariness of the method is highlighted. Indeed, no obvious criterion can be used to select a particular exit point or another. In the present work, the criterion was set to retain the point with the smallest Pythagorean distance to the ground state. This Pythagorean distance will be defined in the following.

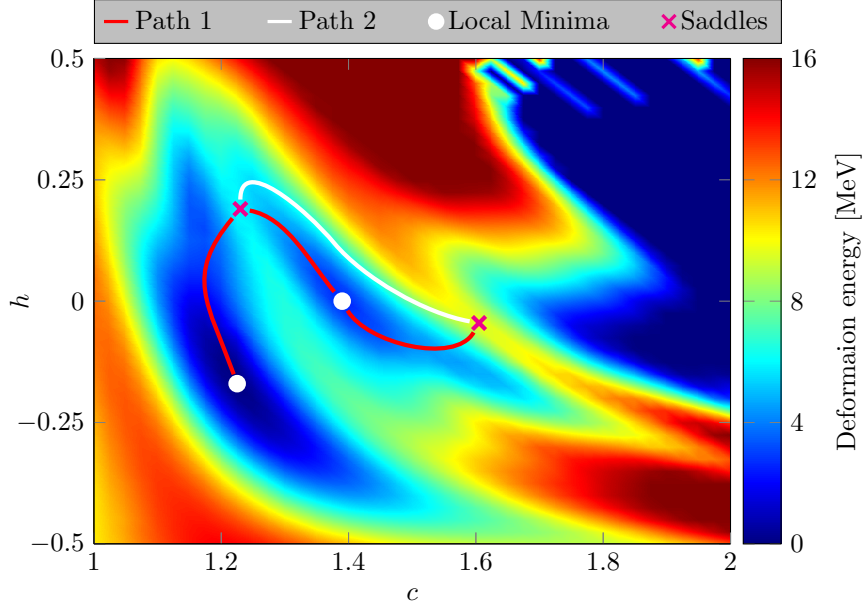


Figure 6.2 – Example of path options that can be used to determine which local minima are “connected” to a given saddle point.

To perform the next step, *i.e.* determining the succession of saddle points and intermediate wells, one starts knowing the ground state shape (entrance point) and the exit point selected from the previous step. From the mapping between pairs of minima, the corresponding saddle point can be obtained (*cf.* step 2). Then the full path must be obtained. One path may be found to go directly from the saddle point to the entrance and exit points but this path would miss possible intermediate wells. The algorithm operates as follow and can be understood using Fig. 6.3 as guideline.

- Starting from the saddle point (① in Fig. 6.3) and, for instance, the exit point (⊗ in Fig. 6.3). The program selects all minima (blue dots in Fig. 6.3) that are connected to the saddle point by an “only-going-down” path (arrowhead lines in Fig. 6.3).
- The program then selects the minima that is related to the exit point with the lowest intermediate saddle point. This latter is ③ in the present case.
- A new saddle point ③ is now selected between two minima ② and ⊗. The same procedure is then applied recursively.

The final step consists in obtaining the full path (*i.e.* not only the succession of saddles and local minima points. This is done assuming that the correct connection between pairs of minima and related saddle points is provided by the latter step. Given a saddle point (running point) and one of the two corresponding minima (the targeted minimum), the program searches the lowest point among the neighbors of the saddle point that has an “only-going-down” path to the targeted minimum. This lowest neighbor becomes the running point and the same search is performed again until the running point becomes the targeted minimum. At this points all saddles of the path have been identified, and two “continuous” set of points are defined from each saddle point down to the related minima. The program finally connects these partial paths by identifying common minima in the subpaths related to two different saddle points.

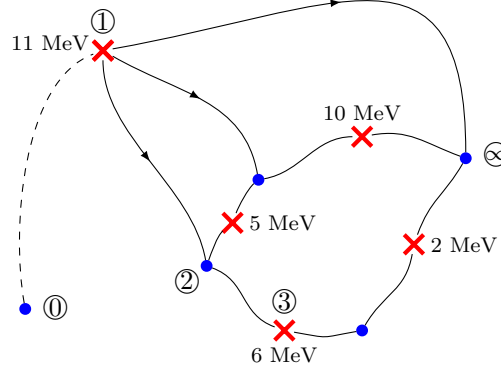


Figure 6.3 – Illustration for the least-energy path searching method. Saddle points are shown with red crosses, local minima with blue dots, arrows indicate “only-going-down” paths. The heights of the saddle points are also shown.

### 6.1.3 2D-Verification and 3D-Application

Figure 6.4 shows the results for the least-energy method that has been detailed above. It is applied to a 2D PES related to the  $^{240}\text{Pu}$  compound nucleus (using a 2D generalized spheroid parameterization). On this 2D image, the agreement between the code results (orange curve) and the background “hilly area” is quite satisfactory. The “fission line” (red curve) corresponds to shapes with the smallest elongation and for which the deformation potential value is identical to the ground state one. It can be noticed that not only *one* intermediate local minima is found, additionally more than *two* saddle points are found whereas one would have expected to obtain two properly defined humps separated with a single intermediate well. Yet these extra minima correspond to very shallow wells, and thus these and the related extra saddle points (to escape from these shallow wells) have very little effects on the path structure. An example of these shallow wells can be seen in Fig. 6.4 near the ground states. Two local minima (white dots) can be observed near  $(c, h) = (1.2, -0.2)$ . The presence of two close local minima may be due to numerical issue, as near the ground state point the potential slope is very low and small numerical fluctuations can produce local minima. It can be observed in Fig. 6.4 that no fission valley can be identified in the area delimited “on the left” of the fission line. This means that, in this case, the fission valleys appear for elongations beyond the fission line. This may actually be different in the case of 3D PES, but this information cannot be obtained by visual checks.

From the least-energy results such as those shown in Fig. 6.4, it is difficult to obtain a one-dimensional deformation energy as no abscissa is defined. The intuitive method would consist in projecting the path (orange curve in Fig. 6.4) on the elongation axis  $c$ . Unfortunately such a method may lead to one-dimensional barrier that is unusable for eventual transmission coefficient calculation. An example is shown in Fig. 6.5. It can be seen that the related projected potential  $V_{\text{def}}^{\text{proj}}(c)$  is not a proper function as a given elongation  $c$  can correspond to several deformation energies. Results from Fig. 6.5 cannot be further used to obtain a transmission coefficient. This effect for the 2D case is even worse if the mass-asymmetry degree of freedom is explored (3D curve).

To avoid this problem, the *ad hoc* Pythagorean rule has been used for the present study with the least-energy technique. For instance with the 2D  $(c, h)$  or 3D  $(c, h, \alpha)$  generalized spheroid shape parameterization, the “distance”  $\text{dist}(P_1, P_2)$  between two points  $P_1$  and  $P_2$  of the least-energy path is given by Tab. 6.1.

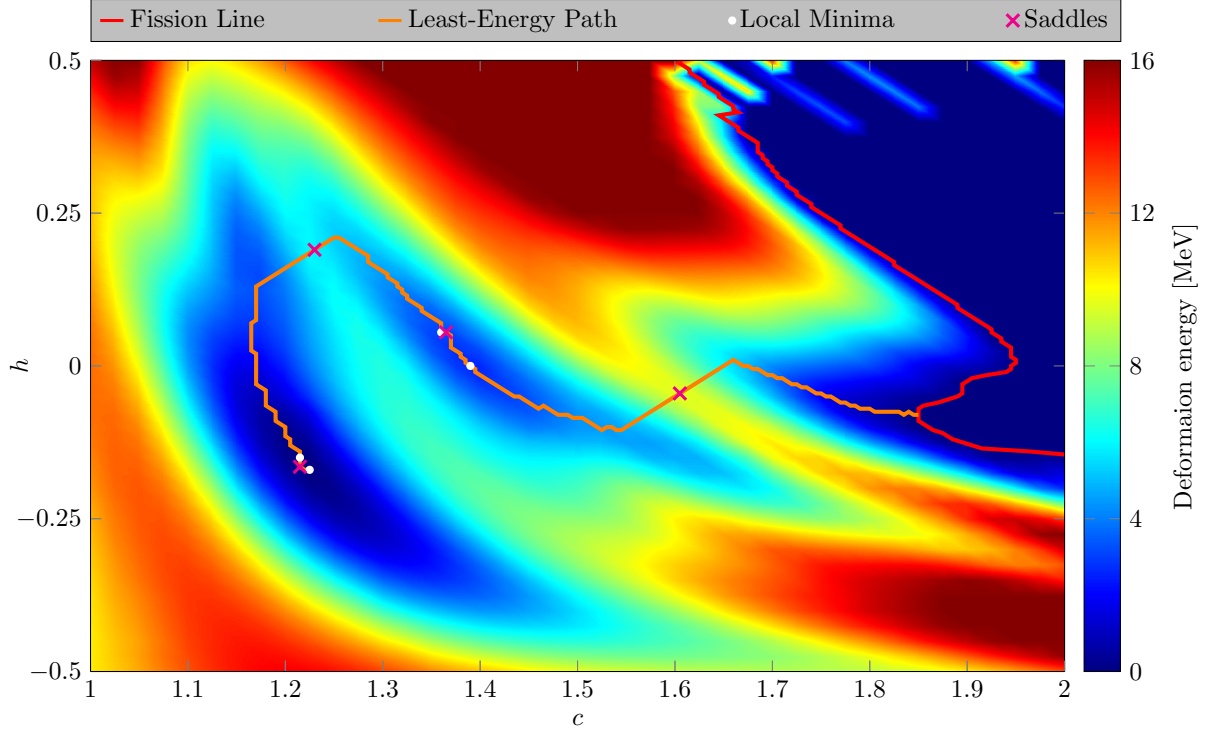


Figure 6.4 – PES of the  $^{240}\text{Pu}$  based on the FRLDM and using the 2D generalized spheroid parameterization. The path obtained with the least-energy (immersion) technique [16] is shown as an orange solid line. The fission line is shown in red, and corresponds to points  $\vec{q}$  with the smallest  $c$  deformations that have the property  $V(\vec{q}) = V(\vec{q}^{\text{GS}})$ . The saddle points are shown with magenta cross marks and the path local minima are marked with white dots.

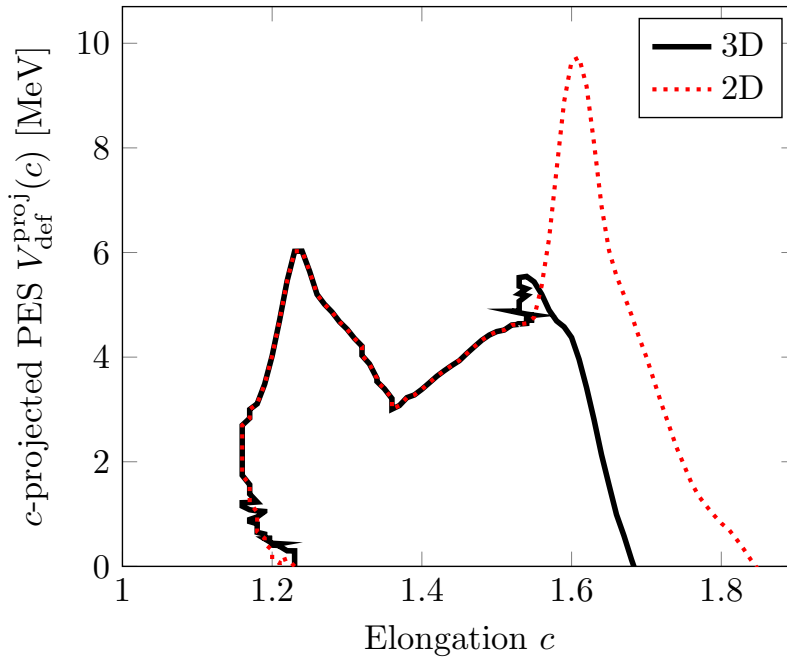


Figure 6.5 – Projection of the least-energy path of the  $^{240}\text{Pu}$  on the elongation axis  $c$ . The original PES is obtained using the generalized spheroid shape parameterization with two (2D) or three (3D) degrees of freedom.

Table 6.1 – Definition of the Pythagorean one-dimensional distance used for the least-energy method.

dimension	$P_1$	$P_2$	$\text{dist}(P_1, P_2)$
2D	$(c_1, h_1)$	$(c_2, h_2)$	$\sqrt{(c_1 - c_2)^2 + (h_1 - h_2)^2}$
3D	$(c_1, h_1, \alpha_1)$	$(c_2, h_2, \alpha_2)$	$\sqrt{(c_1 - c_2)^2 + (h_1 - h_2)^2 + (\alpha_1 - \alpha_2)^2}$

The one-dimensional projection using the Pythagorean distance rule is shown in the left part of Fig. 6.6. It can be seen that the shape is somehow scaled along the “ $x$ -axis” between the 2D and the 3D case. This highlights the fact that the Pythagorean distance is not a sound definition for the deformation abscissa. This “ $x$  scaling” is caused by the fact that, while deforming from the ground state to the first saddle point, the nucleus takes small mass-asymmetric shapes. This fact must be taken cautiously because, as can be seen in Fig. B.4 of Appendix B.1, the mass asymmetry parameter has small effect for shapes with small elongation. The first saddle point is reached for  $(c \approx 1.2)$  and the maximum of mass asymmetry for shapes between the ground state and the first saddle point is  $\alpha = 0.12$ , which is about half the mass asymmetry for shapes shown in Fig. B.4. The saddle point area is yet completely mass-symmetric ( $\alpha = 0$ ), which results in similar shapes for first saddle points shown in Fig. 6.6 (blue dots). One can get convinced that the path are quite similar between the 2D and 3D paths by examining again Fig. 6.5. Except in the vicinity of the ground state, the 2D and 3D projections are identical up to the second hump.

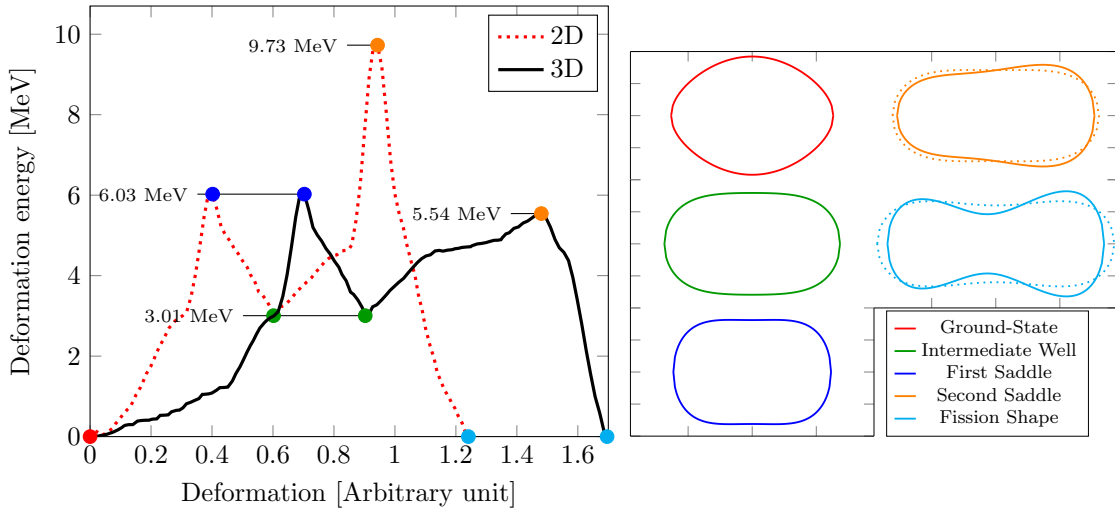


Figure 6.6 – (Left) One dimension reduction of the  $^{240}\text{Pu}$  PES using the Pythagorean distance rule for the 2D and 3D cases. (Right) Illustration of the shapes obtained for the ground state, the saddle points, the intermediate well bottom and the “fission point”. Data related to the 2D PES are shown with dotted lines.

Even if the  $x$ -axis of Fig. 6.6 is not completely justified, one can notice interesting features concerning the curve height. For the second saddle point, the mass-asymmetry has a significant effect and leads to a significant reduction of the second barrier height. This effect has been noticed for a long time but remains yet a comforting result for testing of the present implementation. The barrier heights, about 10 MeV for the mass-symmetric path and about 6 MeV for the mass-asymmetric path are quite realistic for actinides [144–146].

From the shape of the curves, the ground state, the saddle points, the intermediate well bottoms and the “fission points” can be identified for both 2D and 3D cases. It can be noticed that, for the ground state, the first saddle point and the intermediate well bottom, shapes and energies obtained in the 2D and 3D cases are identical. The corresponding shapes are shown on the right part of Fig. 6.6. The solid (respectively dotted) lines correspond to shapes obtained with the 3D (respectively 2D) model. One can also notice that in the case of fission shapes (and also second saddle point shapes), the 2D configurations are more elongated, which is expected from measurements analyses of fragments total kinetic energy [147].

## 6.2 Least-Action Path

The least-energy path searching method explained above contains some arbitrariness, for instance the path abscissa is not well justified. Also, paths down saddles to local minima are not uniquely defined, and even the choice of the sequence of saddles and minima can be questioned. An alternative approach to find a one-dimensional path in a multidimensional PES is the least-action method. This method has two main advantages: it provides a more satisfactory one-dimensional “fission abscissa”, and the definition of the “fission path” between two points is unambiguous. However the method requires the introduction of an additional quantity, the deformation inertia tensor.

### 6.2.1 Deformation Inertia Tensor

Assuming that the deformation degrees of freedom of the nucleus are labeled  $\vec{q}$ , the kinetic energy  $T^{\text{kin}}$  of the deforming nucleus given by [20]

$$T^{\text{kin}} = \sum_{ij} \frac{1}{2} B_{ij}(\vec{q}) \dot{q}_i \dot{q}_j, \quad (6.1)$$

where  $B_{ij}$  are the components of the *deformation inertia tensor*. Assuming that this tensor is known, several methods can be used to find the *least-action path*  $L$  that minimizes the *action integral*  $S$  [20] defined by

$$S = \int_L ds \sqrt{\sum_{ij} B_{ij}(\vec{q}) \frac{dq_i}{ds} \frac{dq_j}{ds} [V(\vec{q}) - V(\vec{q}^{\text{GS}})]}, \quad (6.2)$$

where  $V$  is the deformation potential provided by the PES,  $\vec{q}^{\text{GS}}$  is the ground state deformation and  $ds$  is the infinitesimal path abscissa. Two models for the inertia tensor will be presented in the following.

#### 6.2.1.1 Werner-Wheeler Approximation

Using the same image than for the Liquid Drop Model (*cf.* Chapter 5, Section 5.2), the deformation inertia of the nucleus is expressed as the deformation inertia of an irrotational incompressible liquid drop. In this case, the deformation kinetic energy is given by [148]

$$T^{\text{kin}} = \frac{1}{2} \rho_m \int_V d^3\vec{r} v^2(\vec{r}), \quad (6.3)$$

where  $v$  is the velocity field of the nuclear liquid and  $\rho_m$  is the mass density of the matter contained in the sharp-edge volume  $V$ . This expression can also be written in terms of time derivatives of the shape coordinates  $\vec{q}$  as

$$T^{\text{kin}} = \frac{1}{2} \sum_{ij} B_{ij}^{\text{irr}}(\vec{q}) \dot{q}_i \dot{q}_j. \quad (6.4)$$

The velocity potential  $\varphi$  defined by  $v(\vec{r}) = \vec{\nabla}\varphi$  is solution of a Laplace equation

$$\Delta\varphi = 0, \quad (6.5)$$

and has Dirichlet boundary conditions on the nuclear surface  $S$  containing  $V$ :

$$\forall \vec{r} \in S, \quad \vec{\nabla}\varphi(\vec{r}) \cdot \vec{n}(\vec{r}) = \vec{v}(\vec{r}) \cdot \vec{n}(\vec{r}) = \sum_i \dot{q}_i \frac{\partial \vec{r}}{\partial q_i} \cdot \vec{n}(\vec{r}), \quad (6.6)$$

where  $\vec{n}$  is a normal vector to the surface at  $\vec{r}$ . Additionally, in the Werner-Wheeler approximation, an additional hypothesis is made, stating that the  $z$  component  $v_z$  of the velocity does not depend on the  $\rho$  coordinate. Using these relations and the volume conservation conditions

$$\frac{\partial}{\partial t} \int_V d^3\vec{r} = \sum_i \dot{q}_i \frac{\partial}{\partial q_i} \int_V d^3\vec{r} = 0, \quad (6.7)$$

the tensor  $B_{ij}^{\text{WW}}$  can be expressed using of shape parameterization function  $\rho(z) = \rho(z; \vec{q})$  [17] as

$$B_{ij}^{\text{WW}}(\vec{q}) = \pi \rho_m \int_{z_{\min}}^{z_{\max}} dz \rho^2(z) \left[ A_i(z) A_j(z) + \frac{1}{8} \rho^2(z) A'_i(z) A'_j(z) \right], \quad (6.8)$$

where  $z_{\min}$  and  $z_{\max}$  are the minimum and maximum  $z$  coordinates of the nucleus surface that verify  $\rho(z_{\min}) = \rho(z_{\max}) = 0$ , and where the  $A_i$  functions are given by

$$A_i(z) = \frac{1}{\rho^2(z)} \frac{\partial}{\partial q_i} \int_z^{z_{\max}} \rho^2(z') dz'. \quad (6.9)$$

Figure 6.7 shows an example of the inertia tensor obtained using a 2D generalized spheroid shape parameterization ( $c, h$ ). Since this tensor is of order two, *i.e.* a matrix, a simple “graphical” representation can be used<sup>3</sup> for  $B_{cc}$ ,  $B_{hh}$  and  $B_{ch}$ . The  $\mathbf{B}$  matrix is symmetric, thus only one of the off-diagonal component ( $B_{ch}$ ) needs to be shown. The structure on the upper-right part of the figures corresponds to the scission line, beyond this line the Werner-Wheeler model implementation does not hold. This is not necessarily an issue in the present study as such highly deformed shapes are not be investigated. The validation of the Werner-Wheeler model implementation has not been completed as analytical solutions exist for only few shape parameterizations [149], but not for those used in this study. Because of the nature of the deformation inertia, the inertia tensor must have only positive eigenvalues. It was verified that the eigenvalues of the inertia tensor  $B^{\text{WW}}$  remain positives in the whole deformation range, as part of the proof, the square root of the matrix determinant is shown in Fig. 6.7.

<sup>3</sup>The graphical limitation is more related to the fact that the inertia tensor components depend on 2 or 3 deformation coordinates. The inertia tensor is always of order two but if three deformation coordinates are used, 7 components would be shown and each of them would depend on 3 parameters.



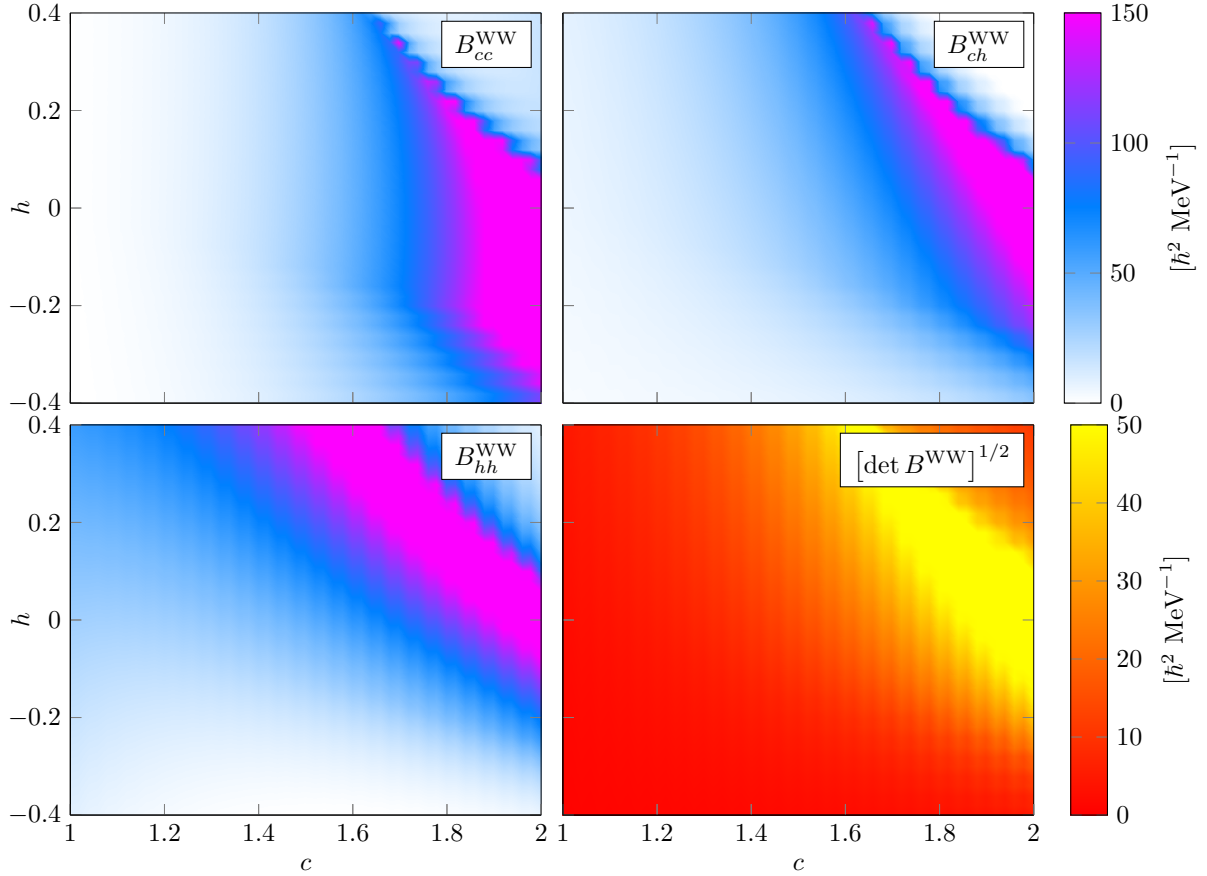


Figure 6.7 – Deformation inertia tensor  $B^{\text{WW}}$  calculated with the Werner-Wheeler approximation for  $^{240}_{94}\text{Pu}$ . The shape is parameterized with generalized spheroid shape parameterization  $(c, h)$ , the three components of the tensor  $B_{cc}^{\text{WW}}$ ,  $B_{ch}^{\text{WW}}$  and  $B_{hh}^{\text{WW}}$  are shown. The square-root of the inertia tensor determinant  $\sqrt{\det B^{\text{WW}}}$  is also shown. The triangular structure on the upper-right parts of the plots is due to inertia calculation failure as this area corresponds to separated fragments.

### 6.2.1.2 Cranking Model for Deformation Inertia Tensor Calculation

In a symmetric way to the PES computation, a microscopic approach for the deformation inertia can be made by using the cranking model. In this approach the single-particle energies and wave functions obtained with the microscopic model described in Chapter 5 will be used to obtain a collective inertia tensor. The cranking model was first developed by Inglis [18] to obtain the *rotational inertia momentum* (not the *deformation inertia tensor*). This former rotational inertia momentum will be detailed later in this chapter. Yet this approach is quite general to any collective coordinates. It was also further developed by Belyaev to include effects of the pairing interaction. The cranking inertia tensor  $B_{ij}^{\text{cr}}$  is defined as [20]

$$B_{ij}^{\text{cr}}(\vec{q}) = 2\hbar^2 \sum_m \frac{\langle 0 | \frac{\partial}{\partial q_i} | m \rangle \langle m | \frac{\partial}{\partial q_j} | 0 \rangle}{E_m - E_0}, \quad (6.10)$$

where 0 stands for the ground state and  $m$  for an excited state. The excited state  $m$  can be written as the superposition of two quasiparticle excitations  $|m\rangle = |\nu\mu\rangle$ , and thus

Belyaev derived [19]

$$\left\langle \nu\mu \left| \frac{\partial}{\partial q_i} \right| 0 \right\rangle = -i(u_\nu v_\mu \pm v_\nu u_\mu) \left\langle \nu \left| \frac{\partial}{\partial q_i} \right| \mu \right\rangle - \frac{\delta_{\nu\mu}}{v_\nu} \frac{\partial u_\nu}{\partial q_i}, \quad (6.11)$$

where  $v_\nu$  and  $u_\nu$  are the occupancy and vacuum numbers of the pairing model (*cf.* Section 5.3 of Chapter 5). Here again for this introduction of the model, only even numbers of particles are considered. The  $\pm$  sign depends on the property of the operator  $\partial/\partial q_i$ , according to

$$\left\langle \bar{\mu} \left| \frac{\partial}{\partial q_i} \right| \bar{\nu} \right\rangle = \pm \left\langle \nu \left| \frac{\partial}{\partial q_i} \right| \mu \right\rangle. \quad (6.12)$$

In the following, it will be assumed a positive sign for this expression. The diagonal terms of Eq. 6.12 are assumed to vanish, meaning that inserting Eq. 6.11 into Eq. 6.10, and using the quasi-particle energies  $E_m - E_0 = E_\nu + E_\mu$ , it leads to

$$B_{ij}^{\text{cr}}(\vec{q}) = 2\hbar^2 \sum_{\mu\nu} \frac{\left\langle \nu \left| \frac{\partial}{\partial q_i} \right| \mu \right\rangle \left\langle \mu \left| \frac{\partial}{\partial q_j} \right| \nu \right\rangle}{E_\nu + E_\mu} (u_\nu v_\mu + v_\nu u_\mu)^2 + \hbar^2 \sum_{\nu} \frac{1}{v_\nu^2} \frac{\partial u_\nu}{\partial q_i} \frac{\partial u_\nu}{\partial q_j} \frac{1}{E_\nu}. \quad (6.13)$$

Brack et al. [20] modified this expression using the Fermi energy  $\lambda$  and pairing energy  $\Delta$  that are involved in the pairing model (the BCS model in this case). They used the following relation [150]

$$(E_m - E_0) \left\langle 0 \left| \frac{\partial}{\partial q_i} \right| m \right\rangle = \left\langle 0 \left| \left[ \hat{H}, \frac{\partial}{\partial q_i} \right] \right| m \right\rangle = - \left\langle 0 \left| \frac{\partial \hat{H}}{\partial q_i} \right| m \right\rangle, \quad (6.14)$$

where  $\hat{H}$  is the single-particle Hamiltonian, and obtained

$$B_{ij}^{\text{cr}}(\vec{q}) = 2\hbar^2 \sum_{\mu\nu} \frac{\left\langle \nu \left| \frac{\partial \hat{H}}{\partial q_i} \right| \mu \right\rangle \left\langle \mu \left| \frac{\partial \hat{H}}{\partial q_j} \right| \nu \right\rangle}{(E_\nu + E_\mu)^3} (u_\nu v_\mu + v_\nu u_\mu)^2 + P_{ij}, \quad (6.15)$$

where

$$\begin{aligned} P_{ij} = \frac{\hbar^2}{4} \sum_{\nu} \frac{1}{E_\nu^5} & \left[ \Delta^2 \frac{\partial \lambda}{\partial q_i} \frac{\partial \lambda}{\partial q_j} + (\epsilon_\nu - \lambda)^2 \frac{\partial \Delta}{\partial q_i} \frac{\partial \Delta}{\partial q_j} + \Delta(\epsilon_\nu - \lambda) \left( \frac{\partial \lambda}{\partial q_i} \frac{\partial \Delta}{\partial q_j} + \frac{\partial \lambda}{\partial q_j} \frac{\partial \Delta}{\partial q_i} \right) \right. \\ & - \Delta^2 \left( \frac{\partial \lambda}{\partial q_i} \left\langle \nu \left| \frac{\partial \hat{H}}{\partial q_j} \right| \nu \right\rangle + \frac{\partial \lambda}{\partial q_j} \left\langle \nu \left| \frac{\partial \hat{H}}{\partial q_i} \right| \nu \right\rangle \right) \\ & \left. - \Delta(\epsilon_\nu - \lambda) \left( \frac{\partial \Delta}{\partial q_i} \left\langle \nu \left| \frac{\partial \hat{H}}{\partial q_j} \right| \nu \right\rangle + \frac{\partial \Delta}{\partial q_j} \left\langle \nu \left| \frac{\partial \hat{H}}{\partial q_i} \right| \nu \right\rangle \right) \right], \quad (6.16) \end{aligned}$$

where  $\epsilon_\nu$  are the single-particle energies (not the quasiparticle energies  $E_\nu$ ). Even if Eqs. 6.15 and 6.16 seem complex, they are directly derived from Eq. 6.11, the BCS equations (*cf.* Chapter 5) and the relation

$$\frac{\partial \epsilon_\nu}{\partial q_i} = \left\langle \nu \left| \frac{\partial \hat{H}}{\partial q_i} \right| \nu \right\rangle. \quad (6.17)$$

Here Eq. 6.16 has been corrected from a misprint reported in Ref. [151]. Brack et al. [20] also derived expressions for the derivatives  $\partial\lambda/\partial q_i$  and  $\partial\Delta/\partial q_i$  that simplify the computations (the only remaining derivatives are related to the Hamiltonian), these derivatives are expressed as

$$\frac{\partial\lambda}{\partial q_i} = \frac{ac_i + bd_i}{a^2 + b^2} \quad \text{and} \quad \frac{\partial\Delta}{\partial q_i} = \frac{bc_i - ad_i}{a^2 + b^2}, \quad (6.18)$$

where

$$\begin{aligned} a &= \Delta \sum_{\nu} \frac{1}{E_{\nu}^3}, & b &= \sum_{\nu} \frac{\epsilon_{\nu} - \lambda}{E_{\nu}^3}, \\ c_i &= \Delta \sum_{\nu} \frac{\langle \nu | \frac{\partial \hat{H}}{\partial q_i} | \nu \rangle}{E_{\nu}^3}, & d_i &= \sum_{\nu} (\epsilon_{\nu} - \lambda) \frac{\langle \nu | \frac{\partial \hat{H}}{\partial q_i} | \nu \rangle}{E_{\nu}^3}. \end{aligned} \quad (6.19)$$

For the computation of the  $\partial\hat{H}/\partial q_i$  term, it is usually assumed [20] that

$$\frac{\partial \hat{H}}{\partial q_i} \approx \frac{\partial \hat{V}}{\partial q_i} \quad (6.20)$$

where  $\hat{V}$  is the scalar potential of the Hamiltonian.

The cranking inertia tensor as described above has been implemented during this work. In the cranking model, the two types of nucleons provide two components  $B^{\text{Cr(n)}}$  and  $B^{\text{Cr(p)}}$ , respectively for neutrons and protons, that are summed to obtain the eventual nucleus deformation inertia  $B^{\text{Cr}}$ .

$$B^{\text{Cr}} = B^{\text{Cr(n)}} + B^{\text{Cr(p)}} \quad (6.21)$$

An example is shown in Fig. 6.8 for the neutron contribution of  $^{240}_{94}\text{Pu}$ . On the contrary to the very regular variation in the Werner-Wheeler approach (*cf.* Fig. 6.7), the cranking model leads to many fluctuations related to the nuclear structure and to the changes in the nucleon wave functions as the nucleus deforms. The tendency of the  $B_{cc}$  and  $B_{ch}$  components to raise as  $c$  increases can be seen for both the Werner-Wheeler and the cranking models. Yet, the order of magnitude of the inertia is quite different for both models. As said earlier, the Werner-Wheeler still needs deeper verification, and this difference of magnitude may be caused by an error in the implementation. But it is to be expected that such different approaches may lead to very different results. In Ref. [151], it is reported that a difference between the two approaches could be as large as one order of magnitude, which is quite consistent with the present results. Finally, in Fig. 6.8, the square root of the  $B^{\text{Cr(n)}}$  determinant is also shown as a verification of the positiveness of  $\det[B^{\text{Cr(n)}}]$ .

To verify the implementation of the cranking model the method described in Ref. [151] was applied. In this method, the single-particle model described in Chapter 5 is used with a perturbed spheroid shape parameterization. In the analytical test case that will be described now, a single shape parameter  $\epsilon_2$  is retained to describe the shape (*cf.* Appendix B.1). The nuclear scalar potential used in the single-particle Hamiltonian is a deformed harmonic oscillator (not a Yukawa-folded potential). No Coulomb potential and no spin-orbit coupling are present in the Hamiltonian. Thus the analytical base functions  $|n_r n_z \Lambda \Sigma\rangle$  defined in Chapter 5 are the exact single-particle wave functions. The Hamiltonian potential  $\hat{V}^{\text{HO}}$  is defined by

$$\hat{V}^{\text{HO}} = \frac{1}{2}m(\omega_{\perp}^2 \rho^2 + \omega_z^2 z^2) = \frac{1}{2} [\hbar\omega_{\perp}\eta + \hbar\omega_z\xi^2], \quad (6.22)$$

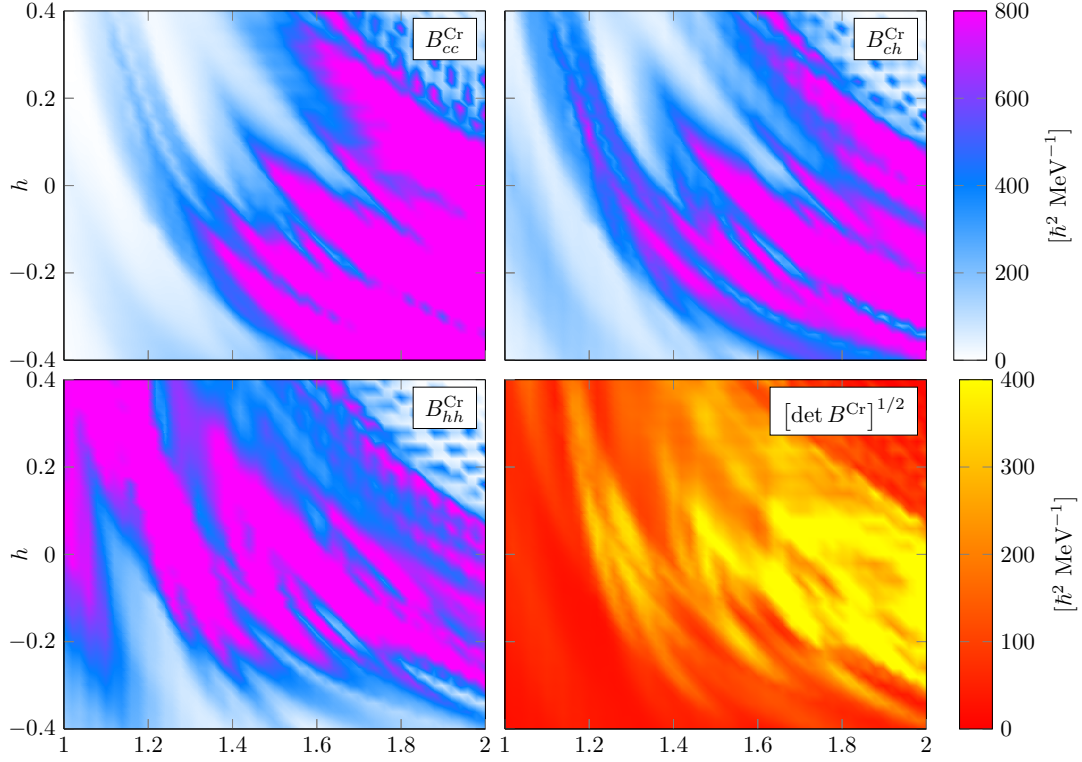


Figure 6.8 – Neutron contribution to the deformation inertia tensor  $B^{\text{Cr}(n)}$  calculated with the cranking model for  $^{240}\text{Pu}$ . The shape is described with generalized spheroid shape parameterization  $(c, h)$ . The three components of the tensor ( $B_{cc}^{\text{Cr}(n)}$ ,  $B_{ch}^{\text{Cr}(n)}$  and  $B_{hh}^{\text{Cr}(n)}$ ) are shown. The square-root of inertia tensor determinant  $\sqrt{\det B^{\text{Cr}(n)}}$  is also shown.

where  $m$  is the mass of the nucleon,  $\eta$  and  $\xi$  are the reduced coordinates defined in Chapter 5 (*cf.* Eq. 5.55), and

$$\omega_{\perp} = \omega_0 \left(1 + \frac{\epsilon_2}{3}\right) \quad \text{and} \quad \omega_z = \omega_0 \left(1 - \frac{2\epsilon_2}{3}\right). \quad (6.23)$$

The  $\omega_0$  parameter is defined so that  $\omega_{\perp}^2 \omega_z$  is independent of  $\epsilon_2$  and is given by

$$\omega_0 = \omega_0^0 \left[1 - \epsilon_2^2 \left(\frac{1}{3} + \frac{2\epsilon_2}{27}\right)\right]^{-1/3}. \quad (6.24)$$

The  $\omega_0^0$  parameter is similar to the one introduced in Chapter 5, *cf.* Eq. 5.54. The Hamiltonian derivative of Eq. 6.20 can be written

$$\frac{d\hat{H}}{d\epsilon_2} \approx \frac{d\hat{V}^{\text{HO}}}{d\epsilon_2} = 3\hbar\omega_0^0 [f_1(\epsilon_2)\eta + f_2(\epsilon_2)\xi^2], \quad (6.25)$$

where

$$f_1(\epsilon_2) = \frac{\epsilon_2(\epsilon_2 + 6) + 9}{[27 - \epsilon_2^2(9 + 2\epsilon_2)]^{4/3}} \quad \text{and} \quad f_2(\epsilon_2) = 2 \frac{\epsilon_2(2\epsilon_2 + 3) - 9}{[27 - \epsilon_2^2(9 + 2\epsilon_2)]^{4/3}}. \quad (6.26)$$

Equation 6.25 differs from the corresponding expression in Ref. [151] by a factor of 2. It seems that the authors of Ref. [151] derived the right-hand side of Eq. 6.22 with respect of  $\epsilon_2$  without considering the  $\eta$  and  $\xi$  dependency on  $\epsilon_2$ . This is unfortunately propagated through the whole paper.

The inertia tensor is reduced to a scalar function (as only one deformation parameter is considered). Its expression (Eq. 6.15) reduces to

$$B^{\text{cr}}(\epsilon_2) = 18\hbar^2[\hbar\omega_0^0]^2 \underbrace{\sum_{\mu\nu} \frac{|\langle\nu|f_1(\epsilon_2)\eta + f_2(\epsilon_2)\xi^2|\mu\rangle|^2}{(E_\nu + E_\mu)^3}}_{D(\epsilon_2)} (u_\nu v_\mu + v_\nu u_\mu)^2 + P_{\epsilon_2}(\epsilon_2). \quad (6.27)$$

The coupling matrix elements  $\langle\nu|f_1(\epsilon_2)\eta + f_2(\epsilon_2)\xi^2|\mu\rangle$  can be computed analytically using the expression of the wave functions  $\langle\nu| = \langle n'_r n'_z \Lambda' \Sigma' |$  and  $|\mu\rangle = |n_r n_z \Lambda \Sigma\rangle$  (defined in Chapter 5). The analytical derivation eventually yields

$$\begin{aligned} \langle\nu|f_1(\epsilon_2)\eta + f_2(\epsilon_2)\xi^2|\mu\rangle &= \delta_{\Lambda,\Lambda'}\delta_{\Sigma,\Sigma'}\delta_{n'_z,n_z}f_1(\epsilon_2)\left[(2n_r+1+\Lambda)\delta_{n'_r,n_r}\right. \\ &\quad \left.-\sqrt{n_r(n_r+\Lambda)}\delta_{n'_r,n_r-1}-\sqrt{(n_r+1)(n_r+\Lambda+1)}\delta_{n'_r,n_r+1}\right] \\ &\quad +\delta_{\Lambda,\Lambda'}\delta_{\Sigma,\Sigma'}\delta_{n'_r,n_r}f_2(\epsilon_2)\left[(n_z+\tfrac{1}{2})\delta_{n'_z,n_z}\right. \\ &\quad \left.+\tfrac{1}{2}\sqrt{n_z(n_z-1)}\delta_{n'_z,n_z-2}+\tfrac{1}{2}\sqrt{(n_z+2)(n_z+1)}\delta_{n'_z,n_z+2}\right]. \end{aligned} \quad (6.28)$$

Here again, this result differs from the corresponding expression in Ref. [151] in which two non-diagonal terms were omitted. The  $P_{\epsilon_2}$  expression is obtained from Eq. 6.16 and reduces to [151]

$$\begin{aligned} P_{\epsilon_2}(\epsilon_2) &= \frac{2\hbar^2}{8} \sum_{\nu} \frac{1}{E_{\nu}^5} \left[ \left( \Delta \frac{d\lambda}{d\epsilon_2} \right)^2 + (\epsilon_{\nu} - \lambda)^2 \left( \frac{d\Delta}{d\epsilon_2} \right)^2 + 2\Delta(\epsilon_{\nu} - \lambda) \frac{d\lambda}{d\epsilon_2} \frac{d\Delta}{d\epsilon_2} \right. \\ &\quad \left. - 2\Delta^2 \frac{d\lambda}{d\epsilon_2} \left\langle \nu \left| \frac{d\hat{V}}{d\epsilon_2} \right| \nu \right\rangle - 2\Delta(\epsilon_{\nu} - \lambda) \frac{d\Delta}{d\epsilon_2} \left\langle \nu \left| \frac{d\hat{V}}{d\epsilon_2} \right| \nu \right\rangle \right]. \end{aligned} \quad (6.29)$$

The pairing and Fermi energies involved in Eq. 6.29 are computed using the usual BCS formalism and Eqs. 6.18 and 6.19.

A comparison between the implemented general model and the derived analytical model is shown in Fig. 6.9 where both  $D(\epsilon_2)$  defined in Eq. 6.27 and  $P_{\epsilon_2}$  obtained from Eq. 6.29 are shown.

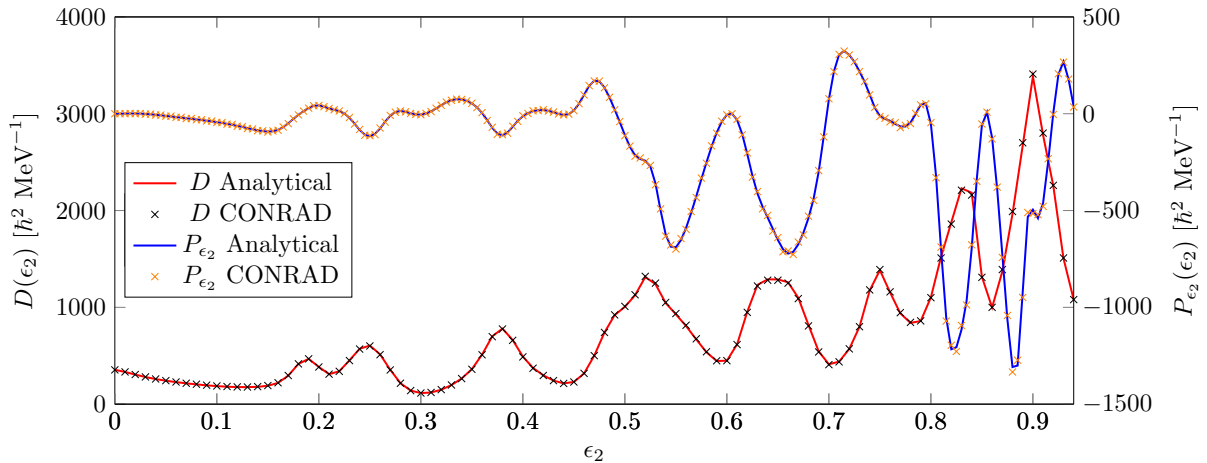


Figure 6.9 – Comparison of results obtained with the analytical cranking model and the CONRAD cranking model.

The two models for the inertia tensor are thus available in the CONRAD code, the Werner-Wheeler model and the cranking model. They can now be used to investigate the effect of the two very different approaches on the determination of the fission path.

### 6.2.2 Action Minimization and Path

Finding the least-action path consists in finding the sequence  $L$  of shapes the deforming nucleus will take, so that the action integral (Eq. 6.2) is minimized. Several techniques can be used to obtain such a path  $L$ . When the PES  $V(\vec{q})$  is given as a grid, for instance when each coordinate  $q_i$  spans over an equally spaced range of values, the Dijkstra [152] or the  $A^*$  algorithms [153] can be used. They consist in an exploratory approach of the grid. The two algorithms will not be detailed here, only a simplified version of the Dijkstra algorithm will be explained. Given two points of the grid, a starting point and an ending point, the algorithm will explore from the starting point, all paths to “neighboring” points, then to the neighboring points of this neighbor, *etc.* At each step the algorithm tests if a shortest path has been found from the starting point to the current neighbors. This approach, has two main liabilities. First, the computation time can be prohibitive if the calculation grid is refined, especially using the Dijkstra algorithm. Additionally, the amount of required memory can be very large, even for current computers, depending on the implementation. The Dijkstra approach has been tested with a procedure implemented in the Boost C++ library [154]. Yet, it was necessary to make an internal implementation to reduce the memory use. It must also be noticed that the exploring graph (*i.e.* the grid) cannot be interpolated without increasing the number of points of the grid and thus the computational cost. The paths obtained with this method have a coarse shape even if the grid is fine enough to perform proper interpolations. The second issue related to these methods is that the definition of a one-dimensional deformation parameter is not straightforward. It should yet be noted that the Dijkstra algorithm has the advantage of yielding the exact solution. In addition, it has some advantages when the “ending point” is not defined *a priori* as the Dijkstra algorithm compute the shortest path from a starting point to all points without too much extra computation time.

Other methods exist, the one retained for this study is the Ritz method [155]. In this method the starting point  $\vec{q}^{\text{GS}}$  and ending point  $\vec{q}^{\text{FIS}}$  must be known *a priori*. An evolution function  $q_i(x)$  is associated to each coordinate.

$$q_i(x) = \sum_{k=1}^N a_k^i \sin(k\pi x) + (q_i^{\text{FIS}} - q_i^{\text{GS}})x + q_i^{\text{GS}}, \quad (6.30)$$

where  $x$  is a parameter evolving in  $[0, 1]$ . Here the  $a_k^i$  parameters must be found to minimize Eq. 6.2; that becomes

$$S = \int_0^1 dx \sqrt{\sum_{ij} B_{ij}(\vec{q}) \frac{dq_i}{dx} \frac{dq_j}{dx} [V(\vec{q}) - V(\vec{q}^{\text{GS}})]}. \quad (6.31)$$

The problem becomes a minimization of a function, Eq. 6.31, over its range of definition that is related to the  $a_k^i$ . For the global minimum search the NLOpt [156] optimization library has been used<sup>4</sup>. One disadvantage of this Ritz representation is that the parameters  $a_k^i$  are strongly correlated with each-other, and thus several sets of parameter values can describe very similar paths (no uniqueness of the solution). This property is not yet a problem for eventual applications because the similar paths would lead to similar fission barriers. However this feature can be an issue for the global optimum search. Indeed the

---

<sup>4</sup>The global optimum search can be done using several algorithms, to simplify the comparisons presented in this work, the GN\_DIRECT algorithm has been used in all calculations. Yet a sensitivity study of the optimum search results with respect of the algorithm should be done.



program searches for the *global* optimum and several parameter sets can lead to similar path (and thus to similar value of the action integral). It would take time for the program to determine which path is the best. In practice a timeout is set to the optimization. If the computation time of the minimization exceeds the timeout, the NLopt program returns the best path that has been found.

Several ending points  $\vec{q}^{\text{GS}}$  are tested to get the one with the smallest action integral. The tested points are those contained in the “fission line” defined for the least-energy method. In the case of three or more dimensions, this line becomes a surface or a hyper surface. It should be stated here that the algorithm, while searching for the  $a_k^i$  coefficients, may “explore” deformation area where the  $V(\vec{q}) < V(\vec{q}^{\text{GS}})$ . This occurs for example when the path is close to the chosen ending point. Indeed the ending point is defined as the first point of the grid that has an energy  $V(\vec{q})$  below  $V(\vec{q}^{\text{GS}})$ . As the grid can be coarse, the integration method computing Eq. 6.31 may need to evaluate the function in a deformation region where  $V(\vec{q}) < V(\vec{q}^{\text{GS}})$  and thus the square root results in complex values. This is avoided in practice by taking the real part of the square root, the action integral remains unchanged. Another feature concerning this method is that the final one-dimensional path may need to be rescaled along the  $x$  axis so that the potential for  $x = 1$  is equal to  $V(\vec{q}^{\text{GS}})$ . This has in practice no effects on the eventual fission transmission coefficient if the one-dimensional deformation inertia is also scaled. It can be stated here that it is possible to operate a variable change [157] so that the deformation inertia matrix is diagonal and independent of the deformation. In such cases, it is the potential that “absorbs” the deformation dependency of the inertia tensor. The deformation inertia still needs to be computed but the subsequent equations can be simplified.

### 6.3 Least-Energy V.S. Least-Actions

To illustrate the difference between the least-energy and the least-action methods, the paths resulting from the  $^{240}\text{Pu}$  2D PES are shown in Fig. 6.10. The least-action path search is performed using the Werner-Wheeler inertia tensor (white curve) and the Cranking inertia tensor (purple curve). In the beginning of the paths, the cranking path seems to follow the least-energy path (orange curve), then it differs to reach the fission line in a more “direct” way than the least-energy path. On the opposite, the Werner-Wheeler path crosses the hill between the first and intermediate wells then avoids the bottom of the intermediate well and directly reaches the fission line. The Werner-Wheeler inertia tensor has very slow variations for  $c < 1.4$  (cf. Fig. 6.7); thus one would have expected the path to follow the PES valleys. On the contrary, the Werner-Wheeler path seems to “ignore” the structures of the PES. This may indicate an issue with the present Werner-Wheeler implementation.

The practical advantage of the least-action technique is that it provides a convenient deformation abscissa  $x$  (cf. Eq. 6.30). It also provides one-dimensional deformation-dependent *inertia parameter*  $\mu(x)$  defined by

$$\mu(x) = \sum_{ij} B_{ij}(\vec{q}) \frac{dq_i}{dx} \frac{dq_j}{dx}. \quad (6.32)$$

For least-energy paths, a constant inertia parameter  $\mu^{\text{const}}$  is considered. Its value is given by [22]

$$\mu^{\text{const}} = 0.054 A^{5/3} \hbar^2 \text{ MeV}^{-1}, \quad (6.33)$$



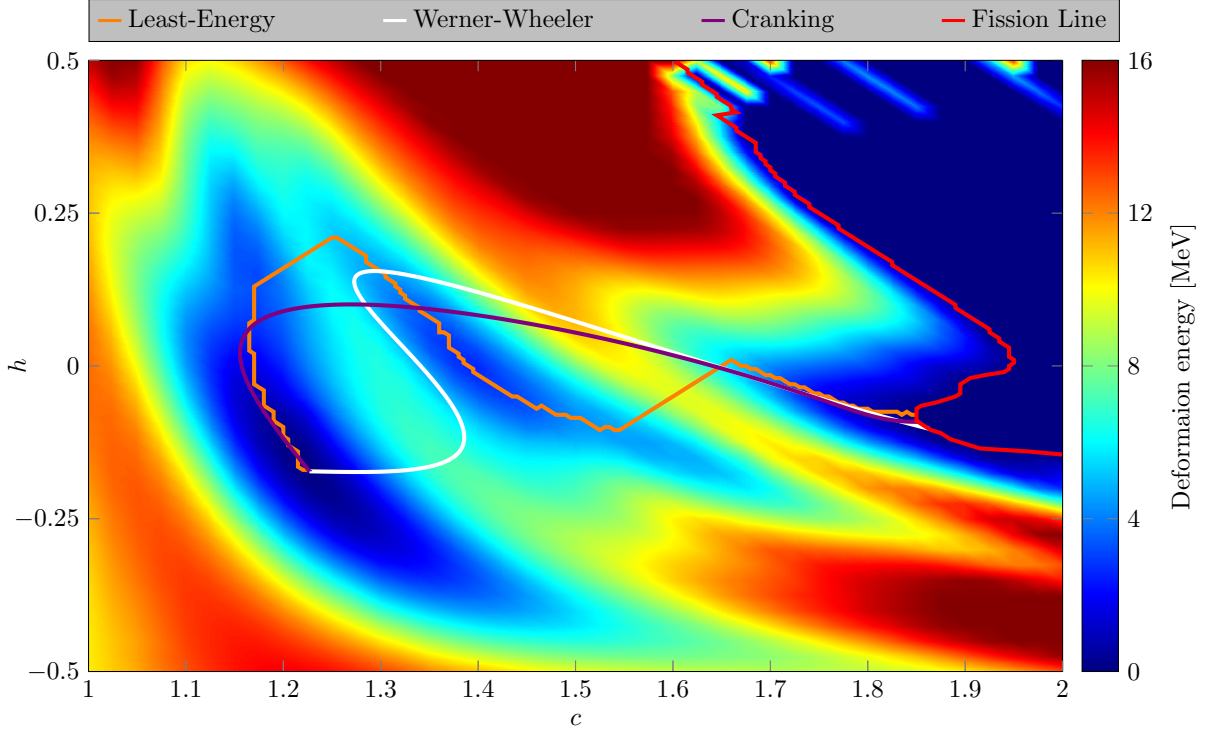


Figure 6.10 – Fission paths obtained with the least-energy and least-action methods. For the least-action method, two types of deformation inertia tensor are used (Cranking and Werner-Wheeler).

where  $A$  is the mass number of the fissioning nucleus. In the present case, it is  $^{240}\text{Pu}$ , so that

$$\mu^{\text{const}} \approx 500\hbar^2 \text{ MeV}^{-1}. \quad (6.34)$$

Figure 6.11 shows the least action paths obtained with the  $^{240}\text{Pu}$  2D PES where the inertia parameter  $\mu$  is either obtained from the Werner-Wheeler model or the cranking model. The constant inertia parameter  $\mu^{\text{const}}$  is also shown for comparison. It can be seen that the saddle points heights are quite similar in the two approaches. The second saddle point is of course very high due to the 2D limitation of the PES in this case. The widths of the first barriers differ significantly between the two methods, so do the widths of intermediate wells. The deformation inertiae differ significantly in terms of magnitude and shape (*cf.* Figs 6.7 and 6.8). These differences in deformation inertia, as exemplified by Fig. 6.11, this will have a dramatic effect on the eventual transmission coefficient calculation, as it will be demonstrated later in this chapter.

Similar calculations were attempted in the case of the 3D PES, however it happened that the present Werner-Wheeler implementation make the inertia tensor have negative eigenvalues. This is nonphysical as it would imply that a shape parameterization could be found, in which the inertia tensor is diagonal with at least one of the diagonal term being negative. This is incompatible with the physical definition of inertia that is always a positive quantity. Therefore *only the cranking inertia tensor is used for the rest of the present study* while considering **3D** PES. The corresponding result are shown in the left part of Fig. 6.12. Contrary to the least-energy case, it can be seen that the barriers obtained from the 2D and 3D PES are completely different. In the 3D case, it seems that the first barrier height is lower than in the least-energy case, which is not possible because of the way the least energy path is constructed. The results comes for the fact that the least-action path does not reached the true intermediate well. The first low

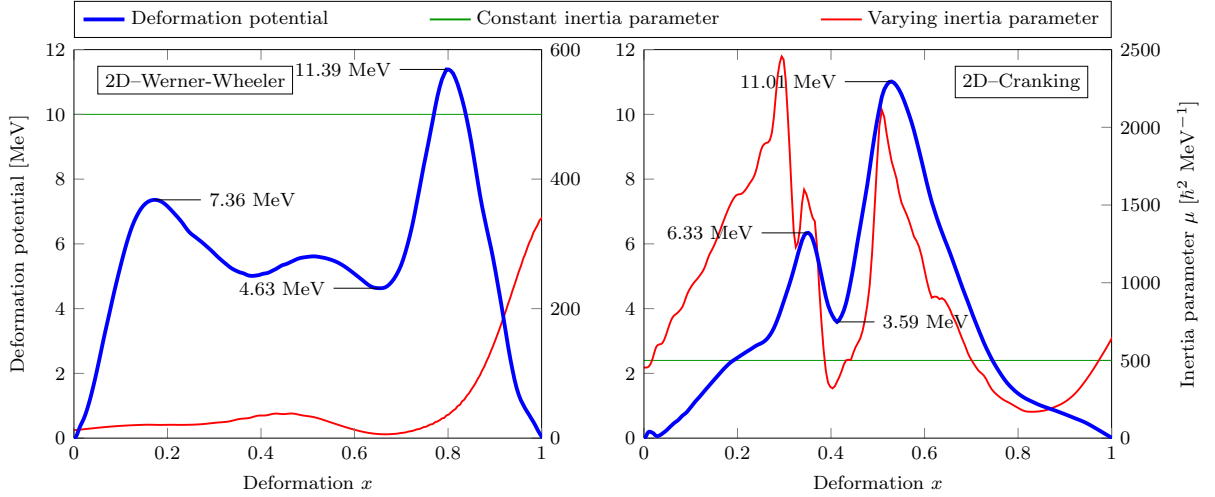


Figure 6.11 – One-dimensional least-action potentials (blue curves) and inertia parameters (red curves) obtained from the 2D PES of  $^{240}\text{Pu}$  using either the Werner-Wheeler (left) and cranking (right) deformation inertia tensors. The constant inertia parameter (green curve) is shown for comparison.

barrier, about 2 MeV height is not a barrier leading to the same intermediate well as in the least-energy case. The explanation of this smaller “first” saddle point height can be understood if one considers the projection of the path (defined in a 3D space  $(c, h, \alpha)$ ) on the 2D plane  $(c, h, \alpha = 0)$ . The path obtained in this case shows that the nucleus “remains” in the first well prior to deforms towards fission. The effects of the *second well* (visible on the PES figure background near  $(c, h) = (1.5, 0)$ ) are only slightly reproduced in the one-dimension barrier (left part of the figure) at the top of the “second barrier”. The fluctuations observed on the top of the “second barrier” do not correspond to the background potential because in this part of the path, the nucleus shape has a non-zero  $\alpha$  value.

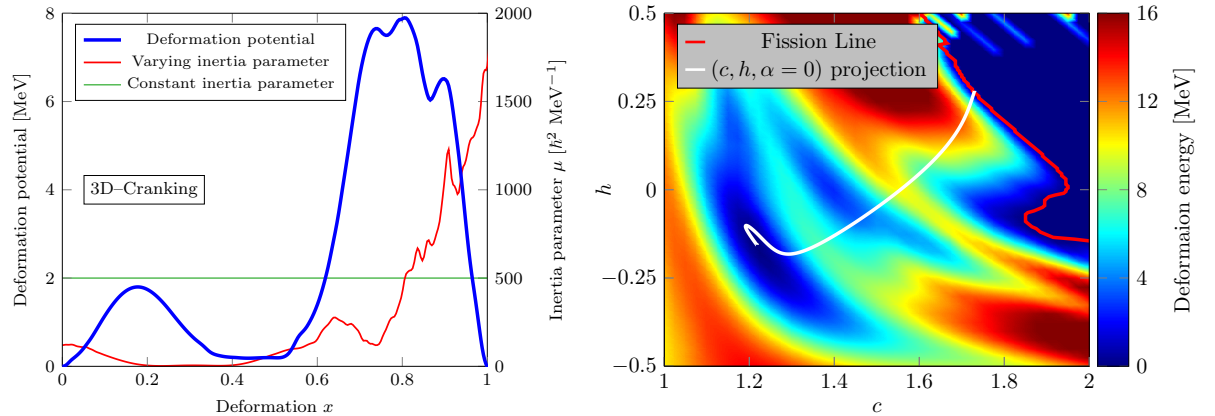


Figure 6.12 – (Left) One-dimensional potential (blue curve) and inertia parameter (red curve) obtained for the  $^{240}\text{Pu}$  with the least-action method applied to the 3D PES and using cranking deformation inertia tensor. The constant inertia parameter (green curve) is shown for comparison. (Right) Projection of the corresponding 3D path on the  $(c, h, \alpha = 0)$  plane. The deformation potential also corresponds to the  $(c, h, \alpha = 0)$  “slice”.

An alternative method in the search of the least action path consists in changing the selected ending point. The ending point is no longer the point of the fission line having

the smallest calculated action integral (calculated by Eq. 6.31). The new ending point is the one related to the lowest barrier height of the path (which is specific to the ending-point). The corresponding results, 3D-Cranking- $V_{\min}$ , are shown in Fig. 6.13. In this case, the one-dimensional fission barrier leads to first saddle point and intermediate well heights that are similar to those obtained with the 2D PES (*cf.* Fig. 6.11). Additionally it can be noted that in this case, the one-dimensional deformation inertia behavior seems anti-correlated to the barrier shape.

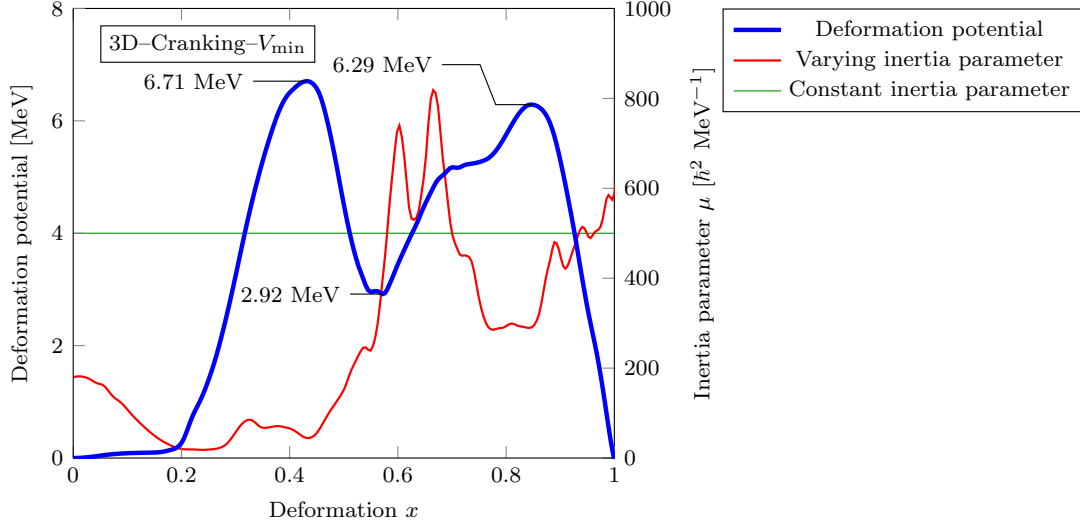


Figure 6.13 – One-dimensional potential (blue curve) and inertia parameters (red curve) obtained for the  $^{240}\text{Pu}$  with the least-action- $V_{\min}$  method for the 3D PES and using the cranking deformation inertia tensor. The constant inertia parameter (green curve) is shown for comparison. The least-action method used here differs from the one used in Fig. 6.12 as the ending point is chosen to be the one related the lowest barrier height.

At this point, two main options seem promising for the final application of fission cross section modeling: the least-energy method and the least-action- $V_{\min}$  method (because of the reasonable values of the barrier heights). Yet the regular least-action method will be preserved in the next step (barrier transmission coefficient calculation), so that the difference between the two least-action methods can be highlighted.

## 6.4 Numerical Transmission Coefficients

Now that the one-dimensional potential has been extracted from the PES, the related transmission coefficient can be calculated. As the shape of the potential can be very general, a numerical method must be used to obtain the fission barrier transmission coefficient out of a numerical deformation potential. Two cases will be treated depending if the one-dimensional deformation inertia deformation-dependent or not.

### 6.4.1 Deformation-Independent Effective Mass Parameter

The barrier transmission coefficient can be computed with the same approach than the in Hill-Wheeler and Cramer-Nix models (*cf.* Chapter 4). The fission process can be modeled as a fictive particle tunneling through a potential barrier. The difference in this case is that the deformation potential is numerical, thus no analytical solution can be given

and a numerical approach must be found. If the deformation inertia  $\mu$  is constant with deformation, the particle tunneling process is described by a wave function  $\Psi$  solution of

$$\underbrace{\frac{-\hbar^2}{2\mu} \frac{d^2\Psi}{d\eta^2}}_{\hat{T}\Psi} + V(\eta)\Psi = E\Psi. \quad (6.35)$$

This equation can be written in the general form

$$f''(x) + W(x)f(x) = 0, \quad (6.36)$$

for which many numerical methods exist. Several methods have been implemented, namely:

- The piece-wise *constant* discretization of the potential, analytical solving on each piece. In this method, the potential  $V$  is transformed into a piece-wise constant function. On each constant fragment, an analytical solution of the wave function can be found. The piece-wise wave functions are then smoothly matched to obtain the complete wave function.
- The piece-wise *linear* discretization of the potential. This method differs from the former only by the definition of the analytical solutions that are defined on each piece of linear potential segment.
- The Jeffreys-Wentzel-Kramers-Brillouin method (JWKB) [158]. This method relies on a quasi-classical approximation of the physical tunneling problem.
- The Numerov method [21]. This is “only” a numerical method that can be used to solve differential equation of type of Eq. 6.36. This method is especially efficient in transmission coefficient calculation problems.

In the interest of simplicity and clarity, only the Numerov method will be presented here. The piece-wise and JWKB methods are described in Appendix D.1. The performances of the different numerical methods will then be compared.

#### 6.4.1.1 Numerov Method

The Numerov method does not rely on physical assumptions but only on mathematical hypotheses regarding Eq. 6.36. The variable  $x$  is discretized and the equation is solved “backward” from  $x = x_{\max}$  to  $x = 0$ . If  $\{x_n\}_n$  stand for the discrete abscissae – all separated by a *constant* step  $h$ , a recurrence relation is provided by the method between corresponding ordinates  $\{f_n\}_n$ . The mathematical assumption would be that in this recurrence relation, terms higher than  $h^6$  are neglected. See Appendix D.1.3 for the derivation of the method. The recurrence relation is

$$f_{n-1} = \frac{\left(2 - \frac{5h^2}{6}W_n\right)f_n + \left(1 - \frac{h^2}{12}W_{n+1}\right)f_{n+1}}{1 - \frac{h^2}{12}W_{n-1}}, \quad (6.37)$$

where  $W_n = W(\eta_n)$ . The wave function  $\Psi$  for  $\eta = \eta_N$  can be written in the form

$$\Psi(\eta_N) = b_\infty e^{ik_\infty \eta_N}, \quad (6.38)$$

where  $b_\infty \in \mathbb{C}^*$ . Using this expression, the wave function derivative is

$$\Psi'(\eta_N) = ik_\infty b_\infty e^{ik_\infty \eta_N}. \quad (6.39)$$

Using these expressions for  $\Psi$  and  $\Psi'$ , one assumes that  $h = \eta_N - \eta_{N-1}$  is small enough, so that the wave function for  $\eta = \eta_{N-1}$  can be expressed as

$$\Psi(\eta_{N-1}) = \Psi(\eta_N) - h\Psi'(\eta_N). \quad (6.40)$$

Thus the two first points of the recurrence (Eq. 6.37) are defined and the wave can be computed down to  $\eta = \eta_0$ . Then a same approach than for Eq. 6.40 can be used to obtain from  $\Psi(\eta_0)$  and  $\Psi(\eta_1)$  the values  $\Psi'(\eta_0)$ , then coefficients  $c_0$  and  $b_0$  can be found using the relations

$$\Psi(\eta_0) = b_0 e^{ik_0 \eta_0} + c_0 e^{-ik_0 \eta_0}, \quad (6.41)$$

$$\Psi'(\eta_0) = ik_0 b_0 e^{ik_0 \eta_0} - ik_0 c_0 e^{-ik_0 \eta_0}. \quad (6.42)$$

The transmission coefficient can thus be obtained using Eq. D.7; here recalled

$$T(E) = \frac{k_\infty}{k_0} \left| \frac{b_\infty}{b_0} \right|^2. \quad (6.43)$$

#### 6.4.1.2 Verification and Comparison of the Methods

To check the accuracy and to compare performances of the implemented methods, analytical test cases were analyzed. These analytical cases are detailed in Appendix D.2, they consist in a step (or square) potential, a triangular potential and a triple, smoothly-joint parabola potential. As detailed in Appendix D.2, the Cramer-Nix analytical solution has to be slightly modified to provide a practical baseline. The tests performed with the square and triangular potential will not be presented here but were quite satisfactory. Instead, focus is made on methods comparison with the triple, smoothly-joint, parabola potential.

First, the JWKB method is compared with the analytical case. Even if the JWKB method has the significant advantage to be applicable for general shapes of the potential, and to consist in a single integral, it cannot be used in all cases. As it is shown in analytical examples in Appendix D.2, transmission coefficients can have resonant structures for energies above the barrier maximum that cannot be obtained with the present JWKB approach. In practice the JWKB approximation becomes inaccurate for energies just below and above the barrier maximum. This can be seen in Fig. 6.14, where the analytical “modified” Cramer-Nix model, described in Appendix D.2, has been used as a reference for the calculation. The last resonance before the JWKB method fails is shifted by about 20 keV with respect of the analytical result. For energies above the barrier height, Eq. D.18 cannot be used anymore. In such cases the transmission coefficient value could be arbitrarily set to one but structures observed in the analytical case (black curve in Fig. 6.14) cannot be reproduced. In practice this means that this approach cannot be used for fissile isotopes.

Other methods do not have such restrictions. To compare performances of the implemented methods, an error score  $\delta$  is defined as

$$\delta = \frac{\int dE |T^{\text{num}}(E) - T^{\text{exact}}(E)|}{\int dE T^{\text{exact}}(E)}, \quad (6.44)$$

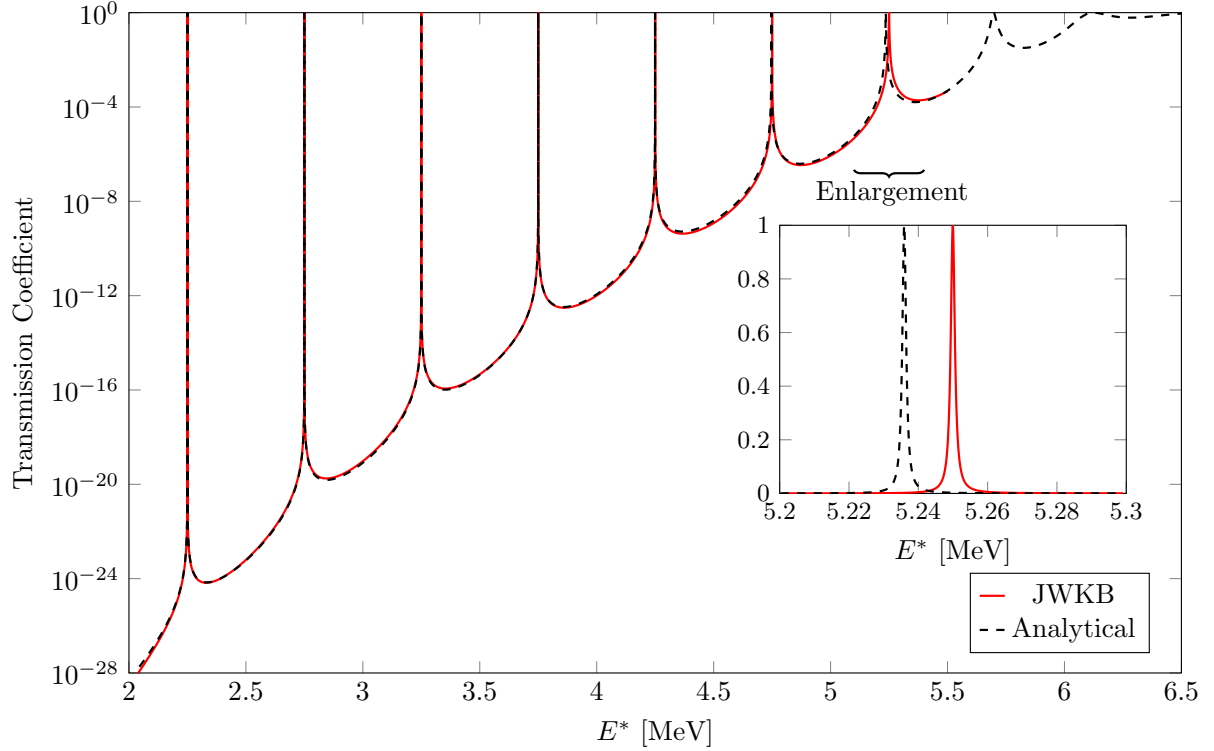


Figure 6.14 – Calculation of the transmission coefficient for the Cramer-Nix potential using the JWKB approximation. Analytical results are also shown. The triple parabola test case potential is defined by  $E_1 = E_3 = 6$  MeV,  $E_2 = 2$  MeV,  $\hbar\omega_1 = \hbar\omega_3 = 1$  MeV,  $\hbar\omega_2 = 0.5$  MeV,  $\mu/\hbar^2 = 0.054A^{5/3}$  (in MeV $^{-1}$ ) where  $A = 240$  (*cf.* Appendix D.2).

where  $T^{\text{num}}$  is the transmission coefficient obtained with a given numerical method, and  $T^{\text{exact}}$  is the corresponding value obtained with a reference analytical model. The integrals are performed over an arbitrary testing energy range. The smaller  $\delta$ , the better the performance. To compare methods, a performance diagram is used where the running time (driven by changing the discretization step) is represented as a function of the error score  $\delta$ . Figure 6.15 shows such a diagram.

The same calculation is performed with the three methods several times with varying discretization, thus yielding different running times and different error scores  $\delta$ . It can be seen that the piecewise linear method has more fluctuating performances than the other methods. This is due to the inherent numerical issues of the method that are explained in Appendix D.2. Unfortunately, the “mixing” with the piecewise constant method does not solve completely the problem. One can also see that this method is significantly less efficient than the two others, because of the time required for the evaluation of the Airy functions. Even if the potential is accurately described with less points than in the constant piecewise method, this gain in discretization is overwhelmed by the computational cost of the Airy functions. It should be noted here that the discretization was performed using the constant deformation step. Unlike in the Numerov method, a uniform discretization grid is not necessary for the piecewise methods and a smartly tuned mesh could change somehow the performance of the method. Finally the Numerov and the piecewise constant methods have similar performances. In general the piecewise constant method is better but if rapidity must prevail over accuracy, the Numerov method should be used instead.

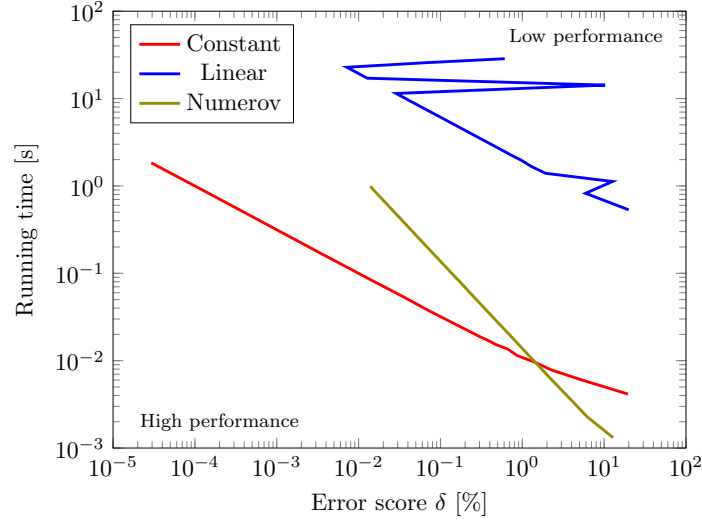


Figure 6.15 – Performance diagram related to the piecewise constant method (Constant), the piecewise linear method (Linear) and the Numerov method (Numerov). The potential used is the triple, smoothly-joint, parabola potential described in Appendix D.2. To make this test representative, each run consists in 500 transmission coefficient calculations defined for energies between 2 and 7 MeV.

### 6.4.2 Deformation-Dependent Effective Mass Parameter

In this case the kinetic operator  $\hat{T}$  of Eq. 6.35 must be modified. A general form satisfying the Hermitian property of the operator and yielding the usual equation when inertia is constant with deformation is

$$\hat{T} = \frac{1}{4} (\mu^\alpha \hat{p} \mu^\beta \hat{p} \mu^\gamma + \mu^\gamma \hat{p} \mu^\beta \hat{p} \mu^\alpha) , \quad (6.45)$$

where  $\alpha$ ,  $\beta$  and  $\gamma$  are real arbitrary parameters satisfying the von Roos [159] condition:  $\alpha + \beta + \gamma = -1$ . If  $\mu$  does not vary, one gets the usual operator

$$\hat{T} = \frac{\hat{p}^2}{2\mu} . \quad (6.46)$$

After some algebraic manipulations, Eq. 6.45 applied to a given wave function  $\Psi$  becomes

$$\hat{T}\Psi = -\frac{\hbar^2}{2\mu} \left[ \Psi'' - \frac{\mu'}{\mu} \Psi' + \left[ [(\beta + \gamma)(\gamma + 1) + 1] \frac{\mu'^2}{\mu^2} - \frac{1}{2}(1 + \beta) \frac{\mu''}{\mu} \right] \Psi \right] . \quad (6.47)$$

To get rid of the  $\alpha$ ,  $\beta$  and  $\gamma$  parameters, the BenDaniel-Duke [160] conditions  $\alpha = \gamma = 0$  and  $\beta = -1$  are used. Equation 6.47 simplifies to

$$\hat{T}\Psi = \frac{1}{2} \hat{p} \frac{1}{\mu} \hat{p} \Psi = -\frac{\hbar^2}{2\mu} \left[ \Psi'' - \frac{\mu'}{\mu} \Psi' \right] . \quad (6.48)$$

As this expression involves a *first* order derivative  $\Psi'$ , the Numerov method described in the previous section cannot be used. A fourth-order Runge-Kutta method has thus been implemented to treat problems with varying inertia.

The fourth-order Runge-Kutta method is a numerical method that can be used to solve differential equation of types

$$u'(\eta) = F[\eta, u(\eta)] . \quad (6.49)$$



In the present case, the differential equation

$$\hat{T}\Psi + V(\eta)\Psi = E\Psi \quad (6.50)$$

can be written

$$\Psi'' - \frac{\mu'}{\mu}\Psi' - \frac{2\mu}{\hbar^2}(V(\eta) - E)\Psi = 0. \quad (6.51)$$

Equation 6.51 can be turned into a form of Eq. 6.49 by defining

$$u = \begin{pmatrix} u_0 \\ u_1 \end{pmatrix} = \begin{pmatrix} \Psi \\ \Psi' \end{pmatrix} \quad \text{and} \quad F[\eta, u] = \begin{pmatrix} \frac{\mu'(\eta)}{\mu(\eta)}u_1 + \frac{2\mu(\eta)}{\hbar^2}(V(\eta) - E)u_0 \\ u_1 \end{pmatrix}. \quad (6.52)$$

Just like in the piecewise methods used when  $\mu$  is constant, the deformation range is discretized, and initial condition

$$u_N = b_\infty e^{ik_\infty \eta_{\max}} \begin{pmatrix} 1 \\ ik_\infty \end{pmatrix} \quad \text{with} \quad b_\infty \in \mathbb{C}^*, \quad (6.53)$$

is imposed on the outermost part of the potential  $\eta = \eta_N = \eta_{\max}$ , where

$$k_\infty = \sqrt{\frac{2\mu}{\hbar^2}[V(\eta_{\max}) - E]}. \quad (6.54)$$

At a given step  $\eta_n$ , the function  $u_n = u(\eta_n)$  can be computed from  $u_{n+1}$  by

$$u_n = u_{n+1} - \frac{h}{6}(k_1 + 2k_2 + 2k_3 + k_4), \quad (6.55)$$

where  $h$  is the constant distance between two points  $\eta_n$  and  $\eta_{n+1}$  and

$$k_1 = F[\eta_n, u_n], \quad (6.56)$$

$$k_2 = F[\eta_n + \frac{h}{2}, u_n + \frac{h}{2}k_1], \quad (6.57)$$

$$k_3 = F[\eta_n + \frac{h}{2}, u_n + \frac{h}{2}k_2], \quad (6.58)$$

$$k_4 = F[\eta_n + h, u_n + hk_3]. \quad (6.59)$$

Once  $u(\eta_0)$  is computed, one can define

$$b_0 = \frac{1}{2ik_0} [ik_0\Psi(\eta_0) - \Psi'(\eta_0)] e^{-ik_0\eta_0}, \quad (6.60)$$

and obtain the transmission coefficient using a slightly modified version of Eq. 6.43:

$$T(E) = \frac{k_\infty \mu(\eta_0)}{k_0 \mu(\eta_{\max})} \left| \frac{b_\infty}{b_0} \right|^2. \quad (6.61)$$

Both accuracy and performance of the method can be analyzed with the same method than in the case of constant inertia. For the analytical case, the same “modified” Cramer-Nix model, described in Appendix D.2 has been used as a baseline. Even though, in this analytical case, inertia is constant, it is still a good verification of the implemented algorithm. The performances of the piecewise constant and Numerov methods (*cf.* Fig. 6.15) are reported in Fig. 6.16 for a comparison with the benefits brought by the Runge-Kutta method. Results of the Numerov method are reported here, yet this method cannot be used when deformation inertia is deformation-dependent. The performances of the method is quite similar to those of the piecewise constant method and even slightly better.

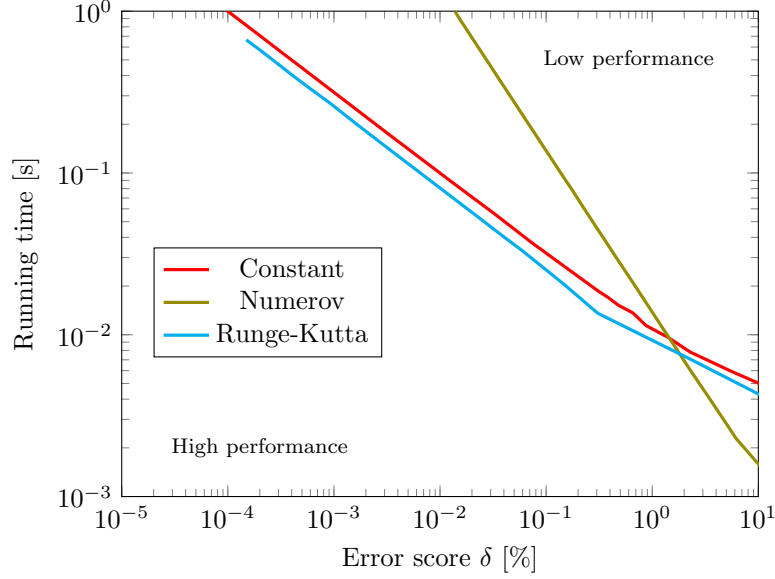


Figure 6.16 – Performance diagram for the piecewise constant method (Constant), the Numerov method (Numerov) and the Runge-Kutta method (Runge-Kutta). The potential used is the triple, smoothly-joint parabola potential described in Appendix D.2. For this test, 500 transmission coefficients are computed for energies between 2 and 7 MeV.

### 6.4.3 Effects of Path Searching Method and Deformation Inertia Tensor on Transmission Coefficient

#### 6.4.3.1 A Test Case

Prior to tackle transmission coefficient calculation for actual potentials, the effect of the deformation-dependent inertia parameter  $\mu(x)$  is analyzed here on a test case. The triple, smoothly-joint, parabola potential described in Appendix D.2 is considered. To highlight the effect of inertia parameter  $\mu$ , four cases are considered.

- The inertia parameter  $\mu(x) = \mu^{\text{const}}$  is constant and given by Eq. 6.33.
- The inertia parameter varies according to<sup>5</sup>

$$B_{\epsilon_2}^{\text{irr}}(\epsilon_2) = \mu^{\text{const}} \left[ 1 - X + X \frac{1 + \frac{2}{9}x^2}{(1 - \frac{1}{3}x^2)^2} \left( 1 - \frac{1}{3}x^2 - \frac{2}{27}x^3 \right)^{-4/3} - 1 \right], \quad (6.62)$$

where  $X$  takes values between 0% (*i.e.*  $\mu(x) = \mu^{\text{const}}$ ) and 100%, namely  $X = 0\%, 1\%, 5\%, 10\%$  and 100%. To avoid over cluttered figures, only the first four values will be used to compute transmission coefficients.

These choices of parameterization of  $\mu$  are illustrated on the left side of Fig. 6.17. It can be seen that the difference between the constant case and the 1% variation is minute. The related transmission coefficients are calculated using the implemented Range-Kutta method, corresponding results are shown on the right side of Fig. 6.17. It can be seen that change in inertia has small effect for the low-energy resonances. However for resonances located just below the barrier maximum (here 6 MeV), the change is dramatic, even for small values of  $X$ . The overall increase of inertia with deformation on transmission coefficient densify the number of observed resonances.

<sup>5</sup>This parameterization is chosen to be consistent with Eq. 5.121.

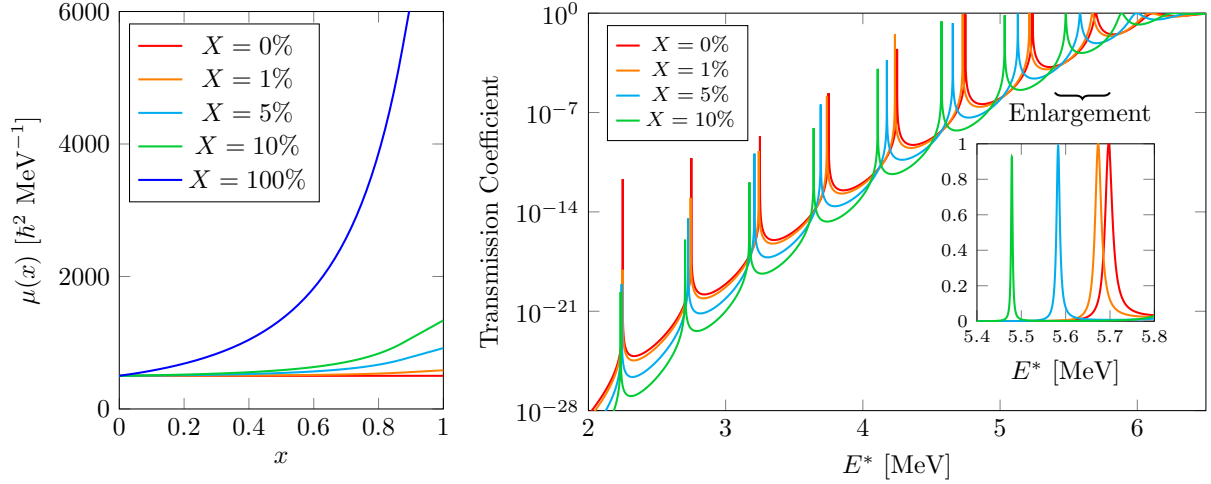


Figure 6.17 – (Left) Inertia parameters used in the test case. (Right) Corresponding transmission coefficients. The triple parabola test case potential is defined by  $E_1 = E_3 = 6$  MeV,  $E_2 = 2$  MeV,  $\hbar\omega_1 = \hbar\omega_3 = 1$  MeV,  $\hbar\omega_2 = 0.5$  MeV,  $\mu/\hbar^2 = 0.054A^{5/3}$  (in  $\text{MeV}^{-1}$ ), where  $A = 240$  (*cf.* Appendix D.2).

#### 6.4.3.2 Actual Barriers and Inertia Parameters

To highlight the dramatic effect of the deformation dependence of the inertia tensor, five different test cases have been treated. All test cases are related to the 3D PES of  $^{240}\text{Pu}$  reduced to a one-dimensional barrier. In all cases the transmission coefficient is calculated using the Runge-Kutta method described here above. These tests will show the effect of the searching method, least-energy (LE), least-action (LA) or least-action with smallest barrier height retained (LA- $V_{\min}$ ). Two cases will be considered in the least-action methods, one using the inertia parameter  $\mu(x)$  obtained with the cranking model, the other using the constant value  $\mu^{\text{const}}$  given by Eq. 6.33. The constant inertia is only related to the one-dimensional calculation, the PES reduction to a one-dimensional potential is always done using the cranking inertia tensor. Present five test cases are:

- Least-energy potential and constant inertia parameter (LE- $\mu^{\text{const}}$ ), *cf.* Fig. 6.6.
- Least-action potential and a varying inertia parameter (LA- $\mu(x)$ ), *cf.* Fig. 6.12.
- Least-action potential and constant inertia parameter (LA- $\mu^{\text{const}}$ ) *i.e.* the least-action path is obtained with the Cranking inertia tensor, but it is a constant inertia parameter that is considered with the one-dimensional barrier, *cf.* Fig. 6.12.
- Least-action potential (with smallest barrier height retained) and a varying inertia parameter (LA- $V_{\min}$ - $\mu(x)$ ), *cf.* Fig. 6.13.
- Least-action potential (with smallest barrier height retained) and constant inertia parameter (LA- $V_{\min}$ - $\mu^{\text{const}}$ ), *cf.* Fig. 6.13.

The four least-action methods are compared in Fig. 6.18. It can be seen that the LA methods (green curves) produce less structures than the LA- $V_{\min}$  methods, this is especially true for LA- $\mu^{\text{const}}$ . This is due to the fact that the LA potential (*cf.* Fig. 6.12) consists almost in a single barrier. This barrier height is also about 2 MeV higher than

the corresponding one of the  $\text{LA-}V_{\min}$  potential. This explain the energy shift (of about 2 MeV) that can be seen between methods (*i.e.* between blue curves on one side and green curves on the other side). A surprising effect is observed comparing the  $\text{LA-}\mu^{\text{const}}$  and  $\text{LA-}\mu(x)$  results; the inclusion of a varying inertia parameter restores structures in the transmission coefficient. This type of phenomenon is proven here to have spectacular effects, but is never considered in evaluation techniques. This effect is less visible for the  $\text{LA-}V_{\min}$  methods because the intermediate well (Fig. 6.13) already induces resonance structures. A last feature can be observed from Fig. 6.18; the deformation-dependent cases (*i.e.* solid lines) exhibit fluctuations up to quite higher energies than the corresponding deformation-independent cases (dashed lines).

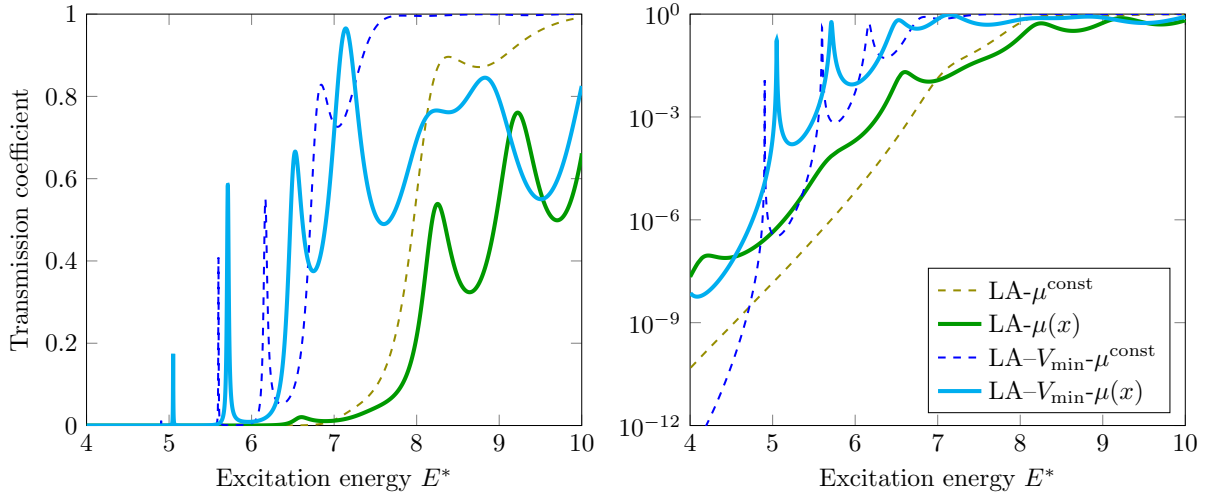


Figure 6.18 – Transmission coefficients calculated using the least-action potential (LA) and using either a constant inertia parameter (dashed curves) or a deformation-dependent inertia parameter (solid curves). The transmission coefficients are shown in linear scale (left) and logarithmic scale (right).

Finally the  $\text{LE-}\mu^{\text{const}}$  and  $\text{LA-}V_{\min}\text{-}\mu(x)$  methods are compared. The related results are shown in Fig. 6.19. Two main features should be noticed. First, the LE method produces many more resonances than the  $\text{LA-}V_{\min}\text{-}\mu(x)$  method, this is probably due to the difference in the shape of the intermediate wells. Second, in the LE case, the transmission coefficient tends to its asymptotic value much faster than in the  $\text{LA-}V_{\min}\text{-}\mu(x)$  case. For energies much above the barrier heights (about 6 MeV in both cases), the  $\text{LA-}V_{\min}\text{-}\mu(x)$  method still exhibits strong fluctuations whereas, in the LE case, the resonances are almost completely damped. One could finally notice that  $\text{LA-}V_{\min}\text{-}\mu(x)$  (respectively LE) leads to a resonance near 5 MeV (respectively 4.5 MeV) that are observed experimentally with surrogate reactions [161, 162].

At this point it is not possible to determine which method is the best suited for cross section modeling as transmission coefficients cannot be confronted with experimental data. To obtain transmission coefficients usable in fission cross section modeling, it is necessary to introduce transition states. To the difference of the usual evaluation method, these transition states must be defined all along the fission path. The method used to deduce them is described in the following section.

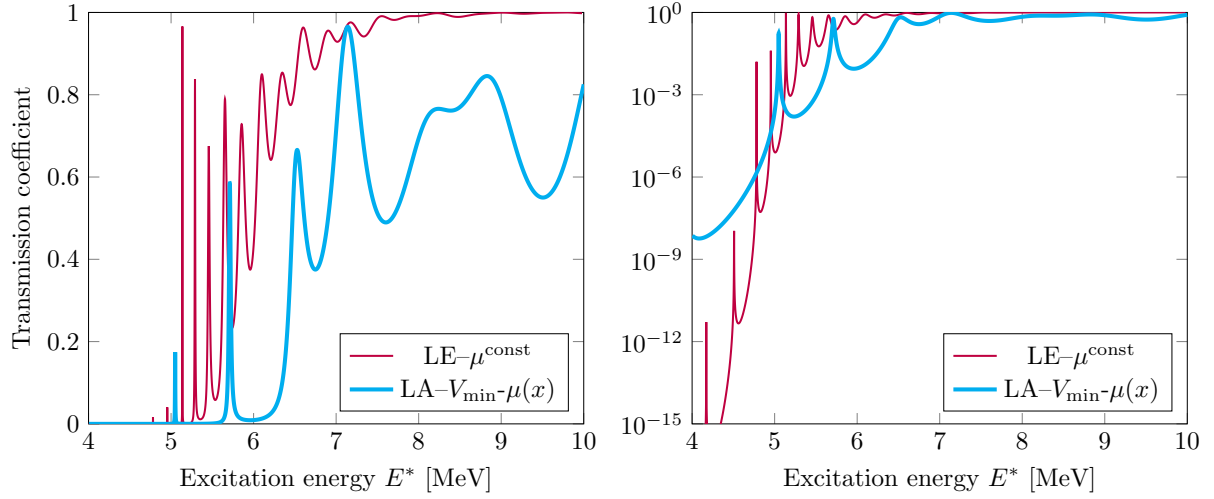


Figure 6.19 – Transmission coefficient calculated using the  $LE-\mu^{\text{const}}$  and  $LA-V_{\text{min}}-\mu(x)$  methods. The transmission coefficients are shown in linear scale (left) and logarithmic scale (right).

## 6.5 Transition states

As was explained in Chapter 4, the transmission coefficient calculated with a barrier shape as obtained with the macroscopic-microscopic model stands for *one* way the nucleus can fission. This latter barrier shape corresponds to configurations where the intrinsic energy (*i.e.* the amount of energy that is not “taken” by the deformation) is minimal. This is why this latter barrier is called the *fundamental* barrier. Additional states can be built “above” the fundamental barrier standing for the configurations where part of the total energy is “consumed” by the intrinsic degrees of freedom. These are the present extension of the single-hump transition states. Several fission “channels” can be defined for each of these configurations, they will be related to a specific new barrier shape that will be somehow “shifted” with respect to the fundamental barrier. As the energy shift, corresponding to the intrinsic energy, will depend on the deformation, the shift is not constant all along the fission path. In the following, it will be assumed that these new barrier shapes do not cross each other, this corresponds to the *adiabatic* assumptions. By analogy with the transition states of Chapter 4 defined separately at each barrier hump, these new barrier shapes will be called continuous *global* transition states. An illustration of such *global* transition states is shown in Fig. 6.20.

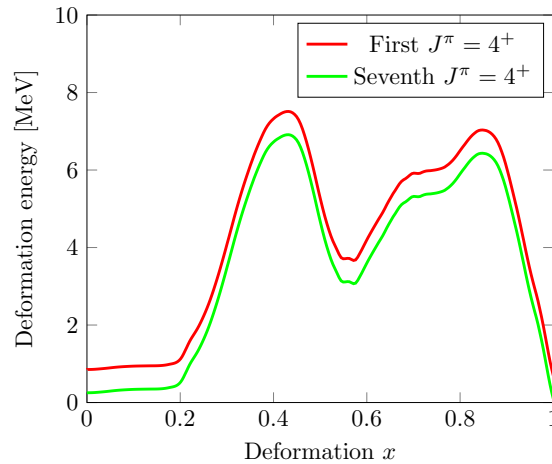


Figure 6.20 – Example of global transition states obtained with the  $LA-V_{\text{min}}$  path. The two transition states correspond to the first and the seventh transition states related to the quantum numbers  $J^\pi = 4^+$ .

In this section the determination of these global transition states will be detailed so that *in fine* a fission transmission coefficient  $T_f^{J^\pi}$  can be defined for each compound nucleus  $J^\pi$  state defined as a sum of a certain set of barrier-related transmission coefficients related individually to a unique global transition state.

### 6.5.1 Rotational Band

The global transition states that are “built” on the fundamental barrier are obtained as a set of excited states having shapes similar to the corresponding fundamental barrier below. The nature of these latter excited states are due to an internal configuration (intrinsic excitation) or from collective excitations. These collective excitations can be related to collective vibrations, with different modes (*i.e.* related to different degrees of freedom). They can also be related to the rotation of the whole nucleus. There is an analytical relation between the energy of a nucleus in its lower rotational state and the energy of a “higher” rotational state (*i.e.* with a higher total angular momentum  $J$ ). Therefore, for a given deformation, the excited states are defined as a *rotational band* built on the lowest rotational state having this deformation (plus a possible intrinsic and vibrational energy  $E_{\text{int.}+\text{vib.}}^{K^\pi}$ ).

As only axially symmetric shapes are considered here, the global transition state energy  $E_{\text{g.t.s.}}^{J^\pi K}$  is given by [89]

$$E_{\text{g.t.s.}}^{J^\pi K} = E_{\text{int.}+\text{vib.}}^{K^\pi} + \frac{\hbar^2}{2I_\perp} [J(J+1) - K^2] \quad (6.63)$$

$$= \underbrace{E_{\text{int.}+\text{vib.}}^{K^\pi} + \frac{\hbar^2}{2I_\perp} K}_{E_{\text{B.H.}}^{K^\pi}} + \frac{\hbar^2}{2I_\perp} [J(J+1) - K(K+1)] , \quad (6.64)$$

where  $I_\perp$  is the *rotational inertia momentum* related to an axis perpendicular to the nucleus symmetry axis. Equation 6.64 also defines the band-head energy  $E_{\text{B.H.}}^{K^\pi}$ , *i.e.* the energy of the first excited state of the rotational band.

For a given a band-head energy  $E_{\text{B.H.}}^{K^\pi}$ , some global transition states cannot be obtained using Eq. 6.64 because selection rules prevent the possibility to obtain some  $J^\pi$  states from a given  $K^\pi$  band-head. These selection rules are given by [163]

$$\begin{aligned} J &= K, K+1, K+2, \dots & K &\neq 0, \\ J &= 0, 2, 4, \dots & K &= 0 \text{ and } \pi = +1, \\ J &= 1, 3, 5, \dots & K &= 0 \text{ and } \pi = -1. \end{aligned} \quad (6.65)$$

In the following, explanations will be given on how the band-head state is obtained (more specifically, how the  $E_{\text{int.}+\text{vib.}}^{K^\pi}$  term is obtained). Then two models for the rotational inertia momentum  $I_\perp$  will be presented, so that fission transmission coefficient  $T_f^{J^\pi}$  could be calculated and used to finally obtain a fission cross section.

### 6.5.2 Rotational Band-Heads

The rotational band-head energy  $E_{\text{B.H.}}^{K^\pi}$  is obtained from a coupling between an intrinsic excitation state and a vibrational state<sup>6</sup> using Eq. 6.64, so that

$$E_{\text{B.H.}}^{K^\pi} = E_{\text{int.}+\text{vib.}}^{K^\pi} + \frac{\hbar^2}{2I_\perp} K. \quad (6.66)$$

---

<sup>6</sup>This vibrational state can be composed of several phonons in several vibrational modes.

The “int.+vib.” state is obtained by a combinatorial method, see for example Ref. [24], so that energy  $E_{\text{int.}+\text{vib.}}^{K\pi}$  is obtained by

$$E_{\text{int.}+\text{vib.}}^{K\pi} = \sum_i n_i E_i^{\text{vib.}} + \sum_i m_i E_i^{\text{q.p.}}, \quad (6.67)$$

where  $E_i^{\text{vib.}}$  is the elementary photon energy of the mode  $i$  (here the multi-phonon energy is obtained assuming a harmonic oscillator model for the vibrations<sup>7</sup>). The  $E_i^{\text{q.p.}}$  term is the quasiparticle energy of the intrinsic excitation  $i$ . It is supplied by the Yukawa-folded model described in Chapter 5 combined with one of the pairing model described in the same chapter. The  $m_i$  and  $n_i$  numbers correspond to the number of phonons or to the number of the quasiparticle states of the excited configuration that is provided by the combinatorial method.

The combinatorial method used was extracted from the AVXSF code [23, 24] and coupled with the CONRAD code so that the computation of the global transition states is completely automated. For an excited configuration yielding  $E_{\text{int.}+\text{vib.}}^{K\pi}$ , the  $K$  and  $\pi$  quantum numbers of the band-head are obtained by the following expression

$$K = |K_1^{\text{vib.}} \pm \dots \pm K_M^{\text{vib.}} \pm K_1^{\text{q.p.}} \dots \pm K_N^{\text{q.p.}}|, \quad (6.68)$$

$$\pi = \prod_{i=1}^M \pi_i^{\text{vib.}} \prod_{j=1}^N \pi_j^{\text{q.p.}}, \quad (6.69)$$

where  $M$  is the number of vibrational phonons, and  $N$  is the number quasiparticle states, that are involved in the configuration leading to  $E_{\text{int.}+\text{vib.}}^{K\pi}$ . They are also provided by the AVXSF routine. The vibrational states are poorly known except for the ground state shape, where spectrometry can be used to deduce experimental values. Therefore in the present study it was assumed that only three basic vibrational states are involved with no dependence on the deformation. Other vibrational states are built from these basic states assuming harmonicity. The three basic states [164] are given in Tab. 6.2. These states correspond to one-phonon vibrational states, assuming harmonicity and no coupling between vibrational modes, the many-phonon states can be obtained from the basis states by combinatorial calculation.

Table 6.2 – Vibrational one-phonon states used in the rotational band-head combinatorial computation.

n	$E^{\text{vib.}}$ [MeV]	$K$	$\pi$
1	0.15	2	+
2	0.7	0	–
3	0.8	1	–

### 6.5.3 Rotational Moments of Inertia

To obtain the band-head energy  $E_{\text{B.H.}}^{K\pi}$  (Eq. 6.66) and the global transition state  $E_{\text{g.t.s.}}^{J\pi K}$  (Eq. 6.63), the rotational moment of inertia  $I_{\perp}$  must be obtained. In a similar way than in the PES determination (*cf.* Chapter 5) and the deformation inertia tensor modeling, two approaches (“macroscopic” and “microscopic”) for the determination of  $I_{\perp}$  will be presented.

<sup>7</sup>This implies that the two-phonon state has an energy twice larger than the one-phonon state, *etc.*



### 6.5.3.1 Rigid Body (Sharp- and Diffuse-edge)

In the “macroscopic” approach, the nuclear matter is considered a rigid, homogeneous body<sup>8</sup>. The rotational moment of inertia can thus be obtained in the framework of classical mechanics [93] as

$$I_{\perp} = \pi \rho_M \int_{z_{\min}}^{z_{\max}} dz \left( z^2 \rho^2(z) + \frac{\rho^4(z)}{4} \right) \underbrace{+ 4Ma^2}_{\text{If shape has diffuse edge}}, \quad (6.70)$$

where  $M$  is the mass of the nucleus, and  $\rho_M$  is the nuclear matter mass density. The last term in Eq. 6.70 must be added if the nuclear shape has diffuse edge. The diffuseness parameter  $a$  corresponds to the range of the Yukawa-folded density function (*cf.* Chapter 5). Yet, as it will be shown below, the diffuse-edge model has not been investigated as the rigid body model already overestimates experimental data and the diffuseness of the shape would increase this discrepancy.

### 6.5.3.2 Cranking Model

In the microscopic approach, the rotational inertia can be obtained with a cranking model [18, 19, 166]. It is the same model that has been used to obtain the deformation inertia tensor can also be used to get the rotational inertia momentum. Just like in the case of the deformation inertia tensor, the rotational inertia momentum  $I_{\perp}$  is the sum of the neutron inertia momentum  $I_{\perp}^{(n)}$  and the proton inertia momentum  $I_{\perp}^{(p)}$ , namely

$$I_{\perp} = I_{\perp}^{(n)} + I_{\perp}^{(p)}. \quad (6.71)$$

The rotational inertia momentum, for instance for neutron, is given by

$$I_{\perp}^{(n)} = 2\hbar^2 \sum_{\nu\mu} \frac{|\langle \nu | j_x | \mu \rangle|^2}{E_{\nu} + E_{\mu}} (u_{\nu} v_{\mu} - u_{\mu} v_{\nu})^2, \quad (6.72)$$

where  $|\nu\rangle$  and  $|\mu\rangle$  are the single-particle wave functions obtained with the Yukawa-folded independent particle model presented in Chapter 5. Energies  $E_{\nu}$  and  $E_{\mu}$  are the quasi-particle energies obtained by the BCS or the Lipkin-Nogami model, and  $v_{\nu}$ ,  $v_{\mu}$ ,  $u_{\nu}$  and  $u_{\mu}$  are the related occupancy numbers.

In the Yukawa-folded independent particle model, the single-particle wave functions are obtained as a linear combination of the deformed harmonic oscillator eigenfunctions  $|n_r n_z \Lambda \Sigma\rangle$ . Therefore the coupling matrix elements  $\langle n'_r n'_z \Lambda' \Sigma' | j_x | n_r n_z \Lambda \Sigma \rangle$  must be known so that Eq. 6.72 can be computed with the wave functions provided by the independent particle model. The only non-vanishing matrix elements are [20, 167]

$$\langle n_r, n_z - 1, \Lambda - 1, \Sigma | j_x | n_r, n_z, \Lambda, \Sigma \rangle = \alpha_2 \sqrt{2n_z(n_r + \Lambda)}, \quad (6.73)$$

$$\langle n_r + 1, n_z + 1, \Lambda - 1, \Sigma | j_x | n_r, n_z, \Lambda, \Sigma \rangle = -\alpha_2 \sqrt{2(n_z + 1)(n_r + 1)}, \quad (6.74)$$

$$\langle n_r - 1, n_z - 1, \Lambda + 1, \Sigma | j_x | n_r, n_z, \Lambda, \Sigma \rangle = -\alpha_2 \sqrt{2n_z n_r}, \quad (6.75)$$

$$\langle n_r, n_z + 1, \Lambda + 1, \Sigma | j_x | n_r, n_z, \Lambda, \Sigma \rangle = \alpha_2 \sqrt{2(n_z + 1)(n_r + \Lambda + 1)}, \quad (6.76)$$

$$\langle n_r, n_z + 1, \Lambda - 1, \Sigma | j_x | n_r, n_z, \Lambda, \Sigma \rangle = -\alpha_1 \sqrt{2(n_z + 1)(n_r + \Lambda)}, \quad (6.77)$$

<sup>8</sup>The macroscopic approach for the rotational moment of inertia considers here the nucleus a rigid body, not a liquid drop. The most exact analogy with PES calculation of Chapter 5 would involve the irrotational flow model [165].

$$\langle n_r + 1, n_z - 1, \Lambda - 1, \Sigma | j_x | n_r, n_z, \Lambda, \Sigma \rangle = \alpha_1 \sqrt{2n_z(n_r + 1)}, \quad (6.78)$$

$$\langle n_r - 1, n_z + 1, \Lambda + 1, \Sigma | j_x | n_r, n_z, \Lambda, \Sigma \rangle = \alpha_1 \sqrt{2(n_z + 1)n_r}, \quad (6.79)$$

$$\langle n_r, n_z - 1, \Lambda + 1, \Sigma | j_x | n_r, n_z, \Lambda, \Sigma \rangle = -\alpha_1 \sqrt{2n_z(n_r + \Lambda + 1)}, \quad (6.80)$$

$$\langle n_r, n_z, \Lambda, -\Sigma | j_x | n_r, n_z, \Lambda, \Sigma \rangle = \frac{\hbar}{2}, \quad (6.81)$$

where

$$\alpha_1 = \frac{\hbar}{4} \left( \sqrt{\frac{\omega_z}{\omega_\perp}} + \sqrt{\frac{\omega_\perp}{\omega_z}} \right) \quad \text{and} \quad \alpha_2 = \frac{\hbar}{4} \left( \sqrt{\frac{\omega_z}{\omega_\perp}} - \sqrt{\frac{\omega_\perp}{\omega_z}} \right), \quad (6.82)$$

and where  $\omega_z$  and  $\omega_\perp$  are the deformed oscillator frequencies defined in Chapter 5.

### 6.5.3.3 Model Comparison and Validation

The two models implemented to calculate the rotational inertia momentum  $I_\perp$  can be benchmarked on a practical case. For ground state deformation the rotational inertia momentum can be obtained for some isotopes from the analysis of their low-lying excited states. For the present work, these low-lying levels have been analyzed using data from the ENSDF database [168]. The results are shown in Fig. 6.21 and are rather consistent with those reported in Ref. [169]. It can be seen that the rigid body model overestimates, at least by a factor two, the experimental data, whereas the cranking model is in better agreement for small and medium size isotopes but underestimates  $I_\perp$  for heavy nuclei. The ground state shape used to obtain the results shown in Fig. 6.21 are taken from Ref. [12].

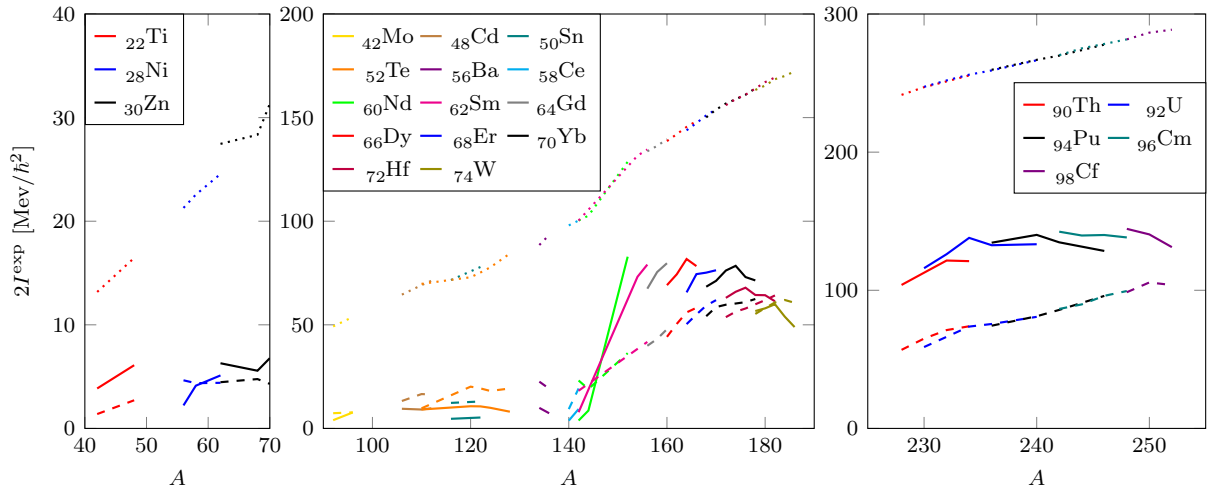


Figure 6.21 – Rotational inertia momentum calculated with the cranking model (dashed lines) and the rigid body model (dotted lines). Experimental data are also shown (solid lines).

The rotational moment of inertia varies as the nucleus deforms towards fission shapes. Figure 6.22 shows results obtained with both models as a function of the  $x$  deformation. The path (set of shapes) used here is the least-action path LA- $V_{\min}$  (*cf.* Fig. 6.6). It can be seen that the dependency of the rotational inertia is quite similar for both models, which is quite astonishing when it is reminded that they are obtained with completely different pictures of the nuclear matter.

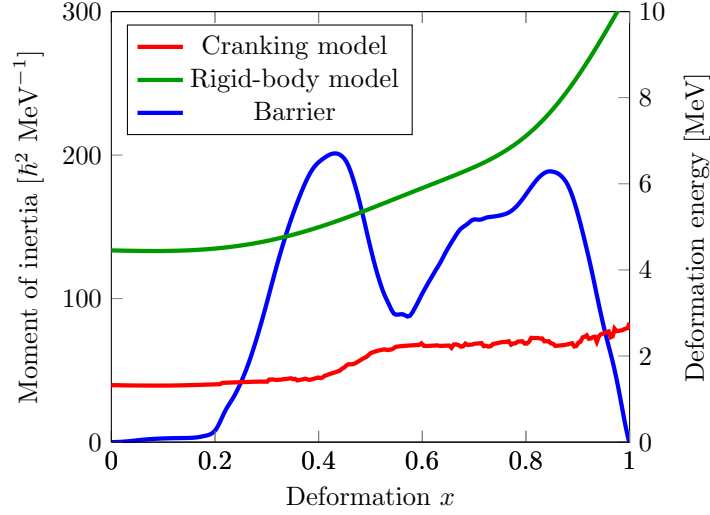


Figure 6.22 – Rotational moments of inertia calculated along the LA- $V_{\min}$  path for the  $^{240}\text{Pu}$ . The red curve stands for moments of inertia calculated with the cranking model, the green curve for the same quantity obtained with the rigid body model. The shape of the corresponding fission barrier is displayed on the background (blue curve).

As can be seen in Fig. 6.21, the cranking model gives “slightly” better results than the rigid body model for ground state moments of inertia. In the interest of simplicity and representativity, it is only the cranking model that will be used in the next section related to fission cross section modeling.

## 6.6 Fission Cross Section

To complete this chapter, an actual calculation of the fission cross section for the  $(n + ^{239}\text{Pu})$  reaction is performed. In a first approach, the least-energy method is used. The steps in the calculation of the eventual fission cross section are recalled below:

1. Considering a shape parameterization (here the  $(c, h, \alpha)$  Brack parameterization), the potential energy of  $^{240}\text{Pu}$  is computed for a large number of shapes spanning corresponding to given ranges of the shape parameters.
2. From this PES, the least-energy path is obtained using the method described in Section 6.1.
3. Once this one-dimensional path is obtained, the single-particle orbits are calculated again for the shapes of the path, *cf.* Chapter 5.
4. From the single-particle states ( $\epsilon_i$  and  $\psi_i$ ) and occupation numbers ( $v_\nu$  and  $u_\nu$ ), the rotational inertia  $I_\perp$  is calculated for both neutrons and protons.
5. For each point of the path, the rotational band-heads are computed by the combinatorial combining of the single-particle energies and the elementary collective phonons (*cf.* Tab. 6.2) using the AVXSf routine.
6. These band-heads are calculated for all points along the path, then the transition states are reconstructed using the moment of inertia  $I_\perp$ .
7. Several *continuous* transition states are thus obtained assuming adiabaticity of the fission process.

8. A *continuous* transition state is related to given  $J^\pi$  quantum numbers, thus each couple  $J^\pi$  is related to a set of transition states.
9. For given  $J^\pi$  and energy  $E^*$  of the compound nucleus, a fission transmission coefficient can be calculated using the numerical methods described above, here considering the inertia parameter to be deformation-independent and equal to  $\mu^{\text{const}}$ .
10. Using the Hauser-Feshbach modeling framework described in Chapter 4, the average fission cross section is computed.

The eventual fission cross section is shown in Fig. 6.23. It can be seen that the calculated cross section is “only” about 30% higher than the evaluated and experimental data. This is actually fortunate as many “loose” assumptions were used in the whole treatment, for instance the definition of the fission abscissa, or the use of single-particle states obtained from a phenomenological average field. Additionally some less-arbitrary hypothesis were also made, for instance the inertia parameter is assumed to be constant and equal to a somehow arbitrary value.

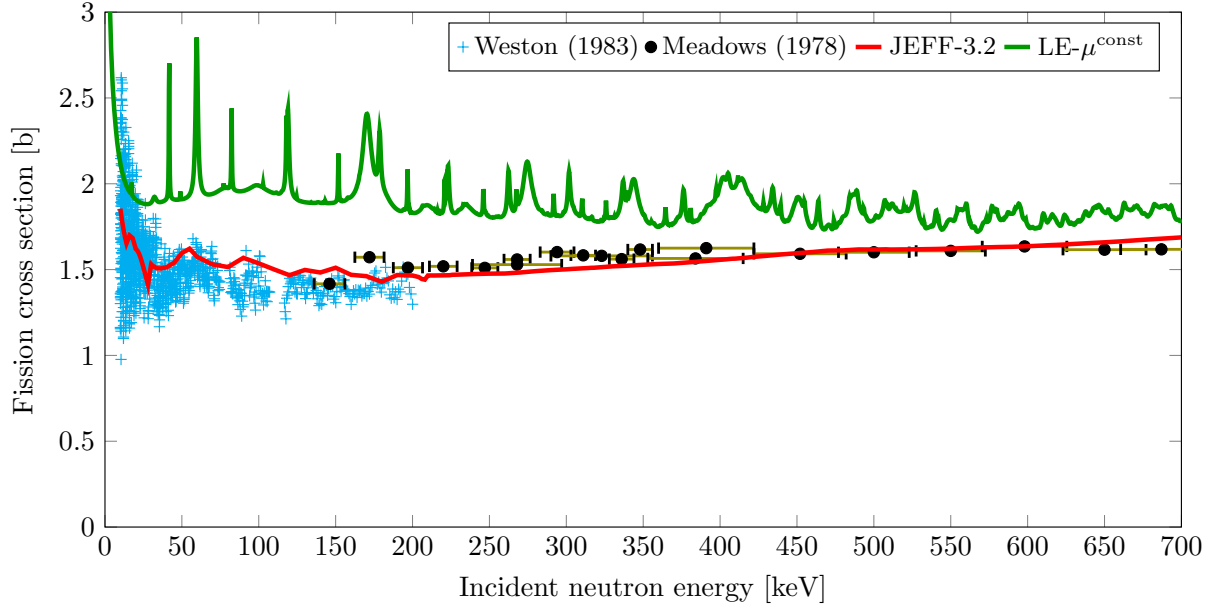


Figure 6.23 – Fission cross section of  $^{239}\text{Pu}$  obtained using an underlying macroscopic-microscopic model (least-energy path). Evaluated (JEFF-3.2) and experimental data (Weston [170] and Meadows [171]) are also shown for comparison.

It can be seen that, even if the order of magnitude is correct, the model cannot be used directly to provide evaluation-quality data. Additionally, the results shown in Fig. 6.23 have some unsatisfactory features. In the low-energy region, the calculated values are quite higher than the experimental data. For higher energies, the calculated cross section seems to *decrease*, whereas the evaluated data seem to *increase*. This feature should be analyzed comparing also total and other partial cross sections with evaluated data. There was just enough time in this PhD to perform a theoretical calculation (because of the quantity of development that were necessary in the CONRAD code; the theoretical calculation itself takes few hours). Yet it was investigated if these features could be explained (and balanced) by varying parameters involved in the fission modeling only.

The effect of two parameters has been investigated, namely the value of the inertia parameter  $\mu^{\text{const}}$  and the cut-off energy used in the combinatorial calculation. In the

combinatorial calculation all combination of excitation states having an energy higher than the cut-off energy are discarded. This cut-off energy is analog to the continuum energy  $E_X^{\text{cont.}}$  in Eq. 4.68 of Chapter 4. The effect of changing the value of the constant inertia parameter is illustrated in Fig. 6.24. The theoretical calculation is performed using increasing values of the inertia parameter:  $\mu^{\text{const}}$ ,  $2 \times \mu^{\text{const}}$ ,  $3 \times \mu^{\text{const}}$  and  $4 \times \mu^{\text{const}}$ , where  $\mu^{\text{const}}$  is given by Eq. 6.33. It can be seen that the increase in the value of the inertia parameter reduces the global level of the fission cross section. This effect is “global” in the sense that it operates similarly at low and high energies.

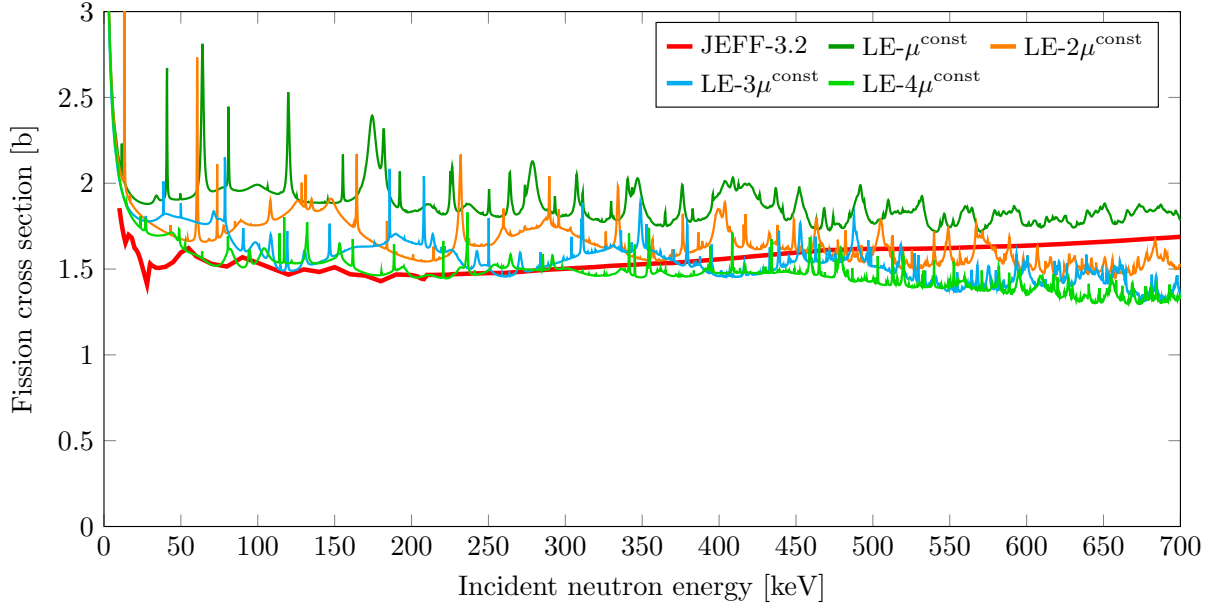


Figure 6.24 – Effect of varying the constant inertia-parameter value in the calculation of the  $^{239}\text{Pu}$  fission cross section (least-energy path). Evaluated data (JEFF-3.2) are also shown for comparison.

The effect of the cut-off energy is however less “global” as illustrated in Fig. 6.25. It can be seen that increasing the cut-off energy increases the value of the fission cross section specifically in the high-energy range. This is expected because the cut-off energy is given with reference to the ground-state energy (and is independent of the incident neutron energy), whereas the number of significant transition states depends on the excitation energy, which depends on the incident neutron energy. It can thus be expected that a proper treatment of the “continuum” of *continuous* transition states could partially restore the proper trend of the fission cross section in the high energy region. It should also be noted here that the results here are obtained with a constant inertia parameter of  $4 \times \mu^{\text{const}}$ , and that this effect is more pronounced if smaller values are considered.

The last analysis that will be shown here is related to the effect of having a deformation-dependent inertia parameter. This effect is illustrated using the LA- $V_{\text{min}}$  fission barrier, using either the inertia parameter obtained from the least-action method, or the constant inertia parameter  $\mu^{\text{const}}$  (cf. Fig. 6.13). Figure 6.26 shows the fission cross section obtained with both least-action methods and with the least-energy method. The difference between the least-action methods, on one side, and the least-energy method, on the other side, is believed to be due to the difference in the related barrier heights. It can be noted from Fig. 6.26 that the deformation-dependent inertia parameter produces a “smoother” fission cross section. This should be kept in mind while attempting to compare the resonant structures of the least-energy method with experimental data. The differences between

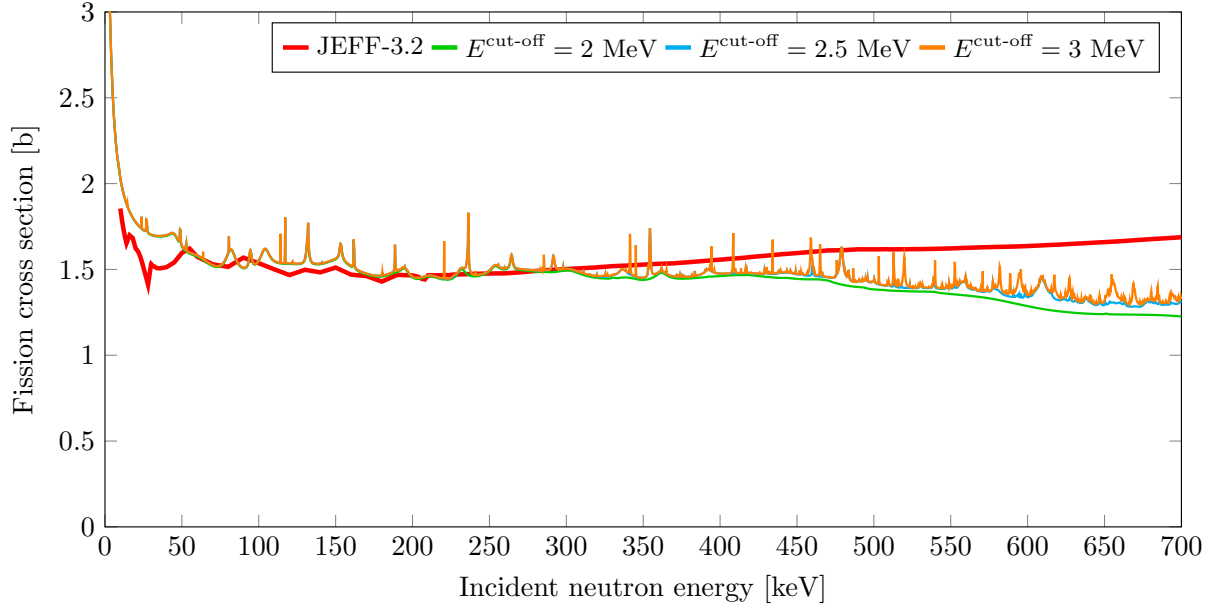


Figure 6.25 – Effect of the combinatorial cut-off energy in the calculation of the  $^{239}\text{Pu}$  fission cross section (least-energy path). Evaluated data (JEFF-3.2) are also shown for comparison. Here the inertia parameter is chosen to be equal to  $4 \times \mu^{\text{const}}$ .

the two least-action method (and thus the effect of considering a deformation-dependent inertia parameter) seem to vanish as the incident neutron energy increases. From about 350 keV, the two methods yield similar gross structures even if the  $\text{LA-}V_{\text{min}} - \mu^{\text{const}}$  exhibit much more narrow resonances.

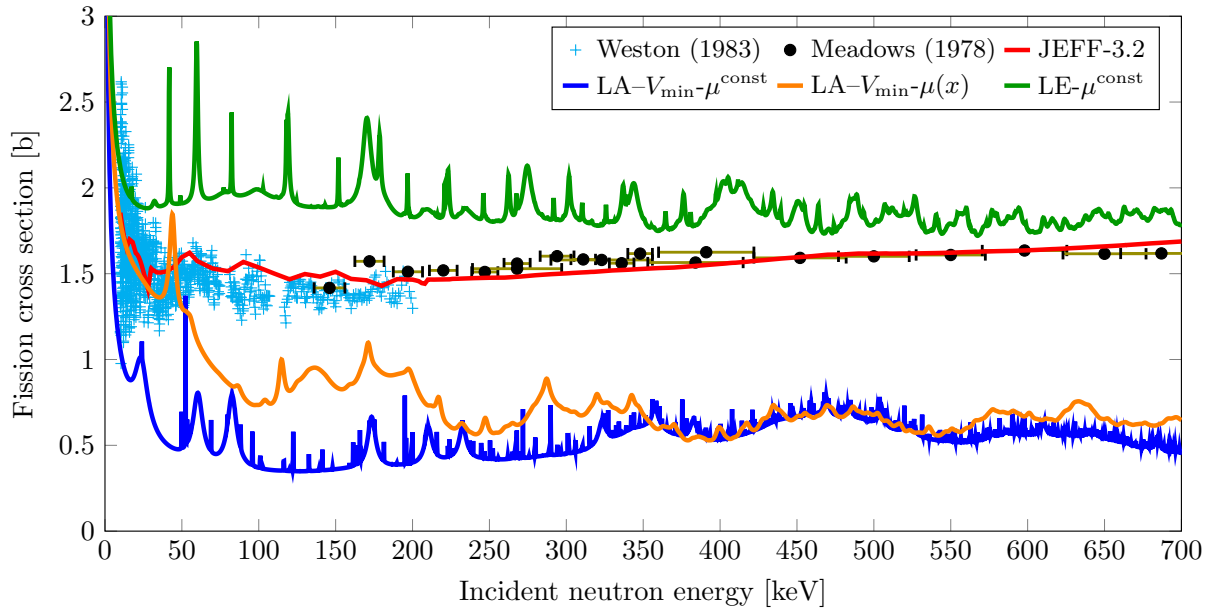


Figure 6.26 – Effect of having a deformation-dependent inertia parameter on the  $^{239}\text{Pu}$  fission cross section (least-action paths). Evaluated (JEFF-3.2) and experimental data (Weston [170] and Meadows [171]) are also shown for comparison as long as the results obtained with the least-energy path.

Due to lack of time, it was not possible to investigate further the effect of the other parameters involved in the calculation. For instance additional details should be carefully

investigated:

- The barrier heights obtained by both methods are still slightly larger than the values commonly used in evaluation. As the shapes used involves “only” three degrees of freedom, it can be expected that the use of a shape parameterization relying on more degrees of freedom (such as the 3QS parameterization *cf.* Appendix B.1) may reduce the second-hump height of the calculated barrier.
- In the present study, only axially symmetric shapes are considered. Yet similar calculations considering axially asymmetric shapes showed that the first barrier can be lowered.
- In Fig. 6.21, it was shown that the cranking model used here to calculate the rotational inertia momentum underestimates experimental data for actinides. According to Eq. 6.63, this would lead to lower the transition state energy and thus, considering the overall trends of transmission coefficients, it should increase the value of the fission cross section.
- Finally, the selection rules given by Eq. 6.65 prevent the compound nuclei formed in a  $J^\pi = 0^-$  from fissioning, which seems unphysical. In the present study, the transmission coefficients for  $J^\pi = 0^+$  were used instead.



# Chapter 7

## Conclusion & Perspectives

*In this chapter, the main results and conclusions of this work are recalled. Additionally, some perspectives for further developments are detailed.*

### Contents

---

<b>7.1 Overview of the Work . . . . .</b>	<b>152</b>
7.1.1 Impact of the Fission Barrier in the RRR . . . . .	152
7.1.2 Integration of a Nuclear Structure Model . . . . .	152
7.1.3 Fission Cross Section in the Statistical Energy Range . . . . .	153
7.1.4 Summary of the Developments . . . . .	154
<b>7.2 To Be Continued... . . . .</b>	<b>154</b>
7.2.1 Consistency and Accuracy of the Current Method . . . . .	154
7.2.2 Further Refinements of the Presented Method . . . . .	155

---

## 7.1 Overview of the Work

This PhD work highlights the importance of the fission-barrier shape as the sound physical quantity fission cross section evaluation should rely on. This demonstration has been performed successfully in both energy ranges involved in cross section evaluation: the Resolved Resonance Range (RRR) and the statistical energy range. The fission barrier corresponds to the variation of the deformation potential that a nucleus “feels” when it deforms from the ground-state shape to scission configurations.

### 7.1.1 Impact of the Fission Barrier in the RRR

Assuming a double-humped shape of the deformation potential, it has been shown that, for some excitation energies, the nucleus has a high probability to be in a deformation state corresponding to intermediate potential well. For these energies the probability of fissioning is thus enhanced due to the fact that a part of the fission barrier has already been crossed. The inclusion of these considerations in the general theoretical framework describing resonant cross sections leads to extending the standard Reich-Moore model. This extension provides a true physical meaning for the fission reduced width amplitude. This is done by modifying the  $\mathfrak{R}$ -matrix penetration factors, related usually to particle channels only, to fission channels (related to transition states). This extension is formally done by using an underlying description of the fission barrier that leads to defining wave function related to the fission “degree of freedom”. This wave function reveals the most probable deformation state of the excited nucleus. A fission-related penetration factor can be obtained from this wave with Lynn’s extension of the  $\mathfrak{R}$ -matrix formalism to the fission reaction. The resulting fission penetration factor presents an energy dependence where the usual evaluation approach prescribes a one-unit arbitrary value. Not only does it depend on energy, but it also exhibits well-defined resonance structures. The structures of the fission penetration factor have been analyzed here and are satisfactorily well reproduced by Lorentzian functions. For fertile isotopes, the Lorentzian parameters can be estimated from the general shape of the fission cross section. For such isotopes, the use of Lorentzian-shaped fission penetration factors to evaluate fission resonance parameters (reduced width amplitudes), effectively compensates the energy dependency that is usually mathematically absorbed by parameter adjustment on experimental data.

### 7.1.2 Integration of a Nuclear Structure Model

This impact of the fission barrier shape on the fission cross section calls for modeling of the former. The study of nuclear deformation energy involves Potential Energy Surfaces (PES) that relates macroscopic shape coordinates to the related deformation energy. Evaluation requires adjustment of model parameters and thus physics is sometimes disregarded in favor of faster and more flexible models. To comply with realistic evaluation constraints, namely in terms of computation time, the macroscopic-microscopic approach has been selected over alternative approaches such as Hartree-Fock-Bogoliubov (HFB) microscopic descriptions.

The macroscopic-microscopic models combine the macroscopic picture of the nucleus being a homogeneous liquid to the corresponding microscopic description of individual nucleons. The Finite-Range Liquid-Drop Model (FRLDM) was chosen for its long-standing success in describing several nuclear properties. This composite model consists in a principal macroscopic energy corrected for microscopic shell and pairing effects. These latter corrections are obtained from single-particle states related to an average mean potential

felt by the nucleons. This parameterized potential is chosen to be consistent with the former macroscopic description. This model is the outcome of many successive improvements that have refined the original liquid-drop model. Implementing this model in the CONRAD code has been a colossal work because of the model complexity and the related 50 year of legacy. An operational FRLDM has been added to the CONRAD toolbox and verified by various means. Despite this pragmatism, deepest care has been brought in the implementation in order to meet the speed requirements of evaluation. Advanced numerical and computational (hardware) solutions have been found and put into effect. The PES obtained using the macroscopic-microscopic FRLDM describes the deformation energy of a nucleus allowed to deform according to a related geometrical shape parameterization. At least three parameters are necessary to satisfactorily describe the shape of the fission barrier: elongation, neck size and mass-asymmetry. The corresponding multidimensional PES must be reduced into a one-dimensional deformation potential. Two algorithms have been implemented in the CONRAD code to obtain such a one-dimensional path: the least-energy and least-action paths searching methods. To study the barrier penetrability, the deformation inertia “along” the fission path must be defined. In many studies this parameter is explicitly or implicitly chosen to be deformation-independent. The natural fission abscissa describing the position along the path provided by these methods has been discussed. The present conclusions advocate for the least-action method as both the fission abscissa and the inertia parameter are naturally provided by the model. Yet the least-energy path provides, for the time being, results closer to the experimental data. It is this pragmatism approach that has been selected in the last section of this chapter to investigate the impact of some parameters on the eventual fission cross section. The one-dimensional deformation potential and the related inertia parameter are obtained with both of the reduction methods and their effect on barrier penetrability has been compared with special focus set on the impact of the deformation dependency of the inertia parameter.

### 7.1.3 Fission Cross Section in the Statistical Energy Range

The barrier penetrability (more specifically the fission barrier transmission coefficient), can be used to model average fission cross section. This latter involves the Hauser-Feshbach theoretical framework that relies on transmission coefficients obtained independently for the different nuclear reactions. Prior to the start of the PhD work, the CONRAD code had very limited capability of modeling average cross sections. The TALYS code has been used as a guideline to identify the missing pieces that needed to be implemented in order to settle a proper Hauser-Feshbach framework. Analogous transmission coefficient models have been implemented for neutron elastic and inelastic emission, direct and compound reactions. A brand new coupled channel optical model was also implemented based on the approach of the ECIS reference code. Corresponding gamma transmission coefficient has been introduced in the CONRAD code, so that the complete average cross section framework makes possible the computation of various partial cross sections. Both the ECIS and TALYS codes have been used to verify the related implementations and remaining differences have been analyzed carefully. Finally, this complete machinery makes possible to calculate average fission cross sections based on an underlying sophisticated macroscopic-microscopic model deeply rooted in nuclear physics.

### 7.1.4 Summary of the Developments

The work reported in this document involves a large number of models, spanning the large energy range of interest for reactor physics. The related developments enclose:

- A Reich-Moore model extension ( $\Re$ -matrix theory approximation) to treat fission channels with Lynn's extension in the RRR.
- A generic Hauser-Feshbach framework for average cross section modeling.
- *Gamma* transmission coefficients from various already-implemented level density and strength function models.
- *Neutron* transmission coefficients, by driving ECIS calculations or using already-implemented spherical optical model and an average  $\Re$ -matrix model.
- A brand new C++ coupled channel optical model, based on the ECIS algorithm, able to treat deformed nuclei.
- Both the FRLDM and an alternative macroscopic-microscopic model, the Finite-Range Droplet Model (FRDM), have been implemented from scratch. This implies namely that a single-particle program had to be written. As this represents the most time-consuming part of the macroscopic-microscopic calculation, it was decided to write a program able to run on Graphics Processing Units (GPUs).
- Two models providing the deformation inertia tensor (Werner-Wheeler and cranking approximations).
- Two PES reduction algorithms, used to reduce the multidimensional PES to a one-dimensional fission barrier.
- Two models related to the rotation inertia momentum (cranking and rigid-body models).
- Several numerical methods to obtain fission barrier transmission coefficients (from the one-dimensional fission barrier) that can be used in the already mentioned Hauser-Feshbach model.

About 80k lines of C++/CUDA-C code have been written in CONRAD, boosting its modeling capabilities well beyond its original resolved-resonance cross section specialty.

## 7.2 To Be Continued...

### 7.2.1 Consistency and Accuracy of the Current Method

The global method presented and carried out here opens the possibility of pouring advanced nuclear physics more directly into fission cross section modeling and evaluation. It has been emphasized that models used in practice for current evaluations suffer from several deficiencies. These deficiencies are related to both non-reproduced features (fluctuations in fission cross section) and lack of predictivity (shape of the fission barrier). Even if the present attempt tends to resolve some of these issues, the proposed method is not yet completely rigorous.

### 7.2.1.1 PES Reduction to a One-Dimensional Fission Barrier

The fission barrier used in the calculation is indeed obtained from a sound nuclear structure model (the FRLDM), but the connection between the multidimensional PES and the one-dimensional fission barrier relies on some arbitrary choices. The validation of the one-dimensional reduction methods requires a dedicated investigation to verify if such an approach yield similar results to those obtained if a complete PES is used. To address this point, one should be able to calculate transmission coefficient from – at least – a 2D PES without performing a one-dimensional reduction.

In the present work, the PES reduction contains some arbitrariness and unexpected results. For instance the least-action method (which is expected to described the phenomenon with better physics than the least-energy method) failed to yield a fission barrier with reliable barrier heights. It is necessary to verify that the method used to obtained the least-action path from the PES is correct. Analytical cases are thus required to perform the related investigation.

If the least-action method shows no inconsistency, the inertia tensor should also be verified. It should be reminded here that the inertia tensor is obtained with a cranking model that uses the single-particle energies and wave functions. These single-particle results are obtained from a “simple” phenomenological model. An equivalent inertia tensor obtained with a self-consistent approach may lead to different least-action paths. Yet to make consistent comparisons between inertia tensors and least-actions paths, the collective coordinates should be consistent. This means that the shape coordinates (for instance  $c$  and  $h$ ) should be replaced by the quantities used in HFB approaches (for instance  $Q_{20}$  and  $Q_{40}$ ). Yet even with such variable changes, the HFB method would lead to a PES, for which energy is already minimized with respect to implicit degrees of freedom. An alternative approach consists in enforcing the self-consistent mean field to have “shapes” similar to the ones obtained in the macroscopic-microscopic approach.

### 7.2.1.2 Inertia Parameter

The least-energy method seems pragmatically promising considering results shown in Chapter 6. In this approach however, the value of the constant inertia parameter is quite arbitrary and may seem to only balance model defects. No direct measurements of the inertia parameter is possible, and thus it is difficult to say that the adjusted value is reliable or not. It should be nevertheless stated here that this method has the advantage of highlighting the effect of this parameter where the “traditional” models ignore it completely.

### 7.2.1.3 Continuum of Transition States

Finally the treatment of the continuum of the transition state is also somehow tedious. The combinatorial approach cannot be performed up to sufficient energies. In the present method, transition states higher than a cut-off energy are simply omitted. It has been shown that the remaining transition states may have significant effect, thus a proper treatment should be found to include states above the cut-off energy.

## 7.2.2 Further Refinements of the Presented Method

In the previous section, some points are discussed and aim to strengthen the presented approach. The present work yields a completely integrated method that can be used to investigate the effect of options in the nuclear structure model on various observables.

### 7.2.2.1 Fission Barrier Described down to the Scission Point

It was mentioned in Chapter 6 that to properly describe the nucleus shape when to nascent fragments appear, the Brack shape parameterization  $(c, h, \alpha)$  may be insufficient. Indeed, in this parameterization the  $\alpha$  parameter and the deformations of individual fragments are correlated. To obtain a proper description, more degrees of freedom should be considered and alternative shape parameterizations must be used, for instance the three quadratic surfaces (3QS) (*cf.* Appendix B.1). This refined description of the shape becomes necessary if the PES is expected to describe shapes beyond the “fission line”. To study the effect of describing the fission barrier “below” the fission point, down to the scission point, the 3QS parameterization should be used. As was mentioned in Chapter 3, this domaine of the fission barrier may have a significant effect on transmission coefficients.

### 7.2.2.2 Axially-Asymmetric Shapes

In the present study, only axially-symmetric shapes are considered. To investigate if the nucleus takes axially-asymmetric shapes as it deforms from ground-state shape to fission, the present implementation of the macroscopic-microscopic model should be modified. For axially-asymmetric shapes, the shape-dependent terms in the macroscopic models become more complex to evaluate as some trivial integrations cannot be performed anymore. In the microscopic model, the treatment of axially-asymmetric shapes is even more tedious because the expansion method described in Chapter 5 cannot be used. Instead of the axial harmonic-oscillator base, one should use a triaxial harmonic-oscillator base. This base would lead to calculate matrix elements consisting of triple integrals whereas it was only double integrals in the present method. Additionally, the splitting of the Hamiltonian matrix into  $\Omega$ -sub-matrices cannot be performed as  $\Omega$  is not a good quantum number anymore. The matrix to be diagonalized is thus much larger in this case. Considering axially-asymmetric shapes increases a lot the computation time for a given shape and thus the study of axial asymmetry is not as “simple” of the investigation of an additional shape (axially-symmetric) degree of freedom. Yet some actinides are expected to have axially-asymmetric shape corresponding to the first barrier hump. This can significantly reduces the corresponding hump height and thus increases the value of the fission transmission coefficient and consequently the fission cross section. For comprehensiveness, the code should be extended to be able to treat axially-asymmetric shapes.

### 7.2.2.3 Vibrational Phonons, Inertia Momentum and Transition States

In the calculation of global transition states as described in Chapter 6, the elementary vibrational phonons are shape-independent. Additionally, the harmonic composition of phonons used in the presented method is a crude approximation. In current phenomenological approaches, these phonons are described individually and do not combine “harmonically”. They are also described differently for the two barrier humps on the basis of the expected symmetries of the nucleus for these states. It could also be expected that advanced theories such as the Random Phase Approximation could yield such phonons and could thus bring more consistency in the current approach.

The Inglis-Belyaev cranking model has been used to calculate rotational inertia momenta. This model has been extended to include excitation energy dependency [172], this could also be studied as it is expected to have an impact on global transition states.

The rotational band-heads calculation uses a combinatorial method. The calculation of rotational states on these band-heads relies on the assumption of axially-symmetric shape

of the nucleus. For the shapes considered in the present study it is strictly valid, but if axially-asymmetric shapes are considered, for instance to study the first barrier hump, then this point must be questioned. Additionally, the selection rules used in the present method yield no  $0^-$  transition states, which inherently prevent a compound nucleus in a  $0^-$  state from fissioning. As mentioned in Chapter 6, it is nonphysical and should be investigated.

#### 7.2.2.4 Odd Compound Nuclei

In the present state of the code, only odd compound nuclei can be studied. This is not due to the PES calculation, as in the related implementation, the different cases are specifically treated. The present limitation is due to the calculation of the inertia quantities: the deformation inertia tensor and the rotational inertia momentum. For both of them, treating an odd number of nucleons is not possible for the time being. Models readily exist in literature but there was not enough time to implement them in the code.

#### 7.2.2.5 Nuclear Structure Models

Several refinements or alternative routes to obtain the PES can also be studied. It could be of course considered to use a HFB model to calculate the PES. Alternatively, the HFB model could be used to provide intermediate data, for instance the single-particle energies required for the macroscopic-microscopic model. This would imply to establish a correspondence between “shapes” obtained with the HFB approach<sup>1</sup> and the geometrical definition of the shape used in the macroscopic model. This is similar to the correspondence that is necessary to use HFB inertia tensor. This approach mixing could be an interesting method to identify the origin of differences between the two “mainstream” models.

In a more short-term view, the presented “standard” approach could be also slightly modified to investigate the impact of some features discussed in this manuscript. For instance the impact of using diffuse-edge potential in the microscopic part of the FRLDM can be considered. Thus a better consistency could be ensured between the macroscopic and microscopic description of the models. The impact of the continuum removal as described in Appendix B.2.2 could be also investigated to see the effect on masses, PES (and fission cross section), and also on the plateau condition of the shell correction. It could also be interesting, as this method allows to use an expansion base (containing a larger number of functions) in the microscopic model, to verify the convergence of the results with respect of the size of the expansion base. It would be also interesting to see the related impact on the pairing correction.

---

<sup>1</sup>In HFB approaches, there is no notion of generating shapes, yet an idea of the shape can be obtained considering the volume containing a certain amount of the nuclear matter.





# Appendix A

## Coupled Channel Equations

*The purpose of this appendix is to detail the general equations that must be computed by a coupled channel program.*

### Contents

---

<b>A.1 Overview</b>	<b>160</b>
<b>A.2 Expansion of the Interaction Potential</b>	<b>161</b>
A.2.1 Nucleus Coupling Matrix Element $\langle I_f M_f   Y_\lambda^\mu(\hat{r}')^*   I_i M_i \rangle_{\hat{r}'}$	163
A.2.2 Particle Coupling Matrix Element $\langle j_f m_f   Y_\lambda^\mu(\hat{r})   j_i m_i \rangle_{\hat{r}}$	164
A.2.3 Full Matrix Element $\langle \Psi_f^{JM}   Y_\lambda^\mu(\hat{r}) Y_\lambda^\mu(\hat{r}')^*   \Psi_i^{JM} \rangle_{\hat{r}, \hat{r}'}$	165
<b>A.3 Special Cases</b>	<b>167</b>
A.3.1 Spin- $\frac{1}{2}$ Projectile	167
A.3.2 Spin-0 Projectile	168
<b>A.4 Spin-Orbit Term</b>	<b>168</b>

---

## A.1 Overview

For comprehensive information about optical models see Refs. [1, 66–70]. In the interest of simplicity, the following derivation will be restrained to spinless particles, its generalization to particles with spin does not lead to special issues. The equation derived in the following are a synthesis of the references mentioned here-above. In the case of an incoming particle scattered by a target nucleus, the wave function  $\Psi$  of the system is solution of

$$\left[ \hat{T} + \hat{V}(\vec{r}, \xi) + \hat{H}_T(\xi) \right] \Psi(\vec{r}, \xi) = E \Psi(\vec{r}, \xi), \quad (\text{A.1})$$

where  $\hat{T} = -d^2_{\vec{r}} \Delta_{\vec{r}}$  is the projectile kinetic-energy operator,  $H_T$  is the target Hamiltonian (that operates only on the intrinsic coordinates  $\xi$ ) and  $\hat{V}(\vec{r}, \xi)$  is the interaction potential that also operates on the degrees of freedom  $\vec{r}$  if relevant (*cf.* Chapter 2 Section 2.1), meaning the distance between the target and projectile centers of mass and the relative orientation of the nucleus and projectile. Here  $\mu$  is the reduced mass of the system and  $E$  the energy of the incident particle in the center-of-mass framework. Let  $\chi_\alpha(\xi)$  be an eigenfunction of  $H_T$  and  $\epsilon_\alpha$  its related eigenvalue so that

$$\hat{H}_T \chi_\alpha(\xi) = \epsilon_\alpha \chi_\alpha(\xi). \quad (\text{A.2})$$

The set of orthonormal wave functions  $(\chi_\alpha)_\alpha$  is assumed to be complete, thus  $\Psi$  can be expanded as

$$\Psi(\vec{r}, \xi) = \sum_{\alpha} \Psi_{\alpha}(\vec{r}_{\alpha}) \chi_{\alpha}(\xi), \quad (\text{A.3})$$

where  $\vec{r}_{\alpha}$  is defined differently wherever it may be a relevant degree of freedom. Inserting Eq. A.3 into Eq. A.1 it becomes

$$\sum_{\alpha'} \left[ \hat{T} + \hat{V}(\vec{r}_{\alpha'}, \xi) + \hat{H}_T(\xi) \right] \Psi_{\alpha'}(\vec{r}_{\alpha'}) \chi_{\alpha'}(\xi) = \sum_{\alpha'} E \Psi_{\alpha'}(\vec{r}_{\alpha'}) \chi_{\alpha'}(\xi), \quad (\text{A.4})$$

which can be multiplied from the left by  $\chi_{\alpha}^*(\xi)$  and integrated over the internal coordinates  $\xi$ , so that one gets

$$\left[ \hat{T} + \epsilon_{\alpha} - E \right] \Psi_{\alpha}(\vec{r}) = - \sum_{\alpha'} \left[ \int d\xi \chi_{\alpha}^*(\xi) \hat{V}(\vec{r}_{\alpha'}, \xi) \chi_{\alpha'}(\xi) \right] \Psi_{\alpha'}(\vec{r}). \quad (\text{A.5})$$

The coupled interaction potential  $V_{\alpha\alpha'}(\vec{r})$  can be defined as

$$\hat{V}_{\alpha\alpha'}(\vec{r}_{\alpha}) = \int d\xi \chi_{\alpha}^*(\xi) \hat{V}(\vec{r}_{\alpha'}, \xi) \chi_{\alpha'}(\xi). \quad (\text{A.6})$$

It can be introduced in Eq. A.4, which becomes

$$\left[ \hat{T} + \epsilon_{\alpha} - E \right] \Psi_{\alpha}(\vec{r}_{\alpha}) = - \sum_{\alpha'} V_{\alpha\alpha'}(\vec{r}_{\alpha'}) \Psi_{\alpha'}(\vec{r}_{\alpha'}). \quad (\text{A.7})$$

To simplify the following derivation, the left-hand-side indices of Eq. A.7 are modified, so that the equation becomes

$$\left[ \hat{T} + \epsilon_{\alpha''} - E \right] \Psi_{\alpha''}(\vec{r}_{\alpha''}) = - \sum_{\alpha'} V_{\alpha''\alpha'}(\vec{r}_{\alpha'}) \Psi_{\alpha'}(\vec{r}_{\alpha'}). \quad (\text{A.8})$$

If the potential is central<sup>1</sup> the wave function  $\Psi_\alpha(\vec{r})$  can be further expanded using the spherical harmonics functions  $Y_\ell^m$  as

$$\Psi_\alpha(\vec{r}_\alpha) = \sum_{\ell=0}^{\infty} \sum_{m=-\ell}^{\ell} \frac{u_c(r_\alpha)}{r_\alpha} Y_\ell^m(\hat{\Omega}_\alpha), \quad (\text{A.9})$$

where the channel notation  $c$  is introduced to take into account the dependence of  $u$  on  $\ell$  and  $m$  (*cf.* Chapter 2 Section 2.1). Here the hat sign above  $\hat{\Omega}_\alpha$  means that it is a direction vector (unitary), not an operator like  $\hat{H}$ . Inserting Eq. A.9 into Eq. A.8, multiplying by  $Y_\ell^{m*}(\hat{\Omega}_{\alpha''})$  from the left and integrating over the solid angle  $\hat{\Omega}_{\alpha''}$ , it yields

$$\left[ -\frac{\hbar^2}{2m} \left( \frac{d^2}{dr_{\alpha''}^2} - \frac{\ell''(\ell''+1)}{r_{\alpha''}^2} \right) + \epsilon_{\alpha''} - E \right] \delta_{\ell\ell''} \delta_{mm''} u_{c''}(r_{\alpha''}) = - \sum_{\alpha'} \sum_{\ell', m' |_{\alpha'}} \left[ \int_{4\pi} d^2\hat{\Omega}_{\alpha''} Y_\ell^{m*}(\hat{\Omega}_{\alpha''}) \hat{V}_{\alpha''\alpha'}(\vec{r}_{\alpha'}) Y_{\ell'}^{m'}(\hat{\Omega}_{\alpha'}) \right] u_{c'}(r_{\alpha'}). \quad (\text{A.10})$$

Choosing  $Y_\ell^{m*}(\hat{\Omega}_{\alpha''})$  so that  $\ell = \ell''$  and  $m = m''$ , Eq. A.10 can be refurbished as

$$\left[ -\frac{\hbar^2}{2m} \left( \frac{d^2}{dr_\alpha^2} - \frac{\ell(\ell+1)}{r_\alpha^2} \right) + \epsilon_\alpha - E \right] u_c(r_\alpha) = - \sum_{\alpha'} \sum_{\ell', m' |_{\alpha'}} \left[ \int_{4\pi} d^2\hat{\Omega}_\alpha Y_\ell^{m*}(\hat{\Omega}_\alpha) \hat{V}_{\alpha\alpha'}(\vec{r}_{\alpha'}) Y_{\ell'}^{m'}(\hat{\Omega}_{\alpha'}) \right] u_{c'}(r_{\alpha'}). \quad (\text{A.11})$$

The channel wave number  $k_c$  and the radial coupling potential  $\hat{W}_{cc'}$  can be defined as

$$k_c^2 = \frac{2m}{\hbar^2} (E - \epsilon_\alpha), \quad (\text{A.12})$$

$$\hat{W}_{cc'}(r_{\alpha'}) = \frac{2m}{\hbar^2} \int_{4\pi} d^2\hat{\Omega}_\alpha Y_\ell^{m*}(\hat{\Omega}_\alpha) \hat{V}_{cc'}(\vec{r}) Y_{\ell'}^{m'}(\hat{\Omega}_{\alpha'}). \quad (\text{A.13})$$

Using Eqs. A.12 and A.13 into Eq. A.11, one finally obtains the general coupled channel equation

$$\left[ \frac{d^2}{dr_\alpha^2} - \frac{\ell(\ell+1)}{r_\alpha^2} + k_c^2 \right] u_c(r_\alpha) = \sum_{c'} W_{cc'}(r_{\alpha'}) u_{c'}(r_{\alpha'}). \quad (\text{A.14})$$

## A.2 Expansion of the Interaction Potential

The dependence of the interaction potential  $V(\vec{r}, \xi)$  on the internal coordinates  $\xi$  is made through a dependence on the orientation of the nucleus  $\hat{r}'$  (expressed in the laboratory framework). More precisely, the potential is made dependent on the angle between the incidence direction of the projectile and the orientation axis of the target nucleus ( $\hat{r} \cdot \hat{r}'$ ). The potential is also dependent on the distance  $r$  between the centers of mass of the projectile and the target, it can be written as

$$V(\vec{r}, \xi) = V(r, \hat{r} \cdot \hat{r}'). \quad (\text{A.15})$$

---

<sup>1</sup>This approximation is valid only when the distance between the target and the nucleus is “large enough”.

Such a potential can be expanded using the Legendre polynomials base

$$V(r, \hat{r} \cdot \hat{r}') = \sum_{\lambda=0}^{\infty} (2\lambda + 1) V_{\lambda}(r) P_{\lambda}(\hat{r} \cdot \hat{r}'), \quad (\text{A.16})$$

where  $V_{\lambda}$  is given by

$$V_{\lambda}(r) = \frac{1}{2} \int_{-1}^{+1} dx P_{\lambda}(x) V(r, x). \quad (\text{A.17})$$

The spherical harmonics addition theorem gives

$$P_{\lambda}(\hat{r} \cdot \hat{r}') = \frac{4\pi}{2\lambda + 1} \sum_{\mu=-\lambda}^{\lambda} Y_{\lambda}^{\mu}(\hat{r}) Y_{\lambda}^{\mu}(\hat{r}')^*. \quad (\text{A.18})$$

Using Eq. A.18 into Eq. A.16, the interaction potential can be expanded as

$$V(\vec{r}, \xi) = V(r, \hat{r} \cdot \hat{r}') = 4\pi \sum_{\lambda=0}^{\infty} V_{\lambda}(r) \sum_{\mu=-\lambda}^{\lambda} Y_{\lambda}^{\mu}(\hat{r}) Y_{\lambda}^{\mu}(\hat{r}')^*. \quad (\text{A.19})$$

The projectile is assumed to be in a state  $|j_i m_i\rangle$  coupled with a nucleus in a state  $|I_i M_i\rangle$ . Additionally the ejectile, in a state  $|j_f m_f\rangle$  leaves the residual nucleus in a state  $|I_f M_f\rangle$ . In this whole process, there is conservation of the total angular momentum  $\vec{J} = \vec{j}_i + \vec{I}_i = \vec{j}_f + \vec{I}_f$  and its  $z$ -projected component  $J_z = j_z + I_z$ . Only channels having the same  $J$  and  $M$  quantum numbers can be coupled. The coupling matrix element is defined as

$$\langle \Psi_f^{JM} | V(\vec{r}, \xi) | \Psi_i^{JM} \rangle. \quad (\text{A.20})$$

The integration must be performed over the coordinates  $\xi$  and  $\hat{r}$ . In the present case  $\xi$  is only  $\hat{r}'$ , the matrix element can thus be written as

$$\langle \Psi_f^{JM} | V(r, \hat{r} \cdot \hat{r}') | \Psi_i^{JM} \rangle_{\hat{r}, \hat{r}'} . \quad (\text{A.21})$$

Using the expansion of  $V$  on the spherical harmonics (Eq. A.19), the coupling matrix element can be written as

$$\langle \Psi_f^{JM} | V(\vec{r}, \xi) | \Psi_i^{JM} \rangle = 4\pi \sum_{\lambda=0}^{\infty} V_{\lambda}(r) \sum_{\mu=-\lambda}^{\lambda} \langle \Psi_f^{JM} | Y_{\lambda}^{\mu}(\hat{r}) Y_{\lambda}^{\mu}(\hat{r}')^* | \Psi_i^{JM} \rangle_{\hat{r}, \hat{r}'} . \quad (\text{A.22})$$

As the integration is not performed over  $r$ ,  $V_{\lambda}(r)$  has been moved out of the integral. The wave function  $|\Psi_i^{JM}\rangle$  can be expressed, using the Clebsch-Gordan coefficients, as a sum of coupled target and projectile states (respectively  $|I_i M_i\rangle$  and  $|j_i m_i\rangle$ ), so that

$$|\Psi_i^{JM}\rangle = \sum_{m_i M_i} \langle JM | I_i j_i M_i m_i \rangle |I_i M_i\rangle |j_i m_i\rangle . \quad (\text{A.23})$$

Hence, the coupling matrix element that needs to be computed is

$$\begin{aligned} & \langle \Psi_f^{JM} | Y_{\lambda}^{\mu}(\hat{r}) Y_{\lambda}^{\mu}(\hat{r}')^* | \Psi_i^{JM} \rangle_{\hat{r}, \hat{r}'} \\ &= \sum_{m_i M_i m_f M_f} \langle JM | I_i j_i M_i m_i \rangle \langle JM | I_f j_f M_f m_f \rangle \langle j_f m_f | Y_{\lambda}^{\mu}(\hat{r}) | j_i m_i \rangle_{\hat{r}} \langle I_f M_f | Y_{\lambda}^{\mu}(\hat{r}')^* | I_i M_i \rangle_{\hat{r}'} . \end{aligned} \quad (\text{A.24})$$

### A.2.1 Nucleus Coupling Matrix Element $\langle I_f M_f | Y_\lambda^\mu(\hat{r}')^* | I_i M_i \rangle_{\hat{r}'}$

To compute the nucleus coupling matrix element  $\langle I_f M_f | Y_\lambda^\mu(\hat{r}')^* | I_i M_i \rangle_{\hat{r}'}$ , the following property is used (*cf.* Eq. 4.17 of Ref. [56])

$$\langle I_f M_f | Y_\lambda^\mu(\hat{r}')^* | I_i M_i \rangle_{\hat{r}'} = (-1)^\mu \langle I_f M_f | Y_\lambda^{-\mu}(\hat{r}') | I_i M_i \rangle_{\hat{r}'}, \quad (\text{A.25})$$

$$= (-1)^\mu \langle I_f M_f | I_i \lambda M_i(-\mu) \rangle \left[ \frac{(2I_i + 1)(2\lambda + 1)}{4\pi(2I_f + 1)} \right]^{1/2} \langle I_f 0 | \lambda I_i 00 \rangle. \quad (\text{A.26})$$

A connection can be made between the Clebsch-Gordan coefficients and the Wigner 3- $j$  symbols

$$\langle I_f M_f | I_i \lambda M_i(-\mu) \rangle = \begin{pmatrix} I_i & \lambda & I_f \\ M_i & -\mu & -M_f \end{pmatrix} (2I_f + 1)^{1/2} (-1)^{I_i - \lambda + M_f}, \quad (\text{A.27})$$

and in particular (*cf.* Eq. 3.3 of Ref. [56])

$$\langle I_f 0 | \lambda I_i 00 \rangle = \begin{pmatrix} \lambda & I_i & I_f \\ 0 & 0 & 0 \end{pmatrix} (2I_f + 1)^{1/2} (-1)^{\lambda - I_i}. \quad (\text{A.28})$$

Inserting Eqs. A.27 and A.28 into Eq. A.26 it yields

$$\begin{aligned} \langle I_f M_f | Y_\lambda^\mu(\hat{r}')^* | I_i M_i \rangle_{\hat{r}'} = \\ (-1)^{M_f + \mu} \left[ \frac{(2I_i + 1)(2\lambda + 1)(2I_f + 1)}{4\pi} \right]^{\frac{1}{2}} \begin{pmatrix} I_i & \lambda & I_f \\ M_i & -\mu & -M_f \end{pmatrix} \begin{pmatrix} \lambda & I_i & I_f \\ 0 & 0 & 0 \end{pmatrix}. \end{aligned} \quad (\text{A.29})$$

The Wigner 3- $j$  symbols are invariant by circular permutation of the columns, so that

$$\begin{aligned} \langle I_f M_f | Y_\lambda^\mu(\hat{r}')^* | I_i M_i \rangle_{\hat{r}'} = \\ (-1)^{M_f + \mu} \left[ \frac{(2I_i + 1)(2\lambda + 1)(2I_f + 1)}{4\pi} \right]^{\frac{1}{2}} \begin{pmatrix} I_f & I_i & \lambda \\ -M_f & M_i & -\mu \end{pmatrix} \begin{pmatrix} I_i & I_f & \lambda \\ 0 & 0 & 0 \end{pmatrix}. \end{aligned} \quad (\text{A.30})$$

The Wigner 3- $j$  symbols property

$$\begin{pmatrix} a & b & c \\ \alpha & \beta & \gamma \end{pmatrix} = (-1)^{a+b+c} \begin{pmatrix} a & b & c \\ -\alpha & -\beta & -\gamma \end{pmatrix}, \quad (\text{A.31})$$

is used for both Wigner 3- $j$  symbols of Eq. A.30, so that it becomes

$$\begin{aligned} \langle I_f M_f | Y_\lambda^\mu(\hat{r}')^* | I_i M_i \rangle_{\hat{r}'} = \\ (-1)^{M_f + \mu} \left[ \frac{(2I_i + 1)(2\lambda + 1)(2I_f + 1)}{4\pi} \right]^{\frac{1}{2}} \begin{pmatrix} I_f & I_i & \lambda \\ M_f & -M_i & \mu \end{pmatrix} \begin{pmatrix} I_i & I_f & \lambda \\ 0 & 0 & 0 \end{pmatrix}. \end{aligned} \quad (\text{A.32})$$

The first Wigner 3- $j$  symbol is different from zero only if  $M_f - M_i + \mu = 0$ . Hence the nucleus coupling matrix element  $\langle I_f M_f | Y_\lambda^\mu(\hat{r}')^* | I_i M_i \rangle_{\hat{r}'}$  can be written

$$\begin{aligned} \langle I_f M_f | Y_\lambda^\mu(\hat{r}')^* | I_i M_i \rangle_{\hat{r}'} = \\ (-1)^{M_i} \left[ \frac{(2I_i + 1)(2\lambda + 1)(2I_f + 1)}{4\pi} \right]^{\frac{1}{2}} \begin{pmatrix} I_f & I_i & \lambda \\ M_f & -M_i & \mu \end{pmatrix} \begin{pmatrix} I_i & I_f & \lambda \\ 0 & 0 & 0 \end{pmatrix}. \end{aligned} \quad (\text{A.33})$$

### A.2.2 Particle Coupling Matrix Element $\langle j_{\mathbf{f}}m_{\mathbf{f}}|Y_{\lambda}^{\mu}(\hat{r})|j_{\mathbf{i}}m_{\mathbf{i}}\rangle_{\hat{r}}$

To compute the particle coupling matrix element  $\langle j_{\mathbf{f}}m_{\mathbf{f}}|Y_{\lambda}^{\mu}(\hat{r})|j_{\mathbf{i}}m_{\mathbf{i}}\rangle_{\hat{r}}$ , the following properties are used (*cf.* Eq. 4.15 of Ref. [56])

$$\langle j_{\mathbf{f}}m_{\mathbf{f}}|Y_{\lambda}^{\mu}(\hat{r})|j_{\mathbf{i}}m_{\mathbf{i}}\rangle_{\hat{r}} = \langle \ell_{\mathbf{f}}s_{\mathbf{f}}j_{\mathbf{f}}m_{\mathbf{f}}|Y_{\lambda}^{\mu}(\hat{r})|\ell_{\mathbf{i}}s_{\mathbf{i}}j_{\mathbf{i}}m_{\mathbf{i}}\rangle \quad (\text{A.34})$$

$$= (-1)^{2\lambda} \langle \ell_{\mathbf{f}}s_{\mathbf{f}}j_{\mathbf{f}}||Y_{\lambda}(\hat{r})||\ell_{\mathbf{i}}s_{\mathbf{i}}j_{\mathbf{i}}\rangle \langle j_{\mathbf{f}}m_{\mathbf{f}}|j_{\mathbf{i}}\lambda m_{\mathbf{i}}\mu\rangle, \quad (\text{A.35})$$

and (*cf.* Eq. 5.9 of Ref. [56])

$$\langle \ell_{\mathbf{f}}s_{\mathbf{f}}j_{\mathbf{f}}||Y_{\lambda}(\hat{r})||\ell_{\mathbf{i}}s_{\mathbf{i}}j_{\mathbf{i}}\rangle = (-1)^{j_{\mathbf{f}}-\lambda-s+\ell_{\mathbf{i}}} [(2\ell_{\mathbf{f}}+1)(2j_{\mathbf{i}}+1)]^{1/2} W(\ell_{\mathbf{f}}\ell_{\mathbf{i}}j_{\mathbf{f}}j_{\mathbf{i}}; \lambda s) \langle \ell_{\mathbf{f}}||Y_{\lambda}||\ell_{\mathbf{i}}\rangle, \quad (\text{A.36})$$

where  $W$  is the Racah coefficient. Finally one has (*cf.* Eq. 4.17 of Ref. [56])

$$\langle \ell_{\mathbf{f}}||Y_{\lambda}||\ell_{\mathbf{i}}\rangle = \left[ \frac{(2\ell_{\mathbf{i}}+1)(2\lambda+1)}{4\pi(2\ell_{\mathbf{f}}+1)} \right]^{1/2} \langle \ell_{\mathbf{f}}0|\lambda\ell_{\mathbf{i}}00\rangle. \quad (\text{A.37})$$

Using Eq. A.37 into Eq. A.36, it yields

$$\begin{aligned} \langle \ell_{\mathbf{f}}s_{\mathbf{f}}j_{\mathbf{f}}||Y_{\lambda}(\hat{r})||\ell_{\mathbf{i}}s_{\mathbf{i}}j_{\mathbf{i}}\rangle = \\ (-1)^{j_{\mathbf{f}}-\lambda-s+\ell_{\mathbf{i}}} \left[ \frac{(2\ell_{\mathbf{i}}+1)(2\lambda+1)(2j_{\mathbf{i}}+1)}{4\pi} \right]^{1/2} W(\ell_{\mathbf{i}}\ell_{\mathbf{f}}j_{\mathbf{i}}j_{\mathbf{f}}; \lambda s) \langle \ell_{\mathbf{f}}0|\lambda\ell_{\mathbf{i}}00\rangle. \end{aligned} \quad (\text{A.38})$$

The last Clebsch-Gordan coefficient of Eq. A.38 can be turned into a Wigner 3- $j$  symbol using Eq. A.28

$$\langle \ell_{\mathbf{f}}0|\lambda\ell_{\mathbf{i}}00\rangle = \begin{pmatrix} \lambda & \ell_{\mathbf{i}} & \ell_{\mathbf{f}} \\ 0 & 0 & 0 \end{pmatrix} (2\ell_{\mathbf{f}}+1)^{1/2} (-1)^{\lambda-\ell_{\mathbf{i}}}, \quad (\text{A.39})$$

So that Eq. A.38 becomes

$$\begin{aligned} \langle \ell_{\mathbf{f}}s_{\mathbf{f}}j_{\mathbf{f}}||Y_{\lambda}(\hat{r})||\ell_{\mathbf{i}}s_{\mathbf{i}}j_{\mathbf{i}}\rangle = \\ (-1)^{j_{\mathbf{f}}-s} \left[ \frac{(2\ell_{\mathbf{i}}+1)(2\ell_{\mathbf{f}}+1)(2\lambda+1)(2j_{\mathbf{i}}+1)}{4\pi} \right]^{1/2} W(\ell_{\mathbf{i}}\ell_{\mathbf{f}}j_{\mathbf{i}}j_{\mathbf{f}}; \lambda s) \begin{pmatrix} \lambda & \ell_{\mathbf{i}} & \ell_{\mathbf{f}} \\ 0 & 0 & 0 \end{pmatrix}. \end{aligned} \quad (\text{A.40})$$

The remaining Clebsch-Gordan of Eq. A.35 can be turned into a Wigner 3- $j$  symbol using Eq. A.27:

$$\langle j_{\mathbf{f}}m_{\mathbf{f}}|j_{\mathbf{i}}\lambda m_{\mathbf{i}}\mu\rangle = \begin{pmatrix} j_{\mathbf{i}} & \lambda & j_{\mathbf{f}} \\ m_{\mathbf{i}} & \mu & -m_{\mathbf{f}} \end{pmatrix} (2j_{\mathbf{f}}+1)^{1/2} (-1)^{j_{\mathbf{i}}-\lambda+m_{\mathbf{f}}}. \quad (\text{A.41})$$

Inserting Eqs. A.41 and A.40 into Eq. A.35, the particle coupling matrix element can be finally obtained as

$$\begin{aligned} \langle j_{\mathbf{f}}m_{\mathbf{f}}|Y_{\lambda}^{\mu}(\hat{r})|j_{\mathbf{i}}m_{\mathbf{i}}\rangle_{\hat{r}} = (-1)^{\lambda+j_{\mathbf{f}}-s+j_{\mathbf{i}}+m_{\mathbf{f}}} \left[ \frac{(2\ell_{\mathbf{i}}+1)(2\ell_{\mathbf{f}}+1)(2\lambda+1)(2j_{\mathbf{i}}+1)(2j_{\mathbf{f}}+1)}{4\pi} \right]^{1/2} \\ \times W(\ell_{\mathbf{i}}\ell_{\mathbf{f}}j_{\mathbf{i}}j_{\mathbf{f}}; \lambda s) \begin{pmatrix} \lambda & \ell_{\mathbf{i}} & \ell_{\mathbf{f}} \\ 0 & 0 & 0 \end{pmatrix} \begin{pmatrix} j_{\mathbf{i}} & \lambda & j_{\mathbf{f}} \\ m_{\mathbf{i}} & \mu & -m_{\mathbf{f}} \end{pmatrix}. \end{aligned} \quad (\text{A.42})$$



### A.2.3 Full Matrix Element $\langle \Psi_f^{JM} | Y_\lambda^\mu(\hat{r}) Y_\lambda^\mu(\hat{r}')^* | \Psi_i^{JM} \rangle_{\hat{r}, \hat{r}'}$

The full matrix element is calculated using the nucleus and particle matrix elements as in Eq. A.24 recalled below

$$\begin{aligned} & \langle \Psi_f^{JM} | Y_\lambda^\mu(\hat{r}) Y_\lambda^\mu(\hat{r}')^* | \Psi_i^{JM} \rangle_{\hat{r}, \hat{r}'} \\ &= \sum_{m_i M_i m_f M_i} \langle JM | I_i j_i M_i m_i \rangle \langle JM | I_f j_f M_f m_f \rangle \langle j_i m_i | Y_\lambda^\mu(\hat{r}) | j_i m_i \rangle_{\hat{r}} \langle I_f M_f | Y_\lambda^\mu(\hat{r}')^* | I_i M_i \rangle_{\hat{r}'} . \end{aligned} \quad (\text{A.43})$$

The Clebsch-Gordan coefficients of Eq. A.43 are then turned into Wigner 3- $j$  symbols (cf. Eq. 3.3 of Ref. [56])

$$\langle JM | I_i j_i M_i m_i \rangle = \begin{pmatrix} I_i & j_i & J \\ M_i & m_i & -M \end{pmatrix} (2J+1)^{1/2} (-1)^{I_i - j_i + M}, \quad (\text{A.44})$$

$$\langle JM | I_f j_f M_f m_f \rangle = \begin{pmatrix} I_f & j_f & J \\ M_f & m_f & -M \end{pmatrix} (2J+1)^{1/2} (-1)^{-I_f + j_f - M}. \quad (\text{A.45})$$

Using both of these expressions into Eq. A.43 it leads to

$$\begin{aligned} & \langle \Psi_f^{JM} | Y_\lambda^\mu(\hat{r}) Y_\lambda^\mu(\hat{r}')^* | \Psi_i^{JM} \rangle_{\hat{r}, \hat{r}'} = \\ & \sum_{m_i M_i m_f M_i} (2J+1) (-1)^{I_i - j_i - I_f + j_f} \begin{pmatrix} I_i & j_i & J \\ M_i & m_i & -M \end{pmatrix} \begin{pmatrix} I_f & j_f & J \\ M_f & m_f & -M \end{pmatrix} \\ & \times \langle j_f m_f | Y_\lambda^\mu(\hat{r}) | j_i m_i \rangle_{\hat{r}} \langle I_f M_f | Y_\lambda^\mu(\hat{r}')^* | I_i M_i \rangle_{\hat{r}'} . \end{aligned} \quad (\text{A.46})$$

The  $\mu$ -summation is introduced back, as in Eq. A.22, so that

$$\begin{aligned} & \langle \Psi_f^{JM} | \sum_{\mu=-\lambda}^{\lambda} Y_\lambda^\mu(\hat{r}) Y_\lambda^\mu(\hat{r}')^* | \Psi_i^{JM} \rangle_{\hat{r}, \hat{r}'} \\ &= \sum_{m_i M_i m_f M_i \mu} (2J+1) (-1)^{I_i - j_i - I_f + j_f} \begin{pmatrix} I_i & j_i & J \\ M_i & m_i & -M \end{pmatrix} \begin{pmatrix} I_f & j_f & J \\ M_f & m_f & -M \end{pmatrix} \\ & \times \langle j_f m_f | Y_\lambda^\mu(\hat{r}) | j_i m_i \rangle_{\hat{r}} \langle I_f M_f | Y_\lambda^\mu(\hat{r}')^* | I_i M_i \rangle_{\hat{r}'} . \end{aligned} \quad (\text{A.47})$$

Replacing the particle matrix element  $\langle j_f m_f | Y_\lambda^\mu(\hat{r}) | j_i m_i \rangle_{\hat{r}}$  and the nucleus matrix elements  $\langle I_f M_f | Y_\lambda^\mu(\hat{r}')^* | I_i M_i \rangle_{\hat{r}'}$  given by Eqs. A.42 and A.33 respectively, it yields

$$\begin{aligned} & \langle \Psi_f^{JM} | \sum_{\mu=-\lambda}^{\lambda} Y_\lambda^\mu(\hat{r}) Y_\lambda^\mu(\hat{r}')^* | \Psi_i^{JM} \rangle_{\hat{r}, \hat{r}'} \\ &= \frac{(2J+1)(2\lambda+1)}{4\pi} [(2I_i+1)(2I_f+1)(2j_i+1)(2j_f+1)]^{\frac{1}{2}} \\ & \times \begin{pmatrix} I_i & I_f & \lambda \\ 0 & 0 & 0 \end{pmatrix} [(2\ell_i+1)(2\ell_f+1)]^{1/2} W(\ell_i \ell_f j_i j_f; \lambda s) \begin{pmatrix} \lambda & \ell_i & \ell_f \\ 0 & 0 & 0 \end{pmatrix} (-1)^{J+\lambda-s} \\ & \times \sum_{m_i M_i m_f M_i \mu} \left[ (-1)^{-J+I_i-I_f+2j_f+M_i+m_f} \begin{pmatrix} I_i & j_i & J \\ M_i & m_i & -M \end{pmatrix} \begin{pmatrix} I_f & j_f & J \\ M_f & m_f & -M \end{pmatrix} \right. \\ & \left. \times \begin{pmatrix} j_i & \lambda & j_f \\ m_i & \mu & -m_f \end{pmatrix} \begin{pmatrix} I_f & I_i & \lambda \\ M_f & -M_i & \mu \end{pmatrix} \right]. \end{aligned} \quad (\text{A.48})$$

As  $(-1)^{I_i+I_f+\lambda} = 1$ , Eq. A.48 “simplifies” to

$$\begin{aligned}
& \langle \Psi_f^{JM} | \sum_{\mu=-\lambda}^{\lambda} Y_{\lambda}^{\mu}(\hat{r}) Y_{\lambda}^{\mu}(\hat{r}')^* | \Psi_i^{JM} \rangle_{\hat{r}, \hat{r}'} \\
&= \frac{(2J+1)(2\lambda+1)}{4\pi} [(2I_i+1)(2I_f+1)(2j_i+1)(2j_f+1)]^{\frac{1}{2}} \\
&\times \begin{pmatrix} I_i & I_f & \lambda \\ 0 & 0 & 0 \end{pmatrix} [(2\ell_i+1)(2\ell_f+1)]^{1/2} W(\ell_i \ell_f j_i j_f; \lambda s) \begin{pmatrix} \lambda & \ell_i & \ell_f \\ 0 & 0 & 0 \end{pmatrix} (-1)^{J+\lambda-s} \\
&\times \sum_{m_i M_i m_f M_i \mu} \left[ (-1)^{-J+2I_i+\lambda+2j_f+M_i+m_f} \begin{pmatrix} I_i & j_i & J \\ M_i & m_i & -M \end{pmatrix} \begin{pmatrix} I_f & j_f & J \\ M_f & m_f & -M \end{pmatrix} \right. \\
&\quad \left. \times \begin{pmatrix} j_i & \lambda & j_f \\ m_i & \mu & -m_f \end{pmatrix} \begin{pmatrix} I_f & I_i & \lambda \\ M_f & -M_i & \mu \end{pmatrix} \right]. \quad (\text{A.49})
\end{aligned}$$

The following sum  $X$  can be calculated

$$\begin{aligned}
X = \sum_{m_i M_i m_f M_i \mu} & (-1)^{-J+2I_i+\lambda+2j_f+M_i+m_f} \begin{pmatrix} I_i & j_i & J \\ M_i & m_i & -M \end{pmatrix} \begin{pmatrix} I_f & j_f & J \\ M_f & m_f & -M \end{pmatrix} \\
& \times \begin{pmatrix} j_i & \lambda & j_f \\ m_i & \mu & -m_f \end{pmatrix} \begin{pmatrix} I_f & I_i & \lambda \\ M_f & -M_i & \mu \end{pmatrix}. \quad (\text{A.50})
\end{aligned}$$

By successive indices permutations, it yields

$$\begin{aligned}
X = \sum_{m_i M_i m_f M_i \mu} & (-1)^{-J+2I_i+\lambda+2j_f+M_i+m_f} \begin{pmatrix} I_i & j_i & J \\ M_i & m_i & -M \end{pmatrix} \begin{pmatrix} j_i & \lambda & j_f \\ m_i & \mu & -m_f \end{pmatrix} \\
& \times \begin{pmatrix} I_f & I_i & \lambda \\ M_f & -M_i & \mu \end{pmatrix} \begin{pmatrix} I_f & j_f & J \\ M_f & m_f & -M \end{pmatrix}, \quad (\text{A.51})
\end{aligned}$$

and

$$\begin{aligned}
X = \sum_{m_i M_i m_f M_i \mu} & (-1)^{I_i+j_i+4j_f+\lambda+M_i+m_f} \begin{pmatrix} I_i & j_i & J \\ M_i & m_i & -M \end{pmatrix} \begin{pmatrix} j_i & \lambda & j_f \\ -m_i & -\mu & m_f \end{pmatrix} \\
& \times \begin{pmatrix} \lambda & I_i & I_f \\ \mu & -M_i & M_f \end{pmatrix} \begin{pmatrix} j_f & I_f & J \\ m_f & M_f & -M \end{pmatrix}. \quad (\text{A.52})
\end{aligned}$$

As  $j_f$  is either an integer or a half-integer, therefore  $(-1)^{4j_f} = 1$ . One has  $m_f = m_i + \mu$ , and  $(-1)^{m_f} = (-1)^{-m_f} = (-1)^{-m_i}(-1)^{-\mu}$ . As  $\mu$  is an integer,  $(-1)^{-\mu} = (-1)^{\mu}$ . Finally,  $(-1)^{m_f} = (-1)^{-m_i+\mu}$ , so that Eq. A.52 becomes

$$\begin{aligned}
X = \sum_{m_i M_i m_f M_i \mu} & (-1)^{I_i+\lambda+j_i+M_i-m_i+\mu} \begin{pmatrix} I_i & j_i & J \\ M_i & m_i & -M \end{pmatrix} \begin{pmatrix} j_i & \lambda & j_f \\ -m_i & -\mu & m_f \end{pmatrix} \\
& \times \begin{pmatrix} \lambda & I_i & I_f \\ \mu & -M_i & M_f \end{pmatrix} \begin{pmatrix} j_f & I_f & J \\ m_f & M_f & -M \end{pmatrix}. \quad (\text{A.53})
\end{aligned}$$

The  $X$  sum can be turned into a Wigner 6- $j$  symbol using (*cf.* Appendix II of Ref. [56])

$$\sum_{\alpha\beta\gamma\alpha'\beta'} (-1)^{A+B+C+\alpha+\beta+\gamma} \begin{pmatrix} A & B & c \\ \alpha & -\beta & \gamma' \end{pmatrix} \begin{pmatrix} B & C & a \\ \beta & -\gamma & \alpha' \end{pmatrix} \begin{pmatrix} C & A & b \\ \gamma & -\alpha & \beta' \end{pmatrix} \begin{pmatrix} a & b & c \\ \alpha' & \beta' & \gamma' \end{pmatrix}$$

$$= \frac{1}{2c+1} \begin{Bmatrix} a & b & c \\ A & B & C \end{Bmatrix}. \quad (\text{A.54})$$

Applied to  $X$ , one gets

$$X = \frac{1}{2J+1} \begin{Bmatrix} j_f & I_f & J \\ I_i & j_i & \lambda \end{Bmatrix} = \frac{1}{2J+1} \begin{Bmatrix} I_i & I_f & \lambda \\ j_f & j_i & J \end{Bmatrix}. \quad (\text{A.55})$$

Gathering all terms, Eq. A.49 becomes

$$\begin{aligned} \langle \Psi_f^{JM} | \sum_{\mu=-\lambda}^{\lambda} Y_{\lambda}^{\mu}(\hat{r}) Y_{\lambda}^{\mu}(\hat{r}')^* | \Psi_i^{JM} \rangle_{\hat{r}, \hat{r}'} &= \frac{2\lambda+1}{4\pi} [(2I_i+1)(2I_f+1)(2j_i+1)(2j_f+1)]^{\frac{1}{2}} \\ &\times \begin{pmatrix} I_i & I_f & \lambda \\ 0 & 0 & 0 \end{pmatrix} (-1)^{J+\lambda-s} [(2\ell_i+1)(2\ell_f+1)]^{1/2} W(\ell_i \ell_f j_i j_f; \lambda s) \\ &\times \begin{pmatrix} \lambda & \ell_i & \ell_f \\ 0 & 0 & 0 \end{pmatrix} \begin{Bmatrix} I_i & I_f & \lambda \\ j_f & j_i & J \end{Bmatrix}. \end{aligned} \quad (\text{A.56})$$

Equation A.56 can be written using Racah coefficients only

$$\begin{aligned} \langle \Psi_f^{JM} | \sum_{\mu=-\lambda}^{\lambda} Y_{\lambda}^{\mu}(\hat{r}) Y_{\lambda}^{\mu}(\hat{r}')^* | \Psi_i^{JM} \rangle_{\hat{r}, \hat{r}'} &= \frac{2\lambda+1}{4\pi} [(2I_i+1)(2I_f+1)(2j_i+1)(2j_f+1)]^{\frac{1}{2}} \begin{pmatrix} I_i & I_f & \lambda \\ 0 & 0 & 0 \end{pmatrix} (-1)^{J+\lambda-s+I_f+j_f+I_i+j_i} \\ &\times [(2\ell_i+1)(2\ell_f+1)]^{1/2} W(\ell_i \ell_f j_i j_f; \lambda s) \begin{pmatrix} \lambda & \ell_i & \ell_f \\ 0 & 0 & 0 \end{pmatrix} W(I_i I_f j_i j_f; \lambda J). \end{aligned} \quad (\text{A.57})$$

Finally, one obtains the full matrix element:

$$\begin{aligned} \langle \Psi_f^{JM} | V(\vec{r}, \xi) | \Psi_i^{JM} \rangle &= \sum_{\lambda=0}^{\infty} V_{\lambda}(r) (2\lambda+1) [(2I_i+1)(2I_f+1)(2j_i+1)(2j_f+1)]^{1/2} \begin{pmatrix} I_i & I_f & \lambda \\ 0 & 0 & 0 \end{pmatrix} \\ &\times (-1)^{J+\lambda-s+I_f+j_f+I_i+j_i} [(2\ell_i+1)(2\ell_f+1)]^{1/2} \\ &W(\ell_i \ell_f j_i j_f; \lambda s) \begin{pmatrix} \lambda & \ell_i & \ell_f \\ 0 & 0 & 0 \end{pmatrix} W(I_i I_f j_i j_f; \lambda J). \end{aligned} \quad (\text{A.58})$$

## A.3 Special Cases

Two special cases are treated here, depending if the the incident particle has a 0- or  $\frac{1}{2}$ -spin.

### A.3.1 Spin- $\frac{1}{2}$ Projectile

For  $s = \frac{1}{2}$ , the following relation can be used

$$[(2\ell_i+1)(2\ell_f+1)]^{1/2} W(\ell_i \ell_f j_i j_f; \lambda \frac{1}{2}) \begin{pmatrix} \lambda & \ell_i & \ell_f \\ 0 & 0 & 0 \end{pmatrix} = - \begin{pmatrix} j_i & j_f & \lambda \\ -\frac{1}{2} & \frac{1}{2} & 0 \end{pmatrix}. \quad (\text{A.59})$$

Hence, Eq. A.58 reduces to

$$\langle \Psi_f^{JM} | V(\vec{r}, \xi) | \Psi_i^{JM} \rangle = \sum_{\lambda=0}^{\infty} V_{\lambda}(r) (2\lambda + 1) [(2I_i + 1)(2I_f + 1)(2j_i + 1)(2j_f + 1)]^{1/2} \\ \begin{pmatrix} I_i & I_f & \lambda \\ 0 & 0 & 0 \end{pmatrix} (-1)^{J+\frac{1}{2}+\lambda} \begin{pmatrix} j_f & \lambda & j_i \\ -\frac{1}{2} & 0 & \frac{1}{2} \end{pmatrix} \begin{Bmatrix} I_i & I_f & \lambda \\ j_f & j_i & J \end{Bmatrix}. \quad (\text{A.60})$$

### A.3.2 Spin-0 Projectile

Using Appendix II of Ref. [56], it can be shown that

$$W(\ell_i \ell_f j_i j_f; \lambda 0) = W(j_i \ell_i j_f \ell_f; 0 \lambda) = \frac{(-1)^{j_i+j_f-\lambda}}{\sqrt{(2j_i+1)(2j_f+1)}} \delta_{j_i \ell_i} \delta_{j_f \ell_f}. \quad (\text{A.61})$$

Hence, Eq. A.58 reduces to

$$\langle \Psi_f^{JM} | \sum_{\mu=-\lambda}^{\lambda} Y_{\lambda}^{\mu}(\hat{r}) Y_{\lambda}^{\mu}(\hat{r}')^* | \Psi_i^{JM} \rangle_{\hat{r}, \hat{r}'} \\ = \frac{2\lambda+1}{4\pi} [(2I_i+1)(2I_f+1)(2l_i+1)(2l_f+1)]^{\frac{1}{2}} \begin{pmatrix} I_i & I_f & \lambda \\ 0 & 0 & 0 \end{pmatrix} \\ \times (-1)^{J+\ell_f+\ell_i} \begin{pmatrix} \lambda & \ell_i & \ell_f \\ 0 & 0 & 0 \end{pmatrix} \begin{Bmatrix} I_i & I_f & \lambda \\ j_f & j_i & J \end{Bmatrix}, \quad (\text{A.62})$$

$$= \frac{2\lambda+1}{4\pi} [(2I_i+1)(2I_f+1)(2l_i+1)(2l_f+1)]^{1/2} \begin{pmatrix} I_i & I_f & \lambda \\ 0 & 0 & 0 \end{pmatrix} \\ \times (-1)^{J+\lambda} \begin{pmatrix} \lambda & \ell_i & \ell_f \\ 0 & 0 & 0 \end{pmatrix} \begin{Bmatrix} I_i & I_f & \lambda \\ \ell_f & \ell_i & J \end{Bmatrix}, \quad (\text{A.63})$$

$$= \frac{2\lambda+1}{4\pi} [(2I_i+1)(2I_f+1)(2l_i+1)(2l_f+1)]^{1/2} \begin{pmatrix} I_i & I_f & \lambda \\ 0 & 0 & 0 \end{pmatrix} \\ \times (-1)^{J+\lambda} \begin{pmatrix} \ell_i & \ell_f & \lambda \\ 0 & 0 & 0 \end{pmatrix} \begin{Bmatrix} \ell_f & \ell_i & \lambda \\ I_i & I_f & J \end{Bmatrix}. \quad (\text{A.64})$$

## A.4 Spin-Orbit Term

The spin orbit coupling potential has a different nature than the scalar potential treated so far in this appendix. It has a general form named the *full Thomas term*

$$V_{\text{s.o.}}(\vec{r}) = \vec{\nabla} V(\vec{r}) \times \frac{\vec{\nabla}}{i} \cdot \vec{\sigma}, \quad (\text{A.65})$$

where  $V$  can be any function. First apply the expansion method is applied to a particular multipole  $V_{\lambda}(r)Y_{\lambda}^{\mu}(\hat{r})$ . Then the following property of the Pauli vector  $\vec{\sigma}$  is used:

$$\forall \vec{a}, \vec{b}, \quad (\vec{\sigma} \cdot \vec{a}) \cdot (\vec{\sigma} \cdot \vec{b}) = (\vec{a} \cdot \vec{b}) + i(\vec{a} \times \vec{b}) \cdot \vec{\sigma}. \quad (\text{A.66})$$

Applying Eq. A.66 to Eq. A.65 it yields

$$V_{\text{s.o.}}(\vec{r}) = \left( \vec{\nabla} [V_{\lambda}(r)Y_{\lambda}^{\mu}(\hat{r})] \cdot \vec{\nabla} \right) - \left( \vec{\sigma} \cdot \vec{\nabla} [V_{\lambda}(r)Y_{\lambda}^{\mu}(\hat{r})] \right) \cdot (\vec{\sigma} \cdot \vec{\nabla}). \quad (\text{A.67})$$

It can be observed that  $\vec{L} = -i\hbar\vec{r} \times \vec{\nabla}$ , so that by taking the triple cross product

$$\vec{r} \times \vec{L} = -i\hbar\vec{r} \times \vec{r} \times \vec{L} = -i\hbar \left( \vec{r} \cdot (\vec{r} \times \vec{\nabla}) - r^2 \vec{\nabla} \right). \quad (\text{A.68})$$

The gradient operator  $\vec{\nabla}$  can be expressed as

$$\vec{\nabla} = \frac{\vec{r}}{r} \frac{\partial}{\partial r} - \frac{i\vec{r} \times \vec{L}}{\hbar r^2}. \quad (\text{A.69})$$

Using Eq. A.69 for the  $\vec{\sigma} \cdot \vec{\nabla}$  operator, one obtains

$$\vec{\sigma} \cdot \vec{\nabla} = \vec{\sigma} \cdot \left( \frac{\vec{r}}{r} \frac{\partial}{\partial r} - \frac{i\vec{r} \times \vec{L}}{\hbar r^2} \right) = \frac{\vec{\sigma} \cdot \vec{r}}{r} \frac{\partial}{\partial r} - \frac{i}{\hbar r^2} \vec{\sigma} \cdot (\vec{r} \times \vec{L}), \quad (\text{A.70})$$

$$= \frac{\vec{\sigma} \cdot \vec{r}}{r} \frac{\partial}{\partial r} - \frac{1}{\hbar r^2} \left[ (\vec{\sigma} \cdot \vec{r}) \cdot (\vec{\sigma} \cdot \vec{L}) - \vec{r} \cdot \vec{L} \right]. \quad (\text{A.71})$$

As  $\vec{r} \cdot \vec{L} = 0$  (triple product containing two identical vectors), one gets

$$\vec{\sigma} \cdot \vec{\nabla} = \frac{(\vec{\sigma} \cdot \vec{r})}{r} \left[ \frac{\partial}{\partial r} - \frac{1}{\hbar r} (\vec{\sigma} \cdot \vec{L}) \right]. \quad (\text{A.72})$$

Gathering terms into Eq. A.67, it yields

$$\begin{aligned} V_{\text{s.o.}}(\vec{r}) = & \left( \left[ \frac{\vec{r}}{r} \frac{\partial}{\partial r} - \frac{i\vec{r} \times \vec{L}}{\hbar r^2} \right] [V_\lambda(r) Y_\lambda^\mu(\hat{r})] \cdot \left[ \frac{\vec{r}}{r} \frac{\partial}{\partial r} - \frac{i\vec{r} \times \vec{L}}{\hbar r^2} \right] \right) \\ & - \left( \frac{(\vec{\sigma} \cdot \vec{r})}{r} \left[ \frac{\partial}{\partial r} - \frac{1}{\hbar r} (\vec{\sigma} \cdot \vec{L}) \right] [V_\lambda(r) Y_\lambda^\mu(\hat{r})] \right) \cdot \frac{(\vec{\sigma} \cdot \vec{r})}{r} \left[ \frac{\partial}{\partial r} - \frac{1}{\hbar r} (\vec{\sigma} \cdot \vec{L}) \right]. \end{aligned} \quad (\text{A.73})$$

The general properties of the Pauli vectors (Eq. A.66) imply that  $(\vec{L} \cdot \vec{\sigma})$  and  $(\vec{\sigma} \cdot \vec{r})$  anticommute, so that

$$(\vec{L} \cdot \vec{\sigma}) \cdot (\vec{\sigma} \cdot \vec{r}) = i(\vec{r} \times \vec{L}) \cdot \vec{\sigma} = -i(\vec{L} \times \vec{r}) \cdot \vec{\sigma} = -(\vec{r} \cdot \vec{\sigma}) \cdot (\vec{\sigma} \cdot \vec{L}). \quad (\text{A.74})$$

The second term of Eq. A.73 becomes

$$\begin{aligned} & - \left( \frac{(\vec{\sigma} \cdot \vec{r})}{r} \left[ \frac{\partial}{\partial r} - \frac{1}{\hbar r} (\vec{\sigma} \cdot \vec{L}) \right] [V_\lambda(r) Y_\lambda^\mu(\hat{r})] \right) \cdot \frac{(\vec{\sigma} \cdot \vec{r})}{r} \left[ \frac{\partial}{\partial r} - \frac{1}{\hbar r} (\vec{\sigma} \cdot \vec{L}) \right] \\ & = - \left( \frac{(\vec{\sigma} \cdot \vec{r})^2}{r^2} \left[ \frac{\partial}{\partial r} + \frac{1}{\hbar r} (\vec{\sigma} \cdot \vec{L}) \right] [V_\lambda(r) Y_\lambda^\mu(\hat{r})] \right) \cdot \left[ \frac{\partial}{\partial r} - \frac{1}{\hbar r} (\vec{\sigma} \cdot \vec{L}) \right]. \end{aligned} \quad (\text{A.75})$$

From Eq. A.66 it can be seen that  $(\vec{\sigma} \cdot \vec{r})^2 = r^2$ , so that

$$\begin{aligned} V_{\text{s.o.}}(\vec{r}) = & \left( \left[ \frac{\vec{r}}{r} \frac{\partial}{\partial r} - \frac{i\vec{r} \times \vec{L}}{\hbar r^2} \right] [V_\lambda(r) Y_\lambda^\mu(\hat{r})] \cdot \left[ \frac{\vec{r}}{r} \frac{\partial}{\partial r} - \frac{i\vec{r} \times \vec{L}}{\hbar r^2} \right] \right) \\ & - \left[ \frac{\partial}{\partial r} + \frac{1}{\hbar r} (\vec{\sigma} \cdot \vec{L}) \right] [V_\lambda(r) Y_\lambda^\mu(\hat{r})] \cdot \left[ \frac{\partial}{\partial r} - \frac{1}{\hbar r} (\vec{\sigma} \cdot \vec{L}) \right]. \end{aligned} \quad (\text{A.76})$$

The first term of Eq. A.76 simplifies because  $\vec{r} \cdot (\vec{r} \times \vec{L}) = 0$ . One obtains

$$V_{\text{s.o.}}(\vec{r}) = \frac{\vec{r}}{r} \frac{\partial}{\partial r} [V_\lambda(r) Y_\lambda^\mu(\hat{r})] \cdot \frac{\vec{r}}{r} \frac{\partial}{\partial r} - \frac{\vec{r} \times \vec{L}}{\hbar r^2} [V_\lambda(r) Y_\lambda^\mu(\hat{r})] \cdot \frac{\vec{r} \times \vec{L}}{\hbar r^2} - \left[ \frac{\partial}{\partial r} + \frac{1}{\hbar r} (\vec{\sigma} \cdot \vec{L}) \right] [V_\lambda(r) Y_\lambda^\mu(\hat{r})] \cdot \left[ \frac{\partial}{\partial r} - \frac{1}{\hbar r} (\vec{\sigma} \cdot \vec{L}) \right]. \quad (\text{A.77})$$

The terms with two derivatives in Eq. A.77 cancel, and thus

$$V_{\text{s.o.}}(\vec{r}) = -\frac{\vec{r} \times \vec{L}}{\hbar r^2} [V_\lambda(r) Y_\lambda^\mu(\hat{r})] \cdot \frac{\vec{r} \times \vec{L}}{\hbar r^2} - \frac{1}{\hbar r} (\vec{\sigma} \cdot \vec{L}) [V_\lambda(r) Y_\lambda^\mu(\hat{r})] \cdot \left[ \frac{\partial}{\partial r} - \frac{1}{\hbar r} (\vec{\sigma} \cdot \vec{L}) \right] + \frac{\partial}{\partial r} [V_\lambda(r) Y_\lambda^\mu(\hat{r})] \cdot \left[ \frac{1}{\hbar r} (\vec{\sigma} \cdot \vec{L}) \right]. \quad (\text{A.78})$$

In the two first terms of Eq. A.78, the first  $\vec{L}$  operators act only on the spherical harmonics  $Y_\lambda^\mu(\hat{r})$ , so that

$$\vec{r} \times \vec{L} [Y_\lambda^\mu(\hat{r})] \cdot \vec{r} \times \vec{L} = \left[ (\vec{r} \times \vec{L} [Y_\lambda^\mu(\hat{r})]) \times \vec{r} \right] \cdot \vec{L}, \quad (\text{A.79})$$

$$= \left[ r^2 \vec{L} [Y_\lambda^\mu(\hat{r})] - (\vec{L} [Y_\lambda^\mu(\hat{r})] \cdot \vec{r}) \vec{r} \right] \cdot \vec{L}, \quad (\text{A.80})$$

$$= r^2 \vec{L} [Y_\lambda^\mu(\hat{r})] \cdot \vec{L}. \quad (\text{A.81})$$

Using Eq. A.81 into Eq. A.78, one obtains

$$V_{\text{s.o.}}(\vec{r}) = -\frac{V_\lambda(r)}{\hbar^2 r^2} \vec{L} [Y_\lambda^\mu(\hat{r})] \cdot \vec{L} - \frac{1}{\hbar r} (\vec{\sigma} \cdot \vec{L}) [V_\lambda(r) Y_\lambda^\mu(\hat{r})] \cdot \left[ \frac{\partial}{\partial r} - \frac{1}{\hbar r} (\vec{\sigma} \cdot \vec{L}) \right] + \frac{\partial}{\partial r} [V_\lambda(r) Y_\lambda^\mu(\hat{r})] \cdot \left[ \frac{1}{\hbar r} (\vec{\sigma} \cdot \vec{L}) \right], \quad (\text{A.82})$$

$$= -\frac{V_\lambda(r)}{\hbar^2 r^2} \vec{L} [Y_\lambda^\mu(\hat{r})] \cdot \vec{L} - \frac{V_\lambda(r)}{\hbar r} (\vec{\sigma} \cdot \vec{L}) [Y_\lambda^\mu(\hat{r})] \frac{\partial}{\partial r} + \frac{V_\lambda(r)}{\hbar^2 r^2} (\vec{\sigma} \cdot \vec{L}) [Y_\lambda^\mu(\hat{r})] \cdot (\vec{\sigma} \cdot \vec{L}) + \frac{\partial}{\partial r} [V_\lambda(r) Y_\lambda^\mu(\hat{r})] \cdot \frac{1}{\hbar r} (\vec{\sigma} \cdot \vec{L}). \quad (\text{A.83})$$

In the last term of Eq. A.83,  $(\vec{L} \cdot \vec{\sigma})$  operates only on the right-hand side and thus can be replaced by the related eigenvalue  $\gamma_i$ . In the second term,  $(\vec{L} \cdot \vec{\sigma})$  operates only on the spherical harmonics  $Y_\lambda^\mu(\hat{r})$ . One can see that it is equivalent to the case it were operating on the whole term, minus  $\gamma_i$ . This can be seen from the fact that  $\vec{L}$  is a sum of first order differential operators, namely

$$\hat{\vec{L}} = \begin{pmatrix} \hat{L}_x \\ \hat{L}_y \\ \hat{L}_z \end{pmatrix}_{\vec{e}_x, \vec{e}_y, \vec{e}_z} = -i\hbar \begin{pmatrix} -\sin\varphi \frac{\partial}{\partial\theta} - \frac{\cos\varphi}{\tan\theta} \frac{\partial}{\partial\varphi} \\ \cos\varphi \frac{\partial}{\partial\theta} - \frac{\sin\varphi}{\tan\theta} \frac{\partial}{\partial\varphi} \\ \frac{\partial}{\partial\varphi} \end{pmatrix}_{\vec{e}_x, \vec{e}_y, \vec{e}_z}. \quad (\text{A.84})$$

And thus the following property can be obtained:

$$\begin{aligned} \vec{L}[ab] &= a\vec{L}b + b\vec{L}a \rightarrow \ell_{ab}ab = a\ell_b b + b\ell_a a, \\ a\vec{L}b &= \vec{L}[ab] - b\vec{L}a \rightarrow a\ell_b b = \ell_{ab}ab - b\ell_a a. \end{aligned} \quad (\text{A.85})$$

The related eigenvalue is written  $\gamma_f - \gamma_i$ . In the penultimate term of Eq. A.83, the operators can be replaced by  $(\gamma_f - \gamma_i)\gamma_i$ . For the remaining term (the first one in Eq. A.83)

$\vec{L}[Y_\lambda^\mu(\hat{r})] \cdot \vec{L}$ , which is equivalent to  $\vec{\lambda} \cdot \vec{\ell}_i$  must be studied. Again, as  $\vec{L}$  is a sum of first order differential operators, one has

$$\vec{L}[Y_\lambda^\mu(\hat{r})b] = Y_\lambda^\mu(\hat{r})\vec{L}[b] + b\vec{L}[Y_\lambda^\mu(\hat{r})] \rightarrow \ell_{ab}Y_\lambda^\mu(\hat{r})b = Y_\lambda^\mu(\hat{r})\ell_b b + b\ell_\lambda Y_\lambda^\mu(\hat{r}). \quad (\text{A.86})$$

The notation  $\vec{\ell}_f = \vec{\ell}_i + \vec{\lambda}$  is introduced, so that

$$\vec{\ell}_f^2 = (\vec{\ell}_i + \vec{\lambda})^2 = \vec{\ell}_i^2 + \vec{\lambda}^2 + 2\vec{\ell}_i \cdot \vec{\lambda}, \quad (\text{A.87})$$

which is justified because  $\vec{\ell}_i$  and  $\vec{\lambda}$  commute. This corresponds to

$$\vec{L}^2 Y_\lambda^\mu(\hat{r}) = Y_\lambda^\mu(\hat{r})\vec{L}^2 + \vec{L}^2[Y_\lambda^\mu(\hat{r})] + 2\vec{L}[Y_\lambda^\mu(\hat{r})] \cdot \vec{L}. \quad (\text{A.88})$$

The special case of spin- $\frac{1}{2}$  incident particle is now considered to show the relation:

$$\vec{L}^2 = (\vec{L} \cdot \vec{\sigma})^2 + (\vec{L} \cdot \vec{\sigma}). \quad (\text{A.89})$$

Starting from

$$\begin{aligned} \vec{L} \cdot \vec{\sigma} &= \ell & \text{for } j = \ell + \frac{1}{2}, \\ \vec{L} \cdot \vec{\sigma} &= -\ell - 1 & \text{for } j = \ell - \frac{1}{2}, \end{aligned} \quad (\text{A.90})$$

one obtains

$$\begin{aligned} (\vec{L} \cdot \vec{\sigma})^2 &= (\ell + 1)^2 & \text{for } j = \ell + \frac{1}{2}, \\ (\vec{L} \cdot \vec{\sigma})^2 &= \ell^2 & \text{for } j = \ell - \frac{1}{2}, \end{aligned} \quad (\text{A.91})$$

and

$$\begin{aligned} (\vec{L} \cdot \vec{\sigma})^2 + (\vec{L} \cdot \vec{\sigma}) &= (\ell + 1)^2 - (\ell + 1) = \ell(\ell + 1) & \text{for } j = \ell + \frac{1}{2}, \\ (\vec{L} \cdot \vec{\sigma})^2 + (\vec{L} \cdot \vec{\sigma}) &= \ell^2 - \ell = \ell(\ell + 1) & \text{for } j = \ell - \frac{1}{2}, \end{aligned} \quad (\text{A.92})$$

Hence

$$\vec{L}^2 = (\vec{L} \cdot \vec{\sigma})^2 + (\vec{L} \cdot \vec{\sigma}), \quad (\text{A.93})$$

so that the term

$$\vec{L}[Y_\lambda^\mu(\hat{r})] \cdot \vec{L} = \frac{1}{2} \left[ \vec{L}^2 Y_\lambda^\mu(\hat{r}) - Y_\lambda^\mu(\hat{r})\vec{L}^2 - \vec{L}^2[Y_\lambda^\mu(\hat{r})] \right], \quad (\text{A.94})$$

can be replaced by

$$\frac{1}{2} Y_\lambda^\mu(\hat{r}) [\gamma_f^2 + \gamma_f - \gamma_i^2 - \gamma_i - \lambda(\lambda + 1)]. \quad (\text{A.95})$$

Finally the spin-orbit coupling term can be written

$$\begin{aligned} V_{\text{s.o.}}(\vec{r}) &= Y_\lambda^\mu(\hat{r}) \left( -\frac{V_\lambda(r)}{2\hbar^2 r^2} [\gamma_f^2 + \gamma_f - \gamma_i^2 - \gamma_i - \lambda(\lambda + 1)] \right. \\ &\quad \left. - \frac{V_\lambda(r)}{\hbar r} (\gamma_f - \gamma_i) \frac{\partial}{\partial r} + \frac{V_\lambda(r)}{\hbar^2 r^2} (\gamma_f - \gamma_i) \gamma_i + \frac{1}{\hbar r} \frac{\partial V_\lambda(r)}{\partial r} \cdot \gamma_i \right), \end{aligned} \quad (\text{A.96})$$

$$\begin{aligned} &= Y_\lambda^\mu(\hat{r}) \left( -\frac{V_\lambda(r)}{2\hbar^2 r^2} [\gamma_f^2 + \gamma_f - 2\gamma_i \gamma_f + \gamma_i^2 - \gamma_i - \lambda(\lambda + 1)] \right. \\ &\quad \left. - \frac{V_\lambda(r)}{\hbar r} (\gamma_f - \gamma_i) \frac{\partial}{\partial r} + \frac{\gamma_i}{\hbar r} \frac{\partial V_\lambda(r)}{\partial r} \right), \end{aligned} \quad (\text{A.97})$$

$$= Y_\lambda^\mu(\hat{r}) \left( \frac{V_\lambda(r)}{2\hbar^2 r^2} [\lambda(\lambda + 1) + (\gamma_i - \gamma_f)(\gamma_f - \gamma_i)] + \frac{V_\lambda(r)}{\hbar r} (\gamma_i - \gamma_f) \frac{\partial}{\partial r} + \frac{\gamma_i}{\hbar r} \frac{\partial V_\lambda(r)}{\partial r} \right). \quad (\text{A.98})$$





# Appendix B

## Macroscopic-Microscopic Models in the CONRAD code

*In this appendix, details are given about the actual FRLDM and FRDM implementation in the CONRAD code.*

### Contents

---

<b>B.1</b>	<b>Generating Shapes . . . . .</b>	<b>174</b>
B.1.1	Legendre Polynomials Expansion . . . . .	174
B.1.2	Hill-Wheeler Parameterization . . . . .	175
B.1.3	Perturbed Spheroid . . . . .	175
B.1.4	Generalized Spheroid . . . . .	176
B.1.5	Three Quadratic Surfaces (3QS) . . . . .	178
<b>B.2</b>	<b>About Shell and Pairing Correction . . . . .</b>	<b>179</b>
B.2.1	Shell Correction . . . . .	179
B.2.2	Discussion about the Shell Correction . . . . .	183
B.2.3	Pairing Correction . . . . .	185
<b>B.3</b>	<b>Finite Range Droplet Model . . . . .</b>	<b>185</b>
B.3.1	Droplet Model . . . . .	185
B.3.2	Finite Range Droplet Model . . . . .	189
<b>B.4</b>	<b>Computational Forms . . . . .</b>	<b>194</b>
B.4.1	Reduction of Integration Domain . . . . .	194
B.4.2	Coulomb Potential in $\rho(z)$ Parameterization . . . . .	198
B.4.3	Principal Curvatures of 2D-Surfaces . . . . .	203

---

## B.1 Generating Shapes

The starting point of the macroscopic, microscopic and thus macroscopic-microscopic models, as described in the document, relies on the definition of the nucleus shape. This shape can be given as a “geometrical” function (*e.g.*  $\rho(z)$  or  $r(\theta)$ ), that depends on shape parameters  $\vec{q}$  (*cf.* Chapter 5). In the following, the shape parameterizations that have been used in the present study will be presented.

### B.1.1 Legendre Polynomials Expansion

In a quite general treatment, the nuclear radius is expanded using the spherical harmonics

$$r(\theta, \varphi) = \frac{R}{\lambda} \left[ 1 + \sum_{\ell=1}^{\infty} \sum_{m=-\ell}^{\ell} a_{\ell m} Y_{\ell m}(\theta, \varphi) \right], \quad (\text{B.1})$$

where  $R = r_0 A^{1/3}$  is the radius of the equivalent spherical shape, the  $a_{\ell m}$  coefficients are the  $\vec{q}$  parameters describing the shape, and the  $\lambda$  parameter is used to enforce volume conservation as the shape evolves ( $\vec{q}$  varies). Real value of the radius is ensured by the condition  $a_{\ell-m} = (-1)^m a_{\ell m}^*$ . For axially-symmetric shapes, the alternative definition is often favored:

$$r(\theta) = R/\lambda(\beta_2, \beta_3, \dots) \left[ 1 + \sum_{i=2}^{\infty} \beta_i P_i(\cos \theta) \right], \quad (\text{B.2})$$

where  $P_i$  are the Legendre polynomials and where the  $\beta_i$  parameters play a role similar to  $a_{\ell m}$ . Figure B.1 shows nuclear shape layouts using this parameterization (exploring only the  $(\beta_2, \beta_4)$  plane).

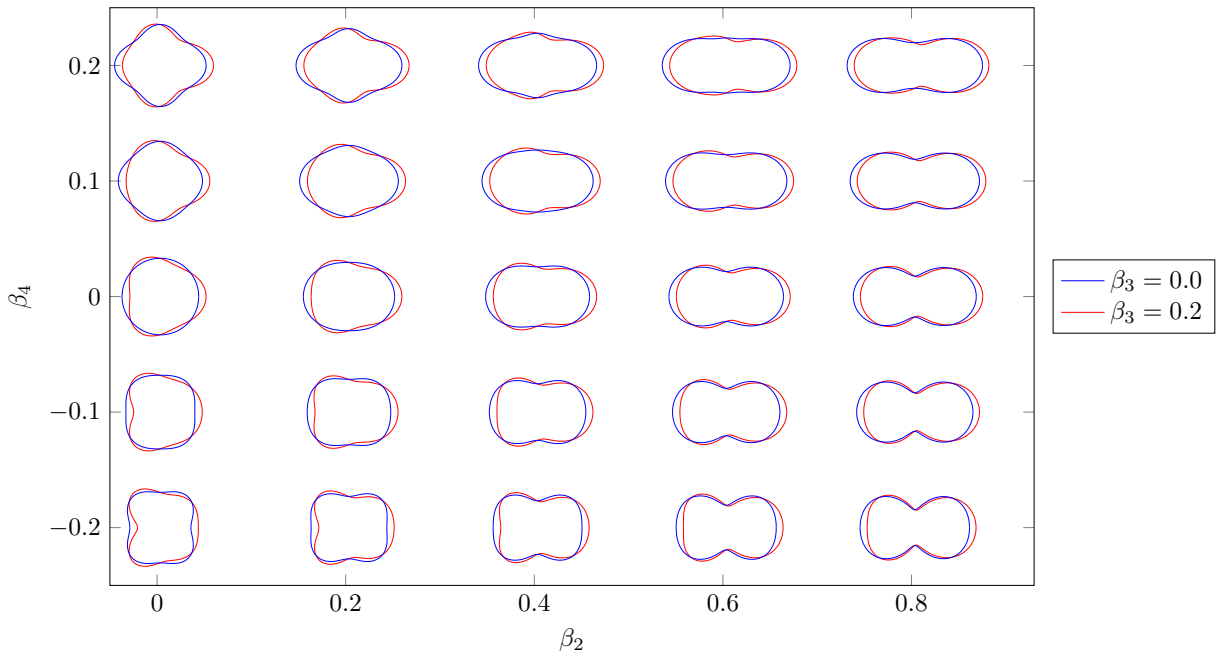


Figure B.1 – Nuclear shape layouts obtained using the Legendre polynomials expansion of the nuclear radius (*cf.* Eq. B.2). Examples of mass asymmetric shapes are also shown (red curves).

One can notice from the red curves that the first “mass-asymmetric” term (*i.e.*, the first odd term in the Legendre polynomial expansion), does not describe properly the

mass-asymmetry but rather the deformations of the nascent fragments. To investigate mass-asymmetric fission path, one would need higher order (odd) terms. Adding terms increases exponentially the computation time, hence this parameterization is not suitable for mass-asymmetry exploration.

### B.1.2 Hill-Wheeler Parameterization

Hill and Wheeler [11] gave a prescription for the nucleus shape in terms of a single parameter  $y$ , called *fissility*. The nucleus radius  $r(\theta)$  is given by

$$r(\theta) = a_0(y) \left[ 1 + \sum_{i=1}^4 a_{2i}(y) P_{2i}(\cos \theta) \right], \quad (\text{B.3})$$

where

$$\begin{aligned} a_0(y) &= 1 - y^2 \left[ 1.06 + \frac{9.76 \times 10^{-4}}{(0.49 - y)^4} \right], & a_2(y) &= y \left[ 2.3 + \frac{5.42 \times 10^{-4}}{(0.49 - y)^4} \right], \\ a_4(y) &= y^2 \left( 1.6 + y \left[ 3.0 + \frac{2.84 \times 10^{-3}}{(0.49 - y)^4} \right] \right), & a_6(y) &= -\frac{2.36 \times 10^{-5}}{(0.49 - y)^4}, \\ a_8(y) &= -\frac{4.72 \times 10^{-5}}{(0.49 - y)^4}, & \forall i > 8 &\Rightarrow a_i(y) = 0. \end{aligned} \quad (\text{B.4})$$

This parameterization is somehow outdated as it was defined using the Liquid Drop Model version of that time. For instance this parameterization does not yield mass-asymmetric shapes. However it can be seen as a “satisfactory” 1-D parameterization because it results from a model rather than just from a geometrical description (as in the Legendre expansion presented above with only a  $\beta_2$  term). Figure B.2 shows layouts of nuclear surfaces using this parameterization.

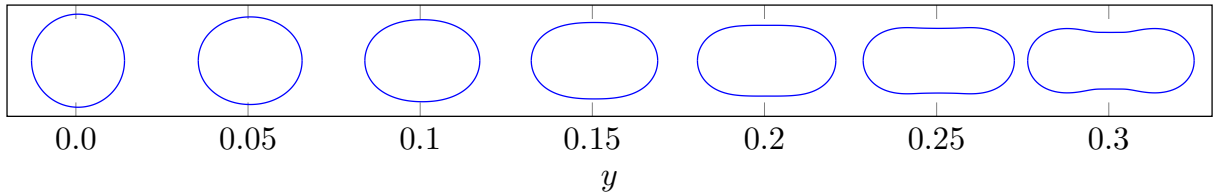


Figure B.2 – Nuclear shape layouts obtained using the Hill-Wheeler prescription of the nuclear radius (*cf.* Eq. B.4). No mass asymmetric shapes are described by this parameterization.

### B.1.3 Perturbed Spheroid

An alternative approach of the polynomial expansion of the nuclear radius can be the perturbed spheroids [12, 173]. For these shapes the radius is given by

$$r(\theta) = \frac{R_0}{\omega_0/\dot{\omega}_0} \left[ \frac{1 - \frac{1}{3}\epsilon_2 - \frac{2}{9}\epsilon_2^2 + \epsilon_2 \left( 1 + \frac{1}{3}\epsilon_2 \right) u^2}{\left( 1 + \frac{1}{3}\epsilon_2 \right)^2 \left( 1 - \frac{2}{3}\epsilon_2 \right) \left[ 1 - \frac{2}{3}\epsilon_2 P_2(u) + 2 \sum_{i=3}^6 \epsilon_i P_i(u) \right]} \right]^{\frac{1}{2}}, \quad (\text{B.5})$$

where the  $\epsilon_i$  are the shape parameters  $\vec{q}$ , and

$$u = \left[ \frac{1 - \frac{2}{3}\epsilon_2}{1 - \frac{1}{3}\epsilon_2(3\cos^2\theta - 1)} \right]^{\frac{1}{2}} \cos\theta, \quad (\text{B.6})$$

and where the  $\omega_0/\dot{\omega}_0$  term ensures the volume conservation. It satisfies

$$\left( \frac{\omega}{\dot{\omega}_0} \right)^3 = \frac{1}{2} \left[ \left( 1 + \frac{1}{3}\epsilon_2 \right)^2 \left( 1 - \frac{2}{3}\epsilon_2 \right) \right]^{-\frac{1}{2}} \int_{-1}^1 du \left[ 1 - \frac{2}{3}\epsilon_2 P_2(u) + 2 \sum_{i=3}^6 \epsilon_i P_i(u) \right]^{-\frac{3}{2}}. \quad (\text{B.7})$$

This expression seems fairly complex compared to the Legendre polynomial expansion. Their origins are in fact, rather similar. In the Legendre expansion, the *radius* is expanded on Legendre polynomials. In the perturbed spheroids approach, one considers a deformed Nilsson harmonic oscillator potential that is expanded on Legendre polynomials. If one considers an equipotential surface of this potential and “scales” it so that the nuclear volume is conserved and equal to  $\frac{4}{3}\pi R^3$ , one finally obtains the perturbed spheroid formula. Figure B.3 shows nuclear surface layouts using this parameterization (exploring only the  $(\epsilon_2, \epsilon_4)$  plane).

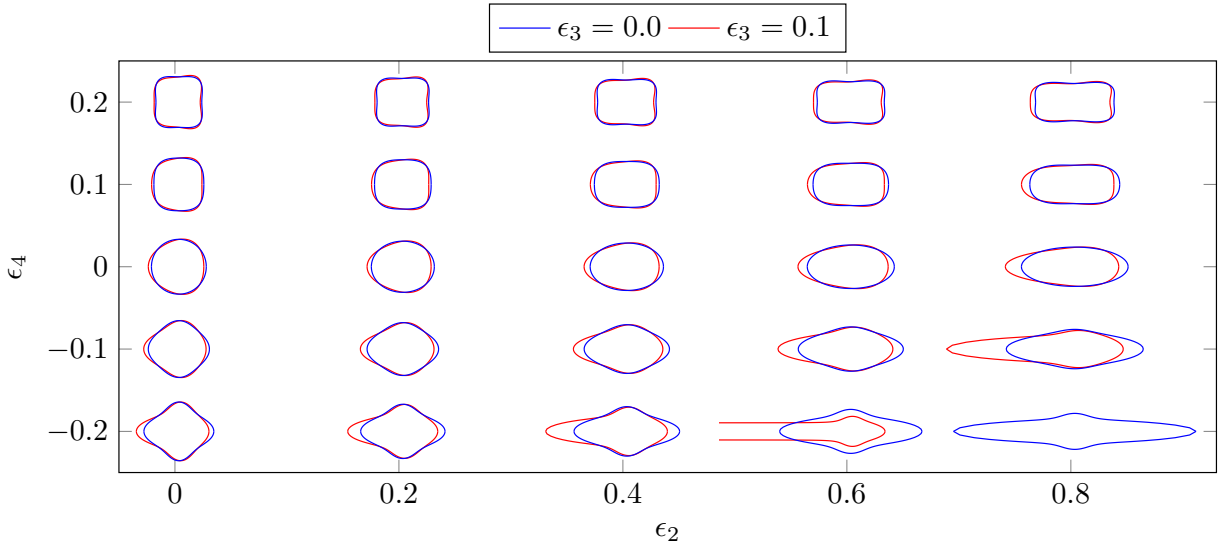


Figure B.3 – Example of perturbed spheroid surfaces defined by Eq. B.5. Examples of mass asymmetric shapes are also shown (red curves).

One can notice that for negative values of  $\epsilon_4$ , one obtains rapidly nonphysical shapes as  $\epsilon_2$  increases. If axially-asymmetric shapes are to be investigated, a “ $\gamma$ ” deformation term can be added in a generalization of this expression [12]. One can also notice from Fig. B.3 that this parameterization is not particularly relevant to describe mass-asymmetric nascent fragments. Just like in the Legendre polynomials expansion, Fig. B.3 shows that odd terms lead to different shapes for the fragments, not really in different masses.

#### B.1.4 Generalized Spheroid

Studies of fission process requires a better description of the scission configurations and mass-asymmetric shapes have to be investigated. A new shape parameterization was

introduced [20] so that asymmetric shapes are described as well as spherical, elongated shapes and diamond-like shapes. This class of shapes is the *generalized spheroids* family. This parameterization allows nuclei to have diamond-like shapes, as such shapes are believed to be closer to actual ground-state shapes than the spherical shape. In this parameterization, the nuclear radius is given in terms of the distance  $\rho$  of the surface to the symmetry axis  $z$ :

$$\rho^2(z) = \begin{cases} (1 - z^2)(a + bz^2 + \alpha z), & b \geq 0 \\ (1 - z^2)(a + \alpha z) \exp(bc^3 z^2), & b < 0 \end{cases}, \quad (\text{B.8})$$

where

$$b = \frac{1}{2}(c - 1) + 2h, \quad a = \begin{cases} \frac{1}{c^3} - \frac{b}{5}, & b \geq 0 \\ -\frac{4b}{3} \left[ e^p + \sqrt{-\pi p} \left( 1 + \frac{1}{2p} \right) \text{erf}(\sqrt{-p}) \right]^{-1}, & b < 0 \end{cases}, \quad (\text{B.9})$$

and  $p = bc^3$ . Examples of shapes provided by this parameterization are shown in Fig. B.4. One can notice that shapes with  $\alpha \neq 0$  render mass-asymmetry in a better way than in the Legendre expansion or in the perturbed spheroid approaches, especially for scission shapes or for shapes with well separated fragments. This parameterization leads to fragments at scission with unsatisfactory deformations. The ground state obtained with this parameterization (and also with the perturbed spheroid parameterization) has a diamond-like shape (for instance  $(c, h) = (1.2, -0.4)$  in Fig. B.4). It is thus interesting to investigate scission shapes where fragments can have such diamond-like shapes. Yet the generalized spheroid parameterization leads to scission shapes where fragments are flattened on a plane perpendicular to the symmetry axis (as can be seen for instance for  $(c, h) = (2.2, 0.4)$  in Fig. B.4). This seems nonphysical and shows the limitations of such a 3D parameterization where only elongation, “neck size” and mass-asymmetry can be easily handled.

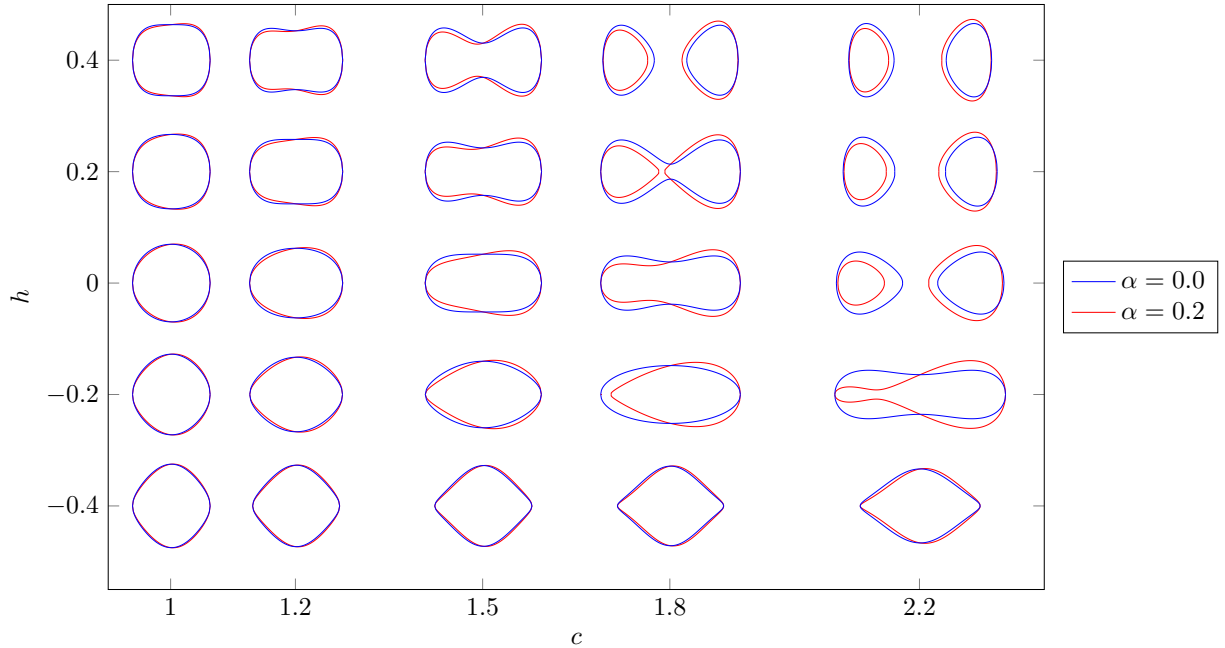


Figure B.4 – Example of nuclear shapes using the generalized spheroid parameterization (cf. Eq. B.8). Examples of mass-asymmetric shapes are shown with red solid curves.

### B.1.5 Three Quadratic Surfaces (3QS)

A proper way of getting rid of the drawbacks of the previous parameterizations is to increase the number of degrees of freedom. Nix introduced another parameterization [174, 175] that relies on two additional degrees of freedom. In this case, as for the generalized spheroid parameterization, the radius is given in terms of  $\rho(z)$  instead of  $r(\theta)$ :

$$\rho(z)^2 = \begin{cases} a_1^2 - \frac{a_1^2}{c_1^2}(z - l_1)^2, & l_1 - z_{\min} \leq z \leq z_1 \\ a_2^2 - \frac{a_2^2}{c_2^2}(z - l_2)^2, & z_2 \leq z \leq l_2 + z_{\max} \\ a_3^2 - \frac{a_3^2}{c_3^2}(z - l_3)^2, & z_1 \leq z \leq z_2 \end{cases}, \quad (\text{B.10})$$

where  $z_{\max} = l_2 + c_2$  and  $z_{\min} = l_1 - c_1$ . One can see that, in this formula, eleven parameters are necessary to describe this shape. However from the smooth continuity relations at  $z = z_1$  and  $z = z_2$ , four parameters can be dropped. Additionally the volume conservation and the center-of-mass position are two degrees of freedom that can be removed. Finally only five parameters are necessary to provide a proper description of the shape. This shape parameterization is particularly suitable for the description of scission configurations because it makes possible to set specific deformations for each fragment. It seems well adapted to describe the fission process.

For such a parameterization with five degrees of freedom, it is difficult to give a layout of the available shapes. However in Fig. B.5, one can see the geometrical meaning of the parameters involved in the shape formula (Eq. B.10) and some examples of related shapes.

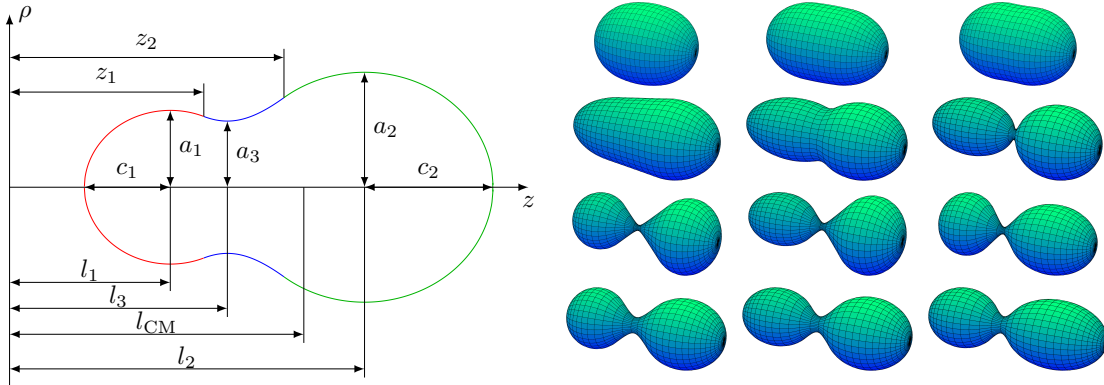


Figure B.5 – Examples of three quadratic surfaces

Out of the eleven geometrical parameters used in Eq. B.5, one could select only five and use them as the degrees of freedom. Yet these geometrical parameters do not linearly and independently affecting the expected degrees of freedom (elongation, neck size, mass-asymmetry and deformation of nascent fragments). The *symmetric*  $\sigma_1, \sigma_2, \sigma_3$  and *asymmetric*  $\alpha_1, \alpha_2, \alpha_3$  parameters are used to get closer to the targeted degrees of freedom. These parameters are defined in Tab. B.1. Six parameters are involved as the degree of freedom related to the center-of-mass position in not yet removed. Additionally a size parameter  $u$  is introduced so that the volume degree of freedom can be removed later.

These parameters are not yet quite satisfactory, instead the global parameters  $Q_2, \alpha_g, d, \varepsilon_1$  and  $\varepsilon_2$ , defined in Ref. [16] operate on the desired degrees of freedom. A connection



Table B.1 – Relations between global and symmetrical/asymmetrical parameters used in the 3QS parameterization.

symmetrical	asymmetrical	dimensional
$\sigma_1 = \frac{l_2 - l_1}{u}$	$\alpha_1 = \frac{1}{2} \frac{l_2 + l_1}{u}$	$u = [\frac{1}{2}(a_1^2 + a_2^2)]^{1/2}$
$\sigma_2 = \frac{a_3^2}{c_3^2}$	$\alpha_2 = \frac{a_1^2 - a_2^2}{u^2}$	
$\sigma_3 = \frac{1}{2} \left( \frac{a_1^2}{c_1^2} + \frac{a_2^2}{c_2^2} \right)$	$\alpha_3 = \frac{a_1^2}{c_1^2} - \frac{a_2^2}{c_2^2}$	

between the symmetric and asymmetric parameters and the global parameters is shown in Tab. B.2. More detailed can be found in Ref. [16, 175].

Table B.2 – Global shape parameters used in the 3QS parameterization.

From global to symmetrical/asymmetrical	From symmetrical/asymmetrical to global
$\sigma_3 = \frac{1}{2} \left[ \left( \frac{3 - 2\varepsilon_{f1}}{3 + \varepsilon_{f1}} \right)^2 + \left( \frac{3 - 2\varepsilon_{f2}}{3 + \varepsilon_{f2}} \right)^2 \right]$	$\varepsilon_{f1} = \frac{1 - \sqrt{2\sigma_3 + \alpha_3}}{\sqrt{2\sigma_3 + \alpha_3} + 2}$
$\alpha_3 = \frac{1}{2} \left[ \left( \frac{3 - 2\varepsilon_{f1}}{3 + \varepsilon_{f1}} \right)^2 - \left( \frac{3 - 2\varepsilon_{f2}}{3 + \varepsilon_{f2}} \right)^2 \right]$	$\varepsilon_{f2} = \frac{1 - \sqrt{2\sigma_3 - \alpha_3}}{\sqrt{2\sigma_3 - \alpha_3} + 2}$
$\alpha_2 = 2 \frac{\left[ \left( \frac{\alpha_g + 1}{\alpha_g - 1} \right)^2 \frac{2\sigma_3 + \alpha_3}{2\sigma_3 - \alpha_3} \right]^{1/3} - 1}{\left[ \left( \frac{\alpha_g + 1}{\alpha_g - 1} \right)^2 \frac{2\sigma_3 + \alpha_3}{2\sigma_3 - \alpha_3} \right]^{1/3} + 1}$	$\alpha_g = \frac{\left[ \frac{2\sigma_3 - \alpha_3}{2\sigma_3 + \alpha_3} \left( \frac{1 + \frac{1}{2}\alpha_2}{1 - \frac{1}{2}\alpha_2} \right)^3 \right]^{1/2} + 1}{\left[ \frac{2\sigma_3 - \alpha_3}{2\sigma_3 + \alpha_3} \left( \frac{1 + \frac{1}{2}\alpha_2}{1 - \frac{1}{2}\alpha_2} \right)^3 \right]^{1/2} - 1}$

The  $Q_2$  parameter is defined by

$$Q_\lambda = 2 \left( \frac{Z}{\frac{4}{3}\pi R^3} \right) \int_V d^3\vec{r} r^\lambda P_\lambda(\cos\theta) = \left( \frac{3Z}{R^3} \right) \int_{z_{\min}}^{z_{\max}} dz \int_0^{\rho(z)} d\rho' [\rho'^2 + z^2]^{\lambda/2} \rho' P_\lambda \left( \frac{z}{\sqrt{\rho'^2 + z^2}} \right). \quad (\text{B.11})$$

Handling this parameterization is quite tedious, especially for shapes with small elongation, and robust numerical methods must be settled. This parameterization has been only used for some tests in the present document. Yet it should be used more extensively in future studies.

## B.2 About Shell and Pairing Correction

Once single-particle energies are obtained from the Yukawa-folded microscopic model, the shell and pairing corrections must be calculated.

### B.2.1 Shell Correction

The method used in the present study for the calculation of the shell energy correction is described in Ref. [87]. Additional calculation details of interest are provided in the

following. As explained in Chapter 5.4.1, the shell correction is calculated as

$$\delta E_{\text{shell}} = \sum_{n=1}^N \epsilon_n - \int_0^N \bar{\epsilon}(n) dn. \quad (\text{B.12})$$

As a starting point, one can consider Eq. 5.84 giving the discrete state density, recalled here

$$g(\epsilon) = \frac{1}{\gamma} \sum_{n=0}^{\infty} \delta(u_n), \quad (\text{B.13})$$

where

$$u_n = \frac{\epsilon - \epsilon_n}{\gamma}. \quad (\text{B.14})$$

The delta function Dirac  $\delta$  can be expanded using the Hermite polynomials:

$$\delta(x) = \sum_{m=0}^{\infty} \frac{e^{-x^2}}{\sqrt{\pi}} \frac{H_m(x) H_m(0)}{2^m m!}. \quad (\text{B.15})$$

From the orthogonality condition of the Hermite polynomials, namely

$$\int_{-\infty}^{\infty} dx e^{-x^2} H_n(x) H_m(x) = \frac{\delta_{nm}}{\sqrt{\pi} 2^n n!}, \quad (\text{B.16})$$

it can be verified that:

$$\int_{-\infty}^{\infty} \delta(x) dx = \sum_{m=0}^{\infty} \frac{H_m(0)}{\sqrt{\pi} 2^m m!} \int_{-\infty}^{\infty} e^{-x^2} H_m(x) dx, \quad (\text{B.17})$$

$$= \sum_{m=0}^{\infty} \frac{H_m(0)}{\sqrt{\pi} 2^m m!} \sqrt{\pi} 2^m m! \delta_{m0}, \quad (\text{B.18})$$

$$= H_0(0), \quad (\text{B.19})$$

$$= 1. \quad (\text{B.20})$$

The value of the Hermite polynomials at the origin is given by

$$H_m(0) = \begin{cases} (-1)^{m/2} \frac{m!}{(m/2)!}, & m \text{ even}, \\ 0, & m \text{ odd}, \end{cases} \quad (\text{B.21})$$

Hence  $g(\epsilon)$  defined in Eq. B.13 can be written

$$g(\epsilon) = \frac{1}{\gamma} \sum_{n=0}^{\infty} \sum_{m=0}^{\infty} \frac{e^{-u_n^2}}{\sqrt{\pi}} \frac{H_m(u_n) H_m(0)}{2^m m!}. \quad (\text{B.22})$$

The cumulative number of state  $n(\epsilon)$  is given by

$$n(\epsilon) = \int_{-\infty}^{\epsilon} g(\epsilon') d\epsilon', \quad (\text{B.23})$$

$$= \frac{1}{\gamma\sqrt{\pi}} \sum_{n=0}^{\infty} \left( \int_{-\infty}^{\epsilon} e^{-v_n^2} H_0(v_n) dv_n + \sum_{m=1}^{\infty} \frac{H_m(0)}{2^m m!} \int_{-\infty}^{\epsilon} e^{-v_n^2} H_m(v_n) dv_n \right), \quad (\text{B.24})$$

where

$$v_n = \frac{\epsilon' - \epsilon_n}{\gamma}. \quad (\text{B.25})$$

Making the variable change  $\epsilon' \rightarrow v_n$ , one obtains

$$n(\epsilon) = \frac{1}{\sqrt{\pi}} \sum_{n=0}^{\infty} \left( \int_{-\infty}^{u_n} e^{-v_n^2} H_0(v_n) dv_n + \sum_{m=1}^{\infty} \frac{H_m(0)}{2^m m!} \int_{-\infty}^{u_n} e^{-v_n^2} H_m(v_n) dv_n \right). \quad (\text{B.26})$$

As  $H_0(x) = 1$  and using Ref. [48] (p. 298), one gets

$$\frac{1}{\sqrt{\pi}} \int_{-\infty}^{\frac{x}{\sqrt{2}}} e^{-t^2} dt = \frac{1}{2} \left[ 1 + \operatorname{erf} \left( \frac{x}{\sqrt{2}} \right) \right], \quad (\text{B.27})$$

so that  $n(\epsilon)$  can be written

$$n(\epsilon) = \sum_{n=0}^{\infty} \left( \frac{1}{2} [1 + \operatorname{erf}(v_n)] + \frac{1}{\sqrt{\pi}} \sum_{m=1}^{\infty} \frac{H_m(0)}{2^m m!} \int_{-\infty}^{u_n} e^{-v_n^2} H_m(v_n) dv_n \right). \quad (\text{B.28})$$

The integral in Eq. B.28 can be put in the form

$$\int_{-\infty}^{u_n} e^{-v_n^2} H_m(v_n) dv_n = \int_{-\infty}^0 e^{-v_n^2} H_m(v_n) dv_n + \int_0^{u_n} e^{-v_n^2} H_m(v_n) dv_n. \quad (\text{B.29})$$

For  $m$  even,  $H_m$  is an even function and thus

$$\int_{-\infty}^0 e^{-v_n^2} H_m(v_n) dv_n = \frac{1}{2} \int_{-\infty}^{+\infty} e^{-v_n^2} H_m(v_n) dv_n = \frac{1}{2} \frac{\delta_{0m}}{\sqrt{\pi} 2^n n!}. \quad (\text{B.30})$$

As  $m = 0$  is not included in the second sum of Eq. B.28, one gets

$$n(\epsilon) = \sum_{n=0}^{\infty} \left( \frac{1}{2} [1 + \operatorname{erf}(v_n)] + \frac{1}{\sqrt{\pi}} \sum_{m=1}^{\infty} \frac{H_m(0)}{2^m m!} \int_0^{u_n} e^{-v_n^2} H_m(v_n) dv_n \right). \quad (\text{B.31})$$

Reference [48] (p. 786) gives the following relation

$$\int_0^x e^{-t^2} H_m(t) dt = H_{m-1}(0) - e^{-x^2} H_{m-1}(x), \quad (\text{B.32})$$

which can be used with Eq. B.30 and yield

$$m \text{ even}, m > 0 \Rightarrow \int_{-\infty}^x e^{-t^2} H_m(t) dt = H_{m-1}(0) - e^{-x^2} H_{m-1}(x). \quad (\text{B.33})$$

Hence Eq. B.28 can be written

$$n(\epsilon) = \sum_{n=0}^{\infty} \left( \frac{1}{2} [1 + \operatorname{erf}(v_n)] + \frac{1}{\sqrt{\pi}} \sum_{m=1}^{\infty} \frac{H_m(0)}{2^m m!} [H_{m-1}(0) - e^{-u_n^2} H_{m-1}(u_n)] \right). \quad (\text{B.34})$$

Either  $m$  or  $m - 1$  is odd so the first term of the second sum is null, so that

$$n(\epsilon) = \sum_{n=0}^{\infty} \left( \frac{1}{2} [1 + \operatorname{erf}(v_n)] - \frac{1}{\sqrt{\pi}} \sum_{m=1}^{\infty} \frac{H_m(0)}{2^m m!} e^{-u_n^2} H_{m-1}(u_n) \right). \quad (\text{B.35})$$

The average number of level  $\bar{n}(\epsilon)$ , required in Eq. 5.90 to obtained the Fermi energy  $\bar{\lambda}$  of the smooth distribution, is obtained by restraining the sum over  $m$  up to a cutoff order  $p$ . To obtain the shell correction (*cf.* Eq. 5.91 or Eq. B.12), one also needs to compute expression of the type

$$\int_0^N \epsilon(n) dn = \int_{-\infty}^{\bar{\lambda}} \epsilon g(\epsilon) d\epsilon = \frac{1}{\gamma \sqrt{\pi}} \sum_{n=0}^{\infty} \sum_{m=0}^{\infty} \frac{H_m(0)}{2^m m!} \int_{-\infty}^{\bar{\lambda}} d\epsilon \epsilon e^{-u_n^2} H_m(u_n). \quad (\text{B.36})$$

Making the variable change  $\epsilon \rightarrow u_n$  and separating the  $m = 0$  term from the rest of the sum, one obtains

$$\begin{aligned} \int_0^N \epsilon(n) dn = \frac{1}{\sqrt{\pi}} \sum_{n=0}^{\infty} \left( \int_{-\infty}^{\frac{\bar{\lambda}-\epsilon_n}{\gamma}} du_n (\gamma u_n + \epsilon_n) e^{-u_n^2} \right. \\ \left. + \sum_{m=1}^{\infty} \frac{H_m(0)}{2^m m!} \int_{-\infty}^{\frac{\bar{\lambda}-\epsilon_n}{\gamma}} du_n (\gamma u_n + \epsilon_n) e^{-u_n^2} H_m(u_n) \right). \quad (\text{B.37}) \end{aligned}$$

Defining  $\tilde{u}_n = \frac{\bar{\lambda} - \epsilon_n}{\gamma}$ , the first term in the parentheses of Eq. B.37 becomes

$$\int_{-\infty}^{\tilde{u}_n} du_n (\gamma u_n + \epsilon_n) e^{-u_n^2} = \gamma \int_{-\infty}^{\tilde{u}_n} du_n u_n e^{-u_n^2} + \epsilon_n \int_{-\infty}^{\tilde{u}_n} du_n e^{-u_n^2}, \quad (\text{B.38})$$

$$= -\frac{\gamma}{2} [e^{-u_n^2}]_{-\infty}^{\tilde{u}_n} + \epsilon_n \sqrt{\pi} \frac{1}{2} [1 + \operatorname{erf}(\tilde{u}_n)], \quad (\text{B.39})$$

$$= -\frac{\gamma}{2} e^{-\tilde{u}_n^2} + \frac{\epsilon_n \sqrt{\pi}}{2} [1 + \operatorname{erf}(\tilde{u}_n)]. \quad (\text{B.40})$$

For the second term in the parentheses of Eq. B.37, one has

$$\int_{-\infty}^{\tilde{u}_n} du_n (\gamma u_n + \epsilon_n) e^{-u_n^2} H_m(u_n) = \gamma \int_{-\infty}^{\tilde{u}_n} du_n u_n e^{-u_n^2} H_m(u_n) + \epsilon_n \int_{-\infty}^{\tilde{u}_n} du_n e^{-u_n^2} H_m(u_n). \quad (\text{B.41})$$

Reference [48] (p. 782) gives the recurrence relation between Hermite polynomials:

$$x H_m(x) = \frac{1}{2} H_{m+1}(x) + m H_{m-1}(x). \quad (\text{B.42})$$

The second term in the parentheses of Eq. B.37 becomes

$$\begin{aligned} & \int_{-\infty}^{\tilde{u}_n} du_n (\gamma u_n + \epsilon_n) e^{-u_n^2} H_m(u_n) = \\ & \frac{\gamma}{2} \int_{-\infty}^{\tilde{u}_n} du_n e^{-u_n^2} H_{m+1}(u_n) + \gamma m \int_{-\infty}^{\tilde{u}_n} du_n e^{-u_n^2} H_{m-1}(u_n) + \epsilon_n \int_{-\infty}^{\tilde{u}_n} du_n e^{-u_n^2} H_m(u_n). \end{aligned} \quad (\text{B.43})$$

Equation B.33 cannot be used because  $m+1$  and  $m-1$  are both even. However for  $m$  even, one can use Ref. [48] (p. 786), namely

$$\int_{-\infty}^x dt e^{-t^2} H_{m+1}(t) = \int_{-\infty}^0 dt e^{-t^2} H_{m+1}(t) + \int_0^x dt e^{-t^2} H_{m+1}(t), \quad (\text{B.44})$$

$$= - \int_0^{+\infty} dt e^{-t^2} H_{m+1}(t) + \int_0^x dt e^{-t^2} H_{m+1}(t), \quad (\text{B.45})$$

$$= -H_m(0) + H_m(0) - e^x H_m(x) = -e^x H_m(x). \quad (\text{B.46})$$

Hence, using Eqs. B.46 and B.33, the second term in the parentheses of Eq. B.37 becomes

$$\begin{aligned} & \int_{-\infty}^{\tilde{u}_n} du_n (\gamma u_n - \epsilon_n) e^{-u_n^2} H_m(u_n) = \\ & - \frac{\gamma}{2} e^{-\tilde{u}_n^2} H_m(\tilde{u}_n) - \gamma m e^{-\tilde{u}_n^2} H_{m-2}(\tilde{u}_n) + \epsilon_n \left[ H_{m-1}(0) - e^{-\tilde{u}_n^2} H_{m-1}(\tilde{u}_n) \right]. \end{aligned} \quad (\text{B.47})$$

As  $m$  is even,  $m-1$  is odd and  $H_{m-1}(0) = 0$ , inserting Eqs. B.40 and B.47 into Eq. B.37, one obtains the smooth energy term

$$\begin{aligned} \int_0^N \epsilon(n) dn = \sum_{n=0}^{\infty} & \left( \frac{\epsilon_n}{2} [1 + \text{erf}(\tilde{u}_n)] - \frac{\gamma}{2\sqrt{\pi}} e^{-\tilde{u}_n^2} \right. \\ & \left. - \frac{e^{-\tilde{u}_n^2}}{\sqrt{\pi}} \sum_{m=1}^{\infty} \frac{H_m(0)}{2^m m!} \left[ \frac{\gamma}{2} H_m(\tilde{u}_n) + \gamma m H_{m-2}(\tilde{u}_n) + \epsilon_n H_{m-1}(\tilde{u}_n) \right] \right). \end{aligned} \quad (\text{B.48})$$

To obtain the smooth equivalent to Eq. B.48, namely

$$\int_0^N \bar{\epsilon}(n) dn, \quad (\text{B.49})$$

used in Eq. 5.91 and Eq. B.12 for the calculation of the actual shell correction energy, one should limit, in Eq. B.48, the second sum on  $m$  up to the cutoff parameter  $p$ .

### B.2.2 Discussion about the Shell Correction

In Fig. B.6, one can see an example for  $^{208}_{82}\text{Pb}_{126}$  that was calculated and put into the same format than in Ref [87] for comparison. The calculation is done for neutrons only. The

number of cumulative levels for the discrete distribution  $n(\epsilon)$  using Eqs. 5.83 and 5.84 and for the corresponding smooth distribution  $\bar{n}(\epsilon)$  using Eq. 5.89 is shown. The Fermi energy  $\bar{\lambda}$  of the smooth distribution can be read from the smooth curves at the point where  $\bar{n}(\bar{\lambda}) = N = 126$ . As is explained later in Chapter 5 Section 5.5.1, levels are computed using a base expansion method. The accuracy of the calculation depends on the choice of the base and on the size of the base. The largest the base, the more accurately the level energies are computed. This method provides level energies for positive and negative energies and the number of energies provided by the method is equal to the number of elements in the base. Only a limited physically-constrained number of negative energy levels exist, therefore as the base size increases, the number of positive energies increases while the number of negative energies remains identical.

In Fig. B.6, one can additionally see the dependence of the number of cumulative levels as the base size increases. The size of the expansion base is characterized by a cutoff number  $N_0$  that is not the number of elements in the base, but as  $N_0$  increases the base size increases. As the size increases, the single-particle energies converge for bound levels ( $\epsilon_n < 0$ ). For unbound energy levels the change is more effective. As all positive energies are eigenvalues of the Hamiltonian (they are related to the continuum), hence in a small interval of positive energies  $d\epsilon$ , an infinity of energy levels are possible. As the base size increases these levels are better described by the expansion method and the infinity of levels tends to be reproduced. In such positive energy region,  $n$  in Fig. B.6 should be completely flat and one should consider instead the level density  $dn/d\epsilon$  where  $dn$  is the variation in the cumulative number of levels in the range  $d\epsilon$ .

This yields unsatisfactory features for the shell correction. As the sum over  $n$  in Eq. 5.93 goes to infinity (and thus related to positive levels) this would bend downwards the smooth curves in the negative energy region too. The eventual effect on the shell correction is also shown in Fig. B.6b. This kind of analysis led to limit the size of the expansion base.

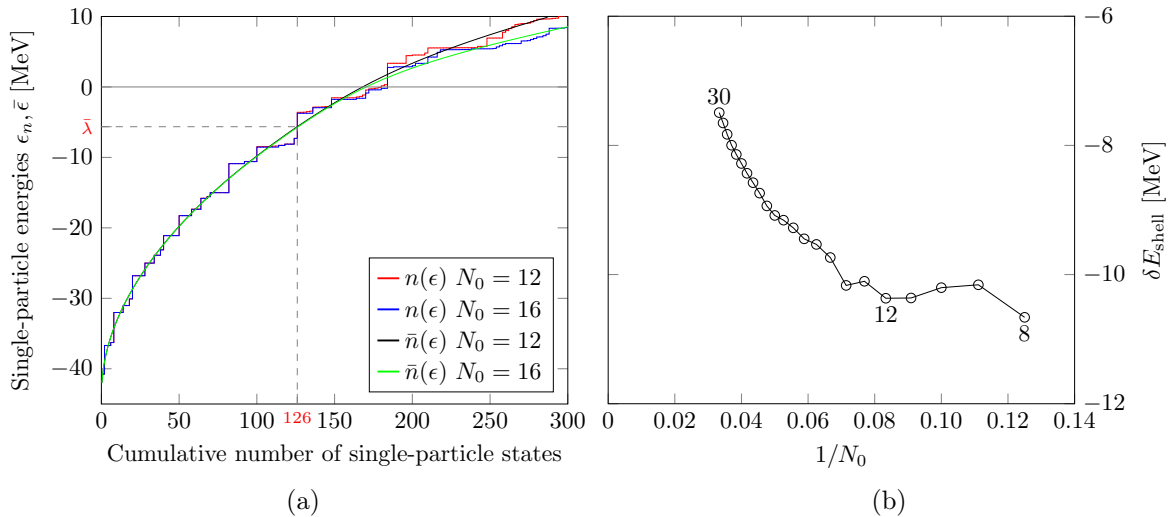


Figure B.6 – Energies of neutron single-particle states of the  $^{208}_{82}\text{Pb}_{126}$  (B.6a) and corresponding shell correction convergence as a function of the base size criterion  $N_0$  (B.6b). Results reproduced for comparison with Ref [87].

This issue can be avoided by using of the following *ad hoc* method given in Ref. [176].

In this approach, the level density  $g$  of Eq. 5.84 is replaced by

$$g_{\text{bound}}(\epsilon) = \sum_{n=1}^{\infty} \delta(\epsilon - \epsilon_n) - \sum_{n=1}^{\infty} \delta(\epsilon - \epsilon_n^0), \quad (\text{B.50})$$

where  $\epsilon_n^0$  are eigenvalues of the “free” Hamiltonian  $\hat{H} = \hat{T}$  as given in Chapter 5, Section 5.5.1. It has been shown that this method leads to converged shell correction as the base size increases [177] and thus corrects the unsatisfactory divergent behavior of the shell correction that is shown in Fig. B.6b.

### B.2.3 Pairing Correction

Two pairing models are used this study, the BCS and the Lipkin-Nogami models, that have been well presented in Ref. [110]. Therefore the related development will not be reported here. It could yet be noted that for the BCS model a slightly different version [87] has been implemented for the present study.

## B.3 Finite Range Droplet Model

The Finite-Range Droplet Model (FRDM) has also been implemented as long as the Finite-Range Liquid-Drop Model (FRLDM) for the present work (*cf.* Chapter 5). This was made in order to perform additional verifications of the FRLDM implementation (*cf.* Section 5.4.2). The droplet model, which is the original version of the macroscopic model used in the FRDM will be detailed below.

### B.3.1 Droplet Model

Myers and Swiatecki elaborated [106, 178] an alternative macroscopic model to the liquid drop model named the droplet model. In this approach different densities are considered for the neutrons and protons ( $\rho_n(\vec{r})$  and  $\rho_p(\vec{r})$ ). The evolution of the different energy terms (Volume, Surface and Coulomb) is analyzed as  $\rho_n(\vec{r})$  and  $\rho_p(\vec{r})$  differ from their standard (liquid drop model) value  $\rho_0 = [\frac{4}{3}\pi r_0^3]^{-1}$ . The density functions  $\rho_n(\vec{r})$  and  $\rho_p(\vec{r})$  considered here are called *bulk density functions*. One can also define the total bulk density  $\rho(\vec{r}) = \rho_n(\vec{r}) + \rho_p(\vec{r})$ . These densities are illustrated, in the case of spherical nucleus, by dashed line in Fig. B.7, along with the actual densities shown in solid line. The bulk density is a continuation of the actual density in the nucleus interior up to a given radius. For instance the neutron bulk density  $\rho_n$  extends from  $r = 0$  up to  $R_n$ , with an excess of density with respect to the actual density for  $r < R_n$  which is equal to the corresponding density deficiency beyond  $R_n$ . In particular this implies

$$\int_{\infty}^{\infty} d^3\vec{r} \rho_n^{\text{actual}}(\vec{r}) = N = \int_{V_{\Sigma_n}} d^3\vec{r} \rho_n^{\text{bulk}}(\vec{r}). \quad (\text{B.51})$$

The definition of the radii  $R_n$ ,  $R_p$  and  $R_{\Sigma}$  and the related densities, as shown in Fig B.7, are defined for a spherical nucleus, but the extension to arbitrary shapes is straightforward. In this latter case, the surface  $\Sigma_n$ ,  $\Sigma_p$  and  $\Sigma$  are considered instead of radii  $R_n$ ,  $R_p$  and  $R_{\Sigma}$ . In the following of this presentation of the droplet model, densities  $\rho_n$ ,  $\rho_p$  and  $\rho$  refer to the bulk quantities. Assuming a normal vector  $\vec{n}$  to both surfaces  $\Sigma_n$  and  $\Sigma_p$ , if  $n_n$  is a



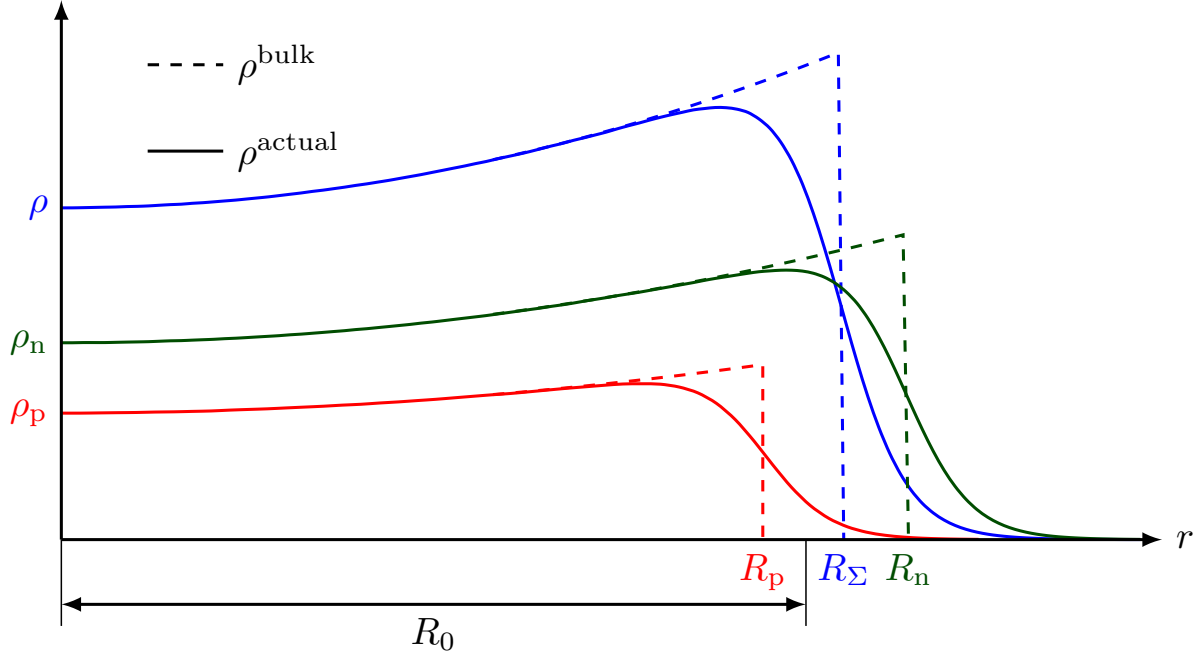


Figure B.7 – Generating functions of the Droplet model, reproduced from Ref. [106].

normal coordinate (along  $\vec{n}$ ) locating  $\Sigma_n$  and  $n_p$  is the similar quantity locating  $\Sigma_p$ , then the position  $n_\Sigma$  of  $\Sigma$  is given by

$$n_\Sigma = \frac{n_n \rho_n(n_n) + n_p \rho_p(n_p)}{\rho_n(n_n) + \rho_p(n_p)}. \quad (\text{B.52})$$

Thus the excess of neutrons in the generating distribution between  $\Sigma$  and  $\Sigma_n$  is the same than the deficiency of protons between  $\Sigma_p$  and  $\Sigma$ . The *density deviation function*  $\epsilon$  and the *neutron-excess deviation function*  $\delta$  are defined by

$$\epsilon(\vec{r}) = -\frac{1}{3} \left( \frac{\rho(\vec{r}) - \rho_0}{\rho_0} \right) \quad \text{and} \quad \delta(\vec{r}) = \frac{\rho_n(\vec{r}) - \rho_p(\vec{r})}{\rho(\vec{r})}. \quad (\text{B.53})$$

Additionally one can define a neutron skin thickness  $\tau$  as

$$\tau = \frac{n_n - n_p}{r_0}. \quad (\text{B.54})$$

This neutron skin thickness is a function of the position on the surface  $\Sigma$ . The derivation of the model final expression is obtained in two steps:

1. The energy terms (Volume, Surface and Coulomb) are written in terms of the volume-averaged quantities  $\bar{\epsilon}$ ,  $\bar{\delta}$ , surface-averaged quantity  $\bar{\tau}$  and the *deviation functions*  $\tilde{\delta}(\vec{r}) = \delta(\vec{r}) - \bar{\delta}$ ,  $\tilde{\epsilon}(\vec{r}) = \epsilon(\vec{r}) - \bar{\epsilon}$  and  $\tilde{\tau}(\vec{r}) = \tau(\vec{r}) - \bar{\tau}$ .
2. The energy expression is made stationary with respect to variations of  $\bar{\epsilon}$ ,  $\bar{\delta}$ ,  $\tilde{\delta}(\vec{r})$ ,  $\tilde{\epsilon}(\vec{r})$  and  $\tilde{\tau}(\vec{r})$ . The expression is not made explicitly stationary with respect of parameter  $\bar{\tau}$  because there is a relation between  $\bar{\tau}$  and  $\bar{\delta}$ , thus it is not a free degree of freedom.

One can notice that a non-zero value of  $\bar{\epsilon}$  corresponds to a nuclear volume  $V_\Sigma = \frac{4}{3}\pi R_\Sigma^3$  that differs from the standard nuclear volume  $V = \frac{4}{3}\pi R_0^3$  where  $R_0 = r_0 A^{1/3}$ . The spherical-equivalent radius  $R_\Sigma$  in the droplet model model is given by

$$R_\Sigma = (1 - 3\bar{\epsilon})^{-1/3} R_0 \approx (1 + \bar{\epsilon}) R_0. \quad (\text{B.55})$$

This is related to the compressibility of the nuclear matter inside the nucleus. The volume energy term  $E_V$  can be written as

$$E_V = \int_{V_\Sigma} d^3\vec{r} \rho(\vec{r}) e(\vec{r}), \quad (\text{B.56})$$

where  $e$  is a local energy density per particle that can be developed in terms of  $\delta$  and  $\epsilon$  according to

$$e(\vec{r}) = -a_1 + J\delta^2(\vec{r}) + \frac{1}{2}K\epsilon^2(\vec{r}) - L\epsilon(\vec{r})\delta^2(\vec{r}) + \frac{1}{2}M\delta^4(\vec{r}), \quad (\text{B.57})$$

where  $a_1$ ,  $J$ ,  $K$ ,  $L$  and  $M$  are constants that will be eventually adjusted on experimental masses. This leads to

$$E_V = \left[ -a_1 + J\bar{\delta}^2 + \frac{1}{2}K\bar{\epsilon}^2 - L\bar{\epsilon}\bar{\delta}^2 + \frac{1}{2}M\bar{\delta}^4 \right] A + \rho_0 \int_{V_\Sigma} d^3\vec{r} \left( J\tilde{\delta}^2(\vec{r}) + \frac{1}{2}K\tilde{\epsilon}^2(\vec{r}) \right). \quad (\text{B.58})$$

Similarly, the surface term  $E_S$  is written as

$$E_S = \frac{1}{4\pi r_0^2} \int_{S_\Sigma} d^2S \left[ a_2 + F\epsilon(\vec{r}) + H\tau^2(\vec{r}) + 2P\tau(\vec{r})\delta(\vec{r}) - G\delta^2(\vec{r}) + \frac{1}{2}a_3 r_0 \kappa(\vec{r}) \right], \quad (\text{B.59})$$

where  $a_2$ ,  $F$ ,  $G$ ,  $P$ ,  $G$  and  $a_3$  are constants and  $\kappa(\vec{r})$  is the local curvature at the surface point  $\vec{r}$ . This leads to

$$E_S = a_2 A^{2/3} (1 + 2\bar{\epsilon}) B_S(\vec{q}) + \frac{1}{3} \rho_0 r_0 \int_{S_\Sigma} d^2S [F\epsilon(\vec{r}) + H\tau^2(\vec{r}) + 2P\tau(\vec{r})\delta(\vec{r}) - G\delta^2(\vec{r})] + a_3 \frac{1}{8\pi r_0} \int_{S_\Sigma} d^2S \kappa(\vec{r}). \quad (\text{B.60})$$

The last term is often written as  $a_3 A^{1/3} B_k(\vec{q})$ , where

$$B_k(\vec{q}) = \frac{1}{8\pi R_\Sigma} \int_{S_\Sigma} d^2S \kappa(\vec{r}). \quad (\text{B.61})$$

Finally the Coulomb energy term  $E_C$  is written

$$E_C = \frac{1}{2} e^2 \int_{V_{\Sigma_p}} d^2\vec{r}_1 \int_{V_{\Sigma_p}} d^3\vec{r}_2 \frac{\rho_p(\vec{r}_1) \rho_p(\vec{r}_2)}{\|\vec{r}_1 - \vec{r}_2\|} + E^{\text{diff}} + E^{\text{exch}}, \quad (\text{B.62})$$

where  $E^{\text{diff}}$  is the correction for the diffuseness of the proton density given by Eq. 5.15 and  $E^{\text{exch}}$  is the exchange correction introduced in Eq. 5.6. This leads to

$$E_C = c_1 \frac{Z^2}{A^{1/3}} (1 - \bar{\epsilon}) B_C(\vec{q}) - \frac{e\rho_0 r_0}{4} \int_{S_\Sigma} d^2S \tau(\vec{r}) \tilde{v}(\vec{r}) - \frac{e\rho_0}{2} \int_{V_\Sigma} d^3\vec{r} v(\vec{r}) (3\tilde{\epsilon}(\vec{r}) + \tilde{\delta}(\vec{r})) + E^{\text{diff}} + E^{\text{exch}}, \quad (\text{B.63})$$

where  $c_1 = \frac{3}{5} \frac{e^2}{r_0}$  and  $v$  is the Coulomb potential generated by an uniform density  $\bar{\rho}_p = \frac{Ze}{V_\Sigma}$  contained in the sharp edge surface  $S_\Sigma$ . It is given by

$$v(\vec{r}_1) = \int_{V_\Sigma} d^3\vec{r}_2 \frac{e\bar{\rho}_p}{\|\vec{r}_1 - \vec{r}_2\|}. \quad (\text{B.64})$$

The average value  $\bar{v}$  of  $v$  over  $V_\Sigma$  and its deviation function  $\tilde{v}$  are defined by

$$\bar{v} = \frac{1}{V_\Sigma} \int_{V_\Sigma} d^3\vec{r}_1 v(\vec{r}_1) \quad \text{and} \quad \tilde{v}(\vec{r}_1) = v(\vec{r}_1) - \bar{v}. \quad (\text{B.65})$$

The total energy  $E = E_V + E_S + E_C$  is thus

$$\begin{aligned} E = & \left[ -a_1 + J\bar{\delta}^2 + \frac{1}{2}K\bar{\epsilon}^2 - L\bar{\epsilon}\bar{\delta}^2 + \frac{1}{2}M\bar{\delta}^4 \right] A \\ & + \rho_0 \int_{V_\Sigma} d^3\vec{r} \left( J\tilde{\delta}^2(\vec{r}) + \frac{1}{2}K\tilde{\epsilon}^2(\vec{r}) \right) + a_2 A^{2/3} (1 + 2\bar{\epsilon}) B_S(\vec{q}) \\ & + \frac{1}{3} \rho_0 r_0 \int_{S_\Sigma} d^2S [F\epsilon(\vec{r}) + H\tau^2(\vec{r}) + 2P\tau(\vec{r})\delta(\vec{r}) - G\delta^2(\vec{r})] + a_3 A^{1/3} B_k(\vec{q}) \\ & + c_1 \frac{Z^2}{A^{1/3}} (1 - \bar{\epsilon}) B_C(\vec{q}) - \frac{e\rho_0 r_0}{4} \int_{S_\Sigma} d^2S \tau(\vec{r}) \tilde{v}(\vec{r}) - \frac{e\rho_0}{2} \int_{V_\Sigma} d^3\vec{r} v(\vec{r}) (3\tilde{\epsilon}(\vec{r}) + \tilde{\delta}(\vec{r})) \\ & + E^{\text{diff}} + E^{\text{exch}}. \quad (\text{B.66}) \end{aligned}$$

Applying all stationary conditions  $\left( \frac{\partial E}{\partial \tilde{\epsilon}} = \frac{\partial E}{\partial \tilde{\delta}} = \frac{\partial E}{\partial \tilde{\tau}} = \frac{\partial E}{\partial \bar{\delta}} = \frac{\partial E}{\partial \bar{\epsilon}} = 0 \right)$  to Eq. B.66 yields

$$\frac{\partial E}{\partial \tilde{\epsilon}} = 0 \Rightarrow \tilde{\epsilon} = \frac{3e}{2K} \tilde{v}, \quad (\text{B.67})$$

$$\frac{\partial E}{\partial \tilde{\delta}} = 0 \Rightarrow \tilde{\delta} = \frac{e\tilde{v}}{4J}, \quad (\text{B.68})$$

$$\frac{\partial E}{\partial \tilde{\tau}} = 0 \Rightarrow \tilde{\tau} = \frac{3}{8} \frac{e}{Q} (\tilde{v}_S - \bar{\tilde{v}}_S), \quad (\text{B.69})$$

$$\frac{\partial E}{\partial \bar{\delta}} = 0 \Rightarrow \bar{\delta} = \frac{I + \frac{c_1}{Q} Z B_v(\vec{q}) \frac{3}{16} A^{-2/3}}{1 + \frac{9}{4} \frac{J}{Q} A^{-1/3} B_S(\vec{q})}, \quad (\text{B.70})$$

$$\frac{\partial E}{\partial \bar{\epsilon}} = 0 \Rightarrow \bar{\epsilon} = \frac{1}{K} \left[ L\bar{\delta}^2 - 2A^{-1/3} a_2 B_S(\vec{q}) + c_1 \frac{Z^2}{A^{4/3}} B_C(\vec{q}) \right], \quad (\text{B.71})$$

where  $\tilde{v}_S$  is the restriction of  $\tilde{v}$  on the surface  $S_\Sigma$ , and  $\bar{\tilde{v}}_S$  is its average value on  $S_\Sigma$  defined by

$$\bar{\tilde{v}}_S = \frac{1}{S_\Sigma} \int_{S_\Sigma} d^2S \tilde{v}_S(\vec{r}), \quad (\text{B.72})$$

and  $Q = \frac{3}{2} \frac{JP}{G}$ . The  $B_v$  term appearing in Eq. B.70 is defined by

$$B_v(\vec{q}) = -\frac{5}{4\pi R_\Sigma Z e} \int_{S_\Sigma} d^2S \tilde{v}(\vec{r}). \quad (\text{B.73})$$

Inserting all stationary conditions into Eq. B.66, it yields

$$\begin{aligned}
E = & \left[ -a_1 + J\bar{\delta}^2 + \frac{1}{2}K\bar{\epsilon}^2 + \frac{1}{2}M\bar{\delta}^4 - L\bar{\epsilon}\bar{\delta}^2 \right] A - c_2 A^{1/3} Z^2 (1 + \bar{\epsilon}) B_r(\vec{q}) \\
& + \left[ a_2 + \frac{9}{4} \frac{J^2}{Q} \bar{\delta}^2 \right] A^{2/3} (1 + 2\bar{\epsilon}) B_S(\vec{q}) - c_5 Z^2 B_w(\vec{q}) \\
& + a_3 A^{1/3} (1 + \bar{\epsilon}) B_k(\vec{q}) + c_1 \frac{Z^2}{A^{1/3}} (1 - \bar{\epsilon}) B_C(\vec{q}) + E^{\text{diff}} + E^{\text{exch}}, \quad (\text{B.74})
\end{aligned}$$

where  $c_5 = \frac{c_1^2}{4^3 Q}$ . The  $B_r$  and  $B_w$  terms are defined by

$$B_r(\vec{q}) = \frac{700\pi}{R_\Sigma Z^2 e^2} \int_{V_\Sigma} d^3\vec{r} \tilde{v}^2 \quad \text{and} \quad B_w(\vec{q}) = \frac{25}{4Z^2 \pi e^2} \int_{S_\Sigma} d^2 S \tilde{v}^2(\vec{r}). \quad (\text{B.75})$$

Finally, as  $\bar{\epsilon} \frac{\partial E}{\partial \bar{\epsilon}} = 0$ , one can consider  $E = E - \bar{\epsilon} \frac{\partial E}{\partial \bar{\epsilon}}$  and the final expression for the total energy becomes

$$\begin{aligned}
E = & \left[ -a_1 + J\bar{\delta}^2 + \frac{1}{2}K\bar{\epsilon}^2 + \frac{1}{2}M\bar{\delta}^4 \right] A - c_2 A^{1/3} Z^2 B_r(\vec{q}) + \left[ a_2 + \frac{9}{4} \frac{J^2}{Q} \bar{\delta}^2 \right] A^{2/3} B_S(\vec{q}) \\
& - c_5 Z^2 B_w(\vec{q}) + a_3 A^{1/3} B_k(\vec{q}) + c_1 \frac{Z^2}{A^{1/3}} B_C(\vec{q}) + E^{\text{diff}} + E^{\text{exch}}. \quad (\text{B.76})
\end{aligned}$$

### B.3.2 Finite Range Droplet Model

Just like the Finite Range Liquid Drop Model (FRLDM) was an extension of the Liquid Drop Model (LDM), the Finite Range Droplet Model (FRDM) is a similar extension of the Droplet Model (DM). The major change between the DM and the FRDM is related to the surface and Coulomb terms. Roughly speaking the  $a_2 A^{2/3} B_S(\vec{q})$  and  $c_1 Z^2 A^{-1/3} B_C(\vec{q})$  terms of Eq. B.76 would be replaced by  $a_2 A^{2/3} B_1(\vec{q})$  and  $c_1 Z^2 A^{-1/3} B_3(\vec{q})$  respectively where  $B_1$  and  $B_3$  are defined by Eq. 5.45 and 5.46. Additionally the effect of nucleus compressibility must be considered. In Eq. B.74 terms  $a_2 A^{2/3} (1 + 2\bar{\epsilon}) B_S(\vec{q})$  and  $c_1 \frac{Z^2}{A^{1/3}} (1 - \bar{\epsilon}) B_C(\vec{q})$  must be seen as the first order expansion of the related surface and Coulomb energy terms with respect of variation of the nuclear volume (*i.e.* of  $\bar{\epsilon}$ ). For instance, defining the standard volume  $V_0 = \frac{4}{3}\pi R_0^3$  and the DM volume  $V_\Sigma = \frac{4}{3}\pi R_\Sigma^3$  (here  $R_\Sigma = R_0(1 + \bar{\epsilon})$ ), the surface energy term  $E_S$  for a volume  $V_0$  is given by

$$E_S(\bar{\epsilon} = 0) = a_2 A^{2/3} \frac{1}{4\pi R_0^2} \int_{S_0} d^2 S, \quad (\text{B.77})$$

where  $S_0$  is the surface containing the volume  $V_0$ . The surface energy term  $E_S$  for a volume  $V_\Sigma$  is

$$E_S(\bar{\epsilon} \neq 0) = a_2 A^{2/3} \frac{1}{4\pi R_0^2} \int_{S_\Sigma} d^2 S, \quad (\text{B.78})$$

where  $S_\Sigma$  is the surface containing the volume  $V_\Sigma$ . As the shapes in Eqs. B.77 and B.78 are identical, the change in volume consists only on a rescale of  $E_S(\bar{\epsilon} = 0)$ , namely

$$E_S(\bar{\epsilon} \neq 0) = E_S(\bar{\epsilon} = 0) \left( \frac{R_\Sigma}{R_0} \right)^2 = E_S(\bar{\epsilon} = 0) (1 + \bar{\epsilon})^2 \approx E_S(\bar{\epsilon} = 0) (1 + 2\bar{\epsilon}). \quad (\text{B.79})$$

Applying this to the finite-range terms  $B_1$ , one obtains for the volume  $V_0$

$$E_S(\bar{\epsilon} = 0) = a_2 A^{2/3} B_1(\vec{q}) = \frac{a_2 A^{2/3}}{8\pi^2 R_0^2 a^4} \int_{V_0} d^3 \vec{r}_1 \int_{V_0} d^3 \vec{r}_2 (2 - \xi) \frac{e^{-\xi}}{\xi}, \quad (\text{B.80})$$

where  $\xi = \|\vec{r}_1 - \vec{r}_2\|/a$ .

Equation B.80 must now be obtained for a volume  $V_\Sigma \neq V_0$ . Considering a function  $f$  of parameters  $\bar{\epsilon}$  and  $a$  defined as the double volume integral of a function  $g$  depending of  $\xi = \|\vec{r}_1 - \vec{r}_2\|/a$  so that for the volume  $V_0$

$$f(\bar{\epsilon} = 0, a) = \int_{z_{\min}}^{z_{\max}} dz \int_{z_{\min}}^{z_{\max}} dz' \int_{y_{\min}}^{y_{\max}} dy \int_{y_{\min}}^{y_{\max}} dy' \int_{x_{\min}}^{x_{\max}} dx \int_{x_{\min}}^{x_{\max}} dx' g(\xi). \quad (\text{B.81})$$

For a non zero value of  $\bar{\epsilon}$ , Eq. B.81 can be written

$$f(\bar{\epsilon} \neq 0, a) = \int_{z_{\min}(1+\bar{\epsilon})}^{z_{\max}(1+\bar{\epsilon})} dz \int_{z_{\min}(1+\bar{\epsilon})}^{z_{\max}(1+\bar{\epsilon})} dz' \int_{y_{\min}(1+\bar{\epsilon})}^{y_{\max}(1+\bar{\epsilon})} dy \int_{y_{\min}(1+\bar{\epsilon})}^{y_{\max}(1+\bar{\epsilon})} dy' \int_{x_{\min}(1+\bar{\epsilon})}^{x_{\max}(1+\bar{\epsilon})} dx \int_{x_{\min}(1+\bar{\epsilon})}^{x_{\max}(1+\bar{\epsilon})} dx' g(\xi). \quad (\text{B.82})$$

Using variable change  $X = x/(1 + \bar{\epsilon})$ , one gets

$$f(\bar{\epsilon} \neq 0, a) = (1 + \bar{\epsilon})^6 \int_{z_{\min}}^{z_{\max}} dZ \int_{z_{\min}}^{z_{\max}} dZ' \int_{y_{\min}}^{y_{\max}} dY \int_{y_{\min}}^{y_{\max}} dY' \int_{x_{\min}}^{x_{\max}} dX \int_{x_{\min}}^{x_{\max}} dX' g(\xi'), \quad (\text{B.83})$$

where  $\xi'$  is now given by

$$\xi' = \frac{\sqrt{(x - x')^2 + (y - y')^2 + (z - z')^2}}{a}, \quad (\text{B.84})$$

$$= \frac{\sqrt{(X - X')^2 + (Y - Y')^2 + (Z - Z')^2}}{a} (1 + \bar{\epsilon}), \quad (\text{B.85})$$

$$= \frac{\sqrt{(X - X')^2 + (Y - Y')^2 + (Z - Z')^2}}{a'}, \quad (\text{B.86})$$

where  $a' = a(1 + \bar{\epsilon})^{-1}$ . Therefore Eq. B.83 becomes

$$f(\bar{\epsilon} \neq 0, a) = (1 + \bar{\epsilon})^6 f(\bar{\epsilon} = 0, \frac{a}{1 + \bar{\epsilon}}), \quad (\text{B.87})$$

$$\approx (1 + 6\bar{\epsilon}) f(\bar{\epsilon} = 0, a(1 - \bar{\epsilon})), \quad (\text{B.88})$$

$$\approx (1 + 6\bar{\epsilon}) \left[ f(\bar{\epsilon} = 0, a) - a\bar{\epsilon} \left. \frac{\partial f}{\partial a} \right|_{\bar{\epsilon}=0, a} \right], \quad (\text{B.89})$$

$$\approx f(\bar{\epsilon} = 0, a) + 6\bar{\epsilon} f(\bar{\epsilon} = 0, a) - a\bar{\epsilon} \left. \frac{\partial f}{\partial a} \right|_{\bar{\epsilon}=0, a}. \quad (\text{B.90})$$

This can be applied to Eq. B.80, where  $f = f_S$  corresponding to  $g(\xi) = (2 - \xi) \frac{e^{-\xi}}{\xi}$ , so that one obtains the surface energy term  $E_S$  related to a volume  $V_\Sigma$  as

$$E_S(\bar{\epsilon} \neq 0) = a_2 A^{2/3} B_1, \quad (\text{B.91})$$

$$= \frac{a_2 A^{2/3}}{8\pi^2 R_0^2 a^4} f_S(\bar{\epsilon}, a), \quad (\text{B.92})$$

$$= a_2 A^{2/3} \left[ (1 + 6\bar{\epsilon}) B_1 - \frac{a\bar{\epsilon}}{8\pi^2 R_0^2 a^4} \frac{\partial f_S}{\partial a} \Big|_{\bar{\epsilon}=0,a} \right]. \quad (\text{B.93})$$

It can be shown that this expression can be written more simply as

$$E_S(\bar{\epsilon} \neq 0) = a_2 A^{2/3} (B_1 + 2\bar{\epsilon} B_2), \quad (\text{B.94})$$

where

$$B_2 = \frac{1}{2\lambda} \frac{d\lambda^2 B_1}{d\lambda} \quad \text{and} \quad \lambda = R_0/a. \quad (\text{B.95})$$

This is justified by

$$E_S(\bar{\epsilon} \neq 0) = a_2 A^{2/3} (B_1 + 2\bar{\epsilon} B_2), \quad (\text{B.96})$$

$$= a_2 A^{2/3} \left[ B_1 + \frac{\bar{\epsilon}}{\lambda} \frac{d\lambda^2 B_1}{d\lambda} \right], \quad (\text{B.97})$$

$$= a_2 A^{2/3} \left[ B_1 + \frac{\bar{\epsilon}}{\lambda} \left( 2\lambda B_1 + \lambda^2 \frac{dB_1}{d\lambda} \right) \right], \quad (\text{B.98})$$

$$= a_2 A^{2/3} \left[ B_1 + 2\bar{\epsilon} B_1 + \bar{\epsilon} \lambda \frac{dB_1}{d\lambda} \right], \quad (\text{B.99})$$

$$= a_2 A^{2/3} \left[ B_1 + 2\bar{\epsilon} B_1 - \frac{R_0}{a} \frac{a^2}{R_0} \bar{\epsilon} \frac{dB_1}{da} \right], \quad (\text{B.100})$$

$$= a_2 A^{2/3} \left[ B_1 + 2\bar{\epsilon} B_1 - a\bar{\epsilon} \frac{dB_1}{da} \right], \quad (\text{B.101})$$

$$= a_2 A^{2/3} \left[ B_1 + 2\bar{\epsilon} B_1 - \frac{a\bar{\epsilon}}{8\pi^2 R_0^2 a^4} \frac{\partial f_S}{\partial a} \Big|_{\bar{\epsilon}=0,a} + 4\bar{\epsilon} B_1 \right], \quad (\text{B.102})$$

$$= a_2 A^{2/3} \left[ B_1 + 6\bar{\epsilon} B_1 - \frac{a\bar{\epsilon}}{8\pi^2 R_0^2 a^4} \frac{\partial f_S}{\partial a} \Big|_{\bar{\epsilon}=0,a} \right]. \quad (\text{B.103})$$

Comparing Eqs. B.93 and B.103 thus justifies Eq. B.96.

A similar procedure is applied to the Coulomb term  $E_C$ , so that for a volume  $V_\Sigma$  it becomes

$$E_C(\bar{\epsilon} = 0, a_{\text{den}}) = \frac{15c_1 Z^2 A^{-1/3}}{32\pi^2 R_0^5 a_{\text{den}}} f_C(\bar{\epsilon} = 0, a_{\text{den}}), \quad (\text{B.104})$$

where  $f_C$  is the equivalent of  $f_S$  and is related to  $g(\xi) = \frac{1}{\xi} (1 - (1 + \frac{\xi}{2}) e^{-\xi})$ . For  $\bar{\epsilon} \neq 0$  this expression becomes

$$E_C(\bar{\epsilon} \neq 0, a_{\text{den}}) = \frac{15c_1 Z^2 A^{-1/3} R_0}{32\pi^2 R_\Sigma^6 a_{\text{den}}} f_C(\bar{\epsilon} \neq 0, a_{\text{den}}), \quad (\text{B.105})$$

$$= \frac{15c_1 Z^2 A^{-1/3} R_0}{32\pi^2 R_0^6 (1 + \bar{\epsilon})^6 a_{\text{den}}} (1 + \bar{\epsilon})^6 f_C(\bar{\epsilon} = 0, a_{\text{den}} (1 - \bar{\epsilon})), \quad (\text{B.106})$$

$$= \frac{15c_1 Z^2 A^{-1/3}}{32\pi^2 R_0^5 a_{\text{den}}} \left[ f_C(\bar{\epsilon} = 0, a_{\text{den}}) - \bar{\epsilon} a_{\text{den}} \frac{\partial f_C}{\partial a_{\text{den}}} \Big|_{\bar{\epsilon}=0,a_{\text{den}}} \right]. \quad (\text{B.107})$$

Applying Eq. B.90 to  $f_C$ , one obtains

$$E_C(\bar{\epsilon} \neq 0) = c_1 Z^2 A^{-1/3} \left[ (1 + 6\bar{\epsilon}) B_3 - \frac{15}{32\pi^2 R_0^5} \bar{\epsilon} \frac{\partial f_C}{\partial a_{\text{den}}} \Big|_{\bar{\epsilon}=0,a_{\text{den}}} \right]. \quad (\text{B.108})$$

It can also be shown that this expression can be written more simply as

$$E_C(\bar{\epsilon} \neq 0) = c_1 Z^2 A^{-1/3} (B_3 - \bar{\epsilon} B_4), \quad (\text{B.109})$$

where

$$B_4 = -\lambda^2 \frac{dB_3/\lambda}{d\lambda} \quad \text{and} \quad \lambda = R_0/a_{\text{den}}. \quad (\text{B.110})$$

This again can be justified because

$$E_C(\bar{\epsilon} \neq 0) = c_1 Z^2 A^{-1/3} \left( B_3 + \bar{\epsilon} \lambda^2 \frac{dB_3/\lambda}{d\lambda} \right), \quad (\text{B.111})$$

$$= c_1 Z^2 A^{-1/3} \left[ B_3 + \bar{\epsilon} \lambda^2 \left( -\frac{1}{\lambda^2} B_3 + \frac{1}{\lambda} \frac{dB_3}{d\lambda} \right) \right], \quad (\text{B.112})$$

$$= c_1 Z^2 A^{-1/3} \left[ B_3(1 - \bar{\epsilon}) + \bar{\epsilon} \lambda \frac{dB_3}{d\lambda} \right], \quad (\text{B.113})$$

$$= c_1 Z^2 A^{-1/3} \left[ B_3(1 - \bar{\epsilon}) - \bar{\epsilon} \frac{R_0}{a_{\text{den}}} \frac{a_{\text{den}}^2}{R_0} \frac{dB_3}{da_{\text{den}}} \right], \quad (\text{B.114})$$

$$= c_1 Z^2 A^{-1/3} \left[ B_3(1 - \bar{\epsilon}) - \bar{\epsilon} a_{\text{den}} \frac{dB_3}{da_{\text{den}}} \right], \quad (\text{B.115})$$

$$= c_1 Z^2 A^{-1/3} \left[ B_3(1 - \bar{\epsilon}) - \bar{\epsilon} a_{\text{den}} \left( \frac{-15f_C}{32\pi^2 R_0^5 a_{\text{den}}^2} + \frac{15}{32\pi^2 R_0^5 a_{\text{den}}} \frac{\partial f_C}{\partial a_{\text{den}}} \bigg|_{\bar{\epsilon}=0, a_{\text{den}}} \right) \right], \quad (\text{B.116})$$

$$= c_1 Z^2 A^{-1/3} \left[ B_3 - \frac{15\bar{\epsilon}}{32\pi^2 R_0^5} \frac{\partial f_C}{\partial a_{\text{den}}} \bigg|_{\bar{\epsilon}=0, a_{\text{den}}} \right]. \quad (\text{B.117})$$

Thus, comparison between Eqs. B.107 and B.117 justifies the definition of  $B_4$  by Eq. B.110.

Now that the surface and Coulomb terms are defined in a “finite range” way, Eqs. B.94 and B.109 can be inserted into Eq. B.66. Then stationary condition Eq. B.71 is applied and yields

$$\bar{\epsilon}(\vec{q}) = \frac{1}{K} \left( C e^{-\gamma A^{1/3}} - 2a_2 \frac{B_2(\vec{q})}{A^{1/3}} + L \bar{\delta}^2(\vec{q}) + c_1 \frac{Z^2}{A^{4/3}} B_4(\vec{q}) \right), \quad (\text{B.118})$$

where the term  $C A e^{-\gamma A^{1/3}}$  is non-analytic and is introduced for empirical reasons. This adds two new adjustable parameters  $C$  and  $\gamma$ . The addition of this term showed to have significant advantages [179]. Finally the dependency of the surface energy on the neutron excess can be taken into account [179] “simply” by replacing  $Q$  by  $Q \frac{B_1}{B_S}$ . Equation B.70 thus becomes

$$\bar{\delta}(\vec{q}) = \frac{I + \frac{3}{16} \frac{c_1}{Q} \frac{Z}{A^{2/3}} \frac{B_v(\vec{q}) B_S(\vec{q})}{B_1(\vec{q})}}{1 + \frac{9}{4} \frac{J}{Q} \frac{1}{A^{1/3}} \frac{B_S^2(\vec{q})}{B_1(\vec{q})}}. \quad (\text{B.119})$$

The final expression of the FRDM can be summarized as [12]

$$E_{\text{macro}}^{\text{FRDM}}(Z, A, \vec{q}) = M_H Z + M_n N + \left[ \left( -a_1 + J \bar{\delta}^2(\vec{q}) - \frac{1}{2} K \bar{\epsilon}^2(\vec{q}) \right) A \right. \\ \left. + \left( a_2 B_1(\vec{q}) + \frac{9}{4} \frac{J^2}{Q} \bar{\delta}^2(\vec{q}) \frac{B_S^2(\vec{q})}{B_1(\vec{q})} \right) A^{2/3} \right]$$



$$\begin{aligned}
& -c_2 Z^2 A^{1/3} B_r(\vec{q}) - c_5 Z^2 \frac{B_w(\vec{q}) B_s(\vec{q})}{B_1(\vec{q})} + a_3 A^{1/3} B_k(\vec{q}) + f_0 \frac{Z^2}{A} \Big] \\
& + a_0 A^0 + c_1 \frac{Z^2}{A^{1/3}} B_3(\vec{q}) - c_4 \frac{Z^{4/3}}{A^{1/3}} - c_a (N - Z) \\
& + W \left( |I| + \frac{1}{A} \delta_{ZN} \delta_{Z\text{odd}} \right) + \begin{cases} \bar{\Delta}_p + \bar{\Delta}_n - \delta_{np}, & Z \text{ and } N \text{ odd} \\ \bar{\Delta}_p, & Z \text{ odd and } N \text{ even} \\ \bar{\Delta}_n, & Z \text{ even and } N \text{ odd} \\ 0, & Z \text{ and } N \text{ even} \end{cases} - a_{\text{el}} Z^{2.39}, \quad (\text{B.120})
\end{aligned}$$

where  $c_2$  and  $c_5$  are given by

$$c_2 = \frac{1}{336} \left( \frac{1}{J} + \frac{18}{K} \right) c_1^2 \quad \text{and} \quad c_5 = \frac{1}{64Q} c_1^2. \quad (\text{B.121})$$

The new shape-dependent terms compared with the FRLDM are given by

$$\begin{aligned}
B_2(\vec{q}) &= \frac{1}{2} \left[ \frac{\partial B_1(\vec{q})}{\partial \bar{\epsilon}} \right]_{\bar{\epsilon}=0}, & B_4(\vec{q}) &= - \left[ \frac{\partial B_3(\vec{q})}{\partial \bar{\epsilon}} \right]_{\bar{\epsilon}=0}, \\
B_v(\vec{q}) &= - \frac{15 A^{-4/3}}{16 \pi^2 r_0^4} \int_S d^2 S_1 \tilde{W}(\vec{r}_1), & B_w(\vec{q}) &= \frac{225 A^{-2}}{64 \pi^3 r_0^6} \int_S d^2 S_1 \tilde{W}^2(\vec{r}_1), \\
B_k(\vec{q}) &= \frac{A^{-1/3}}{8 \pi r_0} \int_S d^2 S_1 \left( \frac{1}{R_1(\vec{r}_1)} + \frac{1}{R_2(\vec{r}_1)} \right), & B_r(\vec{q}) &= \frac{1575 A^{-7/3}}{64 \pi^3 r_0^7} \int_V d^3 \vec{r}_1 \tilde{W}^2(\vec{r}_1),
\end{aligned} \quad (\text{B.122})$$

where

$$W(\vec{r}_1) = \int_V \frac{d^3 \vec{r}_2}{\|\vec{r}_1 - \vec{r}_2\|}, \quad (\text{B.123})$$

$$\bar{W} = \frac{3}{4 \pi r_0^3 A} \int_V d^3 \vec{r}_1 W(\vec{r}_1), \quad (\text{B.124})$$

$$\tilde{W}(\vec{r}_1) = W(\vec{r}_1) - \bar{W}, \quad (\text{B.125})$$

and  $R_1$  and  $R_2$  are the principal radii of curvature, the calculation of which is detailed in Appendix B.4.3. All integrations are made on a volume  $\frac{4}{3} \pi R_0^3$ , or on a surface containing a volume of  $\frac{4}{3} \pi R_0^3$ .

For the numerical validation of the FRDM, it can be noted that all shape-dependent terms, expect  $B_1$ ,  $B_2$ ,  $B_3$  and  $B_4$  in Eqs. B.120 and B.122 are normalized to unity for spherical shapes. For  $B_1$  and  $B_3$ , analytical expressions are given in Eqs. 5.48 and 5.49 respectively. For  $B_2$  and  $B_4$ , analytical expressions also exists for spherical shapes<sup>1</sup>

$$B_2(\vec{q}_{\text{sphere}}) = 1 - (1 + 2x_0 + 2x_0^2) e^{-2x_0}, \quad (\text{B.126})$$

$$B_4(\vec{q}_{\text{sphere}}) = 1 + 5 \left[ -\frac{3}{y_0^2} + \frac{15}{2y_0^3} - \frac{63}{4y_0^5} + \frac{3}{4} \left( \frac{2}{y_0} + \frac{12}{y_0^2} + \frac{32}{y_0^3} + \frac{42}{y_0^4} + \frac{21}{y_0^5} \right) e^{-2y_0} \right], \quad (\text{B.127})$$

where

$$x_0 = \frac{r_0 A^{1/3}}{a} \quad \text{and} \quad y_0 = \frac{r_0 A^{1/3}}{a_{\text{den}}}. \quad (\text{B.128})$$

<sup>1</sup>The  $B_2$  expression is corrected here for a misprint that occurred in [12, 180].

## B.4 Computational Forms

In this section computational forms used in the implementation of the various integrals that are involved in this work are presented.

### B.4.1 Reduction of Integration Domain

In the present study, volume and double volume integrations must be performed many times. Here the volume integration method will be detailed. Similar computational forms can be derived for double volume integrals. In practice, volume integrals can be turned into surface integrals using the divergence theorem, for instance considering a function  $f$  defined within a volume  $V$ . Its volume integral is defined by

$$I_f(\vec{r}_1) = \int_V d^3\vec{r}_2 f(\|\vec{r}_1 - \vec{r}_2\|) = I_F(\vec{r}_1) = \int_S d^2\vec{S}_2 \cdot (\vec{r}_1 - \vec{r}_2) F(\|\vec{r}_1 - \vec{r}_2\|) \quad (\text{B.129})$$

where  $\vec{r}_1$  is the point where the “potential” is evaluated,  $\vec{r}_2$  denotes the running integration point. The divergence theorem transforms the volume integral of  $f$  on a surface integral of a related function  $F$ . Some of the volume-defined  $f$  and surface-defined  $F$  functions used in this work are presented in Tab. B.3.

Table B.3 – Examples of volume- and surface-defined functions used in the present study.

potential	$f$	$F$
Coulomb	$\frac{1}{\ \vec{r}_1 - \vec{r}_2\ }$	$-\frac{1}{2} \frac{1}{\ \vec{r}_1 - \vec{r}_2\ }$
Yukawa	$\frac{\exp(-\ \vec{r}_1 - \vec{r}_2\ /a)}{\ \vec{r}_1 - \vec{r}_2\ /a}$	$-\left(\frac{\ \vec{r}_1 - \vec{r}_2\ }{a}\right)^{-3} \left[1 - \left(1 + \frac{\ \vec{r}_1 - \vec{r}_2\ }{a}\right) \exp\left(-\frac{\ \vec{r}_1 - \vec{r}_2\ }{a}\right)\right]$

In the following the computational forms to obtain  $I_F$  are derived for both shape parameterization types  $r(\theta)$  and  $\rho(z)$ . The cylindrical coordinate system shown in Fig. 5.4 will be used in the following derivations.

#### B.4.1.1 $r(\theta)$ Parameterization

In the surface integral (*cf.* Eq. B.129),  $d^2\vec{S}_2 = \vec{n}_2 d^2S$  where the unit vector  $\vec{n}_2$  normal to the surface  $S$  at  $\vec{r}_2$  is given by

$$\vec{n}_2 = \frac{\vec{r}_{2\theta} \times \vec{r}_{2\varphi}}{\|\vec{r}_{2\theta} \times \vec{r}_{2\varphi}\|}, \quad (\text{B.130})$$

and where  $\vec{r}_{2\theta}$  and  $\vec{r}_{2\varphi}$  are defined by

$$\begin{cases} \vec{r}_{2\theta} = \frac{\partial \vec{r}_2}{\partial \theta_2} = \frac{\partial r_2}{\partial \theta_2} \vec{e}_{r_2} + r_2 \vec{e}_{\theta_2}, \\ \vec{r}_{2\varphi} = \frac{\partial \vec{r}_2}{\partial \varphi_2} = r_2 \sin \theta_2 \vec{e}_{\varphi_2}. \end{cases} \quad (\text{B.131})$$

The cross-product  $\vec{r}_{2\theta} \times \vec{r}_{2\varphi}$  can thus be calculated, and is

$$\vec{r}_{2\theta} \times \vec{r}_{2\varphi} = \begin{pmatrix} \frac{\partial r_2}{\partial \theta_2} \\ r_2 \\ 0 \end{pmatrix}_{r_2 \theta_2 \varphi_2} \times \begin{pmatrix} 0 \\ 0 \\ r_2 \sin \theta_2 \end{pmatrix}_{r_2 \theta_2 \varphi_2} = r_2 \sin \theta_2 \begin{pmatrix} r_2 \\ -\frac{\partial r_2}{\partial \theta_2} \\ 0 \end{pmatrix}_{r_2 \theta_2 \varphi_2}. \quad (\text{B.132})$$

The norm of  $\vec{r}_{2\theta} \times \vec{r}_{2\varphi}$  is given by

$$\|\vec{r}_{2\theta} \times \vec{r}_{2\varphi}\| = r_2 \sin \theta_2 \sqrt{r_2^2 + \left(\frac{\partial r_2}{\partial \theta_2}\right)^2}. \quad (\text{B.133})$$

So the related normalized vector  $\vec{n}_2$  can be written

$$\vec{n}_2 = \frac{(r_2 \vec{e}_{r_2} - \frac{\partial r_2}{\partial \theta_2} \vec{e}_{\theta_2})}{\sqrt{r_2^2 + \left(\frac{\partial r_2}{\partial \theta_2}\right)^2}}. \quad (\text{B.134})$$

The scalar product  $(\vec{r}_1 - \vec{r}_2) \cdot \vec{n}_2$  involved in the surface integral of Eq. B.129 can be calculated

$$(\vec{r}_1 - \vec{r}_2) \cdot \vec{n}_2 = (r_1 \vec{e}_{r_1} - r_2 \vec{e}_{r_2}) \cdot \vec{n}_2, \quad (\text{B.135})$$

$$= - \left( r_2^2 + \left( \frac{\partial r_2}{\partial \theta_2} \right)^2 \right)^{-1/2} \left( r_2^2 - r_1 (r_2 \vec{e}_{r_1} \cdot \vec{e}_{r_2} - \frac{\partial r_2}{\partial \theta_2} \vec{e}_{r_1} \cdot \vec{e}_{\theta_2}) \right). \quad (\text{B.136})$$

Since only axially spherical shapes are considered, the calculation can be performed assuming  $\varphi_1 = 0$ . The base vectors in the cylindrical coordinate system are defined by

$$\begin{cases} \vec{e}_{r_1} = \cos \theta_1 \vec{e}_z + \sin \theta_1 \vec{e}_x, \\ \vec{e}_{r_2} = \cos \theta_2 \vec{e}_z + \sin \theta_2 \cos \varphi_2 \vec{e}_x + \sin \theta_2 \sin \varphi_2 \vec{e}_y, \\ \vec{e}_{\theta_2} = \cos \theta_2 \cos \varphi_2 \vec{e}_x + \cos \theta_2 \sin \varphi_2 \vec{e}_y - \sin \theta_2 \vec{e}_z. \end{cases} \quad (\text{B.137})$$

So that the following scalar products can be computed

$$\begin{cases} \vec{e}_{r_1} \cdot \vec{e}_{r_2} = \cos \theta_1 \cos \theta_2 + \sin \theta_1 \sin \theta_2 \cos \varphi_2, \\ \vec{e}_{r_1} \cdot \vec{e}_{\theta_2} = \cos \theta_2 \cos \varphi_2 \sin \theta_1 - \sin \theta_2 \cos \theta_1. \end{cases} \quad (\text{B.138})$$

As  $r_1 \cos \theta_1 = z_1$  and  $r_1 \sin \theta_1 = x_1$ , one obtains

$$\begin{cases} r_1 \vec{e}_{r_1} \cdot \vec{e}_{r_2} = z_1 \cos \theta_2 + x_1 \sin \theta_2 \cos \varphi_2, \\ r_1 \vec{e}_{r_1} \cdot \vec{e}_{\theta_2} = x_1 \cos \theta_2 \cos \varphi_2 - z_1 \sin \theta_2. \end{cases} \quad (\text{B.139})$$

Using Fig. B.8,  $d^2S$  can be expressed as

$$d^2S = r_2 \sin \theta_2 d\varphi_2 d\ell, \quad (\text{B.140})$$

$$= r_2 \sin \theta_2 d\varphi_2 \left( (r_2 d\theta_2)^2 + \left( \frac{\partial r_2}{\partial \theta_2} d\theta_2 \right)^2 \right)^{1/2}, \quad (\text{B.141})$$

$$= r_2 \sin \theta_2 d\varphi_2 \left( r_2^2 + \left( \frac{\partial r_2}{\partial \theta_2} \right)^2 \right)^{1/2} d\theta_2. \quad (\text{B.142})$$

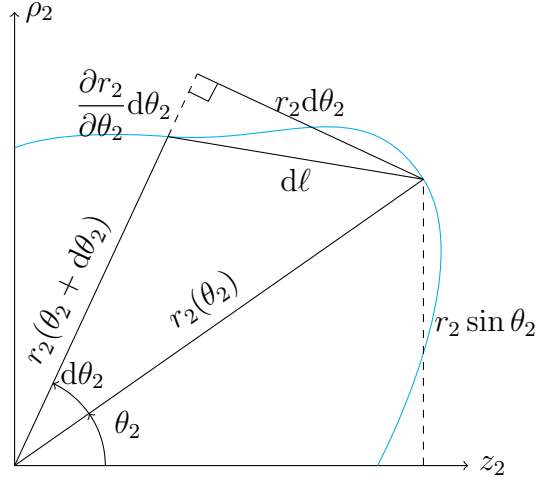


Figure B.8 – Surface element scheme.

So that the  $(\vec{r}_1 - \vec{r}_2) \cdot \vec{n}_2 d^2 S$  term can be written

$$(\vec{r}_1 - \vec{r}_2) \cdot \vec{n}_2 d^2 S = - \left( r_2^2 - r_1 (r_2 \vec{e}_{r_1} \cdot \vec{e}_{r_2} - \frac{\partial r_2}{\partial \theta_2} \vec{e}_{r_1} \cdot \vec{e}_{\theta_2}) \right) r_2 \sin \theta_2 d\varphi_2 d\theta_2. \quad (\text{B.143})$$

This latter results can be inserted into Eq. B.129 so that  $I_F$  can be written

$$I_F(\vec{r}_1) = - \int_0^\pi d\theta_2 \int_0^{2\pi} d\varphi_2 r_2 \sin \theta_2 \left( r_2^2 - r_2 (z_1 \cos \theta_2 + x_1 \sin \theta_2 \cos \varphi_2) + \frac{\partial r_2}{\partial \theta_2} (x_1 \cos \theta_2 \cos \varphi_2 - z_1 \sin \theta_2) \right) F(\|\vec{r}_1 - \vec{r}_2\|). \quad (\text{B.144})$$

Changing the  $\theta_2$  variable into  $\mu_2 = \cos \theta_2$ , and defining  $\nu_2 = \sin \theta_2 = \sqrt{1 - \mu_2^2}$ , Eq. B.144 can be written

$$I_F(\vec{r}_1) = - \int_{-1}^1 d\mu_2 \int_0^{2\pi} d\varphi_2 r_2 \left( r_2^2 - r_2 (z_1 \mu_2 + x_1 \nu_2 \cos \varphi_2) + \frac{\partial r_2}{\partial \theta_2} (x_1 \mu_2 \cos \varphi_2 - z_1 \nu_2) \right) F(\|\vec{r}_1 - \vec{r}_2\|). \quad (\text{B.145})$$

As  $r_2 = r_2(\mu_2)$ , one has

$$I_F(\vec{r}_1) = - \int_{-1}^1 d\mu_2 r_2 \int_0^{2\pi} d\varphi_2 \left[ \left( r_2^2 - r_2 z_1 \mu_2 - \frac{\partial r_2}{\partial \theta_2} z_1 \nu_2 \right) + \cos \varphi_2 \left( \frac{\partial r_2}{\partial \theta_2} x_1 \mu_2 - r_2 x_1 \nu_2 \right) \right] F(\|\vec{r}_1 - \vec{r}_2\|). \quad (\text{B.146})$$

This latter expression is particularly useful for numerical computation. Still a practical expression for  $\|\vec{r}_1 - \vec{r}_2\|$  needs to be given. Using

$$\begin{cases} \vec{r}_1 = x_1 \vec{e}_x + z_1 \vec{e}_z, \\ \vec{r}_2 = r_2 \mu_2 \vec{e}_z + r_2 \nu_2 \cos \varphi_2 \vec{e}_x + r_2 \nu_2 \sin \varphi_2 \vec{e}_y, \end{cases} \quad (\text{B.147})$$

one obtains

$$\|\vec{r}_1 - \vec{r}_2\| = (x_1 - r_2\nu_2 \cos \varphi_2)^2 + (z_1 - r_2\mu_2)^2 + r_2^2\nu_2^2 \sin^2 \varphi_2, \quad (\text{B.148})$$

$$= x_1^2 - 2x_1r_2\nu_2 \cos \varphi_2 + r_2^2\nu_2^2 \cos^2 \varphi_2 + (z_1 - r_2\mu_2)^2 + r_2^2\nu_2^2 \sin^2 \varphi_2, \quad (\text{B.149})$$

$$= x_1^2 + \nu_2^2 r_2^2 + (z_1 - r_2\mu_2)^2 - 2x_1\nu_2 r_2 \cos \varphi_2, \quad (\text{B.150})$$

$$= x_1^2 + \nu_2^2 r_2^2 + z_1^2 - 2z_1r_2\mu_2 + r_2^2\mu_2^2 - 2x_1\nu_2 r_2 \cos \varphi_2, \quad (\text{B.151})$$

$$= x_1^2 + r_2^2 + z_1^2 - 2z_1r_2\mu_2 - 2x_1\nu_2 r_2 \cos \varphi_2. \quad (\text{B.152})$$

#### B.4.1.2 $\rho(z)$ Parameterization

Considering axially symmetric shapes, one can assume that  $\varphi_1 = 0$ . So that  $\vec{r}_1$  and  $\vec{r}_2$  can be written

$$\begin{cases} \vec{r}_1 = \rho_1 \vec{e}_x + z_1 \vec{e}_z, \\ \vec{r}_2 = \rho_2 \cos \varphi_2 \vec{e}_x + \rho_2 \sin \varphi_2 \vec{e}_y + z_2 \vec{e}_z. \end{cases} \quad (\text{B.153})$$

The vector normal to the surface  $\vec{n}_2$  is defined as

$$\vec{n}_2 = \frac{\vec{r}_{2z} \times \vec{r}_{2\varphi}}{\|\vec{r}_{2z} \times \vec{r}_{2\varphi}\|}, \quad (\text{B.154})$$

where

$$\begin{cases} \vec{r}_{2z} = \frac{\partial \vec{r}_2}{\partial z_2} = \frac{\partial \rho_2}{\partial z_2} (\cos \varphi_2 \vec{e}_x + \sin \varphi_2 \vec{e}_y) + \vec{e}_z, \\ \vec{r}_{2\varphi} = \frac{\partial \vec{r}_2}{\partial \varphi_2} = \rho_2 (-\sin \varphi_2 \vec{e}_x + \cos \varphi_2 \vec{e}_y). \end{cases} \quad (\text{B.155})$$

The  $\vec{r}_{2\theta} \times \vec{r}_{2\varphi}$  term can be thus calculated as

$$\vec{r}_{2\theta} \times \vec{r}_{2\varphi} = \begin{pmatrix} \frac{\partial \rho_2}{\partial z_2} \cos \varphi_2 \\ \frac{\partial \rho_2}{\partial z_2} \sin \varphi_2 \\ 1 \end{pmatrix}_{xyz} \times \begin{pmatrix} -\rho_2 \sin \varphi_2 \\ \rho_2 \cos \varphi_2 \\ 0 \end{pmatrix}_{xyz} = \rho_2 \begin{pmatrix} -\cos \varphi_2 \\ -\sin \varphi_2 \\ \frac{\partial \rho_2}{\partial z_2} \end{pmatrix}_{xyz}. \quad (\text{B.156})$$

Its norm  $\|\vec{r}_{2\theta} \times \vec{r}_{2\varphi}\|$  is given by

$$\|\vec{r}_{2\theta} \times \vec{r}_{2\varphi}\| = \rho_2 \left[ 1 + \left( \frac{\partial \rho_2}{\partial z_2} \right)^2 \right]^{1/2}. \quad (\text{B.157})$$

So that  $\vec{n}_2$  can be written

$$\vec{n}_2 = \left[ 1 + \left( \frac{d\rho_2}{dz_2} \right)^2 \right]^{-1/2} \left( \frac{d\rho_2}{dz_2} \vec{e}_z - \cos \varphi_2 \vec{e}_x - \sin \varphi_2 \vec{e}_y \right). \quad (\text{B.158})$$

The integration element  $d^2S$  is defined as

$$d^2S = \rho_2 d\varphi_2 d\ell, \quad (\text{B.159})$$

where  $d\ell$  can be calculated using Fig. B.9.

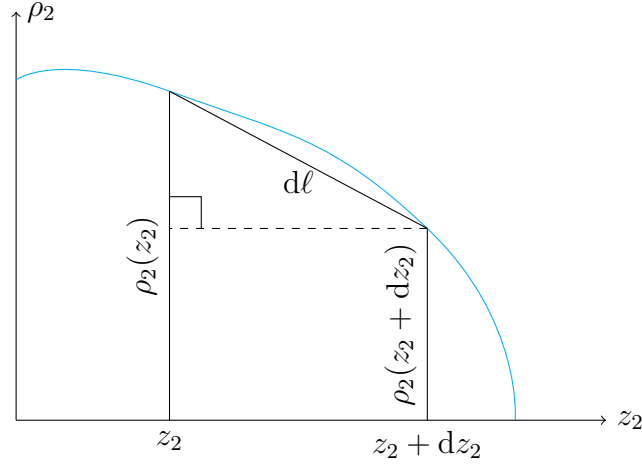


Figure B.9 – Surface element scheme.

And is thus given by

$$\begin{aligned}
 d\ell &= \sqrt{(\rho_2(z_2) - \rho_2(z_2 + dz_2))^2 + (dz_2)^2}, \\
 &= \sqrt{\left(\rho_2(z_2) - \rho_2(z_2) - \frac{d\rho_2}{dz_2}dz_2\right)^2 + (dz_2)^2}, \\
 &= \left[1 + \left(\frac{d\rho_2}{dz_2}\right)^2\right]^{1/2} dz_2.
 \end{aligned} \tag{B.160}$$

To compute Eq. B.129, one also needs to compute

$$\vec{r}_1 - \vec{r}_2 = (\rho_1 - \rho_2 \cos \varphi_2)\vec{e}_x - \rho_2 \sin \varphi_2 \vec{e}_y + (z_1 - z_2)\vec{e}_z, \tag{B.161}$$

so that  $(\vec{r}_1 - \vec{r}_2) \cdot \vec{n}_2 d^2S$  can be written

$$\begin{aligned}
 (\vec{r}_1 - \vec{r}_2) \cdot \vec{n}_2 d^2S &= \rho_2 d\varphi_2 dz_2 \left( \frac{d\rho_2}{dz_2}(z_1 - z_2) - \cos \varphi_2(\rho_1 - \rho_2 \cos \varphi_2) + \rho_2 \sin^2 \varphi_2 \right), \\
 &= \rho_2 d\varphi_2 dz_2 \left( (z_1 - z_2) \frac{d\rho_2}{dz_2} - \rho_1 \cos \varphi_2 + \rho_2 \right).
 \end{aligned} \tag{B.162}$$

Finally the surface integral  $I_F(\vec{r}_1)$  in Eq B.129 can be computed as

$$I_F(\vec{r}_1) = \int_{z_{\min}}^{z_{\max}} dz_2 \rho_2 \int_0^{2\pi} d\varphi_2 \left[ \left( -(z_1 - z_2) \frac{d\rho_2}{dz_2} - \rho_2 \right) + \rho_1 \cos \varphi_2 \right] F(\|\vec{r}_1 - \vec{r}_2\|). \tag{B.163}$$

The form  $\|\vec{r}_1 - \vec{r}_2\|$  is also given explicitly by

$$\begin{aligned}
 \|\vec{r}_1 - \vec{r}_2\|^2 &= (z_1 - z_2)^2 + \rho_2^2 \sin^2 \varphi_2 + (\rho_1 - \rho_2 \cos \varphi_2)^2, \\
 &= (z_1 - z_2)^2 + \rho_1^2 + \rho_2^2 - 2\rho_1 \rho_2 \cos \varphi_2.
 \end{aligned} \tag{B.164}$$

### B.4.2 Coulomb Potential in $\rho(z)$ Parameterization

A term involved very often in many calculations presented here is (or involves) the coulomb potential generated by a uniform charge distribution contained within a given sharp-edge volume  $V$ . The diverge theorem can reduces the volume integration to a surface

integration. A special modification of the surface integral can then turn the surface integral into a one-dimension integral. This can be done only when using the  $\rho(z)$  shape parameterization. This method will be presented in the following.

In the general case, the Coulomb potential is defined as

$$V_C(\vec{r}_1) = \int_V \rho_C(\vec{r}_2) \frac{d^3\vec{r}_2}{\|\vec{r}_1 - \vec{r}_2\|}, \quad (\text{B.165})$$

where  $\rho_C$  is the charge density. The integration is performed over a volume  $V$  that contains all existing charges of the system. In all generality this volume can be the universe. The case we are interested in is when this volume is finite and corresponds to the volume inside the sharp surface of the homogeneous nucleus. Therefore  $\rho_C(\vec{r}_2)$  is constant within the nucleus and can be moved outside the integral. The considered integral is thus

$$\tilde{V}_C(\vec{r}_1) = \int_V \frac{d^3\vec{r}_2}{\|\vec{r}_1 - \vec{r}_2\|}. \quad (\text{B.166})$$

The divergence theorem states that

$$\int_V \text{div} \vec{F} d^3\vec{r}_2 = \int_S \vec{F} \cdot d^2\vec{S}. \quad (\text{B.167})$$

One can notice that

$$\frac{1}{\|\vec{r}_1 - \vec{r}_2\|} = -\frac{1}{2} \text{div} \frac{\vec{r}_1 - \vec{r}_2}{\|\vec{r}_1 - \vec{r}_2\|}, \quad (\text{B.168})$$

which is applied to the Coulomb potential given by Eq. B.166. It yields

$$\tilde{V}_C(\vec{r}_1) = -\frac{1}{2} \int_S \frac{\vec{r}_1 - \vec{r}_2}{\|\vec{r}_1 - \vec{r}_2\|} \cdot d^2\vec{S}. \quad (\text{B.169})$$

The integration element  $d^2\vec{S}$  is decomposed as

$$d^2\vec{S} = d^2S \vec{n}_2, \quad (\text{B.170})$$

where  $\vec{n}_2$  is a normalized vector normal to the nucleus surface at the point  $\vec{r}_2$  and oriented outward. This normal vector can be expressed in the local coordinate system with vectors  $\vec{e}_{\rho_2}$  and  $\vec{e}_z$ . From Fig. B.10, we define the angle  $\theta = \arctan \frac{d\rho_2}{dz_2}$ .

The normal vector coordinates are thus given by

$$n_{\rho_2} = \cos(\arctan \frac{d\rho_2}{dz_2}) = \frac{1}{\sqrt{1 + \left(\frac{d\rho_2}{dz_2}\right)^2}}, \quad (\text{B.171})$$

$$n_z = -\sin(\arctan \frac{d\rho_2}{dz_2}) = \frac{-\frac{d\rho_2}{dz_2}}{\sqrt{1 + \left(\frac{d\rho_2}{dz_2}\right)^2}}. \quad (\text{B.172})$$

It can be seen that vector  $\vec{n}_2 = n_{\rho_2}\vec{e}_{\rho_2} + n_z\vec{e}_z$  is normalized and can finally be written

$$\vec{n}_2 = \left(1 + \left(\frac{d\rho_2}{dz_2}\right)^2\right)^{-1/2} \left(\vec{e}_{\rho_2} - \frac{d\rho_2}{dz_2}\vec{e}_z\right). \quad (\text{B.173})$$

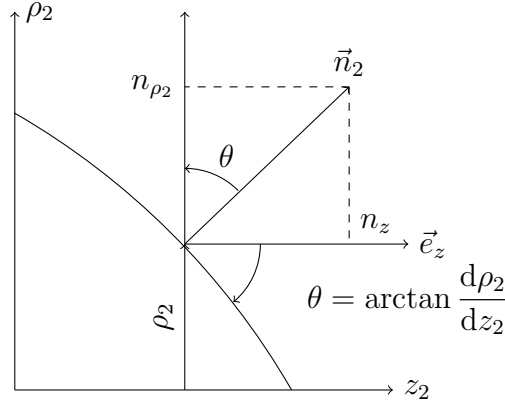


Figure B.10 – Normal vector to the nucleus surface.

From Fig. B.11, one can derive the definition of  $d^2S$  as

$$d^2S = \rho_2 d\varphi_2 dX. \quad (\text{B.174})$$

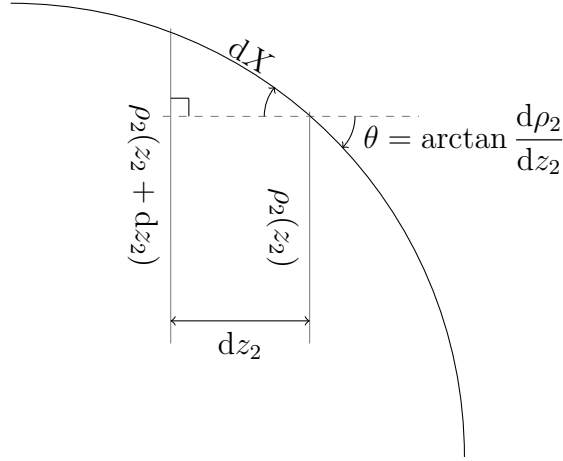


Figure B.11 – Infinitesimal surface element.

As  $dX = \frac{1}{\cos \theta} dz_2 = \sqrt{1 + \left(\frac{d\rho_2}{dz_2}\right)^2} dz_2$ , one has

$$d^2S = \rho_2 d\varphi_2 dz_2 \left(1 + \left(\frac{d\rho_2}{dz_2}\right)^2\right)^{1/2}. \quad (\text{B.175})$$

Using the local coordinate system, one can write  $\vec{r}_1 - \vec{r}_2$  as

$$\vec{r}_1 - \vec{r}_2 = \rho_1 \vec{e}_{\rho_1} + z_1 \vec{e}_z - \rho_2 \vec{e}_{\rho_2} - z_2 \vec{e}_z = \rho_1 \vec{e}_{\rho_1} - \rho_2 \vec{e}_{\rho_2} + (z_1 - z_2) \vec{e}_z. \quad (\text{B.176})$$

Its norm is given by

$$\|\vec{r}_1 - \vec{r}_2\|^2 = (z_1 - z_2)^2 + (\rho_1 \vec{e}_{\rho_1} - \rho_2 \vec{e}_{\rho_2})^2 = (z_1 - z_2)^2 + \rho_1^2 + \rho_2^2 - 2\rho_1 \rho_2 \vec{e}_{\rho_1} \cdot \vec{e}_{\rho_2}. \quad (\text{B.177})$$

Hence the scalar product  $(\vec{r}_1 - \vec{r}_2) \cdot \vec{n}_{\rho_2}$  can be calculated. It yields

$$(\vec{r}_1 - \vec{r}_2) \cdot \vec{n}_{\rho_2} = \left(1 + \left(\frac{d\rho_2}{dz_2}\right)^2\right)^{-1/2} \left[ \rho_1 \vec{e}_{\rho_1} \cdot \vec{e}_{\rho_2} - \rho_2 - \frac{d\rho_2}{dz_2} (z_1 - z_2) \right]. \quad (\text{B.178})$$



Finally the integral can be written

$$\begin{aligned} \tilde{V}_C(\vec{r}_1) = & -\frac{1}{2} \int_{z_{\min}}^{z_{\max}} dz_2 \rho_2 \int_0^{2\pi} d\varphi_2 \left[ \rho_1 \vec{e}_{\rho_1} \vec{e}_{\rho_2} - \rho_2 - \frac{d\rho_2}{dz_2} (z_1 - z_2) \right] \\ & \times \left[ (z_1 - z_2)^2 + \rho_1^2 + \rho_2^2 - 2\rho_1 \rho_2 \vec{e}_{\rho_1} \vec{e}_{\rho_2} \right]^{-\frac{1}{2}}. \end{aligned} \quad (\text{B.179})$$

It can be shown that

$$\vec{e}_{\rho_1} \cdot \vec{e}_{\rho_2} = \cos(\varphi_2 - \varphi_1). \quad (\text{B.180})$$

The variable change  $\varphi'_2 = \varphi_2 - \varphi_1$  is made. This change impacts the integration boundaries but as long as the whole  $2\pi$  are taken into account it does not matter.  $\tilde{V}_C(\vec{r}_1)$  can thus be written

$$\begin{aligned} \tilde{V}_C(\vec{r}_1) = & \frac{1}{2} \int_{z_{\min}}^{z_{\max}} dz_2 \rho_2 \int_0^{2\pi} d\varphi'_2 \left[ \rho_2 + \frac{d\rho_2}{dz_2} (z_1 - z_2) - \rho_1 \cos \varphi'_2 \right] \\ & \times \left[ (z_1 - z_2)^2 + \rho_1^2 + \rho_2^2 - 2\rho_1 \rho_2 \cos \varphi'_2 \right]^{-\frac{1}{2}}. \end{aligned} \quad (\text{B.181})$$

The integration can be performed over the first half of the  $2\pi$  range only, and the result is multiplied by 2. One obtains

$$\begin{aligned} \tilde{V}_C(\vec{r}_1) = & \int_{z_{\min}}^{z_{\max}} dz_2 \rho_2 \int_0^{\pi} d\varphi'_2 \left[ \rho_2 + \frac{d\rho_2}{dz_2} (z_1 - z_2) - \rho_1 \cos \varphi'_2 \right] \\ & \times \left[ (z_1 - z_2)^2 + \rho_1^2 + \rho_2^2 - 2\rho_1 \rho_2 \cos \varphi'_2 \right]^{-\frac{1}{2}}. \end{aligned} \quad (\text{B.182})$$

The  $k$  parameter is defined as

$$k^2 = \frac{4\rho_1 \rho_2}{(\rho_1 + \rho_2)^2 + (z_1 - z_2)^2}. \quad (\text{B.183})$$

One can notice that  $(z_1 - z_2)^2 + \rho_1^2 + \rho_2^2 = (z_1 - z_2)^2 + (\rho_1 + \rho_2)^2 - 2\rho_1 \rho_2$ , so that  $\tilde{V}_C(\vec{r}_1)$  can be written

$$\tilde{V}_C(\vec{r}_1) = \int_{z_{\min}}^{z_{\max}} dz_2 \rho_2 \int_0^{\pi} d\varphi'_2 \left[ \rho_2 + \frac{d\rho_2}{dz_2} (z_1 - z_2) - \rho_1 \cos \varphi'_2 \right] \left[ \frac{4\rho_1 \rho_2}{k^2} - 2\rho_1 \rho_2 - 2\rho_1 \rho_2 \cos \varphi'_2 \right]^{-1/2}, \quad (\text{B.184})$$

$$= \int_{z_{\min}}^{z_{\max}} dz_2 \rho_2 \int_0^{\pi} d\varphi'_2 \left[ \rho_2 + \frac{d\rho_2}{dz_2} (z_1 - z_2) - \rho_1 \cos \varphi'_2 \right] \frac{k}{\sqrt{4\rho_1 \rho_2}} \left[ 1 - k^2 \frac{\cos \varphi'_2 + 1}{2} \right]^{-1/2}. \quad (\text{B.185})$$

Noticing that

$$\frac{k}{\sqrt{4\rho_1 \rho_2}} = \frac{1}{[(\rho_1 + \rho_2)^2 + (z_1 - z_2)^2]^{1/2}}, \quad (\text{B.186})$$

$\tilde{V}_C(\vec{r}_1)$  simplifies to

$$\begin{aligned} \tilde{V}_C(\vec{r}_1) = & \int_{z_{\min}}^{z_{\max}} dz_2 \rho_2 \int_0^\pi d\varphi'_2 \left[ \rho_2 + \frac{d\rho_2}{dz_2} (z_1 - z_2) - \rho_1 \cos \varphi'_2 \right] \\ & \times \left[ 1 - k^2 \frac{\cos \varphi'_2 + 1}{2} \right]^{-\frac{1}{2}} [(\rho_1 + \rho_2)^2 + (z_1 - z_2)^2]^{-\frac{1}{2}}, \quad (\text{B.187}) \end{aligned}$$

which becomes

$$\begin{aligned} \tilde{V}_C(\vec{r}_1) = & \int_{z_{\min}}^{z_{\max}} dz_2 \rho_2 \left[ \left( \rho_1 + \rho_2 + \frac{d\rho_2}{dz_2} (z_1 - z_2) \right) \int_0^\pi d\varphi'_2 \left[ 1 - k^2 \frac{\cos \varphi'_2 + 1}{2} \right]^{-1/2} \right. \\ & \left. - \rho_1 \int_0^\pi d\varphi'_2 \frac{\cos \varphi'_2 + 1}{\left[ 1 - k^2 \frac{\cos \varphi'_2 + 1}{2} \right]^{1/2}} \right] [(\rho_1 + \rho_2)^2 + (z_1 - z_2)^2]^{-1/2}. \quad (\text{B.188}) \end{aligned}$$

The two integrals that are involved in this expression are

$$I_1 = \int_0^\pi \frac{d\varphi'_2}{\left[ 1 - k^2 \frac{\cos \varphi'_2 + 1}{2} \right]^{1/2}} \quad \text{and} \quad I_2 = \int_0^\pi d\varphi'_2 \frac{\cos \varphi'_2 + 1}{\left[ 1 - k^2 \frac{\cos \varphi'_2 + 1}{2} \right]^{1/2}}. \quad (\text{B.189})$$

Using the relation

$$\cos \varphi'_2 + 1 = 2 \cos^2 \frac{\varphi'_2}{2}, \quad (\text{B.190})$$

and making the variable change  $\varphi''_2 = \frac{\varphi'_2}{2}$ , one can write the  $I_1$  and  $I_2$  integrals as

$$I_1 = \int_0^\pi \frac{d\varphi'_2}{\left[ 1 - k^2 \cos^2 \frac{\varphi'_2}{2} \right]^{1/2}} = 2 \int_0^{\pi/2} \frac{d\varphi''_2}{[1 - k^2 \cos^2 \varphi''_2]^{1/2}}, \quad (\text{B.191})$$

$$I_2 = 2 \int_0^\pi d\varphi'_2 \frac{\cos^2 \frac{\varphi'_2}{2}}{\left[ 1 - k^2 \cos^2 \frac{\varphi'_2}{2} \right]^{1/2}} = 4 \int_0^{\pi/2} d\varphi''_2 \frac{\cos^2 \varphi''_2}{[1 - k^2 \cos^2 \varphi''_2]^{1/2}}. \quad (\text{B.192})$$

Using that  $\cos(\frac{\pi}{2} - \varphi''_2) = \sin \varphi''_2$ , the final variable change with  $\varphi'''_2 = \frac{\pi}{2} - \varphi''_2$  is made, so that one obtains

$$I_1 = -2 \int_{\pi/2}^0 \frac{d\varphi'''_2}{[1 - k^2 \sin^2 \varphi'''_2]^{1/2}} = 2 \int_0^{\pi/2} \frac{d\varphi'''_2}{[1 - k^2 \sin^2 \varphi'''_2]^{1/2}}, \quad (\text{B.193})$$

$$I_2 = -4 \int_{\pi/2}^0 d\varphi'''_2 \frac{\sin^2 \varphi'''_2}{[1 - k^2 \sin^2 \varphi'''_2]^{1/2}} = 4 \int_0^{\pi/2} d\varphi'''_2 \frac{\sin^2 \varphi'''_2}{[1 - k^2 \sin^2 \varphi'''_2]^{1/2}}. \quad (\text{B.194})$$

It can be seen that  $I_1 = 2K(k)$  where  $K$  is the *complete elliptic integral of first kind* [48]. Additionally,  $I_2$  can also be expressed in terms of a sum the complete elliptic integrals of first ( $K$ ) and second kinds ( $E$ ). Indeed

$$K(k) = \int_0^{\pi/2} \frac{d\theta}{(1 - k^2 \sin^2 \theta)^{1/2}}, \quad (\text{B.195})$$

$$E(k) = \int_0^{\pi/2} (1 - k^2 \sin^2 \theta)^{1/2} d\theta. \quad (\text{B.196})$$

So that

$$K - E = \int_0^{\pi/2} \left( \frac{1}{(1 - k^2 \sin^2 \theta)^{1/2}} - \frac{1 - k^2 \sin^2 \theta}{(1 - k^2 \sin^2 \theta)^{1/2}} \right) d\theta = k^2 \int_0^{\pi/2} \frac{\sin^2 \theta}{(1 - k^2 \sin^2 \theta)^{1/2}} d\theta. \quad (\text{B.197})$$

And therefore

$$I_1 = 2K(k), \quad (\text{B.198})$$

$$I_2 = 4 \frac{K(k) - E(k)}{k^2}. \quad (\text{B.199})$$

Finally, the Coulomb potential  $\tilde{V}_C(\vec{r}_1)$  is expressed [11] using  $K$  and  $E$

$$\tilde{V}_C(\vec{r}_1) = 2 \int_{z_{\min}}^{z_{\max}} dz_2 \rho_2 \frac{\left( \rho_1 + \rho_2 + \frac{d\rho_2}{dz_2}(z_1 - z_2) \right) K(k) - 2 \frac{\rho_1}{k^2} (K(k) - E(k))}{[(\rho_1 + \rho_2)^2 + (z_1 - z_2)^2]^{1/2}}. \quad (\text{B.200})$$

The implementation of these complete elliptic integrals in the Boost C++ library [154] that is used in CONRAD showed a low efficiency that actually reduce the overall program speed compared with the surface integration. Thus a new implementation of these functions using the Fukushima's method [181] has been done and led to significant speed-ups.

### B.4.3 Principal Curvatures of 2D-Surfaces

A final computational feature is presented in the following and is related to the calculation of the principal radii of curvature involved in the  $B_k$  term of the FRDM model (*cf.* Eq. B.122). It should be noted that this term has actually no effects in the implemented version as its related mass coefficient in Eq. B.120,  $a_3$  is zero when using parameters values given in Ref. [12]. These radii are calculated differently according to the parameterization  $\rho(z)$  or  $r(\theta)$  of the nucleus shape. For more information about differential geometry see for instance Ref. [182].

#### B.4.3.1 $\rho(z)$ Parameterization

In case, the considered surface is defined by the parameterized vector  $\vec{X}$  defined by

$$\vec{X}(z, \varphi) = \begin{pmatrix} \rho(z) \cos \varphi \\ \rho(z) \sin \varphi \\ z \end{pmatrix}_{xyz}. \quad (\text{B.201})$$

The following derivative vectors can be calculated

$$\begin{aligned} \frac{\partial \vec{X}}{\partial z} &= \begin{pmatrix} \rho'(z) \cos \varphi \\ \rho'(z) \sin \varphi \\ 1 \end{pmatrix}, & \frac{\partial \vec{X}}{\partial \varphi} &= \begin{pmatrix} -\rho(z) \sin \varphi \\ \rho(z) \cos \varphi \\ 0 \end{pmatrix}, & \frac{\partial^2 \vec{X}}{\partial \varphi \partial z} &= \begin{pmatrix} -\rho'(z) \sin \varphi \\ \rho'(z) \cos \varphi \\ 0 \end{pmatrix}, \\ \frac{\partial^2 \vec{X}}{\partial z^2} &= \begin{pmatrix} \rho''(z) \cos \varphi \\ \rho''(z) \sin \varphi \\ 0 \end{pmatrix}, & \frac{\partial^2 \vec{X}}{\partial \varphi^2} &= \begin{pmatrix} -\rho(z) \cos \varphi \\ -\rho(z) \sin \varphi \\ 0 \end{pmatrix}, & \frac{\partial \vec{X}}{\partial z} \times \frac{\partial \vec{X}}{\partial \varphi} &= \begin{pmatrix} -\rho(z) \cos \varphi \\ -\rho(z) \sin \varphi \\ \rho'(z) \rho(z) \end{pmatrix}. \end{aligned} \quad (\text{B.202})$$

The norm  $\left\| \frac{\partial \vec{X}}{\partial z} \times \frac{\partial \vec{X}}{\partial \varphi} \right\|$  is given by

$$\left\| \frac{\partial \vec{X}}{\partial z} \times \frac{\partial \vec{X}}{\partial \varphi} \right\| = \sqrt{\rho^2(z) + \rho^2(z)[\rho'(z)]^2} = \rho(z)\sqrt{1 + [\rho'(z)]^2}. \quad (\text{B.203})$$

Therefore the normal vector  $\vec{n}$  orthogonal to the surface at the point  $\vec{X}(z, \varphi)$  is given by

$$\vec{n} = \frac{\frac{\partial \vec{X}}{\partial z} \times \frac{\partial \vec{X}}{\partial \varphi}}{\left\| \frac{\partial \vec{X}}{\partial z} \times \frac{\partial \vec{X}}{\partial \varphi} \right\|} = \frac{1}{\sqrt{1 + [\rho'(z)]^2}} \begin{pmatrix} -\cos \varphi \\ -\sin \varphi \\ \rho'(z) \end{pmatrix}. \quad (\text{B.204})$$

The first and second fundamental forms are defined as

$$\mathbf{I} = \begin{bmatrix} E & F \\ F & G \end{bmatrix}, \quad \mathbf{II} = \begin{bmatrix} L & M \\ M & N \end{bmatrix}, \quad (\text{B.205})$$

where

$$\begin{aligned} E &= \frac{\partial \vec{X}}{\partial z} \cdot \frac{\partial \vec{X}}{\partial z} = [\rho'(z)]^2 + 1, & F &= \frac{\partial \vec{X}}{\partial z} \cdot \frac{\partial \vec{X}}{\partial \varphi} = 0, & G &= \frac{\partial \vec{X}}{\partial \varphi} \cdot \frac{\partial \vec{X}}{\partial \varphi} = \rho^2(z), \\ L &= \frac{\partial^2 \vec{X}}{\partial z^2} \cdot \vec{n} = -\frac{\rho''(z)}{\sqrt{1 + [\rho'(z)]^2}}, & M &= \frac{\partial^2 \vec{X}}{\partial z \partial \varphi} \cdot \vec{n} = 0, & N &= \frac{\partial^2 \vec{X}}{\partial \varphi^2} \cdot \vec{n} = \frac{\rho(z)}{\sqrt{1 + [\rho'(z)]^2}}. \end{aligned} \quad (\text{B.206})$$

The shape operator  $S$  is defined by

$$S = \mathbf{I}^{-1} \mathbf{II}, \quad (\text{B.207})$$

$$= \frac{1}{EG - F^2} \begin{bmatrix} LG - FM & GM - FN \\ ME - FL & EN - FM \end{bmatrix}, \quad (\text{B.208})$$

$$= \frac{1}{\rho^2(z)(1 + [\rho'(z)]^2)} \begin{bmatrix} -\frac{\rho^2(z)\rho''(z)}{\sqrt{1 + [\rho'(z)]^2}} & 0 \\ 0 & \rho(z)\sqrt{1 + [\rho'(z)]^2} \end{bmatrix}, \quad (\text{B.209})$$

$$= \begin{bmatrix} -\frac{\rho''(z)}{(1 + [\rho'(z)]^2)^{3/2}} & 0 \\ 0 & \frac{1}{\rho(z)\sqrt{1 + [\rho'(z)]^2}} \end{bmatrix}. \quad (\text{B.210})$$

The principal curvatures  $k_1$  and  $k_2$  are the eigenvalues of the shape operator. They are given as

$$k_1 = -\frac{\rho''(z)}{(1 + [\rho'(z)]^2)^{3/2}} \quad \text{and} \quad k_2 = \frac{1}{\rho(z)\sqrt{1 + [\rho'(z)]^2}}. \quad (\text{B.211})$$

The principal radii of curvature are the inverse of the curvatures. The shape operator is diagonal in the chosen parameterization  $(z, \varphi)$ . It can be deduced that the directions generated by the derivation of  $\vec{X}$  with respect to these parameters are the principal directions. The definition of the principal curvatures was verified on a practical example shown in Fig. B.12. It was possible to verify that, given a point on the surface (yellow dot on the figure), the normal vector is properly calculated (black line) and the two circles in red and blue are properly tangent to the surface at the chosen point.

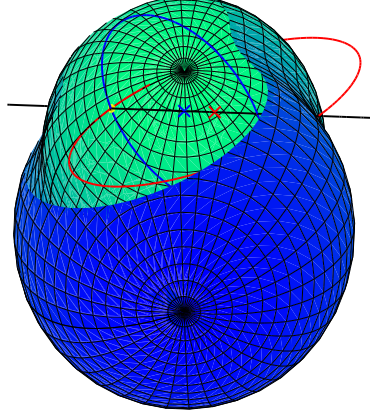


Figure B.12 – Example of verification of the calculation of the principal radii of curvature for a  $\rho(z)$ -defined shape, here a three-quadratic-surface shape.

#### B.4.3.2 $r(\theta)$ Parameterization

For this shape parameterization, the surface is defined using the parameterized vector  $\vec{X}$  given by

$$\vec{X}(\theta, \varphi) = \begin{pmatrix} r(\theta) \sin \theta \cos \varphi \\ r(\theta) \sin \theta \sin \varphi \\ r(\theta) \cos \theta \end{pmatrix}_{xyz}. \quad (\text{B.212})$$

The following derivatives can be computed

$$\begin{aligned} \frac{\partial \vec{X}}{\partial \theta} &= \begin{pmatrix} (r' \sin \theta + r \cos \theta) \cos \varphi \\ (r' \sin \theta + r \cos \theta) \sin \varphi \\ r' \cos \theta - r \sin \theta \end{pmatrix}, & \frac{\partial \vec{X}}{\partial \varphi} &= \begin{pmatrix} -r \sin \theta \sin \varphi \\ r \sin \theta \cos \varphi \\ 0 \end{pmatrix}, \\ \frac{\partial^2 \vec{X}}{\partial \theta \partial \varphi} &= \begin{pmatrix} -(r' \sin \theta + r \cos \theta) \sin \varphi \\ (r' \sin \theta + r \cos \theta) \cos \varphi \\ 0 \end{pmatrix}, & \frac{\partial^2 \vec{X}}{\partial \theta^2} &= \begin{pmatrix} (r'' \sin \theta + 2r' \cos \theta - r \sin \theta) \cos \varphi \\ (r'' \sin \theta + 2r' \cos \theta - r \sin \theta) \sin \varphi \\ r'' \cos \theta - 2r' \sin \theta - r \cos \theta \end{pmatrix}, \\ \frac{\partial^2 \vec{X}}{\partial \varphi^2} &= \begin{pmatrix} -r \sin \theta \cos \varphi \\ -r \sin \theta \sin \varphi \\ 0 \end{pmatrix}, & \frac{\partial \vec{X}}{\partial \theta} \times \frac{\partial \vec{X}}{\partial \varphi} &= \begin{pmatrix} (-r' \cos \theta + r \sin \theta) r \sin \theta \cos \varphi \\ -(r' \cos \theta - r \sin \theta) r \sin \theta \sin \varphi \\ (r' \sin \theta + r \cos \theta) r \sin \theta \end{pmatrix}. \end{aligned} \quad (\text{B.213})$$

So that the norm  $\left\| \frac{\partial \vec{X}}{\partial \theta} \times \frac{\partial \vec{X}}{\partial \varphi} \right\|$  is obtained by

$$\left\| \frac{\partial \vec{X}}{\partial \theta} \times \frac{\partial \vec{X}}{\partial \varphi} \right\| = r \sin \theta \left[ (r' \cos \theta - r \sin \theta)^2 + (r' \sin \theta + r \cos \theta)^2 \right]^{1/2}, \quad (\text{B.214})$$

$$\begin{aligned} &= r \sin \theta \left[ r'^2 \cos^2 \theta - 2r'r \sin \theta \cos \theta + r^2 \sin^2 \theta \right. \\ &\quad \left. + r'^2 \sin^2 \theta + 2r'r \sin \theta \cos \theta + r^2 \cos^2 \theta \right]^{1/2}, \end{aligned} \quad (\text{B.215})$$

$$= r \sin \theta \left[ r'^2 + r^2 \right]^{1/2}. \quad (\text{B.216})$$

Therefore the normalized vector  $\vec{n}$  orthonormal to the surface at the point  $\vec{X}$  is given by

$$\vec{n} = \frac{\frac{\partial \vec{X}}{\partial \theta} \times \frac{\partial \vec{X}}{\partial \varphi}}{\left\| \frac{\partial \vec{X}}{\partial \theta} \times \frac{\partial \vec{X}}{\partial \varphi} \right\|} = \frac{1}{\sqrt{r^2 + r'^2}} \begin{pmatrix} (r \sin \theta - r' \cos \theta) \cos \varphi \\ (r \sin \theta - r' \cos \theta) \sin \varphi \\ r' \sin \theta + r \cos \theta \end{pmatrix}. \quad (\text{B.217})$$

The first fundamental form is defined as

$$\mathbf{I} = \begin{bmatrix} E & F \\ F & G \end{bmatrix}, \quad (\text{B.218})$$

where

$$E = \frac{\partial \vec{X}}{\partial \theta} \cdot \frac{\partial \vec{X}}{\partial \theta} = (r' \sin \theta + r \cos \theta)^2 + (r' \cos \theta - r \sin \theta)^2, \quad (\text{B.219})$$

$$= r'^2 \sin^2 \theta + 2r'r \sin \theta \cos \theta + r^2 \cos^2 \theta + r'^2 \cos^2 \theta - 2r'r \cos \theta \sin \theta + r^2 \sin^2 \theta, \quad (\text{B.220})$$

$$= r'^2 + r^2, \quad (\text{B.221})$$

$$F = \frac{\partial \vec{X}}{\partial \theta} \cdot \frac{\partial \vec{X}}{\partial \varphi} = 0, \quad (\text{B.222})$$

$$G = \frac{\partial \vec{X}}{\partial \varphi} \cdot \frac{\partial \vec{X}}{\partial \varphi} = r^2 \sin^2 \theta. \quad (\text{B.223})$$

The second fundamental form is defined as

$$\mathbf{II} = \begin{bmatrix} L & M \\ M & N \end{bmatrix}, \quad (\text{B.224})$$

where

$$L = \frac{\partial^2 \vec{X}}{\partial \theta^2} \cdot \vec{n} = \sqrt{r^2 + r'^2} [(r \sin \theta - r' \cos \theta)(r'' \sin \theta + 2r' \cos \theta - r \sin \theta) + (r' \sin \theta + r \cos \theta)(r'' \cos \theta - 2r' \sin \theta - r \cos \theta)], \quad (\text{B.225})$$

$$= \sqrt{r^2 + r'^2} [rr'' \sin^2 \theta + 2r'r \sin \theta \cos \theta - r^2 \sin^2 \theta - r'r'' \sin \theta \cos \theta - 2r'^2 \cos^2 \theta + r'r \cos \theta \sin \theta + r'r'' \sin \theta \cos \theta - 2r'^2 \sin^2 \theta - r'r \sin \theta \cos \theta + rr'' \cos^2 \theta - 2rr' \sin \theta \cos \theta - r^2 \cos^2 \theta], \quad (\text{B.226})$$

$$= \sqrt{r^2 + r'^2} [-r^2 - 2r'^2 + rr''], \quad (\text{B.227})$$

$$M = \frac{\partial^2 \vec{X}}{\partial \theta \partial \varphi} \cdot \vec{n} = \sqrt{r^2 + r'^2} [-(r' \sin \theta + r \cos \theta)(r \sin \theta - r' \cos \theta) \cos \varphi \sin \varphi + (r' \sin \theta + r \cos \theta)(r \sin \theta - r' \cos \theta) \sin \varphi \cos \varphi], \quad (\text{B.228})$$

$$N = \frac{\partial^2 \vec{X}}{\partial \varphi^2} \cdot \vec{n} = \sqrt{r^2 + r'^2} [r \sin \theta - r' \cos \theta](-r \sin \theta). \quad (\text{B.229})$$

The shape operator  $S$  is defined by

$$S = \mathbf{I}^{-1} \mathbf{II} = \frac{1}{EG - F^2} \begin{bmatrix} LG - FM & GM - FN \\ ME - FL & EN - FM \end{bmatrix}. \quad (\text{B.230})$$

It can be expressed as

$$S = \frac{1}{r^2 \sin^2 \theta (r^2 + r'^2)} \times \begin{bmatrix} r^2 \sin^2 \theta [r^2 + r'^2]^{-1/2} [-r^2 - 2r'^2 + rr''] & 0 \\ 0 & -\sqrt{r^2 + r'^2} r \sin \theta [r \sin \theta - r' \cos \theta] \end{bmatrix}. \quad (\text{B.231})$$

The principal curvatures  $k_1$  and  $k_2$  are the eigenvalues of the shape operator, and given by

$$k_1 = [r^2 + r'^2]^{-3/2} [rr'' - 2r'^2 - r^2] \quad \text{and} \quad k_2 = -[r^2 + r'^2]^{-1/2} \left[ 1 - \frac{r' \cos \theta}{r \sin \theta} \right]. \quad (\text{B.232})$$

The shape operator is diagonal in the chosen parameterization. It can be deduced that the directions generated by the derivation of  $\vec{X}$  with respect to these parameters are the principal directions. As for the  $\rho(z)$ -parameterization, the definition of the principal curvatures was also verified on a practical example shown in Fig. B.13 for the  $r(\theta)$ -parameterization. It was possible to verify that given a point on the surface (yellow dot on the figure), the normal vector is properly calculated (black line) and the two circles in red and cyan are properly tangent to the surface at the chosen point.

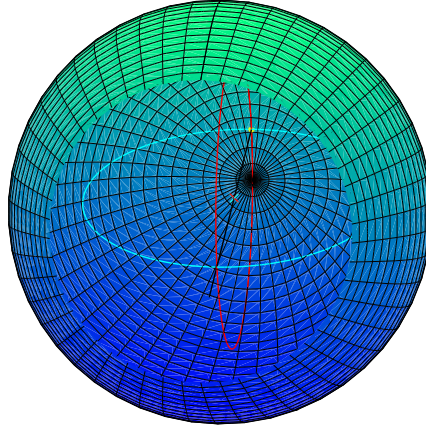


Figure B.13 – Example of verification of the calculation of the principal radii of curvature for a  $r(\theta)$ -defined shape, here a perturbed-spheroid shape.





# Appendix C

## Matrix Elements of the Single Particle Hamiltonian

*This appendix details how to calculate matrix elements involved in the single-particle model presented in Chapter 5. The following explanations are a detailed version of expressions given in Refs.<sup>1</sup> [117, 131].*

### Contents

---

<b>C.1 Wave-Functions Basis</b> $ n_r n_z \Lambda \Sigma\rangle$ . . . . .	<b>210</b>
<b>C.2 Kinetic Matrix Element</b> $\langle \Psi_f   \hat{T}   \Psi_i \rangle$ . . . . .	<b>210</b>
C.2.1 Kinetic Operators . . . . .	210
C.2.2 $\xi$ -Diagonal Matrix Element $\langle \Psi_{n'_z}   \hat{T}_\xi   \Psi_{n_z} \rangle$ . . . . .	211
C.2.3 $\eta$ -Diagonal Matrix Element $\langle \Psi_{n'_r}^\Lambda   \hat{T}_{\Lambda\eta}   \Psi_{n_r}^\Lambda \rangle$ . . . . .	213
C.2.4 General Kinetic Matrix Element . . . . .	215
<b>C.3 Scalar Potential Matrix Element</b> $\langle \Psi_f   \hat{V}_{C+N}   \Psi_i \rangle$ . . . . .	<b>216</b>
<b>C.4 Spin-Orbit Coupling Matrix Element</b> $\langle \Psi_f   \hat{V}_{s.o.}   \Psi_i \rangle$ . . . . .	<b>216</b>
C.4.1 Diagonal Spin-Orbit Matrix Element ( $\Sigma' = \Sigma$ ) . . . . .	217
C.4.2 Cross Spin-Orbit Matrix Element ( $\Sigma' = -\Sigma$ ) . . . . .	219

---

---

<sup>1</sup>Reference [130] corrects misprints of Ref. [131].

## C.1 Wave-Functions Basis $|n_r n_z \Lambda \Sigma\rangle$

In the cylindrical coordinate system  $(\rho, \varphi, z)$  defined in Fig. 5.4, the basis wave functions used in the expansion method are the deformed harmonic oscillator eigenfunction (*cf.* Eq. 5.58) defined as

$$|n_r n_z \Lambda \Sigma\rangle = \Psi(n_r, n_z, \Lambda, \Sigma) = \Psi_{n_r}^\Lambda(\rho) \Psi_{n_z}(z) \Psi_\Lambda(\varphi) \chi(\Sigma), \quad (\text{C.1})$$

where

$$\Psi_\Lambda(\varphi) = \frac{1}{\sqrt{2\pi}} e^{i\Lambda\varphi}, \quad (\text{C.2})$$

$$\Psi_{n_z}(z) = N_{n_z} \left[ \frac{m\omega_z}{\hbar} \right]^{\frac{1}{4}} e^{-\frac{\xi^2}{2}} H_{n_z}(\xi), \quad (\text{C.3})$$

$$\Psi_{n_r}^\Lambda(\rho) = N_{n_r}^{|\Lambda|} \left[ \frac{2m\omega_\perp}{\hbar} \right]^{\frac{1}{2}} \eta^{\frac{|\Lambda|}{2}} e^{-\frac{\eta}{2}} L_{n_r}^{|\Lambda|}(\eta), \quad (\text{C.4})$$

where  $H_{n_z}$  and  $L_{n_r}^{|\Lambda|}$  are respectively the Hermite and associated Laguerre polynomials [48],  $\eta$  and  $\xi$  are the reduced coordinates, and  $N_{n_z}$  and  $N_{n_r}^\Lambda$  are normalization factors defined by

$$\begin{aligned} \eta^{\frac{1}{2}} &= \sqrt{\frac{m\omega_\perp}{\hbar}} \rho, & \xi &= \sqrt{\frac{m\omega_z}{\hbar}} z, \\ N_{n_z} &= \frac{1}{\sqrt{\sqrt{\pi} 2^{n_z} n_z!}}}, & N_{n_r}^\Lambda &= \sqrt{\frac{n_r!}{(n_r + \Lambda)!}}. \end{aligned} \quad (\text{C.5})$$

Only the functions where  $\Lambda \geq 0$  are kept. The corresponding negative states having negative values of  $\Lambda$  can be obtained using Eqs. 5.70 and 5.71. The Pauli spin matrices lead to using the vector representation for the intrinsic spin function  $\chi(\Sigma)$

$$\chi(\Sigma = +\frac{1}{2}) = \begin{pmatrix} 1 \\ 0 \end{pmatrix}, \quad \chi(\Sigma = -\frac{1}{2}) = \begin{pmatrix} 0 \\ 1 \end{pmatrix}. \quad (\text{C.6})$$

## C.2 Kinetic Matrix Element $\langle \Psi_f | \hat{T} | \Psi_i \rangle$

### C.2.1 Kinetic Operators

The kinetic operator  $\hat{T}$  related to the nucleon motion is

$$\hat{T} = -\frac{\hbar^2}{2m} \Delta, \quad (\text{C.7})$$

which can be expressed in the cylindrical coordinate system as

$$\hat{T} = -\frac{\hbar^2}{2m} \left( \frac{1}{\rho} \frac{\partial}{\partial \rho} \left( \rho \frac{\partial}{\partial \rho} \right) + \frac{1}{\rho^2} \frac{\partial^2}{\partial \varphi^2} + \frac{\partial^2}{\partial z^2} \right). \quad (\text{C.8})$$

Using the variable changes  $\rho \rightarrow \eta$  and  $z \rightarrow \xi$  one gets

$$\hat{T} = -\frac{\hbar^2}{2m} \frac{m\omega_\perp}{\hbar} \left( \frac{1}{\eta^{\frac{1}{2}}} \frac{\partial}{\partial \eta^{\frac{1}{2}}} \left( \eta^{\frac{1}{2}} \frac{\partial}{\partial \eta^{\frac{1}{2}}} \right) + \frac{1}{\eta} \frac{\partial^2}{\partial \varphi^2} \right) - \frac{\hbar^2}{2m} \frac{m\omega_z}{\hbar} \left( \frac{\partial^2}{\partial \xi^2} \right), \quad (\text{C.9})$$

$$= -\frac{1}{2} \hbar \omega_\perp \left( \frac{1}{\eta^{\frac{1}{2}}} \frac{\partial}{\partial \eta^{\frac{1}{2}}} \left( \eta^{\frac{1}{2}} \frac{\partial}{\partial \eta^{\frac{1}{2}}} \right) + \frac{1}{\eta} \frac{\partial^2}{\partial \varphi^2} \right) - \frac{1}{2} \hbar \omega_z \frac{\partial^2}{\partial \xi^2}. \quad (\text{C.10})$$

In the following the convention  $\Psi_i = |n_r n_z \Lambda \Sigma\rangle$  and  $\Psi_f = \langle n'_r n'_z \Lambda' \Sigma' |$  will be used. The  $\Sigma$ -independence of  $\hat{T}$  makes the matrix elements  $\langle \Psi_f | \hat{T} | \Psi_i \rangle$  diagonal in  $\Sigma$ . The integration over  $\varphi$  is straightforward and leads to diagonal matrix elements in  $\Lambda$  with a partially integrated kinetic operator  $\hat{T}_\Lambda$  defined by

$$\hat{T}_\Lambda = -\frac{1}{2}\hbar\omega_\perp \left( \frac{1}{\eta^{\frac{1}{2}}} \frac{\partial}{\partial \eta^{\frac{1}{2}}} \left( \eta^{\frac{1}{2}} \frac{\partial}{\partial \eta^{\frac{1}{2}}} \right) - \frac{\Lambda^2}{\eta} \right) - \frac{1}{2}\hbar\omega_z \frac{\partial^2}{\partial \xi^2}. \quad (\text{C.11})$$

Therefore the kinetic matrix elements can be written

$$\langle \Psi_f | \hat{T} | \Psi_i \rangle = \delta_{\Sigma\Sigma'} \delta_{\Lambda\Lambda'} \langle \Psi_{n'_z} \Psi_{n'_r}^{\Lambda'} | \hat{T}_\Lambda | \Psi_{n_z} \Psi_{n_r}^\Lambda \rangle. \quad (\text{C.12})$$

Because  $\Psi_{n'_z}$  and  $\Psi_{n_z}$  on one side, and  $\Psi_{n'_r}^\Lambda$  and  $\Psi_{n_r}^\Lambda$  on the other side, are orthonormal, the matrix elements can be split into two diagonal parts:

$$\langle \Psi_f | \hat{T} | \Psi_i \rangle = \delta_{\Sigma\Sigma'} \delta_{\Lambda\Lambda'} \delta_{n_r n'_r} \langle \Psi_{n'_z} | \hat{T}_\xi | \Psi_{n_z} \rangle + \delta_{\Sigma\Sigma'} \delta_{\Lambda\Lambda'} \delta_{n_z n'_z} \langle \Psi_{n'_r}^{\Lambda'} | \hat{T}_{\Lambda\eta} | \Psi_{n_r}^\Lambda \rangle, \quad (\text{C.13})$$

where  $\hat{T}_\xi$  and  $\hat{T}_{\Lambda\eta}$  are defined by

$$\hat{T}_\xi = -\frac{1}{2}\hbar\omega_z \frac{d^2}{d\xi^2} \quad \text{and} \quad \hat{T}_{\Lambda\eta} = -\frac{1}{2}\hbar\omega_\perp \left( \frac{1}{\eta^{\frac{1}{2}}} \frac{d}{d\eta^{\frac{1}{2}}} \left( \eta^{\frac{1}{2}} \frac{d}{d\eta^{\frac{1}{2}}} \right) - \frac{\Lambda^2}{\eta} \right). \quad (\text{C.14})$$

### C.2.2 $\xi$ -Diagonal Matrix Element $\langle \Psi_{n'_z} | \hat{T}_\xi | \Psi_{n_z} \rangle$

The matrix element related to the  $\hat{T}_\xi$  operator is given by

$$\langle \Psi_{n'_z} | \hat{T}_\xi | \Psi_{n_z} \rangle = -\frac{1}{2}\hbar\omega_z \int_{-\infty}^{+\infty} dz \Psi_{n'_z} \frac{d^2}{dz^2} \Psi_{n_z}. \quad (\text{C.15})$$

By change of the integration variable ( $z \rightarrow \xi$ ), one obtains

$$\langle \Psi_{n'_z} | \hat{T}_\xi | \Psi_{n_z} \rangle = -\frac{1}{2}\hbar\omega_z \left( \frac{m\omega_z}{\hbar} \right)^{-1/2} \int_{-\infty}^{+\infty} d\xi \Psi_{n'_z} \frac{d^2}{d\xi^2} \Psi_{n_z}. \quad (\text{C.16})$$

Replacing  $\Psi_{n_z}$  and  $\Psi_{n'_z}$  by their expressions (cf. Eq. C.3) in Eq. C.16 it yields

$$\langle \Psi_{n'_z} | \hat{T}_\xi | \Psi_{n_z} \rangle = -\frac{1}{2}\hbar\omega_z \left( \frac{m\omega_z}{\hbar} \right)^{-1/2} \int_{-\infty}^{+\infty} d\xi \Psi_{n'_z} \frac{d^2}{d\xi^2} \Psi_{n_z}, \quad (\text{C.17})$$

$$= -\frac{1}{2}\hbar\omega_z \left( \frac{m\omega_z}{\hbar} \right)^{-1/2} \int_{-\infty}^{+\infty} d\xi N_{n'_z} \left[ \frac{m\omega_z}{\hbar} \right]^{\frac{1}{4}} e^{-\frac{\xi^2}{2}} H_{n'_z} \frac{d^2}{d\xi^2} N_{n_z} \left[ \frac{m\omega_z}{\hbar} \right]^{\frac{1}{4}} e^{-\frac{\xi^2}{2}} H_{n_z}, \quad (\text{C.18})$$

$$= -\frac{1}{2}\hbar\omega_z N_{n_z} N_{n'_z} \int_{-\infty}^{+\infty} d\xi e^{-\frac{\xi^2}{2}} H_{n'_z} \frac{d^2}{d\xi^2} e^{-\frac{\xi^2}{2}} H_{n_z}, \quad (\text{C.19})$$

$$= -\frac{1}{2}\hbar\omega_z N_{n_z} N_{n'_z} \int_{-\infty}^{+\infty} d\xi e^{-\frac{\xi^2}{2}} H_{n'_z} \frac{d}{d\xi} \left( -\xi e^{-\frac{\xi^2}{2}} H_{n_z} + e^{-\frac{\xi^2}{2}} \frac{dH_{n_z}}{d\xi} \right), \quad (\text{C.20})$$

$$= -\frac{1}{2} \hbar \omega_z N_{n_z} N_{n'_z} \int_{-\infty}^{+\infty} d\xi e^{-\xi^2} H_{n'_z} \left( -H_{n_z} - \xi \frac{dH_{n_z}}{d\xi} + \xi^2 H_{n_z} - \xi \frac{dH_{n_z}}{d\xi} + \frac{d^2 H_{n_z}}{d\xi^2} \right), \quad (\text{C.21})$$

$$= \frac{1}{2} \hbar \omega_z N_{n_z} N_{n'_z} \int_{-\infty}^{+\infty} d\xi e^{-\xi^2} H_{n'_z} \left( H_{n_z} + 2\xi \frac{dH_{n_z}}{d\xi} - \xi^2 H_{n_z} - \frac{d^2 H_{n_z}}{d\xi^2} \right). \quad (\text{C.22})$$

The Hermite polynomials satisfy the differential equation (*cf.* Ref. [183])

$$\frac{d^2 H_{n_z}}{d\xi^2} = 2\xi \frac{dH_{n_z}}{d\xi} - 2n_z H_{n_z}. \quad (\text{C.23})$$

Equation C.23 can be used into Eq. C.22, so that derivatives vanish

$$\begin{aligned} \langle \Psi_{n'_z} | \hat{T}_\xi | \Psi_{n_z} \rangle &= \frac{1}{2} \hbar \omega_z N_{n_z} N_{n'_z} \int_{-\infty}^{+\infty} d\xi e^{-\xi^2} H_{n'_z} \left( H_{n_z} + 2\xi \frac{dH_{n_z}}{d\xi} - \xi^2 H_{n_z} - 2\xi \frac{dH_{n_z}}{d\xi} + 2n_z H_{n_z} \right), \\ & \quad (\text{C.24}) \end{aligned}$$

$$= \frac{1}{2} \hbar \omega_z N_{n_z} N_{n'_z} \int_{-\infty}^{+\infty} d\xi e^{-\xi^2} H_{n'_z} \left( (1 + 2n_z) H_{n_z} - \xi^2 H_{n_z} \right). \quad (\text{C.25})$$

The Hermite polynomials also satisfy the recurrence relation (*cf.* Ref. [183])

$$\xi H_{n_z} = \frac{1}{2} H_{n_z+1} + n_z H_{n_z-1} \quad (\text{C.26})$$

The recurrence relation (Eq. C.26) can be used into Eq. C.25, so that terms containing  $\xi$  vanish

$$\begin{aligned} \langle \Psi_{n'_z} | \hat{T}_\xi | \Psi_{n_z} \rangle &= \frac{1}{2} \hbar \omega_z N_{n_z} N_{n'_z} \int_{-\infty}^{+\infty} d\xi e^{-\xi^2} H_{n'_z} \left( (1 + 2n_z) H_{n_z} - \xi \left( \frac{1}{2} H_{n_z+1} + n_z H_{n_z-1} \right) \right), \\ & \quad (\text{C.27}) \end{aligned}$$

$$\begin{aligned} &= \frac{1}{2} \hbar \omega_z N_{n_z} N_{n'_z} \int_{-\infty}^{+\infty} d\xi e^{-\xi^2} H_{n'_z} \\ & \quad \times \left( (1 + 2n_z) H_{n_z} - \frac{1}{2} \left( \frac{1}{2} H_{n_z+2} + (n_z + 1) H_{n_z} \right) - n_z \left( \frac{1}{2} H_{n_z} + (n_z - 1) H_{n_z-2} \right) \right), \\ & \quad (\text{C.28}) \end{aligned}$$

$$\begin{aligned} &= \frac{1}{2} \hbar \omega_z N_{n_z} N_{n'_z} \int_{-\infty}^{+\infty} d\xi e^{-\xi^2} H_{n'_z} \\ & \quad \times \left( (1 + 2n_z - \frac{n_z}{2} - \frac{1}{2} - \frac{n_z}{2}) H_{n_z} - \frac{1}{4} H_{n_z+2} - n_z (n_z - 1) H_{n_z-2} \right), \\ & \quad (\text{C.29}) \end{aligned}$$

$$= \frac{1}{2} \hbar \omega_z N_{n_z} N_{n'_z} \int_{-\infty}^{+\infty} d\xi e^{-\xi^2} H_{n'_z} \left( \left( \frac{1}{2} + n_z \right) H_{n_z} - \frac{1}{4} H_{n_z+2} - n_z (n_z - 1) H_{n_z-2} \right). \quad (\text{C.30})$$

Due to the orthogonality property Hermite polynomials (with weight  $e^{-\xi^2}$ ), the matrix element  $\langle \Psi_{n'_z} | \hat{T}_\xi | \Psi_{n_z} \rangle$  has non-zero value only for few values of  $n'_z$  and  $n_z$ , namely

$$\begin{aligned} n'_z &= n_z, \\ n'_z &= n_z + 2, \\ n'_z &= n_z - 2. \end{aligned} \quad (\text{C.31})$$

Using that the normalization  $\int_{-\infty}^{+\infty} d\xi e^{-\xi^2} H_{n_z}^2 = \sqrt{\pi} 2^{n_z} n_z!$  and the definition of  $N_{n_z}$  (cf. Eq. C.5), the matrix elements  $\langle \Psi_{n'_z} | \hat{T}_\xi | \Psi_{n_z} \rangle$  can be expressed as

$$\langle \Psi_{n_z} | \hat{T}_\xi | \Psi_{n_z} \rangle = \frac{1}{2} \hbar \omega_z N_{n_z}^2 \left( \frac{1}{2} + n_z \right) \int_{-\infty}^{+\infty} d\xi e^{-\xi^2} H_{n_z}^2 = \frac{1}{2} \hbar \omega_z \left( \frac{1}{2} + n_z \right), \quad (\text{C.32})$$

$$\langle \Psi_{n_z+2} | \hat{T}_\xi | \Psi_{n_z} \rangle = -\frac{1}{8} \hbar \omega_z N_{n_z} N_{n_z+2} \sqrt{\pi} 2^{n_z+2} (n_z + 2)!, \quad (\text{C.33})$$

$$= -\frac{1}{8} \hbar \omega_z \sqrt{\frac{2^{n_z+2} (n_z + 2)!}{2^{n_z} n_z!}}, \quad (\text{C.34})$$

$$= -\frac{1}{4} \hbar \omega_z \sqrt{(n_z + 2)(n_z + 1)}, \quad (\text{C.35})$$

$$\langle \Psi_{n_z+2} | \hat{T}_\xi | \Psi_{n_z} \rangle = -\frac{1}{2} \hbar \omega_z N_{n_z} N_{n_z-2} n_z (n_z - 1) \sqrt{\pi} 2^{n_z-2} (n_z - 2)!, \quad (\text{C.36})$$

$$= -\frac{1}{2} \hbar \omega_z n_z (n_z - 1) \sqrt{\frac{2^{n_z-2} (n_z - 2)!}{2^{n_z} n_z!}}, \quad (\text{C.37})$$

$$= -\frac{1}{4} \hbar \omega_z \sqrt{n_z (n_z - 1)}. \quad (\text{C.38})$$

### C.2.3 $\eta$ -Diagonal Matrix Element $\langle \Psi_{n'_r}^\Lambda | \hat{T}_{\Lambda\eta} | \Psi_{n_r}^\Lambda \rangle$

The matrix element related to the  $\hat{T}_{\Lambda\eta}$  operator is given by

$$\langle \Psi_{n'_r}^\Lambda | \hat{T}_{\Lambda\eta} | \Psi_{n_r}^\Lambda \rangle = -\frac{1}{2} \hbar \omega_\perp \int_0^{+\infty} \rho d\rho \Psi_{n'_r}^\Lambda \left( \frac{1}{\eta^{\frac{1}{2}}} \frac{d}{d\eta^{\frac{1}{2}}} \left( \eta^{\frac{1}{2}} \frac{d}{d\eta^{\frac{1}{2}}} \right) - \frac{\Lambda^2}{\eta} \right) \Psi_{n_r}^\Lambda. \quad (\text{C.39})$$

Using the variable change  $\rho \rightarrow \eta$  (cf. Eq. C.5), the integration element  $d\rho$  is replaced by  $d\eta$  according to

$$\rho d\rho = \frac{1}{2} d(\rho^2) = \frac{\hbar}{2m\omega_\perp} d\eta. \quad (\text{C.40})$$

The derivative operators are also modified according to

$$\frac{d}{d\eta^{\frac{1}{2}}} = 2\eta^{\frac{1}{2}} \frac{d}{d\eta}, \quad (\text{C.41})$$

so that Eq. C.39 becomes

$$\langle \Psi_{n'_r}^\Lambda | \hat{T}_{\Lambda\eta} | \Psi_{n_r}^\Lambda \rangle = -\frac{1}{2} \hbar \omega_\perp \frac{\hbar}{2m\omega_\perp} \int_0^{+\infty} d\eta \Psi_{n'_r}^\Lambda \left( 4 \frac{d}{d\eta} \left( \eta \frac{d}{d\eta} \right) - \frac{\Lambda^2}{\eta} \right) \Psi_{n_r}^\Lambda, \quad (\text{C.42})$$

$$= -\frac{1}{2}\hbar\omega_{\perp}\frac{\hbar}{2m\omega_{\perp}}\int_0^{+\infty}d\eta\Psi_{n'_r}^{\Lambda}\left(4\left(\frac{d}{d\eta}+\eta\frac{d^2}{d\eta^2}\right)-\frac{\Lambda^2}{\eta}\right)\Psi_{n_r}^{\Lambda}. \quad (C.43)$$

Replacing  $\Psi_{n'_r}^{\Lambda}$  and  $\Psi_{n_r}^{\Lambda}$  by their expressions (cf. Eq. C.4) in Eq. C.43, one obtains

$$\langle \Psi_{n'_r}^{\Lambda} | \hat{T}_{\Lambda\eta} | \Psi_{n_r}^{\Lambda} \rangle = -\frac{1}{2}\hbar\omega_{\perp}\frac{\hbar}{2m\omega_{\perp}}\int_0^{+\infty}d\eta N_{n'_r}^{\Lambda}\left[\frac{2m\omega_{\perp}}{\hbar}\right]^{\frac{1}{2}}\eta^{\frac{\Lambda}{2}}e^{-\frac{\eta}{2}}L_{n'_r}^{\Lambda} \quad (C.44)$$

$$\begin{aligned} &\times \left(4\left(\frac{d}{d\eta}+\eta\frac{d^2}{d\eta^2}\right)-\frac{\Lambda^2}{\eta}\right)N_{n_r}^{\Lambda}\left[\frac{2m\omega_{\perp}}{\hbar}\right]^{\frac{1}{2}}\eta^{\frac{\Lambda}{2}}e^{-\frac{\eta}{2}}L_{n_r}^{\Lambda}, \\ &= -\frac{1}{2}\hbar\omega_{\perp}N_{n_r}^{\Lambda}N_{n'_r}^{\Lambda}\int_0^{+\infty}d\eta\eta^{\frac{\Lambda}{2}}e^{-\frac{\eta}{2}}L_{n'_r}^{\Lambda}\left(4\left(\frac{d}{d\eta}+\eta\frac{d^2}{d\eta^2}\right)-\frac{\Lambda^2}{\eta}\right)\eta^{\frac{\Lambda}{2}}e^{-\frac{\eta}{2}}L_{n_r}^{\Lambda}. \end{aligned} \quad (C.45)$$

The function  $\eta^{\frac{\Lambda}{2}}e^{-\frac{\eta}{2}}L_{n_r}^{\Lambda}$  satisfies the differential equation (cf. Ref. [183])

$$\frac{du}{d\eta}+\eta\frac{d^2u}{d\eta^2}=-\left(\Lambda-2\frac{\Lambda}{2}\right)\frac{du}{d\eta}-\left[n_r+\frac{\Lambda+1}{2}-\frac{\eta}{4}+\frac{\frac{\Lambda}{2}(\frac{\Lambda}{2}-\Lambda)}{\eta}\right]u, \quad (C.46)$$

$$=-\left[n_r+\frac{\Lambda+1}{2}-\frac{\eta}{4}-\frac{\Lambda^2}{4\eta}\right]u. \quad (C.47)$$

Using Eq. C.45 into Eq. C.45 makes the differential operators vanish. Equation C.45 becomes

$$\begin{aligned} &\langle \Psi_{n'_r}^{\Lambda} | \hat{T}_{\Lambda\eta} | \Psi_{n_r}^{\Lambda} \rangle \\ &= -\frac{1}{2}\hbar\omega_{\perp}N_{n_r}^{\Lambda}N_{n'_r}^{\Lambda}\int_0^{+\infty}d\eta\eta^{\frac{\Lambda}{2}}e^{-\frac{\eta}{2}}L_{n'_r}^{\Lambda}\left(-4\left[n_r+\frac{\Lambda+1}{2}-\frac{\eta}{4}-\frac{\Lambda^2}{4\eta}\right]-\frac{\Lambda^2}{\eta}\right)\eta^{\frac{\Lambda}{2}}e^{-\frac{\eta}{2}}L_{n_r}^{\Lambda}, \end{aligned} \quad (C.48)$$

$$= \frac{1}{2}\hbar\omega_{\perp}N_{n_r}^{\Lambda}N_{n'_r}^{\Lambda}\int_0^{+\infty}d\eta\eta^{\Lambda}e^{-\eta}L_{n'_r}^{\Lambda}([4n_r+2(\Lambda+1)]L_{n_r}^{\Lambda}-\eta L_{n_r}^{\Lambda}). \quad (C.49)$$

The associated Laguerre polynomials satisfy the recurrence relation (cf. Ref. [183])

$$\eta L_{n_r}^{\Lambda}=(2n_r+\Lambda+1)L_{n_r}^{\Lambda}-(n_r+1)L_{n_r+1}^{\Lambda}-(n_r+\Lambda)L_{n_r-1}^{\Lambda}. \quad (C.50)$$

So that the recurrence relation (Eq. C.50) can be used into Eq. C.49 so that the term in factor of  $\eta$  vanishes. It yields

$$\langle \Psi_{n'_r}^{\Lambda} | \hat{T}_{\Lambda\eta} | \Psi_{n_r}^{\Lambda} \rangle = \frac{1}{2}\hbar\omega_{\perp}N_{n_r}^{\Lambda}N_{n'_r}^{\Lambda}\int_0^{+\infty}d\eta\eta^{\Lambda}e^{-\eta}L_{n'_r}^{\Lambda}([4n_r+2(\Lambda+1)]L_{n_r}^{\Lambda} \quad (C.51)$$

$$\begin{aligned} &-(2n_r+\Lambda+1)L_{n_r}^{\Lambda}+(n_r+1)L_{n_r+1}^{\Lambda}+(n_r+\Lambda)L_{n_r-1}^{\Lambda}), \\ &= \frac{1}{2}\hbar\omega_{\perp}N_{n_r}^{\Lambda}N_{n'_r}^{\Lambda}\int_0^{+\infty}d\eta\eta^{\Lambda}e^{-\eta}L_{n'_r}^{\Lambda} \\ &\times ([2n_r+\Lambda+1]L_{n_r}^{\Lambda}+(n_r+1)L_{n_r+1}^{\Lambda}+(n_r+\Lambda)L_{n_r-1}^{\Lambda}). \end{aligned} \quad (C.52)$$

Due to the orthogonality property of the associated Laguerre polynomials (with weight  $\eta^\Lambda e^{-\eta}$ ), the matrix element  $\langle \Psi_{n'_r}^\Lambda | \hat{T}_{\Lambda\eta} | \Psi_{n_r}^\Lambda \rangle$  has non-zero value only for few values of  $n'_r$  and  $n_r$ , namely

$$\begin{aligned} n'_r &= n_r, \\ n'_r &= n_r + 1, \\ n'_r &= n_r - 1. \end{aligned} \quad (C.53)$$

Using that  $\int_{-\infty}^{+\infty} d\xi e^{-\eta} \eta^\Lambda (L_{n_r}^\Lambda)^2 = \frac{(n_r + \Lambda)!}{n_r!}$  and the definition of  $N_{n_r}^\Lambda$  (cf. Eq. C.5) the matrix elements  $\langle \Psi_{n'_r}^\Lambda | \hat{T}_{\Lambda\eta} | \Psi_{n_r}^\Lambda \rangle$  can be expressed as

$$\langle \Psi_{n_r}^\Lambda | \hat{T}_{\Lambda\eta} | \Psi_{n_r}^\Lambda \rangle = \frac{1}{2} \hbar \omega_\perp (N_{n_r}^\Lambda)^2 (2n_r + \Lambda + 1) \int_0^{+\infty} d\eta \eta^\Lambda e^{-\eta} (L_{n_r}^\Lambda)^2, \quad (C.54)$$

$$= \frac{1}{2} \hbar \omega_\perp (2n_r + \Lambda + 1), \quad (C.55)$$

$$\langle \Psi_{n_r+1}^\Lambda | \hat{T}_{\Lambda\eta} | \Psi_{n_r}^\Lambda \rangle = \frac{1}{2} \hbar \omega_\perp N_{n_r}^\Lambda N_{n_r+1}^\Lambda (n_r + 1) \frac{(n_r + 1 + \Lambda)!}{(n_r + 1)!}, \quad (C.56)$$

$$= \frac{1}{2} \hbar \omega_\perp (n_r + 1) \sqrt{\frac{(n_r + 1 + \Lambda)!}{(n_r + 1)!} \frac{n_r!}{(n_r + \Lambda)!}}, \quad (C.57)$$

$$= \frac{1}{2} \hbar \omega_\perp \sqrt{(n_r + 1)(n_r + 1 + \Lambda)}, \quad (C.58)$$

$$\langle \Psi_{n_r-1}^\Lambda | \hat{T}_{\Lambda\eta} | \Psi_{n_r}^\Lambda \rangle = \frac{1}{2} \hbar \omega_\perp N_{n_r}^\Lambda N_{n_r-1}^\Lambda (n_r + \Lambda) \frac{(n_r - 1 + \Lambda)!}{(n_r - 1)!}, \quad (C.59)$$

$$= \frac{1}{2} \hbar \omega_\perp (n_r + \Lambda) \sqrt{\frac{(n_r - 1 + \Lambda)!}{(n_r - 1)!} \frac{n_r!}{(n_r + \Lambda)!}}, \quad (C.60)$$

$$= \frac{1}{2} \hbar \omega_\perp \sqrt{n_r(n_r + \Lambda)}. \quad (C.61)$$

## C.2.4 General Kinetic Matrix Element

Using Eqs. C.38 and C.61, the general kinetic matrix element  $\langle \Psi_f | \hat{T} | \Psi_i \rangle$  can be expressed as

$$\begin{aligned} \langle \Psi_f | \hat{T} | \Psi_i \rangle &= \delta_{\Sigma\Sigma'} \delta_{\Lambda\Lambda'} \left[ \delta_{n_r n'_r} \frac{\hbar \omega_z}{4} \left( \delta_{n_z n'_z} (2n_z + 1) \right. \right. \\ &\quad \left. \left. - \delta_{n_z+2, n'_z} \sqrt{(n_z + 2)(n_z + 1)} \right. \right. \\ &\quad \left. \left. - \delta_{n_z-2, n'_z} \sqrt{n_z(n_z - 1)} \right) \right. \\ &\quad \left. + \delta_{n_z n'_z} \frac{\hbar \omega_\perp}{2} \left( \delta_{n_r n'_r} (2n_r + \Lambda + 1) \right. \right. \\ &\quad \left. \left. + \delta_{n_r+1, n'_r} \sqrt{(n_r + 1)(n_r + 1 + \Lambda)} \right. \right. \\ &\quad \left. \left. + \delta_{n_r-1, n'_r} \sqrt{n_r(n_r + \Lambda)} \right) \right]. \quad (C.62) \end{aligned}$$

### C.3 Scalar Potential Matrix Element $\langle \Psi_f | \hat{V}_{C+N} | \Psi_i \rangle$

The matrix element related to the scalar potential is written  $\langle \Psi_f | \hat{V}_{C+N} | \Psi_i \rangle$ . The scalar potential operator is the sum of the Coulomb potential  $V_C$  and nuclear potential  $V_N$ . In our case, the Coulomb scalar potential and the nuclear mean fields are given by

$$V_C(\vec{r}_1) = C\rho_C \iiint_V \frac{d^3\vec{r}_2}{\|\vec{r}_2 - \vec{r}_1\|}, \quad (\text{C.63})$$

$$V_N(\vec{r}_1) = -\frac{V_0}{4\pi a^3} \iiint_V \frac{\exp(-\|\vec{r}_2 - \vec{r}_1\|/a)}{\|\vec{r}_2 - \vec{r}_1\|/a} d^3\vec{r}_2. \quad (\text{C.64})$$

Yet the derivation given in the following is general and does not depend on the properties of the *scalar* potential. The scalar potential matrix elements are diagonal in  $\Lambda$  and  $\Sigma$ , so that it can be written

$$\langle \Psi_f | \hat{V}_{C+N} | \Psi_i \rangle = \delta_{\Lambda'\Lambda} \delta_{\Sigma\Sigma'} \int_{-\infty}^{+\infty} dz \int_0^{+\infty} \rho d\rho \Psi_{n'_z}(z) \Psi_{n'_r}^\Lambda(\rho) V(\rho, z) \Psi_{n_z}(z) \Psi_{n_r}^\Lambda(\rho). \quad (\text{C.65})$$

Performing the variable changes  $z \rightarrow \xi$  and  $\rho \rightarrow \eta^{\frac{1}{2}}$  (*cf.* Eq. C.5), Eq. C.65 becomes

$$\begin{aligned} \langle \Psi_f | \hat{V}_{C+N} | \Psi_i \rangle &= 2\delta_{\Lambda'\Lambda} \delta_{\Sigma\Sigma'} N_{n'_z} N_{n'_r}^\Lambda N_{n_z} N_{n_r}^\Lambda \int_{-\infty}^{+\infty} d\xi \int_0^{+\infty} \eta^{\frac{1}{2}} d\eta^{\frac{1}{2}} e^{-\xi^2} \eta^\Lambda e^{-\eta} \\ &\quad \times H_{n_z}(\xi) H_{n'_z}(\xi) L_{n_r}^\Lambda(\eta) L_{n'_r}^\Lambda(\eta) V(\rho, z). \end{aligned} \quad (\text{C.66})$$

Performing the additional variable change  $\eta^{\frac{1}{2}} \rightarrow \eta$ , Eq. C.66 becomes

$$\begin{aligned} \langle \Psi_f | \hat{V}_{C+N} | \Psi_i \rangle &= \delta_{\Lambda'\Lambda} \delta_{\Sigma\Sigma'} N_{n'_z} N_{n'_r}^\Lambda N_{n_z} N_{n_r}^\Lambda \int_{-\infty}^{+\infty} d\xi \int_0^{+\infty} d\eta e^{-\xi^2} \eta^\Lambda e^{-\eta} \\ &\quad \times H_{n_z}(\xi) H_{n'_z}(\xi) L_{n_r}^\Lambda(\eta) L_{n'_r}^\Lambda(\eta) V(\rho, z). \end{aligned} \quad (\text{C.67})$$

This can be eventually computed numerically using Gauss-Hermite and Gauss-Laguerre quadrature rules.

### C.4 Spin-Orbit Coupling Matrix Element $\langle \Psi_f | \hat{V}_{\text{s.o.}} | \Psi_i \rangle$

The spin-orbit coupling operator has the general form

$$\hat{V}_{\text{s.o.}} = -\lambda \left( \frac{\hbar}{2mc} \right)^2 \vec{\sigma} \cdot \vec{\nabla} V_N \times \frac{\vec{p}}{\hbar}, \quad (\text{C.68})$$

where  $\vec{\sigma}$  is a column vector containing the Pauli matrices, and  $V_N$  is the nuclear scalar potential. As the total angular momentum projection on the symmetry axis  $\Omega = \Lambda + \Sigma$  is a good quantum number, the only possibly non-zero elements are between wave functions having the same  $\Omega$  number, namely

$$\langle n'_r, n'_z, \Lambda, \Sigma | \hat{V}_{\text{s.o.}} | n_r, n_z, \Lambda, \Sigma \rangle,$$



$$\begin{aligned} & \langle n'_r, n'_z, \Lambda + 1, -\frac{1}{2} | \hat{V}_{s.o.} | n_r, n_z, \Lambda, +\frac{1}{2} \rangle, \\ & \langle n'_r, n'_z, \Lambda - 1, +\frac{1}{2} | \hat{V}_{s.o.} | n_r, n_z, \Lambda, -\frac{1}{2} \rangle. \end{aligned}$$

The spin-orbit coupling matrix element can be written

$$\langle n'_r, n'_z, \Lambda', \Sigma' | \hat{V}_{s.o.} | n_r, n_z, \Lambda, \Sigma \rangle = \langle \Psi_f | \hat{V}_{s.o.} | \Psi_i \rangle, \quad (C.69)$$

where the trivial integration over  $\varphi$  has already been performed.

#### C.4.1 Diagonal Spin-Orbit Matrix Element ( $\Sigma' = \Sigma$ )

The direct spin-orbit matrix element is characterized by  $\Lambda' = \Lambda$  and  $\Sigma' = \Sigma$ . Using Eq. 5.69, the spin-orbit coupling can be written as

$$\langle \Psi_f | \hat{V}_{s.o.} | \Psi_i \rangle = \pm \lambda \left( \frac{\hbar}{2mc} \right)^2 \int_{-\infty}^{+\infty} dz \int_0^{+\infty} \rho d\rho \Psi_f^* \frac{\Lambda}{\rho} \frac{\partial V_N}{\partial \rho} \Psi_i, \quad (C.70)$$

where  $V_N$  still depends on  $z$  and  $\rho$ . In the remaining of this appendix, the following color convention will be used

$$\Sigma = +\frac{1}{2}, \quad \Sigma = -\frac{1}{2}. \quad (C.71)$$

Performing again the variable changes  $z \rightarrow \xi$  and  $\rho \rightarrow \eta$  (cf. Eq. C.5), Eq. C.70 becomes

$$\langle \Psi_f | \hat{V}_{s.o.} | \Psi_i \rangle = \pm \lambda \left( \frac{\hbar}{2mc} \right)^2 \Lambda \left( \frac{\hbar}{m\omega_z} \right)^{1/2} \int_{-\infty}^{+\infty} d\xi \int_0^{+\infty} d\eta \frac{\partial V_N}{\partial \eta} \Psi_f^* \Psi_i. \quad (C.72)$$

Integrating Eq. C.72 by parts on  $\eta$ , it yields

$$\begin{aligned} \langle \Psi_f | \hat{V}_{s.o.} | \Psi_i \rangle &= \pm \lambda \left( \frac{\hbar}{2mc} \right)^2 \Lambda \left( \frac{\hbar}{m\omega_z} \right)^{1/2} \\ &\times \int_{-\infty}^{+\infty} d\xi \left( [V_N \Psi_f^* \Psi_i]_0^{+\infty} - \int_0^{+\infty} d\eta V_N \left[ \frac{\partial \Psi_f^*}{\partial \eta} \Psi_i + \frac{\partial \Psi_i}{\partial \eta} \Psi_f^* \right] \right). \end{aligned} \quad (C.73)$$

The integral term  $[V \Psi_f^* \Psi_i]_0^{+\infty}$  in Eq. C.73 is not necessarily zero for  $\eta = 0$  but this can occur only for  $\Lambda = 0$ , value of  $\Lambda$  for which the whole element is zero. Hence Eq. C.73 simplifies to

$$\langle \Psi_f | \hat{V}_{s.o.} | \Psi_i \rangle = \pm \lambda \left( \frac{\hbar}{2mc} \right)^2 \Lambda \left( \frac{\hbar}{m\omega_z} \right)^{1/2} \int_{-\infty}^{+\infty} d\xi \int_0^{+\infty} d\eta V_N \left[ \frac{\partial \Psi_f^*}{\partial \eta} \Psi_i + \frac{\partial \Psi_i}{\partial \eta} \Psi_f^* \right]. \quad (C.74)$$

Replacing  $\Psi_f$  and  $\Psi_i$  by their expressions and using the  $\Psi_{n_z}$  and  $\Psi_{n_r}^\Lambda$  definitions (cf. Eq. C.4), one obtains

$$\begin{aligned} \langle \Psi_f | \hat{V}_{s.o.} | \Psi_i \rangle &= \pm \lambda \left( \frac{\hbar}{2mc} \right)^2 \Lambda \frac{2m\omega_\perp}{\hbar} N_{n'_z} N_{n'_r}^\Lambda N_{n_z} N_{n_r}^\Lambda \int_{-\infty}^{+\infty} d\xi e^{-\xi^2} H_{n_z} H_{n'_z} \int_0^{+\infty} d\eta \\ &\times V_N \left( \eta^{\Lambda/2} e^{-\eta/2} L_{n_r}^\Lambda \frac{d(\eta^{\Lambda/2} e^{-\eta/2} L_{n'_r}^\Lambda)}{d\eta} + \eta^{\Lambda/2} e^{-\eta/2} L_{n'_r}^\Lambda \frac{d(\eta^{\Lambda/2} e^{-\eta/2} L_{n_r}^\Lambda)}{d\eta} \right), \end{aligned} \quad (C.75)$$

where the Hermite ( $H$ ) and associated Laguerre ( $L$ ) polynomials still depend of  $\xi$  and  $\eta$  respectively. Equation C.75 can be developed (the derivatives with respect of  $\eta$  are developed), so that it yields

$$\begin{aligned} \langle \Psi_f | \hat{V}_{s.o.} | \Psi_i \rangle &= \pm \lambda \left( \frac{\hbar}{2mc} \right)^2 \Lambda \frac{2m\omega_{\perp}}{\hbar} N_{n'_z} N_{n'_r}^{\Lambda} N_{n_z} N_{n_r}^{\Lambda} \int_{-\infty}^{+\infty} d\xi e^{-\xi^2} H_{n_z} H_{n'_z} \int_0^{+\infty} d\eta V_N \eta^{\Lambda/2} e^{-\eta/2} \\ &\quad \times \left( L_{n_r}^{\Lambda} \left[ \left( \frac{\Lambda}{2} \eta^{\frac{\Lambda}{2}-1} e^{-\eta/2} - \frac{\eta^{\Lambda/2}}{2} e^{-\eta/2} \right) L_{n'_r}^{\Lambda} + \eta^{\Lambda/2} e^{-\eta/2} \frac{dL_{n'_r}^{\Lambda}}{d\eta} \right] \right. \\ &\quad \left. + L_{n'_r}^{\Lambda} \left[ \left( \frac{\Lambda}{2} \eta^{\frac{\Lambda}{2}-1} e^{-\eta/2} - \frac{\eta^{\Lambda/2}}{2} e^{-\eta/2} \right) L_{n_r}^{\Lambda} + \eta^{\Lambda/2} e^{-\eta/2} \frac{dL_{n_r}^{\Lambda}}{d\eta} \right] \right), \end{aligned} \quad (C.76)$$

$$\begin{aligned} &= \pm \lambda \left( \frac{\hbar}{2mc} \right)^2 \Lambda \frac{m\omega_{\perp}}{\hbar} N_{n'_z} N_{n'_r}^{\Lambda} N_{n_z} N_{n_r}^{\Lambda} \int_{-\infty}^{+\infty} d\xi e^{-\xi^2} H_{n_z} H_{n'_z} \int_0^{+\infty} d\eta V_N \eta^{\Lambda} e^{-\eta} \\ &\quad \times \left( L_{n_r}^{\Lambda} \left[ \left( \frac{\Lambda}{\eta} - 1 \right) L_{n'_r}^{\Lambda} + 2 \frac{dL_{n'_r}^{\Lambda}}{d\eta} \right] + L_{n'_r}^{\Lambda} \left[ \left( \frac{\Lambda}{\eta} - 1 \right) L_{n_r}^{\Lambda} + 2 \frac{dL_{n_r}^{\Lambda}}{d\eta} \right] \right), \end{aligned} \quad (C.77)$$

$$\begin{aligned} &= \pm \lambda \left( \frac{\hbar}{2mc} \right)^2 \Lambda \frac{m\omega_{\perp}}{\hbar} N_{n'_z} N_{n'_r}^{\Lambda} N_{n_z} N_{n_r}^{\Lambda} \int_{-\infty}^{+\infty} d\xi e^{-\xi^2} H_{n_z} H_{n'_z} \int_0^{+\infty} d\eta V_N \eta^{\Lambda-1} e^{-\eta} \\ &\quad \times \left( L_{n_r}^{\Lambda} \left[ (\Lambda - \eta) L_{n'_r}^{\Lambda} + 2\eta \frac{dL_{n'_r}^{\Lambda}}{d\eta} \right] + L_{n'_r}^{\Lambda} \left[ (\Lambda - \eta) L_{n_r}^{\Lambda} + 2\eta \frac{dL_{n_r}^{\Lambda}}{d\eta} \right] \right). \end{aligned} \quad (C.78)$$

The associated Laguerre polynomials satisfy the differential equation (*cf.* Ref. [183])

$$\eta \frac{dL_{n_r}^{\Lambda}}{d\eta} = n_r L_{n_r}^{\Lambda} - (n_r + \Lambda) L_{n_r-1}^{\Lambda}, \quad n_r \geq 1. \quad (C.79)$$

Using the recurrence relation (Eq. C.79) into Eq. C.78, it becomes

$$\begin{aligned} \langle \Psi_f | \hat{V}_{s.o.} | \Psi_i \rangle &= \pm \lambda \left( \frac{\hbar}{2mc} \right)^2 \Lambda \frac{m\omega_{\perp}}{\hbar} N_{n'_z} N_{n'_r}^{\Lambda} N_{n_z} N_{n_r}^{\Lambda} \int_{-\infty}^{+\infty} d\xi e^{-\xi^2} H_{n_z} H_{n'_z} \int_0^{+\infty} d\eta V_N \eta^{\Lambda-1} e^{-\eta} \\ &\quad \times \left( L_{n_r}^{\Lambda} \left[ (\Lambda - \eta) L_{n'_r}^{\Lambda} + 2n'_r L_{n'_r-1}^{\Lambda} - 2(n'_r + \Lambda) L_{n'_r-1}^{\Lambda} \right] \right. \\ &\quad \left. + L_{n'_r}^{\Lambda} \left[ (\Lambda - \eta) L_{n_r}^{\Lambda} + 2n_r L_{n_r-1}^{\Lambda} - 2(n_r + \Lambda) L_{n_r-1}^{\Lambda} \right] \right), \end{aligned} \quad (C.80)$$

$$\begin{aligned} &= \pm \lambda \left( \frac{\hbar}{2mc} \right)^2 \Lambda \frac{2m\omega_{\perp}}{\hbar} N_{n'_z} N_{n'_r}^{\Lambda} N_{n_z} N_{n_r}^{\Lambda} \int_{-\infty}^{+\infty} d\xi e^{-\xi^2} H_{n_z} H_{n'_z} \int_0^{+\infty} d\eta V_N \eta^{\Lambda-1} e^{-\eta} \\ &\quad \times \left( (\Lambda - \eta + n_r + n'_r) L_{n_r}^{\Lambda} L_{n'_r}^{\Lambda} - (n'_r + \Lambda) L_{n_r}^{\Lambda} L_{n'_r-1}^{\Lambda} - (n_r + \Lambda) L_{n'_r}^{\Lambda} L_{n_r-1}^{\Lambda} \right). \end{aligned} \quad (C.81)$$

To simplify the expression obtained, the following notation is introduced

$$\tilde{L}_{n_r}^\Lambda = \Lambda L_{n_r}^\Lambda - \eta L_{n_r}^\Lambda + 2\eta \frac{dL_{n_r}^\Lambda}{d\eta} = (2n_r + \Lambda - \eta) L_{n_r}^\Lambda - 2(n_r + \Lambda) L_{n_r-1}^\Lambda. \quad (C.82)$$

Using  $\tilde{L}_{n_r}^\Lambda$  in Eq. C.81,  $\langle \Psi_f | \hat{V}_{s.o.} | \Psi_i \rangle$  simplifies to

$$\begin{aligned} \langle \Psi_f | \hat{V}_{s.o.} | \Psi_i \rangle = & \pm \lambda \left( \frac{\hbar}{2mc} \right)^2 \Lambda \frac{m\omega_\perp}{\hbar} N_{n'_z} N_{n'_r}^\Lambda N_{n_z} N_{n_r}^\Lambda \\ & \times \int_{-\infty}^{+\infty} d\xi e^{-\xi^2} H_{n_z} H_{n'_z} \int_0^{+\infty} d\eta V_N \eta^{\Lambda-1} e^{-\eta} \left( L_{n_r}^\Lambda \tilde{L}_{n'_r}^\Lambda + L_{n'_r}^\Lambda \tilde{L}_{n_r}^\Lambda \right). \end{aligned} \quad (C.83)$$

Observing that  $2\Sigma = \pm 1$ , the final expression for the direct spin-orbit coupling matrix element can be written

$$\begin{aligned} \langle \Psi_f | \hat{V}_{s.o.} | \Psi_i \rangle = & 2\lambda \left( \frac{\hbar}{2mc} \right)^2 \Sigma \Lambda \frac{m\omega_\perp}{\hbar} N_{n'_z} N_{n'_r}^\Lambda N_{n_z} N_{n_r}^\Lambda \\ & \times \int_{-\infty}^{+\infty} d\xi e^{-\xi^2} H_{n_z} H_{n'_z} \int_0^{+\infty} d\eta V_N \eta^{\Lambda-1} e^{-\eta} \left( L_{n_r}^\Lambda \tilde{L}_{n'_r}^\Lambda + L_{n'_r}^\Lambda \tilde{L}_{n_r}^\Lambda \right). \end{aligned} \quad (C.84)$$

### C.4.2 Cross Spin-Orbit Matrix Element ( $\Sigma' = -\Sigma$ )

The cross spin-orbit coupling matrix elements correspond to the cases where  $\Lambda' \neq \Lambda$  ( $\Sigma' = -\Sigma$ ). Those cases have possibly non-zero values are more specifically given by

$$\langle n'_r, n'_z, \Lambda + 1, -\frac{1}{2} | \hat{V}_{s.o.} | n_r, n_z, \Lambda, +\frac{1}{2} \rangle \quad \text{and} \quad \langle n'_r, n'_z, \Lambda - 1, +\frac{1}{2} | \hat{V}_{s.o.} | n_r, n_z, \Lambda, -\frac{1}{2} \rangle.$$

Both cases will be treated simultaneously using the following convention

$$\langle \Psi_f | \hat{V}_{s.o.} | \Psi_i \rangle = \langle n'_r, n'_z, \Lambda \pm 1, \pm \frac{1}{2} | \hat{V}_{s.o.} | n_r, n_z, \Lambda, \pm \frac{1}{2} \rangle. \quad (C.85)$$

The cross matrix element  $\langle \Psi_f | \hat{V}_{s.o.} | \Psi_i \rangle$  is defined as (*cf.* Eq. 5.69)

$$\langle \Psi_f | \hat{V}_{s.o.} | \Psi_i \rangle = \lambda \left( \frac{\hbar}{2mc} \right)^2 \int_{-\infty}^{+\infty} dz \int_0^{+\infty} \rho d\rho \Psi_f^* \left( \frac{\Lambda}{\rho} \frac{\partial V_N}{\partial z} \pm \frac{\partial V_N}{\partial z} \frac{\partial}{\partial \rho} \pm \frac{\partial V_N}{\partial \rho} \frac{\partial}{\partial z} \right) \Psi_i. \quad (C.86)$$

Performing the the variable changes  $z \rightarrow \xi$  and  $\rho \rightarrow \eta$  (*cf.* Eq. C.5), Eq. C.86 becomes

$$\langle \Psi_f | \hat{V}_{s.o.} | \Psi_i \rangle = \lambda \left( \frac{\hbar}{2mc} \right)^2 \left( \frac{\hbar}{m\omega_\perp} \right)^{\frac{1}{2}} \int_{-\infty}^{+\infty} d\xi \int_0^{+\infty} d\eta \Lambda \eta^{-\frac{1}{2}} \Psi_f^* \left( \frac{\Lambda}{2\eta^{\frac{1}{2}}} \frac{\partial V_N}{\partial \xi} \pm \frac{\partial V_N}{\partial \xi} \eta^{\frac{1}{2}} \frac{\partial}{\partial \eta} \pm \frac{\partial V_N}{\partial \eta} \eta^{\frac{1}{2}} \frac{\partial}{\partial \xi} \right) \Psi_i. \quad (C.87)$$

The partial derivatives of the nuclear potential  $V_N$  will be removed by integration by parts. First Eq. C.87 is expanded and ordered, so that

$$\begin{aligned} \langle \Psi_f | \hat{V}_{s.o.} | \Psi_i \rangle &= \frac{1}{2} \lambda \left( \frac{\hbar}{2mc} \right)^2 \left( \frac{\hbar}{m\omega_\perp} \right)^{\frac{1}{2}} \int_{-\infty}^{+\infty} d\xi \int_0^{+\infty} d\eta \Lambda \eta^{-\frac{1}{2}} \Psi_f^* \frac{\partial V_N}{\partial \xi} \Psi_i \\ &\quad \pm \lambda \left( \frac{\hbar}{2mc} \right)^2 \left( \frac{\hbar}{m\omega_\perp} \right)^{\frac{1}{2}} \int_{-\infty}^{+\infty} d\xi \int_0^{+\infty} d\eta \eta^{\frac{1}{2}} \Psi_f^* \left( \frac{\partial V_N}{\partial \xi} \frac{\partial}{\partial \eta} - \frac{\partial V_N}{\partial \eta} \frac{\partial}{\partial \xi} \right) \Psi_i, \end{aligned} \quad (C.88)$$

$$\begin{aligned}
 &= \frac{1}{2} \lambda \left( \frac{\hbar}{2mc} \right)^2 \left( \frac{\hbar}{m\omega_{\perp}} \right)^{\frac{1}{2}} \int_0^{+\infty} d\eta \Lambda \eta^{-\frac{1}{2}} \int_{-\infty}^{+\infty} d\xi \Psi_f^* \Psi_i \frac{\partial V_N}{\partial \xi} \\
 &\quad + \lambda \left( \frac{\hbar}{2mc} \right)^2 \left( \frac{\hbar}{m\omega_{\perp}} \right)^{\frac{1}{2}} \left[ \int_0^{+\infty} d\eta \eta^{\frac{1}{2}} \int_{-\infty}^{+\infty} d\xi \Psi_f^* \frac{\partial \Psi_i}{\partial \eta} \frac{\partial V_N}{\partial \xi} - \int_{-\infty}^{+\infty} d\xi \int_0^{+\infty} d\eta \eta^{\frac{1}{2}} \Psi_f^* \frac{\partial \Psi_i}{\partial \xi} \frac{\partial V_N}{\partial \eta} \right]. \quad (\text{C.89})
 \end{aligned}$$

Then the integration by parts is performed for the first two terms involving partial derivatives of  $V_N$ . One obtains

$$\begin{aligned}
 \langle \Psi_f | \hat{V}_{\text{s.o.}} | \Psi_i \rangle &= \frac{1}{2} \lambda \left( \frac{\hbar}{2mc} \right)^2 \left( \frac{\hbar}{m\omega_{\perp}} \right)^{\frac{1}{2}} \int_0^{+\infty} d\eta \Lambda \eta^{-\frac{1}{2}} \left[ [\Psi_f^* \Psi_i V_N]_{-\infty}^{+\infty} \right. \\
 &\quad \left. - \int_{-\infty}^{+\infty} d\xi V_N \left( \frac{\partial \Psi_f^*}{\partial \xi} \Psi_i + \Psi_f^* \frac{\partial \Psi_i}{\partial \xi} \right) \right] \\
 &\quad + \lambda \left( \frac{\hbar}{2mc} \right)^2 \left( \frac{\hbar}{m\omega_{\perp}} \right)^{\frac{1}{2}} \left[ \int_0^{+\infty} d\eta \eta^{\frac{1}{2}} \left( [\Psi_f^* \frac{\partial \Psi_i}{\partial \eta} V_N]_{-\infty}^{+\infty} \right. \right. \\
 &\quad \left. \left. - \int_{-\infty}^{+\infty} d\xi V_N \left[ \frac{\partial \Psi_f^*}{\partial \xi} \frac{\partial \Psi_i}{\partial \eta} + \Psi_f^* \frac{\partial^2 \Psi_i}{\partial \eta \partial \xi} \right] \right) - \int_{-\infty}^{+\infty} d\xi \int_0^{+\infty} d\eta \eta^{\frac{1}{2}} \Psi_f^* \frac{\partial \Psi_i}{\partial \xi} \frac{\partial V_N}{\partial \eta} \right]. \quad (\text{C.90})
 \end{aligned}$$

The two integrated terms (terms in brackets [ ]) are zeros because  $\lim_{\xi \rightarrow \pm\infty} \Psi_f^*(\eta, \xi) = 0$ . The last term involving a partial derivative of  $V_N$  is integrate by part. Equation C.90 becomes

$$\begin{aligned}
 \langle \Psi_f | \hat{V}_{\text{s.o.}} | \Psi_i \rangle &= -\frac{1}{2} \lambda \left( \frac{\hbar}{2mc} \right)^2 \left( \frac{\hbar}{m\omega_{\perp}} \right)^{\frac{1}{2}} \int_0^{+\infty} d\eta \Lambda \eta^{-\frac{1}{2}} \int_{-\infty}^{+\infty} d\xi V_N \left( \frac{\partial \Psi_f^*}{\partial \xi} \Psi_i + \Psi_f^* \frac{\partial \Psi_i}{\partial \xi} \right) \\
 &\quad + \lambda \left( \frac{\hbar}{2mc} \right)^2 \left( \frac{\hbar}{m\omega_{\perp}} \right)^{\frac{1}{2}} \left[ \int_0^{+\infty} d\eta \eta^{\frac{1}{2}} \int_{-\infty}^{+\infty} d\xi V_N \left( \frac{\partial \Psi_f^*}{\partial \xi} \frac{\partial \Psi_i}{\partial \eta} + \Psi_f^* \frac{\partial^2 \Psi_i}{\partial \eta \partial \xi} \right) \right. \\
 &\quad \left. + \int_{-\infty}^{+\infty} d\xi \left( [V_N \eta^{\frac{1}{2}} \Psi_f^* \Psi_i]_0^{+\infty} - \int_0^{+\infty} d\eta V_N \left[ \frac{1}{2\eta^{\frac{1}{2}}} \Psi_f^* \frac{\partial \Psi_i}{\partial \xi} + \eta^{\frac{1}{2}} \frac{\partial \Psi_f^*}{\partial \eta} \frac{\partial \Psi_i}{\partial \xi} + \eta^{\frac{1}{2}} \Psi_f^* \frac{\partial^2 \Psi_i}{\partial \xi \partial \eta} \right] \right) \right]. \quad (\text{C.91})
 \end{aligned}$$

The integrated term also vanishes because  $\lim_{\eta \rightarrow +\infty} \Psi_f^*(\eta, \xi) = 0$ . The last term of Eq. C.91 is split according to its power of  $\eta$ , so that Eq. C.91 becomes

$$\begin{aligned}
 \langle \Psi_f | \hat{V}_{s.o.} | \Psi_i \rangle = & -\frac{1}{2} \lambda \left( \frac{\hbar}{2mc} \right)^2 \left( \frac{\hbar}{m\omega_{\perp}} \right)^{\frac{1}{2}} \int_0^{+\infty} d\eta \Lambda \eta^{-\frac{1}{2}} \int_{-\infty}^{+\infty} d\xi V_N \left( \frac{\partial \Psi_f^*}{\partial \xi} \Psi_i + \Psi_f^* \frac{\partial \Psi_i}{\partial \xi} \right) \\
 & \pm \lambda \left( \frac{\hbar}{2mc} \right)^2 \left( \frac{\hbar}{m\omega_{\perp}} \right)^{\frac{1}{2}} \left[ \int_0^{+\infty} d\eta \eta^{\frac{1}{2}} \int_{-\infty}^{+\infty} d\xi V_N \left( \frac{\partial \Psi_f^*}{\partial \xi} \frac{\partial \Psi_i}{\partial \eta} + \Psi_f^* \frac{\partial^2 \Psi_i}{\partial \eta \partial \xi} \right) \right. \\
 & \quad \left. - \int_{-\infty}^{+\infty} d\xi \int_0^{+\infty} d\eta V_N \left( \eta^{\frac{1}{2}} \frac{\partial \Psi_f^*}{\partial \eta} \frac{\partial \Psi_i}{\partial \xi} + \eta^{\frac{1}{2}} \Psi_f^* \frac{\partial^2 \Psi_i}{\partial \xi \partial \eta} \right) \right] \\
 & \pm \lambda \left( \frac{\hbar}{2mc} \right)^2 \left( \frac{\hbar}{m\omega_{\perp}} \right)^{\frac{1}{2}} \int_{-\infty}^{+\infty} d\xi \int_0^{+\infty} d\eta V_N \frac{1}{2\eta^{\frac{1}{2}}} \Psi_f^* \frac{\partial \Psi_i}{\partial \xi}.
 \end{aligned} \tag{C.92}$$

Gathering terms in Eq. C.92, one obtains

$$\begin{aligned}
 \langle \Psi_f | \hat{V}_{s.o.} | \Psi_i \rangle = & -\frac{1}{2} \lambda \left( \frac{\hbar}{2mc} \right)^2 \left( \frac{\hbar}{m\omega_{\perp}} \right)^{\frac{1}{2}} \int_0^{+\infty} d\eta \eta^{-\frac{1}{2}} \int_{-\infty}^{+\infty} d\xi V_N \left( \Lambda \frac{\partial \Psi_f^*}{\partial \xi} \Psi_i + (\Lambda \pm 1) \Psi_f^* \frac{\partial \Psi_i}{\partial \xi} \right) \\
 & \pm \lambda \left( \frac{\hbar}{2mc} \right)^2 \left( \frac{\hbar}{m\omega_{\perp}} \right)^{\frac{1}{2}} \int_0^{+\infty} d\eta \eta^{\frac{1}{2}} \int_{-\infty}^{+\infty} d\xi V_N \left( \frac{\partial \Psi_f^*}{\partial \xi} \frac{\partial \Psi_i}{\partial \eta} - \frac{\partial \Psi_f^*}{\partial \eta} \frac{\partial \Psi_i}{\partial \xi} \right).
 \end{aligned} \tag{C.93}$$

Replacing  $\Psi_f$  and  $\Psi_i$  by their expressions and using the  $\Psi_{n_z}$  and  $\Psi_{n_r}^{\Lambda}$  definitions (cf. Eq. C.4), one obtains

$$\begin{aligned}
 \langle \Psi_f | \hat{V}_{s.o.} | \Psi_i \rangle = & -\lambda \left( \frac{\hbar}{2mc} \right)^2 \left( \frac{m^2 \omega_z \omega_{\perp}}{\hbar^2} \right)^{\frac{1}{2}} N_{n_z} N_{n'_z} N_{n_r}^{\Lambda} N_{n'_r}^{\Lambda \pm 1} \int_0^{+\infty} d\eta \eta^{-\frac{1}{2}} \eta^{\Lambda/2} \eta^{\frac{\Lambda \pm 1}{2}} L_{n_r}^{\Lambda} L_{n'_r}^{\Lambda \pm 1} e^{-\eta} \\
 & \times \int_{-\infty}^{+\infty} d\xi e^{-\xi^2/2} V_N \left( (\Lambda \pm 1) H_{n'_z} \frac{dH_{n_z} e^{-\xi^2/2}}{d\xi} + \Lambda H_{n_z} \frac{dH_{n'_z} e^{-\xi^2/2}}{d\xi} \right) \\
 & \pm 2\lambda \left( \frac{\hbar}{2mc} \right)^2 \left( \frac{m^2 \omega_z \omega_{\perp}}{\hbar^2} \right)^{\frac{1}{2}} N_{n_z} N_{n'_z} N_{n_r}^{\Lambda} N_{n'_r}^{\Lambda \pm 1} \int_0^{+\infty} d\eta \eta^{\frac{1}{2}} \int_{-\infty}^{+\infty} d\xi V_N \\
 & \times \left( H_{n_z} e^{-\xi^2/2} \eta^{\frac{\Lambda \pm 1}{2}} e^{-\eta/2} \frac{dH_{n'_z} e^{-\xi^2/2}}{d\xi} \frac{dL_{n_r}^{\Lambda} e^{-\eta/2} \eta^{\Lambda/2}}{d\eta} L_{n'_r}^{\Lambda \pm 1} \right. \\
 & \quad \left. - H_{n'_z} e^{-\xi^2/2} \eta^{\Lambda/2} e^{-\eta/2} \frac{dH_{n_z} e^{-\xi^2/2}}{d\xi} L_{n_r}^{\Lambda} \frac{dL_{n'_r}^{\Lambda \pm 1} e^{-\eta/2} \eta^{\frac{\Lambda \pm 1}{2}}}{d\eta} \right),
 \end{aligned} \tag{C.94}$$

$$\begin{aligned}
 = & -\lambda \left( \frac{\hbar}{2mc} \right)^2 \left( \frac{m^2 \omega_z \omega_{\perp}}{\hbar^2} \right)^{\frac{1}{2}} N_{n_z} N_{n'_z} N_{n_r}^{\Lambda} N_{n'_r}^{\Lambda \pm 1} \int_0^{+\infty} d\eta \eta^{-\frac{1}{2}} \eta^{\Lambda/2} \eta^{\frac{\Lambda \pm 1}{2}} L_{n_r}^{\Lambda} L_{n'_r}^{\Lambda \pm 1} e^{-\eta} \\
 & \times \int_{-\infty}^{+\infty} d\xi e^{-\xi^2} V_N \left( (\Lambda \pm 1) H_{n'_z} \left[ -\xi H_{n_z} + \frac{dH_{n_z}}{d\xi} \right] + \Lambda H_{n_z} \left[ -\xi H_{n'_z} + \frac{dH_{n'_z}}{d\xi} \right] \right) \\
 & \pm 2\lambda \left( \frac{\hbar}{2mc} \right)^2 \left( \frac{m^2 \omega_z \omega_{\perp}}{\hbar^2} \right)^{\frac{1}{2}} N_{n_z} N_{n'_z} N_{n_r}^{\Lambda} N_{n'_r}^{\Lambda \pm 1} \int_0^{+\infty} d\eta \eta^{\frac{1}{2}} e^{-\eta/2} \int_{-\infty}^{+\infty} d\xi e^{-\xi^2} V_N \\
 & \times \left[ H_{n_z} \eta^{\frac{\Lambda \pm 1}{2}} \left( -\xi H_{n'_z} + \frac{dH_{n'_z}}{d\xi} \right) \right. \\
 & \quad \times \left( \left( \frac{\Lambda}{2} \eta^{\frac{\Lambda}{2}-1} e^{-\eta/2} - \frac{1}{2} \eta^{\Lambda/2} e^{-\eta/2} \right) L_{n_r}^{\Lambda} + e^{-\eta/2} \eta^{\Lambda/2} \frac{dL_{n_r}^{\Lambda}}{d\eta} \right) L_{n'_r}^{\Lambda \pm 1} \\
 & \quad - H_{n'_z} \eta^{\Lambda/2} \left( -\xi H_{n_z} + \frac{dH_{n_z}}{d\xi} \right) L_{n_r}^{\Lambda} \\
 & \quad \left. \times \left( \left( \frac{\Lambda \pm 1}{2} \eta^{\frac{\Lambda \pm 1}{2}-1} e^{-\eta/2} - \frac{1}{2} \eta^{\frac{\Lambda \pm 1}{2}} e^{-\eta/2} \right) L_{n'_r}^{\Lambda \pm 1} + e^{-\eta/2} \eta^{\frac{\Lambda \pm 1}{2}} \frac{dL_{n'_r}^{\Lambda \pm 1}}{d\eta} \right) \right]. \tag{C.95}
 \end{aligned}$$

Equation C.95 can be further simplified to become

$$\begin{aligned}
 \langle \Psi_f | \hat{V}_{\text{s.o.}} | \Psi_i \rangle = & -\lambda \left( \frac{\hbar}{2mc} \right)^2 \left( \frac{m^2 \omega_z \omega_{\perp}}{\hbar^2} \right)^{\frac{1}{2}} N_{n_z} N_{n'_z} N_{n_r}^{\Lambda} N_{n'_r}^{\Lambda \pm 1} \int_0^{+\infty} d\eta \eta^{(2\Lambda \pm 1 - 1)/2} L_{n_r}^{\Lambda} L_{n'_r}^{\Lambda \pm 1} e^{-\eta} \\
 & \times \int_{-\infty}^{+\infty} d\xi e^{-\xi^2} V_N \left[ (\Lambda \pm 1) H_{n'_z} \left( -\xi H_{n_z} + \frac{dH_{n_z}}{d\xi} \right) + \Lambda H_{n_z} \left( -\xi H_{n'_z} + \frac{dH_{n'_z}}{d\xi} \right) \right] \\
 & \pm 2\lambda \left( \frac{\hbar}{2mc} \right)^2 \left( \frac{m^2 \omega_z \omega_{\perp}}{\hbar^2} \right)^{\frac{1}{2}} N_{n_z} N_{n'_z} N_{n_r}^{\Lambda} N_{n'_r}^{\Lambda \pm 1} \int_0^{+\infty} d\eta \eta^{(2\Lambda \pm 1 + 1)/2} e^{-\eta} \int_{-\infty}^{+\infty} d\xi e^{-\xi^2} V_N \\
 & \times \left[ H_{n_z} \left( -\xi H_{n'_z} + \frac{dH_{n'_z}}{d\xi} \right) \left( \left( \frac{\Lambda}{2\eta} - \frac{1}{2} \right) L_{n_r}^{\Lambda} + \frac{dL_{n_r}^{\Lambda}}{d\eta} \right) L_{n'_r}^{\Lambda \pm 1} \right. \\
 & \quad \left. - H_{n'_z} \left( -\xi H_{n_z} + \frac{dH_{n_z}}{d\xi} \right) L_{n_r}^{\Lambda} \left( \left( \frac{\Lambda \pm 1}{2\eta} - \frac{1}{2} \right) L_{n'_r}^{\Lambda \pm 1} + \frac{dL_{n'_r}^{\Lambda \pm 1}}{d\eta} \right) \right], \tag{C.96}
 \end{aligned}$$

$$\begin{aligned}
 &= -\lambda \left( \frac{\hbar}{2mc} \right)^2 \left( \frac{m^2 \omega_z \omega_\perp}{\hbar^2} \right)^{\frac{1}{2}} N_{n_z} N_{n'_z} N_{n_r}^\Lambda N_{n'_r}^{\Lambda \pm 1} \int_0^{+\infty} d\eta \eta^{(2\Lambda \pm 1 - 1)/2} L_{n_r}^\Lambda L_{n'_r}^{\Lambda \pm 1} e^{-\eta} \\
 &\quad \times \int_{-\infty}^{+\infty} d\xi e^{-\xi^2} V_N \left[ (\Lambda \pm 1) H_{n'_z} \left( -\xi H_{n_z} + \frac{dH_{n_z}}{d\xi} \right) + \Lambda H_{n_z} \left( -\xi H_{n'_z} + \frac{dH_{n'_z}}{d\xi} \right) \right] \\
 &\quad \pm \lambda \left( \frac{\hbar}{2mc} \right)^2 \left( \frac{m^2 \omega_z \omega_\perp}{\hbar^2} \right)^{\frac{1}{2}} N_{n_z} N_{n'_z} N_{n_r}^\Lambda N_{n'_r}^{\Lambda \pm 1} \int_0^{+\infty} d\eta \eta^{(2\Lambda \pm 1 - 1)/2} e^{-\eta} \int_{-\infty}^{+\infty} d\xi e^{-\xi^2} V_N \\
 &\quad \times \left[ H_{n_z} \left( -\xi H_{n'_z} + \frac{dH_{n'_z}}{d\xi} \right) \left( (\Lambda - \eta) L_{n_r}^\Lambda + 2\eta \frac{dL_{n_r}^\Lambda}{d\eta} \right) L_{n'_r}^{\Lambda \pm 1} \right. \\
 &\quad \left. - H_{n'_z} \left( -\xi H_{n_z} + \frac{dH_{n_z}}{d\xi} \right) L_{n_r}^\Lambda \left( (\Lambda \pm 1 - \eta) L_{n'_r}^{\Lambda \pm 1} + 2\eta \frac{dL_{n'_r}^{\Lambda \pm 1}}{d\eta} \right) \right]. \tag{C.97}
 \end{aligned}$$

The Hermite and associated Laguerre polynomials satisfy the differential equations (*cf.* Ref. [183])

$$\frac{dH_{n_z}}{d\xi} = 2n_z H_{n_z-1} \quad \text{and} \quad \eta \frac{dL_{n_r}^\Lambda}{d\eta} = n_r L_{n_r}^\Lambda - (n_r + \Lambda) L_{n_r-1}^\Lambda. \tag{C.98}$$

Using the convention  $H_{-1}(\xi) = 0$  and  $L_{-1}^\Lambda(\eta) = 0$ , Eq. C.97 simplifies to

$$\begin{aligned}
 \langle \Psi_f | \hat{V}_{\text{s.o.}} | \Psi_i \rangle &= -\lambda \left( \frac{\hbar}{2mc} \right)^2 \left( \frac{m^2 \omega_z \omega_\perp}{\hbar^2} \right)^{\frac{1}{2}} N_{n_z} N_{n'_z} N_{n_r}^\Lambda N_{n'_r}^{\Lambda \pm 1} \int_0^{+\infty} d\eta \eta^{(2\Lambda \pm 1 - 1)/2} L_{n_r}^\Lambda L_{n'_r}^{\Lambda \pm 1} e^{-\eta} \\
 &\quad \times \int_{-\infty}^{+\infty} d\xi e^{-\xi^2} V_N \left[ (\Lambda \pm 1) H_{n'_z} (-\xi H_{n_z} + 2n_z H_{n_z-1}) + \Lambda H_{n_z} (-\xi H_{n'_z} + 2n'_z H_{n'_z-1}) \right] \\
 &\quad \pm \lambda \left( \frac{\hbar}{2mc} \right)^2 \left( \frac{m^2 \omega_z \omega_\perp}{\hbar^2} \right)^{\frac{1}{2}} N_{n_z} N_{n'_z} N_{n_r}^\Lambda N_{n'_r}^{\Lambda \pm 1} \int_0^{+\infty} d\eta \eta^{(2\Lambda \pm 1 - 1)/2} e^{-\eta} \int_{-\infty}^{+\infty} d\xi e^{-\xi^2} V_N \\
 &\quad \times \left[ H_{n_z} (-\xi H_{n'_z} + 2n'_z H_{n'_z-1}) ([\Lambda - \eta] L_{n_r}^\Lambda + 2n_r L_{n_r}^\Lambda - 2[n_r + \Lambda] L_{n_r-1}^\Lambda) L_{n'_r}^{\Lambda \pm 1} \right. \\
 &\quad \left. - H_{n'_z} (-\xi H_{n_z} + 2n_z H_{n_z-1}) L_{n_r}^\Lambda \right. \\
 &\quad \left. \times ([\Lambda \pm 1 - \eta] L_{n'_r}^{\Lambda \pm 1} + 2n'_r L_{n'_r}^{\Lambda \pm 1} - 2[n'_r + \Lambda] L_{n'_r-1}^{\Lambda \pm 1}) \right]. \tag{C.99}
 \end{aligned}$$

The  $\tilde{L}_{n_r}^\Lambda$  notation (*cf.* Eq. C.82) is used and an equivalent notation for the Hermite polynomials is also introduced

$$\tilde{H}_{n_z} = -\xi H_{n_z} + \frac{dH_{n_z}}{d\xi} = -\xi H_{n_z} + 2n_z H_{n_z-1}. \tag{C.100}$$

Observing that  $\Lambda' = \Lambda \pm 1$ , Eq. C.99 can be written as

$$\begin{aligned}
 \langle \Psi_f | \hat{V}_{\text{s.o.}} | \Psi_i \rangle &= -\lambda \left( \frac{\hbar}{2mc} \right)^2 \left( \frac{m^2 \omega_z \omega_\perp}{\hbar^2} \right)^{\frac{1}{2}} N_{n_z} N_{n'_z} N_{n_r}^\Lambda N_{n'_r}^{\Lambda'} \int_0^{+\infty} d\eta \eta^{(2\Lambda \pm 1 - 1)/2} L_{n_r}^\Lambda L_{n'_r}^{\Lambda'} e^{-\eta} \\
 &\quad \times \int_{-\infty}^{+\infty} d\xi e^{-\xi^2} V_N \left( \Lambda' H_{n'_z} \tilde{H}_{n_z} + \Lambda H_{n_z} \tilde{H}_{n'_z} \right) \\
 &\quad \pm \lambda \left( \frac{\hbar}{2mc} \right)^2 \left( \frac{m^2 \omega_z \omega_\perp}{\hbar^2} \right)^{\frac{1}{2}} N_{n_z} N_{n'_z} N_{n_r}^\Lambda N_{n'_r}^{\Lambda'} \int_0^{+\infty} d\eta \eta^{(2\Lambda \pm 1 - 1)/2} e^{-\eta} \int_{-\infty}^{+\infty} d\xi e^{-\xi^2} V_N \\
 &\quad \times \left( H_{n_z} \tilde{H}_{n'_z} \tilde{L}_{n_r}^\Lambda L_{n'_r}^{\Lambda'} - H_{n'_z} \tilde{H}_{n_z} L_{n_r}^\Lambda \tilde{L}_{n'_r}^{\Lambda'} \right), \tag{C.101}
 \end{aligned}$$

$$\begin{aligned}
 &= -\lambda \left( \frac{\hbar}{2mc} \right)^2 \left( \frac{m^2 \omega_z \omega_\perp}{\hbar^2} \right)^{\frac{1}{2}} N_{n_z} N_{n'_z} N_{n_r}^\Lambda N_{n'_r}^{\Lambda'} \int_0^{+\infty} d\eta \eta^{(2\Lambda \pm 1 - 1)/2} e^{-\eta} \int_{-\infty}^{+\infty} d\xi e^{-\xi^2} V_N \\
 &\quad \times \left( H_{n'_z} \tilde{H}_{n_z} (\Lambda' L_{n_r}^\Lambda L_{n'_r}^{\Lambda'} \pm \tilde{L}_{n'_r}^{\Lambda'} L_{n_r}^\Lambda) + H_{n_z} \tilde{H}_{n'_z} (\Lambda L_{n_r}^\Lambda L_{n'_r}^{\Lambda'} \pm \tilde{L}_{n_r}^\Lambda L_{n'_r}^{\Lambda'}) \right). \tag{C.102}
 \end{aligned}$$

Using again that  $\Lambda - \Lambda' = \pm 1$ , one finally obtains the cross spin-orbit matrix element

$$\begin{aligned}
 \langle \Psi_f | \hat{V}_{\text{s.o.}} | \Psi_i \rangle &= -\lambda \left( \frac{\hbar}{2mc} \right)^2 \left( \frac{m^2 \omega_z \omega_\perp}{\hbar^2} \right)^{\frac{1}{2}} N_{n_z} N_{n'_z} N_{n_r}^\Lambda N_{n'_r}^{\Lambda'} \int_0^{+\infty} d\eta \eta^{(\Lambda + \Lambda' - 1)/2} e^{-\eta} \int_{-\infty}^{+\infty} d\xi e^{-\xi^2} V_N \\
 &\quad \times \left[ H_{n'_z} \tilde{H}_{n_z} (\Lambda' L_{n_r}^\Lambda L_{n'_r}^{\Lambda'} + (\Lambda' - \Lambda) \tilde{L}_{n'_r}^{\Lambda'} L_{n_r}^\Lambda) + H_{n_z} \tilde{H}_{n'_z} (\Lambda L_{n_r}^\Lambda L_{n'_r}^{\Lambda'} + (\Lambda - \Lambda') \tilde{L}_{n_r}^\Lambda L_{n'_r}^{\Lambda'}) \right]. \tag{C.103}
 \end{aligned}$$



# Appendix D

## Numerical Transmission Coefficients

### D.1 Numerical Methods for Transmission Coefficient Calculation

*This appendix describes of the numerical methods that have been implemented to obtain a barrier transmission coefficient from an arbitrary one-dimensional barrier shape cf. Section 6.4 of Chapter 6. It also present some analytical cases that have been used to verify the accuracy of the implemented methods.*

#### Contents

---

<b>D.1 Numerical Methods for Transmission Coefficient Calculation</b>	<b>225</b>
D.1.1 Piece-wise Methods . . . . .	226
D.1.2 JWKB Method . . . . .	228
D.1.3 Derivation of the Numerov Method . . . . .	228
<b>D.2 Analytical Cases . . . . .</b>	<b>229</b>
D.2.1 Step Potential . . . . .	230
D.2.2 Triangular Potential . . . . .	231
D.2.3 Cramer-Nix Original Potential . . . . .	234
D.2.4 Cramer-Nix “Modified” Potential . . . . .	236

---

### D.1.1 Piece-wise Methods

In both piece-wise methods, the potential is locally approximated by either a constant or a linear function thus defining several intervals as illustrated in Fig. D.1.

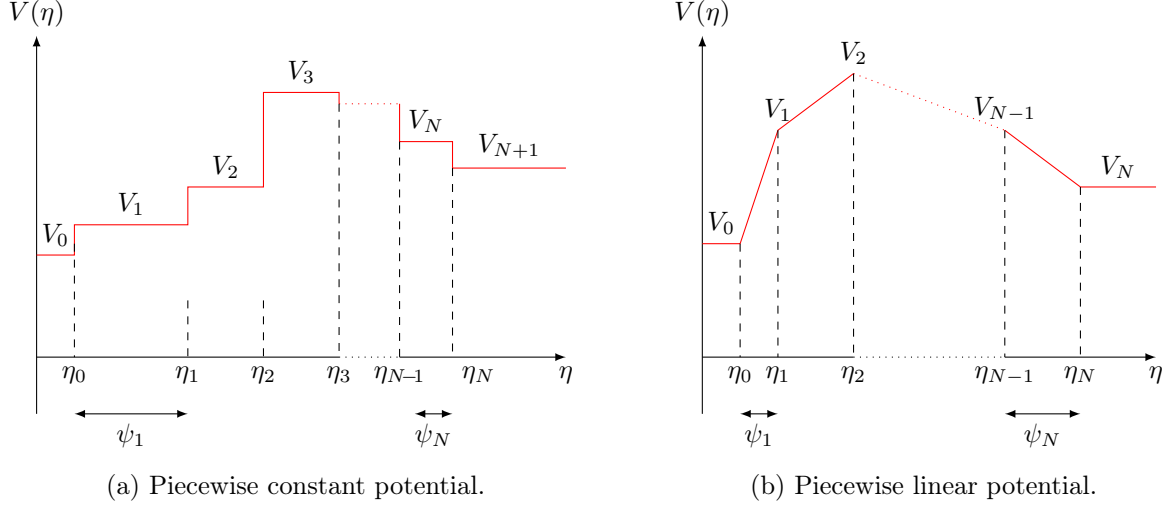


Figure D.1 – Examples of discretization of the potential.

In both methods, two linearly independent solutions can be defined in each interval. They are respectively the positive- and negative-argument exponentials for the piecewise constant potential (Fig D.1a) and the Airy functions  $\text{Ai}$  and  $\text{Bi}$  for piece-wise linear potential (Fig D.1b). In each interval, the analytical solution of the wave function can be expressed as a linear combination of the two linearly independent solutions.

In zone  $n \in \llbracket 1, N \rrbracket$ , the wave function has the form

$$\psi_n(\eta) = \begin{cases} b_n e^{ik_n \eta} + c_n e^{-ik_n \eta} & (\text{constant}) \\ b_n \text{Ai}[X_n(\eta)] + c_n \text{Bi}[X_n(\eta)] & (\text{linear}) \end{cases}, \eta_{n-1} \leq \eta \leq \eta_n \quad (\text{D.1})$$

where  $(b_n, c_n) \in \mathbb{C}^2$  are the expansion coefficients and the  $k_n$  coefficient is given by

$$k_n = \left[ \frac{2\mu}{\hbar^2} (E - V_n) \right]^{1/2} \in \mathbb{C}^*. \quad (\text{D.2})$$

When  $k_n$  is real, it corresponds to the wave number associated with the constant potential in region  $n$ . The parameter  $X_n$  is given by

$$X_n(\eta) = \alpha_n^{1/3} \eta + \frac{\beta_n}{\alpha_n^{2/3}}, \quad (\text{D.3})$$

and is an intermediate linear function of  $\eta$  introduced so that the wave function can be expressed in terms of Airy functions. Parameters  $\alpha_n$  and  $\beta_n$  are defined as

$$\alpha_n = \frac{2\mu}{\hbar^2} \frac{V_n - V_{n-1}}{\eta_n - \eta_{n-1}} \quad \text{and} \quad \beta_n = \frac{2\mu}{\hbar^2} (V_{n-1} - E) - \alpha_n \eta_{n-1}. \quad (\text{D.4})$$

By convention, parameters related to the outermost part of the potential has  $\infty$  subscript. The smooth matching conditions of the wave functions (Eq. D.1) at each interval boundaries provide a linear relation between expansion coefficients  $(c_n, b_c)$  and  $(c_{n+1}, b_{n+1})$ . In

both extremal intervals (and in both methods), the wave function is expanded using the exponential functions.

$$\begin{aligned}\psi_0(\eta) &= b_0 e^{ik_0 \eta} + c_0 e^{-ik_0 \eta} \quad , \quad \eta \leq \eta_0 \quad , \\ \psi_\infty(\eta) = \psi_{N+1}(\eta) &= b_\infty e^{ik_\infty \eta} + c_\infty e^{-ik_\infty \eta} \quad , \quad \eta \geq \eta_N \quad .\end{aligned}\quad (\text{D.5})$$

The conditions  $c_\infty = 0$  and  $b_\infty \in \mathbb{C}^*$ , are often used in order to easily compute the eventual transmission coefficient<sup>1</sup>. From this condition, the smooth continuity relation leads to a recursive relation

$$\begin{bmatrix} b_n \\ c_n \end{bmatrix} = M_n \begin{bmatrix} b_{n+1} \\ c_{n+1} \end{bmatrix} \quad , \quad \begin{bmatrix} b_0 \\ c_0 \end{bmatrix} = \left( \prod_{n=0}^N M_n \right) \begin{bmatrix} b_\infty \\ 0 \end{bmatrix} \quad , \quad (\text{D.6})$$

where  $M_n$  is the matching matrix that defines the relation between coefficients  $b$  and  $c$  related the  $n - 1^{\text{th}}$  segment to those of the  $n^{\text{th}}$  segment. Finally one obtains a linear relation between  $b_0$  and  $b_\infty$ , and the transmission coefficient

$$T(E) = \frac{k_\infty}{k_0} \left| \frac{b_\infty}{b_0} \right|^2 \quad . \quad (\text{D.7})$$

For the piecewise-constant method, the matching matrix  $M_n$  is

$$M_n^{\text{pc}} = \frac{1}{2k_n} \begin{bmatrix} (k_n + k_{n+1})e^{i(k_{n+1}-k_n)\eta_n} & (k_n - k_{n+1})e^{-i(k_{n+1}+k_n)\eta_n} \\ (k_n - k_{n+1})e^{i(k_{n+1}+k_n)\eta_n} & (k_n + k_{n+1})e^{-i(k_{n+1}-k_n)\eta_n} \end{bmatrix} \quad . \quad (\text{D.8})$$

For the linear-constant method the matching matrix  $M_n, n \in \llbracket 1, N - 1 \rrbracket$  is

$$M_n^{\text{lc}} = \pi \begin{bmatrix} \text{Bi}'[X_n^-] \text{Ai}[X_n^+] - \frac{X'_{n+1}}{X'_n} \text{Ai}'[X_n^+] \text{Bi}[X_n^-] & \text{Bi}'[X_n^-] \text{Bi}[X_n^+] - \frac{X'_{n+1}}{X'_n} \text{Bi}'[X_n^+] \text{Bi}[X_n^-] \\ \frac{X'_{n+1}}{X'_n} \text{Ai}'[X_n^+] \text{Ai}[X_n^-] - \text{Ai}'[X_n^-] \text{Ai}[X_n^+] & \frac{X'_{n+1}}{X'_n} \text{Bi}'[X_n^+] \text{Ai}[X_n^-] - \text{Ai}'[X_n^-] \text{Bi}[X_n^+] \end{bmatrix} \quad (\text{D.9})$$

where

$$X'_n = \frac{dX_n}{d\eta} = \alpha_n^{1/3} \quad , \quad (\text{D.10})$$

$$X_n^+ = X_{n+1}(\eta_n) \quad , \quad (\text{D.11})$$

$$X_n^- = X_n(\eta_n) \quad . \quad (\text{D.12})$$

For  $n = 0$  and  $n = N$ , different matching matrices must be used as the potential for  $\eta < \eta_0$  and  $\eta > \eta_N$  is constant. The related  $M_0$  and  $M_N$  matrices are thus given by

$$M_N^{\text{lc}} = \pi \begin{bmatrix} \text{Bi}'[X_N^-] e^{ik_\infty \eta_N} - \frac{ik_\infty}{X'_N} \text{Bi}[X_N^-] e^{ik_\infty \eta_N} & 0 \\ \frac{ik_\infty}{X'_N} \text{Ai}[X_N^-] e^{ik_\infty \eta_N} - \text{Ai}'[X_N^-] e^{ik_\infty \eta_N} & 0 \end{bmatrix} \quad , \quad (\text{D.13})$$

$$M_0^{\text{lc}} = \frac{\pi}{2k_0} \begin{bmatrix} (k_0 \text{Ai}[X_0^+] - iX'_1 \text{Ai}'[X_0^+]) e^{-ik_0 \eta_0} & (k_0 \text{Bi}[X_0^+] - iX'_1 \text{Bi}'[X_0^+]) e^{-ik_0 \eta_0} \\ (k_0 \text{Ai}[X_0^+] + iX'_1 \text{Ai}'[X_0^+]) e^{ik_0 \eta_0} & (k_0 \text{Bi}[X_0^+] + iX'_1 \text{Bi}'[X_0^+]) e^{ik_0 \eta_0} \end{bmatrix} \quad . \quad (\text{D.14})$$

A similar approach can be considered with a piece-wise *quadratic* potential using parabolic cylinder functions as expansion functions, yet the expected gain in the number of intervals is balanced by the cost of “complex” function evaluations.

<sup>1</sup>In practice  $b_\infty$  is set to unity,  $b_\infty = 1$ .

In practice this piecewise-linear method cannot be used alone. Indeed if in a given discretized step  $n$ , the slope of the potential is very low then  $\alpha_n$  (Eq. D.4) tends to zero and  $X_n$  (Eq. D.3) becomes infinite. This leads to numerical issues in the evaluation of the Airy functions. This problem can be solved by considering that for low slopes, the Airy base function are “replaced” by the exponential functions. The method relies thus on a mixed piecewise-constant/linear discretization of the potential.

### D.1.2 JWKB Method

An widely-used alternative method to compute transmission coefficient for arbitrary barrier shapes is the JWKB method [78, 184, 185]. In this so-called semi-classical approach, the wave function of the system  $\Psi$  is expressed as the exponential of another function  $\Phi$ ,  $\Psi = e^\Phi$ , that satisfies the differential equation (*cf.* Eq. 6.35)

$$\Psi''(\eta) + [\Psi'(\eta)]^2 = \frac{2\mu}{\hbar^2}(V(\eta) - E). \quad (\text{D.15})$$

The  $\Phi'$  function is split in its real  $A$  and imaginary  $B$  parts, which are expanded as a power series in  $\hbar$ . To the lowest orders in  $\hbar$ , assuming that  $B$  varies slowly with  $\eta$ , and assuming  $E$  smaller than  $V$  over the considered range of  $\eta$ , one finally obtains [186]

$$\Psi \propto C_{\pm} \left[ \frac{2\mu}{\hbar^2}(V(\eta) - E) \right]^{1/4} \exp \left[ \pm \int d\eta \sqrt{\frac{2\mu}{\hbar^2}(V(\eta) - E)} \right]. \quad (\text{D.16})$$

Finally, for a single-humped barrier, the transmission coefficient can be obtained by [78]

$$T(E) = \exp \left[ -2 \int_{\eta_{\min}}^{\eta_{\max}} d\eta \sqrt{\frac{2\mu}{\hbar^2}(V(\eta) - E)} \right], \quad (\text{D.17})$$

where  $\eta_{\min}$  and  $\eta_{\max}$  are defined by  $V(\eta_{\min}) = V(\eta_{\max}) = E$  and are called *turning points*. In the case of a double-humped barrier, assuming  $a_1$  and  $a_2$  to be the turning points of the first hump and  $a_3$  and  $a_4$  those of the second hump, the transmission coefficient is obtained by [185]

$$T(E) = \frac{64P_AP_B}{(P_AP_B + 16)^2 \cos^2 \varphi + 16(P_A + P_B)^2 \sin^2 \varphi}, \quad (\text{D.18})$$

where

$$\begin{aligned} P_A(E) &= \exp \left[ -2 \int_{a_1}^{a_2} d\eta |k(\eta)| \right], & P_B(E) &= \exp \left[ -2 \int_{a_3}^{a_4} d\eta |k(\eta)| \right], \\ k(\eta) &= \left[ \frac{2\mu}{\hbar^2} [E - V(\eta)] \right]^{1/2}, & \phi(E) &= \int_{a_2}^{a_3} d\eta k(\eta). \end{aligned} \quad (\text{D.19})$$

### D.1.3 Derivation of the Numerov Method

Here the differential equation (Eq. 6.36) is considered

$$f''(x) + W(x)f(x) = 0. \quad (\text{D.20})$$

The  $f$  function can be written, using a Taylor expansion about  $x + h$  and  $x - h$  as

$$f(x + h) = f(x) + hf'(x) + \frac{h^2}{2!}f''(x) + \frac{h^3}{3!}f^{(3)}(x) + \frac{h^4}{4!}f^{(4)}(x) + \frac{h^5}{5!}f^{(5)}(x) + O(h^6), \quad (\text{D.21})$$

$$f(x - h) = f(x) - hf'(x) + \frac{h^2}{2!}f''(x) - \frac{h^3}{3!}f^{(3)}(x) + \frac{h^4}{4!}f^{(4)}(x) - \frac{h^5}{5!}f^{(5)}(x) + O(h^6). \quad (\text{D.22})$$

Using abscissa discretization  $\{x_n\}_n$  and  $\{f_n\}_n$  ( $f_n = f(x_n)$ ), summing the two above expressions yields

$$f_{n+1} + f_{n-1} = h^2 f_n'' + \frac{h^4}{12} f_n^{(4)} + O(h^6), \quad (\text{D.23})$$

$$= -h^2 W_n f_n + \frac{h^4}{12} f_n^{(4)} + O(h^6), \quad (\text{D.24})$$

where the relation in Eq. D.20 has been used and where  $W_n = W(x_n)$ . The double differentiation of Eq. D.20, yields

$$f^{(4)}(x) = -[W(x)f(x)]''. \quad (\text{D.25})$$

The right-hand side of Eq. D.25 can be approximated by its centered finite difference expression

$$[W(x)f(x)]'' \approx \frac{W_{n+1}f_{n+1} - 2W_n f_n + W_{n-1}f_{n-1}}{h^2}. \quad (\text{D.26})$$

Inserting Eqs. D.26 and D.25 into Eq. D.24, one finally obtains

$$f_{n-1} = \frac{\left(2 - \frac{5h^2}{6}W_n\right) f_n - \left(1 + \frac{h^2}{12}W_{n+1}\right) f_{n+1}}{1 + \frac{h^2}{12}W_{n-1}}. \quad (\text{D.27})$$

## D.2 Analytical Cases

To verify the calculation of transmission coefficient for any numerical barrier shape, some analytic cases are tested with the implemented methods. The three types of potential are detailed below:

- The Step Potential.
- The Triangular Potential.
- The Cramer-Nix Original and “Modified” Potentials.

In this section analytical solutions of the Schrödinger equation

$$-\frac{\hbar^2}{2\mu} \frac{d^2\psi}{d\eta^2} + (V(\eta) - E)\psi = 0, \quad (\text{D.28})$$

are given for the three potentials  $V$ , and the related analytical transmission coefficient are derived.

### D.2.1 Step Potential

The step potential is illustrated in Fig. D.2, and is defined by

$$V(\eta) = \begin{cases} 0, & \eta < 0 \\ V_F, & 0 < \eta < a \\ -V_\infty, & \eta > a \end{cases}, \quad (\text{D.29})$$

where  $a$ ,  $V_F$  and  $V_\infty$  are defined in Fig. D.2.

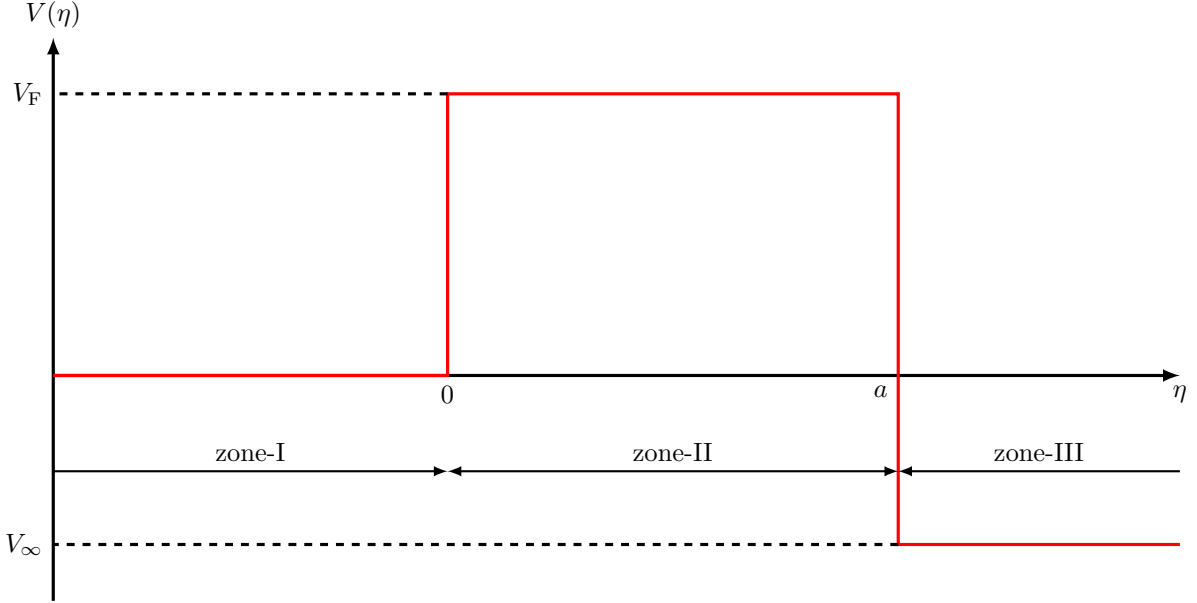


Figure D.2 – Step Potential.

Different analytical wave functions can be defined according to the  $\eta$ -zones shown in Fig. D.2.

$$\psi_{\text{I}}(\eta) = Ae^{ik_0\eta} + Be^{-ik_0\eta}, \quad (\text{D.30})$$

$$\psi_{\text{II}}(\eta) = Ce^{ik_F\eta} + De^{-ik_F\eta}, \quad (\text{D.31})$$

$$\psi_{\text{III}}(\eta) = Fe^{ik_\infty\eta} \quad (\text{D.32})$$

where the wave numbers for the different zones of this potential are defined as

$$k_0 = \sqrt{\frac{2BE}{\hbar^2}}, \quad (\text{D.33})$$

$$k_F = \sqrt{\frac{2B(E - V_F)}{\hbar^2}} \quad (= i\kappa_F, \text{ if } E < V_F), \quad (\text{D.34})$$

$$k_\infty = \sqrt{\frac{2B(E - V_\infty)}{\hbar^2}}. \quad (\text{D.35})$$

Only the plane wave propagating toward  $\eta > 0$  ( $e^{ik_\infty\eta}$ ) is considered in zone III, so that the derivation of the transmission coefficient is eased. The smooth matching conditions for the wave functions at  $\eta = 0$  and  $\eta = a$  leads to a linear relation between  $A$  and  $F$ . The eventual transmission coefficient is obtained by

$$T_f = \frac{k_\infty}{k_0} \left| \frac{F}{A} \right|^2. \quad (\text{D.36})$$

The analytical transmission coefficient, shown in Fig. D.3, is obtained using Eq. D.36 and can be written

$$T(E) = \begin{cases} \frac{4k_F^2 k_0 k_\infty}{[k_F^4 - k_F^2(k_0^2 + k_\infty^2) + k_0^2 k_\infty^2] \sin^2(k_F a) + k_F^2(k_0 + k_\infty)^2}, & E \geq V_F, \\ \frac{4\kappa_F^2 k_0 k_\infty}{[\kappa_F^4 + \kappa_F^2(k_0^2 + k_\infty^2) + k_0^2 k_\infty^2] \sinh^2(\kappa_F a) + \kappa_F^2(k_0 + k_\infty)^2}, & E \leq V_F. \end{cases} \quad (\text{D.37})$$

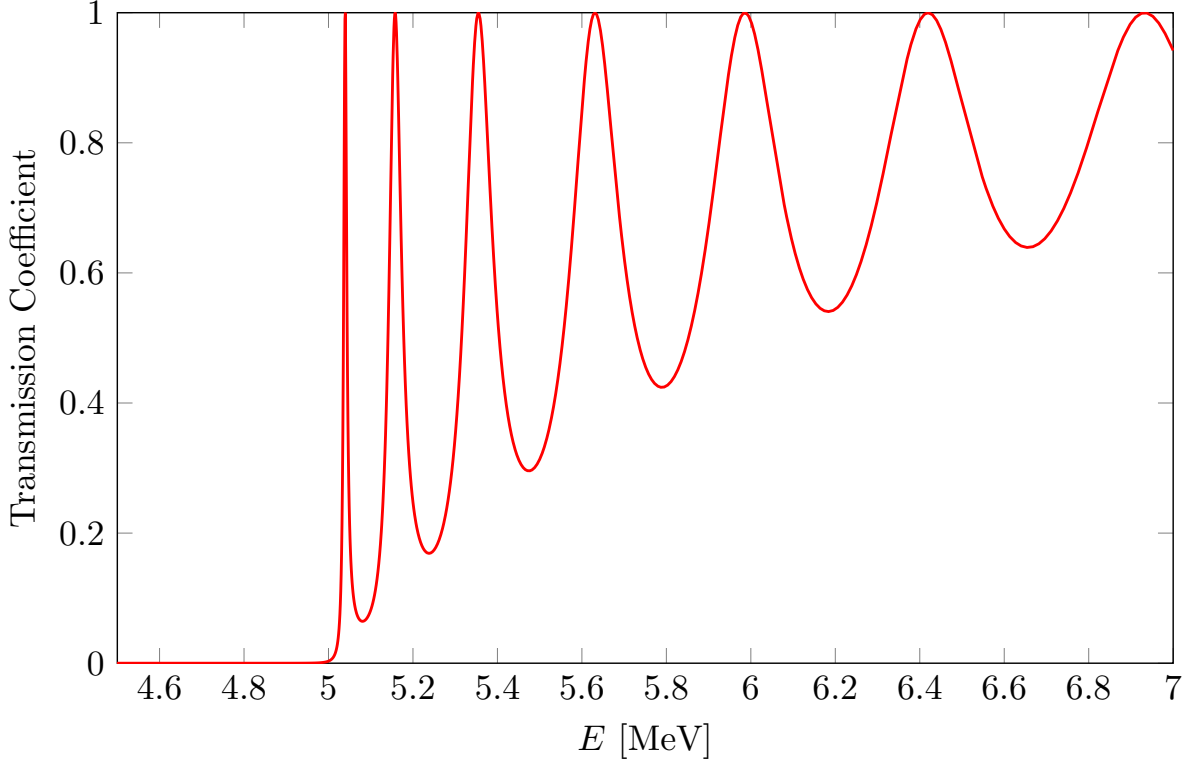


Figure D.3 – Transmission coefficient for a step potential with  $a = 0.5$ ,  $V_F = 5$  MeV,  $V_\infty = 0$  MeV and  $\mu/\hbar^2 = 0.054A^{5/3}$  (in  $\text{MeV}^{-1}$ ) where  $A = 240$ .

### D.2.2 Triangular Potential

In this case the potential is given by

$$V(\eta) = \begin{cases} 0, & \eta < 0 \\ \left(\frac{a-x}{a}\right) V_0, & 0 < \eta \leq a \\ 0, & \eta \geq a \end{cases}, \quad (\text{D.38})$$

where  $a$  and  $V_0$  are defined in Fig. D.4.

In zones I and III the solutions of the Schrödinger equation have the same form than in the case of the step potential, namely

$$\psi_{\text{I}}(\eta) = Ae^{ik\eta} + Be^{-ik\eta}, \quad (\text{D.39})$$

$$\psi_{\text{III}}(\eta) = Fe^{ik\eta}. \quad (\text{D.40})$$

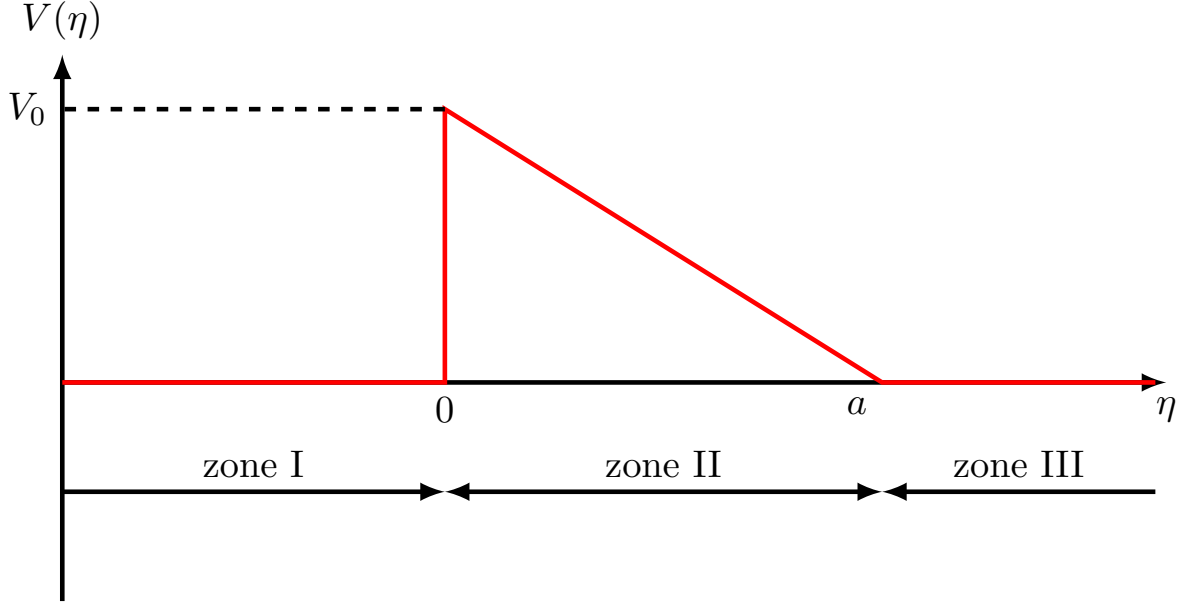


Figure D.4 – Triangular potential.

For zone II, the Schrödinger equation is

$$-\frac{\hbar^2}{2\mu} \frac{d^2\psi_{\text{II}}}{d\eta^2} + \left( \frac{a-\eta}{a} V_0 - E \right) \psi_{\text{II}} = 0. \quad (\text{D.41})$$

It can be turned into

$$\frac{d^2\psi_{\text{II}}}{d\eta^2} - (\alpha\eta + \beta)\psi_{\text{II}} = 0, \quad (\text{D.42})$$

where

$$\alpha = \frac{-2BV_0}{\hbar^2 a} \quad \text{and} \quad \beta = \frac{2B(V_0 - E)}{\hbar^2}. \quad (\text{D.43})$$

The variable change

$$X(\eta) = \alpha^{1/3} \eta + \frac{\beta}{\alpha^{2/3}}, \quad (\text{D.44})$$

is performed. It leads to a simple form of the differential equation

$$\frac{d^2\psi_{\text{II}}}{dX^2} - X\psi_{\text{II}} = 0. \quad (\text{D.45})$$

Two real linearly independent solutions exist for this equation, they are the Airy functions Ai and Bi. The general solution can be expressed as a linear combination of the two, namely

$$\psi_{\text{II}}(\eta) = C \text{Ai}[X(\eta)] + D \text{Bi}[X(\eta)]. \quad (\text{D.46})$$

The continuity conditions of the value and derivative of the wave functions  $\psi_{\text{I}}$  and  $\psi_{\text{II}}$  at  $\eta = a$  leads to the system of equations

$$\begin{cases} C \text{Ai}[X_a] + D \text{Bi}[X_a] = F e^{ika}, \\ C X' \text{Ai}'[X_a] + D X' \text{Bi}'[X_a] = ik F e^{ika}, \end{cases} \quad (\text{D.47})$$

where  $X_a = X(a)$  and  $X' = \frac{dX}{d\eta} = \alpha^{1/3}$ . Using that the Wronskian of the Airy functions [48]  $W(\text{Ai}, \text{Bi}) = \pi^{-1}$ , the system can be solved as long as the slope  $V_0/a$  is not zero.



The coefficients  $C$  and  $D$  are thus obtained by

$$C = \frac{\pi F}{X'} \begin{vmatrix} e^{ika} & \text{Bi}[X_a] \\ ik e^{ika} & X' \text{Bi}'[X_a] \end{vmatrix}, \quad D = \frac{\pi F}{X'} \begin{vmatrix} \text{Ai}[X_a] & e^{ika} \\ X' \text{Ai}'[X_a] & ik e^{ika} \end{vmatrix}. \quad (\text{D.48})$$

The smooth continuity conditions in  $\eta = 0$  leads to a second system of equations

$$\begin{cases} A + B &= C \text{Ai}[X_0] + D \text{Bi}[X_0], \\ ikA - ikB &= CX' \text{Ai}'[X_0] + DX' \text{Bi}'[X_0], \end{cases} \quad (\text{D.49})$$

where again  $X_0 = X(\eta = 0)$ . The system can be written as

$$\begin{cases} A + B &= C \text{Ai}[X_0] + D \text{Bi}[X_0], \\ A - B &= C \frac{X'}{ik} \text{Ai}'[X_0] + D \frac{X'}{ik} \text{Bi}'[X_0]. \end{cases} \quad (\text{D.50})$$

Finally  $A$  can then be expressed as

$$A = \frac{1}{2} \left[ C \left( \text{Ai}[X_0] + \frac{X'}{ik} \text{Ai}'[X_0] \right) + D \left( \text{Bi}[X_0] + \frac{X'}{ik} \text{Bi}'[X_0] \right) \right]. \quad (\text{D.51})$$

The transmission coefficient for this potential can be computed as

$$T = \left| \frac{F}{A} \right|^2. \quad (\text{D.52})$$

Figure D.5 shows an illustration of calculations using this type of transmission coefficient.

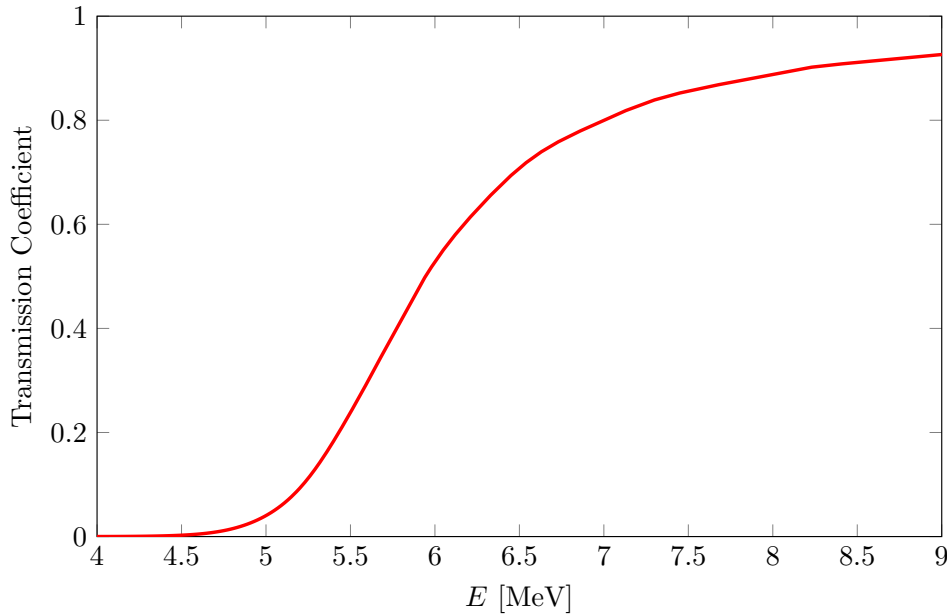


Figure D.5 – Transmission coefficient for triangular potential having  $a = 0.5$ ,  $V_0 = 5$  MeV and  $\mu/\hbar^2 = 0.054A^{5/3}$  (in  $\text{MeV}^{-1}$ ) where  $A = 240$ .

### D.2.3 Cramer-Nix Original Potential

In this case the potential is given by [22]

$$V(\eta) = \begin{cases} E_1 - \frac{1}{2}\mu\omega_1^2(\eta - \eta_1)^2, & \eta \leq a \\ E_2 + \frac{1}{2}\mu\omega_2^2(\eta - \eta_2)^2, & a \leq \eta \leq b \\ E_3 - \frac{1}{2}\mu\omega_3^2(\eta - \eta_3)^2, & \eta \geq b \end{cases} \quad (\text{D.53})$$

and is illustrated in Fig. D.6, where the related parameters  $E_1, E_2, E_3, \eta_1, \eta_2, \eta_3, a$  and  $b$  are shown. Parameters  $\omega_1, \omega_2, \omega_3$  characterize the curvature of the parabola shown in Fig. D.6, and  $\mu$  is the inertia parameter.

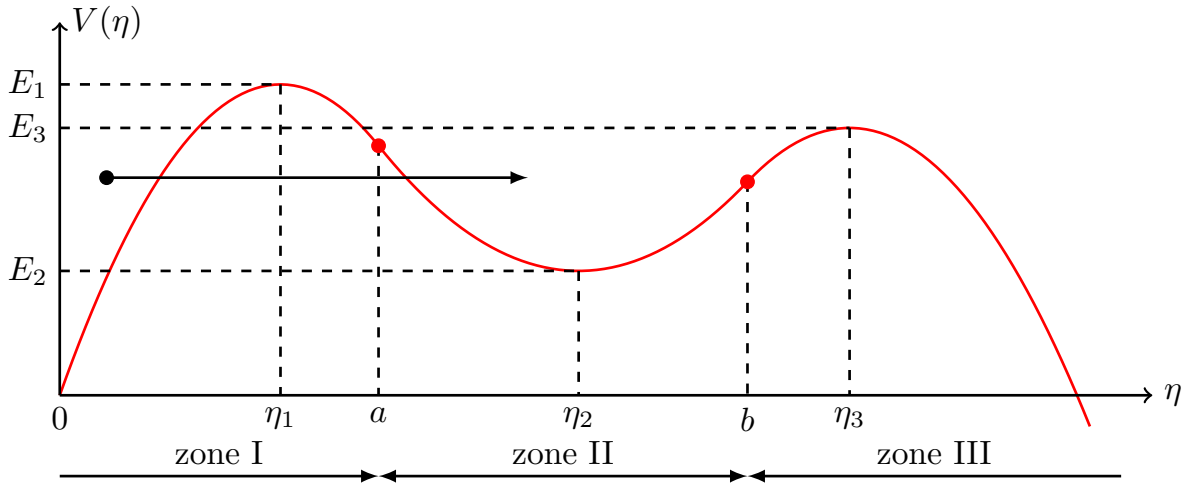


Figure D.6 – Triple parabola barrier.

By imposing a smooth continuity of the potential in  $a$  and  $b$ , the number of parameters required to define the potential can be reduced. By additionally setting  $V(\eta = 0) = 0$  – as shown in Fig. D.6 – the number of required parameters drops to six. Those are chosen to be  $E_1, E_2, E_3, \omega_1, \omega_2$  and  $\omega_3$ . The other parameters are deduced according to

$$\begin{aligned} \eta_1 &= \left[ \frac{2E_1}{\mu\omega_1^2} \right]^{1/2}, \\ a &= \eta_1 + \left[ \frac{2(E_1 - E_2)}{\mu\omega_1^2} \right]^{1/2} \left( 1 + \frac{\omega_1^2}{\omega_2^2} \right)^{-1/2}, \\ \eta_2 &= a + \left[ \frac{2(E_1 - E_2)}{\mu\omega_2^2} \right]^{1/2} \left( 1 + \frac{\omega_2^2}{\omega_1^2} \right)^{-1/2}, \\ b &= \eta_2 + \left[ \frac{2(E_3 - E_2)}{\mu\omega_2^2} \right]^{1/2} \left( 1 + \frac{\omega_2^2}{\omega_3^2} \right)^{-1/2}, \\ \eta_3 &= b + \left[ \frac{2(E_3 - E_2)}{\mu\omega_3^2} \right]^{1/2} \left( 1 + \frac{\omega_3^2}{\omega_2^2} \right)^{-1/2}. \end{aligned} \quad (\text{D.54})$$

In zone I, the Schrödinger equation is

$$-\frac{\hbar^2}{2\mu} \frac{d^2\psi_I}{d\eta^2} + \left( E_1 - \frac{1}{2}\mu\omega_1^2(\eta - \eta_1) - E \right) \psi_I = 0. \quad (\text{D.55})$$

Performing the variable change  $u = \sqrt{\frac{2\mu\omega_1}{\hbar}}(\eta - \eta_1)$ , Eq. D.55 becomes

$$\frac{d^2\psi_I}{du^2} + \left( \frac{E - E_1}{\hbar\omega_1} + \frac{u^2}{4} \right) \psi_I = 0. \quad (\text{D.56})$$

Defining the parameter  $\alpha_1 = \frac{E_1 - E}{\hbar\omega_1}$  and using it in Eq. D.56, one obtains

$$\frac{d^2\psi_I}{du^2} + \left( -\alpha_1 + \frac{u^2}{4} \right) \psi_I = 0. \quad (\text{D.57})$$

The solutions of this equation are known as the *parabolic cylinder functions*  $\mathcal{E}$  and  $\mathcal{E}^*$  (cf. Ref. [48]) and  $\psi_I$  can be expanded using these functions

$$\psi_I(\eta) = A\mathcal{E}^*[\alpha_1, -u(\eta)] + B\mathcal{E}[\alpha_1, -u(\eta)]. \quad (\text{D.58})$$

In zone II, the Schrödinger equation is

$$\frac{-\hbar^2}{2\mu} \frac{d^2\psi_{II}}{d\eta^2} + \left( E_2 + \frac{1}{2}\mu\omega_2^2(\eta - \eta_2) - E \right) \psi_{II} = 0 \quad (\text{D.59})$$

This equation is transformed using the variable change  $v = \sqrt{\frac{2\mu\omega_2}{\hbar}}(\eta - \eta_2)$  into

$$\frac{d^2\psi_{II}}{dv^2} + \left( \frac{E - E_2}{\hbar\omega_2} - \frac{v^2}{4} \right) \psi_{II} = 0. \quad (\text{D.60})$$

Defining the coefficient  $\alpha_2 = \frac{E_2 - E}{\hbar\omega_2}$ , one gets

$$\frac{d^2\psi_{II}}{dv^2} - \left( \alpha_2 + \frac{v^2}{4} \right) \psi_{II} = 0. \quad (\text{D.61})$$

Solutions of this equation are different kinds of parabolic cylinder functions  $\mathcal{U}$  and  $\mathcal{V}$  (cf. Ref. [48]), so that  $\psi_{II}$  can be expressed as

$$\psi_{II}(\eta) = C\mathcal{U}[\alpha_2, v(\eta)] + D\mathcal{V}[\alpha_2, v(\eta)]. \quad (\text{D.62})$$

For zone III, a similar treatment than for zone I is made. Defining  $w = \sqrt{\frac{2\mu\omega_3}{\hbar}}(\eta - \eta_3)$  and  $\alpha_3 = \frac{E_3 - E}{\hbar\omega_3}$ , one obtains

$$\frac{d^2\psi_{III}}{dw^2} + \left( -\alpha_3 + \frac{w^2}{4} \right) \psi_{III} = 0, \quad (\text{D.63})$$

and

$$\psi_{III}(\eta) = F\mathcal{E}[\alpha_3, w(\eta)]. \quad (\text{D.64})$$

Only one term is considered in this case as only the component associated with the wave propagating towards  $\eta > 0$  ( $\mathcal{E}$ ) is kept (in order to obtain the transmission coefficient more easily).

Coefficients  $A$ ,  $B$ ,  $C$ ,  $D$  can be expressed in terms of  $F$  by successively matching the value and derivative of the wave functions at  $\eta = b$  and  $\eta = a$ . The transmission coefficient can be computed as [22]

$$T = \sqrt{\frac{\omega_3}{\omega_1}} \left| \frac{F}{A} \right|^2, \quad (\text{D.65})$$

where

$$\frac{F}{A} = \frac{v'u'2i\sqrt{2/\pi}}{\begin{vmatrix} \mathcal{E}_a(\alpha_1, -u) & -\mathcal{V}_a(\alpha_2, v) & -\mathcal{U}_a(\alpha_2, v) & 0 \\ -u'\mathcal{E}_a^{(-u)}(\alpha_1, -u) & -v'\mathcal{V}_a^{(v)}(\alpha_2, v) & -v'\mathcal{U}_a^{(v)}(\alpha_2, v) & 0 \\ 0 & \mathcal{V}_b(\alpha_2, v) & \mathcal{U}_b(\alpha_2, v) & -\mathcal{E}_b(\alpha_3, w) \\ 0 & v'\mathcal{V}_b^{(v)}(\alpha_2, v) & v'\mathcal{U}_b^{(v)}(\alpha_2, v) & -w'\mathcal{E}_b^{(w)}(\alpha_3, w) \end{vmatrix}}. \quad (\text{D.66})$$

The subscripts on the parabolic cylinder functions specify the value of  $\eta$  at which the second parameter must be evaluated. The superscript on the functions indicates the first order derivative of the function with respect of the variable in parentheses. The prim over  $u$ ,  $v$  or  $w$  stands for their derivatives with respect of  $\eta$ . The energy dependence of the related transmission coefficient is shown in Fig. D.7.

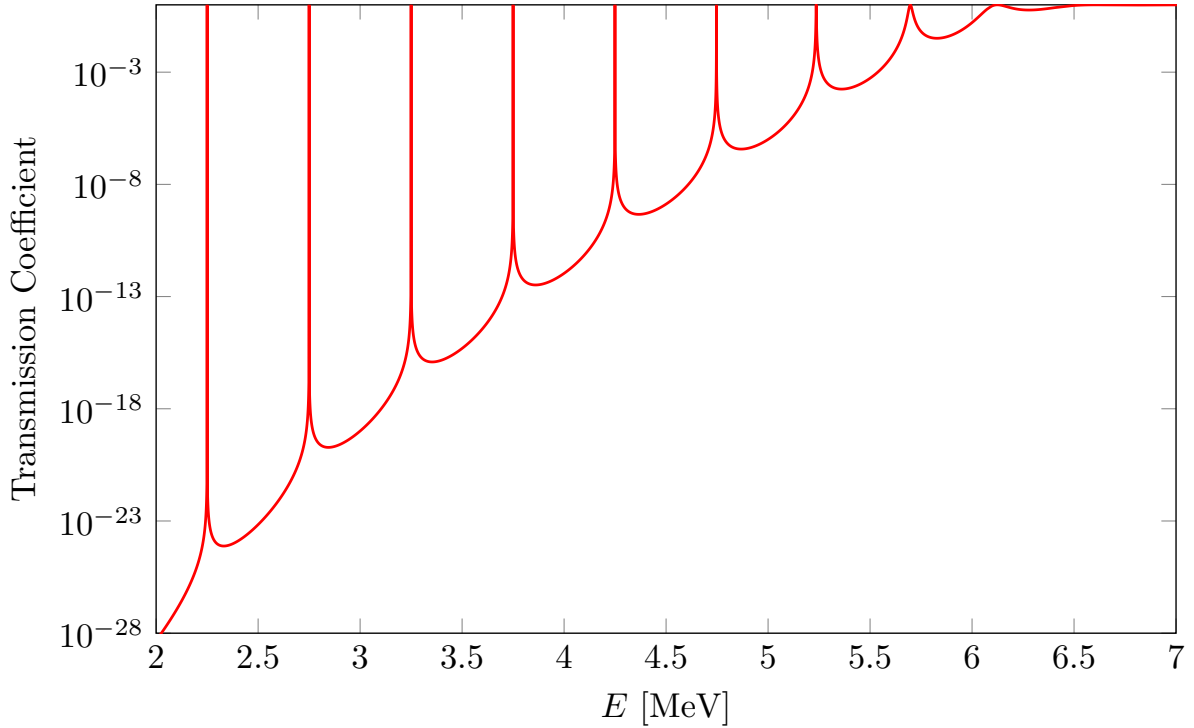


Figure D.7 – Transmission coefficient for a triple parabola potential with values  $E_1 = E_3 = 6$  MeV,  $E_2 = 2$  MeV,  $\hbar\omega_1 = \hbar\omega_3 = 1$  MeV,  $\hbar\omega_2 = 0.5$  MeV,  $\mu/\hbar^2 = 0.054A^{5/3}$  (in  $\text{MeV}^{-1}$ ) where  $A = 240$ .

#### D.2.4 Cramer-Nix “Modified” Potential

With the approach of the previous section, no reflected wave is considered in zone III. In the following, the Cramer-Nix model is modified so that a reflection in the outer barrier

zone can be added. The following potential is considered

$$V(\eta) = \begin{cases} 0, & \eta \leq 0 \\ E_1 - \frac{1}{2}\mu\omega_1^2(\eta - \eta_1)^2, & 0 \leq \eta \leq a \\ E_2 + \frac{1}{2}\mu\omega_2^2(\eta - \eta_2)^2, & a \leq \eta \leq b \\ E_3 - \frac{1}{2}\mu\omega_3^2(\eta - \eta_3)^2, & b \leq \eta \leq c \\ V_\infty, & \eta \geq c \end{cases} \quad (\text{D.67})$$

An illustration is shown in Fig. D.8 where the same parameters than in Fig. D.6 are introduced with the addition of the parameters  $c$  and  $V_\infty$ .

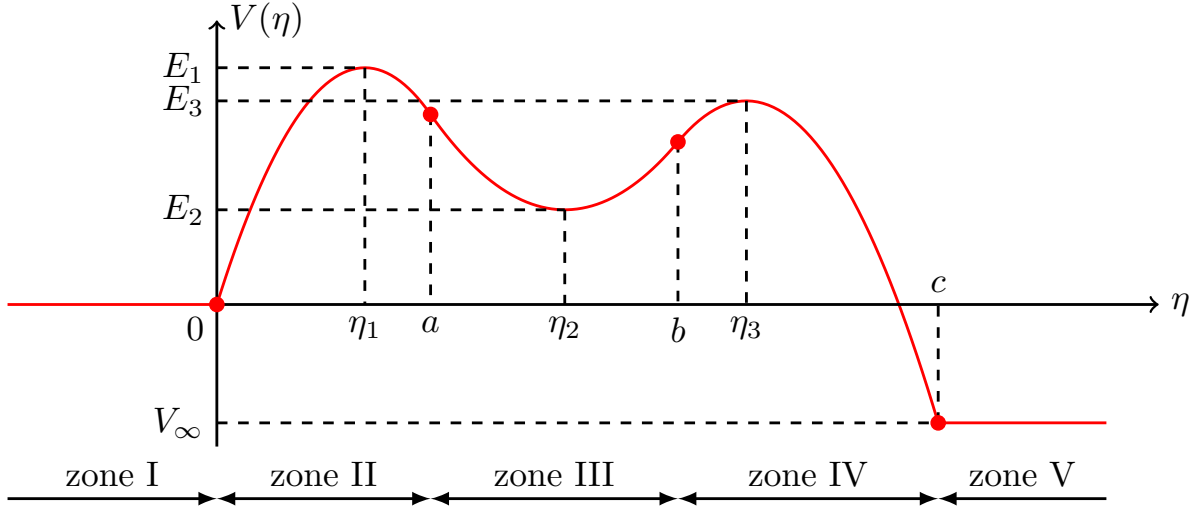


Figure D.8 – Triple parabola barrier with reflection condition.

Relations D.54 are still valid, but there is a need for a new parameter to describe the potential. It can be either  $c$  or  $V_\infty$ , here  $V_\infty$  is selected and  $c$  is deduced by

$$c = \eta_3 + \left[ \frac{2(E_3 - V_\infty)}{B\omega_3^2} \right]^{1/2}. \quad (\text{D.68})$$

The wave numbers related to zone-I and zone-V are given by

$$k_0 = \sqrt{\frac{2BE}{\hbar^2}} \quad \text{and} \quad k_\infty = \sqrt{\frac{2B(E - V_\infty)}{\hbar^2}}. \quad (\text{D.69})$$

The wave function forms can be deduced from the previous sections

$$\psi(\eta) = \begin{cases} \psi_{\text{I}}(\eta) &= Y e^{ik_0\eta} &+ Z e^{-ik_0\eta} & \eta \leq 0 \\ \psi_{\text{II}}(\eta) &= A \mathcal{E}^*[\alpha_1, -u(\eta)] &+ B \mathcal{E}[\alpha_1, -u(\eta)] & 0 \leq \eta \leq a \\ \psi_{\text{III}}(\eta) &= C \mathcal{W}[\alpha_2, v(\eta)] &+ D \mathcal{V}[\alpha_2, v(\eta)] & a \leq \eta \leq b \\ \psi_{\text{IV}}(\eta) &= F \mathcal{E}[\alpha_3, w(\eta)] &+ G \mathcal{E}^*[\alpha_3, w(\eta)] & b \leq \eta \leq c \\ \psi_{\text{V}}(\eta) &= H e^{ik_\infty\eta} & & \eta \geq c \end{cases}. \quad (\text{D.70})$$

A similar attempt was made in Ref. [187], where the original Cramer-Nix model was refined in order to keep a parabolic cylinder function expansion up to the second hump maximum.

The present attempt is more suited for the validation of the numerical methods that have been implemented for the present study. The transmission coefficient is defined by

$$T(E) = \frac{k_\infty}{k_0} \left| \frac{H}{Y} \right|^2. \quad (\text{D.71})$$

The  $H$  coefficient can be chosen arbitrarily in  $\mathbb{C}^*$  (e.g.  $H = 1$ ). The smooth continuity relations at  $\eta = c, b, a, 0$  provide the remaining coefficients. The smooth continuity relation in  $\eta = c$  gives

$$F = \frac{iHe^{ik_\infty c}}{2w'} \left| \begin{array}{cc} 1 & \mathcal{E}_c^*(\alpha_3, w) \\ ik_\infty & w' \mathcal{E}_c^{*(w)}(\alpha_3, w) \end{array} \right|, \quad G = \frac{iHe^{ik_\infty c}}{2w'} \left| \begin{array}{cc} \mathcal{E}_c(\alpha_3, w) & 1 \\ w' \mathcal{E}_c^{(w)}(\alpha_3, w) & ik_\infty \end{array} \right|. \quad (\text{D.72})$$

The smooth continuity relation in  $\eta = b$  gives

$$C = \sqrt{\frac{\pi}{2}} \frac{1}{v'} \left| \begin{array}{cc} L_b & \mathcal{V}_b(\alpha_2, v) \\ R_b & v' \mathcal{V}_b^{(v)}(\alpha_2, v) \end{array} \right|, \quad D = \sqrt{\frac{\pi}{2}} \frac{1}{v'} \left| \begin{array}{cc} \mathcal{U}_b(\alpha_2, v) & L_b \\ v' \mathcal{U}_b^{(v)}(\alpha_2, v) & R_b \end{array} \right|, \quad (\text{D.73})$$

where

$$\begin{aligned} L_b &= F \mathcal{E}_b(\alpha_3, w) + G \mathcal{E}_b^*(\alpha_3, w), \\ R_b &= F w' \mathcal{E}_b^{(w)}(\alpha_3, w) + G w' \mathcal{E}_b^{*(w)}(\alpha_3, w). \end{aligned} \quad (\text{D.74})$$

The smooth continuity relations in  $\eta = a$  give

$$A = \frac{-i}{2u'} \left| \begin{array}{cc} L_a & \mathcal{E}_a(\alpha_1, -u) \\ R_a & -u' \mathcal{E}_a^{(-u)}(\alpha_1, -u) \end{array} \right|, \quad B = \frac{-i}{2u'} \left| \begin{array}{cc} \mathcal{E}_a^*(\alpha_1, -u) & L_a \\ -u' \mathcal{E}_a^{*(u)}(\alpha_1, -u) & R_a \end{array} \right|, \quad (\text{D.75})$$

where

$$\begin{aligned} L_a &= C \mathcal{U}_a(\alpha_2, v) + D \mathcal{V}_a(\alpha_2, v), \\ R_a &= C v' \mathcal{U}_a^{(v)}(\alpha_2, v) + D v' \mathcal{V}_a^{(v)}(\alpha_2, v). \end{aligned} \quad (\text{D.76})$$

The smooth continuity relation in  $\eta = 0$  gives

$$\begin{cases} Y + Z = A \mathcal{E}_0^*(\alpha_1, -u) + B \mathcal{E}_0(\alpha_1, -u) & = L_0, \\ ik_0 Y - ik_0 Z = -u' A \mathcal{E}_0^{*(-u)}(\alpha_1, -u) - u' B \mathcal{E}_0^{(-u)}(\alpha_1, -u) & = R_0. \end{cases} \quad (\text{D.77})$$

So that finally coefficient  $Y$  can be obtained by

$$Y = \frac{1}{2} \left( L_0 + \frac{R_0}{ik_0} \right). \quad (\text{D.78})$$

Finally, the transmission coefficient can be computed inserting Eq. D.78 into Eq. D.71. The energy dependency of this coefficient is shown in Fig. D.9 and is compared with the Cramer-Nix original model. It can be seen that this modification can have significant effects compared with the original model, especially for energies near the barrier height.

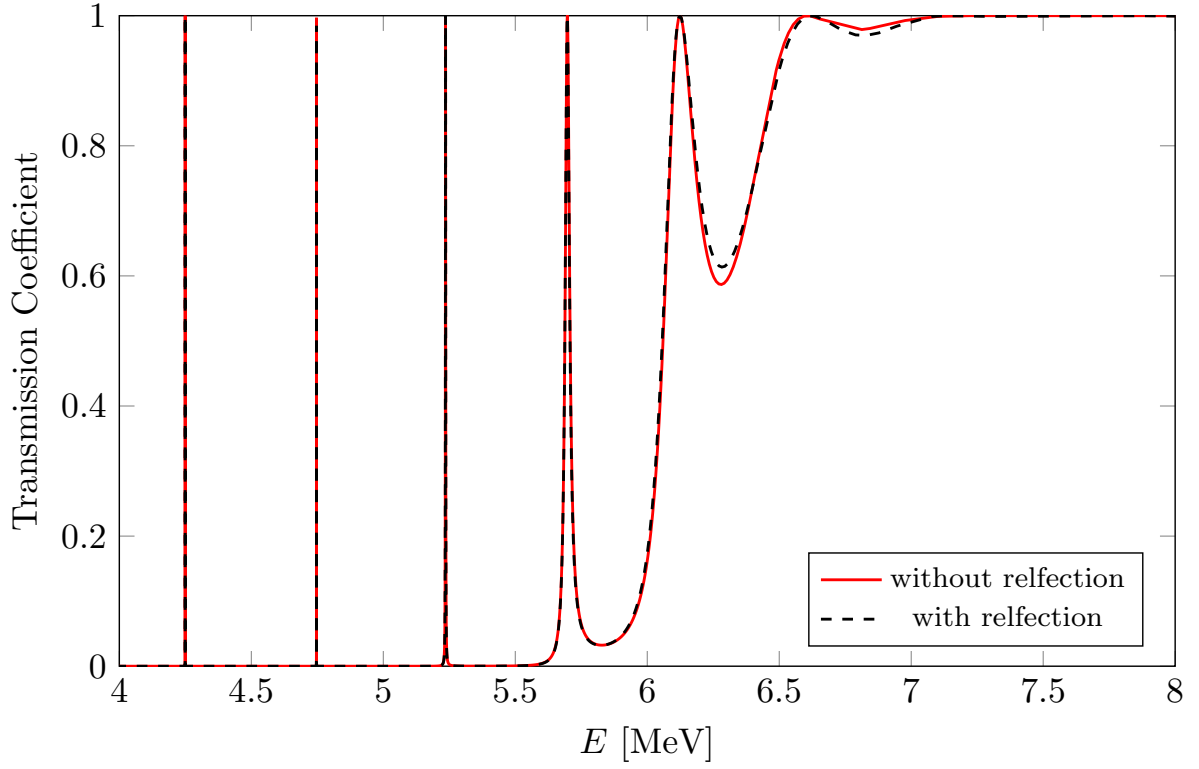


Figure D.9 – Transmission coefficient for a triple parabola potential with values  $E_1 = E_3 = 6$  MeV,  $E_2 = 2$  MeV,  $\hbar\omega_1 = \hbar\omega_3 = 1$  MeV,  $\hbar\omega_2 = 0.5$  MeV,  $\mu/\hbar^2 = 0.054A^{5/3}$  (in  $\text{MeV}^{-1}$ ) where  $A = 240$ .





# Bibliography

- [1] J. Raynal, “Notes on ECIS94,” Tech. Rep. CEA-N-2772, pp. 1–145, Commissariat à l’Énergie Atomique, Saclay, France, 1994.
- [2] A. J. Koning, S. Hilaire, and M. C. Duijvestijn, “Talys-1.0,” in Bersillon *et al.* [51], pp. 211–214. Nice, France, April 22 - 27.
- [3] C. De Saint Jean, B. Habert, O. Litaize, G. Noguère, and C. Suteau, “Status of CONRAD, a nuclear reaction analysis tool,” *EDP Sciences*, vol. 1, pp. 251–254, 2008.
- [4] E. P. Wigner and L. Eisenbud, “Higher Angular Momenta and Long Range Interaction in Resonance Reactions,” *Phys. Rev.*, vol. 72, pp. 29–41, July 1947.
- [5] A. M. Lane and R. G. Thomas, “R-Matrix Theory of Nuclear Reactions,” *Rev. Mod. Phys.*, vol. 30, pp. 257–353, 1958.
- [6] C. W. Reich and M. S. Moore, “Multilevel Formula for the Fission Process,” *Phys. Rev.*, vol. 111, pp. 929–933, Aug. 1958.
- [7] J. E. Lynn, “Fission in nuclear reaction theory,” *Journal of Physics A: Mathematical, Nuclear and General*, vol. 6, no. 4, p. 542, 1973.
- [8] W. Hauser and H. Feshbach, “The Inelastic Scattering of Neutrons,” *Phys. Rev.*, vol. 87, pp. 366–373, July 1952.
- [9] A. Gilbert and A. G. W. Cameron, “A composite nuclear-level density formula with shell corrections,” *Canadian Journal of Physics*, vol. 43, no. 8, pp. 1446–1496, 1965.
- [10] R. Capote, M. Herman, P. Obložinský, P. G. Young, S. Goriely, T. Belgya, A. V. Ignatyuk, A. J. Koning, S. Hilaire, V. A. Plujko, M. Avrigeanu, O. Bersillon, M. B. Chadwick, T. Fukahori, Z. Ge, Y. Han, S. Kailas, J. Kopecky, V. M. Maslov, G. Reffo, M. Sin, S. Soukhovitskii, Efrem, and P. Talou, “RIPL – Reference Input Parameter Library for Calculation of Nuclear Reactions and Nuclear Data Evaluations,” *Nuclear Data Sheets*, vol. 110, no. 12, pp. 3107–3214, 2009. Special Issue on Nuclear Reaction Data.
- [11] D. L. Hill and J. A. Wheeler, “Nuclear Constitution and the Interpretation of Fission Phenomena,” *Phys. Rev.*, vol. 89, pp. 1102–1145, Mar. 1953.
- [12] P. Möller, J. R. Nix, W. D. Myers, and W. J. Swiatecki, “Nuclear Ground-State Masses and Deformations,” *Atomic Data and Nuclear Data Tables*, vol. 59, p. 185, 1995.
- [13] C. Weizsäcker, “Zur Theorie der Kernmassen,” *Zeitschrift für Physik*, vol. 96, no. 7–8, pp. 431–458, 1935.

- [14] H. A. Bethe and R. F. Bacher, “Nuclear Physics A. Stationary States of Nuclei,” *Rev. Mod. Phys.*, vol. 8, pp. 82–229, Apr. 1936.
- [15] V. M. Strutinsky, “Shell effects in nuclear masses and deformation energies,” *Nuclear Physics A*, vol. 95, no. 2, pp. 420–442, 1967.
- [16] P. Möller, A. J. Sierk, T. Ichikawa, A. Iwamoto, R. Bengtsson, H. Uhrenholt, and S. Åberg, “Heavy-element fission barriers,” *Phys. Rev. C*, vol. 79, p. 064304, June 2009.
- [17] K. T. R. Davies, A. J. Sierk, and J. R. Nix, “Effect of viscosity on the dynamics of fission,” *Phys. Rev. C*, vol. 13, pp. 2385–2403, June 1976.
- [18] D. R. Inglis, “Nuclear Moments of Inertia due to Nucleon Motion in a Rotating Well,” *Phys. Rev.*, vol. 103, pp. 1786–1795, Sep 1956.
- [19] S. Belyaev, “Effect of Pairing Correlations on Nuclear Properties,” *Mat. Fys. Medd. Dan. Vid. Selsk.*, vol. 31, no. 11, 1959.
- [20] M. Brack, J. Damgaard, A. S. Jensen, H.-C. Pauli, V. M. Strutinsky, and C.-Y. Wong, “Funny Hills: The Shell-Correction Approach to Nuclear Shell Effects and Its Applications to the Fission Process,” *Rev. Mod. Phys.*, vol. 44, pp. 320–405, Apr. 1972.
- [21] B. V. Numerov, “Note on the numerical integration of  $d^2x/dt^2 = f(x, t)$ ,” *Astronomische Nachrichten*, vol. 230, no. 19, pp. 359–364, 1927.
- [22] J. D. Cramer and J. R. Nix, “Exact Calculation of the Penetrability Through Two-Peaked Fission Barriers,” *Phys. Rev. C*, vol. 2, pp. 1048–1057, Sep 1970.
- [23] J. E. Lynn, “Systematics for Neutron Reactions of the Actinide Nuclei,” tech. rep., UKAEA Research Group, Harwell. Atomic Energy Research Establishment., Nov. 1974. AERE-R-7468.
- [24] O. Bouland, J. E. Lynn, and P. Talou, “*R*-matrix analysis and prediction of low-energy neutron-induced fission cross sections for a range of Pu isotopes,” *Phys. Rev. C*, vol. 88, p. 054612, Nov. 2013.
- [25] A. Carlson, V. Pronyaev, D. Smith, N. Larson, Z. Chen, G. Hale, F.-J. Hambsch, E. Gai, S.-Y. Oh, S. Badikov, T. Kawano, H. Hofmann, H. Vonach, and S. Tegen, “International Evaluation of Neutron Cross Section Standards,” *Nuclear Data Sheets*, vol. 110, no. 12, pp. 3215–3324, 2009. Special Issue on Nuclear Reaction Data.
- [26] R. E. MacFarlane, D. W. Muir, R. M. Boicourt, and A. C. Kahler, “The NJOY Nuclear Data Processing System, Version 2012,” tech. rep., Los Alamos National Laboratory, Dec. 2012.
- [27] J.-C. Sublet and M. Ribon, Pierre Coste-Delclaux, “CALENDF-2010 : User Manual,” tech. rep., CEA, 2011.
- [28] P. Reuss, *Neutron Physics*. Génie Atomique, EDP Sciences, 2012.

- [29] O. H. Bouland, *Amélioration du calcul de l'autoprotection des résonances résolues par un traitement quasi exact du ralentissement des neutrons*. PhD thesis, Université Paris 11, 1994.
- [30] H. C. Honeck, “ENDF Description and Specifications,” Tech. Rep. BNL-8381, Jan. 1965.
- [31] H. C. Honeck, S. Pearlstein, Brookhaven National Laboratory., and U.S. Atomic Energy Commission., “ENDF/B: specifications for an evaluated nuclear data file for reactor applications,” Tech. Rep. BNL-50066, 1967.
- [32] M. Herman and A. Trkov, “ENDF-6 Formats Manual. Data Formats and Procedures for the Evaluated Nuclear Data File ENDF/B-VI and ENDF/B-VII,” Tech. Rep. BNL-90365-2009 Rev.1, Brookhaven National Laboratory, July 2010.
- [33] C. M. Mattoon, B. R. Beck, N. R. Patel, N. C. Summers, G. W. Hedstrom, and D. A. Brown, “Generalized Nuclear Data: A New Structure (with Supporting Infrastructure) for Handling Nuclear Data,” *Nuclear Data Sheets*, vol. 113, no. 12, pp. 3145–3171, 2012. Special Issue on Nuclear Reaction Data.
- [34] P. A. Seeger, A. Hemmendinger, and B. C. Diven, “Fission cross sections of  $^{241}\text{Am}$  and  $^{242m}\text{Am}$ ,” *Nuclear Physics A*, vol. 96, no. 3, pp. 605–616, 1967.
- [35] J. H. McNally, J. W. Barnes, B. J. Dropesky, P. A. Seeger, and K. Wolfsberg, “Neutron-induced fission cross section of  $^{237}\text{U}$ ,” *Phys. Rev. C*, vol. 9, pp. 717–722, Feb 1974.
- [36] E. Privas, *Contribution à l'Évaluation des Incertitudes sur les Sections Efficaces Neutroniques, pour les Réacteurs à Neutrons Rapides*. PhD thesis, Institut polytechnique de Grenoble, 2015.
- [37] K. Shibata, O. Iwamoto, T. Nakagawa, N. Iwamoto, A. Ichihara, S. Kunieda, S. Chiba, K. Furutaka, N. Otuka, T. Ohasawa, T. Murata, H. Matsunobu, A. Zukeran, S. Kamada, and J.-i. Katakura, “JENDL-4.0: A New Library for Nuclear Science and Engineering,” *Journal of Nuclear Science and Technology*, vol. 48, no. 1, pp. 1–30, 2011.
- [38] B. Habert, *Estimation des incertitudes dans l'évaluation des sections efficaces de réactions nucléaires*. PhD thesis, Institut polytechnique de Grenoble, 2009.
- [39] L. W. Weston and J. H. Todd, “Subthreshold Fission Cross Section of  $^{240}\text{Pu}$  and the Fission Cross Sections of  $^{235}\text{U}$  and  $^{239}\text{Pu}$ ,” *Nuclear Science and Engineering*, vol. 88, pp. 567–578, Dec. 1984.
- [40] D. H. Byers, B. C. Diven, and M. G. Silbert, “Capture and fission cross section of  $\text{Pu}^{240}$ ,” in *Nuclear Cross Sections and Technology: Proceedings of a Conference vol. 2, Washington, D.C., March 22–24, 1966*, p. 903, U.S. Department of Commerce, National Bureau of Standards, Mar. 1975.
- [41] F. Tovesson, T. S. Hill, M. Mocko, J. D. Baker, and C. A. McGrath, “Neutron induced fission of  $^{240,242}\text{Pu}$  from 1 eV to 200 MeV,” *Phys. Rev. C*, vol. 79, p. 014613, Jan 2009.

- [42] J.-M. Ruggieri, J. Tommasi, J.-F. Lebrat, C. Suteau, D. Plisson-Rieunier, C. De Saint Jean, G. Rimpault, and J.-C. Sublet, “ERANOS 2.1: International Code System for GEN IV Fast Reactor Analysis,” in *ICAPP 2006 - International Congress on Advances in NPPs*, American Nuclear Society, 2006. Reno, Nevada, USA, June 4–8.
- [43] O. Bouland, H. Derrien, N. M. Larson, and L. L. Leal, “R-Matrix Analysis of the  $^{240}\text{Pu}$  Neutron Cross Sections in the Thermal to 5700-eV Energy Range,” *Nuclear Science and Engineering*, vol. 127, pp. 105–129, Oct. 1997.
- [44] O. Bouland, “Re-evaluation of the  $^{240}\text{Pu}$  Cross Sections in the Unresolved Resonance Energy Range,” tech. rep., NEA/OECD, 2002.
- [45] E. Fort, G. Rimpault, J.-C. Bosq, B. Camous, V. Zammit, E. Dupont, R. Jacqmin, P. Smith, D. Biron, and D. Verrier, “Improved performances of the fast reactor calculational system ERANOS-ERALIB1 due to improved a priori nuclear data and consideration of additional specific integral data,” *Annals of Nuclear Energy*, vol. 30, no. 18, pp. 1879–1898, 2003.
- [46] W. Kolar and K. H. Böckhoff, “Resonance parameters of  $^{240}\text{Pu}$ : Part I-Neutron widths,” *Journal of Nuclear Energy*, vol. 22, no. 5, pp. 299–315, 1968.
- [47] E. Vogt, “Theory of Low Energy Nuclear Reactions,” *Rev. Mod. Phys.*, vol. 34, pp. 723–747, Oct. 1962.
- [48] I. A. Stegun and M. Abramowitz, *Handbook of Mathematical Functions with Formulas, Graphs, and Mathematical Tables*. National Bureau of Standards, 1964.
- [49] O. Bersillon, “SCAT2: un programme de modèle optique sphérique,” Tech. Rep. CEA-N-2227, Commissariat à l’Énergie Atomique et aux énergies alternatives, Saclay, Oct. 1981.
- [50] P. Archier, *Contribution à l’Amélioration des Données Nucléaires Neutroniques du Sodium pour le Calcul des Réacteurs de Génération IV*. PhD thesis, École Doctorale I-MEP2 - Université de Grenoble, 2011.
- [51] A. J. Koning, S. Hilaire, and M. C. Duijvestijn, “TALYS-1.0,” *EDP Sciences*, vol. 1, pp. 211–214, 2008.
- [52] O. Litaize and O. Serot, “Investigation of phenomenological models for the Monte Carlo simulation of the prompt fission neutron and  $\gamma$  emission,” *Phys. Rev. C*, vol. 82, p. 054616, Nov. 2010.
- [53] L. Berge, *Contribution à la modélisation des spectres de neutrons prompts de fission. Propagation d’incertitudes sur un calcul de fluence cuve*. PhD thesis, Institut polytechnique de Grenoble, 2015.
- [54] N. Terranova, O. Serot, P. Archier, C. De Saint Jean, and M. Sumini, “Covariance Matrix Evaluations for Independent Mass Fission Yields,” *Nuclear Data Sheets*, vol. 123, pp. 225–230, 2015. Special Issue on International Workshop on Nuclear Data Covariances April 28 - May 1, 2014, Santa Fe, New Mexico, {USA}.
- [55] E. P. Wigner, “Resonance Reactions and Anomalous Scattering,” *Phys. Rev.*, vol. 70, pp. 15–33, July 1946.

- [56] D. Brink and G. Satchler, *Angular Momentum*. Oxford Science Publications, Clarendon Press, 1993.
- [57] E. Vogt, “R-Matrix theory.” Joint Institute for Nuclear Astrophysics (JINA) at Notre Dame University, South Bend, Indiana., Oct. 2004.
- [58] F. C. Barker, “The boundary condition parameter in R-matrix theory,” *Australian Journal of Physics*, vol. 25, p. 341, Aug. 1972.
- [59] G. Noguère, O. Bouland, S. Kopecky, C. Lampoudis, P. Schillebeeckx, A. Plompen, F. Gunsing, C. Sage, and I. Sirakov, “Partial-wave analysis of  $n + {}^{241}\text{Am}$  reaction cross sections in the resonance region,” *Phys. Rev. C*, vol. 92, p. 014607, Jul 2015.
- [60] J. E. Lynn, “Structure in sub-threshold fission modes,” Tech. Rep. AERE-R-5891, Atomic Energy Research Establishment, Harwell (England), Jan. 1968.
- [61] H. Yamamoto, Y. Kanie, and K. Taniguchi, “Resonant Tunneling in a Symmetrical Rectangular Triple-Barrier Structure,” *Physica Status Solidi (b)*, vol. 167, no. 2, pp. 571–580, 1991.
- [62] C. E. Porter and R. G. Thomas, “Fluctuations of Nuclear Reaction Widths,” *Phys. Rev.*, vol. 104, pp. 483–491, Oct. 1956.
- [63] F. H. Fröhner, “Evaluation and Analysis of Nuclear Resonance Data,” Tech. Rep. JEFF Report 18, Nuclear Energy Agency, 2000.
- [64] E. Fort and J. P. Doat, “ESTIMA - A Code to Calculate Average Parameters from Sets of Resolved Resonance Parameters,” Tech. Rep. NEANDC-161-U, OECD Nuclear Energy Agency Data Bank, Gif-sur-Yvette, France., June 1983.
- [65] E. Rich, , G. Noguère, C. De Saint Jean, and A. Tudora, “Generalization of the SPRT Method for the Modeling of the Neutron Cross Sections in the Unresolved Resonance Range,” *Nuclear Science and Engineering*, vol. 162, pp. 76–86, May 2009.
- [66] T. Tamura, “Analyses of the Scattering of Nuclear Particles by Collective Nuclei in Terms of the Coupled-Channel Calculation,” *Rev. Mod. Phys.*, vol. 37, pp. 679–708, Oct. 1965.
- [67] K. Roberts, L. Kowarski, D. Potter, R. Hockney, J. Killeen, M. Rosenbluth, J. Boris, E. Lohrmann, S. Lindenbaum, S. Ratti, J. Raynal, R. Bullough, R. Nesbet, W. J. Lester, J. Campbell, G. Kuo-Petravic, M. Petravic, S. Cohen, S. Lurié, M. Perrottet, and A. Hearn, *Computing as a Language of Physics: Lectures Presented at an International Seminar Course at Trieste from 2 to 20 Aug. 1971*. Proceedings series, International Atomic Energy Agency, 1972.
- [68] W. von Oertzen, M.-C. Lemaire, J. Raynal, K. Wildermuth, M. Bauer, B. Zakhariev, M. Nagarajan, R. Guardiola, J. Gillespie, C. Ciofi degli Atti, M. Kirson, J. Németh, A. Rimini, T. Weber, S. Boffi, L. Sips, W. Rybarska, K. Dietrich, M. Zielinska-Pfabé, Z. Bochnacki, S. Gabrakov, G. Ripka, M. Grypeos, J. Davies, and S. Ogaza, *The Structure of Nuclei: Lectures Presented at an International Course, Trieste, 13 January-12 March 1971*. Proceedings series, International Centre for Theoretical Physics and International Atomic Energy Agency, 1972.

- [69] J. Raynal, “Recurrence relations for distorted-wave Born approximation Coulomb excitation integrals and their use in coupled channel calculations,” *Phys. Rev. C*, vol. 23, pp. 2571–2585, June 1981.
- [70] P. Hodgson, *Nuclear reactions and nuclear structure*. International series of monographs on physics, Clarendon Press, 1971.
- [71] D. Régnier, *Contribution à l’étude des gammas prompts de fission*. PhD thesis, École Doctorale I-MEP2 - Université de Grenoble, 2013.
- [72] A. V. Ignatyuk, G. N. Smirenkin, and A. S. Tishin, “Phenomenological description of the energy dependence of the level density parameter,” *Sov. J. Nucl. Phys.*, vol. 21, pp. 255–260, 1975.
- [73] A. J. Koning, S. Hilaire, and S. Goriely, *TALYS-1.4*, Dec. 2011.
- [74] P. Axel, “Electric Dipole Ground-State Transition Width Strength Function and 7-Mev Photon Interactions,” *Phys. Rev.*, vol. 126, pp. 671–683, Apr. 1962.
- [75] J. Kopecky and M. Uhl, “Test of gamma-ray strength functions in nuclear reaction model calculations,” *Phys. Rev. C*, vol. 41, pp. 1941–1955, May 1990.
- [76] J. Kopecky, M. Uhl, and R. E. Chrien, “Radiative strength in the compound nucleus  $^{157}\text{Gd}$ ,” *Phys. Rev. C*, vol. 47, pp. 312–322, Jan. 1993.
- [77] R. C. Sharma and J.-N. Leboeuf, “Three-hump potential barrier in the  $^{234}\text{Th}$  nucleus,” *Phys. Rev. C*, vol. 14, pp. 2340–2342, Dec. 1976.
- [78] B. S. Bhandari and A. S. Al-Kharam, “Tunneling through equivalent multihumped fission barriers: Some implications for the actinide nuclei,” *Phys. Rev. C*, vol. 39, pp. 917–926, Mar. 1989.
- [79] S. Bjørnholm and J. E. Lynn, “The double-humped fission barrier,” *Rev. Mod. Phys.*, vol. 52, pp. 725–931, Oct. 1980.
- [80] P. Tamagno, C. De Saint Jean, O. Bouland, G. Noguère, P. Archier, E. Privas, and O. Serot, “From low to high energy nuclear data evaluations,” *The European Physical Journal A - Hadrons and Nuclei*, vol. 51, pp. 181–205, 2015.
- [81] N. Bohr and J. A. Wheeler, “The Mechanism of Nuclear Fission,” *Phys. Rev.*, vol. 56, pp. 426–450, Sep 1939.
- [82] E. Wigner, “The transition state method,” *Trans. Faraday Soc.*, vol. 34, pp. 29–41, 1938.
- [83] A. Bohr and B. R. Mottelson, “Rotational States in Even-Even Nuclei,” *Phys. Rev.*, vol. 90, pp. 717–719, May 1953.
- [84] A. Koning and D. Rochman, “Modern Nuclear Data Evaluation with the TALYS Code System,” *Nuclear Data Sheets*, vol. 113, no. 12, pp. 2841–2934, 2012. Special Issue on Nuclear Reaction Data.
- [85] S. Goriely, S. Hilaire, A. J. Koning, and R. Capote, “Towards an improved evaluation of neutron-induced fission cross sections on actinides,” *Phys. Rev. C*, vol. 83, p. 034601, 2011.

- [86] W. J. Swiatecki, "Systematics of Spontaneous Fission Half-Lives," *Phys. Rev.*, vol. 100, pp. 937–938, Nov 1955.
- [87] M. Bolsterli, E. O. Fiset, J. R. Nix, and J. L. Norton, "New Calculation of Fission Barriers for Heavy and Superheavy Nuclei," *Phys. Rev. C*, vol. 5, pp. 1050–1077, Mar. 1972.
- [88] E. Rutherford, F. W. Aston, J. Chadwick, C. D. Ellis, G. Gamow, R. H. Fowler, O. W. Richardson, and D. R. Hartree, "Discussion on the Structure of Atomic Nuclei," *Proceedings of the Royal Society of London A: Mathematical, Physical and Engineering Sciences*, vol. 123, no. 792, pp. 373–390, 1929.
- [89] D. J. Rowe, *Nuclear Collective Motion: Models and Theory*. World Scientific, 2010.
- [90] G. Audi and A. Wapstra, "The 1993 atomic mass evaluation: (I) Atomic mass table," *Nuclear Physics A*, vol. 565, no. 1, pp. 1–65, 1993.
- [91] W. J. Swiatecki, "Semi-Empirical Interpretation of Nuclear Masses and Deformations," in *Nuclidic Masses* (W. H. J. Johnson, ed.), pp. 58–66, Springer Vienna, 1964.
- [92] W. D. Myers and W. J. Swiatecki, "Nuclear masses and deformations," *Nuclear Physics*, vol. 81, no. 1, pp. 1–60, 1966.
- [93] K. T. R. Davies and J. R. Nix, "Calculation of moments, potentials, and energies for an arbitrarily shaped diffuse-surface nuclear density distribution," *Phys. Rev. C*, vol. 14, pp. 1977–1994, Nov. 1976.
- [94] P. Möller and J. R. Nix, "Nuclear mass formula with a Yukawa-plus-exponential macroscopic model and a folded-Yukawa single-particle potential," *Nuclear Physics A*, vol. 361, no. 1, pp. 117–146, 1981.
- [95] P. Möller and J. R. Nix, "Nuclear masses from a unified macroscopic-microscopic model," *Atomic Data and Nuclear Data Tables*, vol. 39, no. 2, pp. 213–223, 1988.
- [96] H. J. Krappe and J. R. Nix, "Modified definition of the surface energy in the liquid-drop formula," in *Physics and Chemistry of Fission Vol. I*, pp. 159–176, IAEA, Jan. 1973. Proceedings of the Third IAEA Symposium on the Physics and Chemistry of Fission.
- [97] J. R. Nix and A. J. Sierk, "Potential-Energy Surfaces for Heavy-Ion Collisions," *Physica Scripta*, vol. 10, no. A, p. 94, 1974.
- [98] H. J. Krappe, J. R. Nix, and A. J. Sierk, "Unified nuclear potential for heavy-ion elastic scattering, fusion, fission, and ground-state masses and deformations," *Phys. Rev. C*, vol. 20, pp. 992–1013, Sep 1979.
- [99] S. D. Drell, "Electrodynamic Interactions," in *Proceedings of the 13th International Conference on High Energy Physics*, University of California Press, 1967.
- [100] J. W. Negele, "The  $^{41}\text{Sc}$ - $^{41}\text{Ca}$  Coulomb energy difference," *Nuclear Physics A*, vol. 165, no. 2, pp. 305–326, 1971.
- [101] L. L. Foldy, "A Note on Atomic Binding Energies," *Phys. Rev.*, vol. 83, pp. 397–399, July 1951.

- [102] P. Seeger and R. Perisho, "MODEL-BASED MASS LAW AND A TABLE OF BINDING ENERGIES.," Tech. Rep. LA-3751, Los Alamos National Laboratory, Jan. 1967.
- [103] P. A. Seeger, "A MODEL-BASED MASS LAW, AND THE r-PROCESS AS A MASS LAW TEST.," in *Proceedings of the Third International Conference on Atomic Masses, August 28–September 1, 1967*, University of Manitoba, Winnipeg, Canada, Barber, R. C. (ed.). Winnipeg, Can., Univer., Oct. 1969.
- [104] D. Lunney, J. M. Pearson, and C. Thibault, "Recent trends in the determination of nuclear masses," *Rev. Mod. Phys.*, vol. 75, pp. 1021–1082, Aug. 2003.
- [105] L. Wilets, "Neutron and Proton Densities in Nuclei," *Phys. Rev.*, vol. 101, pp. 1805–1809, Mar. 1956.
- [106] W. D. Myers and W. J. Swiatecki, "Average nuclear properties," *Annals of Physics*, vol. 55, no. 3, pp. 395–505, 1969.
- [107] W. D. Myers, "Development of the semiempirical droplet model," *Atomic Data and Nuclear Data Tables*, vol. 17, no. 5–6, pp. 411–417, 1976.
- [108] G. T. Garvey, W. J. Gerace, R. L. Jaffe, I. Talmi, and I. Kelson, "Set of Nuclear-Mass Relations and a Resultant Mass Table," *Rev. Mod. Phys.*, vol. 41, pp. S1–S80, Oct. 1969.
- [109] D. G. Madland and J. Nix, "New model of the average neutron and proton pairing gaps," *Nuclear Physics A*, vol. 476, no. 1, pp. 1–38, 1988.
- [110] P. Möller and J. Nix, "Nuclear pairing models," *Nuclear Physics A*, vol. 536, no. 1, pp. 20–60, 1992.
- [111] S. G. Nilsson, "Binding states of individual nucleons in strongly deformed nuclei," *Dan. Mat. Fys. Medd.*, vol. 29, no. CERN-55-30. 16, pp. 1–69, 1955. This document exists only as a journal publication: it is not in the CERN Official Collection bound volume.
- [112] R. D. Woods and D. S. Saxon, "Diffuse Surface Optical Model for Nucleon-Nuclei Scattering," *Phys. Rev.*, vol. 95, pp. 577–578, Jul 1954.
- [113] W. D. Myers, "Droplet model nuclear density distributions and single-particle potential wells," *Nuclear Physics A*, vol. 145, no. 2, pp. 387–400, 1970.
- [114] P. Möller, S. G. Nilsson, and J. R. Nix, "Calculated ground-state properties of heavy nuclei," *Nuclear Physics A*, vol. 229, no. 2, pp. 292–319, 1974.
- [115] H. Sherif and J. S. Blair, "Inelastic proton scattering and the deformed spin-dependent optical potential," *Physics Letters B*, vol. 26, no. 8, pp. 489–492, 1968.
- [116] F. Dickmann, "Ein Eigenwertverfahren zur Lösung des Einteilchenmodells für Atomkerne in ihrer Sattelpunktsdeformation," *Zeitschrift für Physik*, vol. 203, no. 2, pp. 141–172, 1967.
- [117] D. Vautherin, "Hartree-Fock Calculations with Skyrme's Interaction. II. Axially Deformed Nuclei," *Phys. Rev. C*, vol. 7, pp. 296–316, Jan. 1973.



- [118] J. von Neuman and E. Wigner, “Über merkwürdige diskrete Eigenwerte. Über das Verhalten von Eigenwerten bei adiabatischen Prozessen,” *Zhurnal Physik*, vol. 30, pp. 467–470, 1929.
- [119] H. Koura and M. Yamada, “Single-particle potentials for spherical nuclei,” *Nuclear Physics A*, vol. 671, no. 1–4, pp. 96–118, 2000.
- [120] W. H. Bassichis, A. K. Kerman, C. F. Tsang, D. R. Tuerpe, and L. Wilets, *A Study of Deformation Energy Surfaces Obtained from Single Particle Energies*, p. 15. 1972.
- [121] A. Bohr, B. R. Mottelson, and D. Pines, “Possible Analogy between the Excitation Spectra of Nuclei and Those of the Superconducting Metallic State,” *Phys. Rev.*, vol. 110, pp. 936–938, May 1958.
- [122] J. Bardeen, L. N. Cooper, and J. R. Schrieffer, “Microscopic Theory of Superconductivity,” *Phys. Rev.*, vol. 106, pp. 162–164, Apr. 1957.
- [123] S. G. Nilsson, C. F. Tsang, A. Sobiczewski, Z. Szymański, S. Wycech, C. Gustafson, I.-L. Lamm, P. Möller, and B. Nilsson, “On the nuclear structure and stability of heavy and superheavy elements,” *Nuclear Physics A*, vol. 131, no. 1, pp. 1 – 66, 1969.
- [124] H. J. Lipkin, “Collective motion in many-particle systems: Part 1. The violation of conservation laws,” *Annals of Physics*, vol. 9, no. 2, pp. 272–291, 1960.
- [125] H. C. Pradhan, Y. Nogami, and J. Law, “Study of approximations in the nuclear pairing-force problem,” *Nuclear Physics A*, vol. 201, no. 2, pp. 357–368, 1973.
- [126] J. F. Goodfellow and Y. Nogami, “On the superconductivity approximation for the nuclear pairing interaction,” *Canadian Journal of Physics*, vol. 44, no. 6, pp. 1321–1327, 1966.
- [127] Y. Nogami, “On the superconductivity theory of the nuclear pairing interaction,” *Physics Letters*, vol. 15, no. 4, pp. 335–337, 1965.
- [128] Y. Nogami and I. J. Zucker, “A note on the pairing interaction in nuclei,” *Nuclear Physics*, vol. 60, no. 2, pp. 203–208, 1964.
- [129] P. Möller. personal communication.
- [130] D. Vautherin and D. M. Brink, “Hartree-Fock Calculations with Skyrme’s Interaction. I. Spherical Nuclei,” *Phys. Rev. C*, vol. 5, pp. 626–647, Mar. 1972.
- [131] J. Damgaard, H. C. Pauli, V. V. Pashkevich, and V. M. Strutinsky, “A method for solving the independent-particle Schrödinger equation with a deformed average field,” *Nuclear Physics A*, vol. 135, no. 2, pp. 432–444, 1969.
- [132] G. Guennebaud, B. Jacob, *et al.*, “Eigen v3.” <http://eigen.tuxfamily.org>, 2010.
- [133] T. N. L. Patterson, “The Optimum Addition of Points to Quadrature Formulae,” *Mathematics of Computation*, vol. 22, pp. pp. 847–856+s21–s31, Oct. 1968.
- [134] T. Patterson, “Stratified nested and related quadrature rules,” *Journal of Computational and Applied Mathematics*, vol. 112, no. 1–2, pp. 243–251, 1999.

- [135] W. H. Press, S. A. Teukolsky, W. T. Vetterling, and B. P. Flannery, *Numerical Recipes 3rd Edition: The Art of Scientific Computing*. New York, NY, USA: Cambridge University Press, 3 ed., 2007.
- [136] A. Kronrod, *Nodes and weights of quadrature formulas: sixteen-place tables*. Consultants Bureau, 1965.
- [137] C. Bond, “A New Integration Method Providing the Accuracy of Gauss-Legendre with Error Estimation Capability,” 2002.
- [138] S. Smolyak, “Quadrature and interpolation formulas for tensor products of certain classes of functions,” *Soviet Mathematics, Doklady*, vol. 4, pp. 240–243, 1963.
- [139] J. Burkardt, “Slow Exponential Growth for Gauss Patterson Sparse Grids,” 2014.
- [140] J. Burkardt, “SANDIA\_RULES: Sparse Grid Mixed Growth Anisotropic Rules.”
- [141] Khronos Group, *The OpenCL Specification*, 2010.
- [142] J. Nickolls, I. Buck, M. Garland, and K. Skadron, “Scalable Parallel Programming with CUDA,” *Queue*, vol. 6, pp. 40–53, 2008.
- [143] H. Goutte, J. F. Berger, P. Casoli, and D. Gogny, “Microscopic approach of fission dynamics applied to fragment kinetic energy and mass distributions in  $^{238}\text{U}$ ,” *Phys. Rev. C*, vol. 71, p. 024316, Feb. 2005.
- [144] M. G. Mustafa, U. Mosel, and H. W. Schmitt, “Asymmetry in Nuclear Fission,” *Phys. Rev. C*, vol. 7, pp. 1518–1532, Apr 1973.
- [145] F.-J. Hambsch, G. Vladuca, A. Tudora, S. Oberstedt, and I. Ruskov, “Prediction of fission mass-yield distributions based on cross section calculations,” *Annals of Nuclear Energy*, vol. 32, no. 12, pp. 1297–1304, 2005.
- [146] U. Brosa, H.-H. Knitter, T.-s. Fan, J.-m. Hu, and S.-l. Bao, “Systematics of fission-channel probabilities,” *Phys. Rev. C*, vol. 59, pp. 767–775, Feb 1999.
- [147] F. Gönnenwein, “Mass, charge, and kinetic energy of fission fragments,” in *The nuclear fission process* (C. Wagemans, ed.), pp. 287–473, CRC Press, Inc; Boca Raton, FL (United States), 1991.
- [148] H. J. Krappe and K. Pomorski, *Theory of Nuclear Fission: A Textbook*. Lecture Notes in Physics, Springer Berlin Heidelberg, 2012.
- [149] R. A. Gherghescu, W. Greiner, and D. N. Poenaru, “Two-dimensional nuclear inertia: Analytical relationships,” *Phys. Rev. C*, vol. 52, pp. 2636–2642, Nov. 1995.
- [150] L. Wilets, *Theories of Nuclear Fission*. Oxford library of the physical sciences, Clarendon Press, 1964.
- [151] D. Poenaru, R. Gherghescu, and W. Greiner, “Analytical relationship for the cranking inertia,” *Eur.Phys.J.*, vol. A24, pp. 355–359, 2005.
- [152] P. Festa, “Shortest Path Algorithms,” in *Handbook of Optimization in Telecommunications* (M. Resende and P. Pardalos, eds.), pp. 185–210, Springer US, 2006.

- [153] R. C. Holte, M. B. Perez, R. M. Zimmer, and A. J. MacDonald, “Hierarchical A\*: Searching Abstraction Hierarchies Efficiently,” in *In Proceedings of the National Conference on Artificial Intelligence*, pp. 530–535, 1996.
- [154] B. Schling, *The Boost C++ Libraries*. XML Press, 2011.
- [155] A. Baran, “Some dynamical aspects of the fission process,” *Physics Letters B*, vol. 76, no. 1, pp. 8–10, 1978.
- [156] Steven G. Johnson, “The NLOpt nonlinear-optimization package.”
- [157] J. Berger, M. Girod, and D. Gogny, “Microscopic analysis of collective dynamics in low energy fission,” *Nuclear Physics A*, vol. 428, pp. 23–36, 1984.
- [158] H. Jeffreys, “On Certain Approximate Solutions of Lineae Differential Equations of the Second Order,” *Proceedings of the London Mathematical Society*, vol. s2-23, no. 1, pp. 428–436, 1925.
- [159] O. von Roos, “Position-dependent effective masses in semiconductor theory,” *Phys. Rev. B*, vol. 27, pp. 7547–7552, June 1983.
- [160] D. J. BenDaniel and C. B. Duke, “Space-Charge Effects on Electron Tunneling,” *Phys. Rev.*, vol. 152, pp. 683–692, Dec. 1966.
- [161] B. B. Back, O. Hansen, H. C. Britt, and J. D. Garrett, “Fission of doubly even actinide nuclei induced by direct reactions,” *Phys. Rev. C*, vol. 9, pp. 1924–1947, May 1974.
- [162] P. Glässel, H. Rösler, and H. J. Specht, “Intermediate structure in the  $^{239}\text{Pu}(\text{d},\text{pf})$  reaction,” *Nuclear Physics A*, vol. 256, no. 2, pp. 220–242, 1976.
- [163] S. Bjørnholm, A. Bohr, and B. R. Mottelson, “ROLE OF SYMMETRY OF THE NUCLEAR SHAPE IN ROTATIONAL CONTRIBUTIONS TO NUCLEAR LEVEL DENSITIES,” in *Physics and Chemistry of Fission Vol. 1*, pp. 367–374, IAEA, 1974.
- [164] O. Bouland. personal communication.
- [165] A. Bohr, “The Coupling of Nuclear Surface Oscillations to the Motion of Individual Nucleons,” *Mat. Fys. Medd. Dan. Vid. Selsk.*, vol. 26, no. 14, pp. 1–40, 1952.
- [166] K. Pomorski, B. Nerlo-Pomorska, I. Ragnarsson, R. K. Sheline, and A. Sobiczewski, “Ground state moments of inertia of deformed nuclei around barium,” *Nuclear Physics A*, vol. 205, no. 3, pp. 433–453, 1973.
- [167] P. Olivius, *Extending the nuclear cranking model to tilted axis rotation and alternative mean field potentials*. PhD thesis, Division of Mathematical Physics, Lund Institute of Technology, 2004.
- [168] M. R. Bhat, “Evaluated Nuclear Structure Data File (ENSDF),” in *Nuclear Data for Science and Technology* (S. Qaim, ed.), Research Reports in Physics, pp. 817–821, Springer Berlin Heidelberg, 1992. Data extracted using the NNDC On-Line Data Service from the ENSDF database, file revised as of (May 4, 2015).

- [169] S. G. Nilsson and O. Prior, "The effect of pair correlation on the moment of inertia and the collective gyromagnetic ratio of deformed nuclei," *Mat. Fys. Medd. Dan. Vid. Selsk.*, vol. 32, no. 16, pp. 1–62, 1961.
- [170] L. W. Weston and J. H. Todd, "Neutron Fission Cross Sections of  $^{239}\text{Pu}$  and  $^{240}\text{Pu}$  Relative to  $^{235}\text{U}$ ," *Nuclear Science and Engineering*, vol. 84, pp. 248–259, July 1983.
- [171] J. W. Meadows, "The Fission Cross Sections of Plutonium-239 and Plutonium-242 Relative to Uranium-235 from 0.1 to 10 MeV," *Nuclear Science and Engineering*, vol. 68, pp. 360–363, December 1978.
- [172] Y. T. Grin, "NONADIABATIC CORRECTIONS TO THE ROTATIONAL SPECTRUM OF ATOMIC NUCLEI," *Soviet Physics, J. Exptl. Theoret. Phys.*, vol. 41, pp. 222–225, Jul. 1961.
- [173] D. Poenaru and M. Ivaşcu, *Particle Emission from Nuclei: Nuclear deformation energy*. Particle Emission from Nuclei, Crc Press, 1989.
- [174] J. R. Nix, "Further studies in the liquid-drop theory on nuclear fission," *Nuclear Physics A*, vol. 130, no. 2, pp. 241–292, 1969.
- [175] J. R. Nix, "Further studies in the liquid-drop theory of nuclear fission," tech. rep., Lawrence Radiation Laboratory, University of California, Berkeley, July 1968. UCRL-17958.
- [176] A. T. Kruppa, "Calculation of the continuum level density," *Physics Letters B*, vol. 431, no. 3–4, pp. 237–241, 1998.
- [177] N. Tajima, Y. R. Shimizu, and S. Takahara, "Improved microscopic-macroscopic approach incorporating the effects of continuum states," *Phys. Rev. C*, vol. 82, p. 034316, Sep 2010.
- [178] W. D. Myers and W. J. Swiatecki, "The nuclear droplet model for arbitrary shapes," *Annals of Physics*, vol. 84, no. 1–2, pp. 186–210, 1974.
- [179] P. Möller, W. D. Myers, W. J. Swiatecki, and J. R. Treiner, "Finite Range Droplet Model," in *Proceedings of the 7th International Conference on Atomic Masses and Fundamental Constants* (O. e. Klepper, ed.), (3–7 Sep 1984, Darmstadt, Germany), pp. 457–465, Aug. 1984. LBL-18230.
- [180] P. Möller, W. D. Myers, W. J. Swiatecki, and J. Treiner, "Nuclear mass formula with a finite-range droplet model and a folded-Yukawa single-particle potential," *Atomic Data and Nuclear Data Tables*, vol. 39, no. 2, pp. 225–233, 1988.
- [181] T. Fukushima, "Fast computation of complete elliptic integrals and jacobian elliptic functions," *Celestial Mechanics and Dynamical Astronomy*, vol. 105, no. 4, pp. 305–328, 2009.
- [182] A. Bronstein, M. Bronstein, and R. Kimmel, *Numerical Geometry of Non-Rigid Shapes*. Monographs in Computer Science, Springer New York, 2008.
- [183] N. N. Lebedev and R. A. Silverman, *Special Functions and Their Applications*. Dover Books on Mathematics, Dover Publications, 1972.

- [184] B. S. Bhandari and M. Khaliqzaman, “Comparison of various parametrizations of the double-humped fission barrier,” *Phys. Rev. C*, vol. 44, pp. 292–305, July 1991.
- [185] A. V. Ignatyuk, N. S. Rabotnov, and G. N. Smirenkin, “Two-hump fission barrier in quasiclassical approximation,” *Physics Letters B*, vol. 29, no. 4, pp. 209–210, 1969.
- [186] B. C. Hall, *Quantum Theory for Mathematicians*. Graduate Texts in Mathematics, Springer, 2013.
- [187] J.-N. Leboeuf and R. C. Sharma, “Penetrability Through a Double-Hump Barrier of Strutinsky Type,” *Canadian Journal of Physics*, vol. 51, no. 11, pp. 1148–1154, 1973.